Study of charmless four-body decays of neutral b-baryons with the LHCb spectrometer

Maxime Vernet

EDSF : 178

UNIVERSITÉ CLERMONT-AUVERGNE
(École Universitaire de Physique et Ingénierie)

ÉCOLE DOCTORALE DES SCIENCES FONDAMENTALES

THÈSE

présentée pour obtenir le grade de

DOCTEUR D'UNIVERSITÉ
(SPÉCIALITÉ CONSTITUANTS ÉLÉMENTAIRES)

par

Maxime VERNET

STUDY OF CHARMLESS FOUR-BODY DECAYS OF NEUTRAL b-BARYONS WITH THE LHCB SPECTROMETER

Thèse soutenue le 24 juillet 2018 devant la commission d'examen :

Président :	M.	V.	VAGNONI
Rapporteurs :	Mme	S.	HANSMANN-MENZEMER
	M.	G.	WILKINSON
Examinateurs :	Mme	S.	DAVIDSON
Directeur de thèse :	M.	S.	MONTEIL

Remerciements

Je voudrais dans ces lignes remercier les personnes qui ont, directement ou indirectement, participé à l'aboutissement de ce travail. Ceci est le fruit d'une vaste collaboration. La réalisation du travail reporté dans ce document a été possible grâce, au premier ordre, à l'Université Clermont Auvergne, et à l'hospitalité du Laboratoire de Physique de Clermont.

Mr. Stéphane Monteil a dirigé ce travail de thèse. En plus des immenses apports scientifiques évidents, sa bienveillance m'a permis d'oeuvrer dans les meilleures conditions possibles pour nos efforts communs. J'ai abondamment appris sur la physique et au delà encore, en toute amitié. Je dois beaucoup à notre collaboration, de laquelle je sors indéniablement grandi. Ce fut un réel plaisir de travailler ensemble. Je remercie ici aussi Jan Mickelle Maratas, pour son héritage et sa précieuse aide dans notre entreprise.

J'adresse toute ma sympathie à l'équipe LHCb de Clermont-Ferrand, particulièrement Régis Lefèvre, Olivier Deschamps, Hervé Chanal et Eric Cogneras. Ma bonne entente et mon intégration au sein de ce groupe fut parfois l'occasion d'évoluer plus comme un collègue que comme un doctorant.

Pour leur présence indéfectible, merci à mes très chers et plus proches amis Marian, Lou, Tristan, Romain, Victor, Alex, Aurélien, Étienne, Paulin et Simon. Je remercie également mon ami et collègue Olivier Bleu qui vécut la même aventure, en simultané. Nos discussions m'ont souvent permis de sortir de mon cadre de travail.

Enfin, je remercie ma famille pour son soutien et sa confiance, particulièrement mes parents et ma soeur Justine.

Et parce que cette thèse doit beaucoup à sa patience et à sa présence, merci pour tout, Estelle.

"I didn't see the light until I was already a man,
by then to me it was only blinding."
The Dark Knight Rises, 2012.

Abstract

Keywords:
LHCb, Standard Model, CKM matrix, direct *CP* violation, *b*-flavoured baryons, Flavour Physics, Branching Fractions

The work presented in this document is focused on the study of weak decays of two *b*-baryons, Λ_b^0 ($|udb\rangle$) and Ξ_b^0 ($|usb\rangle$), by making use of data samples recorded by the LHCb experiment in 2011 and 2012. The abundant production of Λ_b^0 and Ξ_b^0 baryons in proton-proton collisions as well as the large probability of the hadronisation of the b quark into *b*-flavoured baryons at the Large Hadron Collider gives the LHCb experiment the opportunity to study multibody charmless decays of *b*-baryons. A significant part of the study is dedicated to the measurements of the branching fractions of Λ_b^0 and Ξ_b^0 in 4-body fully-charged charmless decays. They proceed in the Standard Model simultaneously through $b \to u$ transition or Flavour Changing Neutral Current (FCNC) penguin transition $b \to s$,d. The weak-phase difference induced by this interference pattern is *a priori* a good opportunity to search for *CP* violation in these very same baryons decays. Furthermore, these charmless multibobdy decays of b baryons contain rich resonance structures, both in the low-mass two-body nonbaryonic resonances (*i.e.* the $\pi^+\pi^-$, $K^\pm\pi^\mp$, K^+K^- invariant mass) and the low-mass baryonic resonances (*i.e.* the pK, $p\pi$ invariant mass). Consequently, *CP* asymmetries might receive significant enhancement from the strong-phase differences coming from the interference of these amplitudes. Measurements of $\Delta\mathcal{A}^{CP}$ in the decay modes of interest are presented in this document, including measurements in specific phase space regions (that are meant to favour resonance structures). Henceforth, seven inclusive decays of Λ_b^0 and Ξ_b^0 are simultaneously studied, namely $\Lambda_b^0 \to p\pi^-\pi^+\pi^-$, $\Lambda_b^0 \to pK^-\pi^+\pi^-$, $\Lambda_b^0 \to pK^-K^+\pi^-$, $\Lambda_b^0 \to pK^-K^+K^-$, $\Xi_b^0 \to pK^-\pi^+\pi^-$, $\Xi_b^0 \to pK^-\pi^+K^-$ and $\Xi_b^0 \to pK^-K^+K^-$ as well as additional specific decays that include intermediate resonances, such as, for instance, $\Lambda_b^0 \to pa_1$, $\Lambda_b^0 \to \Delta^{++}K^-\pi^-$ and $\Lambda_b^0 \to \Lambda^*(1520)^0\phi^0$.
Six decay modes are observed, among which four are established for the first time. Six branching fractions measurements are thus performed, and 90% and 95% confidence level intervals, based on the Feldman-Cousins confidence belt inference described are placed on the branching fraction for the $\Xi_b^0 \to pK^-K^+K^-$ decay mode, for which only a hint of its existence is obtained. No significant *CP*-violation effect is observed in any of the $\Delta\mathcal{A}^{CP}$ measurement performed.

Résumé

Mots clés:
LHCb, Modèle Standard, matrice CKM, violation directe de la symétrie *CP*, baryons beaux, Physique des Saveurs, Rapports d'embranchement

Le travail présenté dans ce document est dédié à l'étude des désintégrations faibles de deux baryons beaux, Λ_b^0 ($|udb\rangle$) et Ξ_b^0 ($|usb\rangle$), et utilise des échantillons de données enregistrés par l'expérience LHCb en 2011 et en 2012. La production abondante des baryons Λ_b^0 et Ξ_b^0 dans les collisions proton-proton ainsi que la grande probabilité pour un quark b d'hadroniser en un baryon beau au Large Hadron Collider (LHC), donne à l'expérience LHCb l'opportunité d'étudier les désintégrations multicorps sans charme de baryons beaux. Une part significative de cette étude est dédiée aux mesures des rapports d'embranchements des désintégrations sans charme à quatre corps des baryons Λ_b^0 et Ξ_b^0. Dans le Modèle Standard, ces désintégrations procèdent simultanément via les transitions de quarks $b \to u$ (à l'arbre) et $b \to d$,s (transitions à courant neutre de type pingouin). La différence de phase faible induite par cette interférence est *a priori* une opportunité de rechercher la violation *CP* dans ces désintégrations de baryons beaux. De plus, ces désintégrations sans charme à quatre corps contiennent des structures résonantes, simultanément dans la région non-baryonique de basse masse à deux corps (*i.e.* les masses invariantes de $\pi^+\pi^-$, $K^\pm\pi^\mp$, K^+K^-) ainsi que dans la region baryonique de basse masse (*i.e.* les masses invariantes de pK, $p\pi$). Par conséquent, la différence de phases fortes induite par l'interférence de ces amplitudes peut augmenter l'effet d'une asymétrie *CP*. Des mesures d'asymétries *CP* ($\Delta\mathcal{A}^{CP}$) dans les modes de désintégrations discutés plus haut sont présentées dans ce document. Certaines sont produites dans des régions de l'espace des phases afin de favoriser la présence de structures résonantes. Ainsi, sept désintégrations inclusives de Λ_b^0 et Ξ_b^0 sont simultanément étudiées: $\Lambda_b^0 \to p\pi^-\pi^+\pi^-$, $\Lambda_b^0 \to pK^-\pi^+\pi^-$, $\Lambda_b^0 \to pK^-K^+\pi^-$, $\Lambda_b^0 \to pK^-K^+K^-$, $\Xi_b^0 \to pK^-\pi^+\pi^-$, $\Xi_b^0 \to pK^-\pi^+K^-$ et $\Xi_b^0 \to pK^-K^+K^-$ ainsi que des désintégrations spécifiques qui incluent plusieurs résonances intermédiaires comme, par exemple, $\Lambda_b^0 \to pa_1$, $\Lambda_b^0 \to \Delta^{++}K^-\pi^-$ ou $\Lambda_b^0 \to \Lambda^*(1520)^0\phi^0$.
Six modes de désintégrations sont observés, parmi lesquels quatre sont établis pour la première fois. Six mesures de rapports d'embranchements sont réalisées, et des limites à 90% et 95% degré de confiance sont placées sur le rapport d'embranchement du mode $\Xi_b^0 \to pK^-K^+K^-$ pour lequel seul un indice de son existence est obtenu. Pour les mesures de $\Delta\mathcal{A}^{CP}$ réalisées, aucun signe significatif de violation de *CP* n'est observé.

Note: Un résumé en français des chapitres de la thèse est fourni dans l'annexe G.

Contents

Introduction

Elementary particles and their interactions (strong, weak and electromagnetic) are currently described by the so-called Standard Model (SM) of particle physics. The High-Energy-Physics (HEP) data are (up to date and since decades) satisfactorily described or understood in this theoretical framework. Recent measurements from LHCb revealed tensions with respect to its predictions but it is fair to say that the edification of the SM is a tremendous success that was lately illustrated by the discovery of a narrow bosonic resonance at LHC, consistent with the Brout-Englert-Higgs SM boson. Although it stands on its own, the SM is incomplete in several respect. Should one be highlighted, I would mention the matter-antimatter asymmetry in the Universe that the SM fails to describe with completeness. A part of this document is focused on the search for *CP*-violation and the measurements of *CP*-violation phenomena present, so far, a consistent interpretation within the Standard Model paradigm. Non-vanishing *CP*-violating asymmetries have been observed in the decays of both K and B mesons. In contrast, *CP* violation has not been observed in baryon decays although some indication for non-vanishing *CP* asymmetries in b-flavoured baryon decays has been recently reported by the LHCb collaboration, based at CERN (Geneva).

The work presented in this document is focused on the study of weak decays of two b-baryons, Λ_b^0 ($|udb\rangle$) and Ξ_b^0 ($|usb\rangle$), by making use of data samples recorded by the LHCb experiment in 2011 and 2012. The BaBar and Belle experiments operated at center-of-mass energies below the threshold for b-baryon production. On the contrary, the abundant production of Λ_b^0 and Ξ_b^0 baryons in proton-proton collisions as well as the large probability of the hadronisation of the b quark into b-flavoured baryons at the Large Hadron Collider gives the LHCb experiment the opportunity to study multibody charmless decays of b-baryons.

A significant part of the study is dedicated to the measurements of the branching fractions of Λ_b^0 and Ξ_b^0 in 4-body fully-charged charmless decays. They proceed in the SM simultaneously through $b \to u$ transition or Flavour Changing Neutral Current (FCNC) penguin transition $b \to s,d$. The weak-phase difference induced by this interference pattern is *a priori* a good opportunity to search for *CP* violation in these very same baryons decays. Furthermore, these charmless multibobdy decays of b baryons contain rich resonance structures, both in the low-mass two-body nonbaryonic resonances (*i.e.* the $\pi^+\pi^-$, $K^\pm\pi^\mp$, K^+K^- invariant mass) and the low-mass baryonic resonances (*i.e.* the pK, $p\pi$ invariant mass). Consequently, *CP* asymmetries might receive significant enhancement from the strong-phase differences coming from the interference of these amplitudes. Measurements of $\Delta\mathcal{A}^{CP}$ in the decay modes of interest are presented in this document, including measurements in specific phase space regions (that are meant to favour resonance structures). Henceforth, seven inclusive decays of Λ_b^0 and Ξ_b^0 are simultaneously studied, namely $\Lambda_b^0 \to p\pi^-\pi^+\pi^-$, $\Lambda_b^0 \to pK^-\pi^+\pi^-$, $\Lambda_b^0 \to pK^-K^+\pi^-$, $\Lambda_b^0 \to pK^-K^+K^-$, $\Xi_b^0 \to pK^-\pi^+\pi^-$, $\Xi_b^0 \to pK^-\pi^+K^-$ and $\Xi_b^0 \to pK^-K^+K^-$ as well as additional specific decays that include intermediate resonances, such as, for instance, $\Lambda_b^0 \to pa_1$, $\Lambda_b^0 \to \Delta^{++}K^-\pi^-$ and $\Lambda_b^0 \to \Lambda^*(1520)^0\phi^0$.

The first chapter is meant to briefly introduce the Standard Model theoretical framework. An overview of signatures of *CP* asymmetries is provided and a discussion on the branching fraction predictions is in order. The second chapter is discussing the LHC and the LHCb experiment. The two following chapters are dedicated to the presentation of the analyses and the fit model that is further used to derive both the branching fractions and $\Delta\mathcal{A}^{CP}$ measurements.

Finally, a preliminary work on the partial reconstruction of $B^{\pm} \to \overset{(-)}{K}(892)^{*}\tau^{+}\tau^{-}$, with $\tau^{\pm} \to \mu^{\pm}\overset{(-)}{\nu}$ and/or $\tau^{\pm} \to \pi^{\pm}\pi^{\mp}\pi^{\pm}\overset{(-)}{\nu}$ has been performed on simulated data. This study can be particularly interesting in order to search for lepton-flavour universality violation. The last appendix is dedicated to this preliminary study.

Chapter 1

Theoretical aspects

This chapter is discussing the theoretical aspects related to the work presented in this document. The Standard Model (SM) of particle physics is straightforwardly discussed: fundamental particles and gauge bosons are introduced, the electroweak unification is presented and eventually the spontaneous symmetry breaking mechanism (the so-called Brout-Englert-Higgs mechanism) is discussed. Eventually, a section is dedicated to the branching fraction of the decay modes that have been studied.

Chapter contents

1.1 Fundamental particles

The SM of particle physics is a renormalisable quantum field theory based on local gauge invariance. Elementary particles as well as their interactions are described by a Lagrangian, set to be invariant under continuous local transformations. The symmetry generating the interactions is built on $SU(3)_C$, $SU(2)_L$ and $U(1)_Y$ for the strong, weak and electromagnetic interactions, respectively. Up to date, gravitational force is not embedded in the SM framework and is therefore not further discussed in this document.

1.1.1 Electroweak interaction as a guideline

The SM electroweak sector is based on local gauge invariance of the $SU(2)_L \otimes U(1)_Y$ symmetry group, and has been formalised by S.L.Glashow, S.Weinberg and A.Salam [1–3]. A spontaneous symmetry breaking mechanism is however needed in order to provide a mass to the fundamental fermions and bosons. An overview of the so-called Brout-Englert-Higgs mechanism is further discussed in Subsection 1.1.2. The generators of the $SU(2)_L$ and $U(1)_Y$ symmetry groups are respectively the weak isospin (Pauli's matrices σ_α) and weak hypercharge, which are associated to the gauge fields $\overrightarrow{W}_\mu = (W^1_\mu, W^2_\mu, W^3_\mu)$ and B_μ, respectively. Both are embedded in the covariant derivative that ensures the local gauge invariance:

$$D^\mu = \partial^\mu + igI_3 W^\mu_\alpha \sigma_\alpha + \frac{ig'Y}{2} B^\mu, \tag{1.1}$$

where ∂^μ is the ordinary derivative, g (g') is the coupling constant associated to the $SU(2)_L$ ($U(1)_Y$) group. I_3 is the third component of the weak isospin and Y is the hypercharge defined as $Y = 2(Q - I_3)$, Q being the electric charge operator.
The kinetic term for the fermionic fields is given by

$$\mathcal{L}^f_{\text{kin.}} = i\overline{\psi} D^\mu \gamma_\mu \psi \tag{1.2}$$

where ψ and $\overline{\psi}$ are the Dirac spinors field that contain three fermions generations. They are further displayed in Table 1.1 as

$$Q_L = \begin{pmatrix} q^u_L \\ q^d_L \end{pmatrix} \;\; ; \;\; L_L = \begin{pmatrix} l^u_L \\ l^d_L \end{pmatrix} \;\; ; \;\; q^u_R \;\; ; \;\; q^d_R \;\; ; \;\; l^d_R \;\; .$$

It has been experimentally observed that parity symmetry is highly violated by the weak interaction [4], which means that only left-handed fermions and right-handed antifermions can participate to charged current weak decays, hence $SU(2)_L$. The electroweak theory is accordingly separating left-handed spinor component from the right-handed spinor component, as $\psi = \psi_L + \psi_R$, where $\psi_L(\psi_R)$ are the projection of the spinor field on the left helicity-states (right helicity-states), providing doublets (Q_L, L_L) and singlets (q_R, l^d_R) of $SU(2)$, respectively. It is worth to notice that l^u_R singlet, that would represent right-handed sterile neutrinos is not further discussed. The two components of the doublets, called "up" component (q^u_L, l^u_L) and "down" component (q^d_L, l^d_L), are eigenstates of the weak isospin that are associated to the $+1/2$ and $-1/2$ eigenvalues, respectively.

The electroweak interaction can hence be written in the interaction basis as Eq. (1.3) and Eq. (1.4) for the quarks and the leptons respectively, using Eq. (1.2) and the notation displayed in Table 1.1.

$$\begin{aligned} \mathcal{L}^{\text{quarks}}_{\text{kin.}} &= i\overline{Q}_L(\partial^\mu + \frac{i}{2} g W^\mu_\alpha \sigma_\alpha + \frac{i}{6} g' B^\mu)\gamma_\mu Q_L \\ &+ i\overline{q^u}_R(\partial^\mu + ig'\frac{2}{3} B^\mu)\gamma_\mu q^u_R + i\overline{q^d}_R(\partial^\mu - \frac{i}{3} g' B^\mu)\gamma_\mu q^d_R \end{aligned} \tag{1.3}$$

$$\mathcal{L}^{\text{leptons}}_{\text{kin.}} = i\overline{L}_L(\partial^\mu + \frac{i}{2} g W^\mu_\alpha \sigma_\alpha - \frac{i}{2} g' B^\mu)\gamma_\mu L_L + i\overline{l^d}_R(\partial^\mu - ig' B^\mu)\gamma_\mu l^d_R \tag{1.4}$$

As already written mathematically, only $SU(2)$ doublets (left-handed components) couple to the gauge bosons W^μ_α. Right-handed components couple only to the hypercharge boson

Table 1.1: Fermionic fields per generation in the interaction basis and their associated quantum operators.

	Fermionic field per generation			Quantum operators	
	1st	2nd	3rd	Isospin I_3	Charge Q
Quarks:					
Q_L	$\begin{pmatrix} u \\ d \end{pmatrix}_L$	$\begin{pmatrix} c \\ s \end{pmatrix}_L$	$\begin{pmatrix} t \\ b \end{pmatrix}_L$	$\begin{pmatrix} \frac{1}{2} & 0 \\ 0 & -\frac{1}{2} \end{pmatrix}$	$\begin{pmatrix} \frac{2}{3} & 0 \\ 0 & -\frac{1}{3} \end{pmatrix}$
q_R^u	u_R	c_R	t_R	0	$+\frac{2}{3}$
q_R^d	d_R	s_R	b_R	0	$-\frac{1}{3}$
Leptons:					
L_L	$\begin{pmatrix} \nu_e \\ e \end{pmatrix}_L$	$\begin{pmatrix} \nu_\mu \\ \mu \end{pmatrix}_L$	$\begin{pmatrix} \nu_\tau \\ \tau \end{pmatrix}_L$	$\begin{pmatrix} \frac{1}{2} & 0 \\ 0 & -\frac{1}{2} \end{pmatrix}$	$\begin{pmatrix} 0 & 0 \\ 0 & -1 \end{pmatrix}$
l_R^d	e_R	μ_R	τ_R	0	-1

B^μ. Physical gauge bosons mediating the electroweak interaction can be identified with the following expressions

$$W_\alpha^\mu \sigma_\alpha = \begin{pmatrix} W_3^\mu & W_1^\mu - iW_2^\mu \\ W_1^\mu + iW_2^\mu & -W_3^\mu \end{pmatrix} \tag{1.5}$$

$$Z^\mu = \cos\theta_\mathrm{w} W_3^\mu - \sin\theta_\mathrm{w} B^\mu \tag{1.6}$$

$$A^\mu = \sin\theta_\mathrm{w} W_3^\mu + \cos\theta_\mathrm{w} B^\mu \tag{1.7}$$

where θ_w is the Weinberg electroweak mixing angle, $W_1^\mu \pm iW_2^\mu$, Z^μ are (once they will acquire a mass) identified as the $W^\pm$, Z^0 bosons and A^μ is identified as the photon.

1.1.2 Gauge bosons and fermions masses

Bosons of the weak interaction acquire a mass via spontaneous symmetry breaking mechanism (Brout-Englert-Higgs mechanism [5–7]). The idea is to add to the SM Lagrangian a doublet of complex scalar fields ϕ and its potential $V(\phi^\dagger\phi)$ that are defined as

$$\phi = \begin{pmatrix} \phi_1 + i\phi_2 \\ \phi_3 + i\phi_4 \end{pmatrix} \quad \text{and} \quad V(\phi^\dagger\phi) = -\mu^2\phi^\dagger\phi + \lambda(\phi^\dagger\phi)^2, \tag{1.8}$$

where ϕ_i are 4 real scalar fields, μ and λ are two parameters defined such as $-\mu^2 < 0$ and $\lambda > 0$. The potential Lagrangian is invariant under the $SU(2)_L \otimes U(1)$ symmetry transformations. The symmetry is however spontaneously broken once one of the degenerate minima is chosen. Choosing $\phi_1 = \phi_2 = \phi_4 = 0$, ϕ_3 develops a nonzero vacuum expectation value given by

$$\langle 0|\phi|0\rangle = \frac{1}{\sqrt{2}} \begin{pmatrix} 0 \\ v \end{pmatrix}, \quad \text{with} \quad v = \left(-\frac{\mu^2}{\lambda}\right)^{1/2}. \tag{1.9}$$

When expanding around the minimum $|\phi_3\rangle = (v+H)/\sqrt{2}$, the Lagrangian associated to the scalar filed reads:

$$\begin{aligned} \mathcal{L}_H &= (D_\mu\phi)^\dagger(D_\mu\phi) - V(\phi^\dagger\phi) \\ &= \frac{1}{2}\partial_\mu H\partial^\mu H + \frac{g^2}{4}(v+H)^2(W_\mu^\dagger W^\mu + \frac{Z_\mu^\dagger Z^\mu}{\cos^2\theta_{\rm w}}) + ... \end{aligned} \tag{1.10}$$

which introduce local gauge invariant mass term in the Lagrangian density. Mass of the gauge bosons are related in Eq. 1.11 while the photon remains massless:

$$M_W = \frac{gv}{2} = M_Z\cos\theta_{\rm w}. \tag{1.11}$$

The couplings of the Higgs field to the gauge bosons are explicitly written in Eq. 1.10. Couplings to the fermion fields are described by the Yukawa couplings, written as, still in the interaction basis

$$\mathcal{L}_\mathcal{Y} = -\lambda_{ij}^u\overline{Q}_{Li}\phi u_{Rj} - \lambda_{ij}^d\overline{Q}_{Li}\phi d_{Rj} - \lambda_{ij}^d\overline{L}_{Li}\phi l_{Rj}^d, \tag{1.12}$$

where i,j are generation indices, Q_L and L_L are the left-handed doublets, u_R, d_R and l_R^d are right handed singlets of $SU(2)_L\otimes U(1)_Y$. $\lambda_{ij}^{d,u}$ are 3×3 complex matrices of down-type, up-type quark couplings. When the Higgs field acquires a nonzero vacuum expectation value, mass terms (for the quarks for instance) appear as

$$\begin{aligned} \mathcal{L}_\mathcal{Y} &= -\left(\frac{\lambda_{ij}^d\cdot v}{\sqrt{2}}\right)\overline{d}_{Li}d_{Rj} - \left(\frac{\lambda_{ij}^u\cdot v}{\sqrt{2}}\right)\overline{u}_{Li}u_{Rj} + ... \\ &= -\mathcal{M}_{ij}^d\overline{d}_{Li}d_{Rj} - \mathcal{M}_{ij}^u\overline{u}_{Li}u_{Rj} + ... \end{aligned} \tag{1.13}$$

where $\mathcal{M}_{ij}^{u,d}$ are 3 mass matrices in the interaction basis. It is useful to move from the interaction eigenstates to the mass eigenstates in order to highlight the physical particle masses. Introducing unitary matrices $\mathcal{U}_L^{u(d)}$ and $\mathcal{U}_R^{u(d)}$, one gets

$$M_{ij}^{u(d)} = \mathcal{U}_L^{u(d)}\mathcal{M}_{ij}^{u(d)}\mathcal{U}_R^{u(d)\dagger} = \begin{pmatrix} m_{u(d)} & 0 & 0 \\ 0 & m_{c(s)} & 0 \\ 0 & 0 & m_{t(b)} \end{pmatrix}, \tag{1.14}$$

where the diagonal elements are the physical masses of the fundamental quarks. Bosons and fermions masses are henceforth generated via their coupling with the Higgs field. Bosons mediating the interaction are gathered in Table 1.2.

1.1.3 Colour and gluons

So far, an overview of the electroweak sector which is based on the $SU(2)_L\otimes U(1)_Y$ symmetry group has been presented. Conversely, the strong interaction (responsible of the quark-confinement for instance) is based on local gauge invariance of the $SU(3)_c$ symmetry group. The Lagrangian is invariant under global $SU(3)$ transformation $\psi' = U\psi$ where U is a 3×3 unitary matrix. A generic $SU(3)$ matrix needs 8 real parameters that can be written as

$$U = \exp\left(i\sum_{a=1}^{a=8}\theta_a L_a\right), \tag{1.15}$$

where L_a are the generators of the $SU(3)_c$ group (*i.e.* the 3×3 Gell-Mann matrices : $\lambda_a/2$ for triplets and 0 for singlets). Starting back from the Eq. (1.1) we can introduce eight gluons fields G_a^μ in the covariant derivative as

$$D^\mu = \partial^\mu + ig_s G_a^\mu L_a, \tag{1.16}$$

where g_s is the coupling constant associated to the $SU(3)$ group. Henceforth, regarding the strong interaction, quarks are triplets in the $SU(3)_c$ colour rotation. It means that three states (named red, green and blue) are available, and a colour quantum number is consequently associated to it. Therefore, it happens that the quarks are not free particles, but they interact with each other through the new gauge potentials. The 8 gluons are related to the 8 parameters of a general SU(3) transformation.

Table 1.2: Gauge boson of the Standard Model. The masses of the weak bosons are coming from Ref. [8].

Gauge boson	Mass	Charge	Spin	Interaction
photon γ	0	0	1	Electromagnetic
$W^\pm$	80.385 ± 0.015	± 1	1	Weak charged current
Z	91.188 ± 0.003	0	1	Weak neutral current
gluons g	—	0	1	Strong

1.2 The CKM matrix

Quark mass terms appear while developing Yukawa couplings when the Higgs field acquire a nonzero vacuum expectation value. It is necessary to use unitary matrix in order to pass from the weak eigenstates to the mass eigenstates as done in Eq. 1.14. This diagonalisation is using different transformations for up-type and down-type isospin-doublet components. It is customary to use the transformations for down quarks. The other choice would be equally satisfactorily. Hence, we have

$$Q_L = \begin{pmatrix} u_L \\ d_L \end{pmatrix} = (\mathcal{U}_L^{u\dagger})_j \begin{pmatrix} u_{Lj}^m \\ (\mathcal{U}_L^u \mathcal{U}_L^{d\dagger})_{jk} d_{Lk}^m \end{pmatrix}. \tag{1.17}$$

where m stands for mass eigenstates. It happens that $(\mathcal{U}_L^u \mathcal{U}_L^{d\dagger})_{jk}$ is an element of a 3×3 complex matrix called Cabibbo-Kobayashi-Maskawa [9,10] matrix whose a generic expression is displayed in Eq. 1.18.

$$V_{CKM} = (\mathcal{U}_L^u \mathcal{U}_L^{d\dagger}) = \begin{pmatrix} V_{ud} & V_{us} & V_{ub} \\ V_{cd} & V_{cs} & V_{cb} \\ V_{td} & V_{ts} & V_{tb} \end{pmatrix}. \tag{1.18}$$

Charged weak currents are therefore modified because of the transformation of the weak eigenstates into the mass eigenstates and CKM matrix elements appear on the way. The Lagrangian, invariant under $SU(2)$ rotations (written in Eq. 1.3), becomes, in the mass eigenstates basis (using Eq. 1.17)

$$\mathcal{L}_{\text{kin.}}^{quarks,m} = \frac{ig}{\sqrt{2}} (\overline{u^m}_{Li} \gamma^\mu (\mathcal{U}_{ik}^u \mathcal{U}_{kj}^{d\dagger}) d_{Lj}^m W_\mu^+ + \overline{d^m}_{Li} \gamma^\mu (\mathcal{U}_{ik}^d \mathcal{U}_{kj}^{u\dagger}) u_{Lj}^m W_\mu^-) + \frac{ig}{2} \overline{Q}_{Li} \gamma^\mu \sigma_3 W_3^\mu Q_{Li}, \tag{1.19}$$

where it appears that in the charged current interaction, there is a mixing of quarks between generations. The last term, driving neutral current, is not modified : there is no Flavour-Changing-Neutral-Current (FCNC) at first order.

1.2.1 Parameterisations of the CKM matrix

Several parameterisations of the CKM matrix are possible. Although this matrix is dimensioned to the number of $n = 3$ quark generations and contains consequently 9 complex elements, its unitary is providing 9 independent relations (and hence constraints on 6 real parameters and 3 complex parameters). In addition, there is 6 arbitrary phases related to each quark field and defining a single phase brings a reference for 5 of them. It happens therefore that CKM matrix can be parameterised using 4 independent parameters: 3 real parameters and one CP-violating phase (further discussed in Section 1.3). It is worth noting that standard CP violation requires at least 3 generations of quarks.

There are two parameterisations of the CKM matrix widely used. The first is considering three rotation angles θ_{12}, θ_{23}, θ_{13} and one phase δ_{13} as

$$\begin{aligned} V_{CKM} &= \mathcal{R}_{23}(\theta_{23}, 0) \otimes \mathcal{R}_{13}(\theta_{13}, \delta_{13}) \otimes \mathcal{R}_{12}(\theta_{12}, 0), \\ &= \begin{pmatrix} c_{12}c_{13} & s_{12}c_{13} & s_{13}e^{-i\delta_{13}} \\ -s_{12}c_{23} - c_{12}s_{23}s_{13}e^{i\delta_{13}} & c_{12}c_{23} - s_{12}s_{23}s_{13}e^{i\delta_{13}} & s_{23}c_{13} \\ s_{12}s_{23} - c_{12}c_{23}s_{13}e^{i\delta_{13}} & -c_{12}s_{23} - s_{12}c_{23}s_{13}e^{i\delta_{13}} & c_{23}c_{13} \end{pmatrix}, \end{aligned} \tag{1.20}$$

where $c_{ij} = \cos\theta_{ij}$, $s_{ij} = \sin\theta_{ij}$ and $i = 1, 2, 3$. This parameterisation is used by the Particle Data Group [8]. It is however convenient to have an explicit and a visual idea of the hierarchy between the mixing angles. Altomari and Wolfenstein [11] are providing such a parameterisation considering λ, A, ρ and η as the four matrix parameters, that are defined as [12]

$$\lambda = s_{12} \quad ; \quad A\lambda^2 = s_{23} \quad ; \quad A\lambda^3(\rho - i\eta) = s_{13}e^{-i\delta}. \tag{1.21}$$

Following this parameterisation, the CKM matrix can hence be written as

$$V_{CKM} = \begin{pmatrix} 1 - \lambda^2/2 & \lambda & A\lambda^3(\rho - i\eta) \\ -\lambda & 1 - \lambda^2/2 & A\lambda^2 \\ A\lambda^3(1 - \rho - i\eta) & -A\lambda^2 & 1 \end{pmatrix} + \mathcal{O}(\lambda^4), \tag{1.22}$$

where we can see that the hierarchy of the matrix elements is governed by the order of the λ parameter. Diagonal elements are equal to 1 at first order, which means that processes involving two quarks belonging to the same generation are favoured.

1.2.2 Unitary triangles

The definition of the the CKM-matrix parameters given in Eq. 1.21 is ensuring that the CKM matrix is unitary at every order of λ. Unitary conditions are equations of triangles in the complex plane. They can be gathered as

$$\left(\sum_i V_{ij} V_{ik}^* \right)_{j \neq k} = (d_{jk})_{j \neq k}. \tag{1.23}$$

Only two of them, namely the relations involving the b-quark, lead to triangles whose sides are of the same order $\mathcal{O}(\lambda^3)$, which would mean that we can expect significant CP-violating effects in b-quark flavour-transitions. A representation of such a triangle can be found on Fig. 1.1 as well as several observables used in order to constrain it: the length of the sides of the triangle are proportional to the moduli of the matrix elements $|V_{ub}|$, $|V_{cb}|$ and $|V_{td}|$. They

are constrained by measurements of the semileptonic branching fractions of b-baryons and oscillation frequency of $B^0 - \overline{B}^0$ mixing. The angles α, β and γ are measured through phase difference observables in mixings or decays involving b-quark transitions. There is almost no theoretical uncertainty attached to the determination of the angles. In contrast, the modulus $|V_{ud}|$ suffers from the uncertainties as derived from absolute probabilities of the decays. Yet, the progresses in the understanding of the hadronic processes in quark transitions, singularly obtained with QCD numeric computations on a lattice, allows to use there constraints in the electroweak interpretation of the unitary triangles. A detailed description of the observables can be found in Ref. [12].

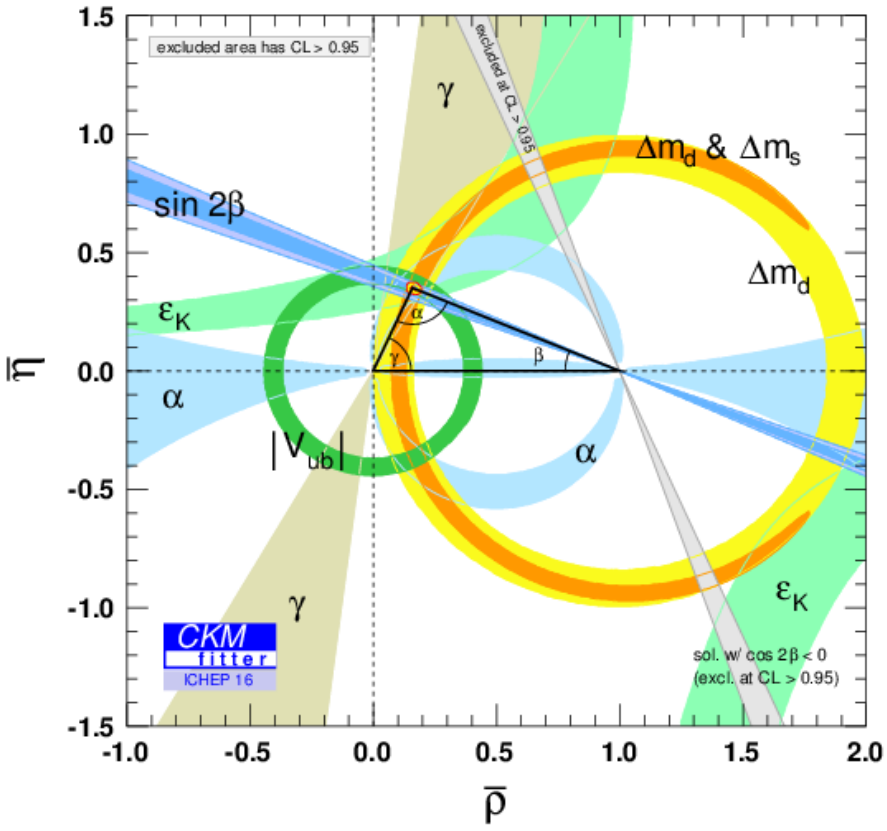

Figure 1.1: Individual constraints on the $(\overline{\rho};\overline{\eta})$ coordinates at 95% C.L. on the apex of the unitary triangle with $\overline{\rho} = (1-\lambda^2/2)\rho + \mathcal{O}(\lambda^4)$ and $\overline{\eta} = (1-\lambda^2/2)\eta + \mathcal{O}(\lambda^4)$. This definition is independent from the phases conventions.

The SM is containing one CP-violating phase through the Kobayashi-Maskawa paradigm. All measurements of CP (-violating or -conserving) observables are up to now consistent within the KM CP violation description[a].

[a]The strong CP problem is not considered here.

1.3 CP violation in the Standard Model

1.3.1 Discrete symmetries

Three discrete space-time-particle symmetries are considered in the SM. They are represented in quantum mechanics by the parity $\mathcal{P}$, the charge conjugation $\mathcal{C}$ and the time reversal $\mathcal{T}$ operators. Parity symmetry states that the physical properties between a given state $|\alpha\rangle$ and the spatially-inverted state $|\alpha_P\rangle$ should be the same. Similarly, charge conjugation symmetry postulates that changing particles into antiparticles and vice-versa (means reversing the sign of the charge quantum numbers) let Nature invariant. Eventually, time reversal symmetry would imply that the physical laws are the same either moving forward or moving backward in time. It has however been experimentally observed that weak interaction is maximally violating $\mathcal{C}$ and $\mathcal{P}$ symmetries. Although CP could appear as a good symmetry, its violation has as well been certified for the first time in 1964 via the observation of the decay $K_L^0 \to \pi^+\pi^-$ [13].

1.3.2 Three signatures of CP violation

Up to date, CP violation can be experimentally observed in three phenomena. They are briefly introduced in this section. In the mean time is discussed the violation of CP symmetry phenomenology. Considering the processes $B^0 \to f$ and $\overline{B}^0 \to \overline{f}$ where initial states B^0, $\overline{B}^0$ and final states f, $\overline{f}$, are CP-conjugates, one can define the respective amplitudes as

$$A = \langle f|\mathcal{H}|B\rangle \tag{1.24}$$
$$\overline{A} = \langle \overline{f}|\mathcal{H}|\overline{B}\rangle \tag{1.25}$$

where $\mathcal{H}$ is the weak Hamiltonian 2×2 matrix describing the evolution of the processes. Let's define

$$\begin{aligned} \mathcal{H} &= \mathcal{M} - \frac{i}{2}\Gamma \\ &= \begin{pmatrix} M_{11} & M_{12} \\ M_{12}^* & M_{22} \end{pmatrix} - \frac{i}{2}\begin{pmatrix} \Gamma_{11} & \Gamma_{12} \\ \Gamma_{12}^* & \Gamma_{22} \end{pmatrix}, \end{aligned} \tag{1.26}$$

where $M_{11} = M_{22}$ and $\Gamma_{11} = \Gamma_{22}$, as imposed by a global CPT symmetry. For instance, this Hamiltonian allows to describe the time-evolution of a mixing between B^0 and $\overline{B^0}$ neutral meson states. Those two states can indeed mix via box diagrams in the SM and the superposition of states can be written as

$$|B(t)\rangle = a(t)\left|B^0(t)\right\rangle + b(t)\left|\bar{B}^0(t)\right\rangle \quad \text{with} \quad |a(t)|^2 + |b(t)|^2 = 1, \tag{1.27}$$

at any t, considering that the time-range is much larger than the interaction scale. The Schrödinger equation is hence providing the time-evolution of the mixing as

$$i\frac{d}{dt}\begin{pmatrix} a(t) \\ b(t) \end{pmatrix} = \mathcal{H}\begin{pmatrix} a(t) \\ b(t) \end{pmatrix}. \tag{1.28}$$

The equation (1.28) has two solutions with eigenstates of definite masses $M_{H,L}$ (H stands for "Heavy" and L for "Light" with the natural convention $M_H > M_L$). The flavour-eigenstates can be written with a linear combination of the B^0 and $\overline{B}^0$ mass eigenstates introducing p and q coefficients, as

$$|B_{H,L}\rangle = \frac{p\,|B^0\rangle \pm q\,\left|\bar{B}^0\right\rangle}{\sqrt{|p|^2 + |q|^2}}. \tag{1.29}$$

1.3.2.1 Direct CP violation

Amplitudes introduced in Eq. (1.24) and (1.25) contain weak phases associated to CKM matrix-elements which are modified under CP-conjugation. Direct CP-violation is hence occurring when the ratio $\left|\frac{\bar{A}}{A}\right|$ is not equal to 1. As a consequence, the branching fraction of the CP-conjugate processes are expected to be different. Experimentally, direct CP-violation has been observed for the first time in K decays in 2001 [14] and in B mesons decays in 2004 [15, 16]. Non-vanishing CP-asymmetries have as well been measured in B^0, B^+ and B_s^0 decays by the LHCb collaboration [17].
A part of the work reported in this document is devoted to the search for direct CP violation in baryon decays. Nonzero asymmetries imply a difference between the partial widths of the two decays rates that are CP-conjugate, such as

$$\Gamma(i \to f) \neq \Gamma(\bar{i} \to \bar{f}) \qquad \text{with} \qquad \begin{cases} \Gamma(i \to f) = |A(i \to f)|^2 \\ \Gamma(\bar{i} \to \bar{f}) = |\bar{A}(\bar{i} \to \bar{f})|^2 \end{cases}. \tag{1.30}$$

If one considers a decay that involves two phase-shifted amplitudes A_1 and A_2, in which strong (weak) phases δ_i (ϕ_i) are (not) CP-conserved, we can write

$$A = A_1 + A_2 = |A_1| e^{i\phi_1} e^{i\delta_1} + |A_2| e^{i\phi_2} e^{i\delta_2}, \tag{1.31}$$
$$\bar{A} = \bar{A}_1 + \bar{A}_2 = |A_1| e^{-i\phi_1} e^{i\delta_1} + |A_2| e^{-i\phi_2} e^{i\delta_2}. \tag{1.32}$$

Computing the CP asymmetry A_{CP} provides the following expression

$$A_{CP} = \frac{|A|^2 - |\bar{A}|^2}{|A|^2 + |\bar{A}|^2} = \frac{2|A_1||A_2| \sin(\phi_1 - \phi_2) \sin(\delta_1 - \delta_2)}{|A_1|^2 + |A_2|^2 + 2|A_1||A_2| \cos(\phi_1 - \phi_2) \cos(\delta_1 - \delta_2)}. \tag{1.33}$$

This A_{CP} expression implies that at least two phase-shifted amplitudes should interfere in order to observe an asymmetry. A non-vanishing weak phase difference (which directly comes from CKM matrix elements) as well as non-vanishing strong phase difference (allowed by interactions in the final states for instance) are necessary for an observation of CP asymmetry. Those conditions are motivating the several measurements that are performed: a rich interference pattern is expected in the decay modes we are interested in. Additional measurements, that meant to include explicit strong resonances, are also performed.

1.3.2.2 Indirect CP violation

Considering p and q coefficients introduced in Eq. (1.29), one can derive

$$\left|\frac{q}{p}\right|^2 = \left|\frac{M_{12}^* - \frac{i}{2}\Gamma_{12}^*}{M_{12} - \frac{i}{2}\Gamma_{12}}\right|. \tag{1.34}$$

The imaginary parts of M_{12} and Γ_{12} imply a CP-violation otherwise the weak eigenstates and the mass eigenstates would be the same. Indirect CP-violation or CP-violation in the mixing is hence occurring when $\frac{q}{p} \neq 1$.

1.3.2.3 CP violation in decays with(out) mixing

The two signatures previously presented can be combined into a phenomenon called CP violation in interferences between decays with and without mixing. Mixing-induced nonzero CP asymmetries have been experimentally measured for the first time in 2001 in $B_s \to$

$J/\psi K^0_s$ decay [18, 19]. The general idea is to compare two initial states B^0 and $\bar{B}^0$ leading to the same final state f_{CP} (eigenstate of CP) which can be reached through a mixing for one of the two initial states. Writing the two amplitudes as

$$A = \langle f_{CP}|\mathcal{H}|B\rangle\,, \tag{1.35}$$
$$\bar{A} = \langle f_{CP}|\mathcal{H}|\bar{B}\rangle\,, \tag{1.36}$$

we can define λ as

$$\lambda = \frac{q}{p}\frac{\bar{A}}{A}. \tag{1.37}$$

The quantity λ is hence independent of any phase-convention and $\lambda \neq 1$ would imply CP violation. This CP-violation signature is particularly of interest in the measurement of parameters of unitary triangles.

1.4 Overview of the modes of interest

Charmless four-body decays of neutral b-baryons are studied in order to (1) measure branching fractions and (2) search for CP-asymmetries by measuring A_{CP} quantities, defined in Eq. 1.33. The scrutinised bottom baryons are Λ^0_b ($|udb\rangle$) and Ξ^0_b($|usb\rangle$), firstly observed by UA1 and CDF collaborations respectively [20, 21].

The decay modes we are interested in are (considering $X_b = \{\Lambda^0_b, \Xi^0_b\}$) $\Lambda^0_b \to p\pi^-\pi^+\pi^-$, $X_b \to pK^-\pi^+\pi^-$, $\Lambda^0_b \to pK^-K^+\pi^-$, $\Xi^0_b \to pK^-\pi^+K^-$ and $X_b \to pK^-K^+K^-$. A simple counting experiment can measure a direct CP-asymmetry up to corrections of instrumental and productions asymmetries. In order to cope with these unknown asymmetries, 4-body decays of X_b involving either a Λ^+_c or Ξ^+_c are used as control channels. The $\Lambda^0_b \to (\Lambda^+_c \to p\pi^-\pi^+)\pi^-$, $\Lambda^0_b \to (\Lambda^+_c \to pK^-\pi^+)\pi^-$ and $\Xi^0_b \to (\Xi^+_c \to pK^-\pi^+)\pi^-$ decays are hence used in the search for CP-asymmetries in order to handle those experimental effects. Eventually, the branching fractions of the modes of interest are determined relative to the known $\Lambda^0_b \to (\Lambda^+_c \to pK^-\pi^+)\pi^-$ branching fraction [8].

1.4.1 A definition of the branching fractions

A significant part of the work presented in this document is hence dedicated to the branching fraction measurements of 4-body charmless decays of Λ^0_b and Ξ^0_b baryons. Up to date, there is no theoretical prediction of such quantities and a complete derivation would exceed the framework of the activities presented in this document. Consequently, this section is only providing a definition of the branching fractions. The measurements of these branching fractions can hopefully motivate a theoretical work on the subject.
The branching fraction (denoted $\mathcal{BF}$) of a process is by definition the ratio between its decay width over the total decay width of the particle decaying. In our case, one of the decay of interest is $\Lambda^0_b \to p\pi^-\pi^+\pi^-$ which can simultaneously proceed via $b \to u$ quark transition at tree level or via a FCNC $b \to d$ quark transitions (implying a penguin loop diagram), as displayed on Fig. 1.3. We restrain the development with the hypothesis that N^* and ρ^0 are the only intermediate hadronic states leading to the final state for sake of simplicity.

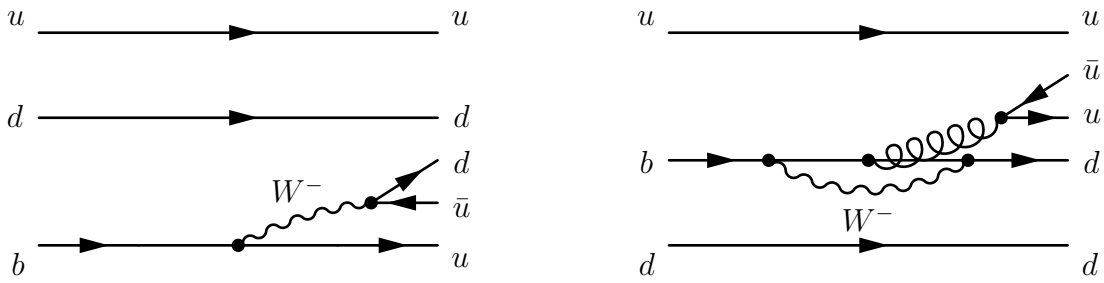

(a) Tree contribution.

(b) Pinguin loop contribution.

Figure 1.2: Feynman diagrams of the decay of $\Lambda_b^0(udb)$ into $N^*(udd)$ and $\rho^0(u\bar{u})$. The hadronisation states are not represented for sake of clearness.

We can subsequently define the $\Lambda_b^0 \to N^*\rho^0(\to p\pi^-\pi^+\pi^-)$ branching fraction as

$$\mathcal{BF} = \frac{\Gamma(\Lambda_b^0 \to N^*\rho^0)}{\Gamma_{\text{total}}} \quad \text{with} \quad \begin{cases} \Gamma_{\text{total}} = \tau_{\Lambda_b^0}^{-1} \\ \hbar = c = 1 \end{cases} \tag{1.38}$$

In order to determine the partial decay width or the Λ_b^0, one can consider the following formula

$$\Gamma(\Lambda_b^0 \to N^*\rho^0) = \left(\frac{E_{N^*} + m_{\Lambda_b^0}}{m_{\Lambda_b^0}}\right) \frac{P_{\rho^0}}{16\pi^2} \int_\Omega \left|A(\Lambda_b^0 \to N^*\rho^0)\right|^2 d\Omega, \tag{1.39}$$

where P_{ρ^0} is the norm of the ρ^0 momentum in the Λ_b^0 rest frame, such as

$$P_{\rho^0} = \frac{1}{2m_{\Lambda_b^0}} \sqrt{[m_{\Lambda_b^0}^2 - (m_{\rho^0} + m_{N^*})^2][m_{\Lambda_b^0}^2 - (m_{\rho^0} - m_{N^*})^2]}. \tag{1.40}$$

The main difficulty is the computation of the amplitude $A(\Lambda_b^0 \to N^*\rho^0)$ which rely essentially on contributions coming from non-perturbative Quantum Chromo-Dynamics (QCD). Electroweak-wise, one can consider diagrams at low-order. Conversely, QCD corrections are requiring to entangle short distance strong interactions (perturbative) and non-trivial long distance interaction (non-perturbative). Generally, the Operator Product Expansion (OPE) method is used in order to separate those two regimes. A discussion of the OPE method is provided in appendix A.1 as well as some inputs on a factorisation hypothesis.

1.4.2 Search for *CP* violation

CP violation has not been clearly observed in baryon decays although evidence for non-vanishing *CP* asymmetries in $\Lambda_b^0 \to p\pi^-\pi^+\pi^-$ has been recently reported by the LHCb collaboration [22], by using T-odd observables. Actually, a comparison between the two types of measurements is not trivial: T-odd *CP*-observables are proportional to the sine of the weak-phase difference while A_{CP} are proportional to the cosine of this very same quantity. To a certain extent, this phase shift brings complementary methods and a null A_{CP} can consequently be consistent with non-zero T-odd asymmetry. The analyses presented in this thesis focus on these decays, where, aside from non-resonant components, it can proceed through baryonic resonances, i.e. Λ^{*0}, N^{*0} and Δ series. In addition, mesonic resonances can also occur. Consequently, the interference pattern is expected to be rich of resonance structures. As explicited in Section 1.3, the direct A_{CP} observable can be enhanced by the presence of significant phase differences from strong resonances of at least two competing

amplitudes. Although it can be beneficial for searching for CP-asymmetries, the expected richness of the phase space of the decays brings some complications in the branching fraction calculation justifying to a certain extent that no prediction of their branching fractions exists.

The figures 1.3 to 1.9 present some diagrammatic possibility (at first order) for the neutral baryon to decay into intermediate strong resonance amplitude and consequently into the different final states.

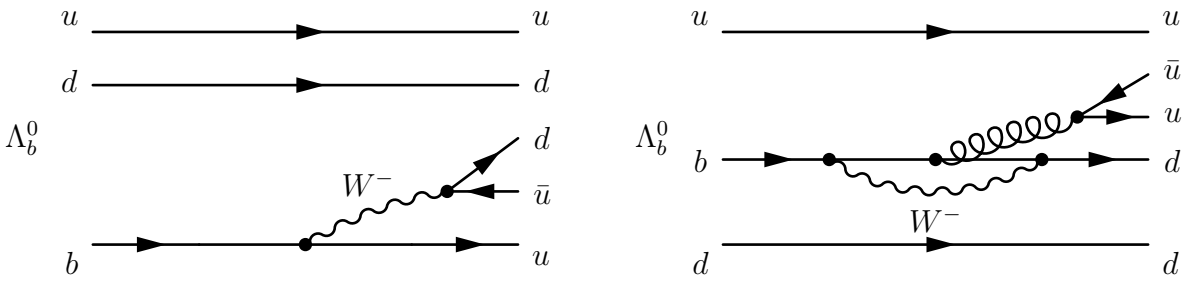

(a) Tree contribution ($\mathcal{O}(\lambda^3)$). (b) Penguin loop contribution ($\mathcal{O}(\lambda^3)$).

Figure 1.3: Feynman diagrams of the decay of $\Lambda_b^0 \to p\pi^-\pi^+\pi^-$.

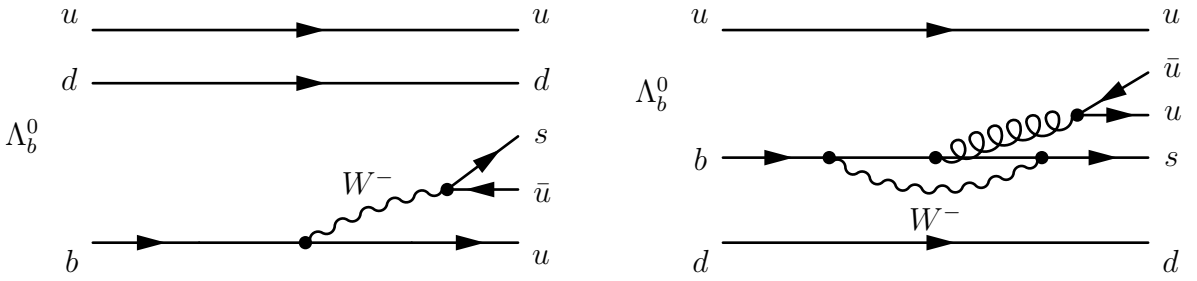

(a) Tree contribution ($\mathcal{O}(\lambda^4)$). (b) Penguin loop contribution ($\mathcal{O}(\lambda^2)$).

Figure 1.4: Feynman diagrams of the decay of $\Lambda_b^0 \to pK^-\pi^+\pi^-$.

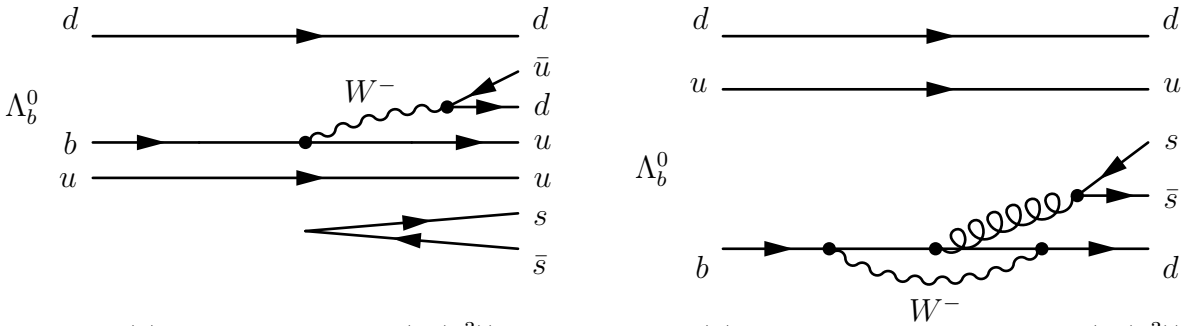

(a) Tree contribution ($\mathcal{O}(\lambda^3)$). (b) Penguin loop contribution ($\mathcal{O}(\lambda^3)$).

Figure 1.5: Feynman diagrams of the decay of $\Lambda_b^0 \to pK^-K^+\pi^-$.

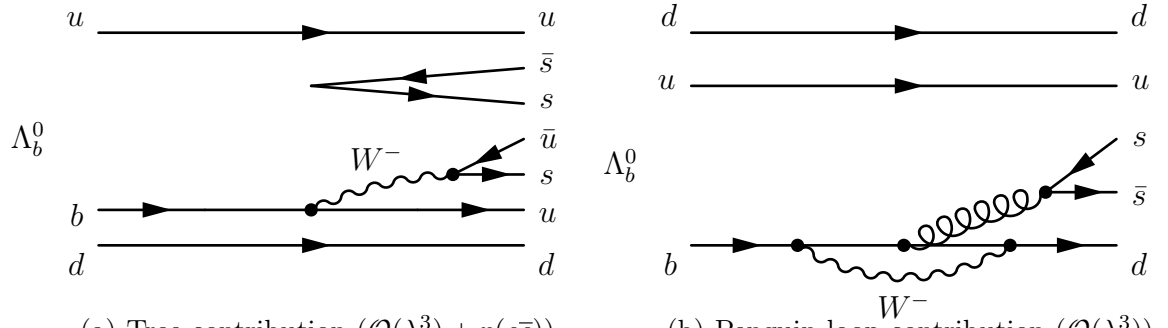

(a) Tree contribution ($\mathcal{O}(\lambda^3) + p(s\bar{s})$). (b) Penguin loop contribution ($\mathcal{O}(\lambda^3)$).

Figure 1.6: Feynman diagrams of the decay of $\Lambda_b^0 \to pK^-K^+K^-$.

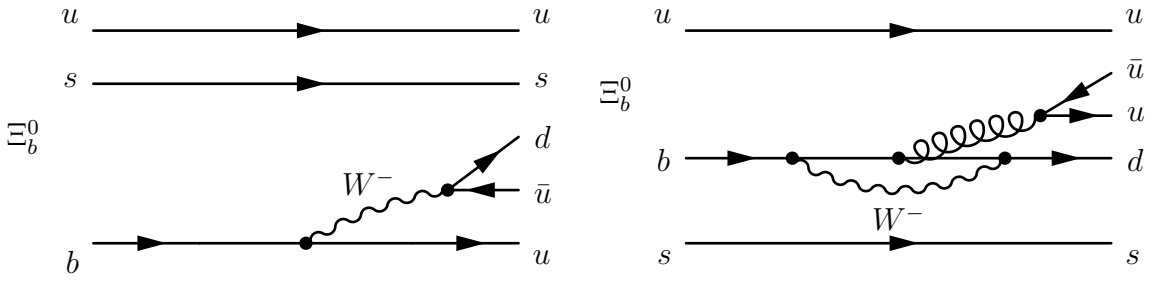

(a) Tree contribution ($\mathcal{O}(\lambda^3)$). (b) Penguin loop contribution ($\mathcal{O}(\lambda^3)$).

Figure 1.7: Feynman diagrams of the decay of $\Xi_b^0 \to pK^-\pi^+\pi^-$.

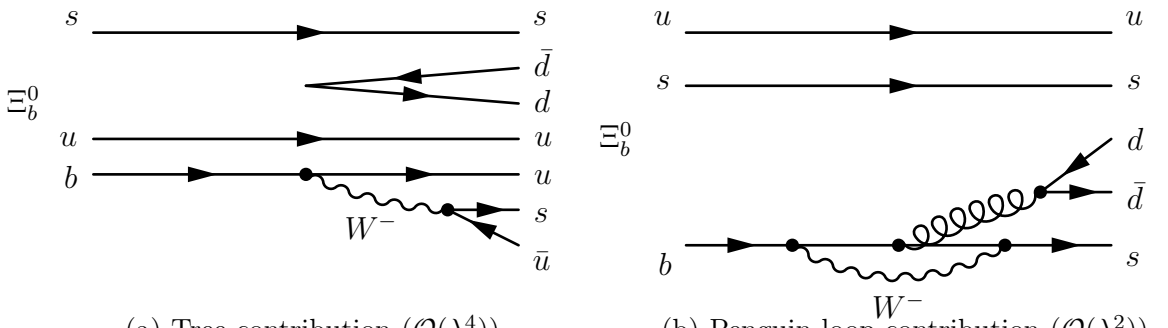

(a) Tree contribution ($\mathcal{O}(\lambda^4)$). (b) Penguin loop contribution ($\mathcal{O}(\lambda^2)$).

Figure 1.8: Feynman diagrams of the decay of $\Xi_b^0 \to pK^-\pi^+K^-$.

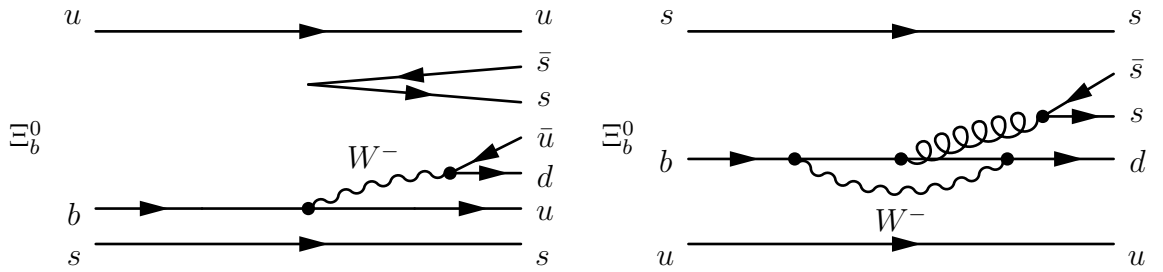

(a) Tree contribution ($\mathcal{O}(\lambda^3) + p(s\bar{s})$). (b) Penguin loop contribution ($\mathcal{O}(\lambda^2)$).

Figure 1.9: Feynman diagrams of the decay of $\Xi_b^0 \to pK^-K^+K^-$.

Chapter 2

A beautiful experiment at the Large Hadron Collider

This chapter is dedicated to the LHC and the LHCb experiment. This part is mostly written according to Refs. [23,24] since it presents the experimental framework in a quite straightforward (but complete) way. The LHC is hence briefly introduced. An overview of the LHCb detector and a description of its sub-components is also provided. Emphasis is brought to the tracking system of the experiment, used extensively in the subsequent analyses reported in this document. Eventually, a specific section will discuss the trigger system in order to introduce one of the most important systematic uncertainties in the measurements that are presented here.

Chapter contents

2.1 The Large Hadron Collider machine

The experimental search for the Brout-Englert-Higgs boson was one of the main motivations for the birth of the Large Hadron Collider, successor of the Large Electron Positron collider at CERN(European Council for Nuclear Research). It consists in two-ring superconducting hadron accelerator and collider, installed underground about 100 meters deep in the historical LEP tunnel. Two proton beams collide at different intersection points with an energy in the center-of-mass of 13 TeV since 2015. This characteristic makes the LHC the highest energy particle accelerator ever built. Previously designed to collide bunches of protons at 14 TeV, the Run I started actually with an energy of 7 TeV in 2011 campaign and 8 TeV in 2012. The Run II (2015) started with collisions close to the nominal LHC energy (13 TeV). It is worth noting that the LHC allows to accelerate and collide lead ions.

2.1.1 From hydrogen to high-energy collisions

The high energy required during the collisions needs a complex accelerator chain whose a representation is displayed on Fig. 2.1. The proton source is as simple as a bottle of hydrogen whose protons are isolated by using electric field. The journey of the protons starts with a linear accelerator (LINAC 2) delivering them into the Proton Synchrotron Booster (PSB) with an energy of 50 MeV. The Booster produces in turn 1.4 GeV beams which circulate right after in the Proton Synchrotron (PS) up to 26 GeV energy. The Super Proton Synchrotron (SPS) follows and accelerates beams up to 450 GeV before delivering them into the main rings, which manage to accelerate proton beams up to the actual LHC energies. The bunch crossing rate is about 40 MHz. Collisions finally happen at four main interaction points where different detectors and experiments take place.

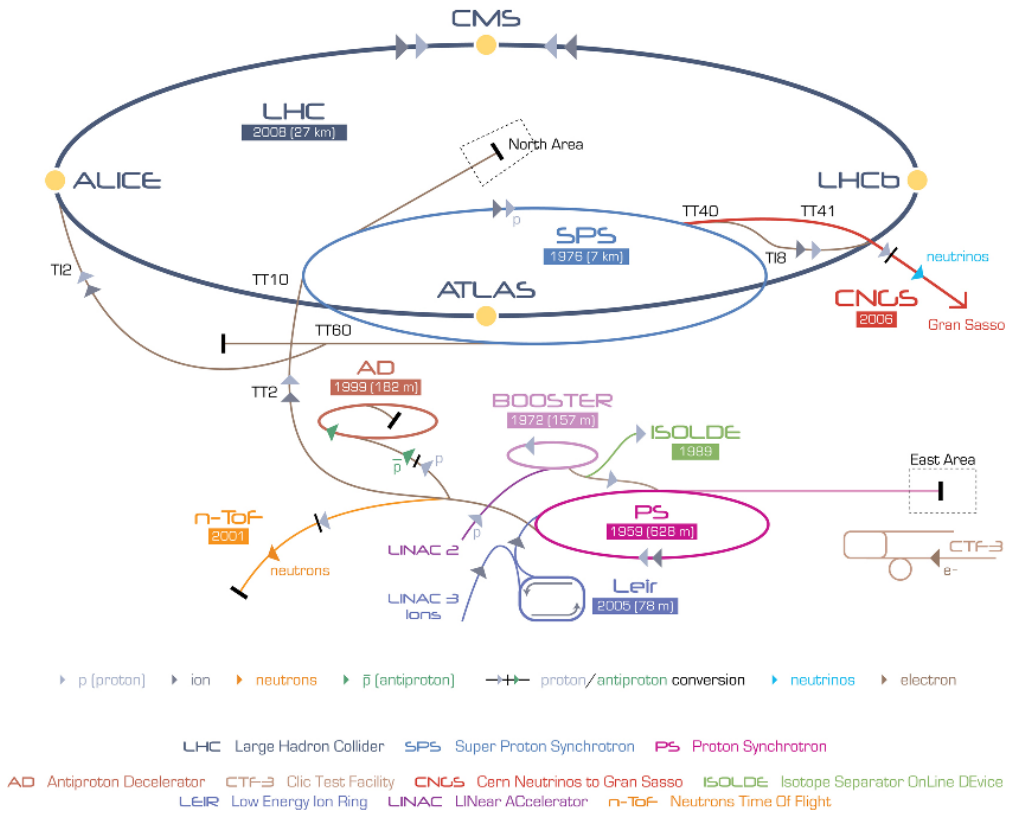

Figure 2.1: Schematic representation of the current LHC accelerator complex.

2.1.2 LHC experiments

At LHC, several experiments take place at different interaction points. The four main are A Large Ion Collider Experiment (ALICE), which uses also Pb-Pb collisions in order to study the quark-gluon plasma. A Torroidal LHC ApparatuS (ATLAS) and Compact Muon Solenoid (CMS) are general-purpose detectors ($\simeq 4\pi$ acceptance) searching for new physics (including super-symmetric particles) and having both confirmed the observation of a narrow bosonic state constant so far with the BEH boson in 2012. Finally, Large Hadron Collider beauty experiments(LHCb), specialised in flavour physics (search for *CP* violation and rare decays).

Few others experiments are based at LHC : TOTal Elastic and diffractive cross-section Measurement (TOTEM), which aims at measuring precisely the total cross-section of proton-proton collisions. Large Hadron Collider forward (LHCf), which measures the neutral-particle production cross-section in the forward region in order to understand the cosmic-rays production. Finally, Monopole and Exotic Detector at LHC (MoEDAL) aims to search for exotics, magnetic monopoles.

2.1.3 Luminosity

In a general way, the luminosity is the proportionality factor between the number of collisions per unity of time and the cross-section of interaction. It is given by :

$$L = \frac{N_1 N_2 k_b f \gamma F}{4\pi\beta^* \epsilon} \tag{2.1}$$

where N_i is the number of protons in each bunch, k_b is the number of proton bunches, f is the frequency of the collisions, F takes account of the reduction due to the crossing angle of the beams , γ is the relativistic factor, β^* is the value of the betatron function at the interaction point and lastly, ϵ is the emittance.

2.2 LHCb experiment

2.2.1 An overview

The LHCb experiment is one of the four main experiments using the LHC collisions and is dedicated to the study of the heavy-flavour sector (processes involving b-, c- quarks or τ-leptons). Beyond the study of *CP*-violating phenomena (and the search for *CP*-violating phases beyond the SM one), LHCb scrutinises the rare decays of heavy-flavoured particles in order to unravel departures from SM predictions.

Since LHCb experiment is dedicated to b-hadron Physics, it makes use of a detector whose geometry is motivated by the direction of the $b\bar{b}$-pair production. The dominant mechanism of $b\bar{b}$ pair production in a hadronic collider is gluon-gluon fusion (as shown on Fig. 2.2a). A direct consequence is that the angular distributions of the final products are dominated by low (or large) polar angles as shown on Fig. 2.2b.

2.2.2 Detector overview

Henceforth, it happens that $b\bar{b}$ pairs are predominantly produced in the same forward of backward cone in LHC collisions. LHCb has consequently been designed as a single-arm spectrometer with a forward angular coverage from 10 mrad to approximately 300 mrad that can be visualised on Fig. 2.3.

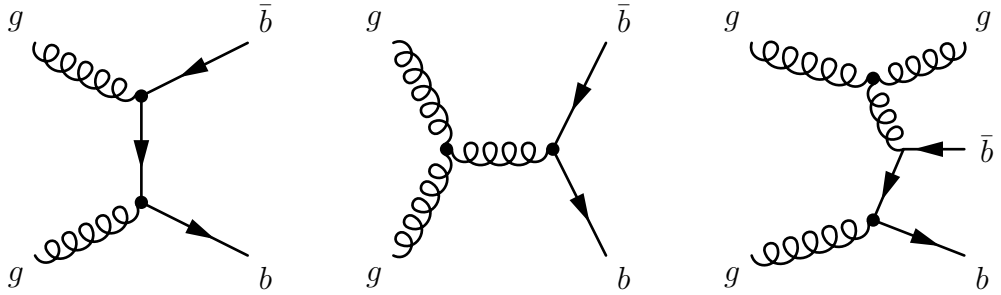

(a) Examples of processes driving the $b\bar{b}$-pair production at order $\mathcal{O}(\alpha_s^2)$ and $\mathcal{O}(\alpha_s^3)$.

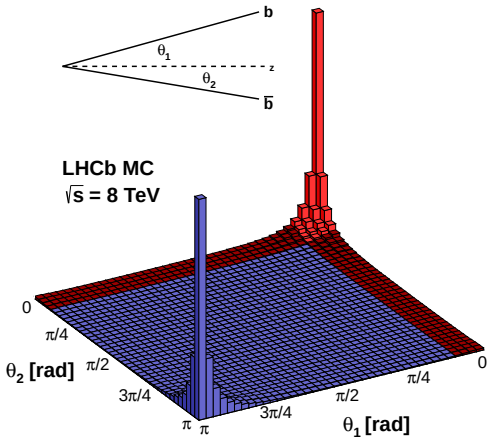

(b) Distribution of the $b\bar{b}$ pair production angle with respect to the beam axis.

Figure 2.2: Production of $b\bar{b}$ pairs at LHC.

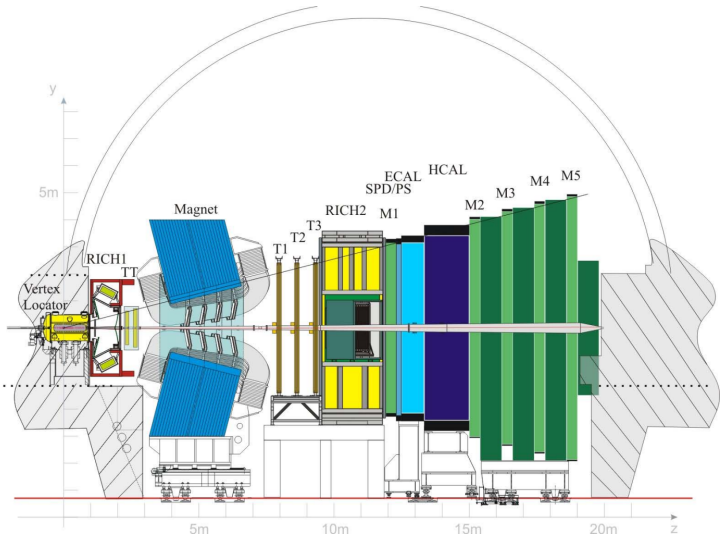

(a) Schematic view.

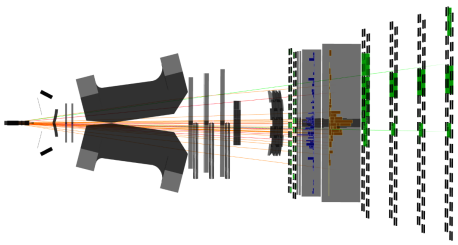

(b) Event display.

Figure 2.3: Views of the LHCb detector. z-axis is aligned with the beam direction and y-axis is along the vertical.

Looking at the layout of the LHCb spectrometer, one can find the tracking system which is built around a dipole magnet providing an integrated field of 4 T.m [25]. Upstream the magnet, it is composed of the high-resolution vertex locator (VELO) [26] and the silicon microchip Trigger Tracker (TT). Three tracking stations T1, T2 and T3 which are made of silicon microstrips in the inner part (IT) and of Kapton/Al straws for the outer part (OT) complete the tracking system [27,28]. An excellent K-π separation (in the momentum range from 2 to 100 GeV/c) is ensured by the presence of two Ring Imaging Cherenkov counters (RICH1 and RICH2) which are respectively located upstream and downstream the magnet [29]. Eventually, the calorimetry system is composed of a Scintillator Pad Detector (SPD) and PreShower (PS), an electromagnetic calorimeter (ECAL) and a hadronic calorimeter (HCAL) [30]. The identification of the muons is strengthened by the presence of a dedicated muon-detection system based on Multi-Wires Proportionnal Chambers (MWPC) and Gas Electron Multiplier (GEM) [31].

2.2.3 The Vertexing and tracking system

2.2.3.1 The Magnet

LHCb detector has a warm dipole magnet delivering an integrated field of 4 T.m, which is used in order to measure the momentum of charged particles. The polarity of the magnetic field is periodically reversed: this is meant to control the systematic effects of the detector that are particularly important in the study of detector asymmetries and CP asymmetries measurements. By convention, LHCb is recording "Down" and "Up" data samples whether the magnet field is along the negative or positive y-axis (as defined on Fig. 2.3a). A representation (as well as a picture) of the magnet are displayed on Fig. 2.4.

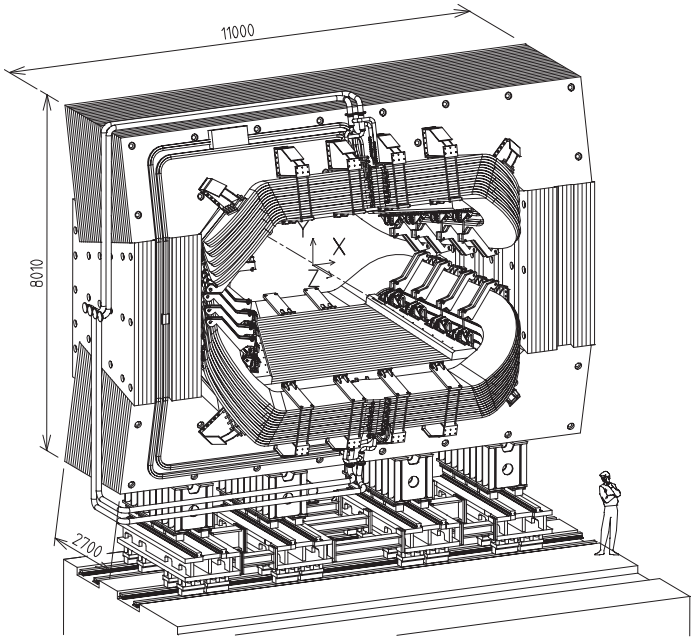

(a) Perspective view of the magnet of LHCb. Units are mm.

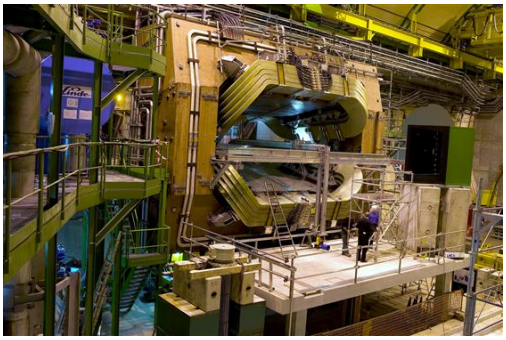

(b) Picture of the magnet.

Figure 2.4: Views of the magnet of LHCb.

2.2.3.2 The Vertex Locator

The Vertex Locator (VELO) is the closest detector to the interaction point. It has been designed to be movable. It's getting to its closed state when the beams are declared stable. When physics data taking is conducted and beams are stable, the first active strip of the VELO is around 8 mm from the beam. The VELO consists in a series of silicon stations spread along the beam axis that have their own z coordinate. A precise measurement of the track coordinates (r and ϕ) is performed by sensors that are placed back-to-back, perpendicularly to the beam pipe. The r-type sensors has silicon strips arranged radially from the beam axis in order to measure the charge energy deposit on the radial position. The ϕ-type sensors have conversely silicon strips arranged as semicircles centered around the beam axis in order to measure the azimutal coordinate. The sensors are used to reconstruct production and displaced secondary vertices[a] whose position is related to the lifetimes of b- and c- hadron decays. Thick aluminium foil (RF foil) is placed between the sensors and the beam vacuum in order to shield electronics from radiations. A representation of the sensors is displayed on Fig. 2.5.

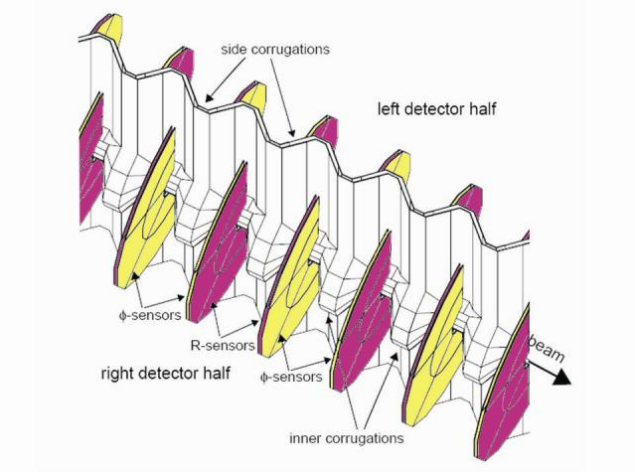

(a) Zoom inside an RF-foil (GEANT modelisation) of the VELO in closed position.

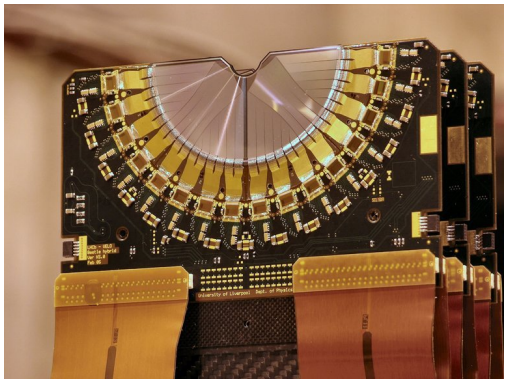

(b) Picture of the sensors.

Figure 2.5: Views of the VELO detector.

Several reconstructed tracks allow the reconstruction of primary vertices (PV) with a given spatial resolution which improves as a function of the number of associated tracks. Although the performance of the VELO detector is well known elsewhere [32, 33], we have explicitly checked from 2012 simulated events used in our analysis, that the PV resolution along x-, y- and z- axes scales as

$$\sigma_{x,y,z} = \frac{A}{N^B} + C, \tag{2.2}$$

where A, B, C are fit parameters determined from the fit displayed on Fig. 2.6. The impact parameter (IP) is defined as the closest approach of a track to the PV and can generally be used in signal selections. By making use of simulated events, we checked that the resolution of the IP of the tracks present in final state (noted as h_i) can be written as

$$\sigma(\mathrm{IP}_{h_i}) = \frac{A}{p_T(h_i)} + B, \tag{2.3}$$

where A, B are fit parameters determined from the fit displayed on Fig. 2.6.

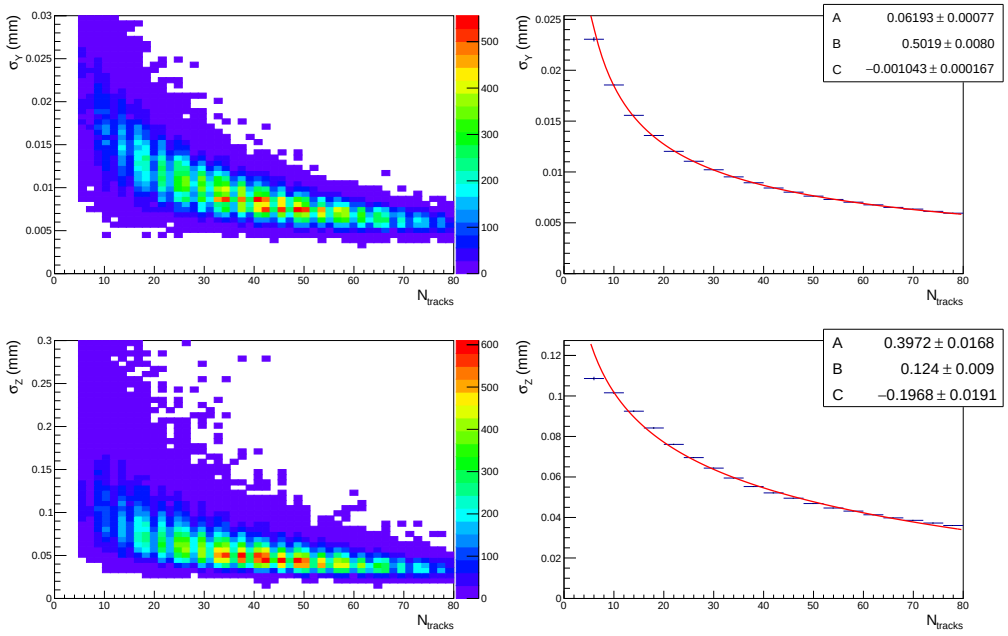

Figure 2.6: PV resolution along (from top to bottom) y- and z-axis as a function of the number of associated tracks. It has been checked that similar results for the resolution along the x-axis are in order. The right column is displaying the fit to the mean value of the resolution for each bin of N_{tracks}.

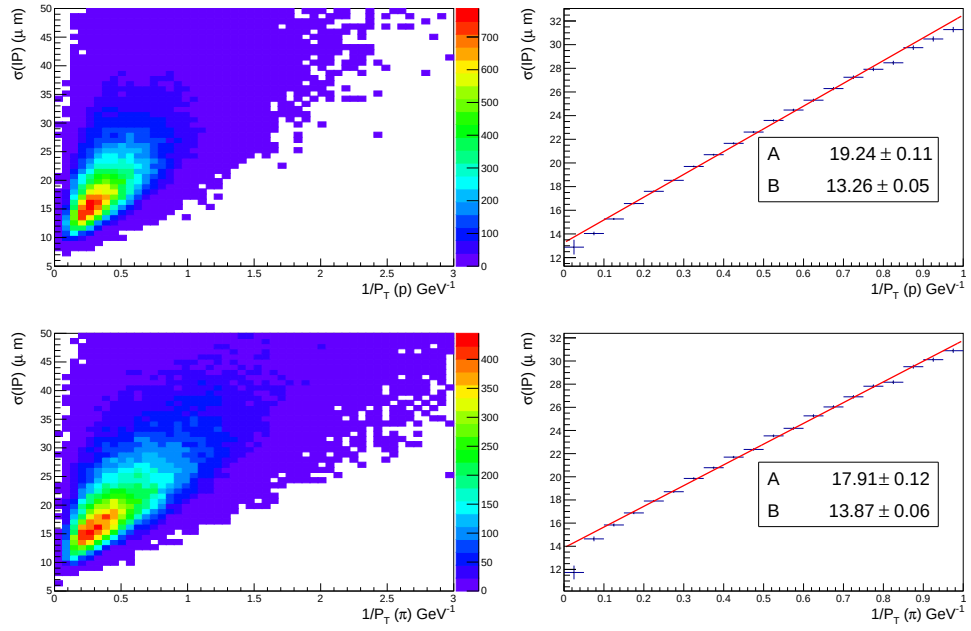

Figure 2.7: IP resolution as a function of the transverse momentum of a proton (top) and a pion (bottom). The right column is displaying the fit to the mean value of the resolution for each bin of $1/p_T$.

As an illustration, the typical PV resolution along the y-(z-) axis is $\sim 10(50)\mu$m for the sample considered. Similarly, the typical resolution on the IP for a proton(pion) is $\sim 17(15)\mu$m. Both IP and PV resolutions are used in the determination of χ^2_{IP} (allowing the discrimination between several PV hypotheses) and χ^2_{PV} (representing the quality of

[a]The primary vertex is conventionally defined as the production vertex.

the vertex reconstruction) that are particularly of interest in the design of the selection of the signal events. It is worth noting that similar variables are considered for the particles flight-distances ($\chi^2_{\rm FD}$).

2.2.3.3 The Silicon Trackers and Outer Tracker

The tracking system of LHCb is completed by a series of four large rectangular stations, each covering an area of about 40 m^2. Two different detector technologies are employed. A representation of the layout of the Silicon Trackers and the Outer Trackers is displayed on Fig. 2.8.

- The Silicon Tracker (ST), uses silicon microstrip detectors to reconstruct tracks close to the beam pipe. One detector is located between the VELO and the magnet (TT) and the others (IT) are located between the magnet and RICH2. IT is further split in three stations T1, T2 and T3. Each of the four ST stations has four detection layers with vertical strips in the first and the last layer and strips rotated by a stereo angle of $-5°$ and $+5°$ in the second and the third layer, respectively.

- The Outer Tracker is situated further from the beam pipe and is made up of thousands of gas-filled straw tubes. It is a drift-chamber detector, means that the position of the track is found by timing how long the electrons take to reach an anode wire situated in the centre of each tube. An excellent momentum resolution is required for a precise determination of the invariant mass of reconstructed b-hadrons.

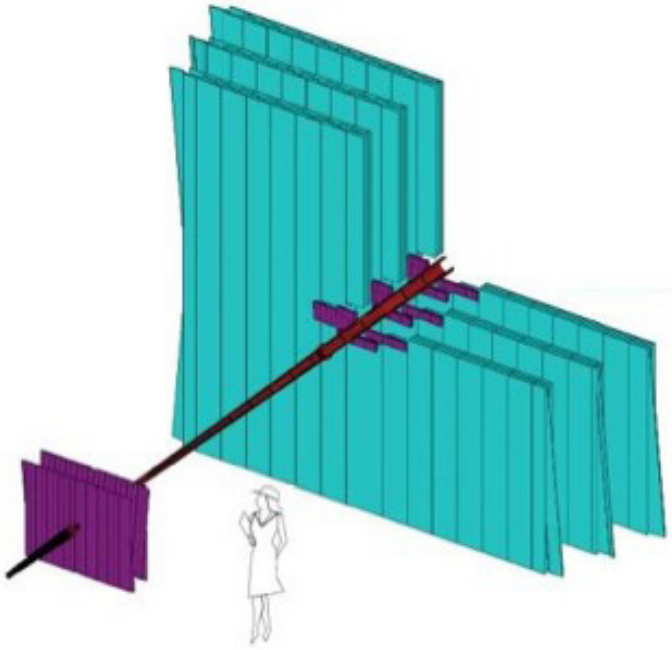

(a) Schematic representation of the layout of the Silicon Tracker (purple) and the Outer Tracker (blue).

(b) Picture of a station.

Figure 2.8: Views of the trackers stations.

2.2.4 The Particle identification system

The tracking system of LHCb is not providing any information on the loss of energy of the particles passing through the detector. The identification of the particles (PID) is ensured by two RICH detectors (Ring Imager Cherenkov) which are designed to get an efficient PID over the full momentum range. A combination of spherical and flat mirrors is used in order to reflect the image of the focused Cherenkov light out of the spectrometer acceptance. Cherenkov photons are detected with Hybrid Photon Detectors that are surrounded by an external iron shield to permit operation in magnetic field. The RICH1 (upstream detector) covers the low momentum charged particle range, from 1 to 60 GeV/c and makes use of aerogel and C_4F_{10} radiators. It has a wide acceptance covering the full LHCb acceptance from $\pm$ 25 mrad to $\pm$ 300 mrad (horizontal) and $\pm$ 250 mrad (vertical). The PID system is completed with RICH2 (downstream detector) which covers the high momentum range from 15 GeV/c up to 100 GeV/c and makes use of CF_4 radiators. Its acceptance is consequently limited from $\pm$ 15 mrad to $\pm$ 120 mrad (horizontal) and $\pm$ 100 mrad (vertical). Cherenkov angle is shown on Fig. 2.10 as a function of the momentum for the different radiators.

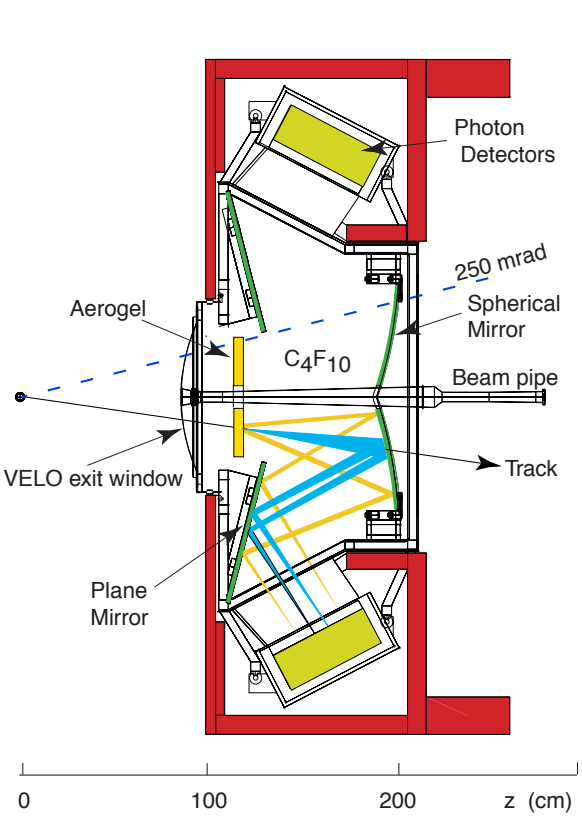

(a) RICH1 layout.

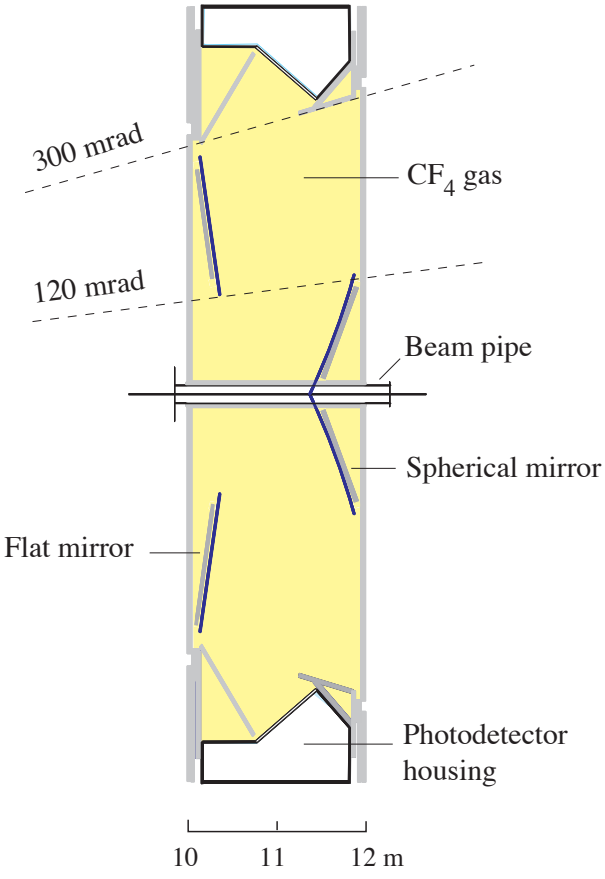

(b) RICH2 layout.

Figure 2.9: Ring Imager Cherenkov detectors layouts.

It is worth noting that information coming from the tracking and the calorimeter systems (taking into account the correlations between the subsystems) can be combined into a single variable called ProbNN by making use of multivariate techniques. Requirements on how likely a particle is a proton (or whatever track reconstructible in LHCb detector) can be hence made by setting cuts on ProbNN variables. Those variables are further used in the selection that is described in the next chapter.

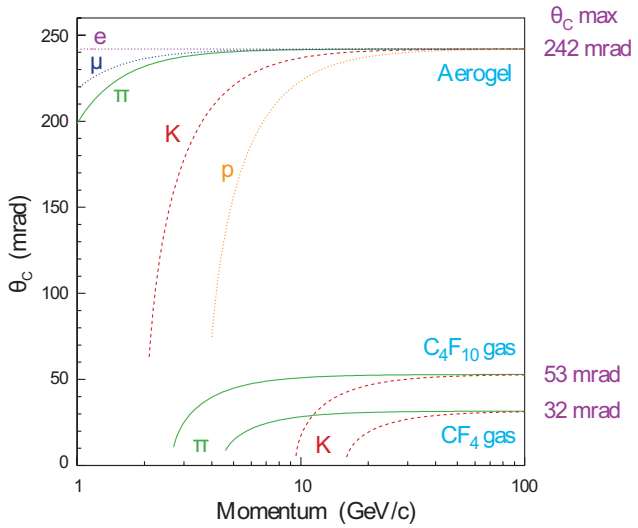

Figure 2.10: Cherenkov angle as a function of different particle momenta for the radiators of RICH1 and RICH2.

2.2.5 The Calorimeter system

The calorimeter system has several functions: on one hand, it selects high-transverse energy candidates, such as hadrons, electrons, photons or π^0, for the first level of trigger of the experiment (L0). On the another hand, it measures electromagnetic energy and position and provides consequently the identification of electrons and photons, that is mandatory for flavour tagging information, lepton flavour universality studies or radiative decays studies. Additionally, the calorimeter system provides identification of π^0 which is a key ingredient for studying *CP*-eigenstates. In order to have a fast identification of an electromagnetic object in a high multiplicity environment, a longitudinal segmentation of the shower is done by making use of several layers: the Scintillating Pad Detector (SPD), the Pre-Shower detector (PS), the Electromagnetic CALorimeter (ECAL) and the Hadronic CALorimeter (HCAL).

- The SPD (installed in front of the PS) determines whether particles hitting the calorimeter system are charged or neutral while the PS indicates the electromagnetic nature of the particle (whether it is an electron or a photon). Both consist of scintillating pads of 15 mm inter-spaced with 2.5 radiation lengths (X_0) lead converter. The lead thickness has been determined as the trade-off between trigger performance and ultimate energy resolution.

- The choice of the ECAL thickness is mostly motivated by having an optimal energy resolution: 25 X_0 has hence been chosen in order to get the full containment of the showers from high energy photons. ECAL is designed with a sampling scintillator/lead structure readout by plastic wavelength shifting (WLS) fibres (Shashlik calorimeter).

- Eventually, the HCAL is 5.6 X_0 thick, since it is mostly used at the L0 trigger stage (and since the place is limited).

A variable lateral segmentation is also in order for the four calorimeter-system sub-detectors, since the hit density varies over the calorimeter surface. Three different sections of elementary cells have been chosen both for the SPD/PS and ECAL. The three sub-detectors are coherently segmented in order to have a projective system. The HCAL in contrast is only segmented into two zones with larger cell sizes because of the hadronic showers dimensions.

2.2.6 The Muon system

The muon system is dedicated both to triggering and muon-identification and is hence providing high-p_T candidates for the L0 trigger decision (further detailed in the next Section). Five rectangular stations are installed along the beam axis (called M1 to M5), gradually increasing in size and covering a combined area of 435 m^2. The first station is placed in front of the calorimeter system while M2 to M5 stations are placed after the HCAL. Each station is divided in four regions (R1 to R4) whose granularity is shaped according to the expected particle density in the region. The outermost part active detectors are equipped with Multi Wire Propotional Chambers (MWPC) while triple-Gas Electron Multipliers (GEM) are used in the innermost part of the M1 detector in order to cope with the high charged tracks multiplicity at this position. Eventually, the last four stations are interleaved with 80 cm thick iron absorbers aiming at stopping hadrons.

2.3 The trigger

The trigger purpose is to reduce the data rate while accepting most of the interesting events. Although the bunch crossing rate is about 40 MHz, the LHC's designed luminosity in the LHCb collision point is producing interactions at a level of 10 MHz. Still, this effective crossing frequency has to be reduced to about 20 kHz which corresponds to the current limitation for writing events to storage. This is achieved in two trigger levels: the hardware Level 0 (L0) and the software High Level Trigger (HLT). The first is part of the front-end electronics and is synchronously operating with the 40 MHz bunch crossing rate. It consequently makes use of the fastest sub-detectors (Pile-up system which is related to the VELO, calorimeters and muon systems). The HLT system is making use of the full event data and aims at reducing the data rate from 1 MHz to about 20 kHz. An illustration of the 2015 trigger scheme is displayed on Fig. 2.11.

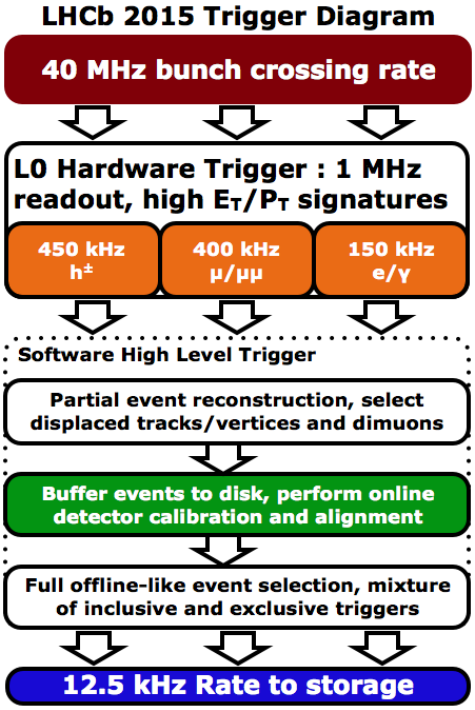

Figure 2.11: LHCb trigger diagram. We take note that the rate of storage steadily increased during the LHCb operation, to reach about 20 kHz in the current operation.

2.3.1 Level L0 - Hardware trigger

As previously emphasised, the L0 trigger makes use of the fastest components of the LHCb detector. Hence, information from the pile-up system, the calorimeters and the muon system are compiled into a single electronics board (Level 0 Decision Unit, L0DU) in order to take a final decision on the event. Each event is thus asked to satisfy a set of requirements, whose a summary is available in Ref. [34] for the years of data taking considered in this analysis. At this hardware stage, events are required to have a muon with high p_{T} or a hadron, photon or electron with high transverse energy. If any of the alley passes the threshold cut, the event is passed to the HLT trigger. Henceforth, trigger signals are associated with reconstructed particles and selection requirements can therefore be made on whether the decision was due to the signal candidate (L0 Trigger On Signal, L0TOS), other particles produce in pp collision (L0 Trigger Independant of Signal, L0TIS) or a combination or both.

2.3.2 HLT - Software trigger

The HLT is requiring a maximal event rate of 1 MHz as input. It is further split in two stages:

- HLT1: the process performs partial reconstruction of the event, combining L0 information with additional inputs coming from the VELO and the tracker. Four selection processes are defined with respect to the reconstructed candidates at the L0 (muon, dimuon, hadron and electromagnetic particles such as photon, electron and π^0). They starts with the PV reconstruction as well as the association of the L0 candidates with the tracks reconstructed by the VELO. Requirements on the position of the displaced vertex and on the Impact parameter (IP) of the candidates are then in order. Eventually, the reconstruction is completed by Trigger Tracker (TT) and all tracker system information that is used in order to require at least one charged particle with a transverse momentum $p_{\mathrm{T}} > 1.7(1.6)\,\mathrm{GeV}/c$ for 2011(2012).

- HLT2: the process applies inclusive and exclusive selections using the full event data. It aims at reducing the data rate to an affordable rate (around 20 Khz) For the analyses presented in this document, we are using HLT2 inclusive trigger based on topological selection of a 2 to 4 tracks displaced vertex.

2.3.3 Trigger requirements for this analysis

Measurements of branching fractions of charmless 4-body decays of Λ_b^0 and/or Ξ_b^0 are provided in this analysis. In addition, $\Delta\mathcal{A}^{CP}$ measurements are performed. The following chapters are discussing the tools that are used in $\mathcal{B}F$ and $\Delta\mathcal{A}^{CP}$ derivations. Although a non-negligible part of the technology employed is shared by the two types of measurements, differences in the trigger requirements are in order.

- For the branching fractions purpose, it is important to minimise the variation of selection efficiency over the phase space of the decays of interest. Consequently, the strategy employed is that signal candidates are selected from events in which the hardware trigger requirements are satisfied by other activity in the event. This choice is further discussed in Section 5.2.

- Conversely, both (L0TOS and L0TIS) requirements are considered for $\Delta\mathcal{A}^{CP}$ measurements. This brings more statistics but implies to correct measured asymmetries for the L0TOS trigger efficiencies. This is further detailed in Section 6.3

Chapter 3

The selection of the signals and the simultaneous fitter

This section is dedicated to the simultaneous fitter technology. The fit model will be further discussed in Section 4. A part of the material presented in this section (*i.e.* part of the Section 3.2) has been developed prior to the beginning of my Ph.D. Few elements of the selection are indeed directly related to the simultaneous fitter strategy and have hence to be briefly presented. This is aiming at providing to the reader a complete understanding of the analysis. Some technical details are also given that a reader external to LHCb can advantageously skip.

Chapter contents

3.1 Data and Monte Carlo samples

The results described in this analysis are obtained using the full Run I data collected by LHCb at the LHC at a center-of-mass energy of $\sqrt{s} = 7$ TeV for the 2011 campaign and $\sqrt{s} = 8$ TeV for the 2012 campaign. The 2011 data sample corresponds to an integrated luminosity of $\int \mathcal{L} dt = 1\,\text{fb}^{-1}$, while the 2012 one data corresponds to $\int \mathcal{L} dt = 2\,\text{fb}^{-1}$. The number of events stored by LHCb is huge, and it requires offline selection (whose first step consits in stripping the data) in order to remove events which are not of interest. Consequently, data used in this analysis are stripped during the Stripping21 campaign using Stripping21r1 for the 2011 data and Stripping21 for the 2012 data, both using the StrippingXb2phhhLine. Monte Carlo (MC) generated samples are used to study the behaviour of the signal and

background events (both signal cross-feeds and B meson decays), in order to model the invariant mass lineshapes of signals, signal cross-feeds and backgrounds. The numbers of MC events produced for each decay mode (signal and background) and year are summarised in Table 3.1. About 50% of these events are produced with MagDown detector configuration, and the other half is produced with MagUp detector configuration. As far as signal events are concerned, the simulated samples contain two extreme decay dynamics: one is nonresonant (phase space) and the other considers quasi-2-body decays involving either a N^{*0} or Λ^{*0} baryon associated with a low-mass meson. This mixture will be advantageously used in order to determine ranges for systematic uncertainties that are related to the phase space of the decay: the true signal dynamics (*a priori* unknown) lies in the range of the two extreme cases.

The stripping line used in this analysis was designed in a way to preserve the low two-body invariant-mass region, specifically the ph invariant mass where the $\Lambda^{*0}(1520)$ and $N^{*0}(1520)$ are expected to be present. As such, only a loose kinematical cut is applied on the daughter tracks and no kinematical cut on the two-body pairs is applied. This is providing two advantages: it allows on one hand to perform branching fraction measurements with an affordable variation of efficiencies over the phase space for a given configuration of trigger (this is further discussed in Section 5). On another hand, it allows to search for CP-asymmetries in low two-body invariant mass region. Measurements of $\Delta\mathcal{A}^{CP}$ are consequently performed in different regions of the phase space of the decays are further discussed in Section 7. Eventually, the summary of the stripping line selection cuts is presented in Table 3.2.

Table 3.1: Number of generated signal and background MC events used in this analysis.

Decay mode	Event type	Year	Yield	Resonances included (in %)
$\Lambda_b^0 \to p\pi^-\pi^+\pi^-$	15204010	2011 (2012)	1033876 (2025489)	PHSP [0.35] + N^{*0} $\{\rho^0, f_2\}$ [0.65]
$\Lambda_b^0 \to pK^-\pi^+\pi^-$	15204011	2011 (2012)	1046073 (2017682)	PHSP [0.30] + Λ^{*0} $\{\rho^0, f_2, K^{*0}, K\pi\}$ [0.70]
$\Lambda_b^0 \to pK^-K^+\pi^-$	15204012	2011 (2012)	1025976 (2011991)	PHSP [0.35] + Λ^{*0} $\{K^{*0}, K\pi\}$ [0.65]
$\Lambda_b^0 \to pK^-K^+K^-$	15204013	2011 (2012)	1032138 (2019736)	PHSP [0.35] + Λ^{*0} $\{\phi^0, f_2'\}$ [0.65]
$\Xi_b^0 \to pK^-\pi^+\pi^-$	16204040	2011 (2012)	1021760 (2037415)	PHSP [0.30] + Λ^{*0} $\{\rho^0, f_2, K^{*0}, K\pi\}$ [0.70]
$\Xi_b^0 \to pK^-\pi^+K^-$	16204041	2011 (2012)	1001562 (2024475)	PHSP [0.35] + Λ^{*0} $\{K^{*0}, K\pi\}$ [0.65]
$\Xi_b^0 \to pK^-K^+K^-$	16204042	2011 (2012)	1051785 (2067281)	PHSP [0.35] + Λ^{*0} $\{\phi^0, f_2'\}$ [0.65]
$\Lambda_b^0 \to (\Lambda_c^+ \to pK\pi)\pi$	15264011	2012	1011237	$\Lambda_b^0 \to (\Lambda_c^+ \to pK^-\pi^+)\pi^-$ [1.00]
$\Lambda_b^0 \to pK^-(\eta' \to \pi^+\pi^-\gamma)$	15104201	2011 (2012)	3036303 (6064043)	$\Lambda_b^0 \to pK^-(\eta' \to \pi^+\pi^-\gamma)$ [1.00]
$B^0 \to \pi^+\pi^-\pi^+\pi^-$	11104061	2011 (2012)	1557242 (3005995)	$B^0 \to \rho^0(\pi^+\pi^-)\rho^0(\pi^+\pi^-)$ [1.00]
$B^0 \to K^+\pi^-\pi^+\pi^-$	11104041	2011 (2012)	2048997 (4021486)	$B^0 \to K^{*0}(K^+\pi^-)\rho^0(\pi^+\pi^-)$ [1.00]
$B^0 \to K^+K^-K^+\pi^-$	11104020	2011 (2012)	2043494 (4017984)	$B^0 \to \phi^0(K^+K^-)K^{*0}(K^+\pi^-)$ [1.00]
$B_s^0 \to K^+\pi^-\pi^+K^-$	13104001	2011 (2012)	1014357 (2037039)	$B_s^0 \to K^{*0}(K^+\pi^-)\overline{K}^{*0}(\pi^+K^-)$ [1.00]
$B_s^0 \to K^+K^-K^+K^-$	13104013	2011 (2012)	1035749 (1025247)	$B_s^0 \to \phi^0(K^+K^-)\phi^0(K^+K^-)$ [1.00]
$B^+ \to K^+\pi^-\pi^+\pi^-\pi^+$	12105011	2011 (2012)	2066498 (4044480)	$B^+ \to K^+\pi^-\pi^+\pi^-\pi^+$ [1.00]

A cut on the $p_{\mathrm{T}} > 400$ MeV of each daughter track is included in the generation of the $B_s^0 \to \phi^0(K^+K^-)\phi^0(K^+K^-)$ MC sample.

3.2 Selection

3.2.1 Offline selection

The neutral b-baryon candidates, henceforth denoted X_b, are formed from a proton candidate selected with particle identification (PID) requirements and three additional charged tracks.

Table 3.2: Cuts applied in the stripping line StrippingXb2phhhLine selecting the candidate events.

Variable definition	Selection requirements
Cuts on daughter tracks (p,π)	
Daughter tracks' momentum	$p > 1500.$ MeV/c
Daughter tracks' transverse momentum	$p_{\mathrm{T}} > 250.$ MeV/c
Daughter tracks' χ^2 over degrees of freedom	Trk. $\chi^2/\mathrm{ndf} < 3.0$
Daughter tracks' minimum impact parameter χ^2 to any PV	Min. $\chi^2_{\mathrm{IP}} > 16.0$
Daughter tracks' probability of being a ghost track	Prob$ghost < 0.40$
Proton track's probability of being a proton	ProbNN$p > 0.05$
Combination cuts (before vertex fit)	
Mass of the X_b^0 candidate with $pKKK$ tracks hypothesis	$m_{pKKK} > 5195.$ MeV/c^2
Mass of the X_b^0 candidate with $p\pi\pi\pi$ tracks hypothesis	$m_{p\pi\pi\pi} < 6405.$ MeV/c^2
X_b^0 candidate's transverse momentum	$p_{\mathrm{T}} > 1500.$ MeV/c
Sum of the daughter tracks' transverse momentum	$\Sigma_{\mathrm{daug.}} p_{\mathrm{T}} > 3500.$ MeV/c
Distance of closest approach χ^2 of any two daughters	$\chi^2_{\mathrm{DOCA}} < 20.$
Combination cuts (after vertex fit)	
X_b^0 candidate's vertex χ^2	$\chi^2_{\mathrm{vtx}} < 20.$
X_b^0 candidate's flight distance χ^2 w.r.t. best PV	$\chi^2_{\mathrm{FD}} > 50.$
X_b^0 candidate's impact parameter χ^2 w.r.t. best PV	$\chi^2_{\mathrm{IP}} < 16.$
Cosine of the X_b^0 candidate pointing angle	$\cos(\theta_{\mathrm{DIRA}}) > 0.9999$

When more than one PV is reconstructed, the X_b candidate is associated with the PV with which it forms the smallest χ^2_{IP}, where χ^2_{IP} is the difference in χ^2 of a given PV reconstructed with and without the considered X_b candidate. Each of the four tracks of the final state is required to have $p < 100\,\mathrm{GeV}/c$, a value beyond which there is little pion/kaon/proton discrimination, and $\chi^2_{\mathrm{IP}} > 16$. The fraction of events containing more than one candidate is below the percent level. The candidate to be retained in each event is chosen randomly and in a reproducible way. The X_b candidates are then required to form a vertex with a fit quality $\chi^2_{\mathrm{vtx}} < 20$ with 5 degrees of freedom and be significantly separated from any PV with $\chi^2_{\mathrm{FD}} > 50$, where χ^2_{FD} is the square of the flight-distance significance. To remove backgrounds from higher-multiplicity decays, the difference in χ^2_{vtx} when adding any other track must be greater than 4. The X_b candidates must have $p_{\mathrm{T}} > 1.5\,\mathrm{GeV}/c$ and invariant mass within the range $5340 < m(phhh) < 6400\,\mathrm{MeV}/c^2$, where h stands for either a charged pion or kaon. They are further required to be consistent with originating from a PV, quantified by both the χ^2_{IP} and the "pointing angle" between the reconstructed momentum of the b-hadron and the vector defined by the associated PV and the decay vertex. Finally, PID requirements are applied to provide discrimination between kaons and pions in order to assign the candidates to one of the five different final-state spectra $p\pi\pi\pi$, $pK\pi\pi$, $pKK\pi$, $pK\pi K$ and $pKKK$.

3.2.2 K/π PID selection optimisation

There are three main categories of background that contribute significantly in the selected invariant-mass regions. Although the identification of the background contributions is further discussed in chapter 4, we already can introduce few of them, since the selection is aiming to reject: the so-called signal "cross-feed" backgrounds resulting from a misidentification of one or more final-state particles; the charmless decays of neutral B mesons to final states

containing four charged mesons, where a pion or a kaon is misidentified as a proton; and the combinatorial backgrounds, which result from a random association of tracks with at least one track unrelated to the vertex of interest. The pion and kaon PID requirements that define mutually exclusive samples are optimised to reduce the signal cross-feed background, and hence to maximise the observation of the signal. The particle identification (PID) variables defined in Eq. 3.1 and Eq. 3.2 are used to select kaons and pions. As a short-hand notation, from hereon we refer PID_K and PID_π as the variables defined in Eq. 3.1 and Eq. 3.2, respectively. It happens that the same optimal cut values are found for kaons and pions, and hence collectively refer them in the later part of this analysis as $\text{PID}_{K\pi}$. Mathematically, the PID cuts are given by,

$$\text{PID}_K : ((h\_\text{ProbNN}\pi - 1.0)^2 + h\_\text{ProbNN}K^2) > a_K^{\text{cut}} \tag{3.1}$$

$$\text{PID}_\pi : ((h\_\text{ProbNN}\pi - 1.0)^2 + h\_\text{ProbNN}K^2) < a_\pi^{\text{cut}} \ , \tag{3.2}$$

where h can be a kaon or a pion depending on which spectrum it is applied.

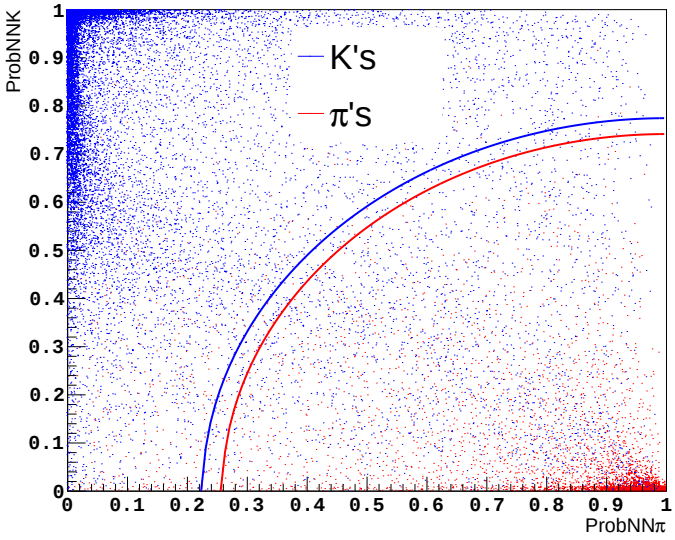

Figure 3.1: Illustration of the distribution of kaons and pions in the ProbNNK-vs-ProbNNπ plane using MC-matched kaons and pions from MC-generated $\Lambda_b^0 \to pK^-\pi^+\pi^-$ events.

The ProbNN variables[a] of kaons and pions from real data are not well described by the MC-calculated ProbNN variables. To correct this discrepancy, a set of PID (mis)identification efficiency maps for each a_π^{cut} and a_K^{cut} cut values is prepared in bins of momentum p and pseudo-rapidity angle η, knowing that the PID (mis)identification efficiency depends on the kinematics of the particles. The binning scheme used in producing the efficiency maps[b] for each year and each particle type is summarised in Table 3.3. A MC-generated event is then used to calculate the kinematics of the tracks, which are in turn employed to calculate the efficiency of an event to pass a certain a_π^{cut} and/or a_K^{cut} cut values taking into account correlations. These event-by-event efficiencies are then averaged to calculate the probability of a certain decay mode to pass the $\text{PID}_{K\pi}$ cut values.

The optimal $\text{PID}_{K\pi}$ cuts for each mode are summarised in Table 3.4. The optimal $\text{PID}_{K\pi}$ a_π^{cut} and a_K^{cut} cuts for the baseline mode are 0.15 and 0.15, as shown in Fig. 3.2. The other

[a] A definition of ProbNN variables is provided in 2.2.4.

[b] The $\text{PID}_{K\pi}$ efficiency maps for the optimal a_π^{cut} and a_K^{cut} are shown in Appendix B.1.

Table 3.3: The binning scheme used to produce the $\mathrm{PID}_{K\pi}$ (mis)identification efficiency maps. Bins boundaries are defined to have approximately the same number of events.

Particle type (year)	p binning boundaries (in GeV/c^2)	η binning boundaries
K's (2011)	{3000; 9300; 15600; 18515; 28325; 40097; 59717; 100000}	{1.5; 2.4975; 2.7075; 3.0575; 3.3725; 3.7225; 4.0025; 5.0}
K's (2012)	{3000; 9300; 15600; 16553; 26363; 38135; 57755; 100000}	{1.5; 2.4625; 2.6725; 2.9875; 3.3025; 3.6525; 3.8975; 5.0}
π's (2011)	{3000; 9300; 15600; 16553; 24401; 36173; 55793; 100000}	{1.5; 2.4625; 2.7075; 3.0225; 3.3375; 3.6875; 3.9675; 5.0}
π's (2012)	{3000; 9300; 14591; 15600; 24401; 34211; 53831; 100000}	{1.5; 2.4275; 2.6375; 2.9525; 3.2675; 3.6175; 3.8975; 5.0}

modes did not satisfy the condition stated above and hence their $\mathrm{PID}_{K\pi}$ cut is chosen to be the same as the $\mathrm{PID}_{K\pi}$ of the baseline mode, i.e., ($a_\pi^{\mathrm{cut}} = 0.15$, $a_K^{\mathrm{cut}} = 0.15$).

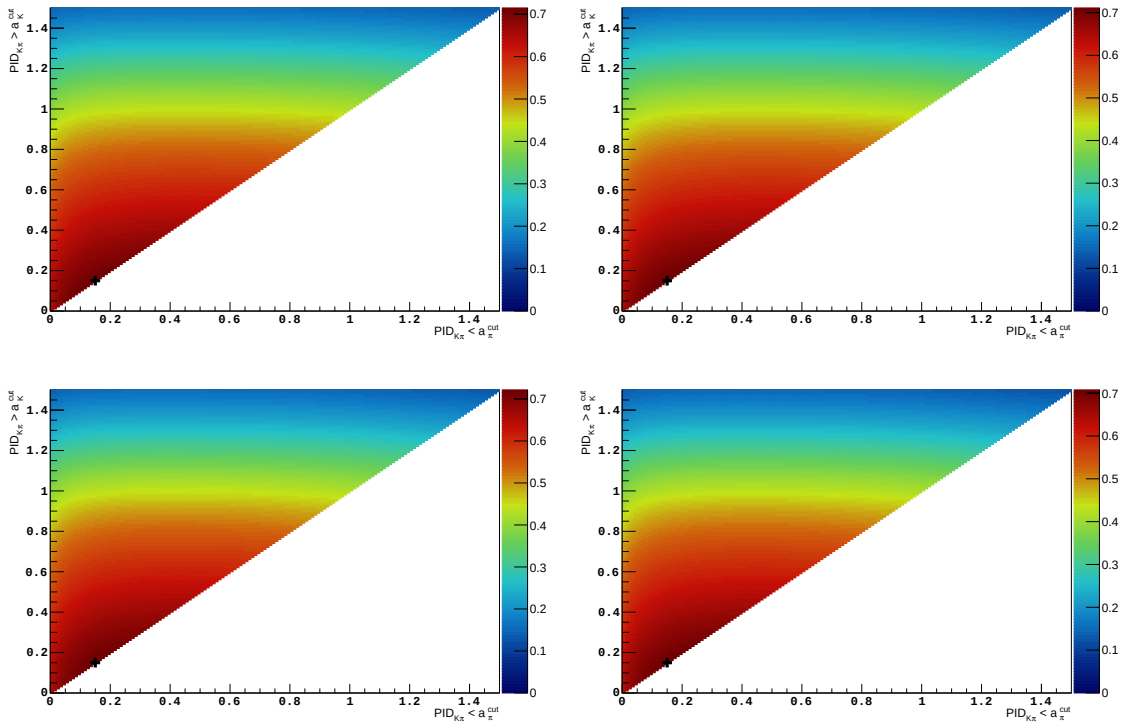

Figure 3.2: Figure of merits of $\mathrm{PID}_{K\pi}$ optimisation of $\Lambda_b^0 \to pK^-K^+\pi^-$ for [top-left] 2011 MagDown, [top-right] 2011 MagUp, [bottom-left] 2012 MagDown and [bottom-right] 2012 MagUp.

3.2.3 MVA selection optimisation

In order to reject combinatorial backgrounds, multivariate discriminators based on a boosted decision tree (BDT) [35] with the AdaBoost algorithm [36] have been designed. Candidates from simulated $\Lambda_b^0 \to p\pi^-\pi^+\pi^-$ events and the data high-mass side-band are used as the signal and background training samples, respectively. This high-mass side-band region is

Table 3.4: The list of optimal $\text{PID}_{K\pi}$ a_π^{cut} and a_K^{cut} cuts.

Signal mode	2011 optimal $\text{PID}_{K\pi}$ cuts (a_π^{cut}, a_K^{cut})		2012 optimal $\text{PID}_{K\pi}$ cuts (a_π^{cut}, a_K^{cut})	
	MagDown	MagUp	MagDown	MagUp
$\Lambda_b^0 \to pK^-K^+\pi^-$	**(0.15, 0.15)**	**(0.15, 0.15)**	**(0.15, 0.15)**	**(0.15, 0.15)**
$\Lambda_b^0 \to p\pi^-\pi^+\pi^-$	(1.00, 1.00)	(1.00, 1.00)	(1.00, 1.00)	(1.00, 1.00)
$\Xi_b^0 \to pK^-\pi^+\pi^-$	(0.55, 0.55)	(0.55, 0.55)	(0.55, 0.55)	(0.55, 0.55)
$\Xi_b^0 \to pK^-\pi^+K^-$	(0.35, 0.35)	(0.35, 0.35)	(0.35, 0.35)	(0.35, 0.35)
$\Xi_b^0 \to pK^-K^+K^-$	(0.30, 0.30)	(0.30, 0.30)	(0.30, 0.30)	(0.30, 0.30)

chosen so that the sample is free of signal cross-feed background. The samples are divided into two data-taking periods and further subdivided into two equally sized sub-samples. Each sub-sample is then used to train an independent discriminant. In the subsequent analysis the BDT trained on one sub-sample is used to select candidates from the other sub-sample, in order to avoid any bias.

The BDTs have as input discriminating quantities the p_{T}, η, χ^2_{IP}, χ^2_{FD}, pointing angle and χ^2_{vtx} of the X_b candidate; the smallest change in the b-baryon χ^2_{vtx} when adding any other track from the event; the sum of the χ^2_{IP} of the four tracks of the final state; and the p_{T} asymmetry

$$p_{\text{T}}^{\text{asym}} = \frac{p_{\text{T}}^B - p_{\text{T}}^{\text{cone}}}{p_{\text{T}}^B + p_{\text{T}}^{\text{cone}}}\,, \tag{3.3}$$

where $p_{\text{T}}^{\text{cone}}$ is the transverse component of the sum of all particle momenta inside a 1.5 rad cone in η and ϕ space around the b-baryon candidate direction. The $p_{\text{T}}^{\text{asym}}$ of the signal candidates are preferentially distributed towards high values. The BDT output is determined to be uncorrelated with the position in the phase space of the decay of interest. The figure 3.3 indicates that there is no obvious sign of overtraining, as also indicated by the Kolmogorov-Smirnov tests.

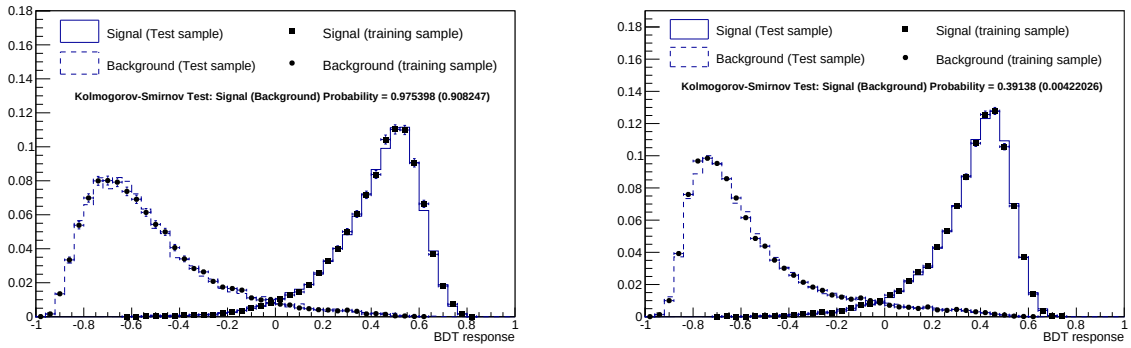

Figure 3.3: BDT response for (left) combined 2011 BDTs and (right) combined 2012 BDTs.

The selection requirement placed on the output of the BDTs is independently optimised for the seven decays of interest by maximising the Figure of Merit [37]

$$\text{FoM} = \frac{\varepsilon_{\text{sig}}}{\frac{a}{2} + \sqrt{N_B}}\,, \tag{3.4}$$

where the signal efficiency (ε_{sig}) is estimated from the simulation and N_B represents the number of expected background events for a given selection, which is calculated by fitting

the high-mass side-band of the data sample, and extrapolating the yield into the signal region defined as the invariant mass window covering $\pm$ 3 times the measured signal width. The value $a = 2$ is used in this analysis. For the branching fraction measurements, a common optimisation of the BDT criteria is found, resulting in a signal efficiency of order 70%. The Figures of Merit for all the modes are displayed on Fig. 3.4. In the case of $X_b^0 \to pK\pi\pi$ and $X_b^0 \to pKKK$ spectra where both Λ_b^0 and Ξ_b^0 signals are present, the Ξ_b^0 signals are chosen to be optimised. The optimal BDT cuts are lying in a range [0.2 - 0.4] for all spectra. Dictated by a sake of simplicity of bookkeeping, a unique BDT cut value of 0.30 is chosen for all the charmless spectra. Eventually, a re-optimisation of the BDT cut is performed for $\Delta\mathcal{A}^{CP}$ measurements. This is further discussed in Chapter 7

3.2.4 Proton PID cut

Common to all the signal modes, both in the charmless and control channels, is the presence of the proton track. Hence, the efficiencies of signal and cross-feeds are basically the same, up to the difference in kinematics, for each ProbNNp cut value. A cut on PID (ProbNNp) is however necessary to reduce and/or reject the physics backgrounds coming from the 4-body and 5-body decays of $B_{d,s}^0$ and B^+. When a pion or a kaon from these decays is mis-identified as a proton, the event can appear in the invariant mass distribution of $phhh$ as a background and potentially yield a CP asymmetry. The inclusive branching fractions of most of the $B_{d,s}^0$ and B^+ decays to fully-charged 4-body and 5-body are yet unmeasured but their experimental upper limits, when they exist, are typically of order $\mathcal{O}(10^{-4})$. Moreover, the hadronisation fraction of b quark to B^0 and B^+ is larger than the hadronisation fraction to Λ_b^0 and Ξ_b^0. Although the hadronisation fraction of b quark to B_s^0 is smaller than its hadronisation fraction to Λ_b^0, it can still populate the spectra significantly if not properly reduced. Hence, to reduce these B physics backgrounds, an arbitrary ProbNN$p > 0.50$ PID cut is applied on the proton track. This is guesstimated to remove significant amount of these backgrounds while keeping most of our signal events. The distributions of these background events and its modelling are discussed in 4.4.4. As for the BDT cut value, a re-optimisation of the ProbNNp cut is eventually performed for $\Delta\mathcal{A}^{CP}$ measurements. This is further discussed in Chapter 7.

For the same reason stated in 3.2.2 that the ProbNN variables are not well-described in MC, a PID re-weighting is needed to properly calculate the (mis)identification efficiency[c]. Proton tracks coming from real data inclusive Λ_c^+ decays are used to produce the identification efficiency map of proton using the PIDCalibTool. The differences in track multiplicity between the proton identification performance in the PID calibration sample and in the signal data (as measured for the normalisation sample) require an enhanced granularity of the binning scheme of the PID calibration sample to derive the signal efficiency. This very scheme will be used as well to correct the modelling of the shapes of the signal, cross-feed signals and B decays backgrounds, described in 4.4.1. In addition to the segmentation in p and η of the tracks, the PID calibration sample is further binned in event track multiplicity N_{tracks}. The binning scheme is reported in 3.5. It has been chosen to also adopt this more complete segmentation for the re-weighting of the K/π candidates. The 3D PID$_p$ and PID$_{K\pi}$ efficiency maps can be found at Appendix B.2 and B.3, respectively.

[c]These numbers are inputs of the Gaussianly-constrained cross-feed yields in the fit as will be detailed in 4.4.3.

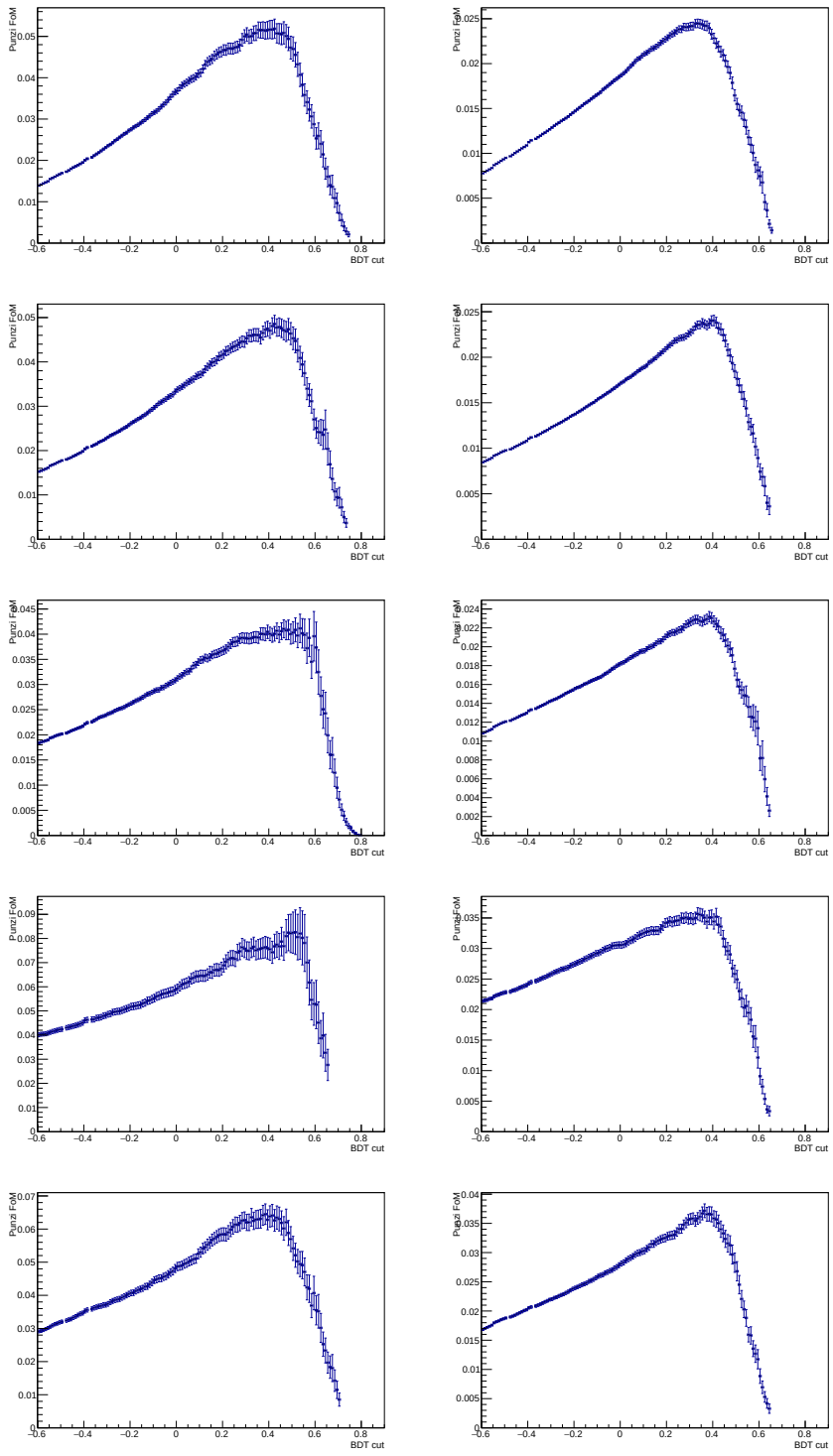

Figure 3.4: Punzi figures of merit for BDT cut optimisation for the spectra (from top to bottom) $X_b^0 \to p\pi\pi\pi$, $X_b^0 \to pK\pi\pi$, $X_b^0 \to pKK\pi$, $X_b^0 \to pKKK$ and $X_b^0 \to pK\pi K$. Figures on the left column are for the 2011 data and figures on the right column are for the 2012 data.

3.2.5 Charm veto cuts

A number of background contributions consisting of fully reconstructed b-baryon decays into the two-body $\Lambda_c^+ h$, $\Xi_c^+ h$, three-body Dph or $(c\bar{c})ph$ combinations, where $(c\bar{c})$ represents a charmonium resonance, may produce the same final state as the signal. Hence, they will have the same b-baryon candidate invariant mass distribution as the signal candidates, as

Table 3.5: The binning scheme used to produce the PID_p (mis)identification efficiency maps. Bins boundaries are defined to have the same number of events.

Particle type (year)	p binning boundaries (in GeV/c^2)	η binning boundaries	N_{tracks}
p's (2011)	{3000; 9300; 15600; 18515; 28325; 40097; 59717; 100000}	{1.5; 2.4975; 2.7075; 3.0575; 3.3725; 3.7225; 4.0025; 5.0}	{0;100;150;200; 270;500}
p's (2012)	{3000; 9300; 15600; 16553; 26363; 38135; 57755; 100000}	{1.5; 2.4625; 2.6725; 2.9875; 3.3025; 3.6525; 3.8975; 5.0}	{0;100;150;200; 270;500}

well as a similar selection efficiency. The presence of a misidentified hadron in the D, Λ_c^+ and Ξ_c^+ decay also produces peaking background under the signal. Therefore, the following decay channels are explicitly reconstructed under the relevant particle hypotheses and vetoed by means of a requirement on the resulting invariant mass, in all experimental spectra: Λ_c^+ ($\to pK^-\pi^+, p\pi^+\pi^-, pK^+K^-$), Ξ_c^+ ($\to pK^-\pi^+$), D^+ ($\to K^-\pi^+\pi^+$), D_s^+ ($\to K^-K^+\pi^+$), D^0 ($\to K^\mp\pi^\pm, \pi^+\pi^-, K^+K^-$), χ_{c0} and J/ψ ($\to \pi^+\pi^-, K^+K^-$). The same set of trigger, PID and BDT requirements is applied to the control channels $\Lambda_b^0 \to (\Lambda_c^+ \to p\pi^-\pi^+)\pi^-$, $\Lambda_b^0 \to (\Lambda_c^+ \to pK^-\pi^+)\pi^-$ and $\Xi_b^0 \to (\Xi_c^+ \to pK^-\pi^+)\pi^-$ to cancel out most of the systematic effects related to the selection criteria. Candidates whose $pK^-\pi^+$ invariant mass is in the range $2213 < m(pK^-\pi^+) < 2313$ MeV/c^2 are retained as normalisation-mode candidates. Conversely, events outside this interval belong to the signal $pK\pi\pi$ spectrum, again ensuring statistically independent samples for the simultaneous fit. The list of charm veto cuts is gathered in Table 3.6. The distributions of the vetoed invariant masses for the dominant mode for 2012 are displayed in Appendix B.4 as an illustration. For labelling purposes, the four charged tracks in each spectrum are arranged in this sequence: $(ph^-h^+h^-)$ or $(\overline{p}h^+h^-h^+)$. Hence, the proton is labelled as h_1, and the remaining h's are labelled h_2, h_3 and h_4 in a charge arrangement defined in the previous sentence. For example, the notation $h_ih_jh_k\_p\pi\pi$ means the reconstructed invariant mass of the combination, where h_i is assigned with the mass of the proton, while h_j and h_k are assigned with the mass of the pion.

3.3 Simultaneous fitter

A simultaneous unbinned extended maximum likelihood fit is performed to the b-hadron candidate invariant-mass distributions under each of the five sets of mass hypotheses for the final-state tracks and control channels. The data samples are further split according to the charge of the proton, to the year of data taking (and to trigger requirements for the $\Delta\mathcal{A}^{CP}$ purpose). The components of the model include, in addition to the signal decays, the partially reconstructed five-body X_b^0 decays, the signal and background cross-feeds, the four- and the five-body decays of B-mesons and the combinatorial background. A detailed background identification as well as the modelling of each of these components are provided in Chapter 4. The independent data samples constructed for each experimental reconstructed spectrum are fitted simultaneously. For each sample, the likelihood is expressed as

$$\ln \mathcal{L} = \sum_i \ln \left(\sum_j N_j P_{j,i} \right) - \sum_j N_j \tag{3.5}$$

where N_j is the number of events related to the component j and P_i the probability of the event i. A modified version of V0hhFitter is used as a tool to simultaneously fit the invariant

Table 3.6: List of charm veto cuts applied on the data.

Charmed resonance	Decay	Cut applied (mass in units of MeV/c^2)
Λ_c^+	$\Lambda_c^+ \to p\pi^-\pi^+$	$\lvert 2283.00 - h_1h_2h_3\_p\pi\pi\rvert > 30.$ and $\lvert 2283.00 - h_1h_4h_3\_p\pi\pi\rvert > 30.$
	$\Lambda_c^+ \to pK^-\pi^+$	$\lvert 2262.50 - h_1h_2h_3\_pK\pi\rvert > 52.5$ and $\lvert 2262.50 - h_1h_4h_3\_pK\pi\rvert > 52.5$
	$\Lambda_c^+ \to pK^-K^+$	$\lvert 2283.00 - h_1h_2h_3\_pKK\rvert > 30.$ and $\lvert 2283.00 - h_1h_4h_3\_pKK\rvert > 30.$
Ξ_c^+	$\Xi_c^+ \to pK^-\pi^+$	$\lvert 2467.80 - h_1h_2h_3\_pK\pi\rvert > 30.$ and $\lvert 2467.80 - h_1h_4h_3\_pK\pi\rvert > 30.$
$\overset{(-)}{D^0}$	$\overset{(-)}{D^0} \to \pi^-\pi^+$	$\lvert 1864.84 - h_2h_3\_\pi\pi\rvert > 30.$ and $\lvert 1864.84 - h_4h_3\_\pi\pi\rvert > 30.$
	$\overset{(-)}{D^0} \to K^-K^+$	$\lvert 1864.84 - h_2h_3\_KK\rvert > 30.$ and $\lvert 1864.84 - h_4h_3\_KK\rvert > 30.$
	$D^0 \to \pi^+K^-$	$\lvert 1864.84 - h_2h_3\_K\pi\rvert > 30.$ and $\lvert 1864.84 - h_4h_3\_K\pi\rvert > 30.$
	$\overline{D}^0 \to \pi^-K^+$	$\lvert 1864.84 - h_2h_3\_\pi K\rvert > 30.$ and $\lvert 1864.84 - h_4h_3\_\pi K\rvert > 30.$
D^+	$D^+ \to \pi^+K^-\pi^+$	$\lvert 1869.61 - h_2h_3h_4\_\pi K\pi\rvert > 30.$
D_s^+	$D_s^+ \to K^+K^-\pi^+$	$\lvert 1968.30 - h_2h_3h_4\_KK\pi\rvert > 30.$ and $\lvert 1968.30 - h_2h_3h_4\_\pi KK\rvert > 30.$
	$D_s^+ \to \pi^+\pi^-\pi^+$	$\lvert 1968.30 - h_2h_3h_4\_\pi\pi\pi\rvert > 30.$
J/ψ	$J/\psi \to \pi^+\pi^-$	$\lvert 3096.92 - h_2h_3\_\pi\pi\rvert > 50.$ and $\lvert 3096.92 - h_4h_3\_\pi\pi\rvert > 50.$
	$J/\psi \to K^+K^-$	$\lvert 3096.92 - h_2h_3\_KK\rvert > 50.$ and $\lvert 3096.92 - h_4h_3\_KK\_\mathrm{M}\rvert > 50.$
χ_{c0}	$\chi_{c0} \to \pi^+\pi^-$	$\lvert 3414.75 - h_2h_3\_\pi\pi\rvert > 50.$ and $\lvert 3414.75 - h_4h_3\_\pi\pi\rvert > 50.$
	$\chi_{c0} \to K^+K^-$	$\lvert 3414.75 - h_2h_3\_KK\rvert > 50.$ and $\lvert 3414.75 - h_4h_3\_KK\_\mathrm{M}\rvert > 50.$
$X \to \mu^+\mu^-$		!(h_1_isMuon == 1 && h_2_isMuon == 1) and !(h_3_isMuon == 1 && h_4_isMuon == 1)
		!(h_2_isMuon == 1 && h_3_isMuon == 1) and !(h_1_isMuon == 1 && h_4_isMuon == 1)

mass spectra. This fitter was originally developed by the LHCb Warwick group for modes involving a V^0 particle in the final state [38], but can actually be used in any 1-dimensional simultaneous fit. It is used in particular for the analysis of the decays $B^0_{d,s}\to K^0_S hh$'. Some modifications to the original code have been implemented to adapt to the blinding strategy of this analysis. We note here that we are fitting separately the X_b^0 and $\overline{X}_b^0$ spectra, which is motivated by the measurement of *CP* observables of the same charmless modes. The philosophy of the simultaneous fit of charmless and charmed signal yields to the corresponding spectra followed a two-fold objective. The information of the charmless spectra (and charmed spectra) are entangled by the presence of signal and background cross-feeds, the common re-weighting of the PID, the physical parameters such as the reconstructed baryon masses or the mass threshold of the partially reconstructed backgrounds (to only cite few of them). The simultaneous adjustment of the shared parameters between the signal and control channel modes, as well as the consistent introduction of data-driven constraints to the fit model for all spectra to account for signal cross-feeds or B physics backgrounds, allows to integrate most of the sources of uncertainties as statistical uncertainty of the fit, and hence minimise the systematic uncertainty budget on the branching fraction measurements as well as on $\Delta\mathcal{A}^{CP}$ determination. Eventually, this strategy presents the advantage of a simple bookkeeping of the fit results given the number of spectra under scrutiny in this analysis. The cross-checks of the measurement (magnet polarity and trigger requirements) proceed in one go.

The total number of floating parameters in the nominal fit for the branching fractions ($\Delta\mathcal{A}^{CP}$) determination is 201 (367) among which 124 (288) are signal yields parameters. The remaining parameters are shape or ratio parameters. The simultaneous fit strategy proceeds with the following constraints

- The nominal mass of Λ_b^0 and Ξ_b^0 are shared by all spectra, both in charmless and

charmed decays.

- The difference of the nominal mass of Λ_b^0 and Ξ_b^0 is Gaussianly-constrained from the PDG value ($m_{\Xi_b^0}$- $m_{\Lambda_b^0}$ = 172.5±0.4).
- The ratio of widths of the charmless signal shapes are Gaussianly-constrained with the values obtained from the fit to MC events. The reference width is the width of $\Lambda_b^0 \to pK\pi\pi$ 2012. These numbers are summarised in the last column of Table 4.5.
- Control modes $\Lambda_b^0 \to (\Lambda_c^+ \to p\pi\pi)\pi$, $\Lambda_b^0 \to (\Lambda_c^+ \to pK\pi)\pi$ and $\Xi_b^0 \to (\Xi_c^+ \to pK\pi)\pi$ have their own signal width parameters floated in the fit.
- The cross-feeds yields are related to their corresponding signal yields by a factor calculated from the ratio of selection efficiencies and PID (mis)-identification efficiencies as discussed in 4.4.3.
- The yields of the background contributions coming from the four- and the five-body decays of B-mesons are similarly constrained to the yields measured in the high invariant-mass region using the method described in 4.3.
- In order to avoid possible bias when the statistics are low, specifically for the signal decays, the signal yields are allowed to go as low as -5% of the total number of events in the spectrum.

Several other constraints related to the sharing of the parameters that are used in the modelling of physical contributions are also embedded in the strategy. They will be presented while discussing the fit model.

3.3.1 Observables of interest

Although not floating parameters of the fit, the branching fractions and $\Delta\mathcal{A}^{CP}$ are calculated directly from the fit taking into account the covariance matrix of the $\mathcal{N}$ parameters as determined by the fit. The observables are presented in the following.

3.3.1.1 Branching fractions

The complete derivation is discussed in Chapter 5. The ratios of efficiencies needed in the branching fractions computation are external parameters to the fit, and are implemented in the branching fraction formula as constant values. Errors associated to these ratios are propagated as a systematic uncertainty in the branching fractions derivation. The branching fraction is given by :

$$
\begin{aligned}
R(X_b^0 \to ph'h''h''') &\equiv \frac{\mathcal{B}(X_b^0 \to ph'h''h''')}{\mathcal{B}(\Lambda_b^0 \to \Lambda_c^+\pi^-)} \cdot \frac{f_{X_b}}{f_{\Lambda_b^0}}, \\
&= \frac{\epsilon^{\text{geo.}}_{\Lambda_b^0 \to \Lambda_c^+\pi^-}}{\epsilon^{\text{geo.}}_{X_b^0 \to ph'h''h'''}} \cdot \frac{\epsilon^{\text{sel.}}_{\Lambda_b^0 \to \Lambda_c^+\pi^-}}{\epsilon^{\text{sel.}}_{X_b^0 \to ph'h''h'''}} \cdot \frac{\epsilon^{\text{PID}}_{\Lambda_b^0 \to \Lambda_c^+\pi^-}}{\epsilon^{\text{PID}}_{X_b^0 \to ph'h''h'''}} \cdot \frac{1}{\epsilon^{\text{veto}}_{X_b^0 \to ph'h''h'''}} \cdot \frac{\mathcal{N}_{X_b^0 \to ph'h''h'''}}{\mathcal{N}_{\Lambda_b^0 \to \Lambda_c^+\pi^-}},
\end{aligned}
$$

where $\mathcal{B}$ represents the relevant branching fraction and $f_{X_b}/f_{\Lambda_b^0}$ is the relative hadronisation fraction of $b \to X_b$ with respect to $b \to \Lambda_b^0$. From left to right, the ratios of efficiencies are related to the geometrical acceptance, the selection criteria, the PID requirements and the veto of charm and charmonium backgrounds. The measured signal and normalisation channel yields are represented by $\mathcal{N}_{X_b^0 \to ph'h''h'''}$ and $\mathcal{N}_{\Lambda_b^0 \to \Lambda_c^+\pi^-}$.

3.3.1.2 $\Delta\mathcal{A}^{CP}$ measurements

The complete derivation is discussed in Chapter 7. The $\mathcal{A}^{CP}$ and $\Delta\mathcal{A}^{CP}$ observables are given by

$$\mathcal{A}^{CP} = \frac{\mathcal{N}(X_b^0) - \overline{\mathcal{N}}(\overline{X}_b^0)}{\mathcal{N}(X_b^0) + \overline{\mathcal{N}}(\overline{X}_b^0)} \quad \text{and} \tag{3.6}$$

$$\Delta\mathcal{A}^{CP} = \frac{\mathcal{N}(X_b^0) - \overline{\mathcal{N}}(\overline{X}_b^0)}{\mathcal{N}(X_b^0) + \overline{\mathcal{N}}(\overline{X}_b^0)} - \frac{\mathcal{N}_{\mathrm{C}}(X_b^0) - \overline{\mathcal{N}}_{\mathrm{C}}(\overline{X}_b^0)}{\mathcal{N}_{\mathrm{C}}(X_b^0) + \overline{\mathcal{N}}_{\mathrm{C}}(\overline{X}_b^0)}, \tag{3.7}$$

respectively, where $\mathcal{N}_{\mathrm{C}}$ and $\overline{\mathcal{N}}_{\mathrm{C}}$ in Eq. 3.7 are the yields of the control decays.
The data sample that is used to perform the measurements is split according to the charge of the proton, to the year of data-taking (and to two trigger requirements in order to correct for asymmetric L0Hadron TOS efficiencies, that are further discussed in Section 6.3). The very same fit model is used for the two types of measurements and is presented in the next chapter.

Chapter 4

Design of the fit model

This section presents the fit model that is used in order to determine the signal yields of the modes of interest. It is worth to mention here that the very same components are used for the measurements of branching fractions (further described in Section 5) and $\Delta\mathcal{A}^{CP}$ measurements (further detailed in Section 7). This section is hence presenting the several background sources as well as the modelling of the contributions. Let me emphasise here that the fit model employed in this analysis is complicated. The shapes of the modelling are fully described in this chapter (Section 4.4) and I apologise in advance to the reader for the austerity of the following lines. Therefore, a first section is discussing the mathematical functions that are used in the fit model, in order to lighten the reading of the last section.

Chapter contents

4.1 The tools of the fit model

This section is introducing the probability density functions (PDF) that are used in order to model the signal and the background contributions.

- **The double Crystal Ball** function (DCB) is, roughly-speaking, a Gaussian with asymmetric tails. It allows to take into account a radiative tail or the imperfections of the tracking, with a left or a right tail, respectively. The mathematical description of a Crystal Ball PDF of variable m is given by:

$$P(m;\alpha,n,\mu,\sigma) = \mathcal{N}\cdot\begin{cases}\exp(-(m-\mu)^2/2\sigma^2), & \text{if } (m-\mu)/\sigma > -\alpha\\ (\frac{n}{|\alpha|})^n\exp(-\alpha^2/2)(\frac{n-\alpha^2}{|\alpha|}-\frac{m-\mu}{\sigma})^{-n}, & \text{if } (m-\mu)/\sigma \leq -\alpha\end{cases}, \tag{4.1}$$

  where $\mathcal{N}$ is the normalisation and m is the invariant mass. The turnover point and the tail parameter are denoted α and n, respectively. This PDF is used in order to model signal and signal cross-feed contributions (composed of true signal events appearing in an other spectrum because of a misidentification of a pion or a kaon).

- **The Cruijff** function is an asymmetric function, composed of two Gaussian functions with shared mean μ but two different width σ's and two tail-correction parameters. Mathematically, the function is given by

$$P(m;\mu,\sigma_L,\sigma_R,\alpha_L,\alpha_R) = \mathcal{N}\cdot\begin{cases}\exp(-(m-\mu)^2/2(\sigma_L^2+\alpha_L(m-\mu)^2)), & \text{if } m \leq \mu\\ \exp(-(m-\mu)^2/2(\sigma_R^2+\alpha_R(m-\mu)^2)), & \text{if } m > \mu\end{cases} \tag{4.2}$$

  where μ, σ_L (σ_R) and α_L (α_R) are the turnover points, the width of the left Gaussian (right Gaussian) and the left tail-correction parameter (right tail-correction parameter), respectively. This shape is used in order to model four-body decays coming from B or B_s^0 with a misidentified kaon or pion as a proton.

- **The ARGUS** function is dedicated to model the partially-reconstructed backgrounds (multibody decays with one particle missing). The generalised ARGUS function has three parameters (m_t, c, p) and is given by:

$$P(m;m_t,c,p) = \frac{2^{-p}c^{2(p+1)}}{\Gamma(p+1)-\Gamma(p+1,c^2/2)}\cdot\frac{m}{m_t}(1-\frac{m^2}{m_t^2})^p\exp\left[-\frac{1}{2}c^2(1-\frac{m^2}{m_t^2})\right], \tag{4.3}$$

  where $\Gamma(n)$ and $\Gamma(n,x)$ are the usual Gamma function and incomplete Gamma function, respectively. The parameter m_t describes the threshold, where if $m > m_t$, the function evaluates to zero. The parameter p controls the curvature of the function and the parameter c controls the falling of the slope.

- **First order Bernstein** polynomial of the second kind[a] is used to model the combinatorial background. This function requires two parameters to get a first order polynomial. One is arbitrarily taken to be equal to 1 which implies that only one parameter c describes the slope of the line describing the decrease of combinatorial background as a function of the reconstructed invariant mass fit-wise. The advantage of using Bersntein polynomial is of numerical nature. They are positively defined and proven robust in complicated fits such as the one presented in this document.

[a]The interested reader can browse the definition and the implementation in https://root.cern.ch/doc/master/classRooBernstein.html

4.2 Identification of backgrounds

The structure of the background of the charmless 4-body fully-charged decays of Λ_b^0 and Ξ_b^0 is rich. There are at least six main categories of backgrounds identified that appears in the mass distribution of the real data candidates:

- **the peaking backgrounds** coming from charmed decays and charmless but charming decays (we are referring here to the tree level $b \to u$ quark transition followed by $W \to \bar{c}s$),

- **the partially reconstructed backgrounds:** Λ_b^0 or Ξ_b^0 5-body decays with one particle missing

- **the cross-feeds from other signal modes** that are true signal events that may appear as background if at least one track is misidentified.

- **the physics backgrounds coming from 4-body decays of B^0 or B_s^0**

- **the physics backgrounds coming from 5-body decays of B^0, B_s^0 or B^+**

- **the random combinatorial** of one or several tracks unrelated to the decay of the interest.

The study of these backgrounds is reported in details in this section.

4.2.1 Peaking backgrounds

Fully-reconstructed charmed and charming decays if not properly removed can appear as peaking background. Since the final state of these decays is the same as the charmless modes, they can not be removed via PID optimisation and neither on using MVA-based requirements without relying on the small topological and kinematical differences. The unique way to reduce them without losing a significant amount of signal events is to properly veto them by cutting on the mass of a given intermediate state. The intermediate states explicitly vetoed in this analysis are Λ_c^+, Ξ_c^+, D^+, D_s^+, D^0, χ_{c0} and J/ψ (Table 3.6). The reconstructed mass of Λ_c^+ is required to be ± 50 MeV/c^2 outside from $m_{\Lambda_c^+} = 2283.$ MeV/c^2, where it is adjusted about 3 MeV/c^2 to the left w.r.t. the PDG value in order to take into account the asymmetry of the distribution as seen in the data, while Ξ_c^+, D^+, D_s^+ and D^0 are required to be ± 30 MeV/c^2 outside from the PDG values. A wider mass window of ± 50 MeV/c^2 from the PDG value is required for vetoing J/ψ and χ_{c0}. The list of final state decays considered for these charmed resonances can be found in Section 3.2.5, where all relevant daughter combinations are considered in the mass reconstruction. Furthermore, these mass veto cuts are applied as a global cut, *e.g.* 3 tracks are reconstructed as $pK\pi$ in order to veto Λ_c^+, regardless of the spectrum. In this way, the candidate is vetoed in all spectra. Let us notice that the vetoed charmed decay modes involving a Λ_c^+ or a Ξ_c^+ are used in turn as control channels for the detection efficiencies and production asymmetries for the $\Delta\mathcal{A}^{CP}$ determination. As far as branching fraction measurements are concerned, the unique normalisation channel is $\Lambda_b^0 \to (\Lambda_c^+ \to pK\pi)\pi$, which will require in some occurrences to correct for π / K detection asymmetries as well.

4.2.2 Partially reconstructed backgrounds

The 5-body decays of Λ_b^0 and/or Ξ_b^0 with one particle missing can still be a significant amount of background events populating the left side of reconstructed invariant-mass distribution. The dominant contributor of the partially-reconstructed backgrounds are the events with a missing π^0. Actually, the partially reconstructed backgrounds with a missing charged pion in the final state are reduced by the isolation variable denoted smallest $\Delta\chi^2_{\text{vtx}}$, which is searching for a better vertex with an additional charged track to the 4-tracks vertex. The mass threshold considered when modelling this background is therefore the difference of Λ_b^0 or Ξ_b^0 mass minus the π^0 mass.

Partially-reconstructed backgrounds with a missing γ are also possible through the decays $\Lambda_b^0 \to pK^-(\eta' \to \pi^+\pi^-\gamma)$ and $\Lambda_b^0 \to p\pi^-(\eta' \to \pi^+\pi^-\gamma)$. Because of the vanishing mass of the photon, the end-point of these partially-reconstructed backgrounds sits at the signal peak. Their relative rate to signal events has been estimated from what is known of analogous B mesons decay modes and, depending on the modes, is fixed in the nominal fit ($p\pi\pi\pi$ spectrum) or left free in the fit and compared to the prediction ($pK\pi\pi$ spectrum). The SM quark level diagrammatic picture for $\Lambda_b^0 \to p\pi^-(\eta' \to \pi^+\pi^-\gamma)$ decay requires the presence of $u\overline{u}$ pair. Hence, we are expecting a hierarchy of $\pi^+\pi^- > \rho^0 > \eta > \eta'$. The analogous decays in the meson systems are: $B^+ \to \pi^+\pi^-\pi^+$, $B^+ \to \rho^0\pi^+$, $B^+ \to \eta\pi^+$, $B^+ \to \eta'\pi^+$, and shows that very hierarchy [8], used to set the ratio of the yield of this partially-reconstructed background to the Λ_b^0 signal to be 1/20. In contrast, the decay mode $\Lambda_b^0 \to pK^-(\eta' \to \pi^+\pi^-\gamma)$ proceeds dominantly in the SM through a gluonic penguin diagram and would constitute a significant background in the fit model. An acceptable diagrammatic proxy to evaluate its relative rate to the signal of interest is the decay $B^0 \to \eta' K_S^0$ compared to the inclusive decay mode $B^0 \to K_S^0\pi^+\pi^-$. The relative rate of $\Lambda_b^0 \to pK^-(\eta' \to \pi^+\pi^-\gamma)$ in the invariant-mass window is estimated to be about 20% of the signal. That contribution is nonetheless left free in the fit given its significance.

Eventually, the dominant quark transitions in the decay of interest in this work are $b \to sq\bar{q}$ where $q = u, d$. This implies that the spectrum $pK\pi\pi$ receives the largest contribution of partially reconstructed b-flavoured baryons. In turn, the events from this category experiencing a misidentification $\pi \to K$ will populate in a significant way the companion spectra $pK^-K^+\pi^-$ and $pK^-\pi^+K^-$. The reciprocal ($K \to \pi$ misidentification) is not relevant here since the events will be shifted to the left-hand part of the spectrum. It has been checked in addition that the partially reconstructed backgrounds in any other spectrum than $pK\pi\pi$ contribute marginally to their companion spectrum and can hence be safely neglected in the fit model.

4.2.3 Cross-feeds or reflections

The PID selection is chosen in a way that a candidate can appear only in one spectrum and not on the other spectra (mutually exclusive selection) in order that a simultaneous fit of all the relevant spectra can be possible. A detailed discussion on the strategy was provided in Section 3.2.2. After optimising the PID selection to reduce the cross-feeds in each spectrum, a significant number of true signal events may still appear as a cross-feed in other spectrum. The dominant cross-feeds are signal events from other spectra with only one particle misidentified, and hence peaks not very far from the signal peak. Henceforth, an accurate handling on the yields and shapes of these background contributions must be achieved. This is realised by constraining in the simultaneous fit their relative yields to the data-driven misidentification probabilities.

4.2.4 $B \to$ 4-body physics backgrounds

Four-body decays coming from B^0 or B_s^0 with a misidentified K or π as a proton can appear in the invariant-mass distribution. Given that the hadronisation fraction of b quark to B^0 is significantly higher the the hadronisation fraction of b quark to neutral baryons Λ_b^0 and Ξ_b^0, they are expected to dominate the mass distribution if not properly reduced. The hadronisation fraction of b quark to B_s^0, although smaller than the hadronisation fraction of b quark to Λ_b^0, can also populate significantly if not handled. Since this background can exhibit significant CP asymmetries, their accurate handling is mandatory and certainly constitutes a challenge of this analysis. Five possible dominant B physics backgrounds are envisioned, which includes $B^0 \to \pi^+\pi^-\pi^+\pi^-$, $B^0 \to K^+\pi^-\pi^+\pi^-$, $B^0 \to K^+K^-K^+\pi^-$, $B_s^0 \to K^+\pi^-\pi^+K^-$ and $B_s^0 \to K^+K^-K^+K^-$. Since they have the same final state particles, except for the proton, as the signal modes, they can not be significantly reduced by the $\text{PID}_{K\pi}$ selection without reducing as well the signal events. Neither MVA-based cuts can reduce them since they are topologically and kinematically similar as the signal events. However, a tight PID cut (ProbNNp) on the proton particle can significantly reduce these B physics events, while retaining signal events with an acceptable efficiency. A dedicated study of the RHSB the invariant-mass distributions for each spectra has been undertaken and is reported in Section 4.3.

4.2.5 $B \to$ 5-body physics backgrounds

Following the very same reasoning as in the previous subsection, five-body decays coming from B^0, B_s^0 or B^+ with a misidentified K or π as a proton with one particle missing in the reconstruction can appear in the invariant-mass distribution. Again, the isolation variable $\Delta\chi^2_{\text{vtx}}$ will reduce the contribution of decays with a missing $\pi^\pm$. These backgrounds can as well exhibit significant CP asymmetries. Their contributions to the different particle/antiparticle spectra are here again determined from the study of the RHSB.

4.2.6 Combinatorial background

Aside from the physical backgrounds described above, there are also combinatorial backgrounds coming solely from the random combination of one or several tracks unrelated to the signal decay. The topology and kinematics[b] of these background events are different enough from the signal events that they can be reduced by a multivariate-based cuts (as what is done in Subsection 3.2.3). It is important to emphasise that the understanding of the different above-mentioned sources of background (not straightforwardly reducible) benefits from the largest as possible suppression of the combinatorial background. This is in particular true for the dominant B physics. Therefore, a special care has been brought to the design of the tool to fight against the combinatorial background. It was previously discussed that a BDT-based MVA is trained using variables with weak linear correlations (but in principle non-linearly correlated) or with different correlations for background and signal events in order to reduce these backgrounds.

[b]Previously discussed in Chapter 3 is the BDT strategy to reduce these combinatorics. No kinematical variables are used in the BDT to avoid the BDT cutting events in the low two-body invariant mass, where the $\Lambda^{*0}(1520)$ and $N^{*0}(1520)$ are expected to appear.

4.2.7 Summary of background contributions

Fit strategy and constraints were already mentioned in the previous Sections. They are spelt again here to wrap-up the whole strategy. Table 4.1 gathers the contributions present in each spectrum. Only dominant cross-feeds are included in the fit. Furthermore, $\Xi_b^0 \to pKKK$ as cross-feed to $X_b^0 \to pKK\pi$ or $X_b^0 \to pK\pi K$ spectra, are not included in the fit since eventually the fit to data found only few events for these contributions. We take note that this observation is inline with the SM expectation where the dominant diagrams of these decays proceed through $b \to d$ penguin loop transition and are hence CKM-suppressed. For the case of the B physics to 4-body backgrounds, singly misidentified decays (π to p and K to p) are modelled in each spectrum. A doubly-misidentified $B^0 \to K^+K^-K^+\pi^-$ as $X_b^0 \to pK\pi\pi$ is also included in the fit model since $B^0 \to K^+K^-K^+\pi^-$ events have been identified using the RHSB events of $X_b^0 \to pK\pi\pi$ spectrum. This background is expected to be the dominant B physics background before any PID cuts are applied and some events still survive in the $X_b^0 \to pK\pi\pi$ spectrum after the PID cuts are applied. Note as well that although $B_s^0 \to K\pi\pi K$ is a background in the $X_b^0 \to pKK\pi$ spectrum, it is triply-misidentified in the $X_b^0 \to pK\pi K$ spectrum since the two kaons should have the same charge. For the case of the B physics to 5-body backgrounds, a PDF is added in each spectrum whose shape is obtained from MC-generated $B^+ \to K\pi\pi\pi + \{\pi^0\}$ events reconstructed as $p\pi\pi\pi$.

Table 4.1: List of contributions in each spectrum.

Spectrum	Signal	Signal cross-feed	$B_{d,s}^0 \to$ 4-body
$X_b^0 \to p\pi\pi\pi$	$\Lambda_b^0 \to p\pi\pi\pi$	$\Lambda_b^0 \to pK\pi\pi$ as $p\pi\pi\pi$ $\Xi_b^0 \to pK\pi\pi$ as $p\pi\pi\pi$	$B^0 \to K\pi\pi\pi$ as $p\pi\pi\pi$ $B^0 \to \pi\pi\pi\pi$ as $p\pi\pi\pi$
$X_b^0 \to pK\pi\pi$	$\Lambda_b^0 \to pK\pi\pi$ $\Xi_b^0 \to pK\pi\pi$	$\Lambda_b^0 \to pKK\pi$ as $pK\pi\pi$ $\Lambda_b^0 \to p\pi\pi\pi$ as $pK\pi\pi$ $\Xi_b^0 \to pK\pi K$ as $pK\pi\pi$	$B_s^0 \to KK\pi\pi$ as $pK\pi\pi$ $B^0 \to \pi K\pi\pi$ as $pK\pi\pi$ $B^0 \to KKK\pi$ as $pK\pi\pi$
$X_b^0 \to pKK\pi$	$\Lambda_b^0 \to pKK\pi$	$\Lambda_b^0 \to pKKK$ as $pKK\pi$ $\Lambda_b^0 \to pK\pi\pi$ as $pKK\pi$ $\Lambda_b^0 \to p\pi\pi\pi$ as $pKK\pi$ $\Xi_b^0 \to pK\pi\pi$ as $pKK\pi$	$B^0 \to KKK\pi$ as $pKK\pi$ $B_s^0 \to \pi KK\pi$ as $pKK\pi$
$X_b^0 \to pKKK$	$\Lambda_b^0 \to pKKK$ $\Xi_b^0 \to pKKK$	$\Lambda_b^0 \to pKK\pi$ as $pKKK$ $\Lambda_b^0 \to pK\pi\pi$ as $pKKK$ $\Xi_b^0 \to pK\pi\pi$ as $pKKK$ $\Xi_b^0 \to pK\pi K$ as $pKKK$	$B_s^0 \to KKKK$ as $pKKK$ $B^0 \to \pi KKK$ as $pKKK$
$X_b^0 \to pK\pi K$	$\Xi_b^0 \to pK\pi K$	$\Lambda_b^0 \to pKKK$ as $pK\pi K$ $\Lambda_b^0 \to pK\pi\pi$ as $pK\pi K$ $\Lambda_b^0 \to p\pi\pi\pi$ as $pK\pi K$ $\Xi_b^0 \to pK\pi\pi$ as $pK\pi K$	$B^0 \to KK\pi K$ as $pK\pi K$
$X_b^0 \to (\Lambda_c^+ \to p\pi\pi)\pi$	$\Lambda_b^0 \to (\Lambda_c^+ \to p\pi\pi)\pi$		
$X_b^0 \to (\Lambda_c^+ \to pK\pi)\pi$	$\Lambda_b^0 \to (\Lambda_c^+ \to pK\pi)\pi$		
$X_b^0 \to (\Xi_c^+ \to pK\pi)\pi$	$\Lambda_b^0 \to (\Xi_c^+ \to pK\pi)\pi$ $\Xi_b^0 \to (\Xi_c^+ \to pK\pi)\pi$		

∘ Each spectrum in the charmless spectra has a PDF for the combinatorics modelled by a first order Bernstein polynomial. Each spectrum contains a PDF for partially-reconstructed background coming from Λ_b^0,$\Xi_b^0 \to$ 4-body + missing π^0 and an additional misidentified partially-reconstructed background is added in the $X_b^0 \to pKK\pi$ and $X_b^0 \to pK\pi K$ spectra..

4.3 Anatomy of the RHSB

In the previously defined right-hand side band (RHSB) of the invariant mass spectra, only combinatorics, signal cross-feed and B physics events are expected to populate that region. The previously-defined Cruijff function is used in order to model B physics events. The shapes can peak under the signal though they cover almost the entire invariant mass spectra with tails reaching up to the end of the RHSB. These events are primarily worrisome because their potential contribution to the CP asymmetry observable we want to measure. A further technical difficulty for the invariant mass fit is that the B physics tail shape is almost the same as the combinatorics and cannot be straightforwardly distinguished from the data themselves. An estimate of their number of expected events is also not yet doable since the inclusive branching fractions of these B physics backgrounds are unmeasured, to date.

A possible method to estimate the yields of B physics backgrounds is to reconstruct explicitly the invariant mass of the 4 daughter particles according to the proper set of expected final daughter particles of the B physics background. For example in the $X_b^0 \to p\pi\pi\pi$ spectrum, the p particle is swapped with a K particle hypothesis to estimate the number of $B^0 \to K\pi\pi\pi$ events. In order to avoid any implicit unblinding of the signal events, only the events in the RHSB are used.

The fit model was empirically built at the ProbNN$p > 0.50$ and BDT > 0.30 working point. It has however been checked that it stands for other working points, in particular for those tested in the companion $\Delta\mathcal{A}^{CP}$ analysis. As far as branching fractions are concerned, the related RHSB spectra fits (where only L0Global TIS events are selected) can be found in Appendix C.1. Another working point result with a milder proton PID cut of ProbNN$p >$ 0.30 is also reported in Appendix C.2.

The chosen PID optimisation favours the modes with larger number of kaons efficiency-wise and induces a hierarchy between misidentification probabilities ($P(\pi \to K) > P(K \to \pi)$). The following lines list the expected contributions feeding RHSB spectra as well as the dedicated fit model. It has to be noticed that this fit model is not aiming at providing a comprehensive fit of the RHSB but identify and quantify the dominant contributions.

- In each RHSB spectrum, a dominant mode coming from B decays must contribute via a $(K \to p)$ misidentification. These modes are cross-feeding the companion spectra via a $(K \to \pi)$ or $(\pi \to K)$ misidentifications. As noted previously, the latter dominates.

- In that respect, the signal cross-feed must populate as well the RHSB. Contributions coming from $\pi \to p$ must be present as well.

- Partially reconstructed background, coming from $B \to$ 5-body where one track is not reconstructed.

- Combinatorial background mostly dominated by random associations of 4 tracks (including a proton) are also expected.

Since only the dominant $B \to$ 4-body are needed to estimate the $B \to$ 4-body background in the nominal fit, we are not aiming at accurately modelling the RHSB. The sub-dominant contributions data-driven constraints are derived for each spectrum from the dominant ones by misidentification factors determined from PID calibration samples, re-weighted as discussed in Section 4.4. For example, knowing the number of expected events of $B \to K\pi\pi\pi$

determined from $p\pi\pi\pi$ spectrum, the corresponding CF yields in $KK\pi\pi$ is constrained using Eq. (4.4).

$$(N_{K\pi\pi\pi})_2 = 2 * \frac{\epsilon_2^{\text{sel.}} * \epsilon_2^{\text{PID}}}{\epsilon_1^{\text{sel.}} * \epsilon_1^{\text{PID}}} * (N_{K\pi\pi\pi})_1 \tag{4.4}$$

where subscript (1) stands for the spectrum where the mode is found ($K\pi\pi\pi$ spectrum in this example) and where subscript (2) stands for the spectrum in which the contribution is cross-feeding ($KK\pi\pi$ spectrum in this example). The factor two is coming from the fact that one of the two pions of same charge can be misidentified for this specific case. Each cross-feed contribution is then implemented in the fit model with this constraint on the yield.

The shapes of the B decays contributions are determined from MC simulated events as listed in the Table 3.1. The invariant mass of the simulated events retained after the whole selection for each dominant B decay category is modelled with a Crystal Ball (CB) function, described in Equation 4.1. The shapes of the B decays cross-feeding to another spectrum with a single $\pi \to K$ or $K \to \pi$ mis-identification are empirically determined on data by selecting the dominant B decay mode and fitting its invariant mass distribution under the relevant reconstruction hypothesis with a single CB function. Conversely, the shapes for signal (charmless baryon decays) CF events, together with the combinatorics, are inferred from data themselves by using a hard cut of ProbNN$p > 0.80$. No B contribution is observed. The model employed is here again a single CB.

Eventually, the partially reconstructed background is modelled with an Argus function convoluted with a normal function sharing its width with the signal one. The threshold of the Argus is set to be equal to the difference of the b-hadron decaying mass and the mass of the π^0 (see Section 4.1). These $B \to$ 5-body contributions are found to be non-negligible sources of background in the charmless 4-body invariant mass spectra. The expected number of events of these backgrounds are hence deduced from the RHSB and are constrain in the fit model.

RHSB fits are presented in Figures 4.1 and 4.2 with BDT > 0.30 using the 2012 data for illustration. As previously emphasised, the fit model is not aiming at providing a comprehensive fit of the RHSB but it provides satisfactory results and allows to identify the dominant contributions. The obtained B decay yields from the RHSB are gathered in the fifth and sixth column of Table 4.2, where the yields are obtained separately for candidates with p and $\overline{p}$ from the original spectrum. These yields are then translated as expected full yields for the whole invariant mass spectra by multiplying it by a factor obtained from the MC shapes. Mathematically, the expected full yield $\mathcal{Y}_{\text{full}}$ and its corresponding uncertainty $\sigma_{\mathcal{Y}_{\text{full}}}$ are proportional to the yield $\mathcal{Y}_{\text{RHSB}}$ obtained in the RHSB and its uncertainty $\sigma_{\mathcal{Y}_{\text{RHSB}}}$, respectively. This is given by,

$$\mathcal{Y}_{\text{full}} \pm \sigma_{\mathcal{Y}_{\text{full}}} = f \cdot (\mathcal{Y}_{\text{RHSB}} \pm \sigma_{\mathcal{Y}_{\text{RHSB}}}) \tag{4.5}$$

where f is the ratio of the integrated PDF of the B physics shape for the full invariant mass region and the RHSB region. Columns seven and eight in Table 4.2 display these translated expected full yields for each dominant B physics background in each spectrum. These expectation values are used to Gaussianly-constrain the yields of the B physics in the nominal fit to data. The former numbers are obtained with the L0 trigger condition (L0Hadron TOS or L0Global TIS). The Table 4.3 gathers the yields obtained for the branching fractions determination under the L0Global TIS condition only.

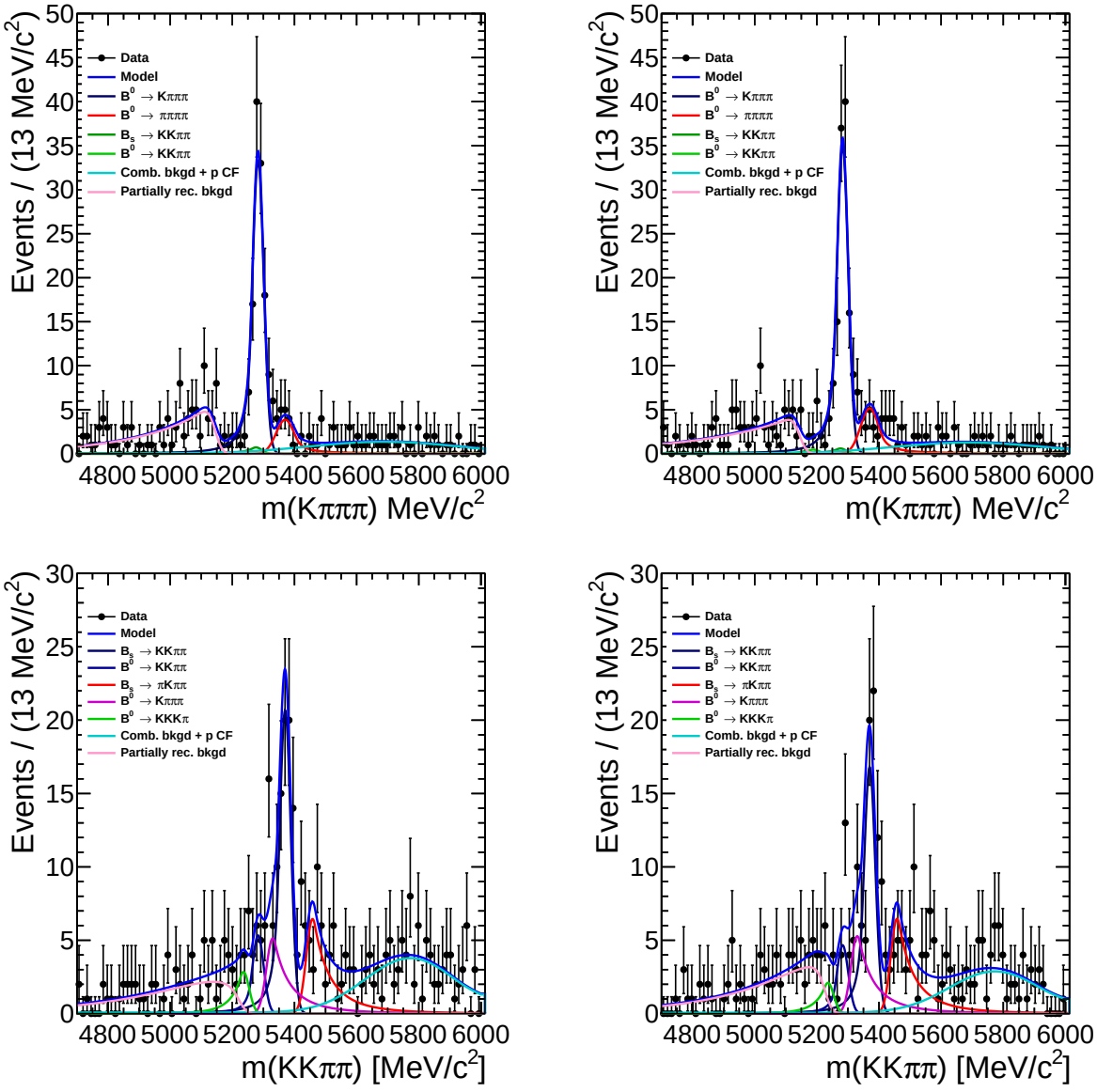

Figure 4.1: Invariant mass spectra of 2012 RHSB events from [from top to bottom] $X_b^0 \to p\pi\pi\pi$ as $B^0 \to K\pi\pi\pi$ and $X_b^0 \to pK\pi\pi$ as $B_s^0 \to KK\pi\pi$ (left-column) with p and (right-column) $\bar{p}$ separated.

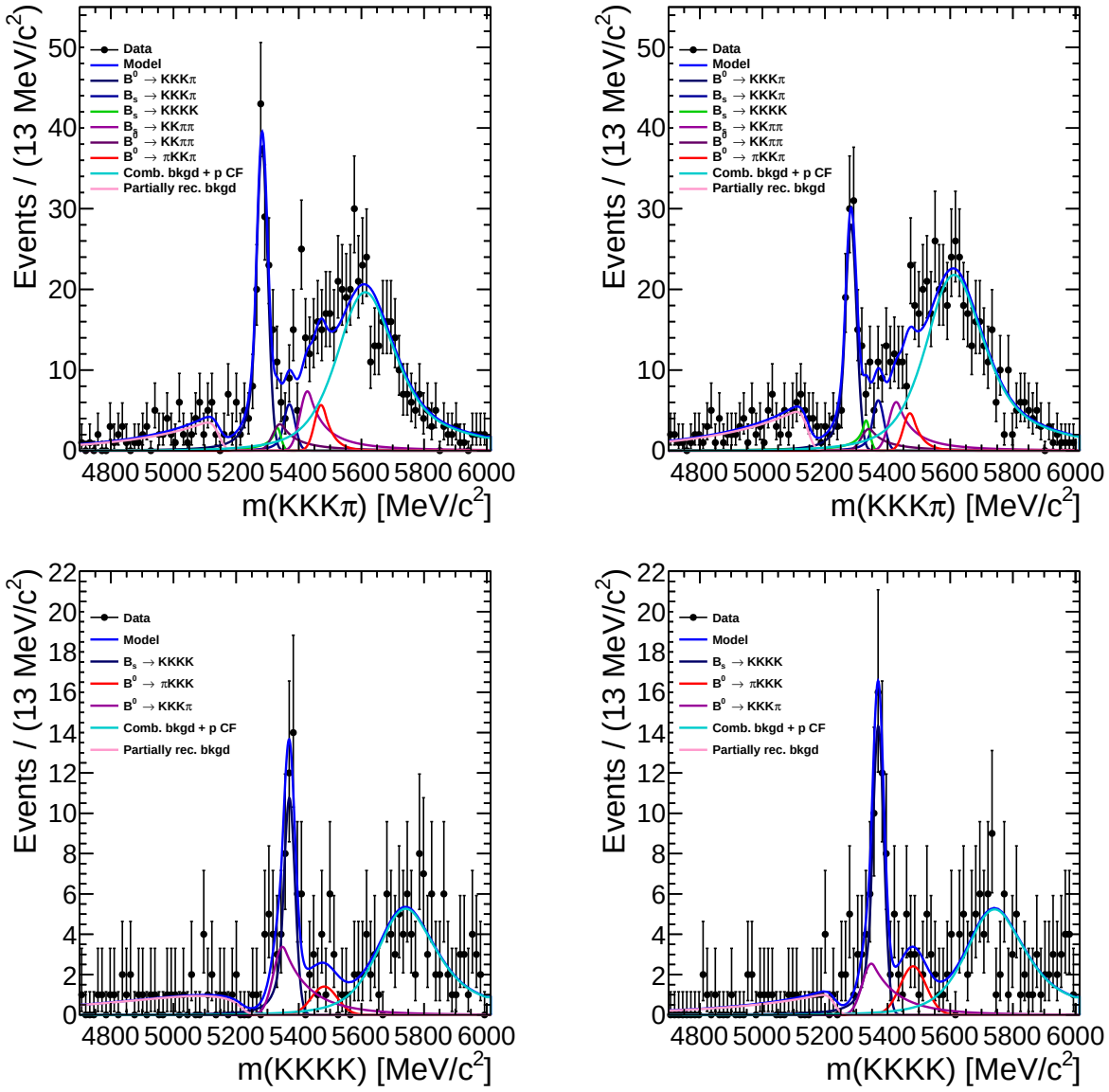

Figure 4.2: Invariant mass spectra of 2012 RHSB events from [from top to bottom] $X_b^0 \to pKK\pi$ as $B^0 \to KKK\pi$ and $X_b^0 \to pKKK$ as $B_s^0 \to KKKK$ (left-column) with p and (right-column) $\bar{p}$ separated.

Table 4.2: The yields of B physics backgrounds from the RHSB of each spectrum.

Spectrum	RHSB cut (in MeV/c^2)	Dominant B	Year	Yields from RHSB		Translated yields	
				w/ p track	w/ $\overline{p}$ track	w/ p track	w/ $\overline{p}$ track
$X_b^0 \to p\pi\pi\pi$	$m_{p\pi\pi\pi} > 5685.$	$B^0 \to K\pi\pi\pi$	2011	35.4 ± 6.4	31.2 ± 6.1	115 ± 25	101 ± 24
			2012	134 ± 12	140 ± 13	433 ± 40	453 ± 41
$X_b^0 \to pK\pi\pi$	$m_{pK\pi\pi} > 5840.$	$B_s^0 \to K\pi\pi K$	2011	16.4 ± 4.8	17.3 ± 5.0	61 ± 18	64 ± 19
			2012	82 ± 11	68 ± 10	307 ± 40	254 ± 37
$X_b^0 \to pKK\pi$	$m_{pKK\pi} > 5685.$	$B^0 \to KKK\pi$	2011	46.7 ± 7.4	37.7 ± 7.0	132 ± 21	107 ± 20
			2012	148 ± 13	111 ± 12	422 ± 38	316 ± 33
$X_b^0 \to pKKK$	$m_{pKKK} > 5840.$	$B_s^0 \to KKKK$	2011	9.2 ± 4.0	7.7 ± 3.5	44 ± 20	37 ± 17
			2012	43.3 ± 8.2	57.4 ± 8.9	210 ± 40	278 ± 43

Table 4.3: The yields of B physics backgrounds from the RHSB of each spectrum for branching fraction measurement.

Spectrum	RHSB cut (in MeV/c^2)	Dominant B	Year	Yields from RHSB		Translated yields	
				w/ p track	w/ $\overline{p}$ track	w/ p track	w/ $\overline{p}$ track
$X_b^0 \to p\pi\pi\pi$	$m_{p\pi\pi\pi} > 5685.$	$B^0 \to K\pi\pi\pi$	2011	20.9 ± 4.9	17.8 ± 4.5	72 ± 17	61 ± 16
			2012	65.8 ± 8.6	77 ± 10	226 ± 30	266 ± 34
$X_b^0 \to pK\pi\pi$	$m_{pK\pi\pi} > 5840.$	$B_s^0 \to K\pi\pi K$	2011	7.5 ± 3.4	10.1 ± 3.8	28 ± 13	38 ± 14
			2012	49.9 ± 8.5	32.9 ± 7.1	191 ± 32	125 ± 27
$X_b^0 \to pKK\pi$	$m_{pKK\pi} > 5685.$	$B^0 \to KKK\pi$	2011	23.0 ± 5.2	25 ± 11	63 ± 14	69 ± 30
			2012	79 ± 11	68.7 ± 9.2	215 ± 29	187 ± 25
$X_b^0 \to pKKK$	$m_{pKKK} > 5840.$	$B_s^0 \to KKKK$	2011	5.4 ± 3.1	5.2 ± 2.8	24 ± 14	22 ± 12
			2012	21.9 ± 5.9	29.1 ± 6.4	96 ± 26	127 ± 28

4.4 Fit model

As previously discussed in Section 3.3, a simultaneous unbinned extended maximum likelihood fit is performed to all the invariant-mass spectra, both in the charmless and charmed decays in order to extract signal yields and hence branching fractions on one hand, $\mathcal{A}^{\text{raw}}$'s and $\Delta\mathcal{A}^{CP}$'s on another hand directly from the fit results. The models used in this fit are described in the following subsections, for the branching fractions purpose. The analogous models used for the $\Delta\mathcal{A}^{CP}$ determination are reported in Appendices C.3 to C.5.

4.4.1 PID re-weighting of the fit model shapes

The differences between the proton identification performance in the PID calibration sample and in the signal data (as measured for the normalisation sample) require an enhanced granularity of the binning scheme of the PID calibration sample to derive the signal efficiency and to model the shapes of the signal, cross-feed signals and B decays backgrounds, described in this Section. In addition to the segmentation in p and η of the tracks, the PID calibration sample is further binned in event track multiplicity N_{tracks}. The binning scheme is reported in Table 4.4. It has been chosen to also adopt this segmentation for the re-weighting of the K/π candidates.

Table 4.4: The binning scheme used to produce the $\text{PID}_{K\pi}$ and PID_p (mis)identification efficiency maps. Bins boundaries are defined to have the same number of events.

Particle type (year)	p binning boundaries (in GeV/c^2)	η binning boundaries	N_{tracks}
K's (2011)	{3000; 9300; 15600; 18515; 28325; 40097; 59717; 100000}	{1.5; 2.4975; 2.7075; 3.0575; 3.3725; 3.7225; 4.0025; 5.0}	{0;100;150;200; 270;500}
K's (2012)	{3000; 9300; 15600; 16553; 26363; 38135; 57755; 100000}	{1.5; 2.4625; 2.6725; 2.9875; 3.3025; 3.6525; 3.8975; 5.0}	{0;100;150;200; 270;500}
π's (2011)	{3000; 9300; 15600; 16553; 24401; 36173; 55793; 100000}	{1.5; 2.4625; 2.7075; 3.0225; 3.3375; 3.6875; 3.9675; 5.0}	{0;100;150;200; 270;500}
π's (2012)	{3000; 9300; 14591; 15600; 24401; 34211; 53831; 100000}	{1.5; 2.4275; 2.6375; 2.9525; 3.2675; 3.6175; 3.8975; 5.0}	{0;100;150;200; 270;500}
p's (2011)	{3000; 9300; 15600; 18515; 28325; 40097; 59717; 100000}	{1.5; 2.4975; 2.7075; 3.0575; 3.3725; 3.7225; 4.0025; 5.0}	{0;100;150;200; 270;500}
p's (2012)	{3000; 9300; 15600; 16553; 26363; 38135; 57755; 100000}	{1.5; 2.4625; 2.6725; 2.9875; 3.3025; 3.6525; 3.8975; 5.0}	{0;100;150;200; 270;500}

4.4.2 Signal shapes

Simulated events are used to obtain the signal shapes. The invariant-mass distribution reconstructed from simulated events is fitted with a double Crystal Ball function (DCB) with shared mean μ and shared width σ. Although the two functions in Eq. (4.1) are independent of the sign of the parameter α, the sign of α governs on which side of the Crystall Ball (CB) function the tail should appear, where positive α means the tail is on the left side of the CB while negative α means the tail is on the right side. This possibility presents the advantage that one can model a radiative tail (for the left tail of signal mass distribution) or the imperfections of the tracking (for the right tail of the mass distribution).

As an illustration, the fit to the signal invariant-mass distribution for the $\Lambda_b^0 \to pK^-K^+K^-$ is reported here, on Fig. 4.3.

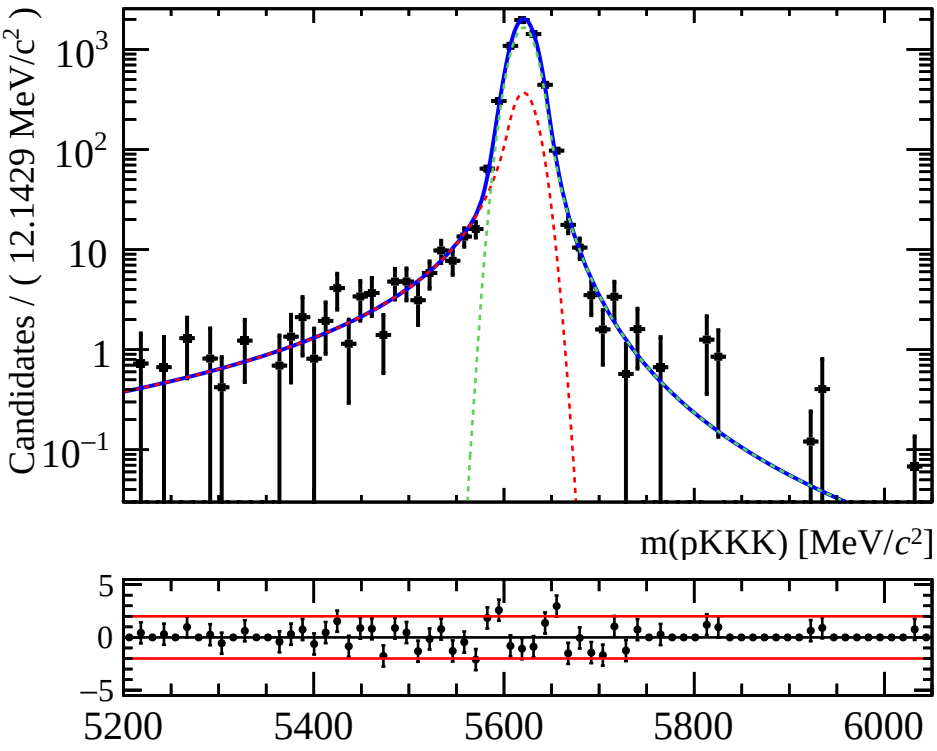

Figure 4.3: Signal invariant-mass distribution fitted with DCB PDF for the $\Lambda_b^0 \to pK^-K^+K^-$ 2011 spectrum. This shapes is used in the fit in order to determine the branching fractions.

Let us notice that no truth-matching is applied onto the candidates in order to take into account for mismatched and mis-reconstructed signals in the signal shape. The full selection is applied to the simulated events, except for the PID cuts since the ProbNN variables are not well-described by the simulation. Since the shape changes with the PID cuts applied, each candidate is weighted by the data-driven efficiency to pass the PID cuts determine from the PID calibration samples. The procedure of applying the weights is the same as what was described in 3.2.2. All the signal shapes are fitted simultaneously in order to obtain the ratios of the widths, which are used as Gaussianly-constrained parameters in the final PDF to be used to fit the real data. The 2012 $\Lambda_b^0 \to pK\pi\pi$ is chosen as the reference for these ratios of widths.

The remaining fit results for branching fraction measurements[c] are shown in Fig. 4.4 and 4.5. The global behaviour of the fit is found to be satisfactory. The extracted parameters α_1, α_2/α_2, n_1, n_2/n_1, f_2, that are reported in Table 4.5, are fixed parameters in the nominal fit to the real data. Systematic uncertainties attached to this assumption are estimated by generating pseudo-experiments according to the distributions of the uncertainties on the fixed parameters as found in the fit to simulated events.

The invariant-mass range used to produce these fits starts from 5200 MeV/c^2. It is worth noticing that the nominal fit to the data starts from 5340 MeV/c^2 (or 5450 MeV/c^2 in the $\Xi_b^0 \to pK\pi K$ spectra). For the latter case, the lower mass bound is chosen to avoid the modelling of partially reconstructed with a missing kaon in the final state.

[c]Similar figures for the $\Delta\mathcal{A}^{CP}$ measurements can be found in Appendix C.3, that are gathered with the shape parameters.

Table 4.5: Fit parameters obtained in the fit to signal shape for the branching fraction measurements.

Year	Fit parameters						
	μ	α_1	α_2/α_1	n_1	n_2/n_1	f_2	σ/σ_{ref}
$\Lambda_b^0 \to p\pi\pi\pi$:							
2011	5620.774±0.323	1.380±0.291	-1.456±0.486	1.793±0.218	1.247±0.321	0.522±0.215	1.027±0.026
2012	5620.709±0.243	0.524±0.337	-4.054±2.700	2.798±1.312	1.057±0.541	0.165±0.070	1.038±0.023
$\Lambda_b^0 \to pK\pi\pi$:							
2011	5620.863±0.278	1.757±0.164	-0.868±0.292	1.625±0.167	2.106±0.636	0.757±0.176	0.998±0.024
2012	5620.807±0.225	1.587±0.330	-1.304±0.370	1.509±0.173	1.539±0.282	0.451±0.217	σ_{ref} = 14.072±0.208
$\Lambda_b^0 \to pKK\pi$:							
2011	5621.416±0.270	1.291±0.270	-1.464±0.416	2.188±0.292	1.296±0.305	0.407±0.165	0.949±0.023
2012	5621.021±0.206	1.351±0.327	-1.585±0.438	1.724±0.222	1.329±0.245	0.281±0.126	0.944±0.019
$\Lambda_b^0 \to pKKK$:							
2011	5620.724±0.218	1.361±0.382	-1.381±0.444	1.997±0.333	1.817±0.437	0.227±0.129	0.898±0.020
2012	5621.300±0.167	1.355±0.384	-1.640±0.502	1.962±0.310	1.362±0.282	0.177±0.100	0.901±0.017
$\Xi_b^0 \to pK\pi\pi$:							
2011	5789.302±0.305	1.035±0.341	-1.600±0.626	1.873±0.274	2.365±0.706	0.270±0.116	1.029±0.027
2012	5789.663±0.219	0.491±0.251	-4.769±2.731	3.146±1.183	0.693±0.403	0.141±0.051	1.022±0.024
$\Xi_b^0 \to pK\pi K$:							
2011	5789.164±0.273	1.328±0.346	-1.337±0.445	1.946±0.263	1.521±0.351	0.337±0.166	1.000±0.023
2012	5789.733±0.211	1.088±0.424	-2.111±0.907	2.228±0.406	1.088±0.300	0.234±0.134	0.989±0.020
$\Xi_b^0 \to pKKK$:							
2011	5789.420±0.209	1.892±0.162	-0.937±0.213	1.987±0.200	1.137±0.243	0.663±0.180	0.918±0.019
2012	5789.508±0.169	1.577±0.291	-1.181±0.295	2.131±0.237	1.899±0.439	0.308±0.150	0.921±0.017

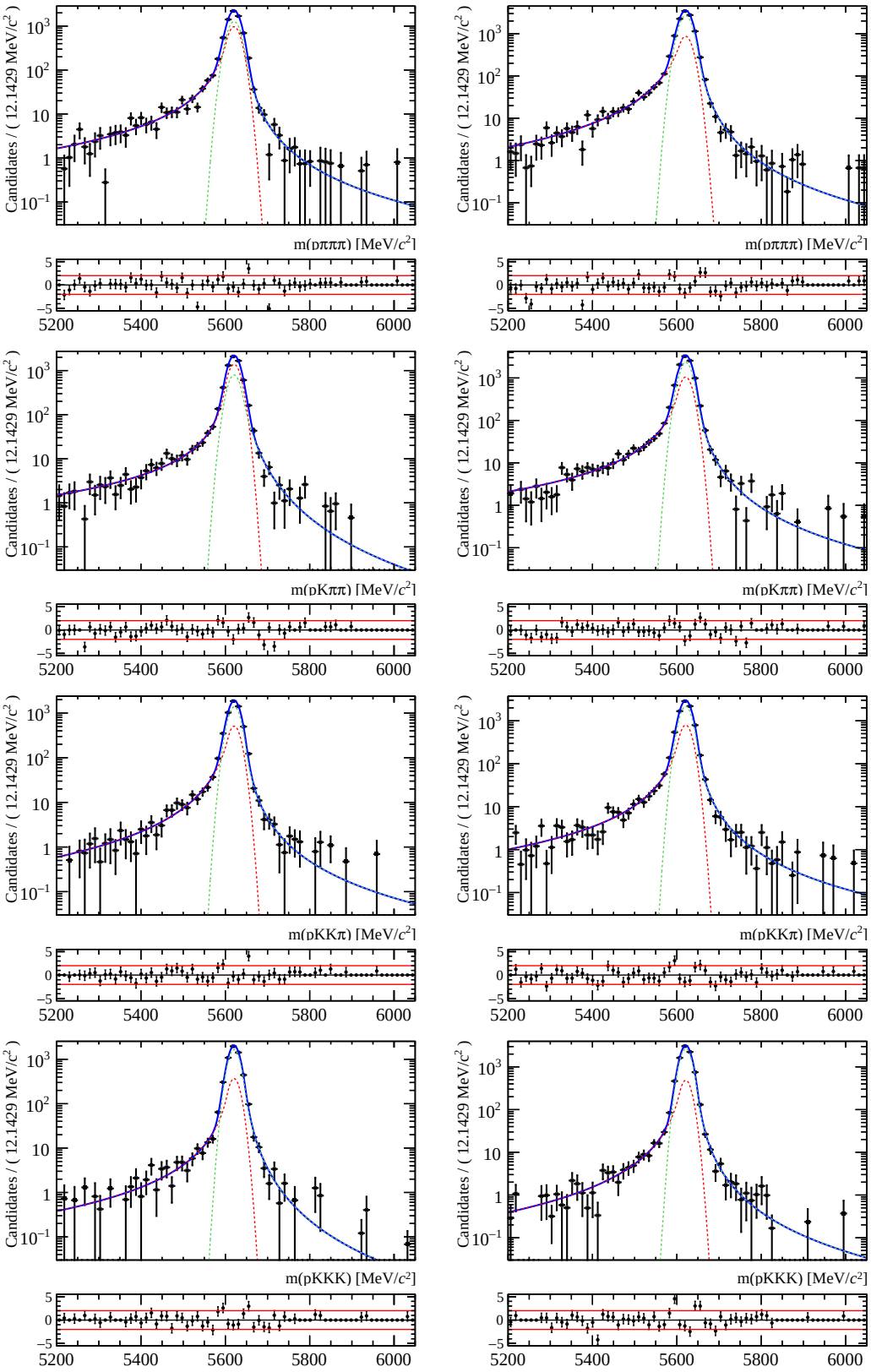

Figure 4.4: Signal invariant-mass distribution fitted with DCB PDF for the modes (in order from top-left to bottom-right) $\Lambda_b^0 \to p\pi\pi\pi$, $\Lambda_b^0 \to pK\pi\pi$, $\Lambda_b^0 \to pKK\pi$ and $\Lambda_b^0 \to pK^-K^+K^-$ for years (left column) 2011 and (right column) 2012. These shapes are used in the fit in order to determine the branching fractions.

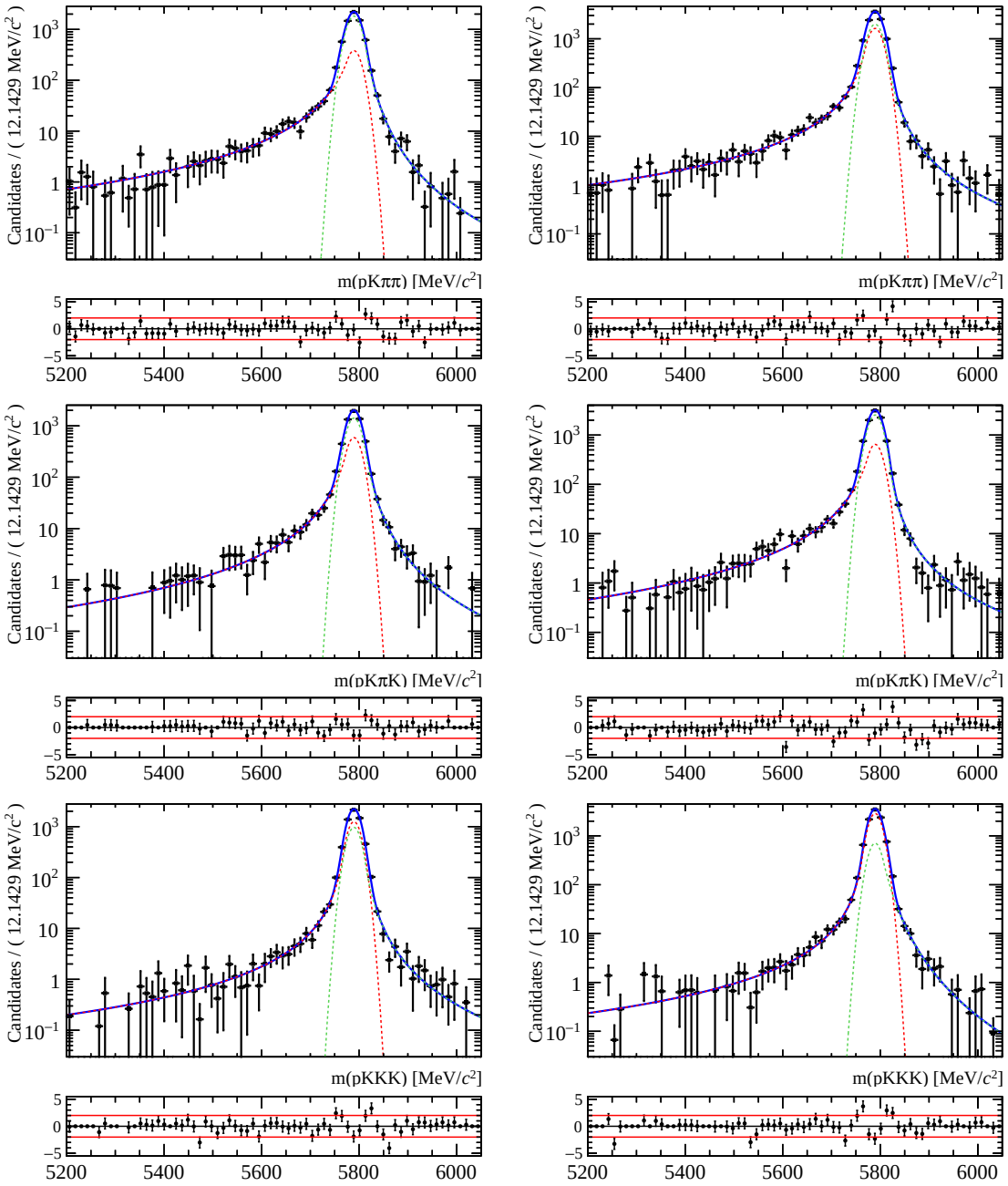

Figure 4.5: Signal invariant-mass distribution fitted with DCB PDF for the modes (in order from top-left to bottom-right) $\Xi_b^0 \to pK\pi\pi$, $\Xi_b^0 \to pK\pi K$ and $\Xi_b^0 \to pKKK$ for years (left column) 2011 and (right column) 2012. These shapes are used in the fit in order to determine the branching fractions.

4.4.3 Cross-feed shapes

There are seven charmless decay modes which are explicitly searched for in this analysis. Significant number of true signal events may still appear as cross-feeds in other spectra. The dominant cross-feeds are those with only one particle misidentified. When a K particle is misidentified as a π particle, the mass distribution of X_b^0 shifts to the left, while it shifts to right if π is misidentified as a K. In both cases, the shift of the most probable value w.r.t. the correct mass is small and hence the singly-misidentified cross-feeds peak near the signal region. As an illustration, the Fig. 4.6 displays the signal cross-feeds invariant-mass distributions for $\Lambda_b^0 \to pK^-K^+\pi^-$ and $\Lambda_b^0 \to p\pi^-\pi^+\pi^-$ events that are reconstructed considering $pK\pi\pi$ mass hypothesis: hence, these shapes aim at modelling true $\Lambda_b^0 \to pK^-K^+\pi^-$ ($\Lambda_b^0 \to p\pi^-\pi^+\pi^-$) signal events that may appear in the $pK\pi\pi$ spectrum if a K (π) is misidentified with a π (K). The fit makes use of a Double Crystal Ball PDF, with shared mean μ but two different widths σ's. In contrast with the signal events modelling, the choice of a DCB function is here taken opportunistically as a satisfactory enough empirical model.

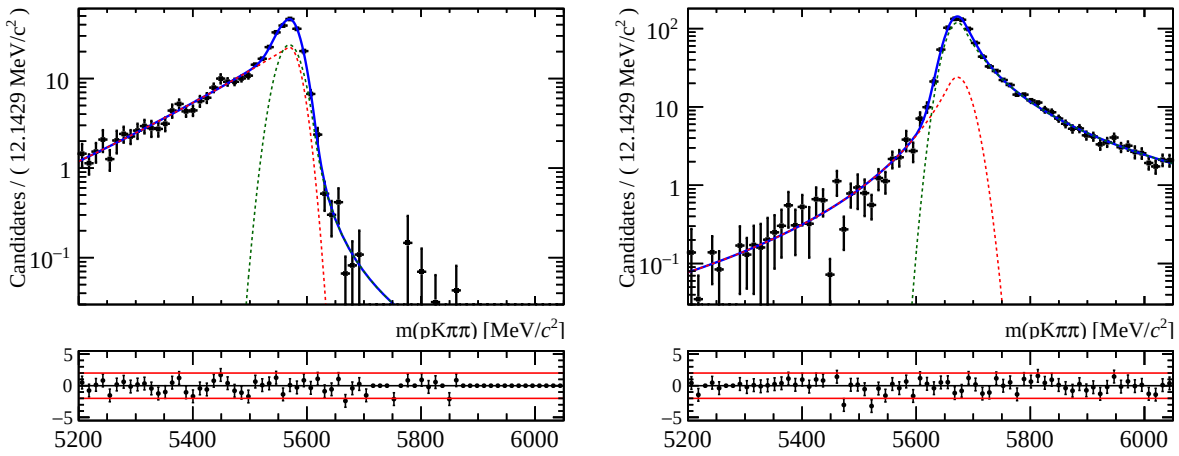

Figure 4.6: Signal cross-feeds invariant-mass distributions fitted with DCB PDF for the modes (in order from left to right) $\Lambda_b^0 \to pKK\pi$ as $pK\pi\pi$ and $\Lambda_b^0 \to p\pi\pi\pi$ as $pK\pi\pi$ for years 2012.

To model the shape of these cross-feeds, the full selection is applied to the events, except for the PID cuts, since the ProbNN variables in the real data are not well-described by simulation, neither for efficiency nor for misidentification probability. For each event, an efficiency weight is applied representing the probability to pass the PID cut. This event-by-event PID weighting is described in Subsection 3.2.2.

The 2012 remaining signal cross-feeds invariant-mass distributions for the branching fraction measurements[d] are shown in Fig. 4.7 and 4.8. All parameters determined from these fits, which are listed in Table 4.6, are fixed in the final nominal fit to the real data. The systematic uncertainty related to the fixing of these parameters is assigned by running pseudo-experiments varying the generated values according to the covariance matrix determined for the fit to the simulated data sample.

For the sake of simplifying the fit model, the cross-feed signals which are found negligible in the data (those which yields have been measured consistent with zero statistically) were a posteriori removed from the nominal mass model. Specifically, the $\Xi_b^0 \to pKKK$ events cross-feeding to $X_b^0 \to pKK\pi$ and $X_b^0 \to pK\pi K$ spectra are not included in the fit.

[d] The cross-feed fits for the $\Delta\mathcal{A}^{CP}$ measurements are displayed at Appendix C.4, that are gathered with the shape parameters and the cross-feed factors.

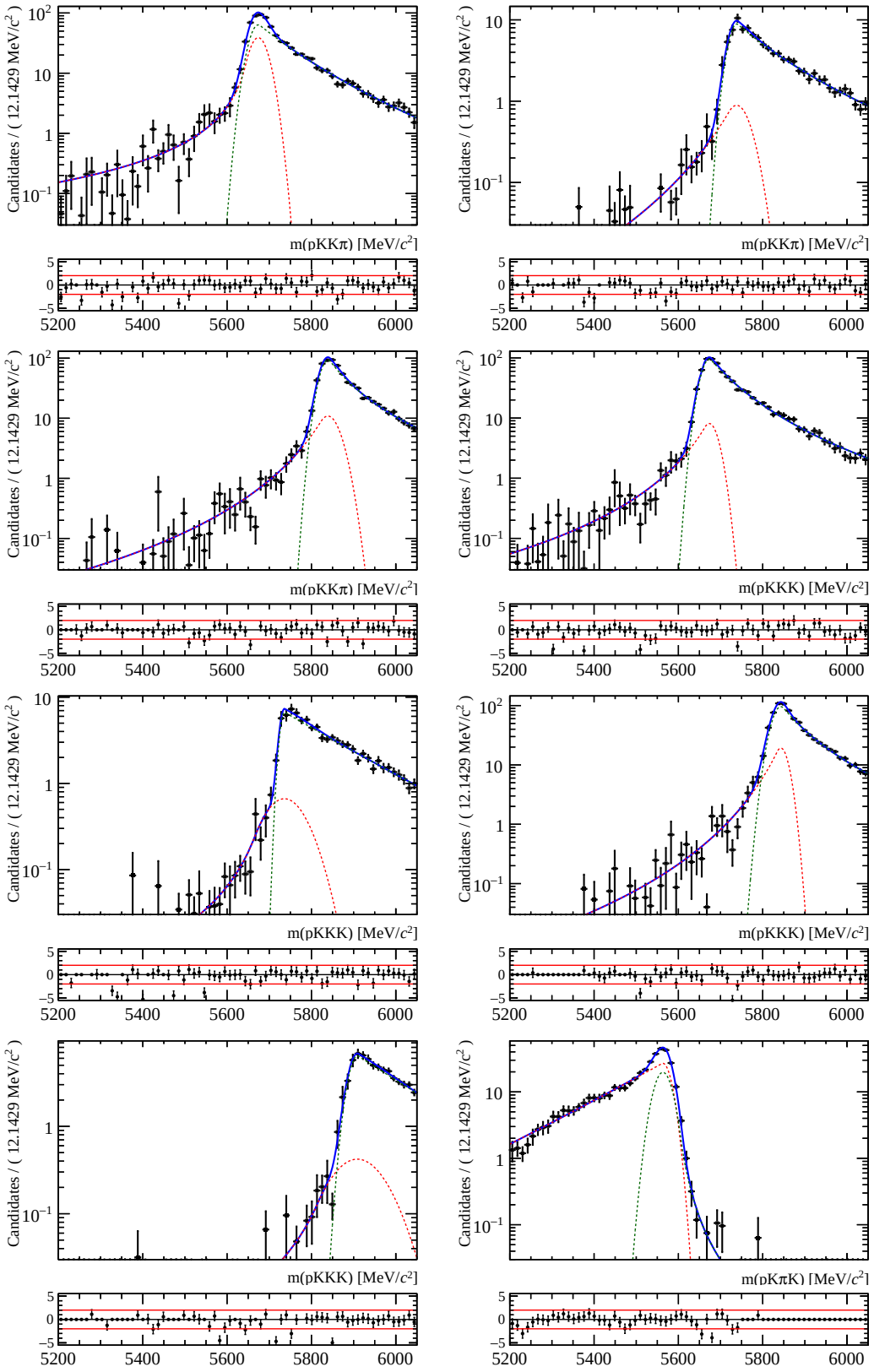

Figure 4.7: Signal cross-feeds invariant-mass distributions fitted with DCB PDF for the modes (in order from top-left to bottom-right) $\Lambda_b^0 \to pK\pi\pi$ as $pKK\pi$, $\Lambda_b^0 \to p\pi\pi\pi$ as $pKK\pi$ $\Xi_b^0 \to pK\pi\pi$ as $pKK\pi$, $\Lambda_b^0 \to pKK\pi$ as $pKKK$, $\Lambda_b^0 \to pK\pi\pi$ as $pKKK$, $\Xi_b^0 \to pK\pi K$ as $pKKK$, $\Xi_b^0 \to pK\pi\pi$ as $pKKK$ and $\Lambda_b^0 \to pKKK$ as $pK\pi K$ for years 2012. These shapes are used in the fit in order to determine the branching fractions.

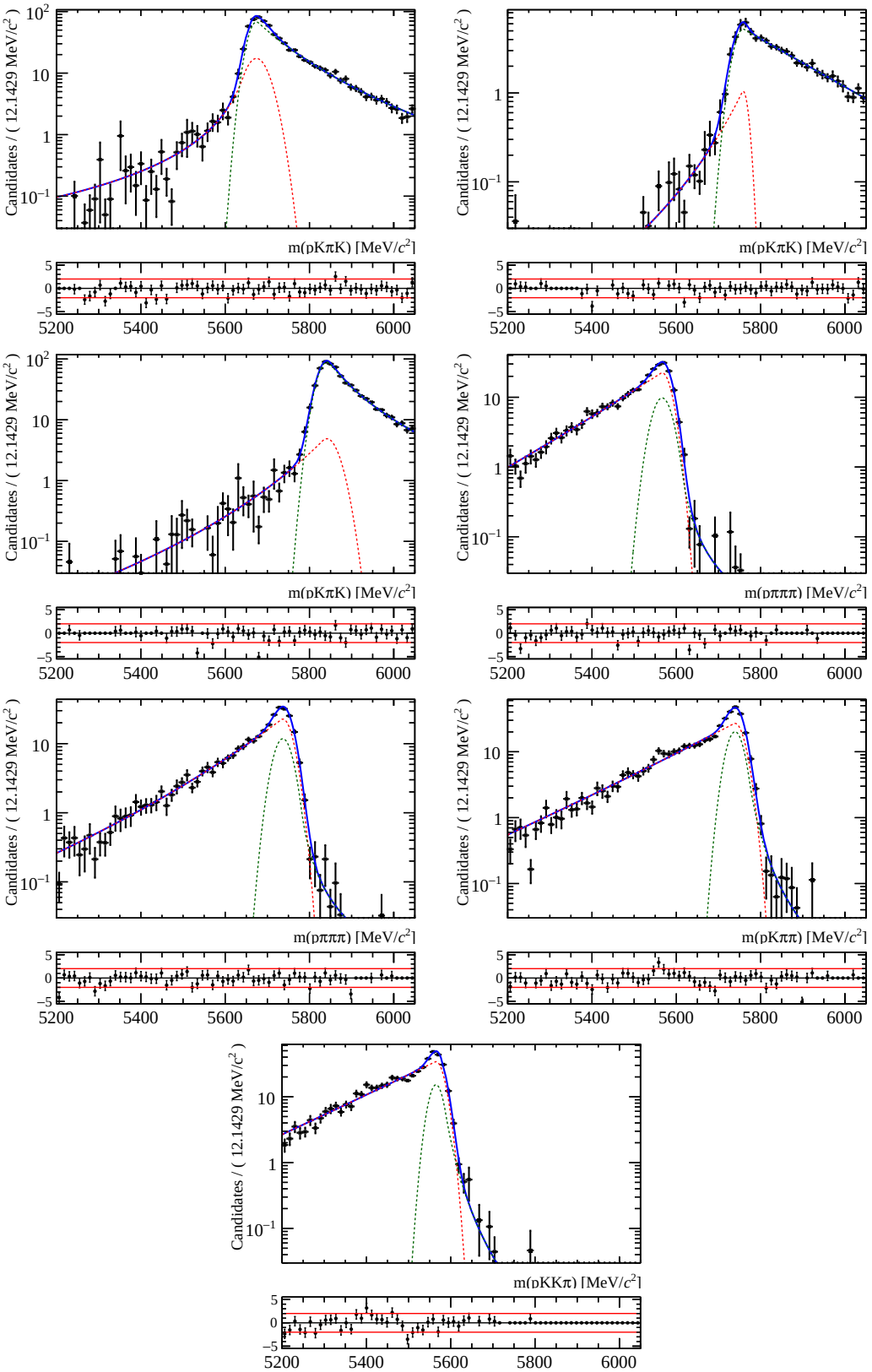

Figure 4.8: Signal cross-feeds invariant-mass distributions fitted with DCB PDF for the modes (in order from top-left to bottom-right) $\Lambda_b^0 \to pK\pi\pi$ as $pK\pi K$, $\Lambda_b^0 \to p\pi\pi\pi$ as $pK\pi K$, $\Xi_b^0 \to pK\pi\pi$ as $pK\pi K$, $\Lambda_b^0 \to pK\pi\pi$ as $p\pi\pi\pi$, $\Xi_b^0 \to pK\pi\pi$ as $p\pi\pi\pi$, $\Xi_b^0 \to pK\pi K$ as $pK\pi\pi$ and $\Lambda_b^0 \to pKKK$ as $pKK\pi$ for years 2012. These shapes are used in the fit in order to determine the branching fractions.

Table 4.6: Fit parameters obtained in the fit to cross-feeds shapes for the branching fraction measurements. The number of digits is automatically defined to be three in order to ensure in all cases the presence of at least two significant digits.

Cross-feed	Year	Fit parameters							
		α_1	α_2/α_1	n_1	n_2/n_1	σ_1	σ_1/σ_2	μ	f_2
$\Lambda_b^0 \to p\pi\pi\pi$ as $pK\pi\pi$	2011	0.542±0.036	-1.047±0.077	2.373±0.237	1.024±0.115	18.939±1.138	1.037±0.066	5672.265±1.271	0.133±0.021
	2012	0.709±0.036	-0.886±0.052	3.111±0.228	0.673±0.054	21.544±0.965	0.912±0.046	5672.266±0.929	0.160±0.020
$\Lambda_b^0 \to p\pi\pi\pi$ as $pKK\pi$	2011	1.186±0.075	-0.240±0.027	0.952±0.148	3.732±0.236	11.563±0.344	2.316±0.088	5750.946±4.085	0.073±0.009
	2012	0.610±0.054	-0.311±0.030	3.960±0.289	1.019±0.136	30.055±1.016	0.627±0.052	5738.252±3.620	0.075±0.009
$\Lambda_b^0 \to p\pi\pi\pi$ as $pK\pi K$	2011	0.160±0.027	-0.987±0.051	1.704±0.252	15.000±0.005	10.158±0.112	2.497±0.089	5760.708±2.588	0.055±0.008
	2012	0.255±0.033	-0.534±0.040	4.909±0.403	14.994±0.010	11.412±0.328	1.902±0.085	5758.644±2.497	0.080±0.010
$\Lambda_b^0 \to pK\pi\pi$ as $p\pi\pi\pi$	2011	0.226±0.025	-10.193±2.499	5.863±2.358	0.302±0.255	22.636±1.808	0.964±0.225	5563.744±2.582	0.862±0.055
	2012	0.177±0.014	-12.602±2.579	29.686±15.686	0.059±0.037	19.640±1.273	1.099±0.227	5566.359±1.999	0.849±0.044
$\Lambda_b^0 \to pK\pi\pi$ as $pKK\pi$	2011	1.594±0.096	-0.104±0.008	1.771±0.307	11.946±9.783	25.300±1.460	0.643±0.050	5672.358±1.579	0.264±0.033
	2012	1.418±0.068	-0.174±0.011	1.476±0.163	4.189±1.075	20.824±0.958	0.924±0.055	5673.921±1.148	0.246±0.026
$\Lambda_b^0 \to pK\pi\pi$ as $pK\pi K$	2011	0.461±0.033	-0.417±0.032	5.480±1.417	1.084±0.322	29.194±1.895	0.509±0.033	5668.500±1.570	0.072±0.015
	2012	1.194±0.067	-0.220±0.015	1.813±0.238	2.380±0.446	26.864±1.362	0.683±0.040	5674.278±1.330	0.159±0.023
$\Lambda_b^0 \to pK\pi\pi$ as $pKKK$	2011	0.354±0.042	-0.319±0.032	6.859±0.345	14.997±0.008	17.177±0.700	1.065±0.070	5741.420±4.355	0.048±0.008
	2012	1.451±0.081	-0.046±0.009	1.800±0.207	14.998±0.006	49.481±1.034	0.209±0.028	5735.995±3.470	0.084±0.010
$\Lambda_b^0 \to pKK\pi$ as $pK\pi\pi$	2011	0.437±0.056	-2.303±1.041	1.580±0.240	4.606±0.922	18.940±1.575	0.784±0.328	5569.561±2.002	0.933±0.048
	2012	0.158±0.013	-13.756±2.160	12.237±4.798	0.170±0.076	17.535±1.110	1.183±0.129	5569.358±1.556	0.707±0.038
$\Lambda_b^0 \to pKK\pi$ as $pKKK$	2011	0.495±0.035	-0.465±0.036	3.148±0.581	1.446±0.325	14.735±0.957	1.085±0.072	5671.982±1.483	0.078±0.018
	2012	0.525±0.029	-0.614±0.036	2.893±0.345	1.218±0.160	19.325±0.906	0.930±0.044	5673.213±1.141	0.067±0.012
$\Lambda_b^0 \to pKKK$ as $pKK\pi$	2011	0.153±0.012	-17.586±4.446	76.644±35.294	0.014±0.011	22.130±1.419	0.586±0.210	5562.391±2.006	0.923±0.031
	2012	0.129±0.007	-10.908±2.447	73.338±36.544	0.057±0.032	18.090±0.988	0.893±0.172	5565.051±1.561	0.890±0.027
$\Lambda_b^0 \to pKKK$ as $pK\pi K$	2011	0.116±0.011	-14.342±3.132	59.641±21.232	0.073±0.050	15.945±1.273	1.292±0.192	5564.078±2.000	0.775±0.040
	2012	0.143±0.011	-14.852±3.022	33.111±11.295	0.083±0.050	17.762±1.059	1.117±0.153	5563.235±1.580	0.795±0.035
$\Xi_b^0 \to pK\pi\pi$ as $p\pi\pi\pi$	2011	0.195±0.016	-8.116±2.524	87.822±29.151	0.045±0.040	21.623±1.605	0.936±0.239	5735.476±2.538	0.839±0.053
	2012	0.217±0.017	-10.001±1.951	9.743±3.497	0.189±0.116	20.587±1.255	0.985±0.178	5736.907±1.887	0.830±0.045
$\Xi_b^0 \to pK\pi\pi$ as $pKK\pi$	2011	0.153±0.013	-2.959±0.182	18.700±2.663	0.125±0.029	14.975±1.018	1.485±0.101	5842.716±1.707	0.066±0.014
	2012	0.665±0.046	-0.560±0.044	3.440±0.505	0.761±0.140	25.715±1.395	0.693±0.039	5839.131±1.183	0.110±0.018
$\Xi_b^0 \to pK\pi\pi$ as $pK\pi K$	2011	0.208±0.019	-2.321±0.230	19.982±2.150	0.105±0.023	18.334±1.336	1.222±0.089	5844.720±1.756	0.070±0.016
	2012	0.409±0.028	-0.983±0.074	5.931±1.222	0.537±0.121	25.665±1.310	0.793±0.041	5841.368±1.274	0.064±0.013
$\Xi_b^0 \to pK\pi K$ as $pK\pi\pi$	2011	0.157±0.011	-13.145±3.573	108.026±0.008	0.018±0.023	21.417±1.428	0.858±2.838	5740.040±6.016	0.842±0.094
	2012	0.154±0.009	-11.842±1.740	30.902±13.780	0.100±0.014	20.010±0.579	0.922±0.094	5739.345±1.498	0.816±0.031
$\Xi_b^0 \to pK\pi K$ as $pKKK$	2011	0.141±0.013	-2.493±0.226	18.912±2.769	0.167±0.048	15.537±0.976	1.302±0.081	5841.439±1.630	0.031±0.009
	2012	0.543±0.035	-0.708±0.053	4.067±0.624	0.768±0.162	16.299±0.813	1.209±0.065	5842.949±1.128	0.124±0.020

In the fit to data, the yield of a cross-feed is constrained to the corresponding signal yield in its respective spectrum by a relevant misidentification efficiency f. These factors are calculated by taking the ratios of selection efficiencies and PID efficiencies as a cross-feed and as a signal. PID efficiencies are measured in simulated events properly re-weighted to match the identification performance as measured in calibration data (see 3.2.2).
This f factor is given by:

$$f = \frac{\epsilon^{\text{Sel.}}_{\text{CF}} \cdot \epsilon^{\text{PID}}_{\text{CF}}}{\epsilon^{\text{Sel.}}_{\text{Sig.}} \cdot \epsilon^{\text{PID}}_{\text{Sig.}}} \tag{4.6}$$

where $\epsilon^{\text{PID}}_{\text{CF}}$ and $\epsilon^{\text{PID}}_{\text{Sig.}}$ are the average efficiencies of misidentifying the candidates as cross-feed and identifying as signal, respectively, while the $\epsilon^{\text{Sel.}}_{\text{CF}}$ and $\epsilon^{\text{Sel.}}_{\text{Sig.}}$ are the average efficiencies in selecting the candidates as cross-feed or signal, respectively. The $\epsilon^{\text{Sel.}}_{\text{CF}}$ and $\epsilon^{\text{Sel.}}_{\text{Sig.}}$ includes the BDT selection efficiency and the mass window cut to be within 5340 MeV/c^2 to 6400 MeV/c^2 (or 5450 MeV/c^2 to 6400 MeV/c^2 in the $\Xi_b^0 \to pK\pi K$ spectra). As expected, these two efficiencies are about the same except for the very small difference in their BDT values because of the slight change in some of the variables due to the refit of the decay tree depending on each spectrum. The uncertainty of these factor is calculated as the linear sum of three contributions : the quadratic addition of the uncertainties on the four efficiencies as they are coming from the PIDCalib data calibration sample, a 2 % relative uncertainty accounting for the PIDCalib samples binning choice and the observed difference on the factors considering the two extreme decay dynamics generated in the signal simulation samples. The factors f are summarised in Table 4.7.

A comment is in order as far as cross-feed contributions proceeding via two π or K misidentifications are concerned: there is no data calibration samples to determine the simultaneous misidentification of two pions in a same event. An estimation of the related cross-feed factor has been determined by letting the relevant contribution free in the fit when they can be measured on one hand and by constraining it to the PID re-weighting estimation on another hand. These two extreme cases allow to get a cross-feed factor estimation when this probability is maximal or minimal respectively and the variation of the yields between the two cases is assigned as a systematic uncertainty estimate.

Table 4.7: Cross-feed factors for the branching fractions measurements. The number of digits is automatically defined to be three in order to ensure in all cases the presence of at least two significant digits. The f factor must receive a factor 2 when two hadrons of the final state can be misidentified.

Cross-feeds	Efficiencies & CF-to-Signal factors (in %)					
	Year	$\epsilon_{\mathrm{CF}}^{\mathrm{PID}}$	$\epsilon_{\mathrm{CF}}^{\mathrm{Sel.}}$	$\epsilon_{\mathrm{Sig.}}^{\mathrm{PID}}$	$\epsilon_{\mathrm{Sig.}}^{\mathrm{Sel.}}$	f
$\Lambda_b^0 \to p\pi\pi\pi$ as $pK\pi\pi$	2011	6.483±0.087	73.495±0.452	47.641±0.298	73.498±0.453	13.607±1.647
	2012	6.673±0.067	65.670±0.366	49.174±0.208	65.332±0.367	13.641±1.562
$\Lambda_b^0 \to p\pi\pi\pi$ as $pKK\pi$	2011	0.889±0.026	69.160±0.474	47.641±0.298	73.498±0.453	5.000±0.194
	2012	0.912±0.022	59.956±0.379	49.174±0.208	65.332±0.367	5.000±0.240
$\Lambda_b^0 \to p\pi\pi\pi$ as $pK\pi K$	2011	0.640±0.015	69.193±0.474	47.641±0.298	73.498±0.453	5.000±0.194
	2012	0.663±0.013	60.006±0.379	49.174±0.208	65.332±0.367	5.000±0.241
$\Lambda_b^0 \to pK\pi\pi$ as $p\pi\pi\pi$	2011	2.211±0.037	72.534±0.470	52.575±0.299	72.868±0.454	4.187±0.741
	2012	2.029±0.027	65.670±0.381	53.633±0.212	66.166±0.369	3.756±0.430
$\Lambda_b^0 \to pK\pi\pi$ as $pKK\pi$	2011	6.071±0.080	68.550±0.474	52.575±0.299	72.868±0.454	10.863±1.114
	2012	6.278±0.066	60.114±0.381	53.633±0.212	66.166±0.369	10.634±0.862
$\Lambda_b^0 \to pK\pi\pi$ as $pK\pi K$	2011	5.681±0.070	68.570±0.474	52.575±0.299	72.868±0.454	10.169±1.114
	2012	5.819±0.059	60.083±0.381	53.633±0.212	66.166±0.369	9.852±0.862
$\Lambda_b^0 \to pK\pi\pi$ as $pKKK$	2011	0.784±0.026	68.544±0.476	52.575±0.299	72.868±0.454	1.403±0.168
	2012	0.787±0.018	59.974±0.383	53.633±0.212	66.166±0.369	1.329±0.123
$\Lambda_b^0 \to pKK\pi$ as $pK\pi\pi$	2011	2.657±0.045	74.093±0.472	57.311±0.308	70.832±0.478	4.849±0.482
	2012	2.490±0.032	65.286±0.384	58.783±0.225	60.491±0.384	4.571±0.428
$\Lambda_b^0 \to pKK\pi$ as $pKKK$	2011	6.454±0.085	69.880±0.482	57.311±0.308	70.832±0.478	11.111±1.389
	2012	6.702±0.070	59.311±0.386	58.783±0.225	60.491±0.384	11.180±1.025
$\Lambda_b^0 \to pKKK$ as $pKK\pi$	2011	3.467±0.053	70.178±0.463	61.921±0.291	70.110±0.445	5.604±0.970
	2012	3.218±0.038	60.038±0.371	64.148±0.209	59.842±0.356	5.033±0.767
$\Lambda_b^0 \to pKKK$ as $pK\pi K$	2011	2.751±0.045	70.203±0.456	61.921±0.291	70.110±0.445	4.449±0.970
	2012	2.560±0.033	60.320±0.365	64.148±0.209	59.842±0.356	4.022±0.767
$\Xi_b^0 \to pK\pi\pi$ as $p\pi\pi\pi$	2011	2.218±0.037	75.337±0.453	53.754±0.298	75.410±0.450	4.122±0.741
	2012	2.058±0.027	68.112±0.368	56.077±0.211	68.331±0.365	3.658±0.430
$\Xi_b^0 \to pK\pi\pi$ as $pKK\pi$	2011	6.095±0.082	71.967±0.471	53.754±0.298	75.410±0.450	10.821±1.114
	2012	6.181±0.066	63.977±0.378	56.077±0.211	68.331±0.365	10.321±0.862
$\Xi_b^0 \to pK\pi\pi$ as $pK\pi K$	2011	5.733±0.078	72.026±0.471	53.754±0.298	75.410±0.450	10.186±1.114
	2012	5.983±0.062	63.994±0.378	56.077±0.211	68.331±0.365	9.992±0.862
$\Xi_b^0 \to pK\pi K$ as $pK\pi\pi$	2011	3.311±0.049	74.811±0.458	58.528±0.305	74.430±0.456	5.685±0.482
	2012	2.958±0.034	66.235±0.376	60.665±0.219	64.091±0.378	5.040±0.428
$\Xi_b^0 \to pK\pi K$ as $pKKK$	2011	6.310±0.079	74.075±0.459	58.528±0.305	74.430±0.456	10.730±1.389
	2012	6.853±0.074	63.728±0.380	60.665±0.219	64.091±0.378	11.233±1.025

4.4.4 B decays shapes

As mentioned in Subsection 4.2.4, $B^0_{d,s} \to$ 4-body decays and $B \to$ 5-body decays populate the invariant-mass spectra of m_{phhh}[e]. The dominant $B^0_{d,s}$ decays backgrounds are those with one π or one K misidentified as a p. Five-body decays coming from $B^0_{d,s}$ and B^+ with a mis-identified π or K and then a missing π also contributes as a background. Despite the hard PID cut on the hypothesised proton track, the $B^0_{d,s}$ and B^+ decays contributions must definitely be included in the nominal fit model and their shapes modelled: these contributions can exhibit significant CP asymmetries and are significant sources of background that consequently need to be properly handled for the $\Delta\mathcal{A}^{CP}$ and the branching fraction measurements. The shapes of the $B^0_{d,s}$ physics backgrounds are empirically modelled by a Cruijff function, mathematically given by Eq. 4.2. An illustration of the fit to the simulated sample is displayed on Fig 4.9. These simulated B decays events proceed through quasi-2-body decays with two low-mass charmless resonances as listed in Table 3.1.
The Cruijff function gives satisfactory results in the modelling of the background coming from B-mesons decays. In the case of $B^0_{d,s}$ and B^+ to 5-body decays, the shapes are as well empirically-modelled by a Cruijff PDF. The shapes are obtained by fitting the mass distribution of simulated $B^+ \to K\pi\pi\pi + \{\pi^0\}$ reconstructed as $p\pi\pi\pi$, *i.e.* K mis-identified as a π and a missing π.

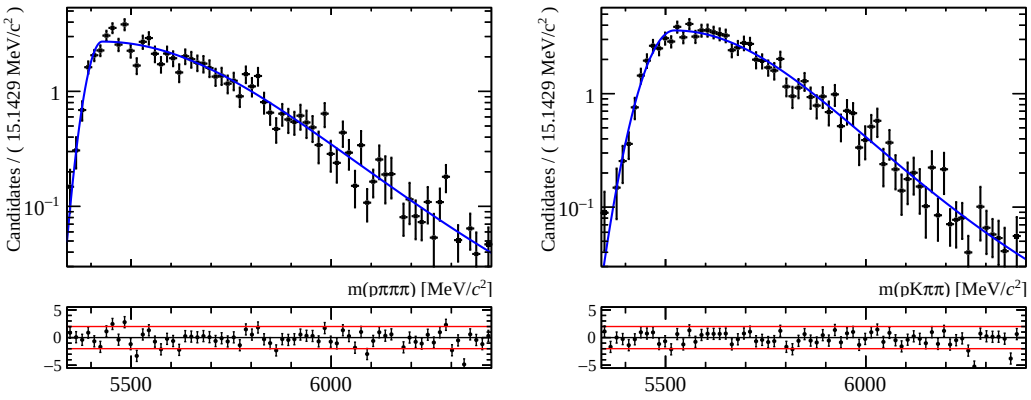

Figure 4.9: B mesons decays backgrounds invariant-mass distribution fitted with Cruijff PDF for the modes (in order from top-left to bottom-right) $B^0 \to \pi\pi\pi\pi$ as $p\pi\pi\pi$, $B^0 \to K\pi\pi\pi$ as $p\pi\pi\pi$, for years (left column) 2011 and (right column) 2012.

Shown in Fig 4.10 and 4.11 are the remaining fits to the simulated B decays and to the $B^0_{d,s}$ and B^+ to 5-body decays events passing the full selection and PID-calibrated in the same way as discussed in Section 3.2.2 for the branching fraction measurements[f]. The fit parameters are summarised in Table 4.8.

[e] Let's remind here that the dominant $B^0_{d,s}$ physics backgrounds included in the simultaneous fit to the data sample are listed in Table 4.1 of Section 4.2.

[f] The shapes for $\Delta\mathcal{A}^{CP}$ purpose are displayed in Appendix C.5, and are gathered with the shape parameters and the cross-feed factors.

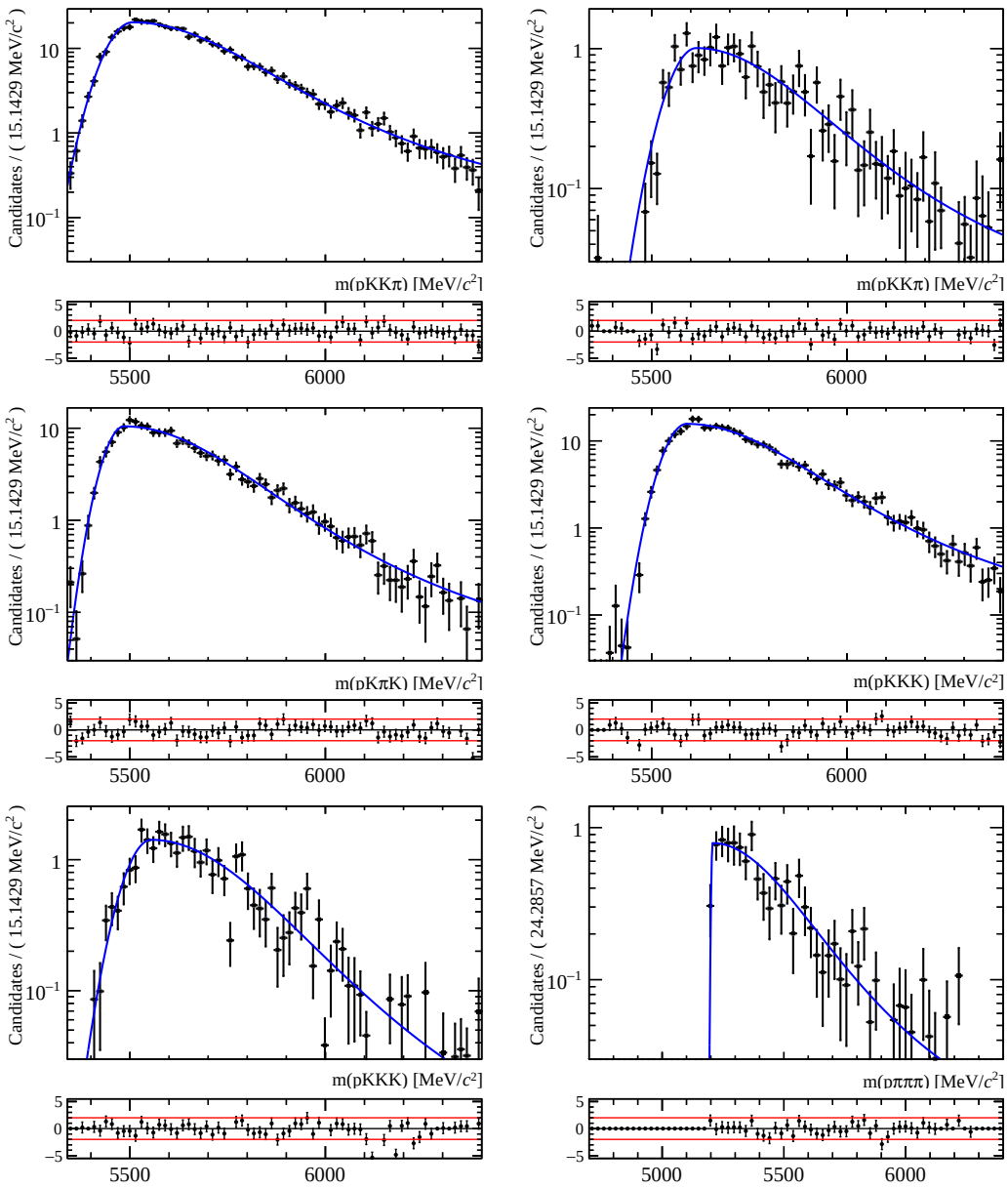

Figure 4.10: B mesons decays backgrounds invariant-mass distribution fitted with Cruijff PDF for the modes (in order from top-left to bottom-right) $B^0 \to KKK\pi$ as $pKK\pi$, $B_s^0 \to \pi KK\pi$ as $pKK\pi$, $B^0 \to KK\pi K$ as $pK\pi K$, $B_s^0 \to KKKK$ as $pKKK$, $B^0 \to \pi KKK$ as $pKKK$ and $B^+ \to K\pi\pi\pi + \{\pi^0\}$ for 2012. These shapes are used in the fit in order to determine the branching fractions. Although the mass range shown in the last plot ranges from 4700 MeV/c^2 in order to obtain the Cruijff shape parameters, in the final fit the mass range starts from 5340. MeV/c^2 (or 5450. MeV/c^2 in the $\Xi_b^0 \to pK\pi K$ spectra).

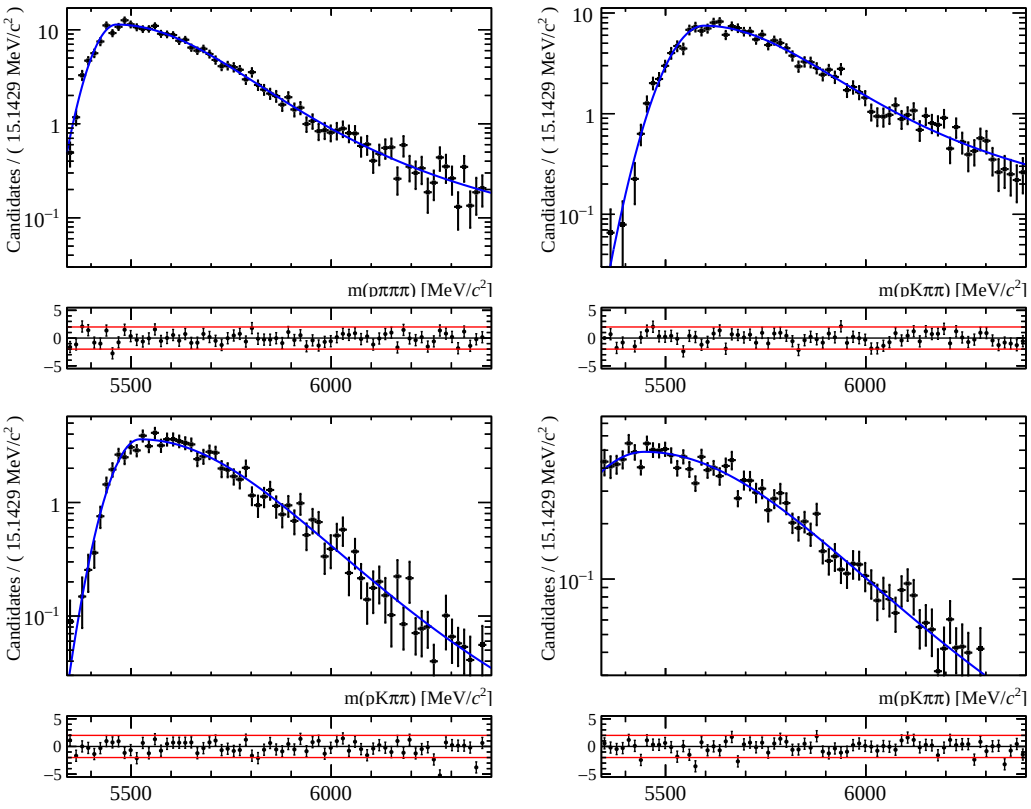

Figure 4.11: B mesons decays backgrounds invariant-mass distribution fitted with Cruijff PDF for the modes (in order from top-left to bottom-right) $B^0 \to K\pi\pi\pi$ as $p\pi\pi\pi$, $B^0_s \to KK\pi\pi$ as $pK\pi\pi$, $B^0 \to \pi K\pi\pi$ as $pK\pi\pi$ and $B^0 \to KKK\pi$ as $pK\pi\pi$ for 2012. These shapes are used in the fit in order to determine the branching fractions.

Table 4.8: Fit parameters obtained in the fit to B physics shapes for the branching fraction determination.

B physics bkg.	Year	Fit parameters σ_L	σ_R	α_R	μ
$B^0 \to \pi\pi\pi\pi$ as $p\pi\pi\pi$	2011	37.989±31.340	255.303±86.125	0.040±0.198	5445.729±49.493
	2012	31.026±22.988	250.001±45.617	0.104±0.080	5427.825±32.689
$B^0 \to K\pi\pi\pi$ as $p\pi\pi\pi$	2011	49.172±13.928	136.292±26.837	0.173±0.050	5471.159±21.586
	2012	49.388±14.447	178.890±26.511	0.170±0.045	5463.551±22.488
$B^0 \to \pi K\pi\pi$ as $pK\pi\pi$	2011	69.867±31.019	150.954±55.271	0.132±0.111	5550.454±51.005
	2012	57.001±23.353	200.550±50.522	0.111±0.099	5521.921±40.306
$B^0_s \to KK\pi\pi$ as $pK\pi\pi$	2011	64.986±20.436	153.472±44.250	0.180±0.087	5585.964±35.730
	2012	70.658±15.881	183.297±38.143	0.211±0.076	5596.293±27.847
$B^0_s \to \pi KK\pi$ as $pKK\pi$	2011	42.118±29.662	249.659±158.052	0.004±0.166	5588.950±44.802
	2012	64.138±33.837	191.301±85.942	0.207±0.216	5614.722±57.361
$B^0 \to KKK\pi$ as $pK\pi\pi$	2011	235.386±45.038	201.018±51.204	0.156±0.217	5485.037±307.501
	2012	152.534±67.555	269.974±26.904	0.157±0.176	5447.530±94.656
$B^0 \to KKK\pi$ as $pKK\pi$	2011	50.876±15.713	152.228±6.656	0.169±0.042	5491.174±18.623
	2012	55.992±9.705	183.605±21.200	0.174±0.038	5506.839±16.401
$B^0 \to KK\pi K$ as $pK\pi K$	2011	39.637±11.906	143.357±27.424	0.157±0.053	5482.050±20.096
	2012	42.295±8.248	178.863±22.423	0.151±0.048	5485.286±13.479
$B^0 \to \pi KKK$ as $pKKK$	2011	46.841±36.820	182.174±83.351	0.140±0.182	5519.164±63.951
	2012	59.389±29.627	185.077±68.274	0.138±0.148	5554.386±50.468
$B^0_s \to KKKK$ as $pKKK$	2011	39.788±8.628	151.498±20.152	0.168±0.039	5571.940±15.479
	2012	47.275±8.995	176.655±24.104	0.169±0.049	5590.037±16.016

The $B^0 \to K\pi\pi\pi$, $B^0 \to KKK\pi$ and $B_s^0 \to K\pi\pi K$ appear in more than one spectrum, as summarised in last column of Table 4.1. The ratios of yields of these B physics backgrounds from one spectrum to a reference spectrum is Gaussianly-constrained according to the selection efficiency computed from the simulation sample and PID mis-identification rate. The reference spectrum for each of these B physics is chosen to be the spectrum where they are expected to be dominant, i.e., $X_b^0 \to p\pi\pi\pi$ for $B^0 \to K\pi\pi\pi$, $X_b^0 \to pK\pi\pi$ for $B_s^0 \to K\pi\pi K$ and $X_b^0 \to pKK\pi$ for $B^0 \to KKK\pi$. The cross-spectra factors are calculated using:

$$f = \frac{\epsilon_{\mathrm{X}}^{\mathrm{Sel.}} \cdot \epsilon_{\mathrm{X}}^{\mathrm{PID}}}{\epsilon_{\mathrm{Ref.}}^{\mathrm{Sel.}} \cdot \epsilon_{\mathrm{Ref.}}^{\mathrm{PID}}}, \tag{4.7}$$

where $\epsilon_{\mathrm{X}}^{\mathrm{PID}}$ and $\epsilon_{\mathrm{Ref.}}^{\mathrm{PID}}$ are the average efficiencies of misidentifying the B physics event as an event in X spectrum and misidentifying as an event in the reference spectrum, respectively, while the $\epsilon_{\mathrm{X}}^{\mathrm{Sel.}}$ and $\epsilon_{\mathrm{Ref.}}^{\mathrm{Sel.}}$ are the average efficiencies of selecting the B physics event as an event in the X spectrum and in the reference spectrum, respectively. The $\epsilon_{\mathrm{X}}^{\mathrm{Sel.}}$ and $\epsilon_{\mathrm{Ref.}}^{\mathrm{Sel.}}$ includes BDT selection and the mass window cut to be within 5340 MeV/c^2 (5450 MeV/c^2 in the $\Xi_b^0 \to pK\pi K$ spectrum) to 6400 MeV/c^2. Table 4.9 summarises these factors.

Table 4.9: B physics cross-spectra factors used for the branching fractions measurement. The number of digits is automatically defined to be three in order to ensure in all cases the presence of at least two significant digits.

B physics	Year	Efficiencies & X-to-Reference factors (in %) $\epsilon_{\mathrm{X}}^{\mathrm{PID}}$	$\epsilon_{\mathrm{X}}^{\mathrm{Sel.}}$	f
$B^0 \to K\pi\pi\pi$ as $p\pi\pi\pi$	2011	2.838±0.040	19.219±0.306	Reference
	2012	3.493±0.022	16.996±0.205	Reference
$B^0 \to \pi K\pi\pi$ as $pK\pi\pi$	2011	3.416±0.077	5.256±0.160	32.924±1.430
	2012	2.844±0.037	6.953±0.131	33.310±0.888
$B^0 \to KKK\pi$ as $pKK\pi$	2011	3.259±0.036	30.825±0.388	Reference
	2012	4.127±0.021	26.727±0.258	Reference
$B^0 \to KK\pi K$ as $pK\pi K$	2011	3.318±0.053	14.407±0.265	47.584±1.410
	2012	4.224±0.032	12.297±0.175	47.099±0.913
$B^0 \to \pi KKK$ as $pKKK$	2011	4.003±0.148	1.953±0.098	7.780±0.502
	2012	3.495±0.077	2.106±0.072	6.672±0.282
$B^0 \to KKK\pi$ as $pK\pi\pi$	2011	0.123±0.003	30.047±0.383	3.682±0.109
	2012	0.149±0.002	26.931±0.259	3.631±0.070
$B_s^0 \to KK\pi\pi$ as $pK\pi\pi$	2011	2.802±0.049	25.658±0.505	Reference
	2012	3.768±0.029	22.729±0.334	Reference
$B_s^0 \to \pi KK\pi$ as $pKK\pi$	2011	3.874±0.160	2.678±0.163	14.432±1.130
	2012	3.080±0.075	3.623±0.133	13.030±0.615

4.4.5 Partially-reconstructed background shapes

The partially-reconstructed backgrounds with no mis-identified particle are modelled by an ARGUS function convoluted by a Gaussian resolution. An ARGUS⊗Gauss PDF is added in each spectrum to model the partially-reconstructed backgrounds with a non-reconstructed π^0 coming from the Λ_b^0 decays, except in the $pK\pi K$ spectrum where no Λ_b^0 signal charmless decay is expected with two and only two same electric charge kaons . In the $pK\pi\pi$, $pK\pi K$ and $pKKK$ spectra, additional ARGUS⊗Gauss shapes are added to model the partially-reconstructed backgrounds coming from the Ξ_b^0 decays. The parameters of the convoluted ARGUSes are directly determined from a fit to the data, with some of the parameters shared or expressed in terms of other parameters of the spectra. This shape is hence an effective model that is meant to cover the background contributions in this region of invariant-mass distributions. The convolution of the ARGUSes with a Gaussian function is numerically and computationally demanding.

The following items list the physical constraints used in order to guide the fit in determining the parameters of the convoluted ARGUSes:

- The slope c and the power p of the ARGUSes are shared among all the charmless spectra, but not shared among years, assuming similar kinematics of the sources.
- The slope c and the power p of the ARGUSes are also shared among charmed spectra. These parameters are also not shared among years.
- Since the main partially-reconstructed backgrounds are $X_b^0 \to 4$ body plus a missing π^0 (an isolated vertex is required in the selection), all the threshold parameters m_t are set to be the difference of the nominal mass of Λ_b^0 (or Ξ_b^0), and the nominal mass of π^0 ($m_{\pi^0}^{\mathrm{PDG}} = 134.9766 \pm 0.0006\,\mathrm{MeV}/c^2$ [8]).
- The resolution of the Gaussian function convoluting the ARGUS function is mainly driven by the detector resolution, and up to first approximation is the same as the resolution of the signal models. The resolutions of the Gaussian functions convoluting the ARGUSes are then set to be the same as the sigma of Λ_b^0 signal shapes (or to Ξ_b^0 in the spectrum $pK\pi K$ where there is no Λ_b^0 signal).
- All the ARGUS⊗Gauss shape parameters are shared by both Λ_b^0 and $\overline{\Lambda}_b^0$ spectra (or Ξ_b^0 and $\overline{\Xi}_b^0$).
- The yield of the partially reconstructed background coming from the Ξ_b^0 decays in $pK\pi\pi$ spectrum is constrained to the yield of the analogous contribution coming from the Λ_b^0 decays as

$$\mathcal{N}(\text{PR from } \Xi_b^0 \to \text{5-body}) = \frac{\mathcal{N}(\text{PR from } \Lambda_b^0 \to \text{5-body})}{\rho} \cdot \frac{\mathcal{N}(\Xi_b^0 \text{ Signal})}{\mathcal{N}(\ \Lambda_b^0 \text{ Signal})} \tag{4.8}$$

where ρ is the ratio of the integrated PDFs of the partially reconstructed from Ξ_b^0 and Λ_b^0 contributions. The computed value for this ratio is found to be $\rho = 0.5 \pm 0.2$. The central value is used in the baseline fit model and a systematic uncertainty (further discussed in Section 6.3) is determined in order to estimate the impact of this 40 % relative uncertainty.

As mentioned in Section 4.2, there are also partially-reconstructed backgrounds due to $\Lambda_b^0 \to p\pi^-(\eta' \to \pi^+\pi^-\gamma)$ and $\Lambda_b^0 \to pK^-(\eta' \to \pi^+\pi^-\gamma)$ in the $p\pi\pi\pi$ and $pK\pi\pi$ spectra, respectively. The shapes of these backgrounds are obtained from the fit to the simulated

$\Lambda_b^0 \to pK^-(\eta' \to \pi^+\pi^-\gamma)$ events reconstructed as $pK\pi\pi$. The same shapes are used for the $\Lambda_b^0 \to p\pi^-(\eta' \to \pi^+\pi^-\gamma)$ as $p\pi\pi\pi$. The shape parameters obtained are then fixed in the nominal fit to data. Also as mentioned in Section 4.2, the ratio of the yield of this partially-reconstructed background with respect to the Λ_b^0 signal reads 1/20 and is fixed in the fit of the $p\pi\pi\pi$ spectrum. It is on the contrary allowed to vary freely in the fit of the $pK\pi\pi$ spectrum.

Due to the significant amount of partially-reconstructed $\Lambda_b^0 \to pK^-\pi^+\pi^- + \{\pi^0\}$, a number of these events are present in the $pKK\pi$ and $pK\pi K$ spectra, where one of the pions is mis-identified as a kaon. We included these contributions in our nominal fit in the $pKK\pi$ and $pK\pi K$ spectra, where their corresponding yields are constrained by the ratio of (mis)identification rates and selection efficiencies. The shape is obtained by selecting the partially-reconstructed backgrounds in the charmed spectra $\Lambda_b^0 \to (\Lambda_c^+ \to pK\pi)\pi$ and reconstructing these events as $pK\pi K$, where the pion coming from the Λ_b^0 (and not from the Λ_c^+) is being mass-swapped as a kaon. The resulting mass distribution is parameterised by a histogram (RooHistPdf). These shapes are then used to model the $\Lambda_b^0 \to pK^-\pi^+\pi^- + \{\pi^0\}$ as $pKK\pi + \{\pi^0\}$ and $pK\pi K + \{\pi^0\}$.

The yields of these mis-identified partially-reconstructed backgrounds are Gaussianly-constrained to be a factor f with respect to the yields of partially-reconstructed background in the $pK\pi\pi$ spectra. Is is found to be $(18.3 \pm 5.1)\%$ for the year 2011 and $(18.4 \pm 5.1)\%$ for the year 2012.

4.4.6 Combinatoric shapes

As previously discussed, first order Bernstein polynomial of the second kind is used to model the combinatorial background. A comment is in order regarding the choice of a polynomial model as the baseline against an exponential shape for the combinatorics: the only valuable information about the combinatorics for most of the modes studied in this analysis lies in the right-hand side-band of the data[g]. The left-handed region of the invariant-mass distribution of most of the spectra of interest is populated by the partially reconstructed background and the signal cross-feeds. Since the mechanics of the adjustment of an exponential shape requires a leverage on the left-handed part of the invariant mass distribution, it is likely that its fit can absorb overlooked background contributions. These considerations drove us to the choice of the polynomial model for the fit model design with blind signal region.

4.4.7 Charmed decay shapes

As discussed in Chapter 5, branching fractions of four-body charmless signals will be determined with respect to the well-known $b \to c$ transition decay $\Lambda_b^0 \to (\Lambda_c^+ \to pK^-\pi^+)\pi^-$. The reconstructed invariant-mass spectra of simulated $\Lambda_b^0 \to (\Lambda_c^+ \to pK^-\pi^+)\pi^-$ events is modelled by a double CB function with shared mean μ and shared width σ. The same selection as applied in charmless spectra except with reversed Λ_c^+ mass window cuts, is applied to the charmed spectra. A PID weight is assigned on an event-by-event basis calculated in the same way as explained in Section 3.2.2. The same shape is eventually used for $\Lambda_b^0 \to (\Lambda_c^+ \to p\pi^-\pi^+)\pi^-$ and $\Xi_b^0 \to (\Xi_c^+ \to pK^-\pi^+)\pi^-$ decay modes, that are used as control channel in the $\Delta\mathcal{A}^{CP}$ determination.

[g] It has been mentioned before that there is however a competition in this region with B physics events which forbids the simultaneous determination of these two contributions from the invariant-mass data distribution only.

Chapter 5

Branching fraction measurements

A part of the analysis presented in this document consists in measuring branching fractions of charmless decay modes. The simultaneous fitter strategy as well as the fit model that have been presented in the previous chapters are used in order to determine the signal yields that are needed in the branching fraction derivation, as explicited in Eq. 3.6. In addition, this chapter is presenting the efficiency derivation, the systematic uncertainties estimates and, eventually, the branching fraction measurements. The results displayed in this chapter have been published [39].

Chapter contents

5.1 Fit results

The figures which are provided in this section correspond to the addition of the charge-separated spectra (p and $\overline{p}$). The fit model was developed with the signal regions blinded. It was blessed by the internal review of the LHCb collaboration and the addition of the p and $\overline{p}$ spectra was unblinded. Note that the individual charge-separated spectra were kept blind for the $\Delta\mathcal{A}^{CP}$ analysis.

Fig 5.1 to 5.5 display the fit results of the simultaneous fit to the invariant mass spectra of the five final states using the whole data sample. The figure 5.6 displays the result of the fit to the normalisation channel. The values of the floating parameters of the simultaneous fit are displayed in Appendix D.1. All signals that were searched for are established unambiguously with the exception of the $\Xi_b^0 \to pK^-K^+K^-$ decay. The signal-to-background ratios vary from mode to mode following the hierarchy of the branching fractions and are summarised in Table 5.1.

Table 5.1: Signal yields for each decay mode, determined by summing the fitted yields in each year of data taking. The signal (S) to background (B, adding all sources) ratios in an invariant mass window, covering ± 3 times the measured signal widths, are provided. The corresponding invariant mass ranges are reported in the fourth column.

Decay mode	Signal yield	S/B	$\pm 3\sigma$ range (MeV/c^2)
$\Lambda_b^0 \to p\pi^-\pi^+\pi^-$	1809 ± 48	4.9 ± 0.3	[5573.9, 5674.6]
$\Lambda_b^0 \to pK^-\pi^+\pi^-$	5193 ± 76	7.7 ± 0.4	[5574.4, 5674.2]
$\Lambda_b^0 \to pK^-K^+\pi^-$	444 ± 30	0.71 ± 0.06	[5577.4, 5671.1]
$\Lambda_b^0 \to pK^-K^+K^-$	1706 ± 46	8.1 ± 0.7	[5579.0, 5674.6]
$\Xi_b^0 \to pK^-\pi^+\pi^-$	183 ± 22	0.59 ± 0.09	[5747.9, 5846.2]
$\Xi_b^0 \to pK^-\pi^+K^-$	199 ± 21	0.81 ± 0.10	[5747.4, 5846.2]
$\Xi_b^0 \to pK^-K^+K^-$	27 ± 14	0.14 ± 0.08	[5752.7, 5840.8]
$\Lambda_b^0 \to (\Lambda_c^+ \to pK^-\pi^+)\pi^-$	16518 ± 133	—	[5573.7, 5674.8]

5.1.1 Fit to the $p\pi\pi\pi$ candidate mass spectrum

Figure 5.1 shows the unambiguous $\Lambda_b^0 \to p\pi^-\pi^+\pi^-$ signal. The background model describes satisfactorily the data. Since the right-hand side-band of the $p\pi\pi\pi$ invariant-mass spectrum is exclusively composed of B and combinatorial backgrounds, it provides confidence in these two modellings. Partially-reconstructed backgrounds are also well accounted for by the ARGUS parameterisation.

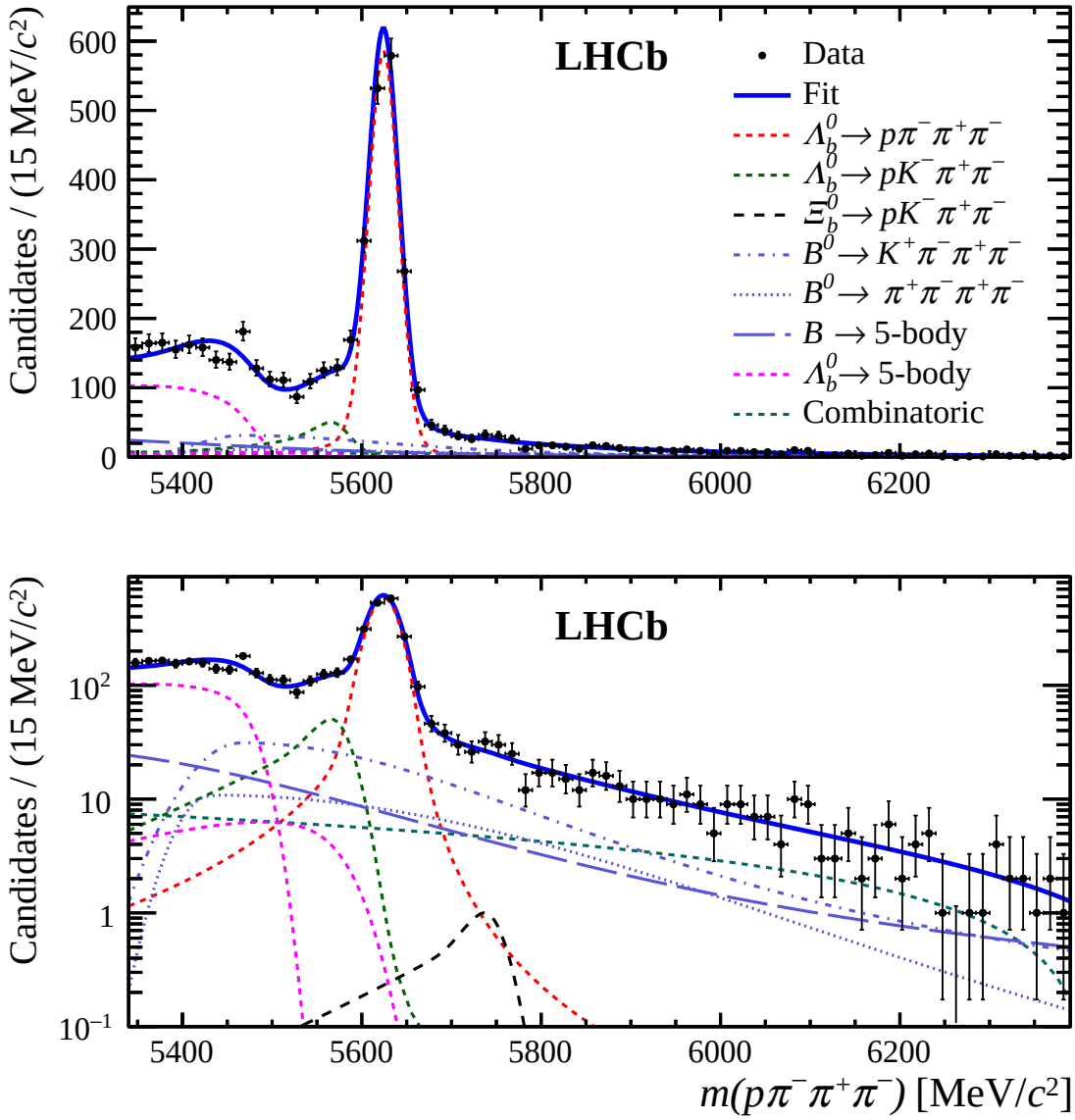

Figure 5.1: Results of the fit to the $p\pi\pi\pi$ candidate mass spectrum with (top) linear and (bottom) logarithmic scales. The different components employed in the fit are indicated in the legend. The $\Lambda_b^0 \to$ 5-body legend describes two components, the radiative partially reconstructed background $\Lambda_b^0 \to p\pi^-\eta'$ and the partially reconstructed background $\Lambda_b^0 \to p\pi^-\pi^+\pi^-\pi^0$ where a π^0 is not reconstructed. The latter has a lower-mass endpoint.

5.1.2 Fit to the $pK\pi\pi$ candidate mass spectrum

Figure 5.2 shows the unambiguous $\Lambda_b^0 \to pK^-\pi^+\pi^-$ signal as well as the $\Xi_b^0 \to pK^-\pi^+\pi^-$ one. One can notice that the background structure is quite rich. As previously emphasised, the advantage of using a simultaneous fit is that information from the previous invariant-mass spectra (and hence from the following) is used in order to constrain some of the contributions that are present in the spectrum (*i.e.* $\Lambda_b^0 \to p\pi^-\pi^+\pi^-$ signal cross-feed). Here again, the partially-reconstructed backgrounds are well accounted for by the ARGUS parameterisation. However, differences between the data and the fit model can be noted in the high-mass sidebands. It happens that the significance of the disagreement is not larger than two standard deviations and those discrepancies are anyway covered within the size of the variations considered in the evaluation of the systematic uncertainties.

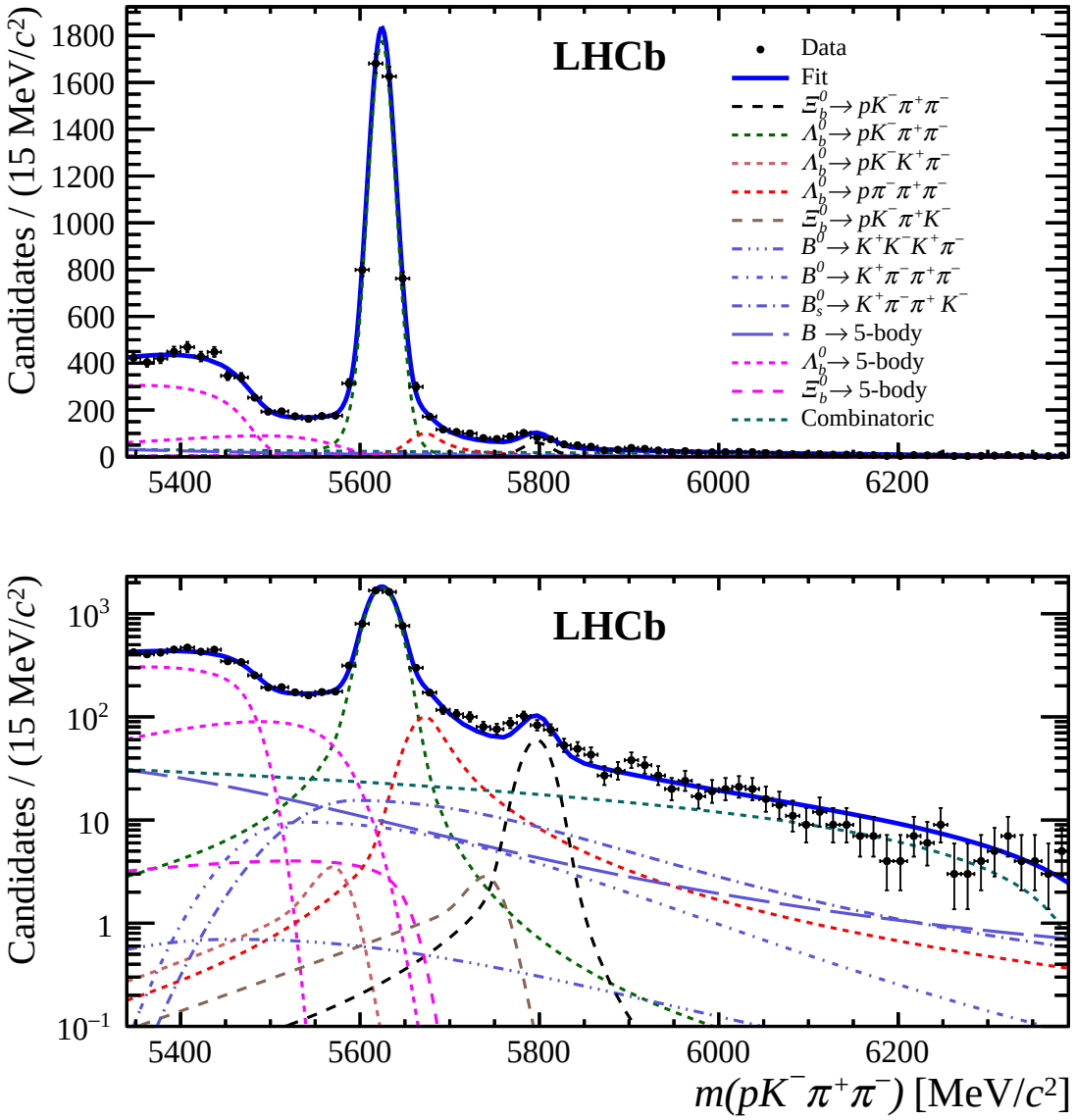

Figure 5.2: Results of the fit to the $pK\pi\pi$ candidate mass spectrum with (top) linear and (bottom) logarithmic scales. The different components employed in the fit are indicated in the legend. The $\Lambda_b^0 \to$ 5-body legend describes two components, the radiative partially reconstructed background $\Lambda_b^0 \to pK^-\eta'$ and the partially reconstructed background $\Lambda_b^0 \to pK^-\pi^+\pi^-\pi^0$ where a π^0 is not reconstructed. The latter has a lower-mass endpoint.

5.1.3 Fit to the $pKK\pi$ candidate mass spectrum

Figure 5.3 shows the unambiguous $\Lambda_b^0 \to pK^-K^+\pi^-$ signal. Here again, one can notice that the background structure is quite rich. A noticeable contribution is the histogram PDF which models the cross-feed of the partially-reconstructed $\Lambda_b^0 \to p\pi^-\pi^+\pi^-\pi^0$. This is the only shape which directly come from the data.

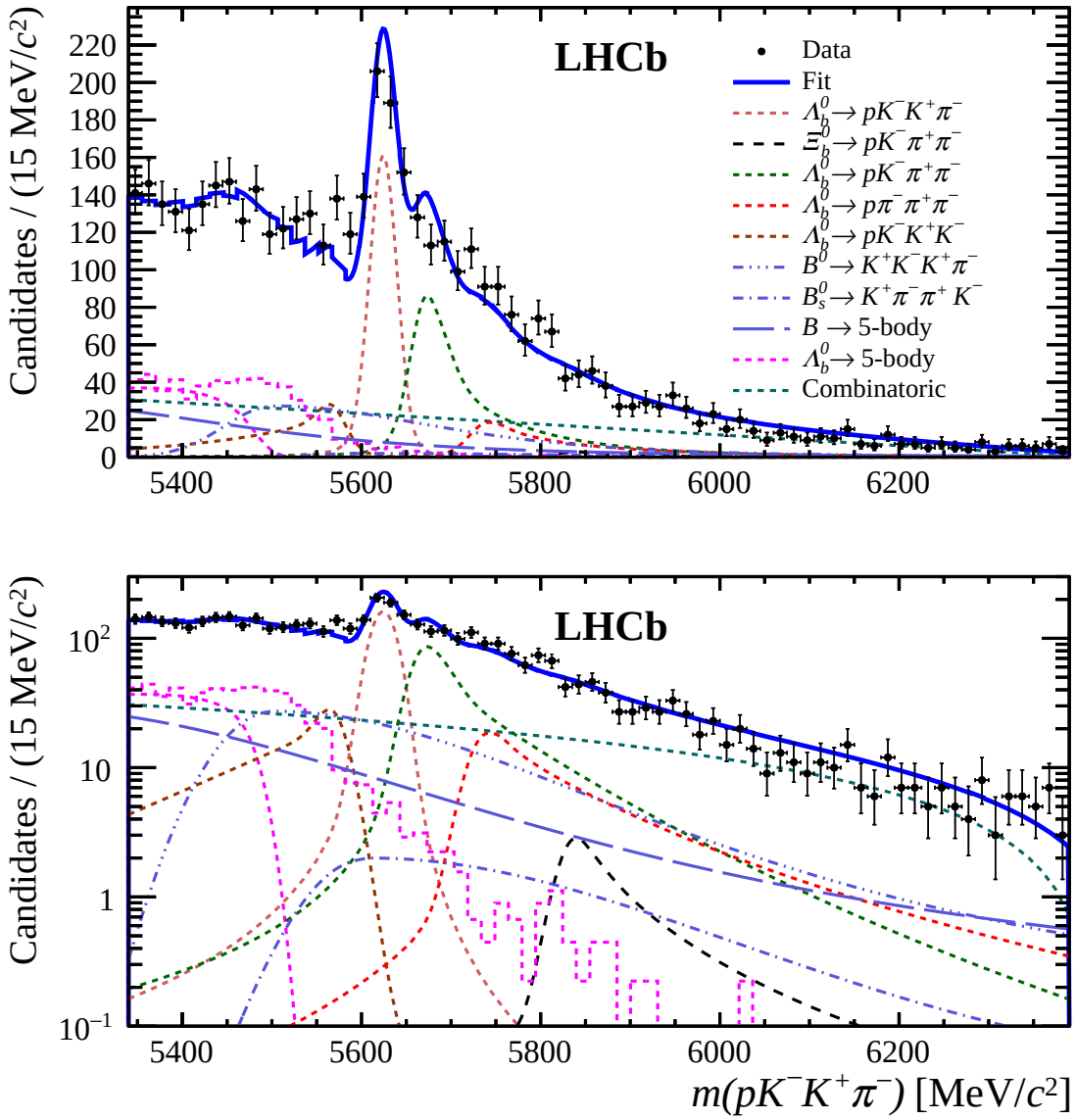

Figure 5.3: Results of the fit to the $pKK\pi$ candidate mass spectrum with (top) linear and (bottom) logarithmic scales. The different components employed in the fit are indicated in the legend. The $\Lambda_b^0 \to$ 5-body legend describes two components where a π^0 is not reconstructed, the partially reconstructed background $\Lambda_b^0 \to pK^-\pi^+\pi^-\pi^0$ where a pion is misidentified as a kaon and the partially reconstructed background $\Lambda_b^0 \to pK^-K^+\pi^-\pi^0$.

5.1.4 Fit to the $pK\pi K$ candidate mass spectrum

Figure 5.4 shows the unambiguous $\Xi_b^0 \to pK^-\pi^+\pi^-$ signal. As for the fit to the $pK\pi\pi$ candidate mass spectrum, differences between the data and the fit model can be noted in the high-mass side-bands. Those effects are covered within the size of the variations considered in the evaluation of the systematic uncertainties.

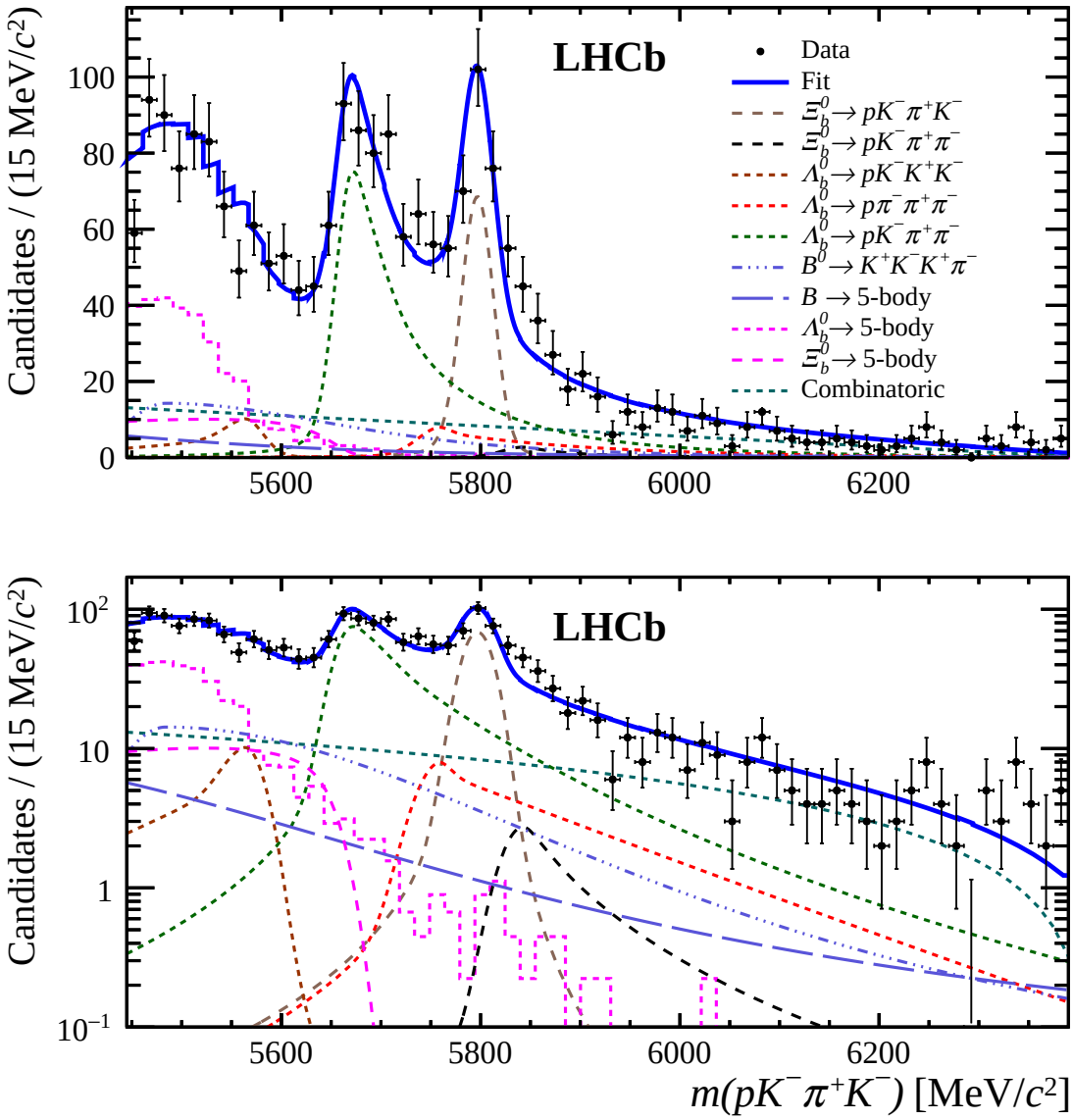

Figure 5.4: Results of the fit to the $pK\pi K$ candidate mass spectrum with (top) linear and (bottom) logarithmic scales. The different components employed in the fit are indicated in the legend.

5.1.5 Fit to the $pKKK$ candidate mass spectrum

Figure 5.5 shows the unambiguous $\Lambda_b^0 \to pK^-K^+K^-$ signal. The $\Xi_b^0 \to pK^-K^+K^-$ decay mode is however measured with a significance of 2.3σ. The partially-reconstructed backgrounds, the combinatorial and the B-mesons backgrounds are well accounted for by the chosen parameterisation.

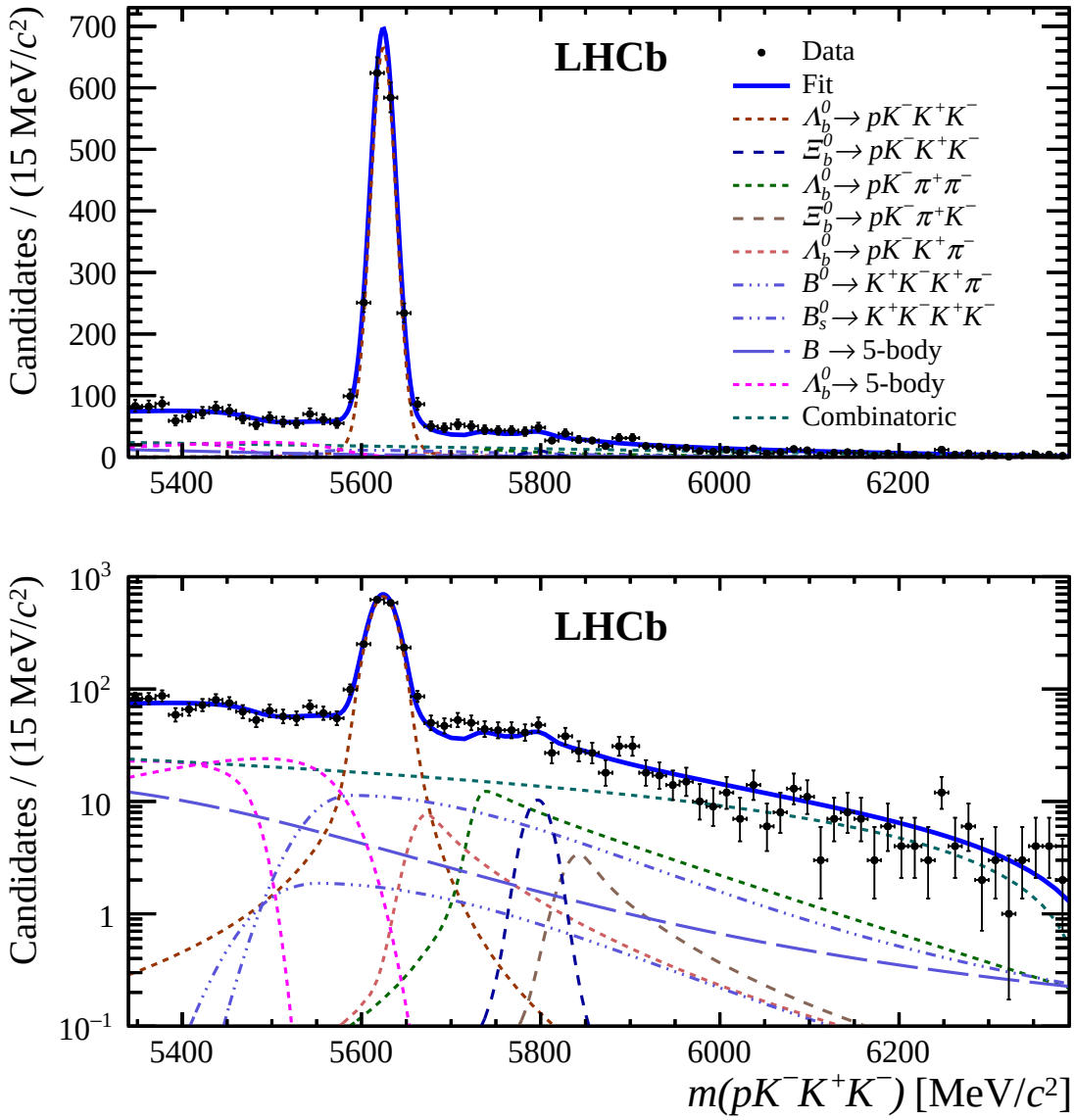

Figure 5.5: Results of the fit to the $pKKK$ candidate mass spectrum with (top) linear and (bottom) logarithmic scales. The different components employed in the fit are indicated in the legend. The $\Lambda_b^0 \to$ 5-body legend includes two decays, partially reconstructed $\Lambda_b^0 \to pK^-K^+K^-\gamma$ and $\Lambda_b^0 \to pK^-K^+K^-\pi^0$, where the γ and π^0 are not reconstructed.

5.1.6 Fit to the $\Lambda_c^+\pi^-$ candidate mass spectrum

Figure 5.6 shows the unambiguous $\Lambda_b^0 \to (\Lambda_c^+ \to p\pi^-\pi^+)\pi^-$ signal. The only source of background is the partially-reconstructed background.

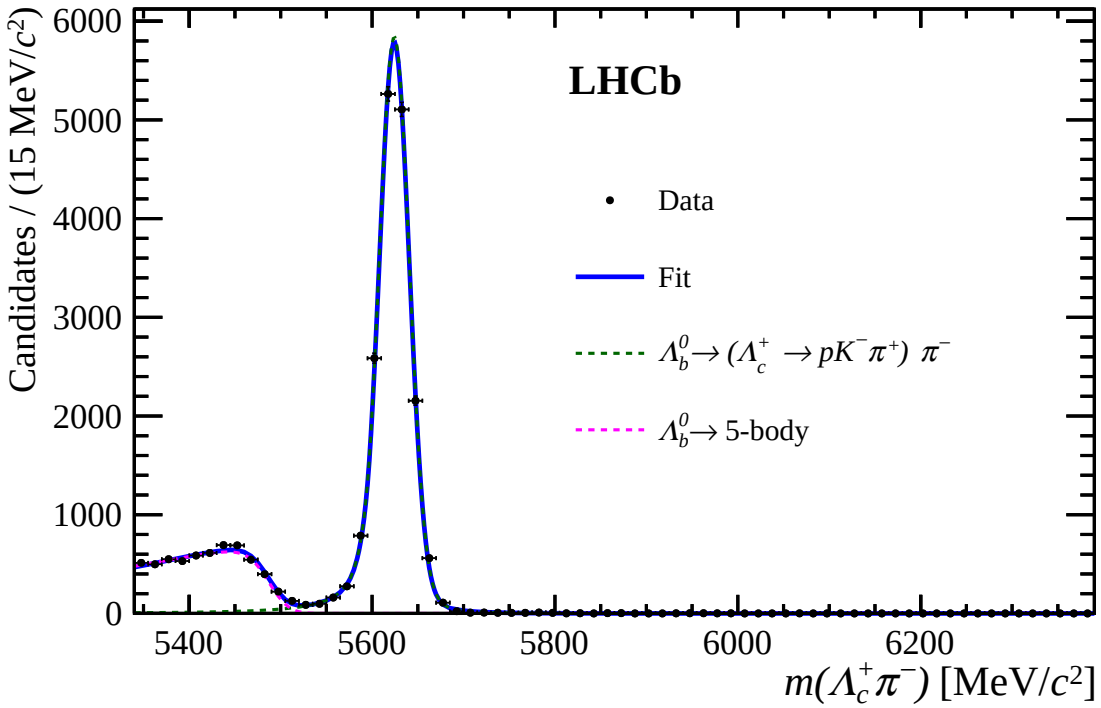

Figure 5.6: Results of the fit to the $\Lambda_c^+\pi^-$ candidate mass spectrum on linear scale. The different components employed in the fit are indicated in the legend.

5.2 Efficiencies derivations

The observable measured for each four-body signal-decay is the quantity R, defined as

$$
\begin{aligned}
R(X_b^0 \to p h^{'} h^{''} h^{'''}) &\equiv \frac{\mathcal{B}(X_b^0 \to p h^{'} h^{''} h^{'''})}{\mathcal{B}(\Lambda_b^0 \to \Lambda_c^+ \pi^-)} \cdot \frac{f_{X_b}}{f_{\Lambda_b^0}}, \\
&= \frac{\epsilon^{\text{geo.}}_{\Lambda_b^0 \to \Lambda_c^+ \pi^-}}{\epsilon^{\text{geo.}}_{X_b^0 \to p h^{'} h^{''} h^{'''}}} \cdot \frac{\epsilon^{\text{sel.}}_{\Lambda_b^0 \to \Lambda_c^+ \pi^-}}{\epsilon^{\text{sel.}}_{X_b^0 \to p h^{'} h^{''} h^{'''}}} \cdot \frac{\epsilon^{\text{PID}}_{\Lambda_b^0 \to \Lambda_c^+ \pi^-}}{\epsilon^{\text{PID}}_{X_b^0 \to p h^{'} h^{''} h^{'''}}} \cdot \frac{1}{\epsilon^{\text{veto}}_{X_b^0 \to p h^{'} h^{''} h^{'''}}} \cdot \frac{\mathcal{N}_{X_b^0 \to p h^{'} h^{''} h^{'''}}}{\mathcal{N}_{\Lambda_b^0 \to \Lambda_c^+ \pi^-}},
\end{aligned}
\tag{5.1}
$$

where $\mathcal{B}$ represents the relevant branching fraction and $f_{X_b}/f_{\Lambda_b^0}$ is the relative hadronisation fraction of $b \to X_b$ with respect to $b \to \Lambda_b^0$. From left to right, the ratios of efficiencies are related to the geometrical acceptance, the selection criteria, the PID requirements and the veto of charm and charmonium backgrounds. The measured signal and normalisation channel yields are represented by $\mathcal{N}_{X_b^0 \to p h^{'} h^{''} h^{'''}}$ and $\mathcal{N}_{\Lambda_b^0 \to \Lambda_c^+ \pi^-}$.

The efficiencies are determined from simulated signal events that have been generated with an arbitrary mixture of phase-space decays and quasi-two-body amplitudes, which feature the production of intermediate resonances close to their kinematic threshold. For instance, the $\Lambda_b^0 \to pK^-\pi^+\pi^-$ decay proceeds in the simulation of quasi-two-body amplitudes

via the decays $\Lambda_b^0 \to \Lambda^*(1520)^0\rho(770)^0$, $\Lambda_b^0 \to \Lambda^*(1520)^0 f_2(1270)$ or $\Lambda_b^0 \to N^*(1520)^0 K^*(892)$. In principle, the selection efficiency of each decay mode depends on the phase-space coordinates, but the actual dynamics of the decays is *a priori* unknown and a data-driven correction of the efficiency determination with simulated events would be required as was done in Ref. [38]. However, the granularity of the problem here is 5 dimensions an the procedure advocated in this reference becomes a daunting task. Yet, the candidate selection has been designed without relying on the kinematics of the daughter particles in the decay. The candidates selected such that the hardware trigger is satisfied independently of the signal particles, provide a sample with an efficiency that is, to a very good approximation, constant over the phase space of the decays. This statement is further discussed in Subsection 5.2.1. The residual variation of the efficiency over the phase space is consequently addressed as a systematic uncertainty.

The imperfections of the simulation are corrected for in several respects. Inaccuracies of the tracking simulation and the PID simulation are mitigated by a weighting of the simulation to match the efficiencies measured in the data calibration samples [40]. The uncertainties related to these corrections are propagated to the branching fraction measurements as systematic uncertainties. Other inaccuracies in the simulation are addressed as systematic uncertainties and discussed in Section 5.3.

A number of two- or three-body invariant-mass criteria have been used to veto charm and charmonium resonances. The efficiency of these vetoes is determined *a posteriori* on the data samples by inferring the number of signal candidates vetoed by each mass criterion from a linear interpolation of the invariant-mass distribution reconstructed under the relevant mass hypotheses of the final-state particles.

5.2.1 Efficiency variation within the Phase Space of the decay

The variation of the total selection efficiency along the Phase Space of the decays has been first examined with simulated events of the decay $\Lambda_b^0 \to pK\pi\pi$. It has been checked that same conclusions can be drawn for the other decays. The dynamics of a 4-body decay can be described with 5 kinematics variables : 2 invariant masses, 2 helicity angles and the angle between the decay planes of the 2-body decays. The definition of the helicity frame considered in this study is provided in Appendix D.2. The simulated events are separated according to the two conditions for the first level of trigger: L0Global TIS and L0Hadron TOS. The entire set of selection cuts, discussed in Section 3.2, has been applied to these samples except the invariant mass vetoes on the charmonia and charmed resonances described in Section 3.2.5 (which are actually cutting the Phase space in a reproducible way).

In order to exhibit the dependence of the selection efficiency along the Phase Space of the decays, we have chosen to determine the average value of the efficiency over the Phase-Space and compute in bins of the 5D space of the decay the distance to the average value in terms of number of standard deviations. The distance to the average value is projected in various two-dimensional figures of the full space. Figures 5.7 and 5.9 display these projections for the sample selected with the L0Global TIS condition. Despite the indication of a variation of the efficiency over the Phase Space when restricting the samples to the L0Global TIS condition, it is possible to mitigate these effects with an affordable systematic uncertainty which does not require the *a priori* knowledge of the dynamics of the decay.

On the contrary, strong variations of the efficiency over the Phase Space of the decay are observed for the sample selected with the L0Hadron TOS condition, which would require to have a measure of the dynamics of the decay as illustrated in Fig. 5.8 and 5.10.

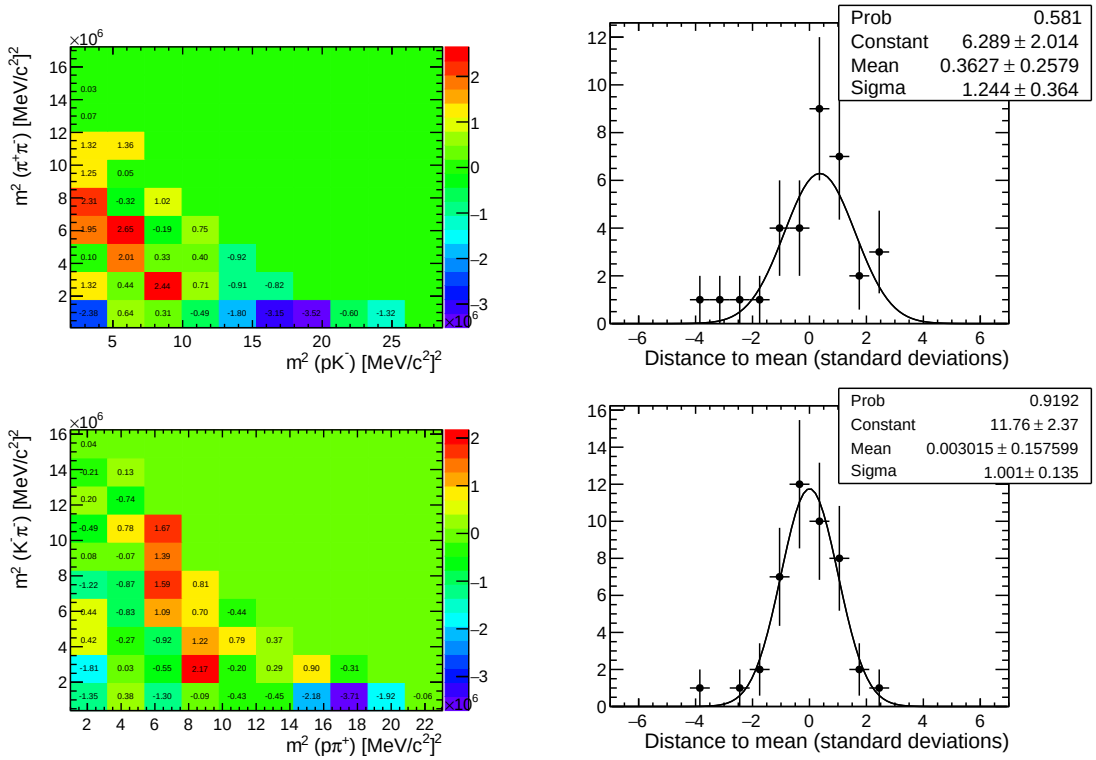

Figure 5.7: Selected simulated events with the L0Global TIS condition. Left: efficiency maps in bins of 2-body invariant masses square, where each bin contains the distance to the mean value of the map expressed in number of standard deviations. Distribution of the distances to the mean value, corresponding to the left plot, are reported in the right column. The consistency with the hypothesis of a flat variation of the efficiency over the phase space of the decay is obtained with mean value at 0 and a sigma at 1.

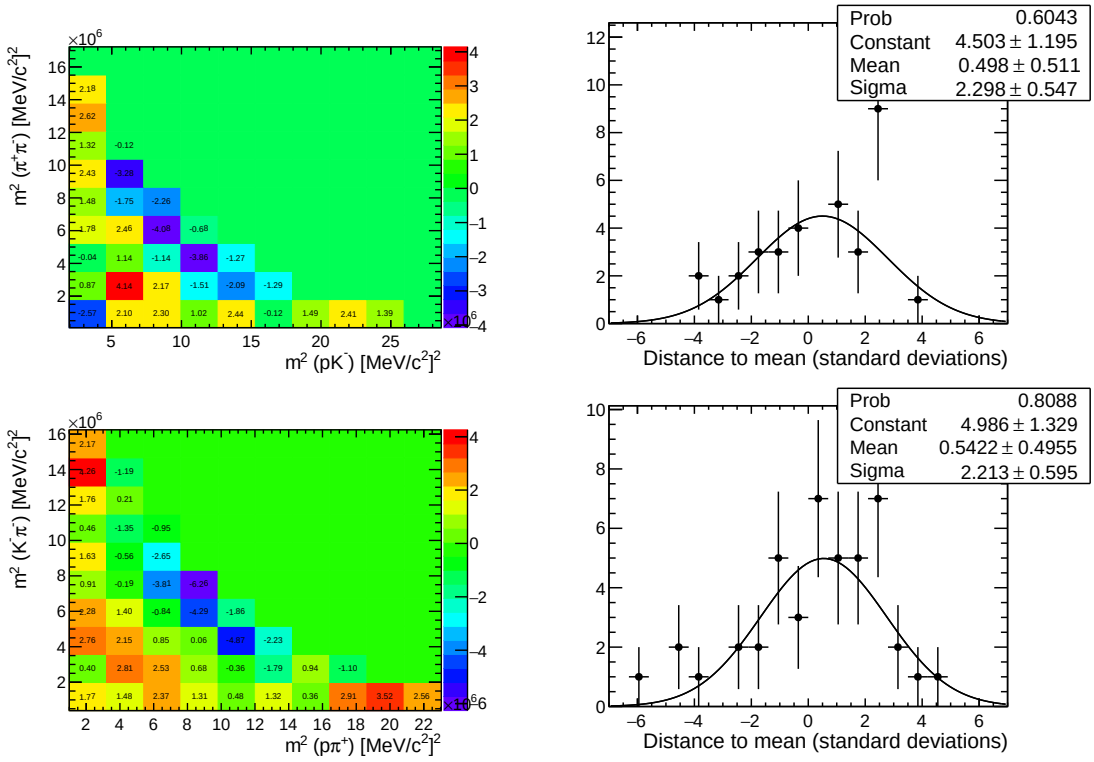

Figure 5.8: Selected simulated events with the L0Hadron TOS condition. Left: efficiency maps in bins of 2-body invariant masses square, where each bin contains the distance to the mean value of the map expressed in number of standard deviations. Distribution of the distances to the mean value, corresponding to the left plot, are reported in the right column. The consistency with the hypothesis of a flat variation of the efficiency over the phase space of the decay is obtained with mean value at 0 and a sigma at 1. Strong inconsistency with the flat variation hypothesis is observed.

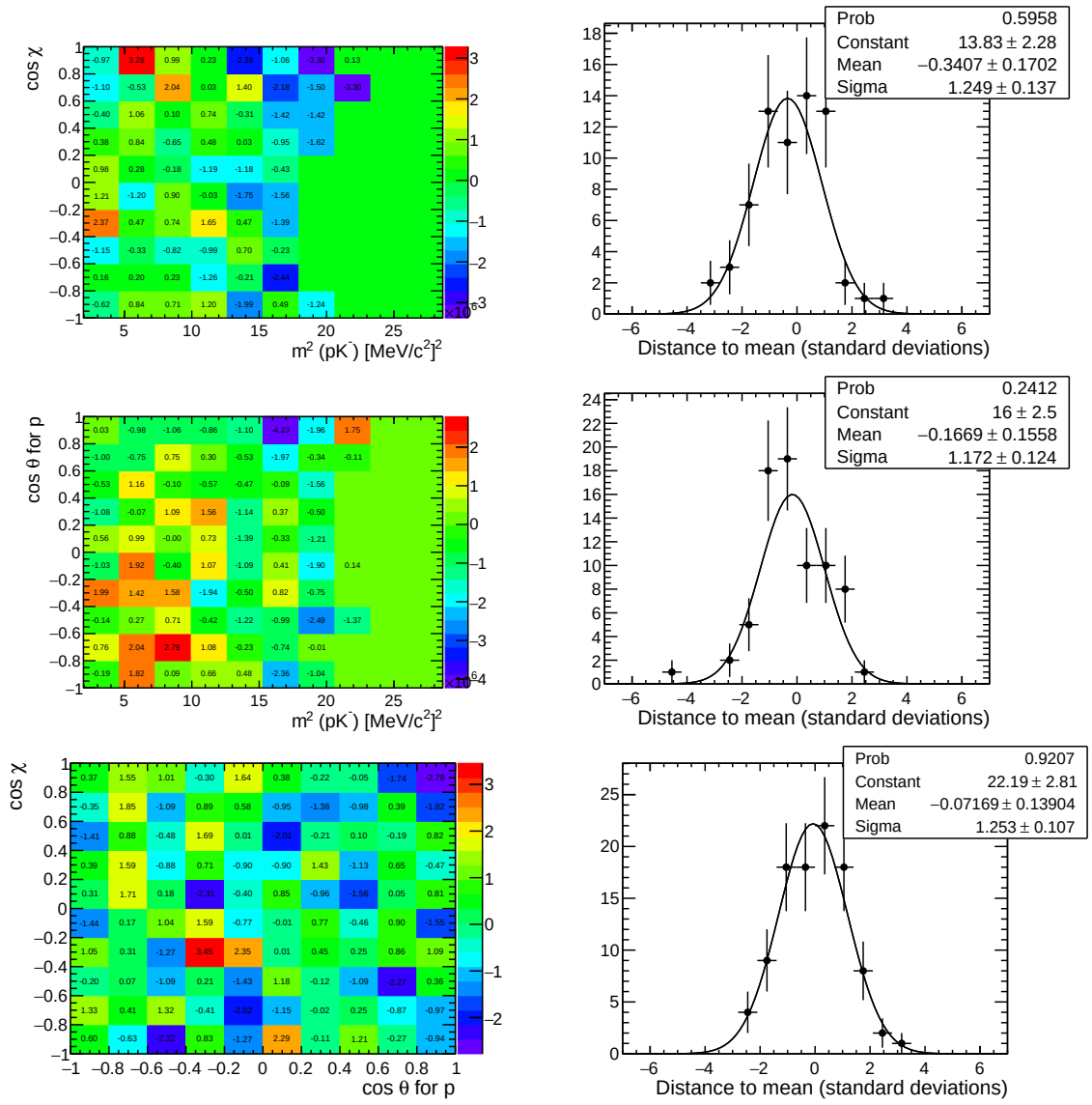

Figure 5.9: Selected simulated events with the L0Global TIS condition. Left: efficiency maps in bins of one invariant mass square and one helicity angle, where each bin contains the distance to the mean value of the map expressed in number of standard deviations. Distribution of the distances to the mean value, corresponding to the left plot, are reported in the right column. The consistency with the hypothesis of a flat variation of the efficiency over the phase space of the decay is obtained with mean value at 0 and a sigma at 1.

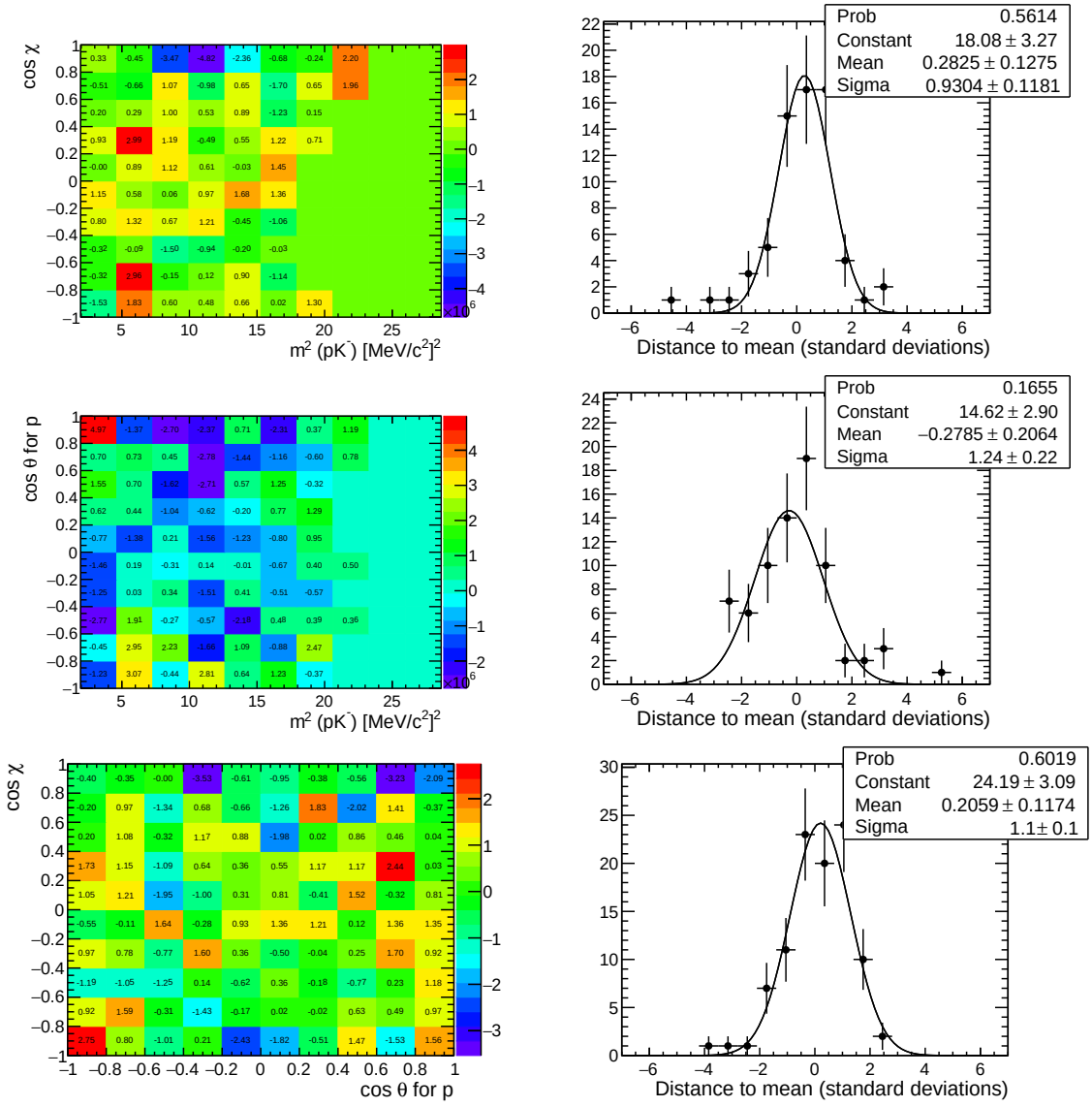

Figure 5.10: Selected simulated events with the L0Hadron TOS condition. Left: efficiency maps in bins of one invariant mass square and one helicity angle, where each bin contains the distance to the mean value of the map expressed in number of standard deviations. Distribution of the distances to the mean value, corresponding to the left plot, are reported in the right column. The consistency with the hypothesis of a flat variation of the efficiency over the phase space of the decay is obtained with mean value at 0 and a sigma at 1. Strong inconsistency with the flat variation hypothesis is observed.

5.2.2 Generator level efficiency

Generator level efficiencies are determined centrally by the collaboration production team and made available for each generated sample. The efficiencies corresponding to the magnet polarities are found consistent and are averaged in Table 5.2, gathering the relevant numbers. The slightly higher efficiency obtained for 2012 production is due to the increase in center-of-mass energy from 7 to 8 GeV.

Table 5.2: Generator level efficiency for each decay mode.

Decay mode	Event type	Year	Generator level efficiency in %
$\Lambda_b^0 \to p\pi^-\pi^+\pi^-$	15204010	2011(2012)	16.185 ± 0.030 (16.621 ± 0.049)
$\Lambda_b^0 \to pK^-\pi^+\pi^-$	15204011	2011(2012)	16.972 ± 0.032 (17.384 ± 0.052)
$\Lambda_b^0 \to pK^-K^+\pi^-$	15204012	2011(2012)	17.705 ± 0.034 (17.990 ± 0.053)
$\Lambda_b^0 \to pK^-K^+K^-$	15204013	2011(2012)	18.673 ± 0.036 (19.070 ± 0.056)
$\Xi_b^0 \to pK^-\pi^+\pi^-$	16204040	2011(2012)	17.004 ± 0.027 (17.301 ± 0.048)
$\Xi_b^0 \to pK^-\pi^+K^-$	16204041	2011(2012)	17.690 ± 0.027 (18.018 ± 0.051)
$\Xi_b^0 \to pK^-K^+K^-$	16204042	2011(2012)	18.639 ± 0.027 (18.940 ± 0.051)
$\Lambda_b^0 \to (\Lambda_c^+ \to pK\pi)\pi$	15264011	2011(2012)	17.322 ± 0.039 (17.459 ± 0.039)

5.2.3 Selection efficiencies

Selection efficiencies for signal and control channels presented in this section are gathering reconstruction, stripping, pre-selection and BDT criteria which are estimated from Monte-Carlo samples. Those efficiencies are defined as the number of events which pass the selection divided by the number of events out of the generation. Selection criteria presented in Section 3.2 are applied, namely trigger, fiducial, BDT and isMuon cuts with the addition of charmed and charmonia invariant mass vetoes for the signal channels. Selection efficiencies are determined separately for each year and each magnet polarity. However they are found consistent for the two magnet polarities samples and are hence averaged for 2011 (2012) samples as reported in Table 5.6. Though the branching fractions derivation requires the total efficiency, we are presenting split efficiencies at each selection step for the sake of the reproducibility of their determination. Each efficiency is calculated with respect to the immediate previous selection step, except for the row labelled "Selection" for which the whole selection efficiency is reported. Absolute efficiencies discussed here are computed with the MC-matched condition. Ratios of efficiencies for tracking and PID corrections presented in the Eq. (5.1) are gathered in the Subsection 5.2.8 and are built up for MC-matched events.

5.2.4 PID efficiency

As discussed in the subsection dedicated to PID selection optimisation , data-driven PID efficiencies are estimated in order to correct for inaccurate simulation of the distribution of ProbNN variables. A set of PID efficiency maps corresponding to the optimal PID selection cuts described in Section 3.2 are built in bins of momentum p of pseudo-rapidity η and in

event track multiplicity N_{tracks}. They are displayed in appendices B.3 and B.2. Each event passing the selection[a] is weighted according to the relevant efficiency maps for each year sample and for each magnet polarity. Numbers for MagDown and MagUp configurations are found consistent and are averaged. Table 5.3 displays for each final state the corresponding PID efficiency split for 2011 and 2012 MC samples.

Table 5.3: PID efficiency for each decay mode split by year.

Decay mode	Year	PID efficiency in %
$\Lambda_b^0 \to p\pi^-\pi^+\pi^-$	2011(2012)	47.64±0.30 (49.17±0.21)
$\Lambda_b^0 \to pK^-\pi^+\pi^-$	2011(2012)	52.58±0.30 (53.63±0.22)
$\Lambda_b^0 \to pK^-K^+\pi^-$	2011(2012)	57.31±0.31 (58.78±0.23)
$\Lambda_b^0 \to pK^-K^+K^-$	2011(2012)	61.92±0.30 (64.15±0.21)
$\Xi_b^0 \to pK^-\pi^+\pi^-$	2011(2012)	53.75±0.30 (56.08±0.22)
$\Xi_b^0 \to pK^-\pi^+K^-$	2011(2012)	58.53±0.31 (60.67±0.22)
$\Xi_b^0 \to pK^-K^+K^-$	2011(2012)	63.49±0.29 (66.67±0.20)
$\Lambda_b^0 \to (\Lambda_c^+ \to pK\pi)\pi$	2011(2012)	48.49±0.53 (51.40±0.39)

5.2.5 Charmed and charmonia invariant-mass vetoes efficiencies

A set of invariant mass vetoes is applied during the selection in order to remove fully-reconstructed charmed and charmonia decays which can appear as peaking background, as described in Subsection 3.2.5. Since the related efficiencies depend on the actual phase space of the decays, all 2- and 3-body vetoed invariant masses distributions of the selected events in the signal region are formed and the efficiency is computed from the counting of the number of vetoed events. The latter is inferred by performing a linear interpolation of the bin centered on the charmed or charmonia vetoed mass. A systematic uncertainty, discussed in Section 5.3, is assigned to integrate this choice. The signal efficiency ϵ_{sig} for a given spectrum is defined as:

$$\epsilon_{\text{sig}} = \frac{N_{\text{sig}}}{N_{\text{sig}} + N_{\text{i}} - N_{\text{bkg}} \cdot (1 - \epsilon_{\text{bkg}})/\epsilon_{\text{bkg}}} \tag{5.2}$$

where N_{sig} is the signal yield measured by the fit and N_{bkg} is the difference between the total number of events in the signal region and the actual signal yield measured by the fit. The background veto efficiency is estimated from the RHSB of the spectra by applying the very procedure employed for the signal region vetoed events determination.

[a] MC-match requirements are implemented for this purpose.

The related uncertainty reads:

$$\left(\frac{\sigma_{\epsilon_{\text{sig}}}}{\epsilon^2_{\text{sig}}}\right)^2 = \left(\frac{N_{\text{sig}} + N_{\text{i}} - N_{\text{tot}} * (1-\epsilon_{\text{bkg}})/\epsilon_{\text{bkg}}}{N^2_{\text{sig}}}\right)^2 \cdot \sigma^2_{N_{\text{sig}}} + \left(\frac{\sigma_{N_{\text{i}}}}{N_{\text{sig}}}\right)^2 + \left(\frac{(1-\epsilon_{\text{bkg}})/\epsilon_{\text{bkg}}}{N_{\text{sig}}}\right)^2 \cdot \sigma^2_{N_{\text{tot}}} + \left(\frac{\sigma_{\epsilon_{\text{bkg}}}}{\epsilon^2_{\text{bkg}}}\right)^2 \tag{5.3}$$

where N_{tot} is the total number of events in the signal region. Finally, the computed veto efficiencies are displayed in Table 5.4.

Table 5.4: Invariant mass veto efficiencies for each decay mode.

Decay mode	Year	Signal vetoes efficiency in %
$\Lambda_b^0 \to p\pi^-\pi^+\pi^-$	2011(2012)	69.3 ± 2.8 (71.2 ± 1.7)
$\Lambda_b^0 \to pK^-\pi^+\pi^-$	2011(2012)	75.8 ± 3.2 (74.4 ± 1.6)
$\Lambda_b^0 \to pK^-K^+\pi^-$	2011(2012)	74.2 ± 9.9 (76.5 ± 5.0)
$\Lambda_b^0 \to pK^-K^+K^-$	2011(2012)	75.1 ± 3.6 (78.7 ± 2.6)
$\Xi_b^0 \to pK^-\pi^+\pi^-$	2011(2012)	65.2 ± 8.2 (65.9 ± 10.9)
$\Xi_b^0 \to pK^-\pi^+K^-$	2011(2012)	68.9 ± 7.4 (75.2 ± 8.1)
$\Xi_b^0 \to pK^-K^+K^-$	2011(2012)	81.9 ± 12.3 (81.9 ± 12.3)

5.2.6 Data-driven tracking efficiency corrections

Inaccurate simulation of the tracking efficiency must be corrected for. The LHCb tracking group provides the ratio of tracking efficiencies determined per track in real and simulated data in (p, η) bins. These tables are displayed on Fig. 5.11. The binned corrective factors are used here to re-weight on a track-by-track basis the MC samples. Each event passing the selection presented in Subsection 5.2.3 hence receives a weight which is defined as the product of the efficiency ratio of each track. The total efficiency ratio is then given in the Eq. 5.4, where $w_i = \prod_{j=1}^{4} w_j$ is the weight of the event i and N the number of events present in the sample after the selection.

$$\epsilon^{\text{ratio}}_{\text{tot}} = \frac{\sum_i^N w_i}{N}. \tag{5.4}$$

The error on the overall efficiency is determined for each MC sample by propagating the uncertainties of the individual track efficiency errors provided by the tracking efficiency tables. Its computation is displayed in the Eq. 5.5 where a_j is the number of tracks in bin j and σ_j is the uncertainty of the efficiency ratio of the bin j. This formula ignores events-correlation in p and η between the tracks in a specific decay which are assumed negligible.

$$\sigma_{\text{tot}} = \sqrt{\sum_j^{10} \left(\frac{a_j}{a}\right)^2 \sigma_j^2}. \tag{5.5}$$

The Table 5.5 gathers the overall tracking efficiency corrections (magnet polarity averaged) for 2011 and 2012 events.

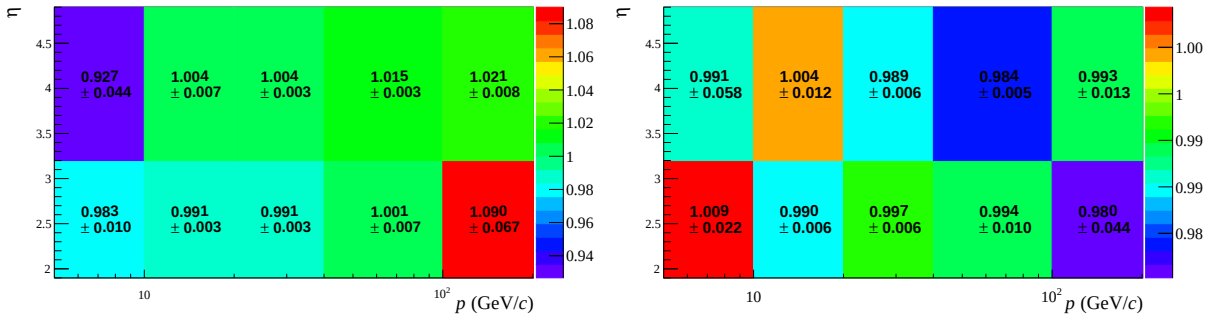

Figure 5.11: Efficiency ratio tables for 2011 [left] and 2012 [right]. Each bin contains the ratio of efficiencies data over MC and the corresponding error.

Table 5.5: Data-driven tracking efficiency correction for each decay mode.

Decay mode	Year	Tracking efficiency correction in %
$\Lambda_b^0 \to p\pi^-\pi^+\pi^-$	2011(2012)	97.87 ± 0.18 (97.79 ± 0.31)
$X_b^0 \to pK^-\pi^+\pi^-$	2011(2012)	98.21 ± 0.16 (97.73 ± 0.30)
$\Lambda_b^0 \to pK^-K^+\pi^-$	2011(2012)	98.30 ± 0.15 (97.64 ± 0.28)
$X_b^0 \to pK^-K^+K^-$	2011(2012)	98.55 ± 0.14 (97.52 ± 0.25)
$\Xi_b^0 \to pK^-\pi^+K^-$	2011(2012)	98.37 ± 0.15 (97.59 ± 0.27)
$\Lambda_b^0 \to (\Lambda_c^+ \to pK\pi)\pi$	2011(2012)	98.37 ± 0.15 (97.59 ± 0.27)

5.2.7 Variation of efficiencies over the Phase Space of the decay

The variation of the total selection efficiency along the Phase Space of the decays has been examined in Subsection 5.2.1. It has been shown that the Phase Space of the decay is strongly biased by the L0Hadron TOS condition. On another hand, the events being triggered at the first level independently of the signal are less biased in that respect, hence driving the choice of using solely the L0Global TIS condition for the branching fraction measurements.

The trigger condition is not the only source of bias of the dynamics of the decay yet. Acceptance and generator level cuts, track reconstruction and particle identification are further sources of decay Phase Space bias. Instead of investigating and correcting each and all effects, we adopted the approach to generate two extreme decay dynamics and evaluate the difference in average efficiency (including selection efficiency). The observed difference will hence be used as a range for the corresponding systematic uncertainty[b]. The two extreme decay dynamics under consideration here are quasi-2 body decay (going through low-mass baryon and meson resonances) and Phase Space decay respectively.

[b]Note that this range uncertainty is not statistically distributed.

The differences of efficiencies will be examined in details in Section 6.3. Let's mention here that the systematic estimate is determined to be at the level of few percents, irrespective of the decay mode.

5.2.8 Ratios of efficiencies: executive summary

This section described all the necessary ingredients required to perform the calculation of the observable R defined in the equation (5.1), efficiency-wise. Table 5.6 gathers the relevant ratios for 2011 and 2012 samples respectively. The associated errors will be propagated as a systematic uncertainty in the branching fractions derivation, as further discussed in Section 5.3.

Table 5.6: Ratios of the normalisation decay mode efficiencies, relative to the signal decay mode as used in Eq. (5.1), for (first row) 2011 and (second row) 2012. The last column shows the efficiency of the veto of charm and charmonium backgrounds (applied to the signal mode only), as discussed in the text. Since the $\Xi_b^0 \to pK^-K^+K^-$ decay mode is not observed, the veto efficiency is determined with the simulated data sample. The difference between the simulation value and the average veto efficiency measured on other Ξ_b^0 modes is reported in the table as the uncertainty.

Decay mode	Ratios of efficiencies			
	Acceptance	Selection	PID	Vetoes
$\Lambda_b^0 \to p\pi^-\pi^+\pi^-$	1.070 ± 0.003	0.433 ± 0.011	1.018 ± 0.013	0.693 ± 0.028
	1.050 ± 0.004	0.425 ± 0.009	1.046 ± 0.010	0.712 ± 0.017
$\Lambda_b^0 \to pK^-\pi^+\pi^-$	1.020 ± 0.003	0.438 ± 0.011	0.922 ± 0.012	0.758 ± 0.032
	1.004 ± 0.004	0.432 ± 0.009	0.958 ± 0.009	0.744 ± 0.016
$\Lambda_b^0 \to pK^-K^+\pi^-$	0.978 ± 0.003	0.462 ± 0.012	0.846 ± 0.011	0.742 ± 0.099
	0.970 ± 0.004	0.468 ± 0.010	0.874 ± 0.008	0.765 ± 0.050
$\Lambda_b^0 \to pK^-K^+K^-$	0.928 ± 0.003	0.445 ± 0.012	0.783 ± 0.010	0.751 ± 0.036
	0.916 ± 0.003	0.452 ± 0.010	0.801 ± 0.007	0.787 ± 0.026
$\Xi_b^0 \to pK^-\pi^+\pi^-$	1.019 ± 0.003	0.431 ± 0.011	0.902 ± 0.011	0.652 ± 0.082
	1.009 ± 0.004	0.424 ± 0.009	0.917 ± 0.008	0.659 ± 0.109
$\Xi_b^0 \to pK^-\pi^+K^-$	0.979 ± 0.003	0.434 ± 0.011	0.829 ± 0.010	0.689 ± 0.074
	0.969 ± 0.004	0.450 ± 0.010	0.847 ± 0.008	0.752 ± 0.081
$\Xi_b^0 \to pK^-K^+K^-$	0.929 ± 0.003	0.425 ± 0.011	0.764 ± 0.009	0.819 ± 0.123
	0.922 ± 0.003	0.429 ± 0.009	0.771 ± 0.007	

5.3 Systematic uncertainties

This section presents the sources of systematic uncertainties that have been identified as well as the methods used in their determinations. Quantitative estimates are provided, separating uncertainties related to the fit model which is presented in Section 4.4, and uncertainties related to the efficiencies determination, discussed in Section 5.2

5.3.1 Systematics related to the fit model

Are described below the systematic uncertainties related to the fit model. The corresponding systematic uncertainty estimates are gathered in Table 5.7.

- **The fixed parameters of the signal, signal cross-feed and B physics background shapes modelling as determined from the MC simulated events:** the parameters are for instance the tail parameters of the signal DCB model. In most cases, they have been determined by a simultaneous fit of several MC simulated events datasets (when relevant parameters can be shared) with a finite number of events and their determination comes with a statistical uncertainty. Pseudo-experiments are generated by varying the fixed parameters of the signal, signal cross-feed and B physics background models according to the results of the MC fits and taking into account its covariance matrix. The distribution of the fit results compared to the generated values of the observable yields (signal and control channel yields) are used as an estimate of the related systematic uncertainty. The procedure is however very demanding CPU-wise but the most rigorous approach to our knowledge.

- **The choice of the combinatorics shape:** the results of the baseline fit model obtained with a modelling of the combinatorial background by a first order Bernstein polynomial are compared to the ones obtained with a modeling by an exponential shape, in a pseudo-experiment. The observed difference of the measured yields is taken as the corresponding systematic uncertainty estimate.

- **Partially reconstructed backgrounds from the $pK\pi\pi$ spectrum cross-feeding into $pK\pi K$ and $pKK\pi$ spectra:** the shape of this contribution is obtained by selecting the decays $\Lambda_b^0 \to (\Lambda_c^+ \to pK\pi)\pi$ and reconstructing these events as $pK\pi K$, where the pion coming from the Λ_b^0 is being mass-swapped as a kaon. The results of the nominal fit model are compared to the ones obtained with an alternative reconstruction of these events, considering that the pion coming from the Λ_c^+ is misidentified as a kaon. These two configurations have different kinematical properties and aimed at covering any systematic effect of modelling. The observed difference of the measured yields in the spectrum of interest between the two shapes is taken as the corresponding systematic uncertainty estimate.

- **Partially reconstructed backgrounds from $\Lambda_b^0 \to p\pi^-(\eta' \to \pi^+\pi^-\gamma)$:** this possible contribution to the $p\pi\pi\pi$ spectrum is a component of the nominal fit model. Its yield relative to the signal in the two spectra where it contributes is fixed to a value estimated from the known branching fractions values of the analogous B mesons decays. The systematic uncertainty related to this assumption is estimated by removing from the nominal fit the $\Lambda_b^0 \to p\pi^-(\eta' \to \pi^+\pi^-\gamma)$ contribution. The differences in the fit results in a pseudo-experiment is taken as the corresponding systematic uncertainty estimate.

- **Partially reconstructed backgrounds from $\Lambda_b^0 \to pK^-(\eta' \to \pi^+\pi^-\gamma)$:** this contribution is left free in the fit. No systematic uncertainty is assigned beyond that related to the fixed parameters of the shape. However, its rate in the invariant mass window relative to the Λ_b^0 signal has been estimated from B^0-mesons decays to be of order 20 %. The corresponding value measured in the fit is 0.25 ± 0.03, in fair agreement with the former indication.

- **Signal, signal cross-feed and B physics background shapes:** as mentioned in the Section 4.4, not only the MC PID efficiency is reweighted according to the data-driven kinematics-dependent PID corrections but also are the MC-derived shapes of all components of the fit model. The arbitrary mixture of quasi 2-body and phase space decays we have devised in our simulation samples is a source of systematics uncertainty. The true signal dynamics (*a priori* unknown) lies in the range of the two extreme cases:

the decays are saturated by quasi 2-body amplitudes or by full phase space amplitude. The shapes of all decays are reweighted according to these two extreme cases and the highest range of variation of the fit results obtained between the two conditions is taken as the corresponding systematic estimate.

- **Cross-feed factors:** as discussed in Section 4.4, there is no data calibration samples to determine the simultaneous misidentification of two pions in a same event. An estimation of the related cross-feed factor has been determined by letting the relevant contribution free in the fit when they can be measured and by constraining it to the PID reweighting estimation when no measured information is at hand. These two extreme cases allow to get a cross-feed factor estimation when this probability is maximal or minimal, respectively, and the variation of the yields between the two cases is assigned as a systematic uncertainty estimate. Only $pKK\pi$, $pK\pi K$, and $pKKK$ modes are concerned. The relative changes on the concerned yields are found to be marginal ($< 0.1\%$) for $pKKK$ modes and up to 5% on $pKK\pi$ and $pK\pi K$ modes. Appendix D.3 displays fit results, in which $p\pi\pi\pi$ and $pK\pi\pi$ cross-feed contributions in $pKK\pi$, $pK\pi K$ and $pKKK$ spectra are free in the fit. It covers most of the discrepancies on the fit to the data that were spotted in Section 5.1

- **Partially reconstructed background from $\Xi_b^0 \to pK\pi\pi$:** as discussed in Section 4.4, the yield of this contribution is contrained to the ratio of the integrated PDFs of the Ξ_b^0 and Λ_b^0 partially reconstructed background contributions. The observed difference of the measured signal yields of this spectrum, considering two extreme values for this ratio, is taken as the related systematic uncertainty. The relative changes on the concerned yields are found to be equal to 1.1% (1.3%) for 2011 (2012) for the $\Xi_b^0 \to pK^-\pi^+\pi^-$ and they are found to be marginal for the $\Lambda_b^0 \to pK^-\pi^+\pi^-$ ($< 0.1\%$) for 2011 and 2012.

5.3.2 Systematics related to the efficiencies determination

Are described below the systematic uncertainties related to the determination of efficiencies. The corresponding systematic uncertainty estimates are gathered in Table 5.9.

- **The tracking efficiency systematic uncertainties:** the detection efficiency of X_b^0 and $\overline{X}_b^0$ in the charmless spectra is cancelled, up to corrections of kinematics differences, by the control channels. As described in the Section 5.2, a data-driven tracking efficiency correction depending on the kinematics of the daughter particles of the decays has been applied on both signal and control channels. The corresponding uncertainty provided by the tracking group is propagated to the efficiency correction, and subsequently to the branching fraction determination.

- PID **efficiency systematic uncertainty:** the very same procedure as employed for the tracking efficiency systematics is in order. The uncertainties coming from the PID calibration samples are propagated to the PID efficiency correction as described in the Section 5.2. Since there is a dependence of the PID efficiency on the kinematical properties of the decay (which are *a priori* unknown), the PID efficiency is determined for quasi 2-body decays and full phase space decays MC events separately. The range of the variation is taken as the corresponding systematic uncertainty estimate.

Table 5.7: Systematic uncertainties related to the fit model for 2011 (first row) and 2012 (second row) data. From left to right, uncertaintes are related to the fixed parameters of the shapes, the choice of the shape for the combinatorial background modelling, the shape for the signal and CF modelling, the $\Lambda_b^0 \to pK^-\pi^+\pi^-\pi^0$ partially reconstructed background (labelled PR1), the $\Lambda_b^0 \to p\pi^-\eta'$ partially reconstructed background (labelled PR2) and the CF factors. The last column presents the overall systematic uncertainties related to the fit model.

Decay mode	Fit model systematic uncertainties (%)							$\sigma_{\text{Tot.}}$ (%)
	$\sigma_{\text{Pars.}}$	$\sigma_{\text{Comb.}}$	$\sigma_{\text{Sig.}}$	$\sigma_{\text{CF.}}$	σ_{PR1}	σ_{PR2}	$\sigma_{f_{\text{CF}}}$	
$\Lambda_b^0 \to p\pi^-\pi^+\pi^-$	$\pm$ 1.1	$<$ 0.1	$\pm$ 0.8	$\pm$ 0.3	—	$\pm$ 0.1	—	$\pm$ 1.4
	$\pm$ 0.7	$<$ 0.1	$\pm$ 0.8	$\pm$ 0.2	—	$<$ 0.1	—	$\pm$ 1.2
$\Lambda_b^0 \to pK^-\pi^+\pi^-$	$\pm$ 0.8	$\pm$ 0.3	$\pm$ 0.7	$<$ 0.1	—	—	—	$\pm$ 1.1
	$\pm$ 0.9	$\pm$ 0.3	$\pm$ 0.7	$\pm$ 0.3	—	—	—	$\pm$ 1.3
$\Lambda_b^0 \to pK^-K^+\pi^-$	$\pm$ 1.5	$\pm$ 1.5	$\pm$ 0.9	$\pm$ 1.2	$\pm$ 7.2	—	$\pm$ 3.5	$\pm$ 8.5
	$\pm$ 1.1	$\pm$ 1.0	$\pm$ 0.7	$\pm$ 1.0	$\pm$ 4.7	—	$\pm$ 3.1	$\pm$ 5.9
$\Lambda_b^0 \to pK^-K^+K^-$	$\pm$ 0.9	$\pm$ 0.6	$\pm$ 1.4	$<$ 0.1	—	—	$<$ 0.1	$\pm$ 1.8
	$\pm$ 0.8	$\pm$ 0.4	$\pm$ 1.0	$<$ 0.1	—	—	$<$ 0.1	$\pm$ 1.4
$\Xi_b^0 \to pK^-\pi^+\pi^-$	$\pm$ 1.8	$\pm$ 1.0	$\pm$ 2.3	$\pm$ 1.5	—	—	$\pm$ 1.8	$\pm$ 3.5
	$\pm$ 1.0	$\pm$ 2.4	$\pm$ 0.5	$\pm$ 1.5	—	—	$\pm$ 1.0	$\pm$ 3.1
$\Xi_b^0 \to pK^-\pi^+K^-$	$\pm$ 1.9	$\pm$ 1.0	$\pm$ 0.7	$\pm$ 0.7	$\pm$ 2.9	—	$\pm$ 3.7	$\pm$ 5.2
	$\pm$ 1.5	$\pm$ 0.7	$\pm$ 0.7	$\pm$ 1.3	$\pm$ 2.2	—	$\pm$ 4.8	$\pm$ 5.8
$\Xi_b^0 \to pK^-K^+K^-$	$\pm$ 6.4	$\pm$ 10	$\pm$ 1.5	$\pm$ 0.5	—	—	$\pm$ 2.2	$\pm$ 13
	$\pm$ 3.9	$\pm$ 8.9	$\pm$ 2.0	$\pm$ 0.6	—	—	$<$ 0.1	$\pm$ 10

- **Pion or kaon detection efficiency:** all branching fractions are measured relative to the control channel $\Lambda_b^0 \to (\Lambda_c^+ \to pK^-\pi^+)\pi^-$. The signal final state might differ w.r.t. to the control channel by the presence or absence of one or two kaons. The kaon detection efficiency as a function of the K momentum and charge is measured in [41]. The simulated signal samples are reweighted accordingly as described in the Section 5.2 and the uncertainties on the kaon detection efficiency correction are conversely propagated to the branching fraction measurements. Only the final states which differ by one kaon with respect to the control channel are considered.

- **Variation of efficiencies over the phase space of the decay:** it has been shown in Subsection 5.2.1 with simulated events that the selection[c] of the signal provides a bias of the phase space of the decay that can be accounted for by a systematics uncertainty if the L0Global TIS condition is required. On top of the selection efficiency, acceptance and generator level cuts, track reconstruction and particle identification are further sources of phase space decay biases. The two extreme decay dynamics presented in Section 3.1 are here again used to determine the difference of the two average efficiencies that is used as a range for the systematic uncertainty estimate. Ranges for systematic uncertainties are gathered with the corresponding value of efficiency for all decay modes of interest in Table 5.8, where the effects are split in terms of

[c]Selection refers here to the entire set of selection cuts applied for the scrutiny of the efficiency variation within the phase space of the decay, *i.e.* without the invariant-mass vetoes on the charmonia and charmed resonances. This uncertainty source is discussed in the next item.

Reconstruction, Trigger, Stripping and Selection cuts on one hand and PID cuts on the other hand and for 2011 and 2012 data samples respectively, in order to understand their hierarchy. The relative range of the integrated difference for acceptance is found to be ±1.6% (±0.28% absolute efficiency difference) for the mode $\Lambda_b^0 \to pK^-\pi^+\pi^-$ [d]. The acceptance efficiency multiplies the efficiencies reported in the table. The numbers reported in the last column of the Table 5.8 are the absolute efficiencies together with the integrated range provided as a symmetrised uncertainty. The latter will be presented in the branching fraction measurement as a non-distributed uncertainty. The effect is depending on the modes and can reach 4 %.

- **Charmed and charmonia invariant mass vetoes:** the efficiency determination and the associated uncertainty (mostly of statistical origin) have been discussed Section 5.2. The obtained uncertainty is propagated to the relative branching fraction observable following the Eq. 5.3.

- **Selection uncertainty:** as described in Section 3.2, ten discriminating variables are considered to train the BDT. The potential or actual inaccuracies in the simulation of these variables results at first in a sub-optimal discrimination of the multivariate tool. In particular, the b-hadron kinematics is a source of differences between simulated events and data. We estimated a systematic uncertainty by reweighting the MC distributions of $p_T X_b^0$ and ηX_b^0 to match those distributions in the selected data for the control channel. The observed difference with the nominal selection efficiency is taken as the uncertainty estimate. It has been found for the mode $\Lambda_b^0 \to pK^-\pi^+\pi^-$ that the MC / data differences are actually contained within the statistical uncertainties of the samples of interest, and results in a relative change of efficiency at the level of 5.10^{-4}

Table 5.8: Relative systematic uncertainty estimates related to the dependence of the efficiency over the phase space of the decay for 2011 (first row) and 2012 (second row). The category RTS2 stands for Reconstruction, Trigger, Stripping and Selection cuts.

Decay mode	RTS2 cuts (%)	PID cuts (%)	All cuts (%)
$\Lambda_b^0 \to p\pi^-\pi^+\pi^-$	± 2.22	± 1.61	± 3.21
	± 3.27	± 1.78	± 4.07
$\Lambda_b^0 \to pK^-\pi^+\pi^-$	± 1.55	± 2.72	± 3.54
	± 1.27	± 2.11	± 2.97
$\Lambda_b^0 \to pK^-K^+\pi^-$	± 0.94	± 2.15	± 2.87
	± 1.10	± 2.41	± 3.13
$\Lambda_b^0 \to pK^-K^+K^-$	± 1.86	± 3.31	± 4.15
	± 2.38	± 2.41	± 3.77
$\Xi_b^0 \to pK^-\pi^+\pi^-$	± 0.49	± 1.88	± 2.56
	± 0.54	± 2.42	± 2.98
$\Xi_b^0 \to pK^-\pi^+K^-$	± 0.48	± 2.33	± 2.90
	± 0.27	± 2.34	± 2.88
$\Xi_b^0 \to pK^-K^+K^-$	± 1.72	± 2.78	± 3.66
	± 2.54	± 2.26	± 3.78

[d]The acceptance biases have been found to be consistent for all modes with samples of 10 k generated events. 200 k events of $\Lambda_b^0 \to pK^-\pi^+\pi^-$ have been generated and the value obtained is used as a proxy for all modes.

Table 5.9: Systematic uncertainties related to the efficiencies for 2011 (first row) and 2012 (second row) data. From left to right, uncertaintes are related to the tracking efficiency, the PID efficiency, the particle detection efficiency, the variation of efficiency and the charmed and charmonia invariane mass vetoes. The last column presents the overall systematic uncertainties related to the fit model.

Decay mode	Efficiencies systematic uncertainties (%)					$\sigma_{\text{Tot.}}$ (%)
	$\sigma_{\text{trk.}}$	$\sigma_{\text{PID.}}$	$\sigma_{\text{Det.}}$	$\sigma_{\text{PhSp.}}$	σ_{Veto}	
$\Lambda_b^0 \to p\pi^-\pi^+\pi^-$	± 0.3	± 1.3	± 0.6	± 3.2	± 4.0	± 5.2
	± 0.5	± 0.8	± 0.4	± 4.1	± 2.4	± 4.8
$\Lambda_b^0 \to pK^-\pi^+\pi^-$	± 0.3	± 1.3	—	± 3.6	± 4.1	± 5.5
	± 0.5	± 0.9	—	± 3.0	± 2.1	± 3.7
$\Lambda_b^0 \to pK^-K^+\pi^-$	± 0.3	± 1.2	± 0.4	± 2.9	± 13	± 14
	± 0.4	± 0.9	± 0.3	± 3.2	± 6.5	± 7.3
$\Lambda_b^0 \to pK^-K^+K^-$	± 0.2	± 1.2	—	± 4.2	± 4.8	± 6.4
	± 0.4	± 0.8	—	± 3.8	± 3.3	± 5.1
$\Xi_b^0 \to pK^-\pi^+\pi^-$	± 0.3	± 1.3	—	± 2.6	± 13	± 14
	± 0.5	± 0.9	—	± 3.0	± 17	± 18
$\Xi_b^0 \to pK^-\pi^+K^-$	± 0.2	± 1.2	± 0.4	± 2.9	± 11	± 12
	± 0.4	± 0.9	± 0.3	± 2.9	± 11	± 13
$\Xi_b^0 \to pK^-K^+K^-$	± 0.2	± 1.2	—	± 3.7	± 15	± 16
	± 0.4	± 0.8	—	± 3.8	± 15	± 16

5.4 Branching fraction measurements and concluding remarks

Six decays are unambiguously observed. The $\Xi_b^0 \to pK^-K^+K^-$ decay mode is measured with a significance of 2.3 σ. Tables 5.10 and 5.11 summarise the relative branching fraction measurements determined from Eq. (5.1), separately for the 2011 and 2012 data samples. The consistency of the two determinations of each decay mode for each year is quantified as the ratio of the signed difference of the central values over the quadratic sum of the related uncertainties. The two measurements are in fair agreement, namely better that 2.1 statistical standard deviations in all cases.

As the decay mode $\Xi_b^0 \to pK^-K^+K^-$ is not observed, 90% and 95% confidence level (C.L.) intervals, based on the Feldman-Cousins confidence belt inference described in Ref. [42], are placed on the branching fraction for this decay mode relative to $\Lambda_b^0 \to (\Lambda_c^+ \to pK^-\pi^+)\pi^-$

$$R(\Xi_b^0 \to pK^-K^+K^-) \in [4.05\text{–}8.86] \cdot 10^{-4} \text{ at } 90\% \text{ C.L.},$$
$$R(\Xi_b^0 \to pK^-K^+K^-) \in [3.82\text{–}9.81] \cdot 10^{-4} \text{ at } 95\% \text{ C.L.}$$

Table 5.10: Measurements of the R ratio from the (first row) 2011 and the (second row) 2012 data samples for Λ_b^0 decay modes expressed in percent as well as their combination. The three uncertainties are statistical, systematic related to the fit model and systematic related to the efficiency, respectively. The consistency of the two determinations for each year, denoted Δ, is quantified as the ratio of the signed difference of the central values over the quadratic sum of the related uncertainties.

R (per decay)	Value (%)	Δ	Combination (%)
$R(\Lambda_b^0 \to p\pi^-\pi^+\pi^-)$	$6.69 \pm 0.33 \pm 0.09 \pm 0.37$ $6.91 \pm 0.23 \pm 0.08 \pm 0.35$	-0.6σ	$6.85 \pm 0.19 \pm 0.08 \pm 0.32$
$R(\Lambda_b^0 \to pK^-\pi^+\pi^-)$	$16.83 \pm 0.49 \pm 0.19 \pm 1.00$ $16.18 \pm 0.33 \pm 0.20 \pm 0.66$	1.2σ	$16.4 \pm 0.3 \pm 0.2 \pm 0.7$
$R(\Lambda_b^0 \to pK^-K^+\pi^-)$	$1.14 \pm 0.15 \pm 0.10 \pm 0.16$ $1.39 \pm 0.11 \pm 0.08 \pm 0.10$	-1.4σ	$1.32 \pm 0.09 \pm 0.09 \pm 0.10$
$R(\Lambda_b^0 \to pK^-K^+K^-)$	$4.49 \pm 0.22 \pm 0.08 \pm 0.29$ $3.97 \pm 0.14 \pm 0.05 \pm 0.20$	2.1σ	$4.11 \pm 0.12 \pm 0.06 \pm 0.19$

Table 5.11: Measurements of the R ratio from the (first row) 2011 and the (second row) 2012 data samples for Ξ_b^0 decay modes expressed in per mil as well as their combination. The three uncertainties are statistical, systematic related to the fit model and systematic related to the efficiency, respectively. The consistency of the two determinations for each year, denoted Δ, is quantified as the ratio of the signed difference of the central values over the quadratic sum of the related uncertainties.

R (per decay)	Value (10^{-3})	Δ	Combination (10^{-3})
$R(\Xi_b^0 \to pK^-\pi^+\pi^-)$	$7.2 \pm 1.4 \pm 0.2 \pm 0.9$ $5.8 \pm 0.9 \pm 0.2 \pm 1.0$	0.9σ	$6.2 \pm 0.8 \pm 0.2 \pm 0.8$
$R(\Xi_b^0 \to pK^-\pi^+K^-)$	$6.4 \pm 1.1 \pm 0.4 \pm 0.7$ $5.3 \pm 0.7 \pm 0.4 \pm 0.6$	0.9σ	$5.6 \pm 0.6 \pm 0.4 \pm 0.5$
$R(\Xi_b^0 \to pK^-K^+K^-)$	$0.59 \pm 0.49 \pm 0.12 \pm 0.10$ $0.56 \pm 0.34 \pm 0.07 \pm 0.09$	0.1σ	$0.57 \pm 0.28 \pm 0.08 \pm 0.10$

Using the world-average values $\mathcal{B}(\Lambda_b^0 \to \Lambda_c^+\pi^-) = (0.430 \pm 0.036)\%$ and $\mathcal{B}(\Lambda_c^+ \to pK^-\pi^+) = (6.46 \pm 0.24)\%$ [43], the branching fractions of the Λ_b^0 decay modes are

$$\begin{aligned}
\mathcal{B}(\Lambda_b^0 \to p\pi^-\pi^+\pi^-) &= (1.90 \pm 0.06 \pm 0.10 \pm 0.16 \pm 0.07) \cdot 10^{-5}, \\
\mathcal{B}(\Lambda_b^0 \to pK^-\pi^+\pi^-) &= (4.55 \pm 0.08 \pm 0.20 \pm 0.39 \pm 0.17) \cdot 10^{-5}, \\
\mathcal{B}(\Lambda_b^0 \to pK^-K^+\pi^-) &= (0.37 \pm 0.03 \pm 0.04 \pm 0.03 \pm 0.01) \cdot 10^{-5}, \\
\mathcal{B}(\Lambda_b^0 \to pK^-K^+K^-) &= (1.14 \pm 0.03 \pm 0.07 \pm 0.10 \pm 0.05) \cdot 10^{-5},
\end{aligned}$$

where the first uncertainty is statistical and the second comes from experimental systematic sources. The two last uncertainties are due to the knowledge of the branching fractions $\mathcal{B}(\Lambda_b^0 \to \Lambda_c^+\pi^-)$ and $\mathcal{B}(\Lambda_c^+ \to pK^-\pi^+)$ in that order.

The product of the branching fractions of the Ξ_b^0 decay modes with the hadronisation fraction of Ξ_b^0 relative to Λ_b^0 are accordingly obtained

$$\begin{aligned}
\mathcal{B}(\Xi_b^0 \to pK^-\pi^+\pi^-) \cdot f_{\Xi_b^0}/f_{\Lambda_b^0} &= (1.72 \pm 0.21 \pm 0.25 \pm 0.15 \pm 0.07) \cdot 10^{-6}, \\
\mathcal{B}(\Xi_b^0 \to pK^-\pi^+K^-) \cdot f_{\Xi_b^0}/f_{\Lambda_b^0} &= (1.56 \pm 0.16 \pm 0.19 \pm 0.13 \pm 0.06) \cdot 10^{-6}, \\
\mathcal{B}(\Xi_b^0 \to pK^-K^+K^-) \cdot f_{\Xi_b^0}/f_{\Lambda_b^0} &\in [0.11\text{–}0.25] \cdot 10^{-6} \text{ at } 90\% \text{ C.L.}
\end{aligned}$$

In summary, the four decay modes $\Lambda_b^0 \to pK^-\pi^+\pi^-$, $\Lambda_b^0 \to pK^-K^+K^-$, $\Xi_b^0 \to pK^-\pi^+\pi^-$ and $\Xi_b^0 \to pK^-\pi^+K^-$ are observed for the first time. Branching fractions (including the ratio of hadronisation fractions in the case of the Ξ_b^0 baryon) of these decay modes and the branching fractions of the two already observed decay modes $\Lambda_b^0 \to p\pi^-\pi^+\pi^-$ and $\Lambda_b^0 \to pK^-K^+\pi^-$ [22] are determined relative to the $\Lambda_b^0 \to \Lambda_c^+\pi^-$ decay. The $\Xi_b^0 \to pK^-K^+K^-$ decay mode is measured with a significance of 2.3 σ and 90% and 95% confidence level intervals are set on its branching fraction relative to $\Lambda_b^0 \to \Lambda_c^+\pi^-$. As previously emphasised in Chapter 1, there is no theoretical predictions of the branching fractions of interest. However, a couple of comments is in order:

- The measured branching fraction scales with the expected CKM hierarchy.
- Only limits are known for inclusive $B \to$ 4-body fully charged decays. By contrast, the branching fractions of $B \to$ 3-body fully-charged decays that contains the very same quark transitions in the Standard Model are measured and can provide a fair qualitative comparison. Here again, consistent order of magnitudes of the branching fractions are obtained.

The establishment of these signals opens new channels in which to search for *CP*-violating asymmetries in these fully charged four-body decays of Λ_b^0 and Ξ_b^0 baryons. The next chapter presents such measurements.

Chapter 6

Blinded $\Delta\mathcal{A}^{CP}$ measurements

This chapter is dedicated to the measurements of $\Delta\mathcal{A}^{CP}$ of the six decay modes which have been unambiguously established in the previous chapter of this thesis. The requirements on ProbNNp and BDT are first re-optimised with respect to the $\Delta\mathcal{A}^{CP}$ sensitivities. Three categories of measurements are then discussed. Eventually, fit results and systematic uncertainties estimates are presented. For the reader's convenience, we recall in this chapter's introduction the definition of the quantities we aim at measuring:

$$\Delta\mathcal{A}^{CP} = \frac{\mathcal{N}(X_b^0) - \overline{\mathcal{N}}(\overline{X}_b^0)}{\mathcal{N}(X_b^0) + \overline{\mathcal{N}}(\overline{X}_b^0)} - \frac{\mathcal{N}_{\rm C}(X_b^0) - \overline{\mathcal{N}}_{\rm C}(\overline{X}_b^0)}{\mathcal{N}_{\rm C}(X_b^0) + \overline{\mathcal{N}}_{\rm C}(\overline{X}_b^0)}, \tag{6.1}$$

where $\mathcal{N}_{\rm C}$ and $\overline{\mathcal{N}}_{\rm C}$ are the yields of the control decays.

Chapter contents

6.1 Re-optimisation of ProbNNp and BDT requirements

As described in Section 3.2, an arbitrary ProbNNp cut is set in order to strongly reduce background contributions coming from B mesons decays. The BDT cut was optimised with a Punzi F.o.M. These two cuts were used in order to build the fit model, to establish the signals and to measure branching fraction. Now that the decay channels have been unravelled, a finer optimisation of the cuts is in order. Since the uncertainty on $\Delta\mathcal{A}^{CP}$ is mostly of statistical nature, the selection requirements for the $\Delta\mathcal{A}^{CP}$ measurements are

optimised separately on the unblinded statistical error of $\Delta\mathcal{A}^{CP}$, while central values are blinded. A simultaneous fit is performed for each ProbNNp and BDT cut value hypothesis. It is worth to notice that the fit model and the quality of the fit remains unchanged while testing other working points (but two hard ProbNNp cuts). For each cut configuration, the signal cross-feed factors, B physics cross-spectra constraints and B physics yields constraints are re-computed. The $\Delta\mathcal{A}^{CP}$ sensitivities of the charmless dominant mode in each spectra are reported in Tables 6.1 and 6.2 for the different ProbNNp cut and BDT cut values tested, respectively. The optimal ProbNNp cut is chosen to be ProbNN$p > 0.50$. This choice is driven by the visible trend which favours the higher cut values and it happens that the fit procedure meets convergence issues, specially for the two higher values (0.55 and 0.60) tested. This PID$_p$ cut significantly reduced the B physics backgrounds, which in turn allows to optimise the BDT cut. The optimal BDT cut value for almost all modes is close to the lowest value tested. It happens that going below 0.075 do not provide a significant decrease of the statistical uncertainty. In addition, the modelling of combinatorial background gets more challenging. BDT > 0.075 is hence chosen as the nominal BDT cut value.

Table 6.1: Absolute $\Delta\mathcal{A}^{CP}$ sensitivities (in %) of the dominant mode in each spectra for different ProbNNp cut values. For each mode and year, the minimum value is highlighted in bold.

		ProbNNp cut					
Decay mode	Year	0.30	0.40	0.45	0.50	0.55	0.60
$\Lambda_b^0 \to p\pi\pi\pi$	2011	5.22	4.96	4.86	4.87	**4.84**	4.86
	2012	3.64	3.35	3.26	**3.21**	3.23	3.28
$\Lambda_b^0 \to pK\pi\pi$	2011	2.41	2.36	**2.32**	2.33	2.35	2.37
	2012	1.61	1.61	**1.59**	**1.59**	1.61	1.63
$\Lambda_b^0 \to pKK\pi$	2011	17.79	14.33	11.76	11.11	**10.25**	10.54
	2012	12.37	8.63	7.72	7.14	6.89	**6.82**
$\Lambda_b^0 \to pKKK$	2011	4.17	3.99	**3.93**	3.97	3.99	3.98
	2012	2.89	2.77	**2.76**	2.78	2.78	2.79
$\Xi_b^0 \to pK\pi K$	2011	14.23	14.19	12.74	12.52	**11.96**	11.98
	2012	10.65	9.87	10.12	9.77	**9.34**	9.80

6.2 The ensemble of measurements

In this Section, we present the blinded fit results and the measurements of *CP* asymmetry observables in several phase space regions. The inclusive measurement, presented in Subsection 6.2.1, considers the whole space of candidates, where no invariant-mass cut is applied to any pair of daughter particles. Conversely, Subsection 6.2.2 presents the study of the anatomy of the phase space of the decays of interest: *CP* asymmetries are first measured in the low invariant mass of $p\pi$ (or pK) pair and low invariant mass on the pairing of the two other tracks. The invariant-mass cut on the $p\pi$ or pK pair is set to be less than 2 GeV/c^2, while the invariant-mass cut on the two remaining tracks depends on whether it is $\pi\pi$ pair, $K\pi$ pair or KK pair. The choice of these values tries to include several known resonances, in particular, $f_0(1500)$ resonance for $\pi\pi$, the broad scalar $K_0^*(1430)$ resonance for $K\pi$ and the $f_2'(1525)$ resonance for KK. The ensemble of measurement that are performed with this phase space selection is hereafter referred to by **Low2x2BodyMass** (LBM) measurements, for sake of readability. Lastly, several *CP* asymmetry measurements are performed for the

Table 6.2: Absolute $\Delta\mathcal{A}^{CP}$ sensitivities (in %) of the dominant mode in each spectra for different BDT cut values. For each mode and year, the minimum value is highlighted in bold.

Decay mode	Year	BDT cut -0.10	0.00	0.075	0.15	0.30
$\Lambda_b^0 \to p\pi\pi\pi$	2011	**4.49**	4.50	4.52	4.56	4.86
	2012	**2.95**	2.96	2.97	3.01	3.21
$\Lambda_b^0 \to pK\pi\pi$	2011	**2.07**	**2.07**	2.09	2.14	2.33
	2012	**1.34**	1.35	1.37	1.40	1.59
$\Lambda_b^0 \to pKK\pi$	2011	10.06	9.95	9.89	**9.76**	10.64
	2012	**5.89**	5.91	6.12	6.31	6.89
$\Lambda_b^0 \to pKKK$	2011	**3.32**	3.37	3.40	3.53	3.96
	2012	**2.31**	2.33	2.36	2.42	2.77
$\Xi_b^0 \to pK\pi K$	2011	10.13	**10.12**	10.31	10.59	12.40
	2012	**7.45**	7.50	7.77	8.20	9.90

dominant modes (namely $\Lambda_b^0 \to p\pi^-\pi^+\pi^-$, $\Lambda_b^0 \to pK^-\pi^+\pi^-$ and $\Lambda_b^0 \to pK^-K^+K^-$ decay modes) with an explicit invariant-mass selection of resonances, which are identified from the invariant-mass distributions of two or three tracks present in the final state, as reported in Appendix E.1. This amounts to a total of 18 measurements of $\Delta\mathcal{A}^{CP}$. The decay modes that are considered for the inclusive measurement as well as for the phase space configurations are reported in Table 6.3.

Table 6.3: List of decay modes used for $\Delta\mathcal{A}^{CP}$ measurements considering the full phase space, the LBM region and with a specific resonance selection.

Spectrum	Full phase space	Low2x2BodyMass	Resonance selection
$X_b^0 \to p\pi\pi\pi$	$\Lambda_b^0 \to p\pi^-\pi^+\pi^-$	$\Lambda_b^0 \to p\pi^-\pi^+\pi^-$	$\Lambda_b^0 \to pa_1$ $\Lambda_b^0 \to \Delta^{++}\pi^-\pi^-$ $\Lambda_b^0 \to N^*(1520)^0\rho^0(f^0)$
$X_b^0 \to pK\pi\pi$	$\Lambda_b^0 \to pK^-\pi^+\pi^-$ $\Xi_b^0 \to pK^-\pi^+\pi^-$	$\Lambda_b^0 \to pK^-\pi^+\pi^-$	$\Lambda_b^0 \to pK_1$ $\Lambda_b^0 \to \Delta^{++}K^-\pi^-$ $\Lambda_b^0 \to \Lambda^*(1520)^0\rho^0(f^0)$ $\Lambda_b^0 \to N^*(1520)^0K^{*0}$
$X_b^0 \to pKKK$	$\Lambda_b^0 \to pK^-K^+K^-$	$\Lambda_b^0 \to pK^-K^+K^-$	$\Lambda_b^0 \to \Lambda^*(1520)^0\phi^0$ $\Lambda_b^0 \to pK^-_{\text{highmass}}\phi^0$
$X_b^0 \to pKK\pi$	$\Lambda_b^0 \to pK^-K^+\pi^-$		
$X_b^0 \to pK\pi K$	$\Xi_b^0 \to pK^-\pi^+K^-$		

6.2.1 Inclusive measurements

The data samples to be simultaneously fit consist of 56 experimental spectra. The data are actually split according to the final state hypotheses, to the proton charge, to the year of data taking and to two L0 triggers requirements (L0TIS and L0TOS, see Section 2.3). Combined plots are produced by summing the 2011 (TIS+TOS), 2012 (TIS+TOS) events (shown as black data points) and the individual PDFs as determined by the fit results for each component (model), without unblinding the signal region. Figures 6.1, 6.2 and 6.3 display the superimposed fit results of the simultaneous fit to the invariant-mass spectra in semi-logarithmic scale. Linear plots can be found in Appendix E.2. The fit parameters are summarised in Tables E.2 and E.1 (reported in Appendix E.3, where it shows which parameters are shared and not shared. The inclusive yields (proton+anti proton) are reported in Table 6.4.

The $\Delta\mathcal{A}^{CP}$ measurements for the Ξ_b^0 decay modes have been determined with respect to two control channels, $\Lambda_b^0 \to (\Lambda_c^+ \to pK^-\pi^+)\pi^-$ and $\Xi_b^0 \to (\Xi_c^+ \to pK^-\pi^+)\pi^-$. The obvious advantage with the latter is that the Ξ_b^0 production asymmetry would be handled. Conversely, a larger statistical uncertainty on the $\Delta\mathcal{A}^{CP}$ measurements is the price to pay.

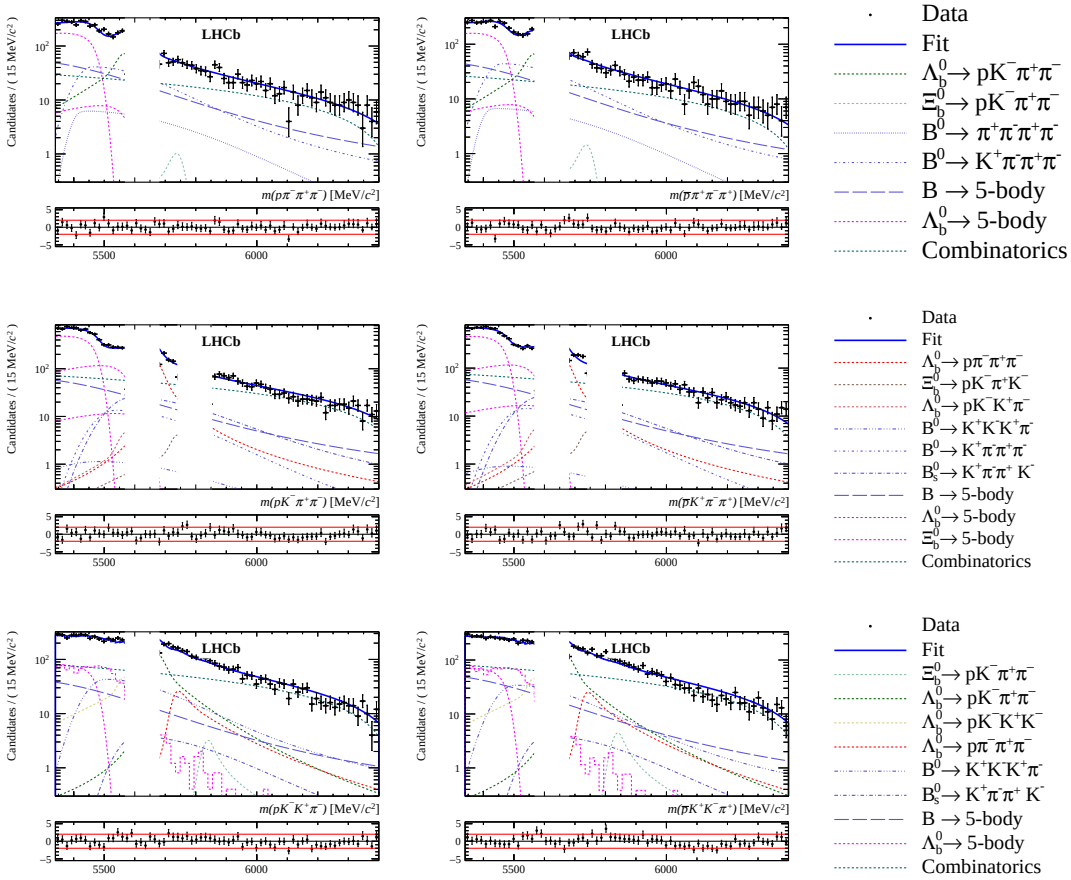

Figure 6.1: Superimposed fit results for the [from top to bottom] $X_b^0 \to p\pi\pi\pi$, $X_b^0 \to pK\pi\pi$ and $X_b^0 \to pKK\pi$ spectra using the full phase space data. Plots in the left-column are for the spectra with X_b^0 and on the right-column for the spectra with $\overline{X}_b^0$.

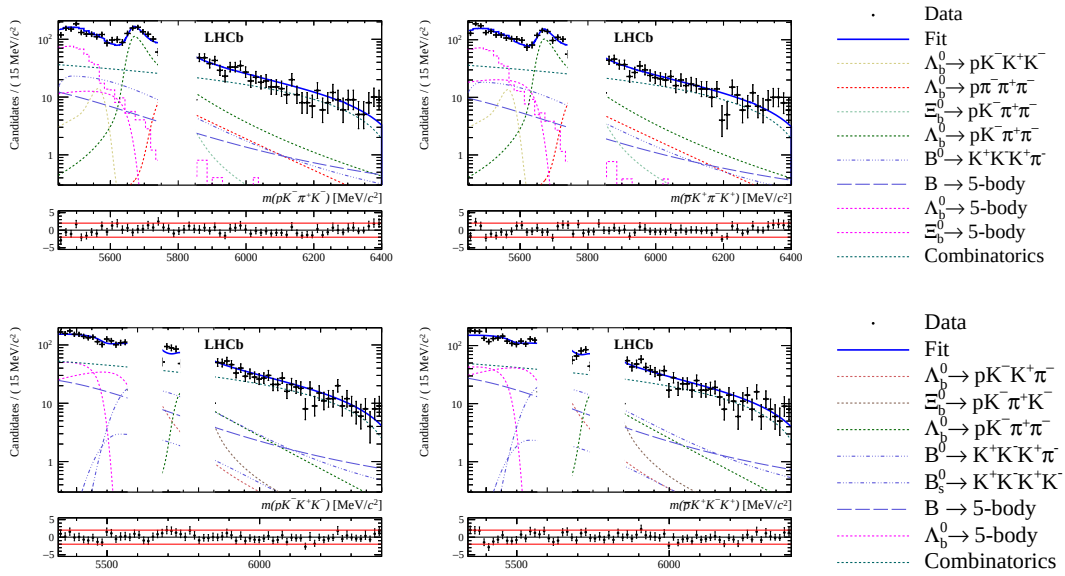

Figure 6.2: Superimposed fit results for the [top] $X_b^0 \to pK\pi K$ and [bottom] $X_b^0 \to pKKK$ spectra using the full phase space data of 2011 and 2012. Plots in the left-column are for the spectra with X_b^0 and on the right-column for the spectra with $\overline{X}_b^0$.

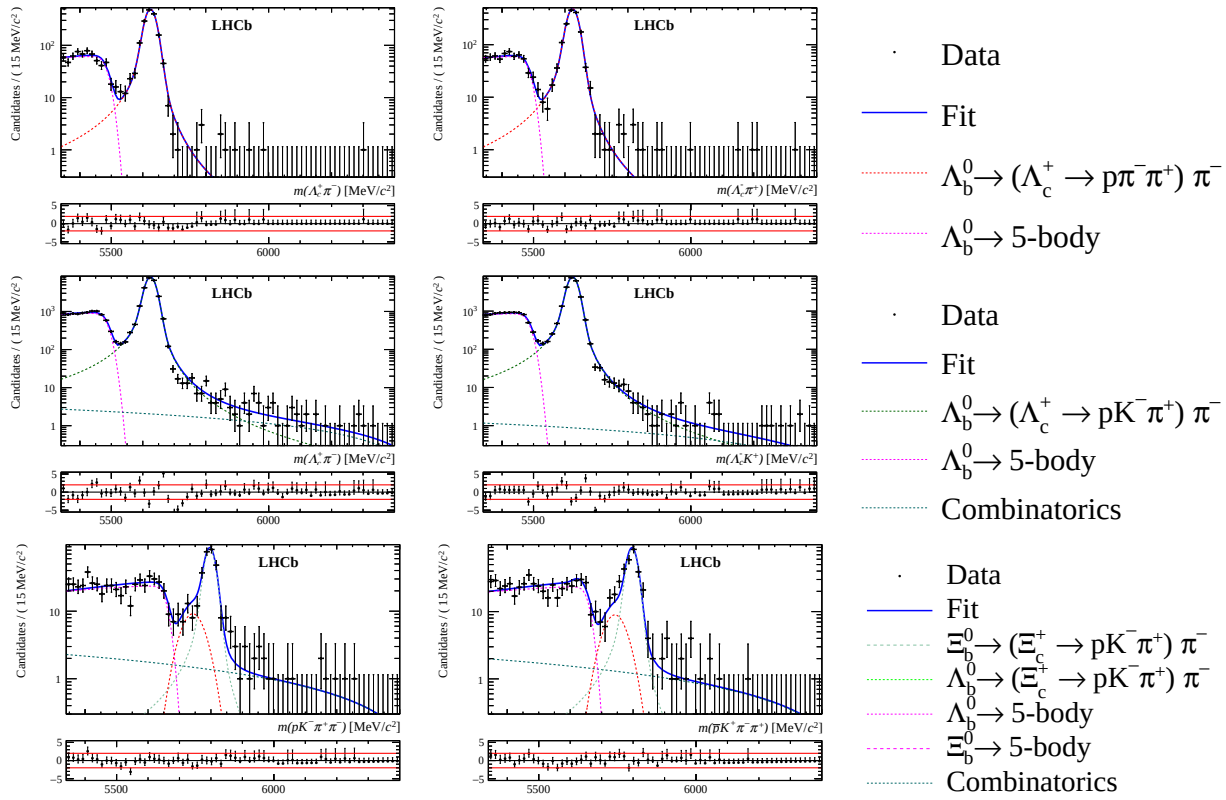

Figure 6.3: Superimposed fit results for the [from top to bottom] $X_b^0 \to (\Lambda_c^+ \to p\pi\pi)\pi$, $X_b^0 \to (\Lambda_c^+ \to pK\pi)\pi$ and $X_b^0 \to (\Xi_c^+ \to pK\pi)\pi$ spectra using the full phase space data of 2011 and 2012. Plots in the left-column are for the spectra with X_b^0 and on the right-column for the spectra with $\overline{X}_b^0$. The pink curve describes the partially reconstructed background $\Lambda_b^0 \to p\pi^-\pi^+\pi^-\pi^0$ where a π^0 is not reconstructed. The blue dotted curve describes the combinatorial background.

Table 6.4: (Blinded) Addition of the (blinded) yields of particle and antiparticle decays, for 2011 and 2012 data.

Decay mode	Yields	
	2011	2012
$\Lambda_b^0 \to p\pi^-\pi^+\pi^-$	1369 ± 42	3230 ± 67
$\Lambda_b^0 \to pK^-\pi^+\pi^-$	3827 ± 68	9212 ± 110
$\Lambda_b^0 \to pK^-K^+\pi^-$	340 ± 28	844 ± 46
$\Lambda_b^0 \to pK^-K^+K^-$	1455 ± 43	3105 ± 64
$\Xi_b^0 \to pK^-\pi^+\pi^-$	114 ± 20	318 ± 35
$\Xi_b^0 \to pK^-\pi^+K^-$	184 ± 20	386 ± 31
$\Xi_b^0 \to pK^-K^+K^-$	23 ± 13	56 ± 22
$\Lambda_b^0 \to (\Lambda_c^+ \to p\pi^-\pi^+)\pi^-$	925 ± 31	2268 ± 48
$\Lambda_b^0 \to (\Lambda_c^+ \to pK^-\pi^+)\pi^-$	13965 ± 120	34774 ± 189
$\Xi_b^0 \to (\Xi_c^+ \to pK^-\pi^+)\pi^-$	169 ± 15	350 ± 22

All signal yields, and hence raw and *CP* asymmetries observables, are blind. Though limited, some comments are however in order concerning the fit results and fit behaviour in general:

- The fit model describes in a satisfactory way all the reconstructed spectra of interest.
- All sources of background seem to be identified and adequately modelled. In particular, signal cross-feeds and B physics backgrounds, data-driven constrained, are in place. No sign of an overlooked contribution is observed. It is remarkable that the slight tensions between the model and the data observed in the fit for the branching fractions measurements are vanishing with the additional statistics brought by the TOS data sample. This gives further confidence that the fit model that we have built provides an accurate description of the LHCb data.
- The empirical adjustment of the partially reconstructed background shapes brings a consistent understanding of this component among the spectra.
- The combinatorial backgrounds are found to be present in all the charmless spectra and described with similar shapes.
- Consistent results are obtained between the two years of data taking for the parameters which can be compared.

The raw asymmetries of the control channels are unblinded and are discussed in Subsection 6.3.2. The fit results are there as well consistent in between the years and the precision basically scales as expected with the luminosity. These asymmetries embody both the detection asymmetries between charges (π, K and proton) and the b-baryon production asymmetries in addition to a *CP* asymmetry expectedly extremely small in the Standard Model.

6.2.2 Anatomy of the Phase Space

The interference pattern of four-body beautiful b-baryon decays is expected to be rich. Difference in strong phases between two competing amplitudes might enhance the weak-induced asymmetries. Following this qualitative statement, $\Delta\mathcal{A}^{CP}$ measurements are performed in several phase space regions in addition to the measurement presented in the previous section, which is performed considering the full phase space.

On one hand, CP asymmetries are measured considering the common region[a] between low invariant mass of $p\pi$ (or pK) and low invariant mass of the pair of the two remaining tracks regions. It consists in a simultaneous fit of the five invariant-mass spectra of interest ($\times 2$ $X_b^0/\overline{X}_b^0$ splitting; $\times 2$ trigger splitting), in which the additional cuts are applied on relevant 2-body invariant masses. The corresponding fit results are described in Subsection 6.2.2.1.

On another hand, using the $\Lambda_b^0 \to p\pi^-\pi^+\pi^-$, $\Lambda_b^0 \to pK^-\pi^+\pi^-$ and $\Lambda_b^0 \to pK^-K^+K^-$ signal modes, the invariant-mass distributions of combinations of two or three tracks (out of the 4 final state tracks) are scrutinised in order to identify at first low baryon or meson resonances (Λ^{*0}, N^{*0}, Δ, ρ^0, f_0 ...). It allows to design a selection of a given resonance by cutting the invariant masses of interest. Contrary to the LBM case, each resonance selection leads to a dedicated simultaneous fit. For the sake of simplicity, only the fit results for the decay mode which receive invariant-mass phase space cuts as well as the corresponding $\Delta\mathcal{A}^{CP}$ measurements are reported. Subsection 6.2.2.2 presents the fit results for each charmless decay mode, considering several resonances hypothesis.

As soon as additional invariant-mass cuts are applied, selection and particle (mis)identification efficiencies, which constrain the cross-feed signal yields, must be re-computed. The two dynamical regimes generated in the simulation (full phase space and 2-body decays) are analysed individually to provide a range of efficiencies that is used as the uncertainty of the Gaussian constraint. B physics background yields are also re-estimated following the procedure described in Section 4.3. Although few contributions might need to be removed depending on the selected resonance (*e.g.* partially reconstructed background coming from $\Lambda_b^0 \to p\pi^-(\eta' \to \pi^+\pi^-\gamma)$ decay is no longer relevant in $\Lambda_b^0 \to \Delta^{++}\pi^-\pi^-$ spectrum), a very similar fit model is used for all the tested hypothesis.

6.2.2.1 Low invariant-mass region

We want to explore in this subsection a semi-inclusive measurement which aims at selecting in the three main spectra the quasi-2-body decays. The rationale behind this selection is to gather quasi-2-body amplitudes where strong phases can be associated to known resonances. Any indication of CP violation in this region of the phase space will point towards specific decays that will be in turn explored one by one (next subsection).

A simultaneous fit is hence performed with invariant-mass cuts on the two pairs of two tracks present in the final state. The cut on $p\pi$ or pK invariant mass is set to be less than 2000 MeV/c^2, while the cut on the invariant mass of the two remaining tracks is set to a value which depends on its nature (π or K). Cuts applied per decay mode are summarised in Table 6.5. Table 6.6 displays the measured yields per decay and Fig. 6.4 displays the fit results of this simultaneous fit in logarithmic scale. Linear plots can be found in Appendix E.4.

6.2.2.2 Resonance selection

Let's come back to the definition of the quasi-2-body decays which we have selected: the $p\pi\pi\pi$ spectrum can proceed through a final state with the N^{*0} resonance series. The latter

[a] Referred to as Low2x2BodyMass (LBM), for sake of readability.

Table 6.5: Set of invariant-mass cuts applied in the LBM regions for *CP* asymmetry measurements.

Decay mode	Invariant-mass cuts (in MeV/c^2)
$\Lambda_b^0 \to p\pi^-\pi^+\pi^-$	$m(p\pi^-) < 2000.$ and $m(\pi^+\pi^-) < 1640.$
$\Lambda_b^0 \to pK^-\pi^+\pi^-$	$(m(pK^-) < 2000.$ and $m(\pi^+\pi^-) < 1640.$ or $(m(p\pi^-) < 2000.$ and $m(\pi^+K^-) < 1600.$
$\Lambda_b^0 \to pK^-K^+K^-$	$(m(pK^-) < 2000.$ and $m(K^+K^-) < 1675.$

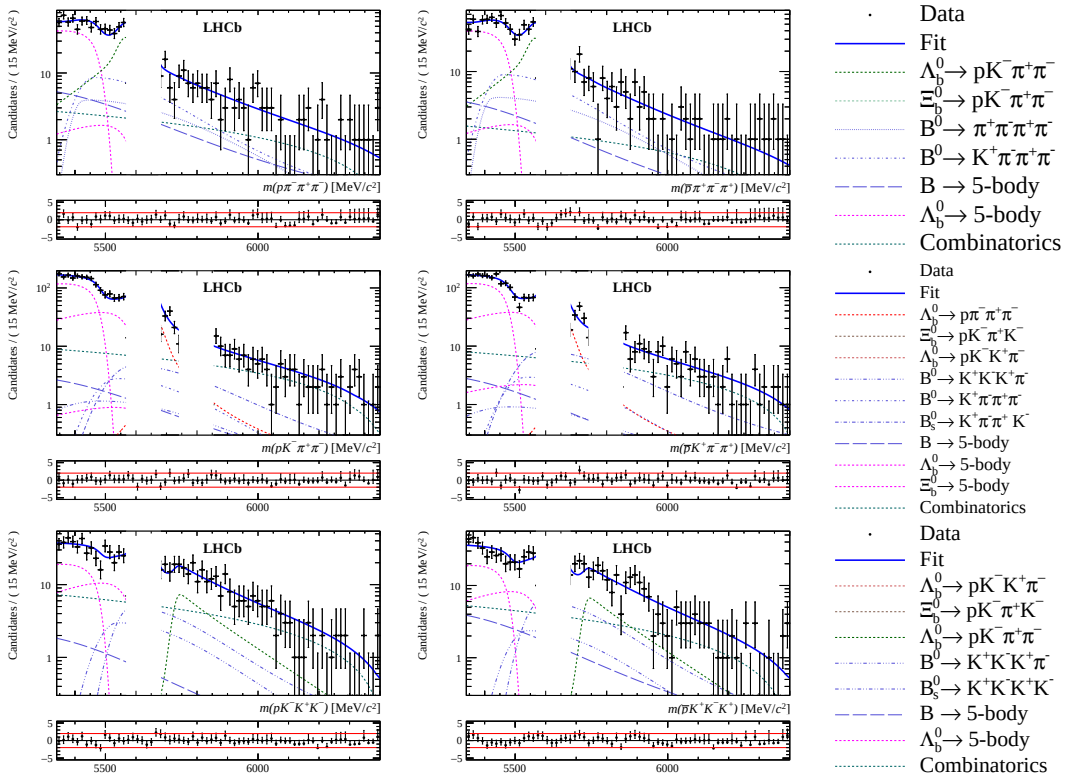

Figure 6.4: Superimposed fit results for (from top to bottom) $X_b^0 \to p\pi\pi\pi$, $X_b^0 \to pK\pi\pi$ and $X_b^0 \to pKKK$ spectra considering the LBM set of cuts on data of 2011 and 2012. Plots in the left-column are for the spectra with X_b^0 and on the right-column for the spectra with $\overline{X}_b^0$.

Table 6.6: Yields measured for LBM configuration, for 2011 and 2012 data.

Decay mode	Yields	
	2011	2012
$\Lambda_b^0 \to p\pi^-\pi^+\pi^-$	280 ± 19	673 ± 30
$\Lambda_b^0 \to pK^-\pi^+\pi^-$	1871 ± 45	4275 ± 70
$\Lambda_b^0 \to pK^-K^+K^-$	762 ± 29	1625 ± 43

is poorly known with the noticeable exception of $N^*(1520)^0$. The analogous comment is in order for $\Lambda^*(1520)^0$ that can be associated with a $\phi(1020)$ that is, to a certain extent, particularly well defined. It has been therefore chosen to highlight this resonance in the selection. Another remarkable (in many respects) resonance is Δ^{++}. The decay under consideration here is $\Lambda_b^0 \to \Delta^{++}\pi^-\pi^-$; there is no $(\pi^+\pi^-)$ strong interacting resonance to our knowledge. Eventually, the quasi-2-body decay $\Lambda_b^0 \to pa_1$ seemed of some interest in our opinion. Though a_1 is a broad resonance, the analogous decay $B^0 \to a_1\pi$ could be accurately studied at the B-factories [44]. The decay $\Lambda_b^0 \to pa_1$ can hence serve as a benchmark in the exploration of the new territory undertaken in this work.

The choice of the phase space regions as well as the related cuts applied are based on the invariant-mass distributions displayed in Appendix E.1. A simultaneous fit is performed for each phase-space configuration. It happens that the different splittings which are used during the simultaneous fit procedure do not provide sub-samples with enough statistics for $\Lambda_b^0 \to \Lambda^*(1520)^0\rho^0(f^0)$, $\Lambda_b^0 \to pK_1$ or $\Lambda_b^0 \to \Lambda^*(1520)^0\phi^0$ phase-space configurations. For these specific cases, the 2011 and 2012 data samples are combined into one data set and then fitted using the model discussed in the previous sections. Cuts applied per decay mode are summarised in Table 6.7. Table 6.8 displays the measured yields per decay mode and per phase-space configuration. Figures E.8, 6.6 and 6.7 display the fit results for the $\Lambda_b^0 \to p\pi^-\pi^+\pi^-$, $\Lambda_b^0 \to pK^-\pi^+\pi^-$ and $\Lambda_b^0 \to pK^-K^+K^-$ phase-space configurations, respectively, in logarithmic scale. Linear plots can be found in Appendix E.4.

Table 6.7: Set of invariant-mass cuts applied for different phase space selection.

Decay mode	Invariant-mass cuts (in MeV/c^2)
$\Lambda_b^0 \to p\pi^-\pi^+\pi^-$	
$\Lambda_b^0 \to pa_1$	$(\ 419 < m(\pi^+\pi^-\pi^+) < 1500\ )$
$\Lambda_b^0 \to N^*(1520)^0\rho^0(f^0)$	$(\ 1078 < m(p\pi^-) < 1800\ )$ and $(m(\pi^+\pi^-) < 1100\ )$
$\Lambda_b^0 \to \Delta^{++}\pi^-\pi^-$	$(\ 1078 < m(p\pi^+) < 1432\ )$
$\Lambda_b^0 \to pK^-\pi^+\pi^-$	
$\Lambda_b^0 \to N^*(1520)^0K^{*0}$	$(\ 1078 < m(p\pi^-) < 1800\ )$ and $(750 < m(\pi^+K^-) < 1100\ )$
$\Lambda_b^0 \to \Lambda^*(1520)^0\rho^0(f^0)$	$(\ 1460 < m(pK^-) < 1580\ )$ and $(\ m(\pi^+\pi^-) < 1100\ )$
$\Lambda_b^0 \to \Delta^{++}K^-\pi^-$	$(\ 1078 < m(p\pi^+) < 1432\ )$
$\Lambda_b^0 \to pK_1$	$(\ 1200 < m(K^-\pi^+\pi^-) < 1600\ )$
$\Lambda_b^0 \to pK^-K^+K^-$	
$\Lambda_b^0 \to \Lambda^*(1520)^0\phi^0$	$(\ 1460 < m(pK^-) < 1600\ )$ and $(\ 1005 < m(K^+K^-) < 1040\ )$
$\Lambda_b^0 \to pK^-_{\text{highmass}}\phi^0$	$(\ m(pK^-) > 1600\ )$ and $(\ 1005 < m(K^+K^-) < 1040\ )$

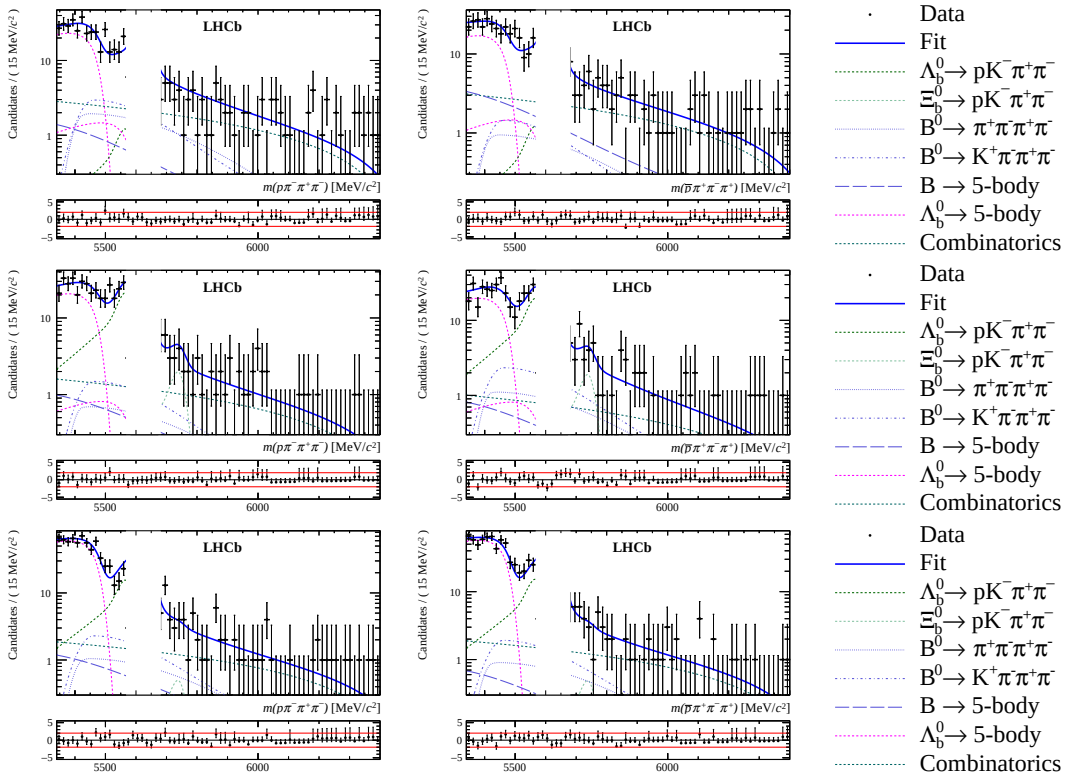

Figure 6.5: $p\pi\pi\pi$ invariant-mass spectra considering (from top to bottom) $\Lambda_b^0 \to pa_1$, $\Lambda_b^0 \to N^{*0}\rho^0$ (f^0), $\Lambda_b^0 \to \Delta^{++}\pi^-\pi^-$ resonances for (first column) X_b^0 data (2011 and 2012 samples combined) and (second column) $\overline{X}_b^0$ data (2011 and 2012 samples combined).

Table 6.8: Yields measured per phase-space configurations, for 2011 and 2012 data. Only one yield is measured for $\Lambda_b^0 \to \Lambda^*(1520)^0\rho^0(f^0)$, $\Lambda_b^0 \to \Lambda^*(1520)^0\phi^0$, $\Lambda_b^0 \to pK^-_{\text{highmass}}\phi^0$ and $\Lambda_b^0 \to pK_1$ since data sample used in the fit is not split with respect to the year of data taking.

Decay mode	Yields	
	2011	2012
$\Lambda_b^0 \to pa_1$	243 ± 17	605 ± 27
$\Lambda_b^0 \to N^*(1520)^0\rho^0(f^0)$	122 ± 12	350 ± 21
$\Lambda_b^0 \to \Delta^{++}\pi^-\pi^-$	475 ± 23	1079 ± 36
$\Lambda_b^0 \to pK_1$	1037 ± 36	
$\Lambda_b^0 \to \Lambda^*(1520)^0\rho^0(f^0)$	327 ± 19	
$\Lambda_b^0 \to N^*(1520)^0K^{*0}$	588 ± 25	1245 ± 37
$\Lambda_b^0 \to \Delta^{++}K^-\pi^-$	577 ± 28	1316 ± 44
$\Lambda_b^0 \to \Lambda^*(1520)^0\phi^0$	363 ± 20	
$\Lambda_b^0 \to pK^-_{\text{highmass}}\phi^0$	1089 ± 36	

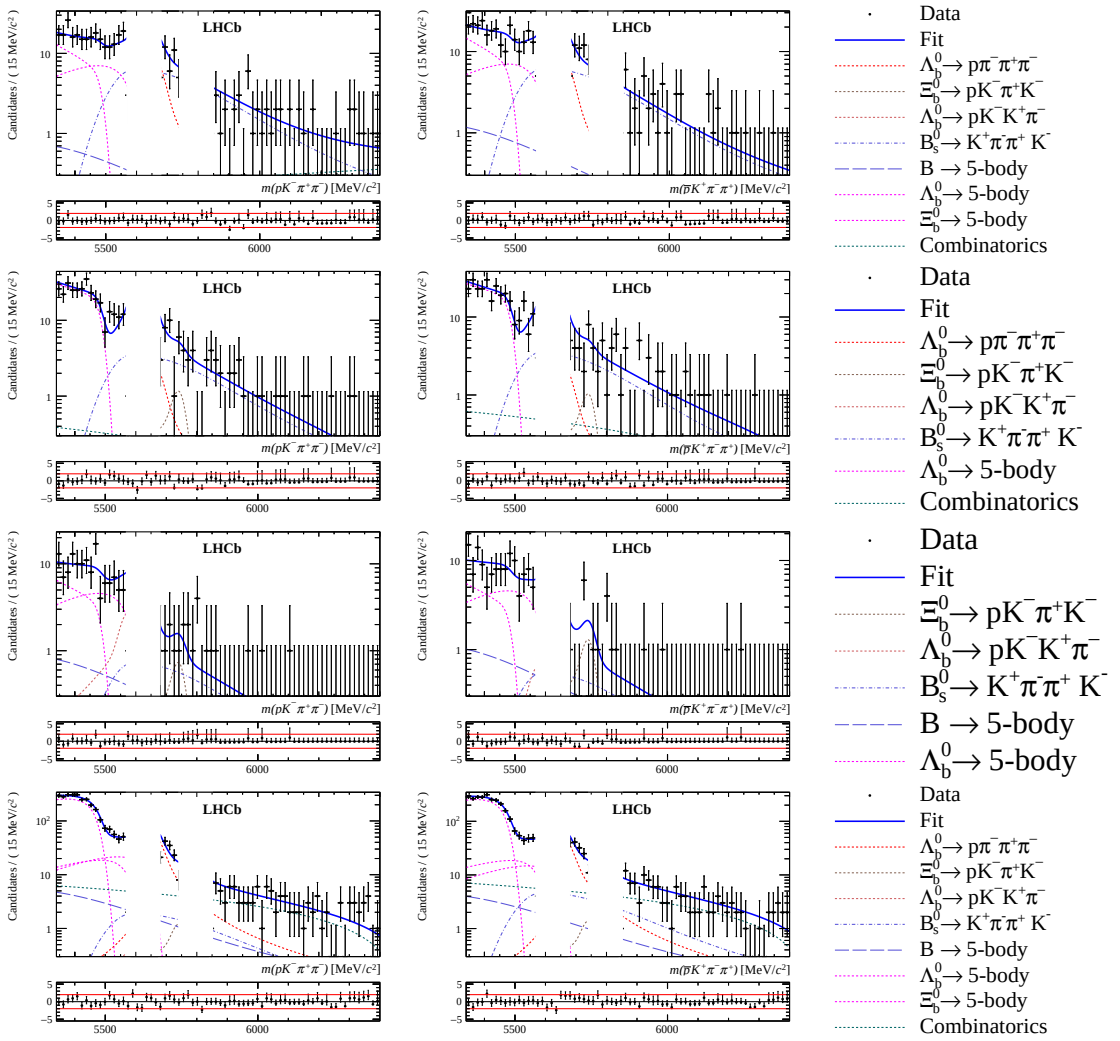

Figure 6.6: $pK\pi\pi$ invariant-mass spectra considering (from top to bottom) $\Lambda_b^0 \to pK_1$, $\Lambda_b^0 \to N^*(1520)^0 K^{*0}$, $\Lambda_b^0 \to \Lambda^*(1520)^0 \rho^0(f^0)$, $\Lambda_b^0 \to \Delta^{++} K^- \pi^-$ decays for (first column) X_b^0 data (2011 and 2012 samples combined) and (second column) $\overline{X}_b^0$ data (2011 and 2012 samples combined).

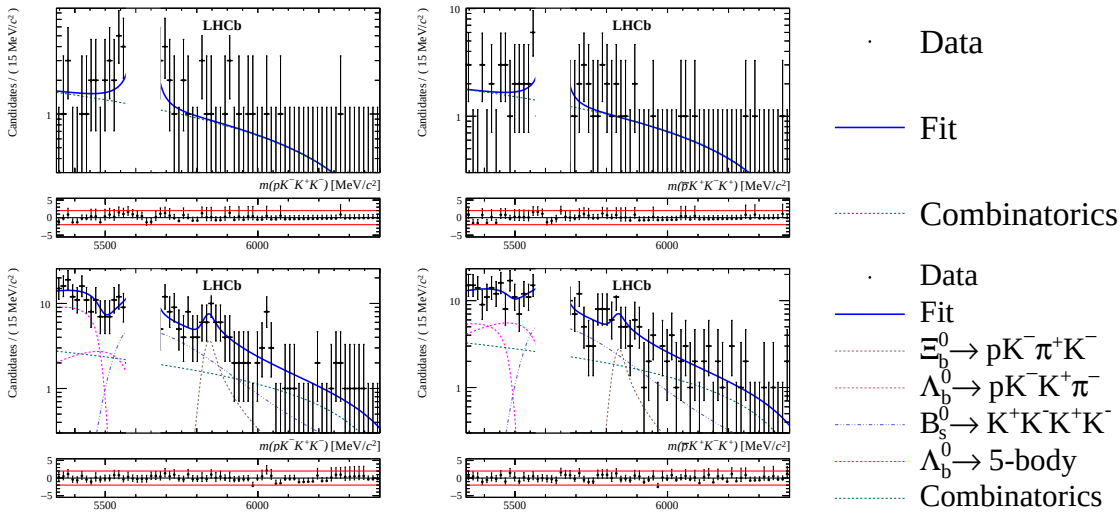

Figure 6.7: $pKKK$ invariant-mass spectra considering (from top to bottom) $\Lambda_b^0 \to \Lambda^*(1520)^0 \phi^0$ and $\Lambda_b^0 \to pK^-_{\text{highmass}} \phi^0$ decays for (first column) X_b^0 data (2011 and 2012 samples combined) and (second column) $\overline{X}_b^0$ data (2011 and 2012 samples combined).

6.3 Corrections of raw asymmetries and systematic uncertainties

Sources of uncertainties (for instance related to the fit model) are charge-independent and are as such, not subjected to systematic uncertainties, contrarily to the branching fractions purpose. It happens that the design of the fit-model and the simultaneous fit strategy (both presented in previous chapters) are taking into account the charge-dependent systematic uncertainties (we are speaking here of the modelling of the combinatorial background and contributions coming from B mesons decays, that are possibly charge asymmetric). Charge-asymmetric uncertainties can however be brought by other sources which are discussed in this section. The systematic uncertainties are first discussed separately (*i.e.* per source) and are eventually gathered at the end of this section in Tables 6.17 and 6.18. Eventually, several crosschecks are also presented.

6.3.1 Systematic uncertainties sources

6.3.1.1 L0Hadron trigger efficiencies

There is a detection asymmetry at the hadron trigger level between particle and antiparticle. Among the different possible reasons, let's mention the fact that the antiparticle will experience a nuclear interaction earlier than the particle in the calorimeter system. These effects have been quantified by studying $K^{\pm}$ and $\pi^{\pm}$ issued from $D^0 \to K^-\pi^+$ decays [45]. It is also necessary to know the p-$\overline{p}$ trigger asymmetry and $\Lambda_b^0 \to (\Lambda_c^+ \to pK^-\pi^+)\pi^-$ decays are used for this purpose. In both cases, the L0 asymmetry is determined as a function of the transverse momentum of the tracks. Those distributions are displayed in Figs. 6.8 and 6.9 for the kaons and pions respectively and in Fig. 6.10 for the proton.

The estimation of the L0 trigger efficiencies makes use of simulated signal and control channel samples (to provide kinematical distributions) re-weighted to match the L0 efficiency as measured in the data. The L0 efficiencies (split by charge) are hence determined for protons, pions and kaons and are used in the $\Delta\mathcal{A}^{CP}$ derivation in order to correct the signal yield measured in the fit to the TOS data sample. Since the analysis has been developed blindly, the correction on the $\Delta\mathcal{A}^{CP}$ measurement (referred to by δ^{L0} defined in Eq. 6.3 in the following) was estimated by measuring the blind difference between the $\Delta\mathcal{A}^{CP}$ fit measurement (not corrected) and ${\Delta\mathcal{A}^{CP}}_{\rm L0}$. The asymmetry corrected for the L0Hadron trigger asymmetry as defined in Eq. 6.2, where α is the ratio of L0HadronTOS efficiencies, reads

$$ {\mathcal{A}^{CP}}_{\rm L0} = \frac{\mathcal{N}(X_b^0) - \alpha\cdot\overline{\mathcal{N}}(\overline{X}_b^0)}{\mathcal{N}(X_b^0) + \alpha\cdot\overline{\mathcal{N}}(\overline{X}_b^0)} \tag{6.2} $$

$$ \delta^{\rm L0} = \Delta\mathcal{A}^{CP} - \left({\mathcal{A}^{CP}}_{\rm L0,sig} - {\mathcal{A}^{CP}}_{\rm L0,cc}\right) \tag{6.3} $$

For the inclusive measurements (using the full phase space of data), there are three sources of systematic uncertainties:

- The δ_{L0} correction is estimated for the two extreme kinematical cases and the difference is taken as a range for a systematic estimate.
- The limited size of the MC sample is an additional systematic uncertainty. It has been explicitly checked that the value of the systematic uncertainty scales as $\left(\sqrt{N_{\rm MC}}\right)^{-1}$

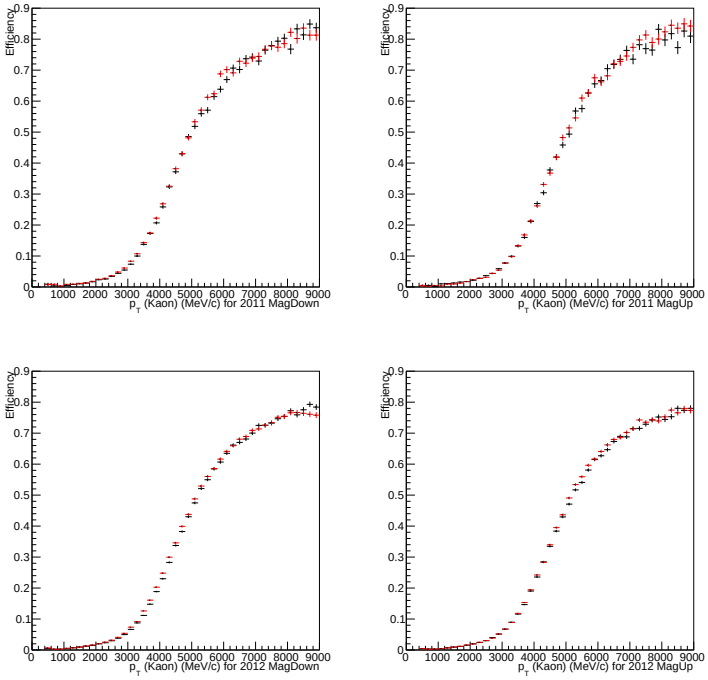

Figure 6.8: L0 trigger efficiency as a function of the momentum of a kaon for (first row) 2011 (second row) 2012, (first column) MagDown (second column) MagUp. Red (black) distribution is for the positive (negative) tracks.

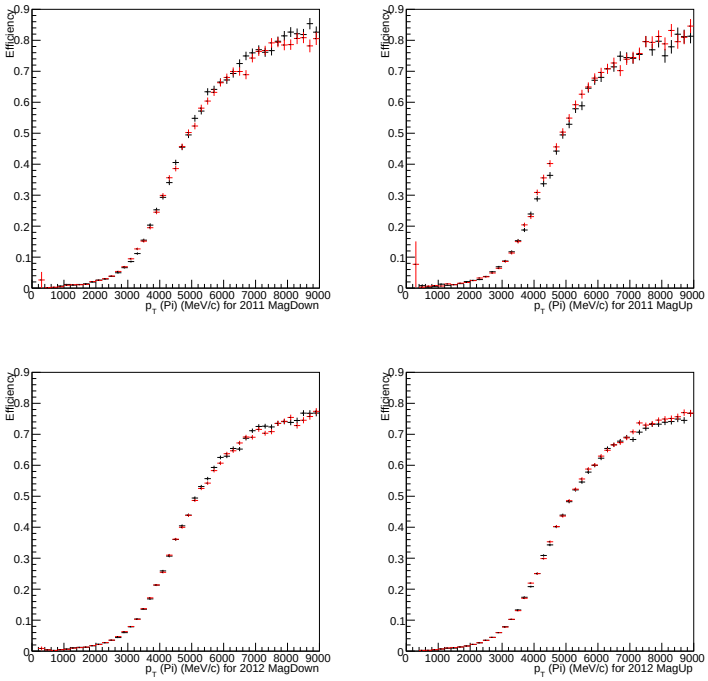

Figure 6.9: L0 trigger efficiency as a function of the momentum of a pion for (first row) 2011 (second row) 2012, (first column) MagDown (second column) MagUp. Red (black) distribution is for the positive (negative) tracks.

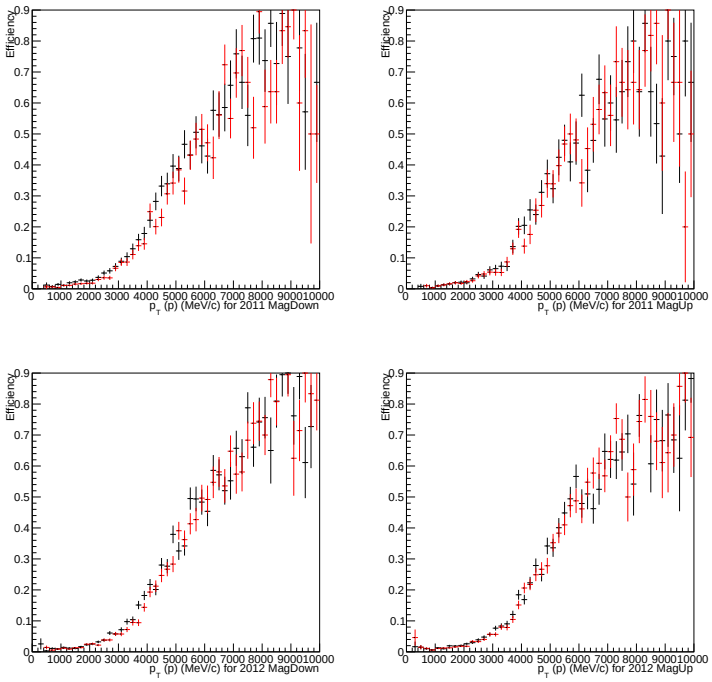

Figure 6.10: L0 trigger efficiency as a function of the momentum of a proton for (first row) 2011 (second row) 2012, (first column) MagDown (second column) MagUp. Red (black) distribution is for the positive (negative) tracks.

where $N_{\rm MC}$ is the number of simulated events used for the estimation. This systematic uncertainty is however not reported for the inclusive measurements, since it is found to be negligibly small.

- Eventually, the uncertainties from the tables used in the efficiency determination is also propagated as systematic uncertainty.

The systematic uncertainties for the $\Delta\mathcal{A}^{CP}$ measurements of specific decays and LBM are reduced to the two latter sources. Relevant numbers are gathered in Tables 6.9 and 6.10 for the inclusive measurements and for the (LBM measurements + quasi 2-body decays measurements), respectively.

6.3.1.2 The proton and kaon detection asymmetry

The LHCb tracking performance group provides kaon detection asymmetries as a function of the momentum of the kaon using double-tagged partially reconstructed D^0 decays [41]. For convenience, the distribution is reported in Fig. 6.11. This distribution is used in order to correct $\Delta\mathcal{A}^{CP}$ measurements for the kinematical dependency of the kaon detection asymmetry of the signal mode and the control channel. It is particularly important when the two final states differ by one kaon.

As for the L0 trigger efficiency case, simulated signal and control channel samples are used to provide kinematical distributions and the kaon detection correction is defined as Eq. 6.4.

$$\Delta A_K(\%) = A_K^{\rm sig.} - A_K^{\rm cc}. \tag{6.4}$$

The uncertainties of the tables and the MC statistics used for the re-weighting are propagated as systematic uncertainties. As soon as the same table is used for signal and control channel,

Table 6.9: L0Hadron correction δ^{L0} in percent, per decay and per year of data taking, for full phase space measurements. The central value is the correction and the uncertainties are the systematic uncertainties on the $\Delta\mathcal{A}^{CP}$ measurements coming from the tables used for the efficiency determination and from the variation over the phase space, respectively. The uncertainties are rounded to the significance of the sub-dominant contribution in order that the reader gets the quantitative hierarchy of the uncertainties.

Decay mode	δ^{L0} (%)	
	2011	2012
$\Lambda_b^0 \to p\pi^-\pi^+\pi^-$	XXX $\pm$ 0.12 $\pm$ 0.03	XXX $\pm$ 0.08 $\pm$ 0.02
$\Lambda_b^0 \to pK^-\pi^+\pi^-$	XXX $\pm$ 0.10 $\pm$ 0.02	XXX $\pm$ 0.07 $\pm$ 0.03
$\Lambda_b^0 \to pK^-K^+\pi^-$	XXX $\pm$ 0.11 $\pm$ 0.03	XXX $\pm$ 0.06 $\pm$ 0.02
$\Lambda_b^0 \to pK^-K^+K^-$	XXX $\pm$ 0.10 $\pm$ 0.06	XXX $\pm$ 0.07 $\pm$ 0.06
$\Xi_b^0 \to pK^-\pi^+\pi^-$	XXX $\pm$ 0.09 $\pm$ 0.03	XXX $\pm$ 0.06 $\pm$ 0.02
$\Xi_b^0 \to pK^-\pi^+K^-$	XXX $\pm$ 0.10 $\pm$ 0.03	XXX $\pm$ 0.06 $\pm$ 0.02

Table 6.10: L0Hadron correction δ^{L0} in percent, per decay and per year of data taking, for LBM measurements and for $\Delta\mathcal{A}^{CP}$ measurements of specific decays. The central value is the correction and the uncertainties are the systematic uncertainties on the $\Delta\mathcal{A}^{CP}$ measurements coming from the tables used for the efficiency determination and from MC statistics, respectively. The uncertainties are rounded to the significance of the sub-dominant contribution in order that the reader gets the quantitative hierarchy of the uncertainties.

Decay mode	δ^{L0} (%)	
	2011	2012
$\Lambda_b^0 \to p\pi^-\pi^+\pi^-$	XXX $\pm$ 0.100 $\pm$ 0.001	XXX $\pm$ 0.074 $\pm$ 0.001
$\Lambda_b^0 \to pK^-\pi^+\pi^-$	XXX $\pm$ 0.090 $\pm$ 0.002	XXX $\pm$ 0.062 $\pm$ 0.001
$\Lambda_b^0 \to pK^-K^+K^-$	XXX $\pm$ 0.090 $\pm$ 0.002	XXX $\pm$ 0.063 $\pm$ 0.001
$\Lambda_b^0 \to pa_1$	XXX $\pm$ 0.177 $\pm$ 0.050	XXX $\pm$ 0.105 $\pm$ 0.002
$\Lambda_b^0 \to N^*(1520)^0\rho^0(f^0)$	XXX $\pm$ 0.078 $\pm$ 0.001	XXX $\pm$ 0.061 $\pm$ 0.001
$\Lambda_b^0 \to \Delta^{++}\pi^-\pi^-$	XXX $\pm$ 0.091 $\pm$ 0.000	XXX $\pm$ 0.065 $\pm$ 0.000
$\Lambda_b^0 \to pK_1$	XXX $\pm$ 0.103 $\pm$ 0.027	
$\Lambda_b^0 \to \Lambda^*(1520)^0\rho^0(f^0)$	XXX $\pm$ 0.037 $\pm$ 0.002	
$\Lambda_b^0 \to N^*(1520)^0K^{*0}$	XXX $\pm$ 0.063 $\pm$ 0.003	XXX $\pm$ 0.044 $\pm$ 0.001
$\Lambda_b^0 \to \Delta^{++}K^-\pi^-$	XXX $\pm$ 0.089 $\pm$ 0.004	XXX $\pm$ 0.060 $\pm$ 0.000
$\Lambda_b^0 \to \Lambda^*(1520)^0\phi^0$	XXX $\pm$ 0.045 $\pm$ 0.001	
$\Lambda_b^0 \to pK^-_{\text{highmass}}\phi^0$	XXX $\pm$ 0.090 $\pm$ 0.002	

the systematic uncertainty on ΔA_K is determined by taking into account the correlation between signal and control channel. Relevant numbers are gathered in Tables 6.11 and 6.12 for the inclusive and for the (LBM measurements + quasi 2-body decays measurements), respectively.

Similarly, tables for proton detection asymmetries are available from ongoing work on measurement of *CP* violation in $\Lambda_b^0 \to pK^-$ and $\Lambda_b^0 \to p\pi^-$ decays[b]. In this work, the

[b]The proton detection asymmetry as a function of the proton momentum can be found in Fig.29 of

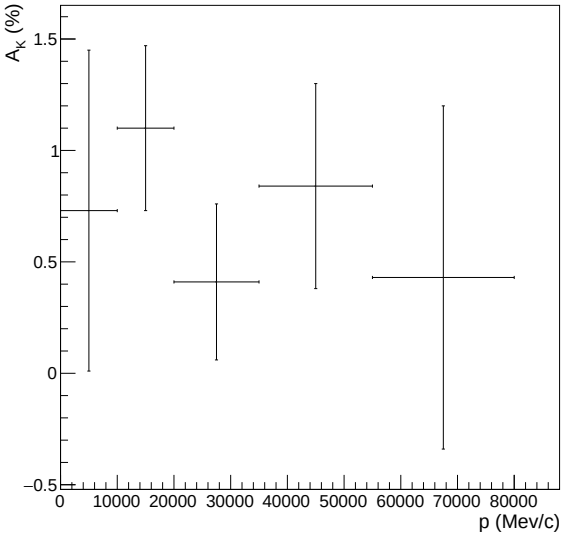

Figure 6.11: Kaon detection asymmetries as a function of the momentum of the kaon as measured in [41].

proton detection asymmetry is derived from simulated events and a dedicated systematic uncertainty due to the material budget modelling is set. The very same procedure is used in order to correct $\Delta\mathcal{A}^{CP}$ for proton detection asymmetries. The difference of proton detection asymmetries ΔA_p is determined with the Eq. 6.4 and the uncertainties of the tables and the MC statistics used for the re-weighting are propagated as systematic uncertainties. Relevant numbers are gathered in Tables 6.13 and 6.14 for the inclusive and for the (LBM measurements + quasi 2-body decays measurements), respectively. There is a noticeable difference with the work in Ref. [46]. Since the observable here is a difference of $\mathcal{A}^{CP}$, the correlated uncertainties between p_T bins do not play a role in the final systematic uncertainty budget.

Table 6.11: Kaon detection correction, per decay and per year of data taking, for full phase space measurements. The central value is the correction and the uncertainties are the systematic uncertainties on the $\Delta\mathcal{A}^{CP}$ measurements.

Decay mode	ΔA_K (%)	
	2011	2012
$\Lambda_b^0 \to p\pi^-\pi^+\pi^-$	—	—
$\Lambda_b^0 \to pK^-\pi^+\pi^-$	XXX ± 0.17	XXX ± 0.18
$\Lambda_b^0 \to pK^-K^+\pi^-$	—	—
$\Lambda_b^0 \to pK^-K^+K^-$	XXX ± 0.16	XXX ± 0.16
$\Xi_b^0 \to pK^-\pi^+\pi^-$	XXX ± 0.18	XXX± 0.18
$\Xi_b^0 \to pK^-\pi^+K^-$	XXX ± 0.16	XXX± 0.16

Ref. [46].

Table 6.12: Kaon detection correction, per decay and per year of data taking, for LBM measurements and for $\Delta\mathcal{A}^{CP}$ measurements of specific decays. The central value is the correction and the uncertainties are the systematic uncertainties on the $\Delta\mathcal{A}^{CP}$ measurements coming from the tables used for the efficiency determination and from MC statistics, respectively. The uncertainties are rounded to the significance of the sub-dominant contribution in order that the reader gets the quantitative hierarchy of the uncertainties.

Decay mode	ΔA_K (%)	
	2011	2012
$\Lambda_b^0 \to p\pi^-\pi^+\pi^-$	—	—
$\Lambda_b^0 \to pK^-\pi^+\pi^-$	XXX ± 0.1711 ± 0.0001	XXX ± 0.1716 ± 0.0010
$\Lambda_b^0 \to pK^-K^+K^-$	XXX ± 0.1623 ± 0.0011	XXX ± 0.1626 ± 0.0012
$\Lambda_b^0 \to pK_1$	XXX ± 0.1615 ± 0.0053	
$\Lambda_b^0 \to \Lambda^*(1520)^0\rho^0(f^0)$	XXX ± 0.1228 ± 0.0003	
$\Lambda_b^0 \to N^*(1520)^0K^{*0}$	XXX ± 0.1535 ± 0.0035	XXX ± 0.1560 ± 0.0051
$\Lambda_b^0 \to \Delta^{++}K^-\pi^-$	XXX ± 0.2153 ± 0.0078	XXX ± 0.2210 ± 0.0122
$\Lambda_b^0 \to \Lambda^*(1520)^0\phi^0$	XXX ± 0.1074 ± 0.0013	
$\Lambda_b^0 \to pK^-_{\text{highmass}}\phi^0$	XXX ± 0.1512 ± 0.0053	

Table 6.13: Proton detection correction, per decay and per year of data taking, for full phase space measurements. The central value is the correction and the uncertainties are the systematic uncertainties on the $\Delta\mathcal{A}^{CP}$ measurements.

Decay mode	ΔA_p (%)	
	2011	2012
$\Lambda_b^0 \to p\pi^-\pi^+\pi^-$	XXX ± 0.201	XXX ± 0.201
$\Lambda_b^0 \to pK^-\pi^+\pi^-$	XXX ± 0.203	XXX ± 0.203
$\Lambda_b^0 \to pK^-K^+\pi^-$	XXX ± 0.206	XXX ± 0.207
$\Lambda_b^0 \to pK^-K^+K^-$	XXX ± 0.202	XXX ± 0.202
$\Xi_b^0 \to pK^-\pi^+\pi^-$	XXX ± 0.202	XXX ± 0.202
$\Xi_b^0 \to pK^-\pi^+K^-$	XXX ± 0.201	XXX ± 0.201

Table 6.14: Proton detection correction, per decay and per year of data taking, for LBM measurements and for $\Delta\mathcal{A}^{CP}$ measurements of specific decays. The central value is the correction and the uncertainties are the systematic uncertainties on the $\Delta\mathcal{A}^{CP}$ measurements coming from the tables used for the efficiency determination and from MC statistics, respectively. The uncertainties are rounded to the significance of the sub-dominant contribution in order that the reader gets the quantitative hierarchy of the uncertainties.

Decay mode	ΔA_p (%)	
	2011	2012
$\Lambda_b^0 \to p\pi^-\pi^+\pi^-$	XXX ± 0.164 ±0.008	XXX ± 0.164 ±0.007
$\Lambda_b^0 \to pK^-\pi^+\pi^-$	XXX ± 0.167 ±0.004	XXX ± 0.166 ±0.005
$\Lambda_b^0 \to pK^-K^+K^-$	XXX ± 0.167 ±0.006	XXX ± 0.167 ±0.006
$\Lambda_b^0 \to pa_1$	XXX ± 0.205 ± 0.019	XXX ± 0.203 ± 0.014
$\Lambda_b^0 \to N^*(1520)^0\rho^0(f^0)$	XXX ± 0.121 ± 0.010	XXX ± 0.121 ± 0.009
$\Lambda_b^0 \to \Delta^{++}\pi^-\pi^-$	XXX ± 0.180 ± 0.115	XXX ± 0.181 ± 0.100
$\Lambda_b^0 \to pK_1$	XXX ± 0.139 ± 0.046	
$\Lambda_b^0 \to \Lambda^*(1520)^0\rho^0(f^0)$	XXX ± 0.117 ± 0.025	
$\Lambda_b^0 \to N^*(1520)^0K^{*0}$	XXX ± 0.136 ± 0.025	XXX ± 0.135 ± 0.025
$\Lambda_b^0 \to \Delta^{++}K^-\pi^-$	XXX ± 0.186 ± 0.070	XXX ± 0.184 ± 0.072
$\Lambda_b^0 \to \Lambda^*(1520)^0\phi^0$	XXX ± 0.100 ± 0.005	
$\Lambda_b^0 \to pK^-_{\text{highmass}}\phi^0$	XXX ± 0.139 ± 0.026	

6.3.1.3 The PID asymmetry

The PID requirements on the tracks of the final state can induce asymmetries that are expected to be cancelled by the $\Delta\mathcal{A}^{CP}$ formalism, up to the kinematical differences between the charmless signal decay mode and charmed decay mode. Performance histograms (from PIDCalib tools) have been built from real data inclusive Λ_c^+ decays, split with respect of the charge of the proton in order to correct the raw asymmetries for residual kinematical differences between signal and control channels. The performance histograms (for the proton) are displayed in Fig. 6.12

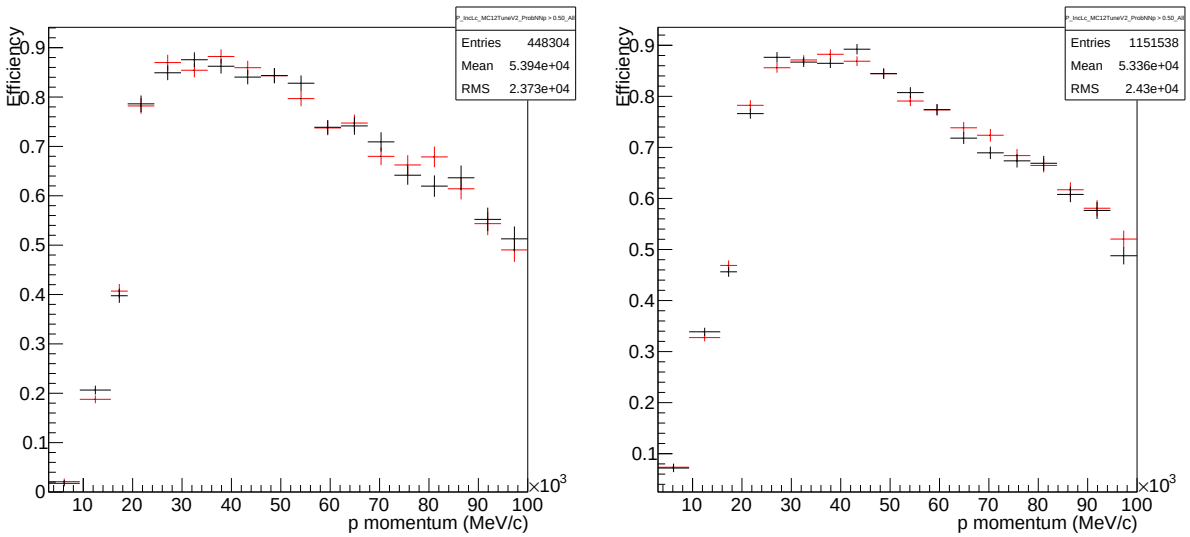

Figure 6.12: PID efficiency (for ProbNN > 0.50) as a function of the transverse momentum of the proton (left) 2011 (right) 2012. Red (black) distribution is for the positive (negative) tracks. It's worth noting that 2012 distributions have ~ 2.6 times more statistics than in 2011.

Here again, charge-dependent PID efficiencies determination makes use of simulated data, that provide kinematical distributions. The PID asymmetries are computed for the signal and the control channel and the correction on the $\Delta\mathcal{A}^{CP}$ variables is similarly determined from the Eq. 6.5. The uncertainties coming from the calibration samples are propagated as a systematic uncertainty on the final measurement. Relevant numbers are gathered in Tables 6.15 and 6.16 for the inclusive measurements and for the (LBM measurements + quasi 2-body decays measurements), respectively.

$$\Delta A_{\text{PID}}(\%) = A_{\text{PID}}^{\text{sig.}} - A_{\text{PID}}^{\text{cc}}. \tag{6.5}$$

6.3.1.4 Fit model uncertainty

The fit model has been built from simulated events (separately from protons and antiprotons) and no difference were observed between particle and antiparticle shapes within the simulated events sample statistics. Should we quote a systematic uncertainty, it would reflect at first the limited size of the MC simulated events. By contrast, we have chosen to assign a systematic uncertainty to the fit biases which can occur in case of significant possible non-vanishing $\Delta\mathcal{A}^{CP}$. The procedure will consist in producing a large number of pseudo-experiments following the fit model and check for the fit biases. Should they be significant, the results will be corrected for and in any case, the uncertainty on their values will be propagated as a systematic uncertainty. This phase can only happen after the unblinding of the results.

Table 6.15: PID correction, per decay and per year of data taking, for full phase space measurements. The central value is the correction and the uncertainties are the systematic uncertainties on the $\Delta\mathcal{A}^{CP}$ measurements.

Decay mode	$\Delta A_{\rm PID}$ (%)	
	2011	2012
$\Lambda_b^0 \to p\pi^-\pi^+\pi^-$	XXX $\pm$ 0.839	XXX $\pm$ 0.479
$\Lambda_b^0 \to pK^-\pi^+\pi^-$	XXX $\pm$ 0.829	XXX $\pm$ 0.477
$\Lambda_b^0 \to pK^-K^+\pi^-$	XXX $\pm$ 0.816	XXX $\pm$ 0.467
$\Lambda_b^0 \to pK^-K^+K^-$	XXX $\pm$ 0.833	XXX $\pm$ 0.478
$\Xi_b^0 \to pK^-\pi^+\pi^-$	XXX $\pm$ 0.836	XXX $\pm$ 0.479
$\Xi_b^0 \to pK^-\pi^+K^-$	XXX $\pm$ 0.833	XXX $\pm$ 0.476

Table 6.16: PID correction, per decay and per year of data taking, for LBM measurements and for $\Delta\mathcal{A}^{CP}$ measurements of specific decays. The central value is the correction and the uncertainties are the systematic uncertainties on the $\Delta\mathcal{A}^{CP}$ measurements coming from the tables used for the efficiency determination and from MC statistics, respectively. The uncertainties are rounded to the significance of the sub-dominant contribution in order that the reader gets the quantitative hierarchy of the uncertainties.

Decay mode	$\Delta A_{\rm PID}$ (%)	
	2011	2012
$\Lambda_b^0 \to p\pi^-\pi^+\pi^-$	XXX $\pm$ 0.717 $\pm$ 0.004	XXX $\pm$ 0.410 $\pm$ 0.003
$\Lambda_b^0 \to pK^-\pi^+\pi^-$	XXX $\pm$ 0.680 $\pm$ 0.005	XXX $\pm$ 0.390 $\pm$ 0.002
$\Lambda_b^0 \to pK^-K^+K^-$	XXX $\pm$ 0.748 $\pm$ 0.005	XXX $\pm$ 0.429 $\pm$ 0.003
$\Lambda_b^0 \to pa_1$	XXX $\pm$ 0.966 $\pm$ 0.060	XXX $\pm$ 0.555 $\pm$ 0.061
$\Lambda_b^0 \to N^*(1520)^0\rho^0(f^0)$	XXX $\pm$ 0.467 $\pm$ 0.006	XXX $\pm$ 0.267 $\pm$ 0.005
$\Lambda_b^0 \to \Delta^{++}\pi^-\pi^-$	XXX $\pm$ 0.957 $\pm$ 0.027	XXX $\pm$ 0.546 $\pm$ 0.004
$\Lambda_b^0 \to pK_1$	XXX $\pm$ 0.582 $\pm$ 0.071	
$\Lambda_b^0 \to \Lambda^*(1520)^0\rho^0(f^0)$	XXX $\pm$ 0.365 $\pm$ 0.006	
$\Lambda_b^0 \to N^*(1520)^0K^{*0}$	XXX $\pm$ 0.638 $\pm$ 0.010	XXX $\pm$ 0.369 $\pm$ 0.005
$\Lambda_b^0 \to \Delta^{++}K^-\pi^-$	XXX $\pm$ 0.964 $\pm$ 0.031	XXX $\pm$ 0.551 $\pm$ 0.006
$\Lambda_b^0 \to \Lambda^*(1520)^0\phi^0$	XXX $\pm$ 0.297 $\pm$ 0.004	
$\Lambda_b^0 \to pK^-_{\rm highmass}\phi^0$	XXX $\pm$ 0.576 $\pm$ 0.011	

Table 6.17: Systematic uncertainties split by sources for each decay mode for 2011 data sample. The "*" index stands for modes for which 2011 and 2012 data samples are combined.

Decay mode	Absolute uncertainties (%)				Total (%)
	σ_{L0}	σ_K	σ_p	σ_{PID}	
$\Lambda_b^0 \to p\pi^-\pi^+\pi^-$	± 0.11	—	± 0.20	± 0.84	± 0.87
$\Lambda_b^0 \to pK^-\pi^+\pi^-$	± 0.10	± 0.17	± 0.20	± 0.83	± 0.88
$\Lambda_b^0 \to pK^-K^+\pi^-$	± 0.11	—	± 0.21	± 0.82	± 0.85
$\Lambda_b^0 \to pK^-K^+K^-$	± 0.11	± 0.15	± 0.20	± 0.83	± 0.88
$\Xi_b^0 \to pK^-\pi^+\pi^-$	± 0.09	± 0.17	± 0.20	± 0.84	± 0.88
$\Xi_b^0 \to pK^-\pi^+K^-$	± 0.09	± 0.15	± 0.20	± 0.83	± 0.88
$\Lambda_b^0 \to p\pi^-\pi^+\pi^-$	± 0.10	—	± 0.16	± 0.72	± 0.74
$\Lambda_b^0 \to pK^-\pi^+\pi^-$	± 0.09	± 0.17	± 0.17	± 0.68	± 0.73
$\Lambda_b^0 \to pK^-K^+K^-$	± 0.09	± 0.16	± 0.17	± 0.75	± 0.79
$\Lambda_b^0 \to pa_1$	± 0.18	—	± 0.20	± 0.97	± 1.01
$\Lambda_b^0 \to N^*(1520)^0\rho^0(f^0)$	± 0.08	—	± 0.12	± 0.47	± 0.49
$\Lambda_b^0 \to \Delta^{++}\pi^-\pi^-$	± 0.09	—	± 0.18	± 0.96	± 0.99
$\Lambda_b^0 \to pK_1$ *	± 0.11	± 0.16	± 0.14	± 0.58	± 0.63
$\Lambda_b^0 \to \Lambda^*(1520)^0\rho^0(f^0)$ *	± 0.04	± 0.12	± 0.12	± 0.36	± 0.40
$\Lambda_b^0 \to N^*(1520)^0K^{*0}$	± 0.06	± 0.15	± 0.14	± 0.64	± 0.67
$\Lambda_b^0 \to \Delta^{++}K^-\pi^-$	± 0.09	± 0.22	± 0.19	± 0.96	± 1.01
$\Lambda_b^0 \to \Lambda^*(1520)^0\phi^0$ *	± 0.05	± 0.11	± 0.10	± 0.30	± 0.33
$\Lambda_b^0 \to pK^-_{\text{highmass}}\phi^0$ *	± 0.06	± 0.15	± 0.14	± 0.58	± 0.61

Table 6.18: Systematic uncertainties split by sources for each decay mode for 2012 data sample.

Decay mode	Absolute uncertainties (%)				Total (%)
	σ_{L0}	σ_K	σ_p	σ_{PID}	
$\Lambda_b^0 \to p\pi^-\pi^+\pi^-$	± 0.08	—	± 0.20	± 0.48	± 0.52
$\Lambda_b^0 \to pK^-\pi^+\pi^-$	± 0.07	± 0.16	± 0.20	± 0.48	± 0.55
$\Lambda_b^0 \to pK^-K^+\pi^-$	± 0.06	—	± 0.21	± 0.47	± 0.51
$\Lambda_b^0 \to pK^-K^+K^-$	± 0.08	± 0.15	± 0.20	± 0.48	± 0.55
$\Xi_b^0 \to pK^-\pi^+\pi^-$	± 0.09	± 0.17	± 0.20	± 0.84	± 0.88
$\Xi_b^0 \to pK^-\pi^+K^-$	± 0.06	± 0.17	± 0.20	± 0.48	± 0.55
$\Lambda_b^0 \to p\pi^-\pi^+\pi^-$	± 0.07	—	± 0.16	± 0.41	± 0.45
$\Lambda_b^0 \to pK^-\pi^+\pi^-$	± 0.06	± 0.17	± 0.17	± 0.39	± 0.46
$\Lambda_b^0 \to pK^-K^+K^-$	± 0.06	± 0.16	± 0.17	± 0.43	± 0.49
$\Lambda_b^0 \to pa_1$	± 0.11	—	± 0.20	± 0.55	± 0.60
$\Lambda_b^0 \to N^*(1520)^0\rho^0(f^0)$	± 0.06	—	± 0.12	± 0.27	± 0.30
$\Lambda_b^0 \to \Delta^{++}\pi^-\pi^-$	± 0.06	—	± 0.18	± 0.55	± 0.59
$\Lambda_b^0 \to N^*(1520)^0K^{*0}$	± 0.04	± 0.16	± 0.14	± 0.37	± 0.43
$\Lambda_b^0 \to \Delta^{++}K^-\pi^-$	± 0.06	± 0.22	± 0.18	± 0.55	± 0.63

6.3.2 Cross-checks

Three main categories of cross-checks have been defined for a sanity check of the results. Raw asymmetries $\mathcal{A}^{\text{raw}}$ of the control modes $\Lambda_b^0 \to (\Lambda_c^+ \to pK^-\pi^+)\pi^-$ and $\Lambda_b^0 \to (\Lambda_c^+ \to p\pi^-\pi^+)\pi^-$ are not blinded and hence can already be discussed. The comparison of the $\Delta\mathcal{A}^{CP}$ measurements will come after the unblinding of the results. It has been decided a priori that a cross-check result will be acceptable if the significance of its consistency is less than two standard deviations. Further investigations will proceed if this criterion is not met.

- The comparison of the results for the independent samples of the two magnet polarities is performed. Consistency of the two $\mathcal{A}^{\text{raw}}$ determinations (Magnet Up and Magnet Down) of each control mode for each year is quantified as the ratio of the signed difference of the central values divided by the quadratic sum of the related statistical uncertainties. The results, reported in Table 6.19, are found to be consistent.

- The comparison of the results obtained for the two categories of L0 trigger requirements: Trigger Independent of Signal (TIS) candidates and Trigger On Signal (TOS) candidates are also determined. Consistency of the two $\mathcal{A}^{\text{raw}}$ determinations (TOS and TIS) of each control mode for each year is also quantified as the ratio of the signed difference of the central values over the quadratic sum of the related statistical uncertainties. Measurements are reported in Table 6.20 for the control modes. They are also found to be consistent.

- *CP* asymmetries in B mesons decays: $\mathcal{A}^{\text{raw}}$ measurements are performed for the dominant background contributions (B mesons decays) by inferring for each component the amount of background in a region defined as $m_{X_b} \pm 3\sigma$. *CP* asymmetries $\mathcal{A}^{CP}$ have been observed in the K and B mesons decays, where large asymmetries have been measured specially in the latter case. B physics background yields are estimated for protons and antiprotons separately in this analysis and allows to properly estimate charge-asymmetries for these contributions. Table 6.21 gathers the measured raw asymmetries for the dominant background contributions, for the dominant modes. All the measurements are compatible with zero asymmetry within 1-2 standard deviation. This does not indicate that background are mastered since B mesons decays can own an actual *CP* asymmetry. The smallnsess of the asymmetries is nonetheless consistent with what has been measured for these B mesons decays.

- *CP* asymmetries in combinatorial background: in contrast with the previous point, it is expected that the charge asymmetry of the combinatorial background is consistent with zero. The results are gathered in Table 6.21 and satisfactorily show a vanishing *CP* asymmetry.

Table 6.19: Raw asymmetries of control modes obtained for the independent samples obtained with each of the magnet polarities in percent. The consistency of the two determination is denoted Δ.

Decay mode	Polarity	$\mathcal{A}^{\text{raw}}$ (in %) 2011 (2012)	Δ 2011 (2012)
$\Lambda_b^0 \to (\Lambda_c^+ \to p\pi^-\pi^+)\pi^-$	MagUp	4.73 ± 5.19 (1.78 ± 3.04)	1.11σ (0.12 σ)
	MagDown	-2.80 ± 4.31 (1.25 ± 2.95)	
$\Lambda_b^0 \to (\Lambda_c^+ \to pK^-\pi^+)\pi^-$	MagUp	0.05 ± 1.34 (0.46 ± 0.78)	-1.66σ (-1.22 σ)
	MagDown	2.94 ± 1.11 (1.79 ± 0.76)	

Table 6.20: Raw asymmetries of control modes obtained for the independent samples obtained with each of the L0 trigger requirements in percent. The consistency of the two determination is denoted Δ.

Decay mode	L0 Trigger	$\mathcal{A}^{\text{raw}}$ (in %) 2011 (2012)	Δ 2011 (2012)
$\Lambda_b^0 \to (\Lambda_c^+ \to p\pi^-\pi^+)\pi^-$	TIS	-1.44 ± 4.15 (2.58 ± 2.67)	0.86 σ (-0.48 σ)
	TOS	4.54 ± 5.53 (0.48 ± 3.49)	
$\Lambda_b^0 \to (\Lambda_c^+ \to pK^-\pi^+)\pi^-$	TIS	2.26 ± 1.07 (2.24 ± 0.67)	-0.02σ (-1.99 σ)
	TOS	2.29 ± 1.42 (-0.02 ± 0.91)	

Table 6.21: Raw asymmetries of dominant background contributions of the spectra of interest.

Decay	Background	$\mathcal{A}^{\text{raw}}$ 2011 (2012)
$\Lambda_b^0 \to p\pi^-\pi^+\pi^-$	$B \to K\pi\pi\pi$	0.025 ± 0.091 (-0.045 ± 0.045)
	$B \to$ 5-body	-0.020 ± 0.126 (0.078 ± 0.051)
	Comb.	0.018 ± 0.080 (0.066 ± 0.087)
$\Lambda_b^0 \to pK^-\pi^+\pi^-$	$B_s \to KK\pi\pi$	-0.047 ± 0.153 (-0.009 ± 0.069)
	$B \to$ 5-body	-0.039 ± 0.193 (-0.003 ± 0.065)
	Comb.	0.037 ± 0.054 (0.023 ± 0.047)
$\Lambda_b^0 \to pK^-K^+K^-$	$B_s \to KKKK$	0.113 ± 0.186 (-0.061 ± 0.091)
	$B \to$ 5-body	-0.429 ± 0.239 (0.036 ± 0.091)
	Comb.	0.047 ± 0.061 (0.023 ± 0.048)

6.4 Results

This section gathers the results of the $\Delta\mathcal{A}^{CP}$ measurements for the different phase space configurations. Since the analysis is still blinded, only the statistical and systematic uncertainties are reported. The latter is found to be of the order of few per mil (absolute). A strategy on how quantify the significance of a CP-violation or the consistency to no CP-violation is provided.

6.4.1 $\Delta\mathcal{A}^{CP}$ measurements

Tables 7.15, 7.16 and 7.17 display the results for the inclusive, the LBM and with the resonances selection measurements, respectively.

Table 6.22: $\Delta\mathcal{A}^{CP}$ measurements in percent, for the full phase space measurements. 2011 (2012) measurements are reported in first (second) row. The combined results is reported in the last column.

Decay mode	$\Delta\mathcal{A}^{CP}$ (%)	
$\Lambda_b^0 \to p\pi^-\pi^+\pi^-$	XXX $\pm$ 4.45 $\pm$ 0.87 XXX $\pm$ 2.90 $\pm$ 0.53	XXX $\pm$ 2.43 $\pm$ 0.47
$\Lambda_b^0 \to pK^-\pi^+\pi^-$	XXX $\pm$ 1.93 $\pm$ 0.88 XXX $\pm$ 1.26 $\pm$ 0.55	XXX $\pm$ 1.05 $\pm$ 0.49
$\Lambda_b^0 \to pK^-K^+\pi^-$	XXX $\pm$ 8.80 $\pm$ 0.85 XXX $\pm$ 5.76 $\pm$ 0.51	XXX $\pm$ 4.82 $\pm$ 0.46
$\Lambda_b^0 \to pK^-K^+K^-$	XXX $\pm$ 3.02 $\pm$ 0.88 XXX $\pm$ 2.09 $\pm$ 0.55	XXX $\pm$ 1.72 $\pm$ 0.49
$\Xi_b^0 \to pK^-\pi^+\pi^-$	XXX $\pm$ 19.58 $\pm$ 0.88 XXX $\pm$ 12.34 $\pm$ 0.55	XXX $\pm$ 10.39 $\pm$ 0.50
$\Xi_b^0 \to pK^-\pi^+K^-$	XXX $\pm$ 13.52 $\pm$ 0.88 XXX $\pm$ 9.87 $\pm$ 0.54	XXX $\pm$ 7.98 $\pm$ 0.49

Table 6.23: $\Delta\mathcal{A}^{CP}$ measurements in percent, for the LBM measurements. 2011 (2012) measurements are reported in first (second) row. The combined results is reported in the last column.

Decay mode	$\Delta\mathcal{A}^{CP}$ (%)	
$\Lambda_b^0 \to p\pi^-\pi^+\pi^-$	XXX ± 7.39 ± 0.74	XXX ± 4.08 ± 0.40
	XXX ± 4.89 ± 0.45	
$\Lambda_b^0 \to pK^-\pi^+\pi^-$	XXX ± 2.57 ± 0.73	XXX ± 1.42 ± 0.42
	XXX ± 1.70 ± 0.46	
$\Lambda_b^0 \to pK^-K^+K^-$	XXX ± 3.90 ± 0.79	XXX ± 2.23 ± 0.44
	XXX ± 2.71 ± 0.49	

Table 6.24: $\Delta\mathcal{A}^{CP}$ measurements in percent, for the phase space measurements. 2011 (2012) measurements are reported in first (second) row. The combined results is reported in the last column.

Decay mode	$\Delta\mathcal{A}^{CP}$ (%)	
$\Lambda_b^0 \to pa_1$	XXX ± 7.83 ± 1.01	XXX ± 4.20 ± 0.53
	XXX ± 4.97 ± 0.60	
$\Lambda_b^0 \to N^*(1520)^0\rho^0(f^0)$	XXX ± 8.82 ± 0.49	XXX ± 4.86 ± 0.27
	XXX ± 5.77 ± 0.30	
$\Lambda_b^0 \to \Delta^{++}\pi^-\pi^-$	XXX ± 5.78 ± 0.99	XXX ± 3.15 ± 0.51
	XXX ± 3.76 ± 0.59	
$\Lambda_b^0 \to pK_1$	—	XXX ± 3.43 ± 0.63
$\Lambda_b^0 \to \Lambda^*(1520)^0\rho^0(f^0)$	—	XXX ± 5.95 ± 0.40
$\Lambda_b^0 \to N^*(1520)^0K^{*0}$	XXX ± 4.35 ± 0.67	XXX ± 2.47 ± 0.38
	XXX ± 3.00 ± 0.43	
$\Lambda_b^0 \to \Delta^{++}K^-\pi^-$	XXX ± 4.55 ± 1.01	XXX ± 2.53 ± 0.56
	XXX ± 3.04 ± 0.63	
$\Lambda_b^0 \to \Lambda^*(1520)^0\phi^0$	—	XXX ± 5.51 ± 0.33
$\Lambda_b^0 \to pK^-_{\text{highmass}}\phi^0$	—	XXX ± 3.28 ± 0.61

6.4.2 About the determination of the significance of CP violation after unblinding

The $\Delta\mathcal{A}^{CP}$ observables are derived quantities from the particle and antiparticle yields which are the actual floating parameters of the fit. Given the complexity of the fit, building a relevant likelihood scan would require impractically large statistics of pseudoexperiments. Instead, fits to data are performed by implementing $\Delta\mathcal{A}^{CP}$ variables as floating parameters of the fits. The determination of the significance can only be conducted after the unblinding of the results.

Chapter 7

Unblinded $\Delta\mathcal{A}^{CP}$ measurements

The blinded simultaneous fits and the estimation of systematic uncertainties have been presented in the previous Chapter. It has been chosen to keep this chapter in the thesis manuscript to display both the logic and the chronology of the measurements. After the scrutiny of a review committee, results have been unblinded within the LHCb collaboration. Henceforth, this chapter presents in a first section the corrections that are applied to the raw asymmetries together with the sanity cross-checks. Secondly, fit results are discussed, and eventually, ΔA_{CP} measurements are presented.

Chapter contents

7.1 Corrections of raw asymmetries after unblinding.

Sources of systematic uncertainties have been identified prior to the unblinding and have been discussed in Section 6.3. Corrections of raw asymmetries have been unblinded with the fit results, and are presented in this Section. Eventually, crosschecks that have been done after unblinding are also presented.

7.1.1 L0Hadron trigger efficiencies

As a reminder, the procedure used in the estimation of the L0 trigger efficiencies is rewritten here: it makes use of simulated signal and control channel samples (to provide kinematical distributions) re-weighted to match the L0 efficiency as measured in the data. The L0 efficiencies (split by charge) are hence determined for protons, pions and kaons and are

used in the $\Delta\mathcal{A}^{CP}$ derivation in order to correct the signal yield measured in the fit to the TOS data sample. The correction on the $\Delta\mathcal{A}^{CP}$ measurements (referred to by δ^{L0} defined in Eq. 7.2 in the following) is estimated by measuring the difference between the $\Delta\mathcal{A}^{CP}$ fit measurement (not corrected) and $\Delta\mathcal{A}^{CP}{}_{\rm L0}$. The asymmetry corrected for the L0Hadron trigger asymmetry as defined in Eq. 7.1, where α is the ratio of L0HadronTOS efficiencies, reads

$$\mathcal{A}^{CP}{}_{\rm L0} = \frac{\mathcal{N}(X_b^0) - \alpha\cdot\overline{\mathcal{N}}(\overline{X}_b^0)}{\mathcal{N}(X_b^0) + \alpha\cdot\overline{\mathcal{N}}(\overline{X}_b^0)} \tag{7.1}$$

$$\delta^{\rm L0} = \Delta\mathcal{A}^{CP} - \left(\mathcal{A}^{CP}{}_{\rm L0,sig} - \mathcal{A}^{CP}{}_{\rm L0,cc}\right) \tag{7.2}$$

For the inclusive measurements (using the full phase space of data), there are three sources of systematic uncertainties that have been discussed and estimated in Section 6.3.1.1. Corrections related to the L0Hadron trigger efficiencies are gathered in Tables 7.1 and 7.2 for the inclusive measurements and for the (LBM measurements + quasi 2-body decays measurements), respectively. The corrections are determined to be of the per mil level, commensurate with its uncertainty.

Table 7.1: L0Hadron correction δ^{L0} in percent, per decay and per year of data taking, for full phase space measurements. The central value is the correction and the uncertainties are the systematic uncertainties on the $\Delta\mathcal{A}^{CP}$ measurements coming from the tables used for the efficiency determination and from the variation over the phase space, respectively. The uncertainties are rounded to the significance of the sub-dominant contribution in order that the reader gets the quantitative hierarchy of the uncertainties.

Decay mode	δ^{L0} (%)	
	2011	2012
$\Lambda_b^0 \to p\pi^-\pi^+\pi^-$	-0.12 ± 0.12 ± 0.03	-0.03 ± 0.08 ± 0.02
$\Lambda_b^0 \to pK^-\pi^+\pi^-$	-0.10 ± 0.10 ± 0.02	-0.05 ± 0.07 ± 0.03
$\Lambda_b^0 \to pK^-K^+\pi^-$	-0.17 ± 0.11 ± 0.03	-0.02 ± 0.06 ± 0.02
$\Lambda_b^0 \to pK^-K^+K^-$	-0.09 ± 0.10 ± 0.06	-0.07 ± 0.07 ± 0.06
$\Xi_b^0 \to pK^-\pi^+\pi^-$	-0.02 ± 0.09 ± 0.03	0.01 ± 0.06 ± 0.02
$\Xi_b^0 \to pK^-\pi^+K^-$	-0.08 ± 0.10 ± 0.03	0.03 ± 0.06 ± 0.02

7.1.2 The proton and kaon detection asymmetry

As for the L0 trigger efficiency case, simulated signal and control channel samples are used to provide a kinematical distributions and the kaon detection correction is defined as Eq. 7.3.

$$\Delta A_K(\%) = A_K^{\rm sig.} - A_K^{\rm cc}. \tag{7.3}$$

The uncertainties of the tables and the MC statistics used for the re-weighting are propagated as systematic uncertainties, as discussed in Section 6.3.1.2. The very same procedure is used in order to correct $\Delta\mathcal{A}^{CP}$ for proton detection asymmetries. The difference of proton detection asymmetries ΔA_p is determined with the Eq. 6.4 and the uncertainties of the tables and the MC statistics used for the re-weighting are propagated as systematic uncertainties. Relevant numbers for the corrections are gathered in Tables 7.5 and 7.6 for the inclusive and for the (LBM measurements + quasi 2-body decays measurements), respectively.

Table 7.2: L0Hadron correction δ^{L0} in percent, per decay and per year of data taking, for LBM measurements and for $\Delta\mathcal{A}^{CP}$ measurements of specific decays. The central value is the correction and the uncertainties are the systematic uncertainties on the $\Delta\mathcal{A}^{CP}$ measurements coming from the tables used for the efficiency determination and from MC statistic, respectively. The uncertainties are rounded to the significance of the sub-dominant contribution in order that the reader gets the quantitative hierarchy of the uncertainties.

Decay mode	δ^{L0} (%)	
	2011	2012
$\Lambda_b^0 \to p\pi^-\pi^+\pi^-$	-0.082 ± 0.100 ± 0.001	-0.043 ± 0.074 ± 0.001
$\Lambda_b^0 \to pK^-\pi^+\pi^-$	-0.094 ± 0.090 ± 0.002	-0.065 ± 0.062 ± 0.001
$\Lambda_b^0 \to pK^-K^+K^-$	-0.098 ± 0.090 ± 0.002	-0.093 ± 0.063 ± 0.001
$\Lambda_b^0 \to pa_1$	-0.465 ± 0.177 ± 0.050	-0.030 ± 0.105 ± 0.002
$\Lambda_b^0 \to N^*(1520)^0\rho^0(f^0)$	-0.061 ± 0.078 ± 0.001	-0.042 ± 0.061 ± 0.001
$\Lambda_b^0 \to \Delta^{++}\pi^-\pi^-$	0.003 ± 0.091 ± 0.000	-0.008 ± 0.065 ± 0.000
$\Lambda_b^0 \to pK_1$	-0.315 ± 0.103 ± 0.027	
$\Lambda_b^0 \to \Lambda^*(1520)^0\rho^0(f^0)$	-0.117 ± 0.037 ± 0.002	
$\Lambda_b^0 \to N^*(1520)^0K^{*0}$	-0.094 ± 0.063 ± -0.003	0.051 ± 0.044 ± 0.001
$\Lambda_b^0 \to \Delta^{++}K^-\pi^-$	-0.063 ± 0.089 ± -0.004	-0.005 ± 0.060 ± 0.000
$\Lambda_b^0 \to \Lambda^*(1520)^0\phi^0$	-0.100 ± 0.045 ± 0.001	
$\Lambda_b^0 \to pK^-_{\text{highmass}}\phi^0$	-0.098 ± 0.090 ± 0.002	

Table 7.3: Kaon detection correction, per decay and per year of data taking, for full phase space measurements. The central value is the correction and the uncertainties are the systematic uncertainties on the $\Delta\mathcal{A}^{CP}$ measurements.

Decay mode	ΔA_K (%)	
	2011	2012
$\Lambda_b^0 \to p\pi^-\pi^+\pi^-$	—	—
$\Lambda_b^0 \to pK^-\pi^+\pi^-$	-0.01 ± 0.17	-0.03 ± 0.18
$\Lambda_b^0 \to pK^-K^+\pi^-$	—	—
$\Lambda_b^0 \to pK^-K^+K^-$	-0.03 ± 0.16	-0.03 ± 0.16
$\Xi_b^0 \to pK^-\pi^+\pi^-$	-0.02 ± 0.18	-0.03± 0.18
$\Xi_b^0 \to pK^-\pi^+K^-$	-0.03 ± 0.16	-0.04± 0.16

Table 7.4: Kaon detection correction, per decay and per year of data taking, for LBM measurements and for $\Delta\mathcal{A}^{CP}$ measurements of specific decays. The central value is the correction and the uncertainties are the systematic uncertainties on the $\Delta\mathcal{A}^{CP}$ measurements coming from the tables used for the efficiency determination and from MC statistic, respectively. The uncertainties are rounded to the significance of the sub-dominant contribution in order that the reader gets the quantitative hierarchy of the uncertainties.

Decay mode	ΔA_K (%)	
	2011	2012
$\Lambda_b^0 \to p\pi^-\pi^+\pi^-$	—	—
$\Lambda_b^0 \to pK^-\pi^+\pi^-$	0.0011 ± 0.1711 ± 0.0001	-0.0236 ± 0.1716 ± 0.0010
$\Lambda_b^0 \to pK^-K^+K^-$	-0.0223 ± 0.1623 ± 0.0011	-0.0312± 0.1626 ± 0.0012
$\Lambda_b^0 \to pK_1$	-0.0183 ± 0.1615 ± 0.0053	
$\Lambda_b^0 \to \Lambda^*(1520)^0\rho^0(f^0)$	0.0047 ± 0.1228 ± 0.0003	
$\Lambda_b^0 \to N^*(1520)^0K^{*0}$	-0.0349 ± 0.1535 ± 0.0035	-0.0643 ± 0.1560 ± 0.0051
$\Lambda_b^0 \to \Delta^{++}K^-\pi^-$	-0.0332 ± 0.2153 ± 0.0078	-0.0680 ± 0.2210 ± 0.0122
$\Lambda_b^0 \to \Lambda^*(1520)^0\phi^0$	-0.0320 ± 0.1074 ± 0.0013	
$\Lambda_b^0 \to pK^-_{\text{highmass}}\phi^0$	-0.0313 ± 0.1512 ± 0.0053	

Table 7.5: Proton detection correction, per decay and per year of data taking, for full phase space measurements. The central value is the correction and the uncertainties are the systematic uncertainties on the $\Delta\mathcal{A}^{CP}$ measurements.

Decay mode	ΔA_p (%)	
	2011	2012
$\Lambda_b^0 \to p\pi^-\pi^+\pi^-$	-0.162 ± 0.201	-0.185 ± 0.201
$\Lambda_b^0 \to pK^-\pi^+\pi^-$	-0.111 ± 0.203	-0.150 ± 0.203
$\Lambda_b^0 \to pK^-K^+\pi^-$	-0.009 ± 0.206	-0.037 ± 0.207
$\Lambda_b^0 \to pK^-K^+K^-$	-0.132 ± 0.202	-0.161 ± 0.202
$\Xi_b^0 \to pK^-\pi^+\pi^-$	-0.126 ± 0.202	-0.171 ± 0.202
$\Xi_b^0 \to pK^-\pi^+K^-$	-0.148 ± 0.201	-0.180 ± 0.201

Table 7.6: Proton detection correction, per decay and per year of data taking, for LBM measurements and for $\Delta\mathcal{A}^{CP}$ measurements of specific decays. The central value is the correction and the uncertainties are the systematic uncertainties on the $\Delta\mathcal{A}^{CP}$ measurements coming from the tables used for the efficiency determination and from MC statistic, respectively. The uncertainties are rounded to the significance of the sub-dominant contribution in order that the reader gets the quantitative hierarchy of the uncertainties.

Decay mode	ΔA_p (%)	
	2011	2012
$\Lambda_b^0 \to p\pi^-\pi^+\pi^-$	-0.137 ± 0.164 ±0.008	-0.158 ± 0.164 ±0.007
$\Lambda_b^0 \to pK^-\pi^+\pi^-$	-0.064 ± 0.167 ±0.004	-0.113 ± 0.166 ±0.005
$\Lambda_b^0 \to pK^-K^+K^-$	-0.124 ± 0.167 ±0.006	-0.152 ± 0.167 ±0.006
$\Lambda_b^0 \to pa_1$	0.054 ± 0.205 ± 0.019	-0.050 ± 0.203 ± 0.014
$\Lambda_b^0 \to N^*(1520)^0\rho^0(f^0)$	-0.120 ± 0.121 ± 0.010	-0.145 ± 0.121 ± 0.009
$\Lambda_b^0 \to \Delta^{++}\pi^-\pi^-$	-0.477 ± 0.180 ± 0.115	-0.502 ± 0.181 ± 0.100
$\Lambda_b^0 \to pK_1$	-0.211 ± 0.139 ± 0.046	
$\Lambda_b^0 \to \Lambda^*(1520)^0\rho^0(f^0)$	0.012 ± 0.117 ± 0.025	
$\Lambda_b^0 \to N^*(1520)^0K^{*0}$	-0.243 ± 0.136 ± 0.025	-0.315 ± 0.135 ± 0.025
$\Lambda_b^0 \to \Delta^{++}K^-\pi^-$	-0.296 ± 0.186 ± 0.070	-0.397 ± 0.184 ± 0.072
$\Lambda_b^0 \to \Lambda^*(1520)^0\phi^0$	-0.155 ± 0.100 ± 0.005	
$\Lambda_b^0 \to pK^-_{\text{highmass}}\phi^0$	-0.141 ± 0.139 ± 0.026	

7.1.3 The PID asymmetry

Here again, charge-dependent PID efficiencies determination makes use of simulated data, that provide kinematical distributions. The PID asymmetries are computed for the signal and the control channel and the correction on the $\Delta\mathcal{A}^{CP}$ variables is similarly determined from the Eq. 7.4.

$$\Delta A_{\text{PID}}(\%) = A_{\text{PID}}^{\text{sig.}} - A_{\text{PID}}^{\text{cc}}. \tag{7.4}$$

The uncertainties coming from the calibration samples are propagated as a systematic uncertainty on the final measurement, following the procedure presented in Section 6.3.1.3. Relevant numbers for the corrections are gathered in Tables 7.7 and 7.8 for the inclusive measurements and for the (LBM measurements + quasi 2-body decays measurements), respectively.

Table 7.7: PID correction, per decay and per year of data taking, for full phase space measurements. The central value is the correction and the uncertainties are the systematic uncertainties on the $\Delta\mathcal{A}^{CP}$ measurements.

Decay mode	ΔA_{PID} (%)	
	2011	2012
$\Lambda_b^0 \to p\pi^-\pi^+\pi^-$	0.053 ± 0.839	0.042 ± 0.479
$\Lambda_b^0 \to pK^-\pi^+\pi^-$	0.077 ± 0.829	0.035 ± 0.477
$\Lambda_b^0 \to pK^-K^+\pi^-$	0.051 ± 0.816	0.030 ± 0.467
$\Lambda_b^0 \to pK^-K^+K^-$	0.072 ± 0.833	0.050 ± 0.478
$\Xi_b^0 \to pK^-\pi^+\pi^-$	0.081 ± 0.836	0.048 ± 0.479
$\Xi_b^0 \to pK^-\pi^+K^-$	0.071 ± 0.833	0.035 ± 0.476

Table 7.8: PID correction, per decay and per year of data taking, for LBM measurements and for $\Delta\mathcal{A}^{CP}$ measurements of specific decays. The central value is the correction and the uncertainties are the systematic uncertainties on the $\Delta\mathcal{A}^{CP}$ measurements coming from the tables used for the efficiency determination and from MC statistic, respectively. The uncertainties are rounded to the significance of the sub-dominant contribution in order that the reader gets the quantitative hierarchy of the uncertainties.

Decay mode	ΔA_{PID} (%)	
	2011	2012
$\Lambda_b^0 \to p\pi^-\pi^+\pi^-$	$0.070 \pm 0.717 \pm 0.004$	$0.054 \pm 0.410 \pm 0.003$
$\Lambda_b^0 \to pK^-\pi^+\pi^-$	$0.091 \pm 0.680 \pm 0.005$	$0.049 \pm 0.390 \pm 0.002$
$\Lambda_b^0 \to pK^-K^+K^-$	$0.092 \pm 0.748 \pm 0.005$	$0.063 \pm 0.429 \pm 0.003$
$\Lambda_b^0 \to pa_1$	$0.176 \pm 0.966 \pm 0.060$	$0.219 \pm 0.555 \pm 0.061$
$\Lambda_b^0 \to N^*(1520)^0\rho^0(f^0)$	$0.069 \pm 0.467 \pm 0.006$	$0.066 \pm 0.267 \pm 0.005$
$\Lambda_b^0 \to \Delta^{++}\pi^-\pi^-$	$0.112 \pm 0.957 \pm 0.027$	$0.016 \pm 0.546 \pm 0.004$
$\Lambda_b^0 \to pK_1$	$0.246 \pm 0.582 \pm 0.071$	
$\Lambda_b^0 \to \Lambda^*(1520)^0\rho^0(f^0)$	$0.082 \pm 0.365 \pm 0.006$	
$\Lambda_b^0 \to N^*(1520)^0K^{*0}$	$0.089 \pm 0.638 \pm 0.010$	$0.063 \pm 0.369 \pm 0.005$
$\Lambda_b^0 \to \Delta^{++}K^-\pi^-$	$0.131 \pm 0.964 \pm 0.031$	$0.029 \pm 0.551 \pm 0.006$
$\Lambda_b^0 \to \Lambda^*(1520)^0\phi^0$	$0.088 \pm 0.297 \pm 0.004$	
$\Lambda_b^0 \to pK^-_{\text{highmass}}\phi^0$	$0.067 \pm 0.576 \pm 0.011$	

7.1.4 Cross-checks after unblinding

We defined a priori cross-checks to qualify whether systematic effects are under control. Those cross-checks are

- the comparison of the results for the independent samples of the two magnet polarities is performed. Consistency of the $\Delta\mathcal{A}^{CP}$ determinations (Magnet Up and Magnet Down) of each mode for each year is quantified as the ratio of the signed difference of the central values divided by the quadratic sum of the related statistical uncertainties.

- the comparison of the results obtained for the two categories of L0 trigger requirements: Trigger Independent of Signal (TIS) candidates and Trigger On Signal (TOS) candidates are also determined. Consistency of the two $\Delta\mathcal{A}^{CP}$ determinations (TOS and TIS) of each mode for each year is also quantified as the ratio of the signed difference of the central values over the quadratic sum of the related statistical uncertainties.

- the comparison of the results for the 2011 and 2012 samples is also performed.

We set a priori the consistency threshold at 2 sigma to investigate further the systematic uncertainties budget. All consistency checks are reported in Table 7.9 and one can notice that all measurements are found to be consistent.

7.2 Fit results

This Section is dedicated to the unblinded fit results. Raw fit results are hence provided here and the actual $\Delta\mathcal{A}^{CP}$ final measurements (for which the corrections coming from experimental effects that have been discussed in the previous Section are applied) are discussed in the next Section.

7.2.1 Inclusive results

The figures 7.1 and 7.2 display the unblinded fit results for the inclusive ΔA_{CP} measurements in linear scale in order to provide a direct visualisation of the (a)symmetry between the particle and the antiparticle spectra. For sake of readability, the plots are the sum of the fits to the 2011 and 2012 and trigger-separated samples. Few comments are in order:

- As emphasised in the previous Chapter, the fit model describes in a satisfactory way all the reconstructed spectra of interest.

- In the plots displayed in this Section, the $\Lambda_b^0 \to pK^-\pi^+\pi^-\pi^0$ contribution of the $pKK\pi$ and $pK\pi K$ spectra is modelled by a generic function in order to have a smoother fit function (instead of an histogram). This is the only contribution that comes directly from the data. One can see that the region before the signal is however not totally mastered in the $pKK\pi$ spectrum: the function used for the $\Lambda_b^0 \to pK^-\pi^+\pi^-\pi^0$ modelling is an histogram of the data that contains statistical fluctuations and the slight differences are hence covered within these statistical fluctuations.

- One can notice some tensions in the residuals, specially in the $pKK\pi$ spectrum (above 5700 MeV/c^2). There is no data calibration sample to determine the simultaneous misidentification of two pions in a same event. However, it has been chosen to constrain the yield of the $\Lambda_b^0 \to p\pi^-\pi^+\pi^-$ cross-feed contribution to the PID re-weighting

Table 7.9: Consistencies between the two trigger configurations (TIS-TOS), the two magnet polarities (Up-Down) and the two year of data sets (2011-2012). All measurements are found to be consistent within the 2σ threshold.

Decay mode	$\Delta A_{CP}^{\text{TIS}}$ vs $\Delta A_{CP}^{\text{TOS}}$		$\Delta A_{CP}^{\text{Down}}$ vs $\Delta A_{CP}^{\text{Up}}$		2011 vs 2012
	2011	2012	2011	2012	
Inclusive					
$\Lambda_b \to p\pi\pi\pi$	1.3	−0.5	0.5	−0.5	0.9
$\Lambda_b \to pK\pi\pi$	0.8	−0.8	0.9	0.8	−1.4
$\Lambda_b \to pKK\pi$	1.0	0.4	−0.8	0.5	0.7
$\Lambda_b \to pKKK$	−0.2	0.1	1.0	1.3	0.4
$\Xi_b \to pK\pi\pi$	−1.6	1.3	−1.5	−0.5	−0.8
$\Xi_b \to pK\pi K$	−1.4	0.8	0.1	−0.9	−0.6
LBM					
$\Lambda_b \to p\pi\pi\pi$	−0.9	−0.1	0.8	0.9	1.4
$\Lambda_b \to pK\pi\pi$	0.9	0.2	0.1	0.3	−0.9
$\Lambda_b \to pKKK$	−1.3	−0.4	0.1	1.1	−0.4
quasi 2-body					
$\Lambda_b \to pa_1$	−0.4	−0.2			−0.1
$\Lambda_b \to \Delta^{++}\pi^-\pi^-$	0.4	−0.3	−1.0	−1.2	−0.2
$\Lambda_b \to N^*\rho^0(f^0)$	−0.7	0.1	−0.4	0.6	1.9
$\Lambda_b \to \Delta^{++}K^-\pi^-$	1.0	−1.8	1.0	0.6	−0.1
$\Lambda_b \to N^*K^*$	0.2	−0.4	0.1	−0.5	0.6
$\Lambda_b \to \Lambda^*\rho^0(f^0)$		0.1		−0.2	—
$\Lambda_b \to pK_1$		0.6		0.3	—
$\Lambda_b \to \Lambda^*\phi^0$		−0.2		−1.1	—
$\Lambda_b \to pK^-_{\text{high mass}}\phi^0$		−0.4		0.9	—

estimation and its value is likely underestimated. It has been checked that letting free this contribution has a marginal impact on the signal yield determination and provide a satisfactory agreement between the data and the model in this region.

- Eventually, the tension at 5700 MeV/c^2 in the $pKKK$ particle spectra is likely a statistical fluctuation, since no equivalent observation can be made from the antiparticle spectrum.

Table 7.10 gathers the raw asymmetries measured from the inclusive fit presented in this Section: the uncertainties reported are only statistical and the corrections discussed in the previous Section are not implemented here. Provided that the corrections are lower than the percent level, one can already infer that $\Delta\mathcal{A}^{CP}$ are compatible with zero asymmetry, within 3σ.

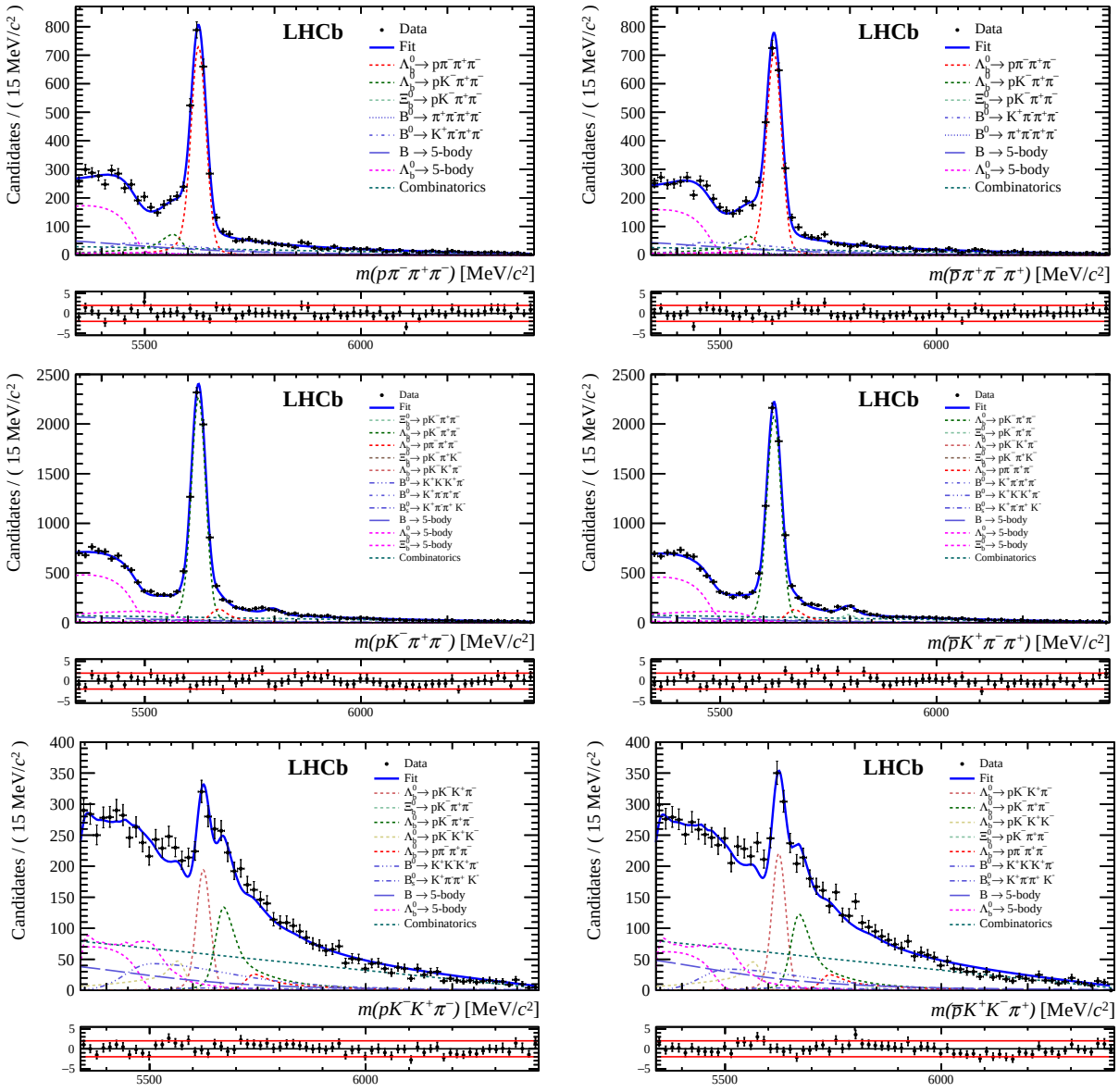

Figure 7.1: Unblinded superimposed fit results for the [from top to bottom] $X_b^0 \to p\pi\pi\pi$, $X_b^0 \to pK\pi\pi$ and $X_b^0 \to pKK\pi$ spectra using the full phase space data. Plots in the left-column are for the spectra with X_b^0 and on the right-column for the spectra with $\overline{X}_b^0$.

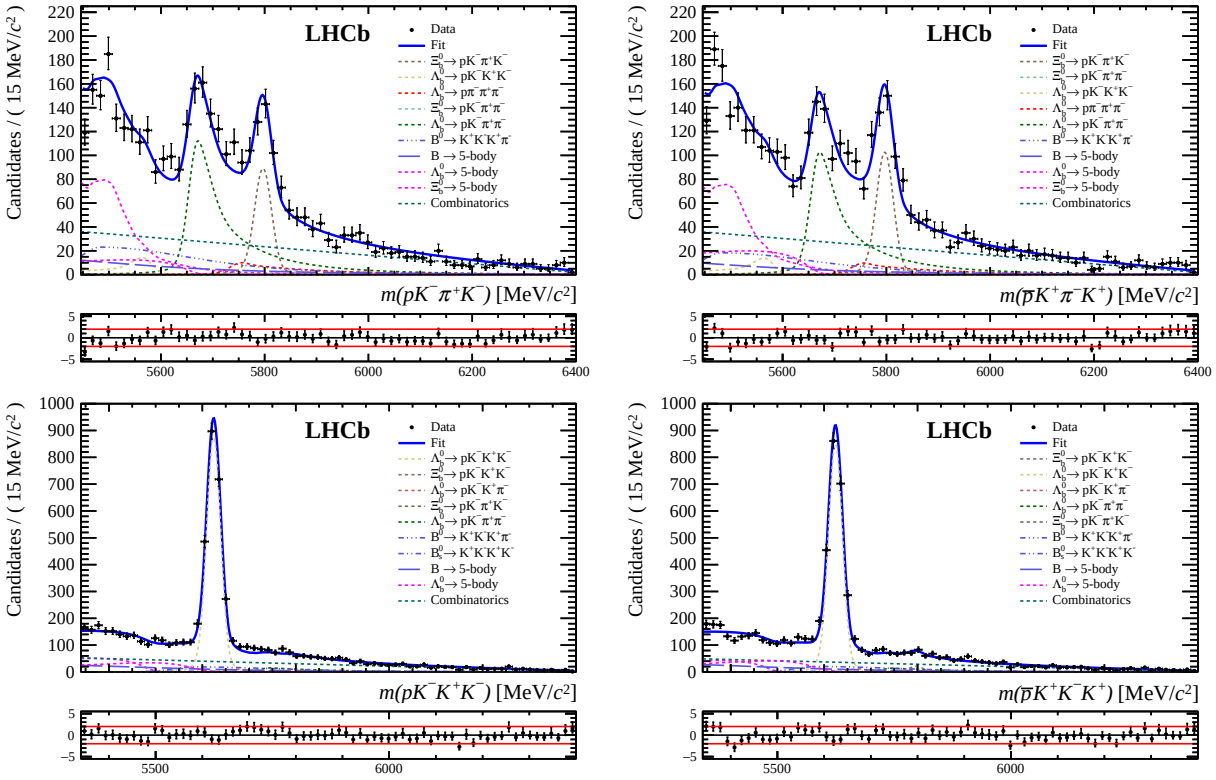

Figure 7.2: Unblinded superimposed fit results for the [top] $X_b^0 \to pK\pi K$ and [bottom] $X_b^0 \to pKKK$ spectra using the full phase space data of 2011 and 2012. Plots in the left-column are for the spectra with X_b^0 and on the right-column for the spectra with $\overline{X}{}_b^0$.

Table 7.10: The *CP* asymmetry observables obtained from the results of the fit to the full phase space data, in percent. The uncertainty reported is related to statistics. The numbers and uncertainties are provided with equal number of digits.

CP asymmetry observable	Value (in %)
2011 spectra:	
$\Delta\mathcal{A}^{CP} = \mathcal{A}^{\text{raw}}$ ($\Lambda_b^0 \to p\pi\pi\pi$) - $\mathcal{A}^{\text{raw}}$ ($\Lambda_b^0 \to (\Lambda_c^+ \to p\pi\pi)\pi$)	4.15 ± 4.45
$\Delta\mathcal{A}^{CP} = \mathcal{A}^{\text{raw}}$ ($\Lambda_b^0 \to pK\pi\pi$) - $\mathcal{A}^{\text{raw}}$ ($\Lambda_b^0 \to (\Lambda_c^+ \to pK\pi)\pi$)	0.88 ± 1.93
$\Delta\mathcal{A}^{CP} = \mathcal{A}^{\text{raw}}$ ($\Lambda_b^0 \to pKK\pi$) - $\mathcal{A}^{\text{raw}}$ ($\Lambda_b^0 \to (\Lambda_c^+ \to p\pi\pi)\pi$)	-2.08 ± 8.80
$\Delta\mathcal{A}^{CP} = \mathcal{A}^{\text{raw}}$ ($\Lambda_b^0 \to pKKK$) - $\mathcal{A}^{\text{raw}}$ ($\Lambda_b^0 \to (\Lambda_c^+ \to pK\pi)\pi$)	0.99 ± 3.02
$\Delta\mathcal{A}^{CP} = \mathcal{A}^{\text{raw}}$ ($\Xi_b^0 \to pK\pi\pi$) - $\mathcal{A}^{\text{raw}}$ ($\Lambda_b^0 \to (\Lambda_c^+ \to pK\pi)\pi$)	-32.32 ± 17.73
$\Delta\mathcal{A}^{CP} = \mathcal{A}^{\text{raw}}$ ($\Xi_b^0 \to pK\pi K$) - $\mathcal{A}^{\text{raw}}$ ($\Lambda_b^0 \to (\Lambda_c^+ \to pK\pi)\pi$)	-14.70 ± 10.68
$\Delta\mathcal{A}^{CP} = \mathcal{A}^{\text{raw}}$ ($\Xi_b^0 \to pK\pi\pi$) - $\mathcal{A}^{\text{raw}}$ ($\Xi_b^0 \to (\Xi_c^+ \to pK\pi)\pi$)	-29.03 ± 19.58
$\Delta\mathcal{A}^{CP} = \mathcal{A}^{\text{raw}}$ ($\Xi_b^0 \to pK\pi K$) - $\mathcal{A}^{\text{raw}}$ ($\Xi_b^0 \to (\Xi_c^+ \to pK\pi)\pi$)	-11.42 ± 13.52
2012 spectra:	
$\Delta\mathcal{A}^{CP} = \mathcal{A}^{\text{raw}}$ ($\Lambda_b^0 \to p\pi\pi\pi$) - $\mathcal{A}^{\text{raw}}$ ($\Lambda_b^0 \to (\Lambda_c^+ \to p\pi\pi)\pi$)	-0.50 ± 2.90
$\Delta\mathcal{A}^{CP} = \mathcal{A}^{\text{raw}}$ ($\Lambda_b^0 \to pK\pi\pi$) - $\mathcal{A}^{\text{raw}}$ ($\Lambda_b^0 \to (\Lambda_c^+ \to pK\pi)\pi$)	4.02 ± 1.26
$\Delta\mathcal{A}^{CP} = \mathcal{A}^{\text{raw}}$ ($\Lambda_b^0 \to pKK\pi$) - $\mathcal{A}^{\text{raw}}$ ($\Lambda_b^0 \to (\Lambda_c^+ \to p\pi\pi)\pi$)	-9.00 ± 5.76
$\Delta\mathcal{A}^{CP} = \mathcal{A}^{\text{raw}}$ ($\Lambda_b^0 \to pKKK$) - $\mathcal{A}^{\text{raw}}$ ($\Lambda_b^0 \to (\Lambda_c^+ \to pK\pi)\pi$)	-0.33 ± 2.09
$\Delta\mathcal{A}^{CP} = \mathcal{A}^{\text{raw}}$ ($\Xi_b^0 \to pK\pi\pi$) - $\mathcal{A}^{\text{raw}}$ ($\Lambda_b^0 \to (\Lambda_c^+ \to pK\pi)\pi$)	-12.95 ± 10.83
$\Delta\mathcal{A}^{CP} = \mathcal{A}^{\text{raw}}$ ($\Xi_b^0 \to pK\pi K$) - $\mathcal{A}^{\text{raw}}$ ($\Lambda_b^0 \to (\Lambda_c^+ \to pK\pi)\pi$)	-5.40 ± 7.90
$\Delta\mathcal{A}^{CP} = \mathcal{A}^{\text{raw}}$ ($\Xi_b^0 \to pK\pi\pi$) - $\mathcal{A}^{\text{raw}}$ ($\Xi_b^0 \to (\Xi_c^+ \to pK\pi)\pi$)	-12.05 ± 12.34
$\Delta\mathcal{A}^{CP} = \mathcal{A}^{\text{raw}}$ ($\Xi_b^0 \to pK\pi K$) - $\mathcal{A}^{\text{raw}}$ ($\Xi_b^0 \to (\Xi_c^+ \to pK\pi)\pi$)	-4.50 ± 9.87
2011+2012 spectra:	
$\Delta\mathcal{A}^{CP} = \mathcal{A}^{\text{raw}}$ ($\Lambda_b^0 \to p\pi\pi\pi$) - $\mathcal{A}^{\text{raw}}$ ($\Lambda_b^0 \to (\Lambda_c^+ \to p\pi\pi)\pi$)	0.88 ± 2.43
$\Delta\mathcal{A}^{CP} = \mathcal{A}^{\text{raw}}$ ($\Lambda_b^0 \to pK\pi\pi$) - $\mathcal{A}^{\text{raw}}$ ($\Lambda_b^0 \to (\Lambda_c^+ \to pK\pi)\pi$)	3.10 ± 1.05
$\Delta\mathcal{A}^{CP} = \mathcal{A}^{\text{raw}}$ ($\Lambda_b^0 \to pKK\pi$) - $\mathcal{A}^{\text{raw}}$ ($\Lambda_b^0 \to (\Lambda_c^+ \to p\pi\pi)\pi$)	-6.93 ± 4.82
$\Delta\mathcal{A}^{CP} = \mathcal{A}^{\text{raw}}$ ($\Lambda_b^0 \to pKKK$) - $\mathcal{A}^{\text{raw}}$ ($\Lambda_b^0 \to (\Lambda_c^+ \to pK\pi)\pi$)	0.09 ± 1.72
$\Delta\mathcal{A}^{CP} = \mathcal{A}^{\text{raw}}$ ($\Xi_b^0 \to pK\pi\pi$) - $\mathcal{A}^{\text{raw}}$ ($\Lambda_b^0 \to (\Lambda_c^+ \to pK\pi)\pi$)	-18.21 ± 9.21
$\Delta\mathcal{A}^{CP} = \mathcal{A}^{\text{raw}}$ ($\Xi_b^0 \to pK\pi K$) - $\mathcal{A}^{\text{raw}}$ ($\Lambda_b^0 \to (\Lambda_c^+ \to pK\pi)\pi$)	-8.69 ± 6.36
$\Delta\mathcal{A}^{CP} = \mathcal{A}^{\text{raw}}$ ($\Xi_b^0 \to pK\pi\pi$) - $\mathcal{A}^{\text{raw}}$ ($\Xi_b^0 \to (\Xi_c^+ \to pK\pi)\pi$)	-16.88 ± 10.39
$\Delta\mathcal{A}^{CP} = \mathcal{A}^{\text{raw}}$ ($\Xi_b^0 \to pK\pi K$) - $\mathcal{A}^{\text{raw}}$ ($\Xi_b^0 \to (\Xi_c^+ \to pK\pi)\pi$)	-6.90 ± 7.98

7.2.2 Low2x2BodyMass (LBM) results

The figure 7.3 displays the unblinded fit results for the LBM ΔA_{CP} measurements in linear scale in order to provide a direct visualisation of the (a)symmetry between the particle and the antiparticle spectra. For sake of readability, the plots are the sum of the fits to the 2011 and 2012 and trigger-separated samples. Here again, the fit model describes in a satisfactory way all the reconstructed spectra of interest and one can notice that signal regions are well described by the fit model. Table 7.11 gathers the raw asymmetries measured from the LBM fit presented in this Section: the uncertainties reported are only statistical and the corrections discussed in the previous Section are not implemented yet.

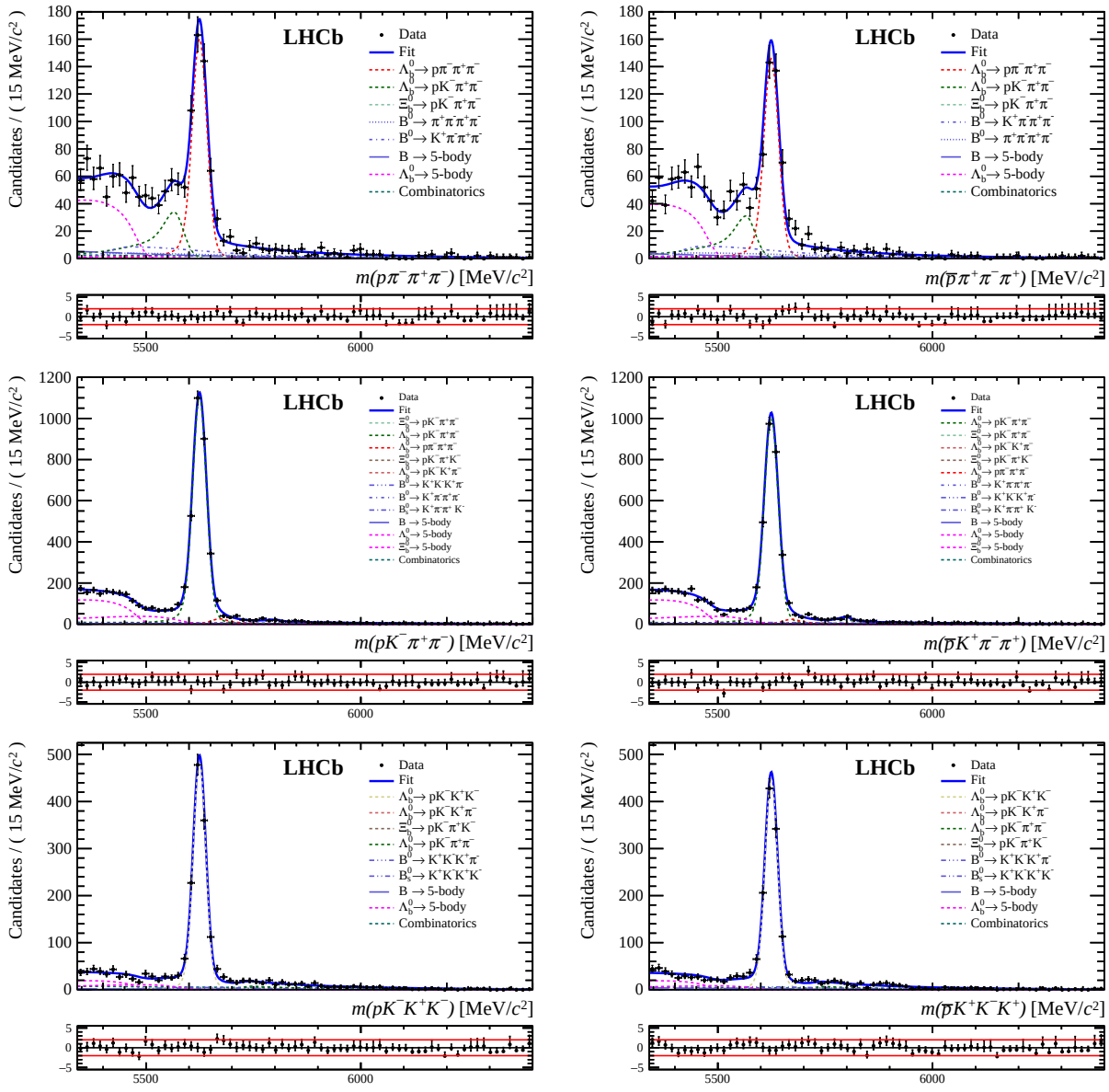

Figure 7.3: (From top to bottom) $p\pi\pi\pi$, $pK\pi\pi$, $pKKK$ invariant-mass spectra for (first column) X_b data 2011 and 2012 samples combined) and (second column) $\bar{X}_b$ data (2011 and 2012 samples combined) considering the LBM set of cuts.

Table 7.11: The *CP* asymmetry observables obtained from the results of the fit to the LBM data, in percent. The uncertainty reported is related to statistics. The numbers and uncertainties are provided with equal number of digits.

CP asymmetry observable	Value (in %)
2011 spectra:	
$\Delta\mathcal{A}^{CP} = \mathcal{A}^{\text{raw}}$ ($\Lambda_b^0 \to p\pi\pi\pi$) - $\mathcal{A}^{\text{raw}}$ ($\Lambda_b^0 \to (\Lambda_c^+ \to p\pi\pi)\pi$)	11.95 ± 7.39
$\Delta\mathcal{A}^{CP} = \mathcal{A}^{\text{raw}}$ ($\Lambda_b^0 \to pK\pi\pi$) - $\mathcal{A}^{\text{raw}}$ ($\Lambda_b^0 \to (\Lambda_c^+ \to pK\pi)\pi$)	1.44 ± 2.57
$\Delta\mathcal{A}^{CP} = \mathcal{A}^{\text{raw}}$ ($\Lambda_b^0 \to pKKK$) - $\mathcal{A}^{\text{raw}}$ ($\Lambda_b^0 \to (\Lambda_c^+ \to pK\pi)\pi$)	1.33 ± 3.90
2012 spectra:	
$\Delta\mathcal{A}^{CP} = \mathcal{A}^{\text{raw}}$ ($\Lambda_b^0 \to p\pi\pi\pi$) - $\mathcal{A}^{\text{raw}}$ ($\Lambda_b^0 \to (\Lambda_c^+ \to p\pi\pi)\pi$)	-0.09 ± 4.89
$\Delta\mathcal{A}^{CP} = \mathcal{A}^{\text{raw}}$ ($\Lambda_b^0 \to pK\pi\pi$) - $\mathcal{A}^{\text{raw}}$ ($\Lambda_b^0 \to (\Lambda_c^+ \to pK\pi)\pi$)	4.18 ± 1.70
$\Delta\mathcal{A}^{CP} = \mathcal{A}^{\text{raw}}$ ($\Lambda_b^0 \to pKKK$) - $\mathcal{A}^{\text{raw}}$ ($\Lambda_b^0 \to (\Lambda_c^+ \to pK\pi)\pi$)	3.16 ± 2.71
2011+2012 spectra:	
$\Delta\mathcal{A}^{CP} = \mathcal{A}^{\text{raw}}$ ($\Lambda_b^0 \to p\pi\pi\pi$) - $\mathcal{A}^{\text{raw}}$ ($\Lambda_b^0 \to (\Lambda_c^+ \to p\pi\pi)\pi$)	3.57 ± 4.08
$\Delta\mathcal{A}^{CP} = \mathcal{A}^{\text{raw}}$ ($\Lambda_b^0 \to pK\pi\pi$) - $\mathcal{A}^{\text{raw}}$ ($\Lambda_b^0 \to (\Lambda_c^+ \to pK\pi)\pi$)	3.35 ± 1.42
$\Delta\mathcal{A}^{CP} = \mathcal{A}^{\text{raw}}$ ($\Lambda_b^0 \to pKKK$) - $\mathcal{A}^{\text{raw}}$ ($\Lambda_b^0 \to (\Lambda_c^+ \to pK\pi)\pi$)	2.57 ± 2.23

7.2.3 Quasi-2 body results

The figures 7.4 to 7.6 display the unblinded fit results for the quasi 2-body decays ΔA_{CP} measurements of $p\pi\pi\pi$, $pK\pi\pi$ and $pKKK$ spectra. Here again, the fit model describes in a satisfactory way all the reconstructed spectra of interest and one can notice that signal regions is well described by the fit model. Table 7.12 to 7.14 gather the raw asymmetries measured from the LBM fit presented in this Section: the uncertainties reported are only statistical and the corrections discussed in the previous Section are not implemented yet.

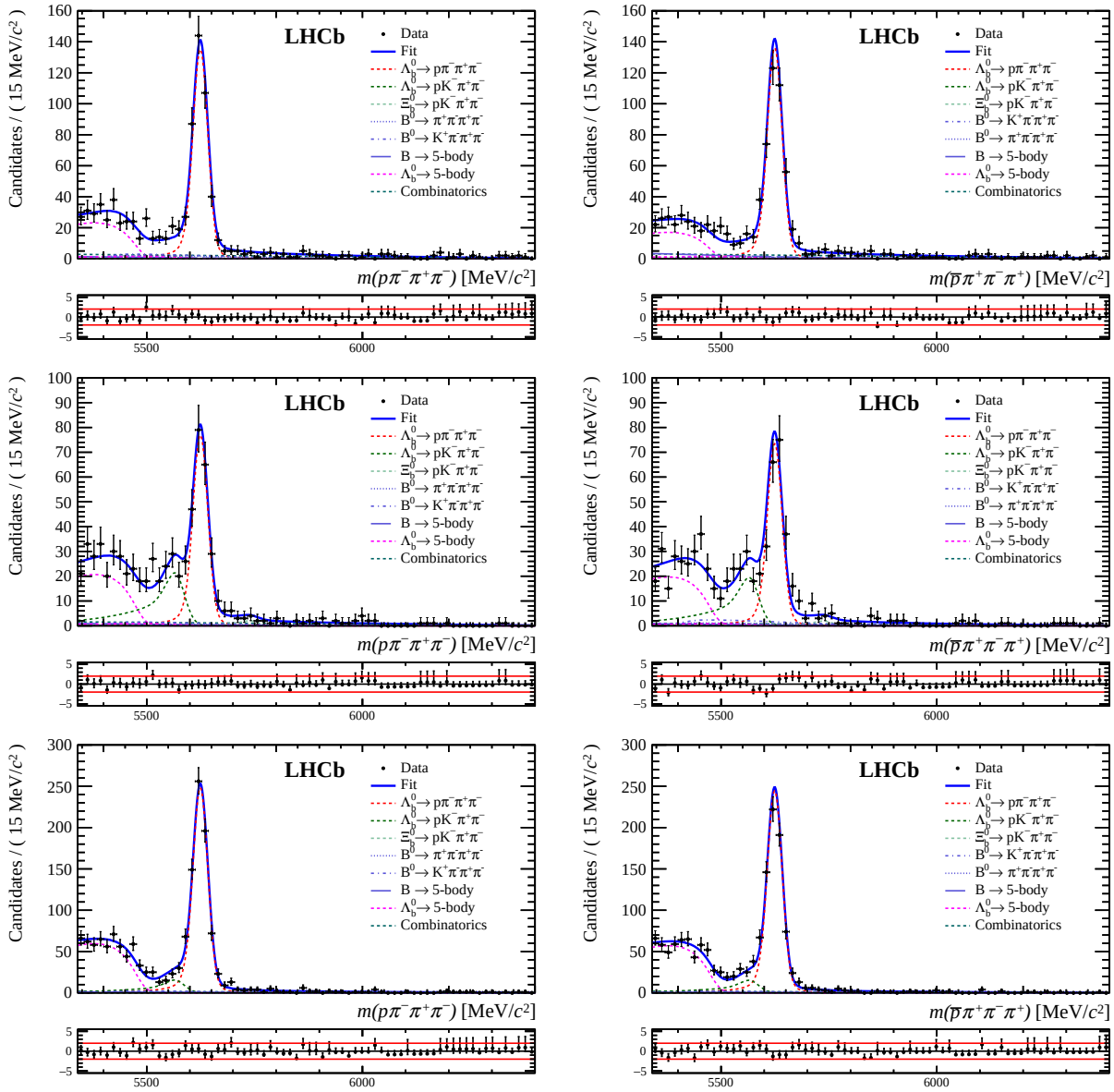

Figure 7.4: $p\pi\pi\pi$ invariant-mass spectra considering (from top to bottom) $\Lambda_b^0 \to pa_1$, $\Lambda_b^0 \to N^{*0}\rho^0$ (f^0), $\Lambda_b^0 \to \Delta^{++}\pi^-\pi^-$ resonances for (first column) X_b^0 data (2011 and 2012 samples combined) and (second column) $\overline{X}_b^0$ data (2011 and 2012 samples combined).

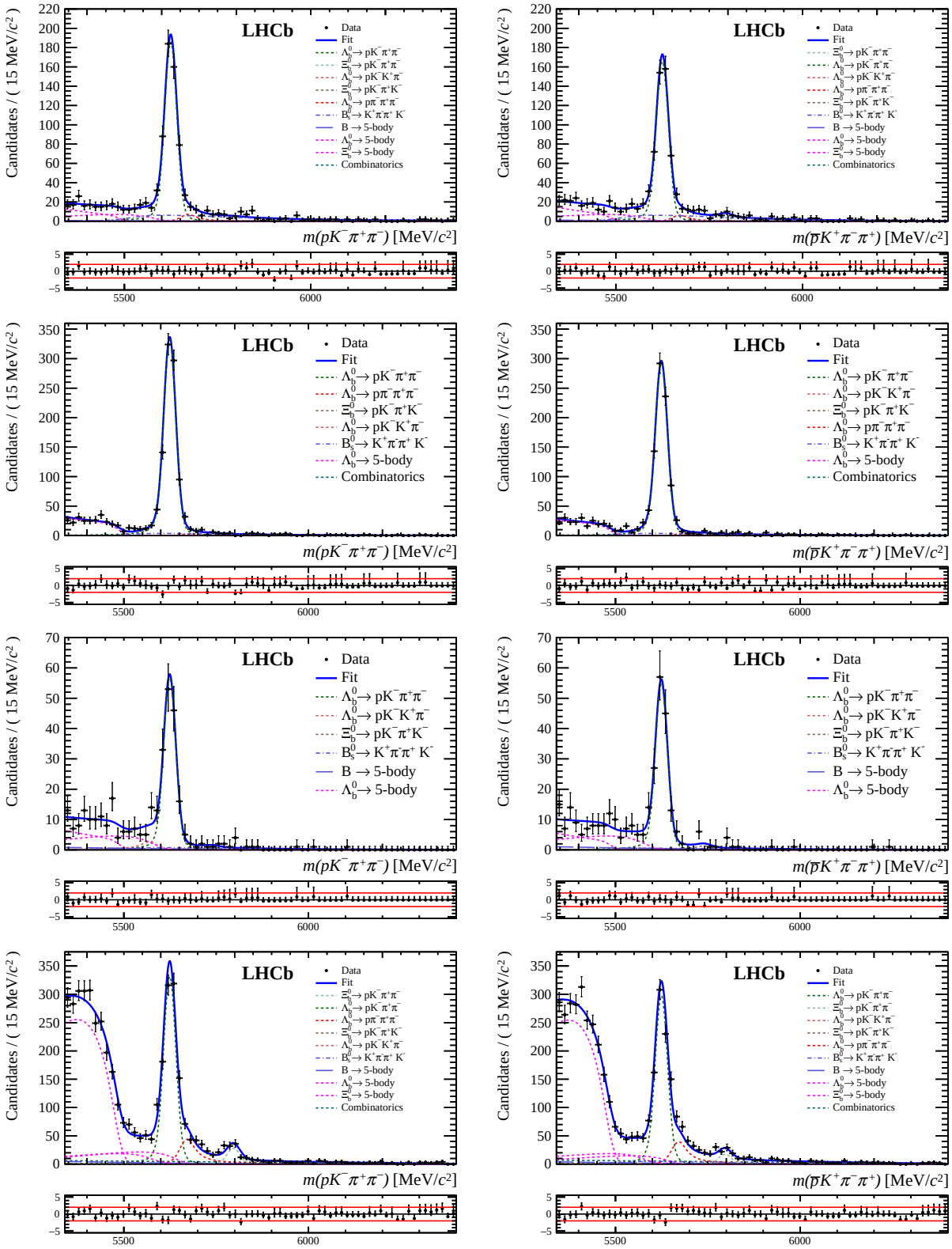

Figure 7.5: $pK\pi\pi$ invariant-mass spectra considering (from top to bottom) $\Lambda_b^0 \to pK_1$, $\Lambda_b^0 \to N^*(1520)^0 K^{*0}$, $\Lambda_b^0 \to \Lambda^*(1520)^0 \rho^0(f^0)$, $\Lambda_b^0 \to \Delta^{++} K^- \pi^-$ decays for (first column) X_b^0 data (2011 and 2012 samples combined) and (second column) $\overline{X}_b^0$ data (2011 and 2012 samples combined).

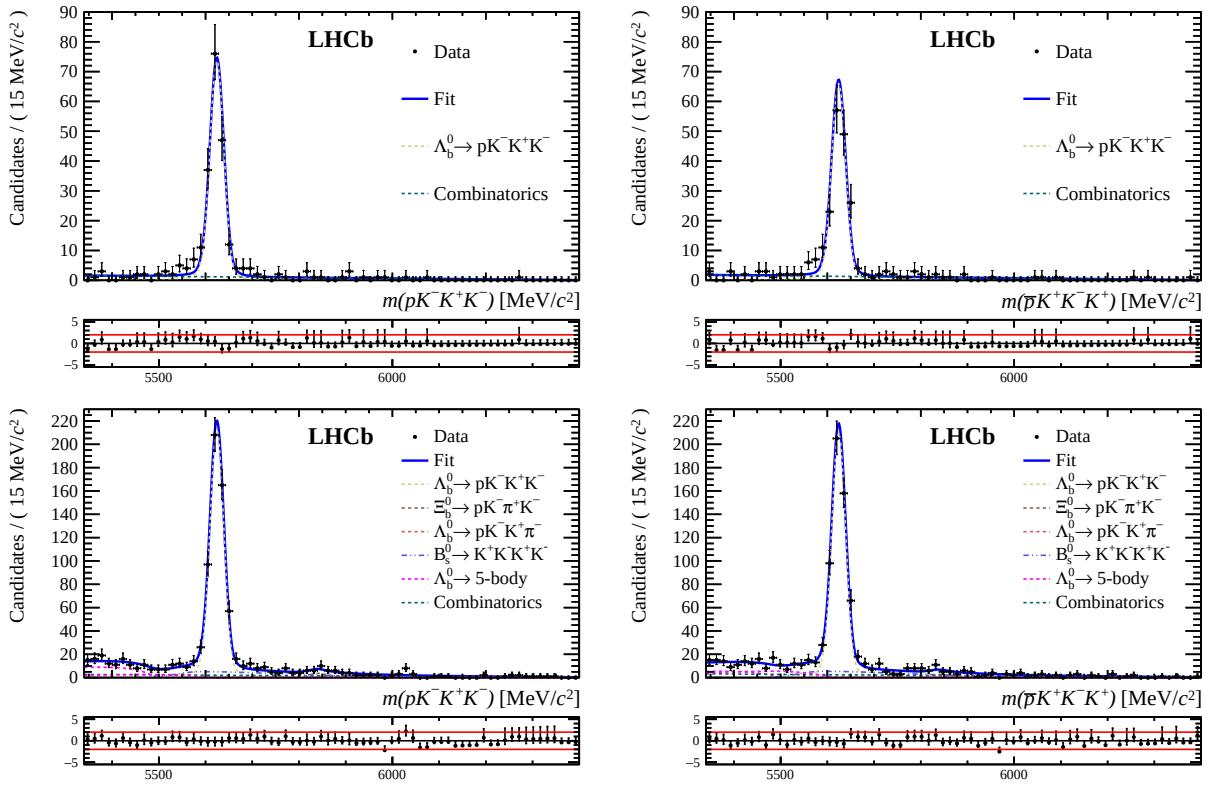

Figure 7.6: $pKKK$ invariant-mass spectra considering (from top to bottom) $\Lambda_b^0 \to \Lambda^*(1520)^0\phi^0$ and $\Lambda_b^0 \to pK^-_{\text{highmass}}\phi^0$ decays for (first column) X_b^0 data (2011 and 2012 samples combined) and (second column) $\overline{X}_b^0$ data (2011 and 2012 samples combined).

Table 7.12: The *CP* asymmetry observables obtained from the different results of the fit to the $p\pi\pi\pi$ phase space data, in percent. The uncertainty reported is related to statistics. The numbers and uncertainties are provided with equal number of digits.

CP asymmetry observable	Value (in %)
2011 spectra:	
$\Delta\mathcal{A}^{CP} = \mathcal{A}^{\text{raw}}$ ($\Lambda_b^0 \to pa_1$) - $\mathcal{A}^{\text{raw}}$ ($\Lambda_b^0 \to (\Lambda_c^+ \to p\pi\pi)\pi$)	-2.22 ± 7.83
$\Delta\mathcal{A}^{CP} = \mathcal{A}^{\text{raw}}$ ($\Lambda_b^0 \to N^*(1520)^0\rho^0(f^0)$) - $\mathcal{A}^{\text{raw}}$ ($\Lambda_b^0 \to (\Lambda_c^+ \to p\pi\pi)\pi$)	16.16 ± 8.82
$\Delta\mathcal{A}^{CP} = \mathcal{A}^{\text{raw}}$ ($\Lambda_b^0 \to \Delta^{++}\pi^-\pi^-$) - $\mathcal{A}^{\text{raw}}$ ($\Lambda_b^0 \to (\Lambda_c^+ \to p\pi\pi)\pi$)	-1.37 ± 5.78
2012 spectra:	
$\Delta\mathcal{A}^{CP} = \mathcal{A}^{\text{raw}}$ ($\Lambda_b^0 \to pa_1$) - $\mathcal{A}^{\text{raw}}$ ($\Lambda_b^0 \to (\Lambda_c^+ \to p\pi\pi)\pi$)	-1.19 ± 4.97
$\Delta\mathcal{A}^{CP} = \mathcal{A}^{\text{raw}}$ ($\Lambda_b^0 \to N^*(1520)^0\rho^0(f^0)$) - $\mathcal{A}^{\text{raw}}$ ($\Lambda_b^0 \to (\Lambda_c^+ \to p\pi\pi)\pi$)	-4.19 ± 5.77
$\Delta\mathcal{A}^{CP} = \mathcal{A}^{\text{raw}}$ ($\Lambda_b^0 \to \Delta^{++}\pi^-\pi^-$) - $\mathcal{A}^{\text{raw}}$ ($\Lambda_b^0 \to (\Lambda_c^+ \to p\pi\pi)\pi$)	0.11 ± 3.76
2011+2012 spectra:	
$\Delta\mathcal{A}^{CP} = \mathcal{A}^{\text{raw}}$ ($\Lambda_b^0 \to pa_1$) - $\mathcal{A}^{\text{raw}}$ ($\Lambda_b^0 \to (\Lambda_c^+ \to p\pi\pi)\pi$)	-1.49 ± 4.20
$\Delta\mathcal{A}^{CP} = \mathcal{A}^{\text{raw}}$ ($\Lambda_b^0 \to N^*(1520)^0\rho^0(f^0)$) - $\mathcal{A}^{\text{raw}}$ ($\Lambda_b^0 \to (\Lambda_c^+ \to p\pi\pi)\pi$)	1.90 ± 4.86
$\Delta\mathcal{A}^{CP} = \mathcal{A}^{\text{raw}}$ ($\Lambda_b^0 \to \Delta^{++}\pi^-\pi^-$) - $\mathcal{A}^{\text{raw}}$ ($\Lambda_b^0 \to (\Lambda_c^+ \to p\pi\pi)\pi$)	-0.32 ± 3.15

Table 7.13: The *CP* asymmetry observables obtained from the different results of the fit to the $pK\pi\pi$ phase space data, in percent. The uncertainty reported is related to statistics. The numbers and uncertainties are provided with equal number of digits.

CP asymmetry observable	Value (in %)
2011 spectra:	
$\Delta\mathcal{A}^{CP} = \mathcal{A}^{\rm raw}$ ($\Lambda_b^0 \to \Delta^{++}K^-\pi^-$) - $\mathcal{A}^{\rm raw}$ ($\Lambda_b^0 \to (\Lambda_c^+ \to pK\pi)\pi$)	3.61 ± 4.55
$\Delta\mathcal{A}^{CP} = \mathcal{A}^{\rm raw}$ ($\Lambda_b^0 \to N^*(1520)^0K^{*0}$) - $\mathcal{A}^{\rm raw}$ ($\Lambda_b^0 \to (\Lambda_c^+ \to pK\pi)\pi$)	7.32 ± 4.35
2012 spectra:	
$\Delta\mathcal{A}^{CP} = \mathcal{A}^{\rm raw}$ ($\Lambda_b^0 \to \Delta^{++}K^-\pi^-$) - $\mathcal{A}^{\rm raw}$ ($\Lambda_b^0 \to (\Lambda_c^+ \to pK\pi)\pi$)	4.31 ± 3.04
$\Delta\mathcal{A}^{CP} = \mathcal{A}^{\rm raw}$ ($\Lambda_b^0 \to N^*(1520)^0K^{*0}$) - $\mathcal{A}^{\rm raw}$ ($\Lambda_b^0 \to (\Lambda_c^+ \to pK\pi)\pi$)	4.22 ± 3.00
2011+2012 spectra:	
$\Delta\mathcal{A}^{CP} = \mathcal{A}^{\rm raw}$ ($\Lambda_b^0 \to pK_1$) - $\mathcal{A}^{\rm raw}$ ($\Lambda_b^0 \to (\Lambda_c^+ \to pK\pi)\pi$)	4.48 ± 3.43
$\Delta\mathcal{A}^{CP} = \mathcal{A}^{\rm raw}$ ($\Lambda_b^0 \to \Lambda^*(1520)^0\rho^0(f^0)$) - $\mathcal{A}^{\rm raw}$ ($\Lambda_b^0 \to (\Lambda_c^+ \to pK\pi)\pi$)	0.56 ± 5.95
$\Delta\mathcal{A}^{CP} = \mathcal{A}^{\rm raw}$ ($\Lambda_b^0 \to \Delta^{++}K^-\pi^-$) - $\mathcal{A}^{\rm raw}$ ($\Lambda_b^0 \to (\Lambda_c^+ \to pK\pi)\pi$)	4.10 ± 2.53
$\Delta\mathcal{A}^{CP} = \mathcal{A}^{\rm raw}$ ($\Lambda_b^0 \to N^*(1520)^0K^{*0}$) - $\mathcal{A}^{\rm raw}$ ($\Lambda_b^0 \to (\Lambda_c^+ \to pK\pi)\pi$)	5.22 ± 2.47

Table 7.14: The *CP* asymmetry observables obtained from the different results of the fit to the $pKKK$ phase space data, in percent. The uncertainty reported is related to statistics. The numbers and uncertainties are provided with equal number of digits.

CP asymmetry observable	Value (in %)
$\Delta\mathcal{A}^{CP} = \mathcal{A}^{\rm raw}$ ($\Lambda_b^0 \to \Lambda^*(1520)^0\phi^0$) - $\mathcal{A}^{\rm raw}$ ($\Lambda_b^0 \to (\Lambda_c^+ \to pK\pi)\pi$)	4.13 ± 5.51
$\Delta\mathcal{A}^{CP} = \mathcal{A}^{\rm raw}$ ($\Lambda_b^0 \to pK^-_{\rm highmass}\phi^0$) - $\mathcal{A}^{\rm raw}$ ($\Lambda_b^0 \to (\Lambda_c^+ \to pK\pi)\pi$)	-0.77 ± 3.28

7.3 Results - $\Delta\mathcal{A}^{CP}$ measurements

This section gathers the results of the $\Delta\mathcal{A}^{CP}$ measurements for the different phase space configurations. The actual $\Delta\mathcal{A}^{CP}$ measurements are determined from the raw asymmetries and the corrections that have been discussed in the previous sections. Henceforth, the $\Delta\mathcal{A}^{CP}$ measurements reads

$$\Delta\mathcal{A}^{CP} = \Delta\mathcal{A}^{CP}{}_{\text{raw}} - \delta^{\text{L0}} + \Delta A_K - \Delta A_P - \Delta A_{PID}, \tag{7.5}$$

where δ^{L0}, ΔA_K, ΔA_P and ΔA_{PID} are corrections related to the trigger, kaon and proton detection and PID asymmetries, respectively. $\Delta\mathcal{A}^{CP}$ measurements are performed for each year of data-taking and the combination is the average weighted by the statistical and the non-correlated systematic uncertainties.

Tables 7.15, 7.16 and 7.17 display the results for the inclusive, the Low2x2BodyMass and quasi 2-body measurements, respectively. All measurements are dominated by the statistical uncertainties and no significant CP violation is observed.

Among the 18 measurements, a naive determination of the significance is highlighting a 2-3σ effect for the $\Lambda_b^0 \to pK^-\pi^+\pi^-$ inclusive $\Delta\mathcal{A}^{CP}$ measurement. However, the measurements in the phase space of the $pK\pi\pi$ spectrum provide less significant asymmetries which seem to indicate that the potential effect is not due to specific regions of phase space that have been scrutinised. We remind here that an enhancement of potential CP asymmetries was expected while scrutinise the phase space because of the presence of strong phases in the final state but the low statistics available for the quasi-2 body measurements prevent from confirming an actual evidence of CP violation.

As previously emphasised, an evidence for CP violation in the $\Lambda_b^0 \to p\pi^-\pi^+\pi^-$ decay mode has been recently reported by the LHCb collaboration [22] (with a significance of 3.3σ), by using T-odd observables. In the analysis presented in this thesis, $\Delta\mathcal{A}^{CP}$ ($\Lambda_b^0 \to p\pi^-\pi^+\pi^-$) is however found to be consistent with zero. Actually, a comparison between the two types of measurements is not trivial: T-odd CP-observables are proportional to the sine of the weak-phase difference while $\Delta\mathcal{A}^{CP}$ are proportional to the cosine of this very same quantity. To a certain extent, this phase shift brings complementary methods and a null $\Delta\mathcal{A}^{CP}$ can consequently be consistent with non-zero T-odd asymmetry. The complete assessement of the CP violation with the two approaches (direct and indirect) would require a five dimensional amplitude analysis in order to pinpoint the amplitudes responsible of the indication of CP violation in both analysis.

Eventually, a wider data sample would reduce the statistical uncertainties but the 2-3σ effect for the $\Lambda_b^0 \to pK^-\pi^+\pi^-$ inclusive measurement can suppose that with the inclusion of the RunII data, the high-mass region of the pK combination (which corresponds to he $p\pi\pi$ low-mass resonances N^*) should be studied as well since the low-mass region is not providing a significant CP asymmetry.

Table 7.15: $\Delta\mathcal{A}^{CP}$ measurements in percent, for the full phase space measurements. 2011 (2012) measurements are reported in first (second) row. The combined results is reported in the last column.

Decay mode	$\Delta\mathcal{A}^{CP}$ (%)	
$\Lambda_b^0 \to p\pi^-\pi^+\pi^-$	4.38 ± 4.45 ± 0.87 -0.32 ± 2.90 ± 0.53	1.07 ± 2.43 ± 0.47
$\Lambda_b^0 \to pK^-\pi^+\pi^-$	1.01 ± 1.93 ± 0.88 4.15 ± 1.26 ± 0.55	3.23 ± 1.05 ± 0.49
$\Lambda_b^0 \to pK^-K^+\pi^-$	-1.95 ± 8.80 ± 0.85 -8.98 ± 5.76 ± 0.51	-6.87 ± 4.82 ± 0.46
$\Lambda_b^0 \to pK^-K^+K^-$	1.12 ± 3.02 ± 0.88 -0.19 ± 2.09 ± 0.55	0.23 ± 1.72 ± 0.49
$\Xi_b^0 \to pK^-\pi^+\pi^-$	-28.98 ± 19.58 ± 0.88 -11.97 ± 12.34 ± 0.55	-16.81 ± 10.39 ± 0.50
$\Xi_b^0 \to pK^-\pi^+K^-$	-11.29 ± 13.52 ± 0.88 -4.43 ± 9.87 ± 0.54	-6.81 ± 7.98 ± 0.49

Table 7.16: $\Delta\mathcal{A}^{CP}$ measurements in percent, for the Low2x2BodyMass measurements. 2011 (2012) measurements are reported in first (second) row. The combined results is reported in the last column.

Decay mode	$\Delta\mathcal{A}^{CP}$ (%)	
$\Lambda_b^0 \to p\pi^-\pi^+\pi^-$	12.10 ± 7.39 ± 0.74 0.06 ± 4.89 ± 0.45	3.72 ± 4.08 ± 0.40
$\Lambda_b^0 \to pK^-\pi^+\pi^-$	1.51 ± 2.57 ± 0.73 4.29 ± 1.70 ± 0.46	3.45 ± 1.42 ± 0.42
$\Lambda_b^0 \to pK^-K^+K^-$	1.44 ± 3.90 ± 0.79 3.31 ± 2.71 ± 0.49	2.71 ± 2.23 ± 0.44

Table 7.17: $\Delta\mathcal{A}^{CP}$ measurements in percent, for the phase space measurements. 2011 (2012) measurements are reported in first (second) row. The combined results is reported in the last column.

Decay mode	$\Delta\mathcal{A}^{CP}$ (%)	
$\Lambda_b^0 \to p a_1$	-1.99 ± 7.83 ± 1.01 -1.33 ± 4.97 ± 0.60	-1.52 ± 4.20 ± 0.53
$\Lambda_b^0 \to N^*(1520)^0 \rho^0(f^0)$	16.28 ± 8.82 ± 0.49 -4.07 ± 5.77 ± 0.30	2.02 ± 4.86 ± 0.27
$\Lambda_b^0 \to \Delta^{++}\pi^-\pi^-$	-1.00 ± 5.78 ± 0.99 0.61 ± 3.76 ± 0.59	0.13 ± 3.15 ± 0.51
$\Lambda_b^0 \to p K_1$	—	4.74 ± 3.43 ± 0.63
$\Lambda_b^0 \to \Lambda^*(1520)^0 \rho^0(f^0)$	—	0.59 ± 5.95 ± 0.40
$\Lambda_b^0 \to N^*(1520)^0 K^{*0}$	7.53 ± 4.35 ± 0.67 4.46 ± 3.00 ± 0.43	5.45 ± 2.47 ± 0.38
$\Lambda_b^0 \to \Delta^{++} K^-\pi^-$	3.80 ± 4.55 ± 1.01 4.62 ± 3.04 ± 0.63	4.37 ± 2.53 ± 0.56
$\Lambda_b^0 \to \Lambda^*(1520)^0 \phi^0$	—	4.27 ± 5.51 ± 0.33
$\Lambda_b^0 \to p K^-_{\text{highmass}} \phi^0$	—	-0.68 ± 3.28 ± 0.61

Conclusion

This document describes the search for 4-body fully charged decays of neutral b-baryons, Λ_b^0 or Ξ_b^0. There are seven decays of interest, namely $\Lambda_b^0 \to p\pi^-\pi^+\pi^-$, $\Lambda_b^0 \to pK^-\pi^+\pi^-$, $\Lambda_b^0 \to pK^-K^+\pi^-$, $\Lambda_b^0 \to pK^-K^+K^-$, $\Xi_b^0 \to pK^-\pi^+\pi^-$, $\Xi_b^0 \to pK^-\pi^+K^-$ and $\Xi_b^0 \to pK^-K^+K^-$, which proceed in the SM simultaneously through $b \to u$ transition or FCNC penguin transition $b \to s$,d.

The decays of interest are selected with a sequential cut-based and multivariate analyses relying on the topological properties (vertexing) of the decays. The kinematical properties of the decay daughters are not used in this selection to maximally preserved the phase space of the decays of interest. Particle identification criteria are further considered to separate the final states and build mutually exclusive data samples to be analysed simultaneously. A simultaneous mass fitter has hence been designed in order to measure the signal yields of interest and their charge conjugate counterparts. This tool is both used in the branching fraction measurements of the decay modes of interest and in the search for *CP*-violating asymmetries in these decays by treating separately the particle and antiparticle invariant-mass spectra. The design of the fit model is detailed in this thesis. The global behaviour of the fit to the data sample (recorded in 2011 and 2012 with the LHCb experiment) is found to be satisfactory and we did not find any sign of an overlooked background.

The individual particle and antiparticle spectra have been first added in order to measure the branching fractions of the modes of interest, while keeping blind the individual charge-separated spectra. The systematic uncertainty budget corresponding to all identified systematic effects have been estimated. All the decay modes have been observed except $\Xi_b^0 \to pK^-K^+K^-$ for which a hint of its existence is obtained. Four decay modes, namely $\Lambda_b^0 \to pK^-\pi^+\pi^-$, $\Lambda_b^0 \to pK^-K^+K^-$, $\Xi_b^0 \to pK^-\pi^+\pi^-$ and $\Xi_b^0 \to pK^-\pi^+K^-$ are established for the first time. The branching fractions of the modes of interest are relative to the $\Lambda_b^0 \to (\Lambda_c^+ \to pK^-\pi^+)\pi^-$ decay mode and are measured to be :

$$
\begin{aligned}
R(\Lambda_b \to p\pi\pi\pi)\ (\%) &= 6.85 \pm 0.19 \pm 0.34, \\
R(\Lambda_b \to pK\pi\pi)\ (\%) &= 16.4 \pm 0.3 \pm 0.7, \\
R(\Lambda_b \to pKK\pi)\ (\%) &= 1.32 \pm 0.09 \pm 0.14, \\
R(\Lambda_b \to pKKK)\ (\%) &= 4.11 \pm 0.12 \pm 0.22, \\
R(\Xi_b \to pK\pi\pi)\ (\%) &= 0.62 \pm 0.08 \pm 0.09, \\
R(\Xi_b \to pK\pi K)\ (\%) &= 0.56 \pm 0.06 \pm 0.07, \\
R(\Xi_b \to pKKK)\ (\%) &\in [0.038 - 0.098] \text{ at } 95\% \text{ C.L.}
\end{aligned}
$$

where the first uncertainty is statistical and the second is systematic. The relative hadronisation fraction is contained in R. The establishment of these signals opens new channels in which to search for *CP*-violating asymmetries in charmless four-body decays of Λ_b^0 and Ξ_b^0 baryons. This work has been published [39].

The *CP* violation in baryons remains unobserved up to date. In the multibody decays of interest, the interference pattern is expected to be rich of resonances structures, in particular in the low mass two-body baryon resonances which come likely in association with two-body non-baryonic resonances. The weak interaction induced *CP* asymmetries might receive significant enhancement from the phase differences coming from these strongly interacting resonances. Henceforth, 18 measurements of *CP* asymmetries are proposed in this document. Upon scrutiny of the invariant mass of the combined two- or three- tracks out of the final tracks of the dominant modes candidate events, several structures are also searched for (*e.g.* a_1, Δ^{++}, $\Lambda^*(1520)^0$...). A simple counting experiment can permit the measurement of a *CP* asymmetry up to corrections of instrumental and productions asymmetries. In order to handle those effects, the measurements are consisting in establishing the differences of the $\mathcal{A}^{CP}$ (denoted $\Delta\mathcal{A}^{CP}$) of the signal with respect to the $\mathcal{A}^{CP}$ of a control channel that require to consider charmed decays such as $\Lambda_b^0 \to (\Lambda_c^+ \to p\pi^-\pi^+)\pi^-$, $\Lambda_b^0 \to (\Lambda_c^+ \to pK^-\pi^+)\pi^-$ and $\Xi_b^0 \to (\Xi_c^+ \to pK^-\pi^+)\pi^-$. Measurements are reported below: all measurements are dominated by the statistical uncertainties and no significant CP violation is observed.
The inclusive $\Delta\mathcal{A}^{CP}$ measurements of the modes of interest are measured to be :

$$\begin{aligned}
\Delta\mathcal{A}^{CP}(\Lambda_b^0 \to p\pi^-\pi^+\pi^-)(\%) &= 1.1 \pm 2.5 \pm 0.5 \\
\Delta\mathcal{A}^{CP}(\Lambda_b^0 \to pK^-\pi^+\pi^-)(\%) &= 3.2 \pm 1.1 \pm 0.5 \\
\Delta\mathcal{A}^{CP}(\Lambda_b^0 \to pK^-K^+\pi^-)(\%) &= -6.9 \pm 4.9 \pm 0.5 \\
\Delta\mathcal{A}^{CP}(\Lambda_b^0 \to pK^-K^+K^-)(\%) &= 0.2 \pm 1.8 \pm 0.5 \\
\Delta\mathcal{A}^{CP}(\Xi_b^0 \to pK^-\pi^+\pi^-)(\%) &= -16.8 \pm 10.4 \pm 0.5 \\
\Delta\mathcal{A}^{CP}(\Xi_b^0 \to pK^-\pi^+K^-)(\%) &= -6.8 \pm 8.0 \pm 0.5.
\end{aligned}$$

The measurements for the 2-body low-invariant mass regions are:

$$\begin{aligned}
\Delta\mathcal{A}^{CP}(\Lambda_b^0 \to p\pi^-\pi^+\pi^-)(\%) &= 3.7 \pm 4.1 \pm 0.5 \\
\Delta\mathcal{A}^{CP}(\Lambda_b^0 \to pK^-\pi^+\pi^-)(\%) &= 3.5 \pm 1.5 \pm 0.5 \\
\Delta\mathcal{A}^{CP}(\Lambda_b^0 \to pK^-K^+\pi^-)(\%) &= 2.7 \pm 2.3 \pm 0.5,
\end{aligned}$$

Eventually $\Delta\mathcal{A}^{CP}$ measurements for the quasi 2-body decays reads:

$$\begin{aligned}
\Delta\mathcal{A}^{CP}(\Lambda_b^0 \to pa_1)(\%) &= -1.5 \pm 4.2 \pm 0.6 \\
\Delta\mathcal{A}^{CP}(\Lambda_b^0 \to N^*(1520)^0\rho^0(f^0))(\%) &= 2.0 \pm 4.9 \pm 0.3 \\
\Delta\mathcal{A}^{CP}(\Lambda_b^0 \to \Delta^{++}\pi^-\pi^-)(\%) &= 0.1 \pm 3.2 \pm 0.6 \\
\Delta\mathcal{A}^{CP}(\Lambda_b^0 \to pK_1)(\%) &= 4.7 \pm 3.5 \pm 0.7 \\
\Delta\mathcal{A}^{CP}(\Lambda_b^0 \to \Lambda^*(1520)^0\rho^0(f^0))(\%) &= 0.6 \pm 6.0 \pm 0.4 \\
\Delta\mathcal{A}^{CP}(\Lambda_b^0 \to N^*(1520)^0K^{*0})(\%) &= 5.5 \pm 2.5 \pm 0.4 \\
\Delta\mathcal{A}^{CP}(\Lambda_b^0 \to \Delta^{++}K^-\pi^-)(\%) &= 4.4 \pm 2.6 \pm 0.6 \\
\Delta\mathcal{A}^{CP}(\Lambda_b^0 \to \Lambda^*(1520)^0\phi^0)(\%) &= 4.3 \pm 5.6 \pm 0.4 \\
\Delta\mathcal{A}^{CP}(\Lambda_b^0 \to pK^-_{\text{highmass}}\phi^0)(\%) &= -0.7 \pm 3.3 \pm 0.7.
\end{aligned}$$

where the first uncertainty is statistical and the second is systematic. No significant *CP* violation is observed. An educated comparison between the results presented in this document and the evidence of *CP* violation in the $\Lambda_b^0 \to p\pi^-\pi^+\pi^-$ decay that have been reported by the LHCb collaboration would require a five dimensional amplitude analysis in order to identify the amplitudes responsible of the indication of *CP* violation in both analysis.

The quest for the first observation of CP violation in baryon decays continues. The LHCb RunII data will multiply by a factor 5 the data sample used in this analysis and will provide a unique data set to complete this program.

Appendix A

Appendix to Chapter 1

A.1 Brief introduction of the Operator Product Expansion

The OPE method consists at first in writing the Hamiltonian as a product of local operators O^i that are 4-quarks current operators (non-perturbative by essence). It allows to consider that the interaction occurs in one point which is weighted by C^i couplings (Wilson's coefficients) which represent the perturbative part of the interaction. The effective Hamiltonian expression is only valid for a given energy scale μ, which is separating the short-distance-interactions domain (energy $> \mu$) from the long-distance-energy interactions domain (energy $< \mu$). In a general way, μ is chosen to be of the order of the baryon mass decaying and the result should be choice-independent. Henceforth, the effective Hamiltonian can be written as

$$\mathcal{H}^{\text{eff}} = \frac{G_F}{\sqrt{2}} \sum_i V^i_{CKM} C^i(\mu) O^i(\mu), \tag{A.1}$$

where G_F is the Fermi coupling constant and V^i_{CKM} stands for a product of CKM-matrix elements. Going from the complete to the effective theory is illustrated for a simple scattering on Fig A.1.

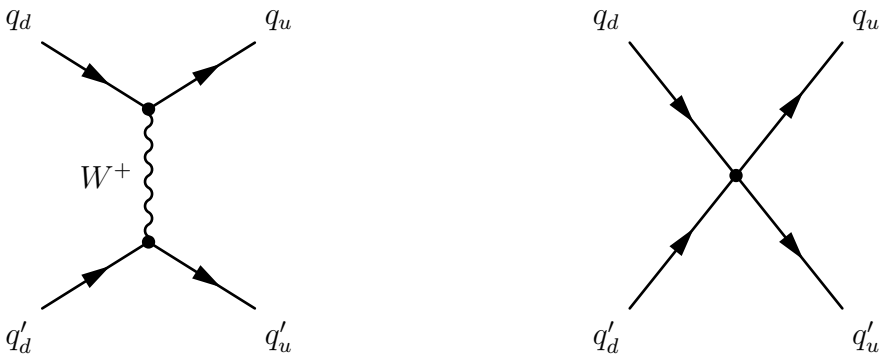

(a) Complete theory (b) Effective theory

Figure A.1: Illustration of the complete theory (left) and of the effective theory (right). $q_{u,d}$ and $q'_{u,d}$ represent up-type, down-type quark fields, respectively.

Considering that the W mass is larger than the k^2_W of the interaction, one can consider a new expression for the amplitude in the effective theory framework, as reported in Eq.(A.3)

$$\text{Fig A.1a}: \quad A = \frac{G_F}{\sqrt{2}} V^*_{q_u q_d} V_{q'_u q'_d} (\overline{q_u} \gamma^\mu (1-\gamma_5) q_d) \frac{M^2_W}{k^2_W - M^2_W} (\overline{q'_u} \gamma^\mu (1-\gamma_5) q'_d) \tag{A.2}$$

$$\text{Fig A.1b}: \quad A = \frac{G_F}{\sqrt{2}} V^*_{q_u q_d} V_{q'_u q'_d} CO + \mathcal{O}(\frac{k^2_W}{M^2_W}) \tag{A.3}$$

A.1.1 Decays topologies

The main difficulty in the branching fraction computation is lying in the amplitude $A(\Lambda^0_b \to N^* \rho^0)$ determination. OPE method, briefly introduced in the previous subsection, is hence providing the following expression

$$A(\Lambda^0_b \to N^* \rho^0) = \left\langle N^* \rho^0 | \mathcal{H}^{\text{eff}} | \Lambda^0_b \right\rangle. \tag{A.4}$$

The ten local operators O_i that are required in the expression $\mathcal{H}^{\text{eff}}$ (Eq. A.1) are reported in the following. They are further split in 3 categories:

- Operators for tree-level

$$O_1 = \left[\overline{d_\alpha}\gamma^\mu(1-\gamma_5)u_\beta\right]\left[\overline{u_\beta}\gamma^\mu(1-\gamma_5)u_\alpha\right] \tag{A.5}$$
$$O_2 = \left[\overline{d_\alpha}\gamma^\mu(1-\gamma_5)u_\alpha\right]\left[\overline{u_\beta}\gamma^\mu(1-\gamma_5)u_\beta\right] \tag{A.6}$$

- Operators for QCD penguin-processes

$$O_3 = \left[\overline{d_\alpha}\gamma^\mu(1-\gamma_5)b_\alpha\right]\sum_{q=u,d,s,c,b}\left[\overline{q_\beta}\gamma^\mu(1-\gamma_5)q_\beta\right] \tag{A.7}$$
$$O_4 = \left[\overline{d_\alpha}\gamma^\mu(1-\gamma_5)b_\beta\right]\sum_{q=u,d,s,c,b}\left[\overline{q_\beta}\gamma^\mu(1-\gamma_5)q_\alpha\right] \tag{A.8}$$
$$O_5 = \left[\overline{d_\alpha}\gamma^\mu(1-\gamma_5)b_\alpha\right]\sum_{q=u,d,s,c,b}\left[\overline{q_\beta}\gamma^\mu(1+\gamma_5)q_\beta\right] \tag{A.9}$$
$$O_6 = \left[\overline{d_\alpha}\gamma^\mu(1-\gamma_5)b_\beta\right]\sum_{q=u,d,s,c,b}\left[\overline{q_\beta}\gamma^\mu(1+\gamma_5)q_\alpha\right] \tag{A.10}$$

- Operators for electroweak penguin-processes

$$O_7 = \frac{3}{2}\left[\overline{d_\alpha}\gamma^\mu(1-\gamma_5)b_\alpha\right]\sum_{q=u,d,s,c,b}e_q\left[\overline{q_\beta}\gamma^\mu(1+\gamma_5)q_\beta\right] \tag{A.11}$$
$$O_8 = \frac{3}{2}\left[\overline{d_\alpha}\gamma^\mu(1-\gamma_5)b_\beta\right]\sum_{q=u,d,s,c,b}e_q\left[\overline{q_\beta}\gamma^\mu(1+\gamma_5)q_\alpha\right] \tag{A.12}$$
$$O_9 = \frac{3}{2}\left[\overline{d_\alpha}\gamma^\mu(1-\gamma_5)b_\alpha\right]\sum_{q=u,d,s,c,b}e_q\left[\overline{q_\beta}\gamma^\mu(1-\gamma_5)q_\beta\right] \tag{A.13}$$
$$O_{10} = \frac{3}{2}\left[\overline{d_\alpha}\gamma^\mu(1-\gamma_5)b_\beta\right]\sum_{q=u,d,s,c,b}e_q\left[\overline{q_\beta}\gamma^\mu(1-\gamma_5)q_\alpha\right] \tag{A.14}$$

where α and β are colour-indexes and e_q is the electric charge of the quark q.

The amplitude can hence be written as

$$A(\Lambda_b^0 \to N^*\rho^0) = \frac{G_F}{\sqrt{2}}\left[V_{ub}^*V_{ud}\sum_{i=1}^{2}C_i(\mu)\left\langle N^*\rho^0|O_i(\mu)|\Lambda_b^0\right\rangle - V_{tb}^*V_{td}\sum_{i=3}^{10}C_i(\mu)\left\langle N^*\rho^0|O_i(\mu)|\Lambda_b^0\right\rangle\right], \tag{A.15}$$

where the first term is related to the tree quark-transitions and the second is related to the penguin-loop quark-transitions. It is however particularly difficult to determine the non-perturbative elements $\langle N^*\rho^0|O_i(\mu)|\Lambda_b^0\rangle$. A possible way out is to consider factorisation hypothesis, which consists in neglecting gluonic-interactions between the quark currents before hadronisation [47, 48]. It allows to factorise $\langle N^*\rho^0|O_i(\mu)|\ ambda_b^0\rangle$ into a term which describes the transition of Λ_b^0 to N^* and a term which describes the creation of ρ^0 from the vacuum. It reads

$$\left\langle N^*\rho^0|O_i(\mu)|\Lambda_b^0\right\rangle \propto \left\langle\rho^0|J_2^i|0\right\rangle \times \left\langle N^*|J_1^i|\Lambda_b^0\right\rangle, \tag{A.16}$$

where $J^i_{1,2}$ are two quark currents. For instance, at the tree-level, one can have the following factorisation:

$$\left\langle N^*\rho^0|O_i(\mu)|\Lambda_b^0\right\rangle \propto \left\langle \rho^0|\overline{u}\gamma^\mu(1-\gamma_5)u|0\right\rangle \times \left\langle N^*|\overline{d}\gamma^\mu(1-\gamma_5)b|\Lambda_b^0\right\rangle . \tag{A.17}$$

For the penguin processes, one has to consider all possible diagrams that correspond to a local operator and are only considered the currents between two colour-singlets. The contributions between two colour-octets are neglected. Wilson's coefficients C^i are thus replaced by 10 linear combinations of these coefficients:

$$\begin{aligned} a_{2j-1} &= C_{2j} + \frac{1}{N_c}C_{2j} \\ a_{2j} &= C_{2j} + \frac{1}{N_c}C_{2j-1} \end{aligned} \tag{A.18}$$

where N_c is the number of colour in the SM and $j \in [0-5]$.
It worth noting that factorisation hypothesis can be enhanced in order to take into account non-factorisable effects [49]. Henceforth, N_c is replaced by an effective number of colour defined as

$$\frac{1}{N_c^{eff}} = \frac{1}{N_c} + \sigma \tag{A.19}$$

where σ is a real parameter related to the corrections coming from contributions between two colour-octets. The effective number of colour should however be adjusted to experimental results. In principle, this number can have different values depending on the process that is considered.

The expressions reported in this section can be used to produce an estimate of the $A(\Lambda_b^0 \to N^*\rho^0)$ amplitude but it would, in addition, require the knowledge of the decay constants of the final-state particles that are involved. Moreover, a proper description of the gluonic-interactions would require additional inputs that exceed the framework of this thesis. Eventually, the full computation of the inclusive branching fraction of the $\Lambda_b^0 \to p\pi^-\pi^+\pi^-$ decay would in any case require to consider other amplitudes, since other intermediate states can lead to the same final state.

Appendix B

Appendix to Chapter 3

B.1 PID K/π (Mis)identification 2D Maps

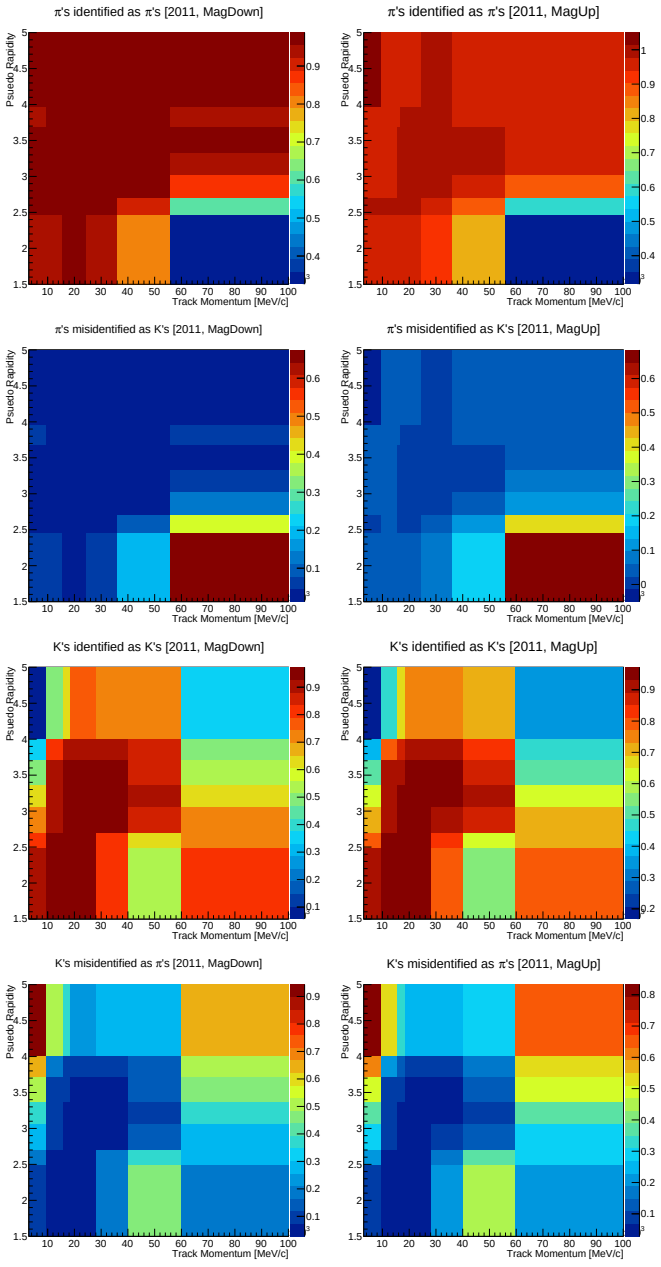

Figure B.1: Efficiency maps of [first-row] pions identified as pions, [second-row] pions misidentified as kaons, [third-row] kaons identified as kaons, and [fourth-row] kaons misidentified as pions for the optimal $\text{PID}_{K\pi}$ cut (0.15,0.15) obtained using the 2011 [first-column] MagDown and [second-column] Mag-Up calibration data.

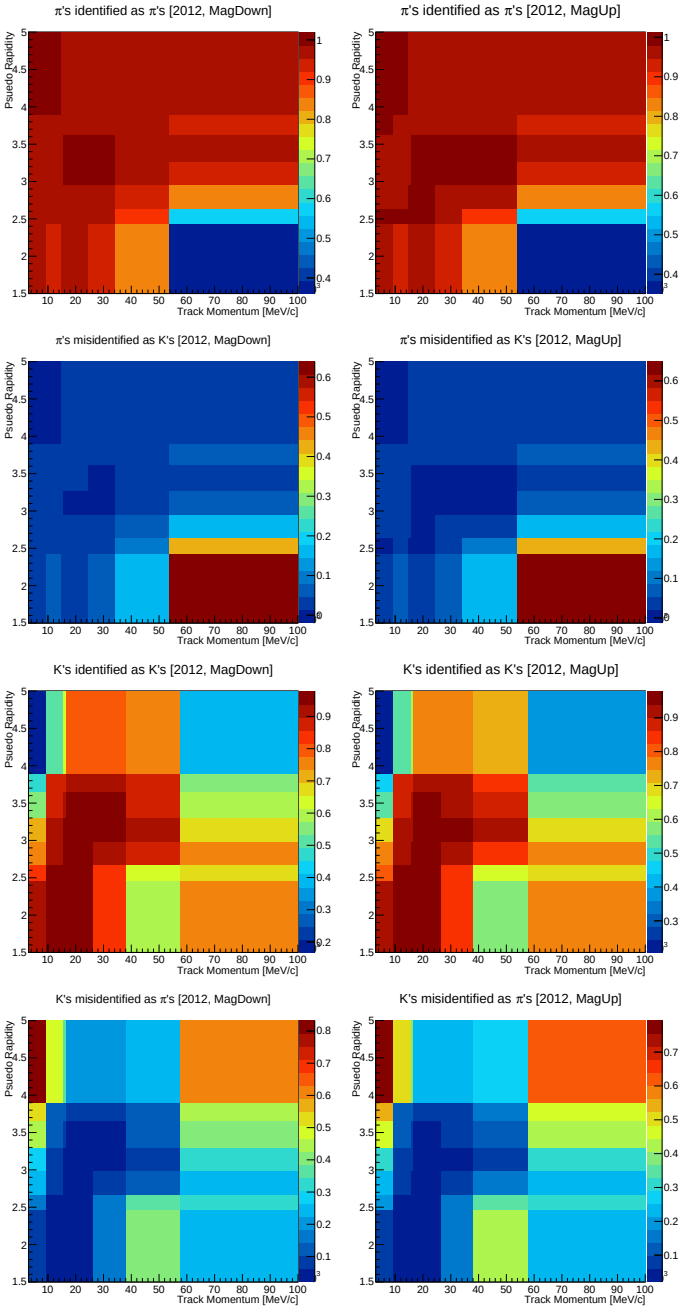

Figure B.2: Efficiency maps of [first-row] pions identified as pions, [second-row] pions misidentified as kaons, [third-row] kaons identified as kaons, and [fourth-row] kaons misidentified as pions for the optimal $\text{PID}_{K\pi}$ cut (0.15,0.15) obtained using the 2012 [first-column] MagDown and [second-column] Mag-Up calibration data.

B.2 PID p (Mis)identification 3D Maps

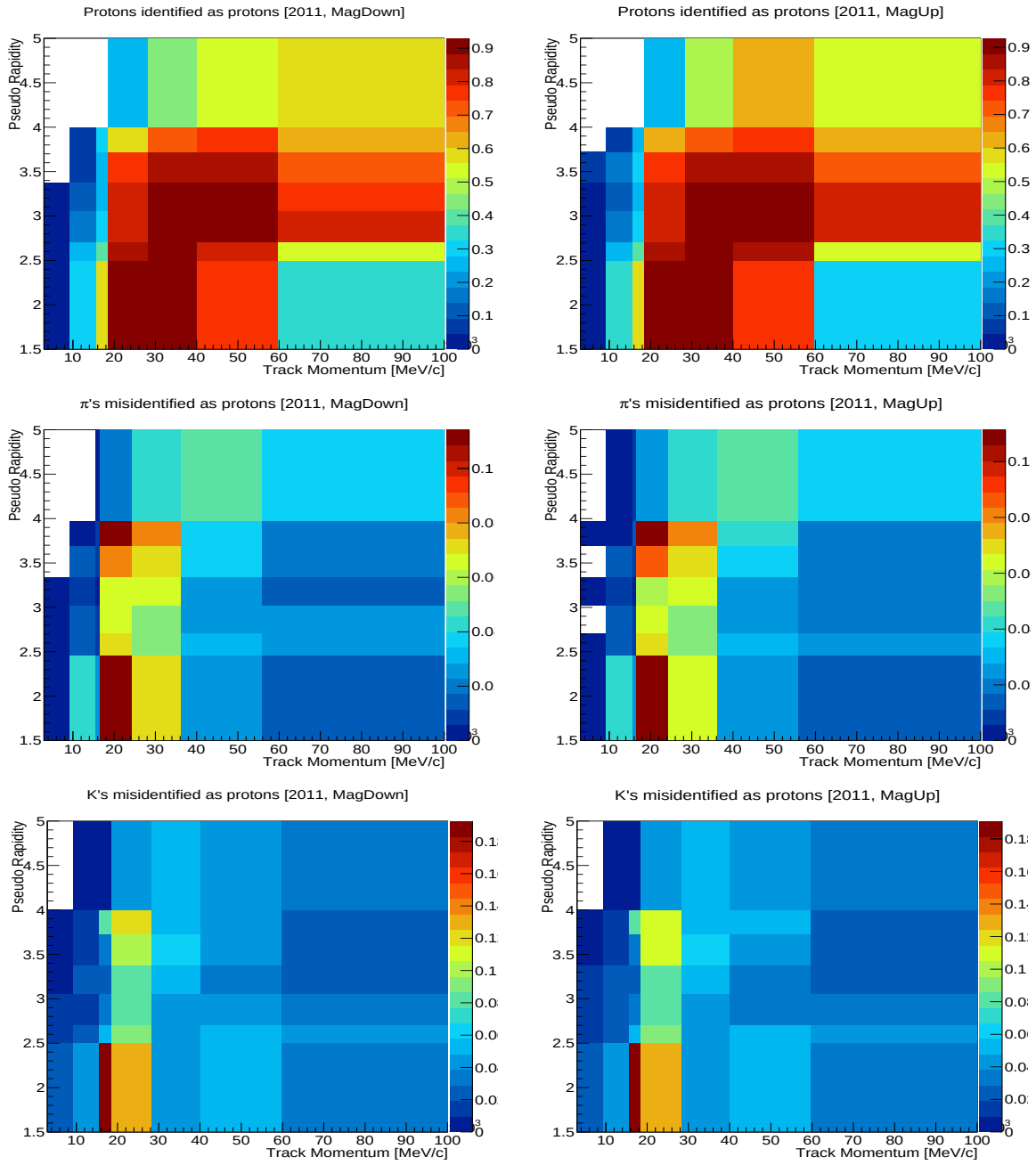

Figure B.3: 2D Projection of three-dimensional efficiency maps of [first-row] protons identified as protons, [second-row] pions misidentified as protons, and [third-row] kaons misidentified as protons for the proton ProbNN$p > 0.50$ cut obtained using the 2011 [first-column] MagDown and [second-column] Mag-Up calibration data. Bins which are poor in term of events and are arbitrarily set to zero in order to avoid division by zero.

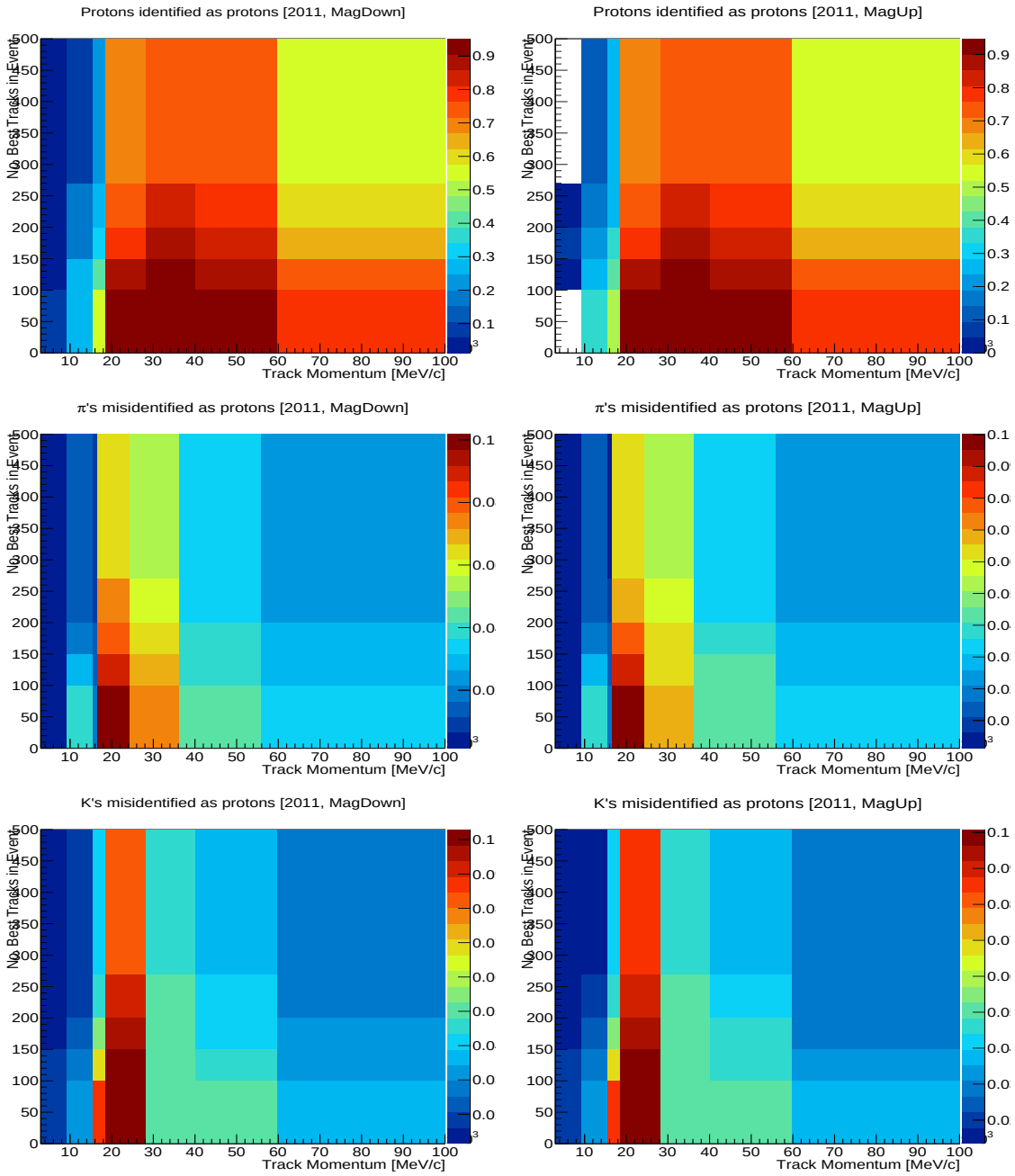

Figure B.4: 2D Projection of three-dimensional efficiency maps of [first-row] protons identified as protons, [second-row] pions misidentified as protons, and [third-row] kaons misidentified as protons for the proton ProbNN$p > 0.50$ cut obtained using the 2011 [first-column] MagDown and [second-column] Mag-Up calibration data. Bins which are poor in term of events and are arbitrarily set to zero in order to avoid division by zero.

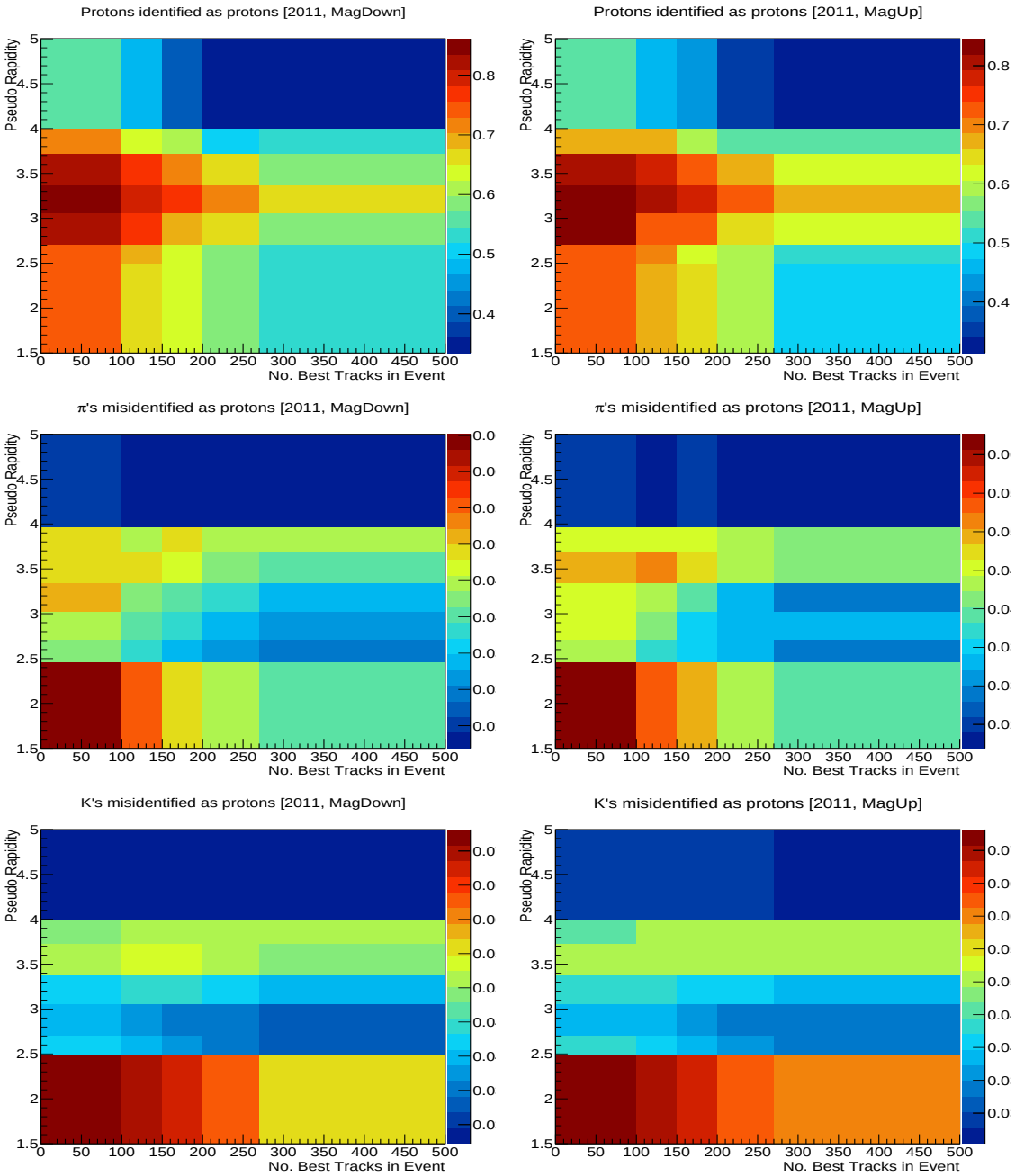

Figure B.5: 2D Projection of three-dimensional efficiency maps of [first-row] protons identified as protons, [second-row] pions misidentified as protons, and [third-row] kaons misidentified as protons for the proton ProbNN$p > 0.50$ cut obtained using the 2011 [first-column] MagDown and [second-column] Mag-Up calibration data. Bins which are poor in term of events and are arbitrarily set to zero in order to avoid division by zero.

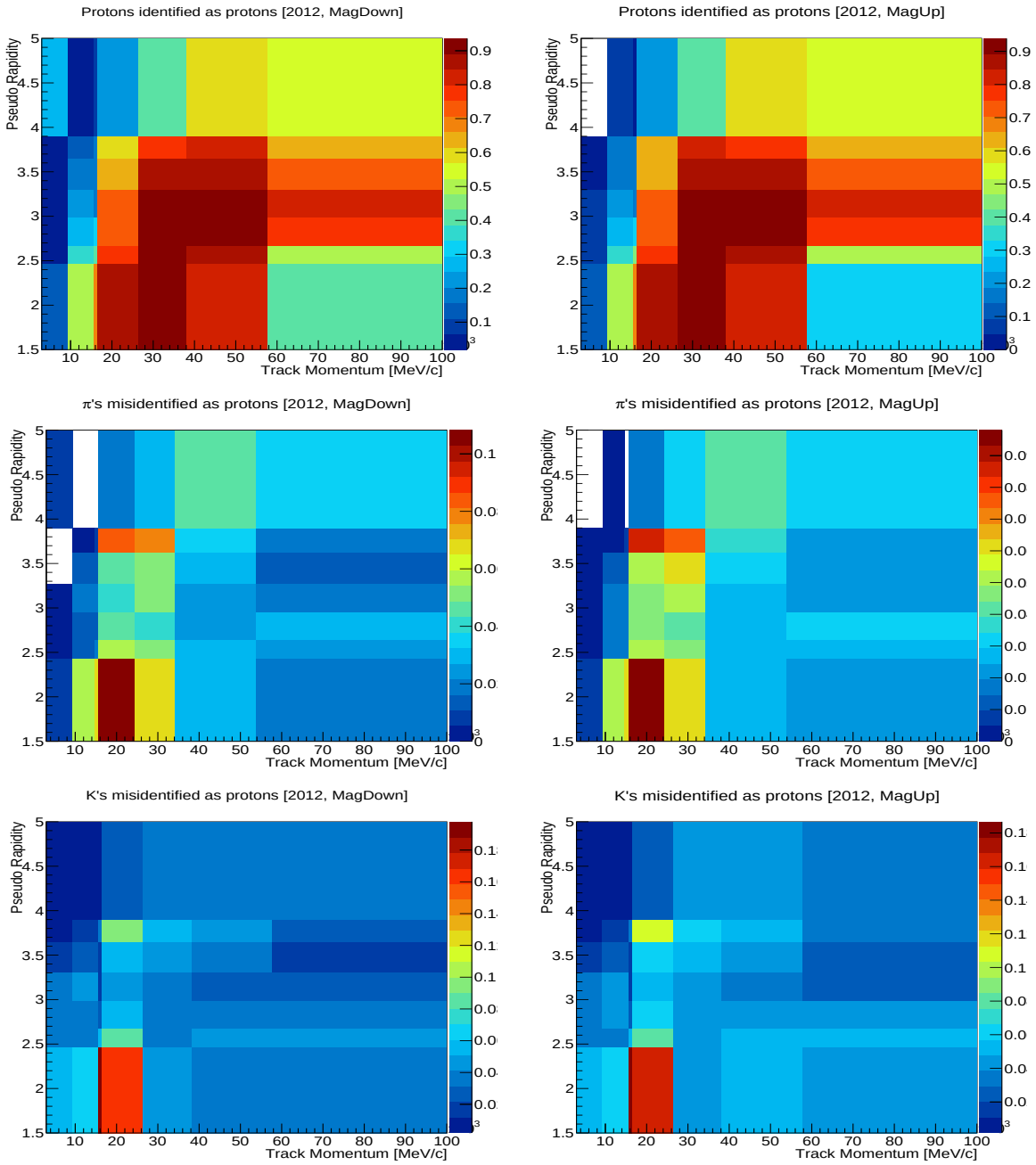

Figure B.6: 2D Projection of three-dimensional efficiency maps of [first-row] protons identified as protons, [second-row] pions misidentified as protons, and [third-row] kaons misidentified as protons for the proton ProbNN$p > 0.50$ cut obtained using the 2012 [first-column] MagDown and [second-column] Mag-Up calibration data. Bins which are poor in term of events and are arbitrarily set to zero in order to avoid division by zero.

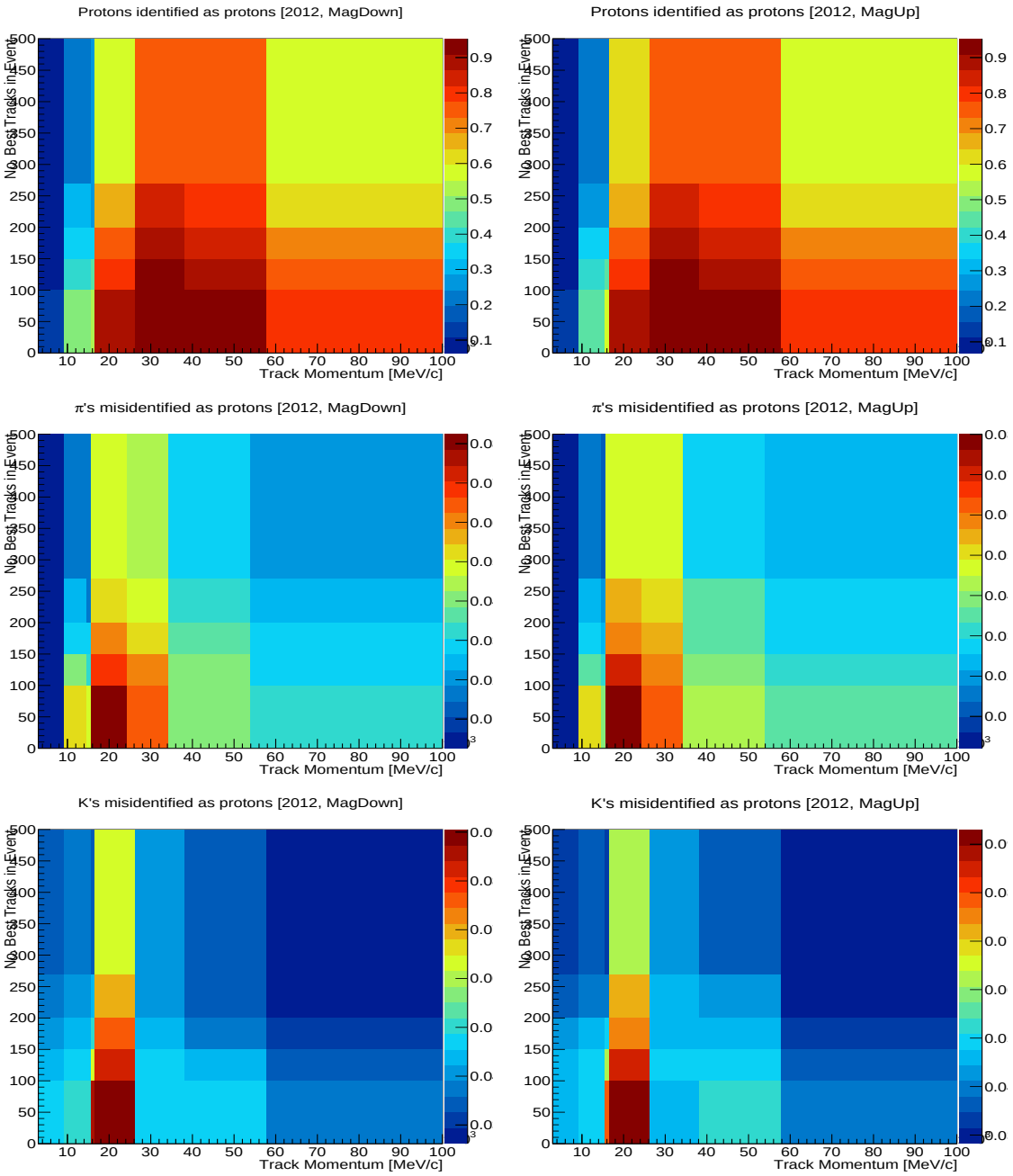

Figure B.7: 2D Projection of three-dimensional efficiency maps of [first-row] protons identified as protons, [second-row] pions misidentified as protons, and [third-row] kaons misidentified as protons for the proton ProbNN$p > 0.50$ cut obtained using the 2012 [first-column] MagDown and [second-column] Mag-Up calibration data. Bins which are poor in term of events and are arbitrarily set to zero in order to avoid division by zero.

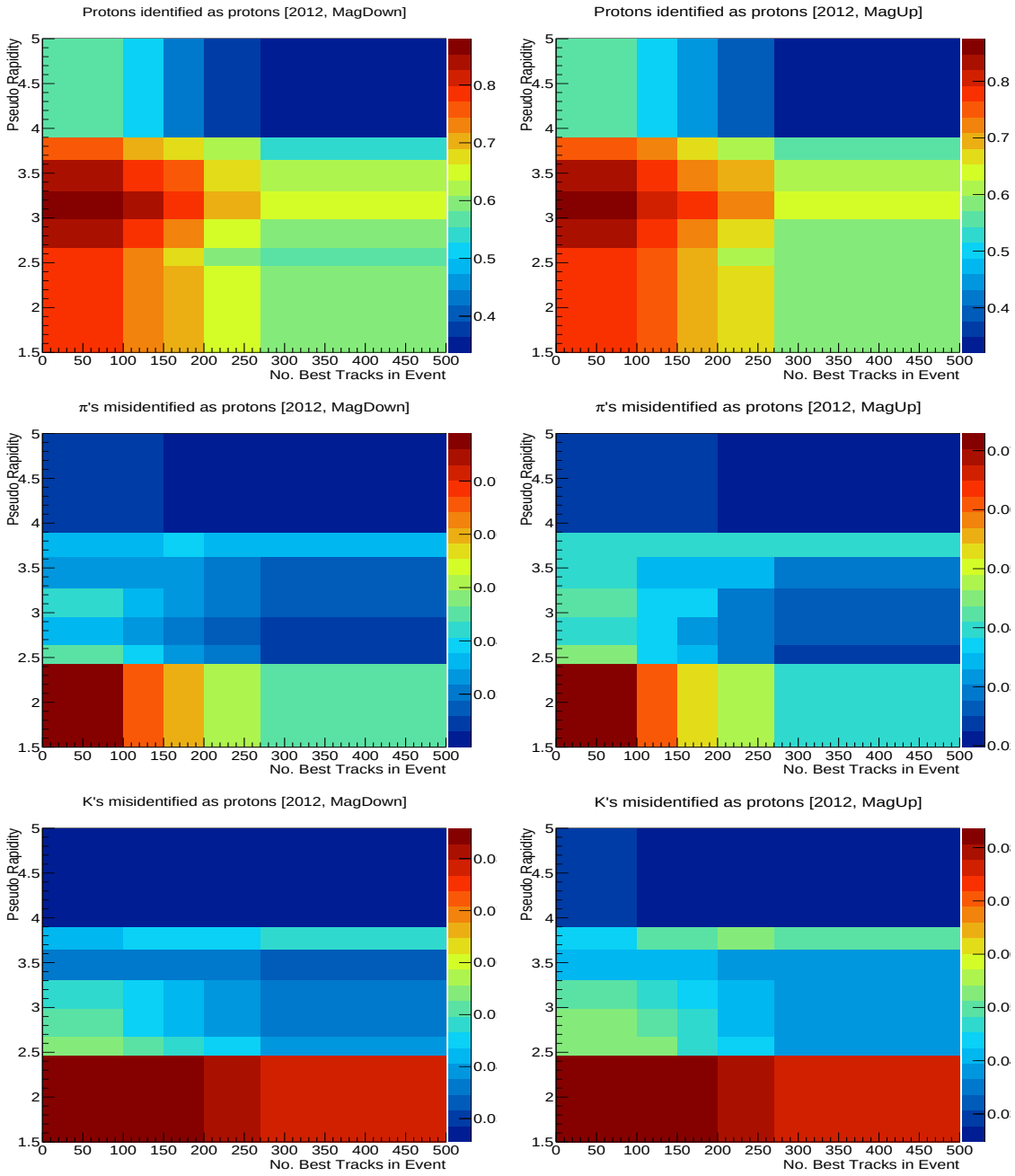

Figure B.8: 2D Projection of three-dimensional efficiency maps of [first-row] protons identified as protons, [second-row] pions misidentified as protons, and [third-row] kaons misidentified as protons for the proton ProbNN$p > 0.50$ cut obtained using the 2012 [first-column] MagDown and [second-column] Mag-Up calibration data. Bins which are poor in term of events and are arbitrarily set to zero in order to avoid division by zero.

B.3 PID K/π (Mis)identification 3D Maps

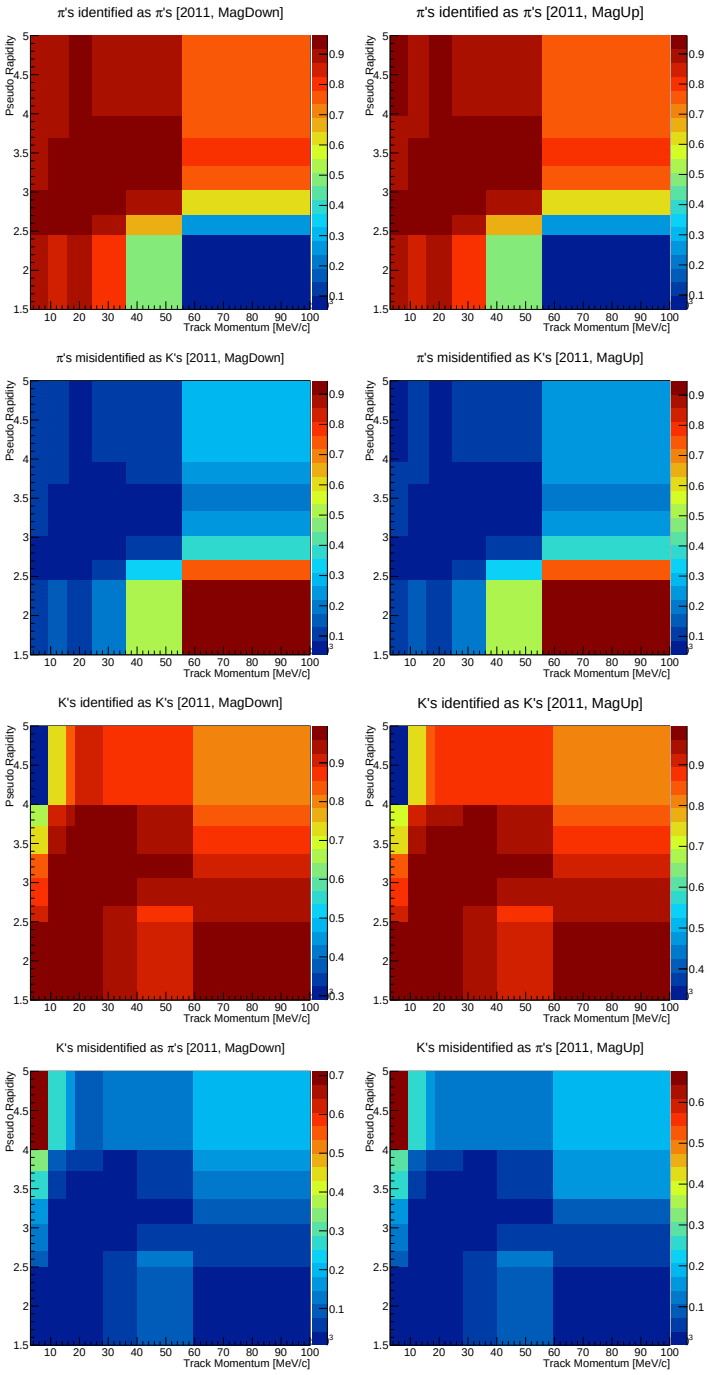

Figure B.9: 2D Projection of three-dimensional efficiency maps of [first-row] pions identified as pions, [second-row] pions misidentified as kaons, [third-row] kaons identified as kaons, and [fourth-row] kaons misidentified as pions for the optimal $\text{PID}_{K\pi}$ cut (0.15,0.15) obtained using the 2011 [first-column] MagDown and [second-column] Mag-Up calibration data. Bins which are poor in term of events and are arbitrarily set to zero in order to avoid division by zero.

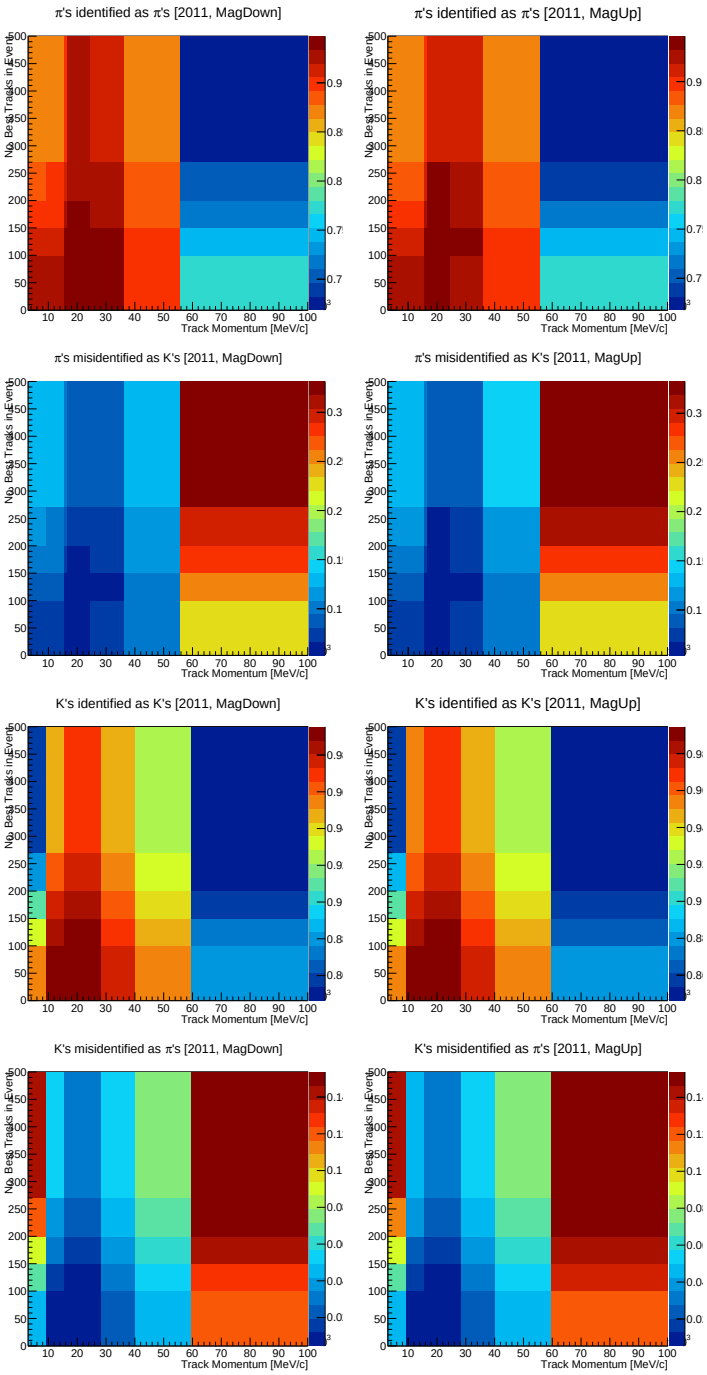

Figure B.10: 2D Projection of three-dimensional efficiency maps of [first-row] pions identified as pions, [second-row] pions misidentified as kaons, [third-row] kaons identified as kaons, and [fourth-row] kaons misidentified as pions for the optimal $\text{PID}_{K\pi}$ cut (0.15,0.15) obtained using the 2011 [first-column] MagDown and [second-column] Mag-Up calibration data. Bins which are poor in term of events and are arbitrarily set to zero in order to avoid division by zero.

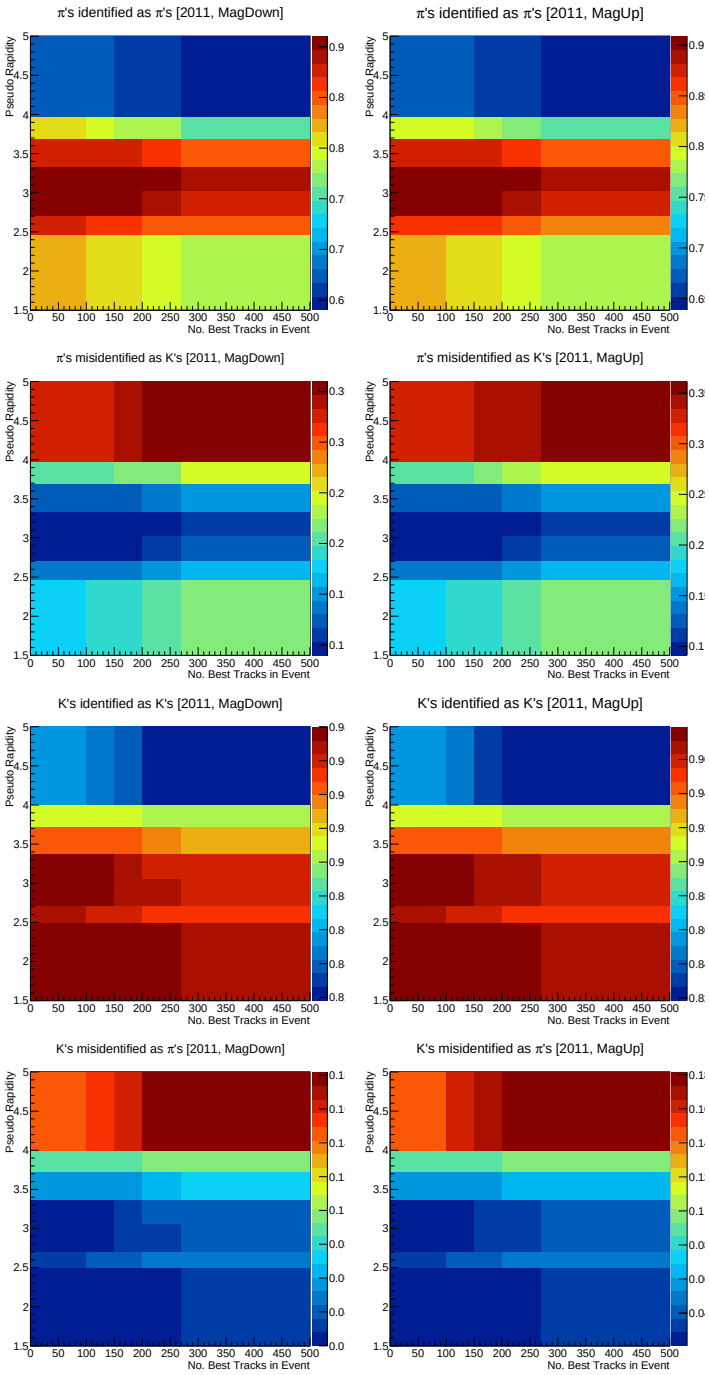

Figure B.11: 2D Projection of three-dimensional efficiency maps of [first-row] pions identified as pions, [second-row] pions misidentified as kaons, [third-row] kaons identified as kaons, and [fourth-row] kaons misidentified as pions for the optimal $\mathrm{PID}_{K\pi}$ cut (0.15,0.15) obtained using the 2011 [first-column] MagDown and [second-column] Mag-Up calibration data. Bins which are poor in term of events and are arbitrarily set to zero in order to avoid division by zero.

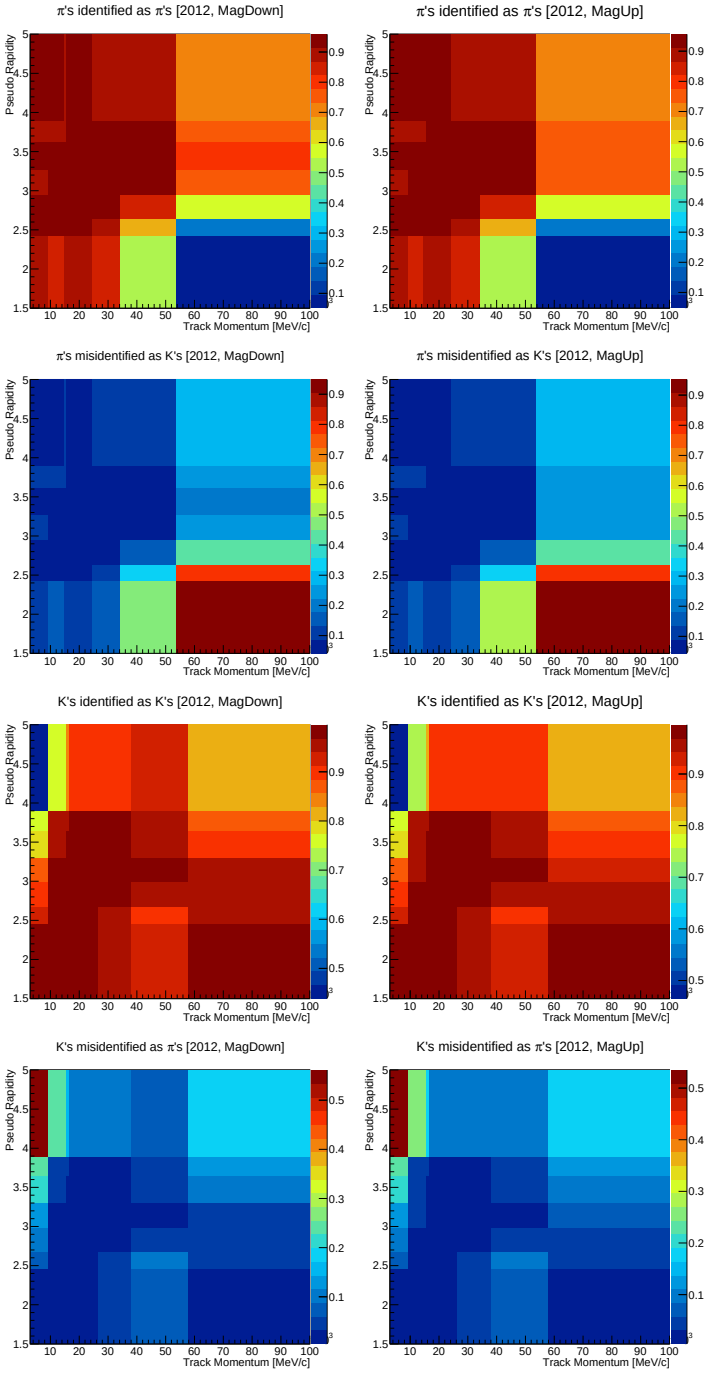

Figure B.12: 2D Projection of three-dimensional efficiency maps of [first-row] pions identified as pions, [second-row] pions misidentified as kaons, [third-row] kaons identified as kaons, and [fourth-row] kaons misidentified as pions for the optimal $\text{PID}_{K\pi}$ cut (0.15,0.15) obtained using the 2012 [first-column] MagDown and [second-column] Mag-Up calibration data. Bins which are poor in term of events and are arbitrarily set to zero in order to avoid division by zero.

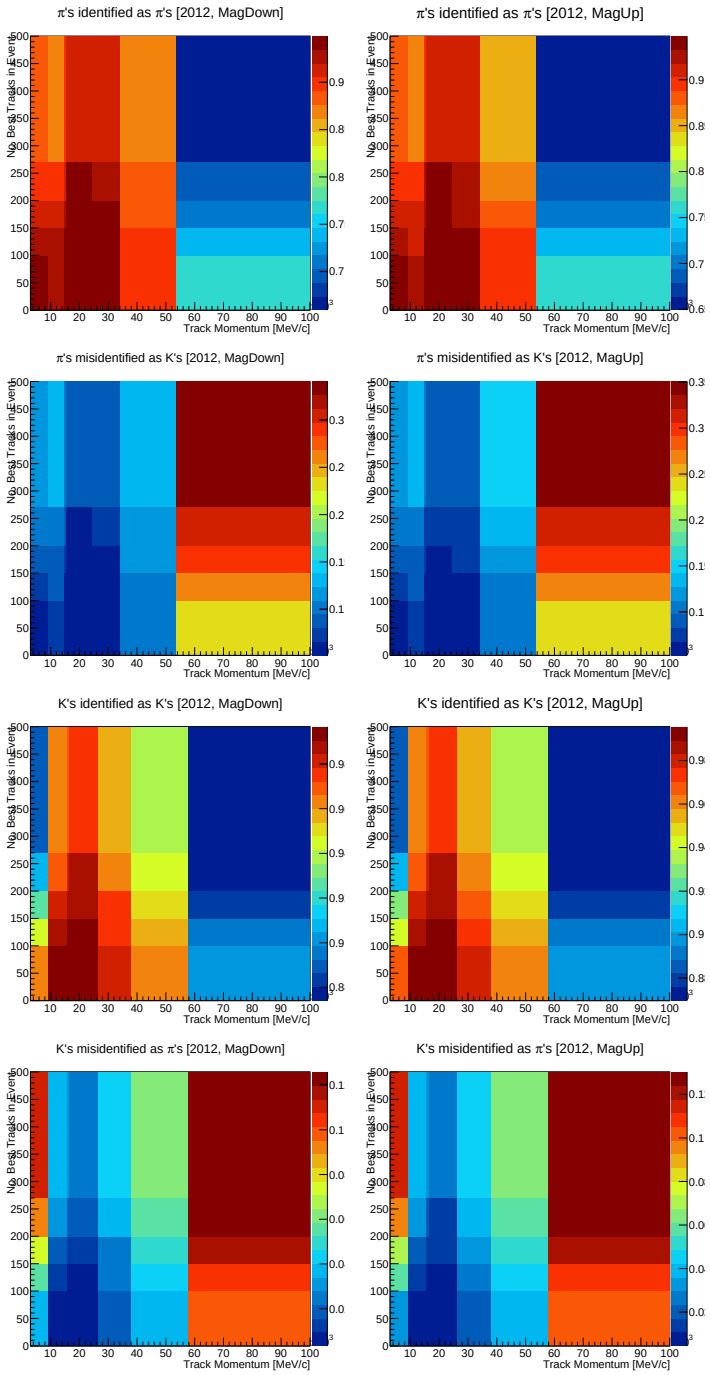

Figure B.13: 2D Projection of three-dimensional efficiency maps of [first-row] pions identified as pions, [second-row] pions misidentified as kaons, [third-row] kaons identified as kaons, and [fourth-row] kaons misidentified as pions for the optimal $\mathrm{PID}_{K\pi}$ cut (0.15,0.15) obtained using the 2012 [first-column] MagDown and [second-column] Mag-Up calibration data. Bins which are poor in term of events and are arbitrarily set to zero in order to avoid division by zero.

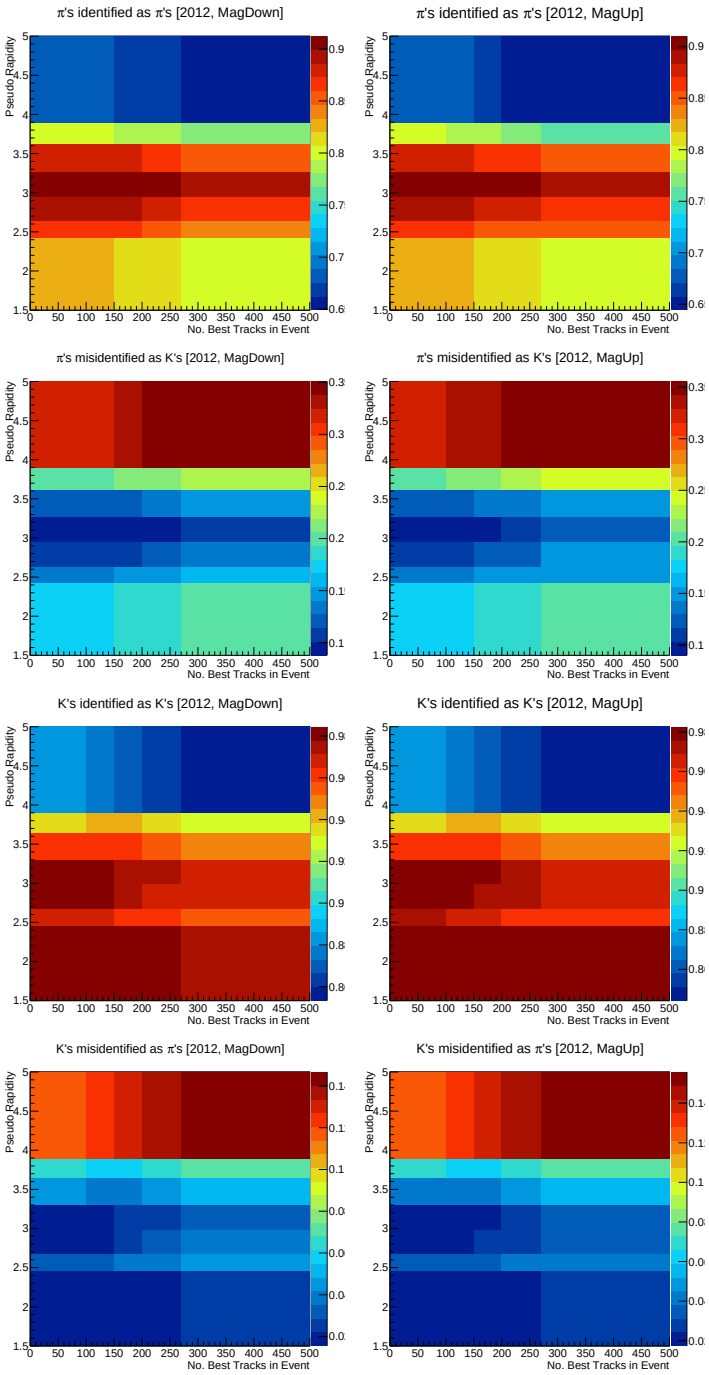

Figure B.14: 2D Projection of three-dimensional efficiency maps of [first-row] pions identified as pions, [second-row] pions misidentified as kaons, [third-row] kaons identified as kaons, and [fourth-row] kaons misidentified as pions for the optimal $\text{PID}_{K\pi}$ cut (0.15,0.15) obtained using the 2012 [first-column] MagDown and [second-column] Mag-Up calibration data. Bins which are poor in term of events and are arbitrarily set to zero in order to avoid division by zero.

B.4 Charmed and charmonia invariant mass vetoes distributions for 2012 dominant modes.

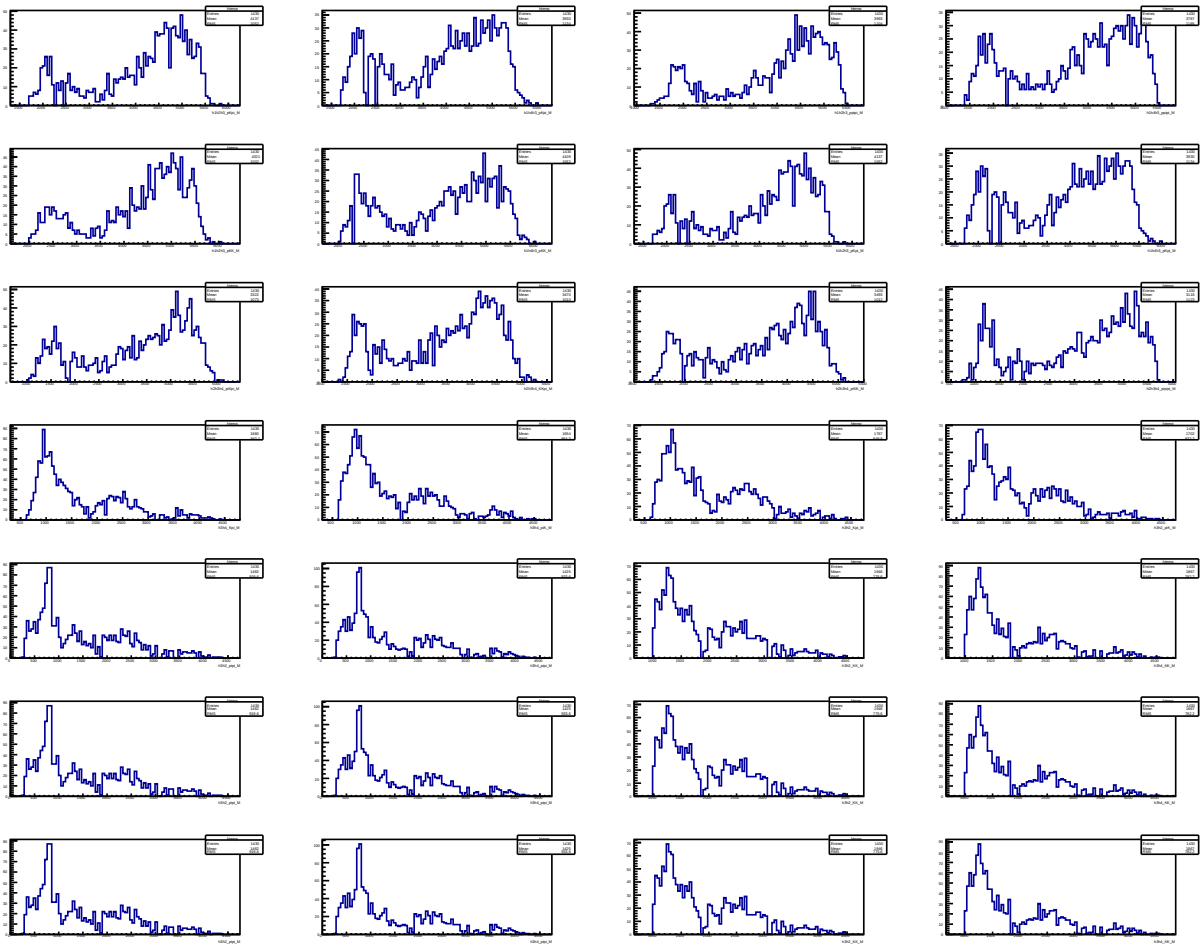

Figure B.15: Charmed and charmonia invariant mass vetoes distributions for $\Lambda_b^0 \to p\pi^-\pi^+\pi^-$ 2012.

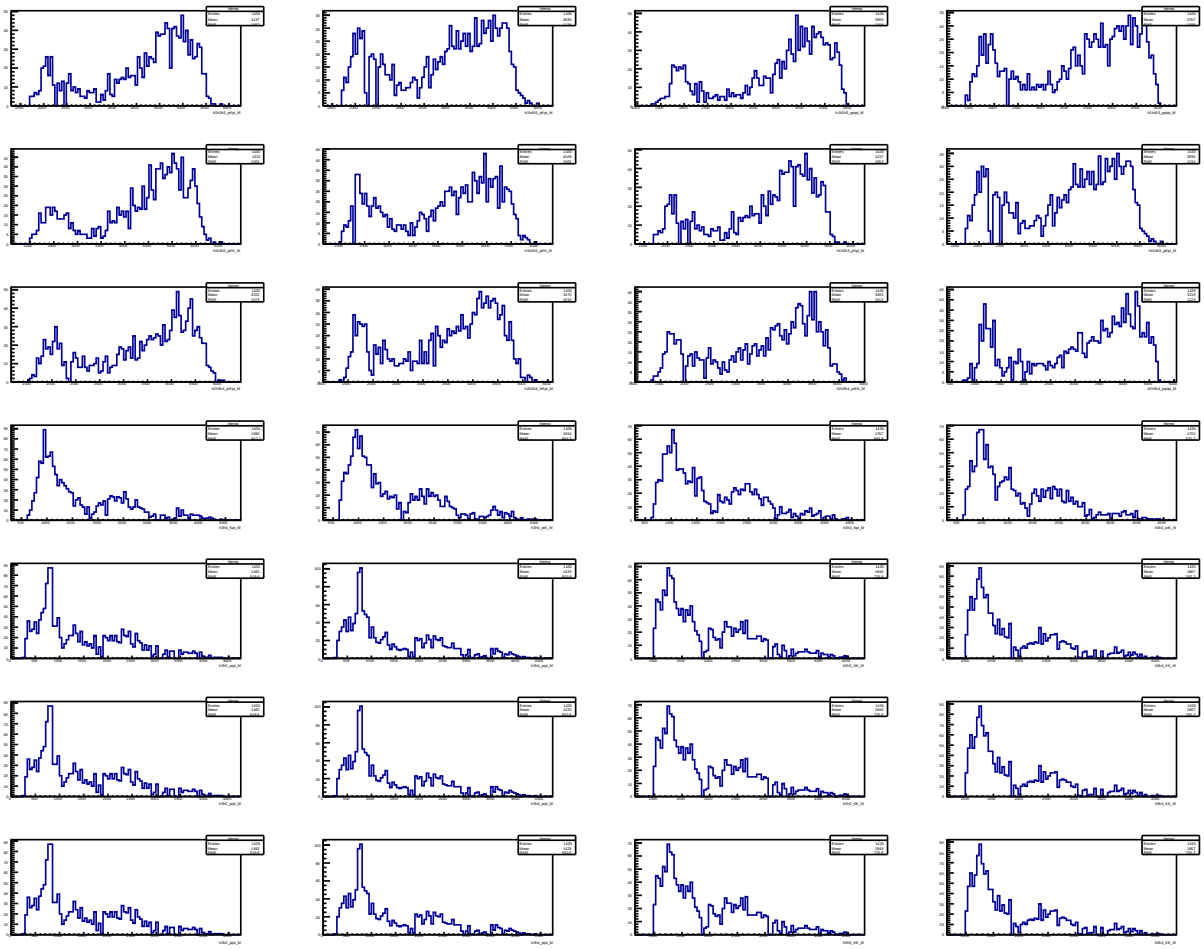

Figure B.16: Charmed and charmonia invariant mass vetoes distributions for $\Lambda_b^0 \to pK^-\pi^+\pi^-$ 2012.

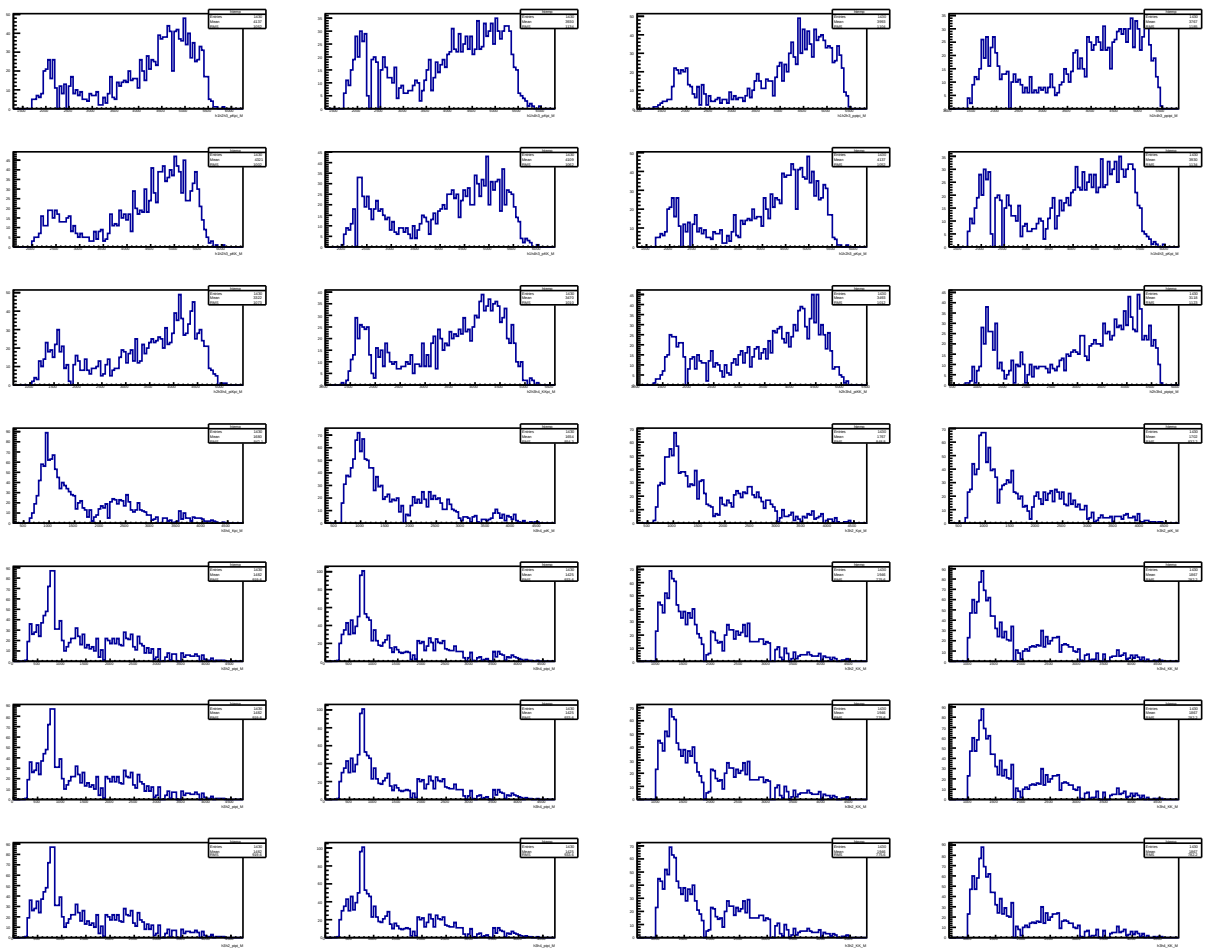

Figure B.17: Charmed and charmonia invariant mass vetoes distributions for $\Lambda_b^0 \to pK^-K^+K^-$ 2012.

Appendix C

Appendix to Chapter 4

C.1 B physics backgrounds from RHSB events of 2011 and 2012 for branching fractions measurement

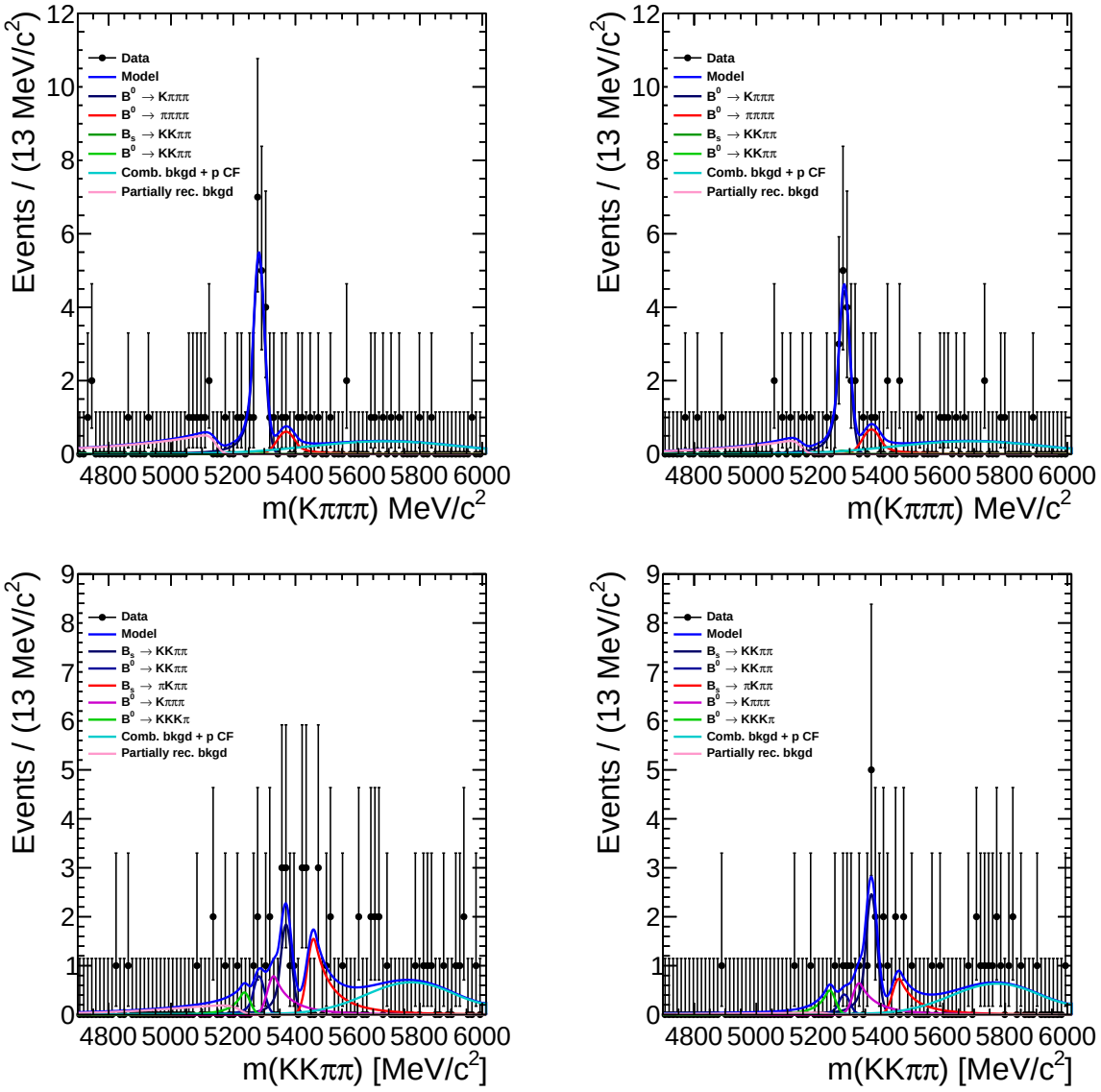

Figure C.1: RHSB selecting L0Global TIS events of 2011 $X_b^0 \to p\pi\pi\pi$ and $X_b^0 \to pK\pi\pi$ spectra reconstructed as $K\pi\pi\pi$ and $KK\pi\pi$, respectively, by selecting a proton (left-column) and an anti-proton (right-column).

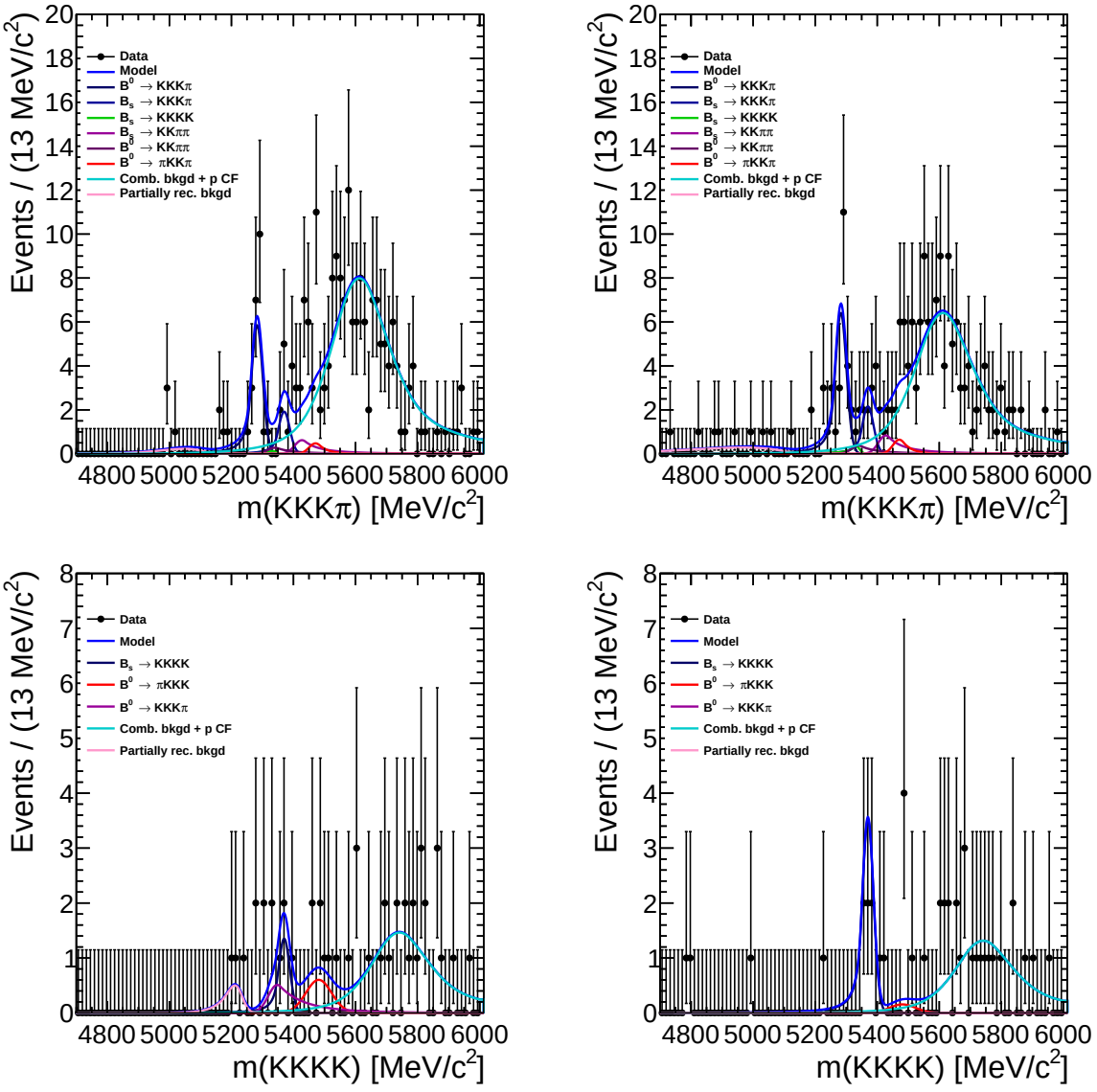

Figure C.2: RHSB selecting L0Global TIS events of 2011 $X_b^0 \to p\pi\pi\pi$ and $X_b^0 \to pK\pi\pi$ spectra reconstructed as $K\pi\pi\pi$ and $KK\pi\pi$, respectively, by selecting a proton (left-column) and an anti-proton (right-column).

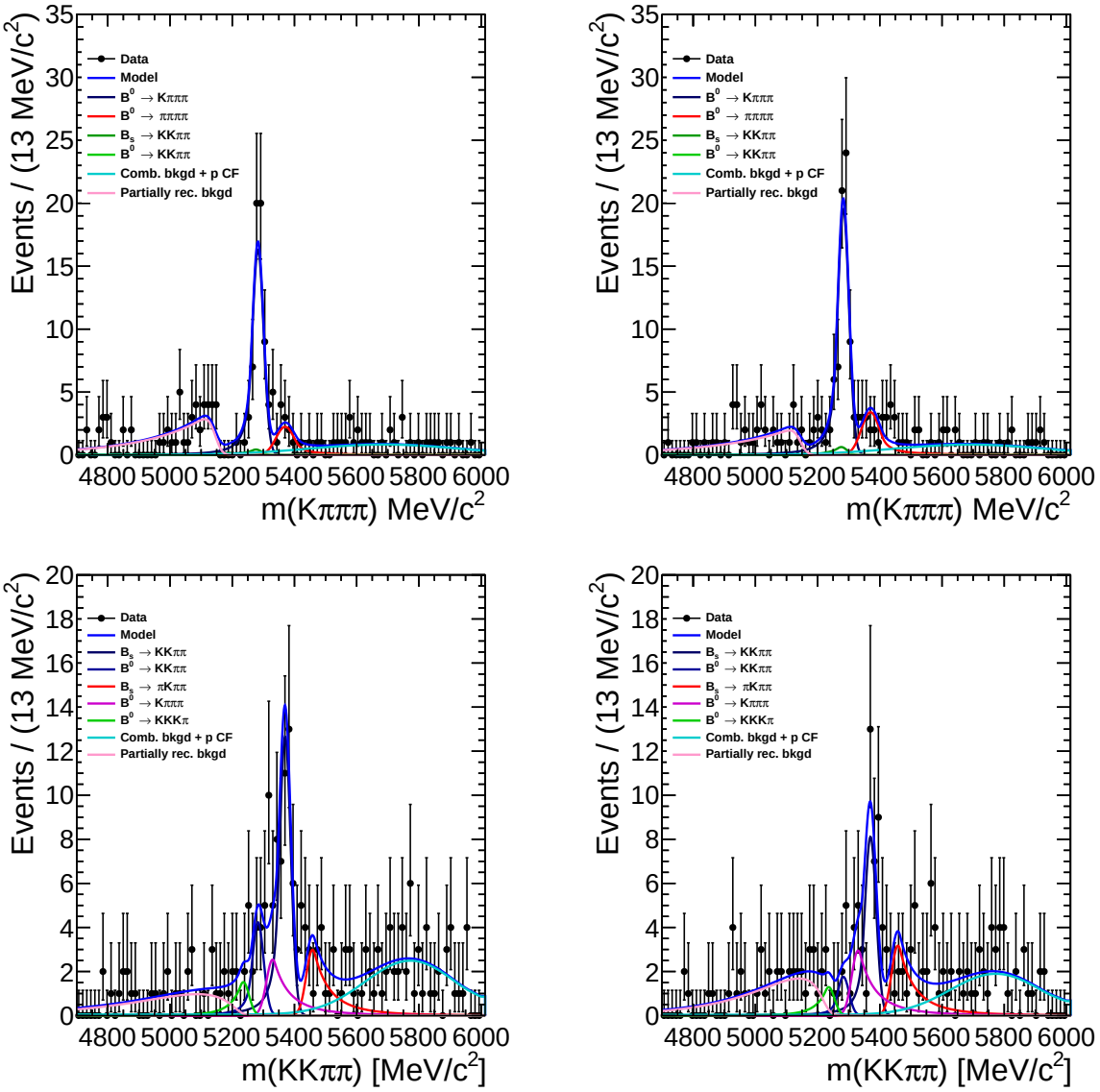

Figure C.3: RHSB events of 2012 $X_b^0 \to p\pi\pi\pi$ and $X_b^0 \to pK\pi\pi$ spectra reconstructed as $K\pi\pi\pi$ and $KK\pi\pi$, respectively, by selecting a proton (left-column) and an anti-proton (right-column), with a milder proton PID cut of ProbNN$p > 0.30$.

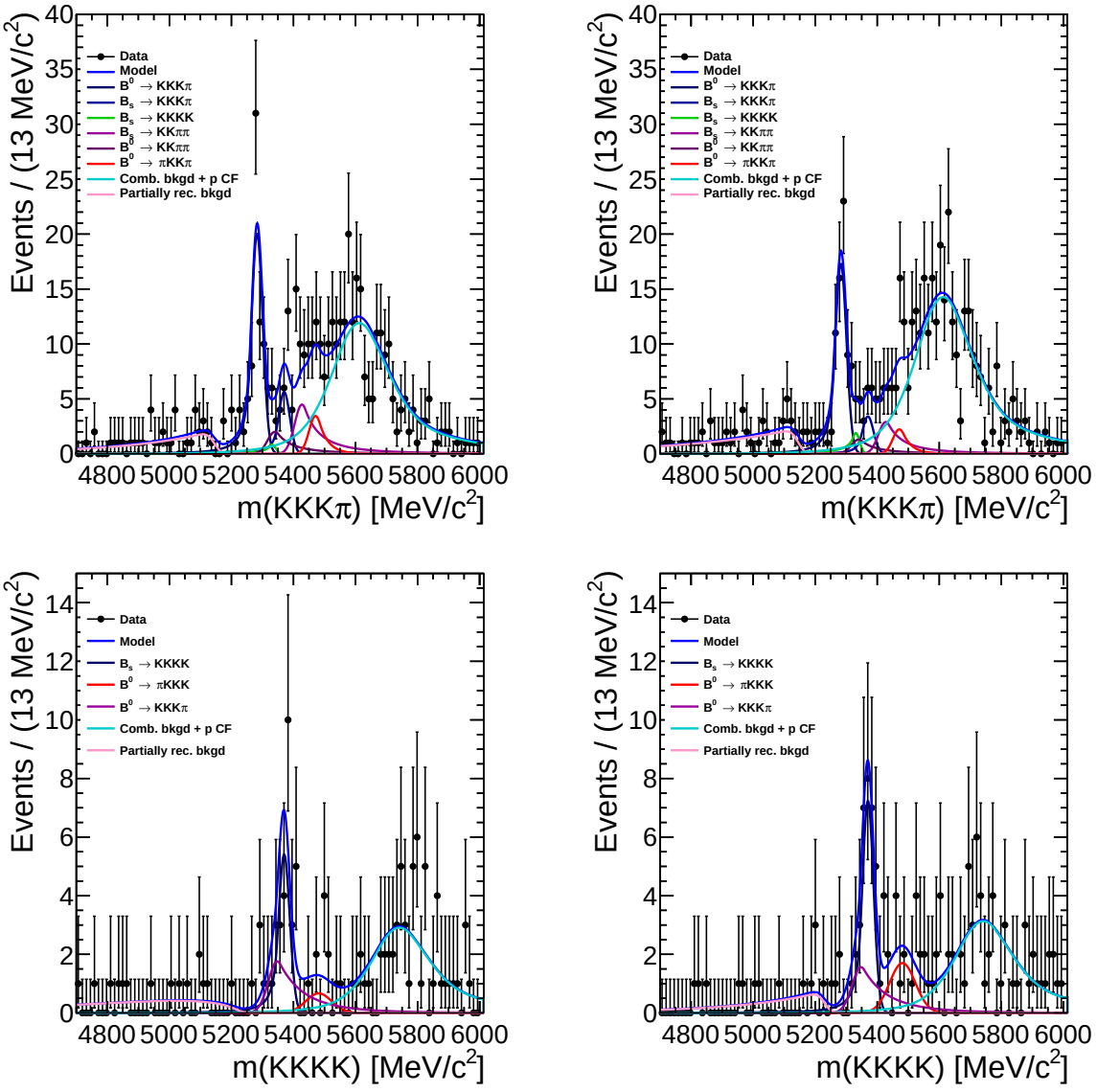

Figure C.4: RHSB events of 2012 $X_b^0 \to pKK\pi$ and $X_b^0 \to pKKK$ spectra reconstructed as $K\pi\pi\pi$ and $KK\pi\pi$, respectively, by selecting a proton (left-column) and an anti-proton (right-column), with a milder proton PID cut of ProbNN$p > 0.30$.

C.2 B physics backgrounds from RHSB events of 2011 and 2012 with a milder proton PID cut

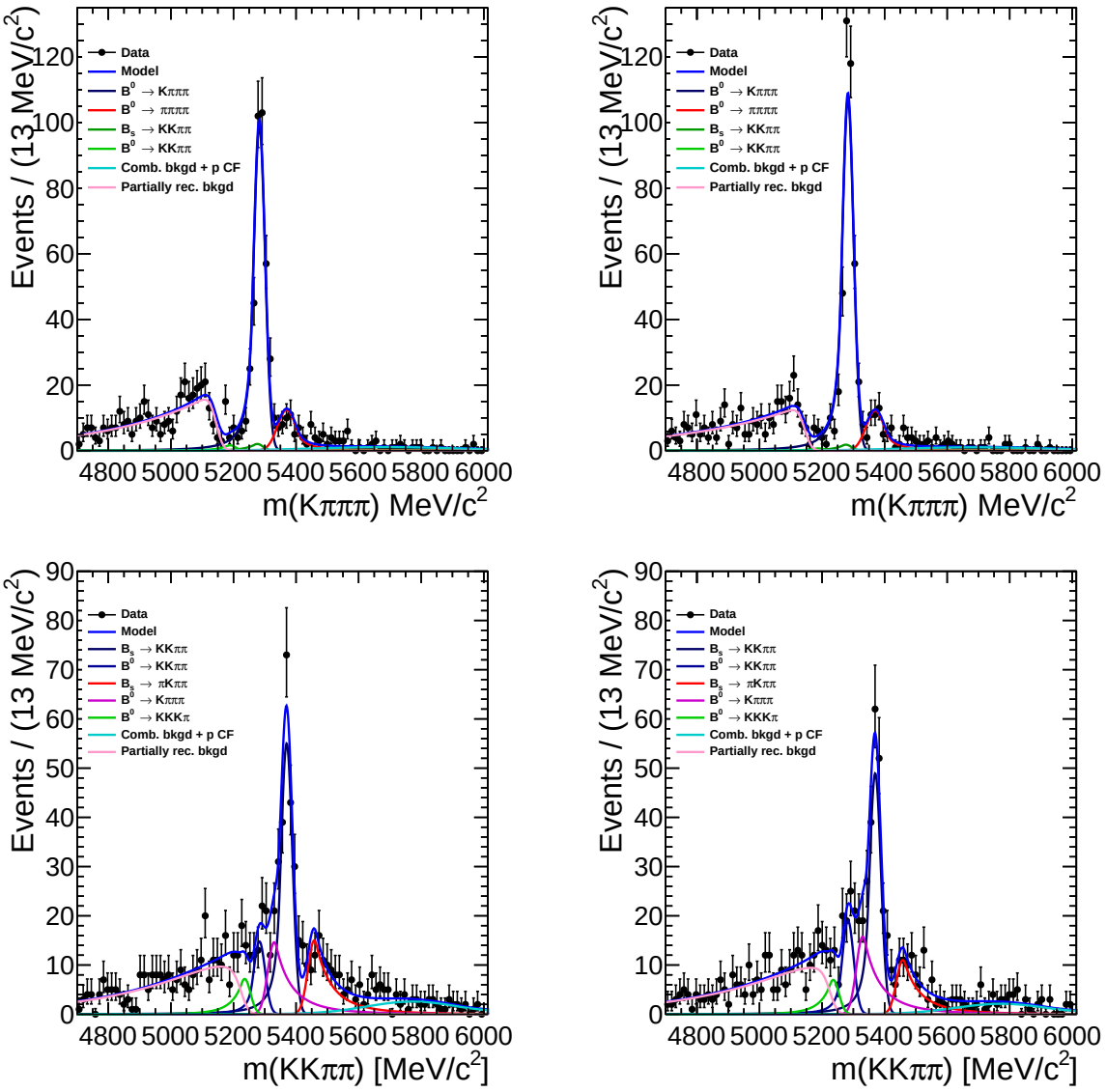

Figure C.5: RHSB events of 2011 $X_b^0 \to p\pi\pi\pi$ and $X_b^0 \to pK\pi\pi$ spectra reconstructed as $K\pi\pi\pi$ and $KK\pi\pi$, respectively, by selecting a proton (left-column) and an anti-proton (right-column), with a milder proton PID cut of ProbNN$p > 0.30$.

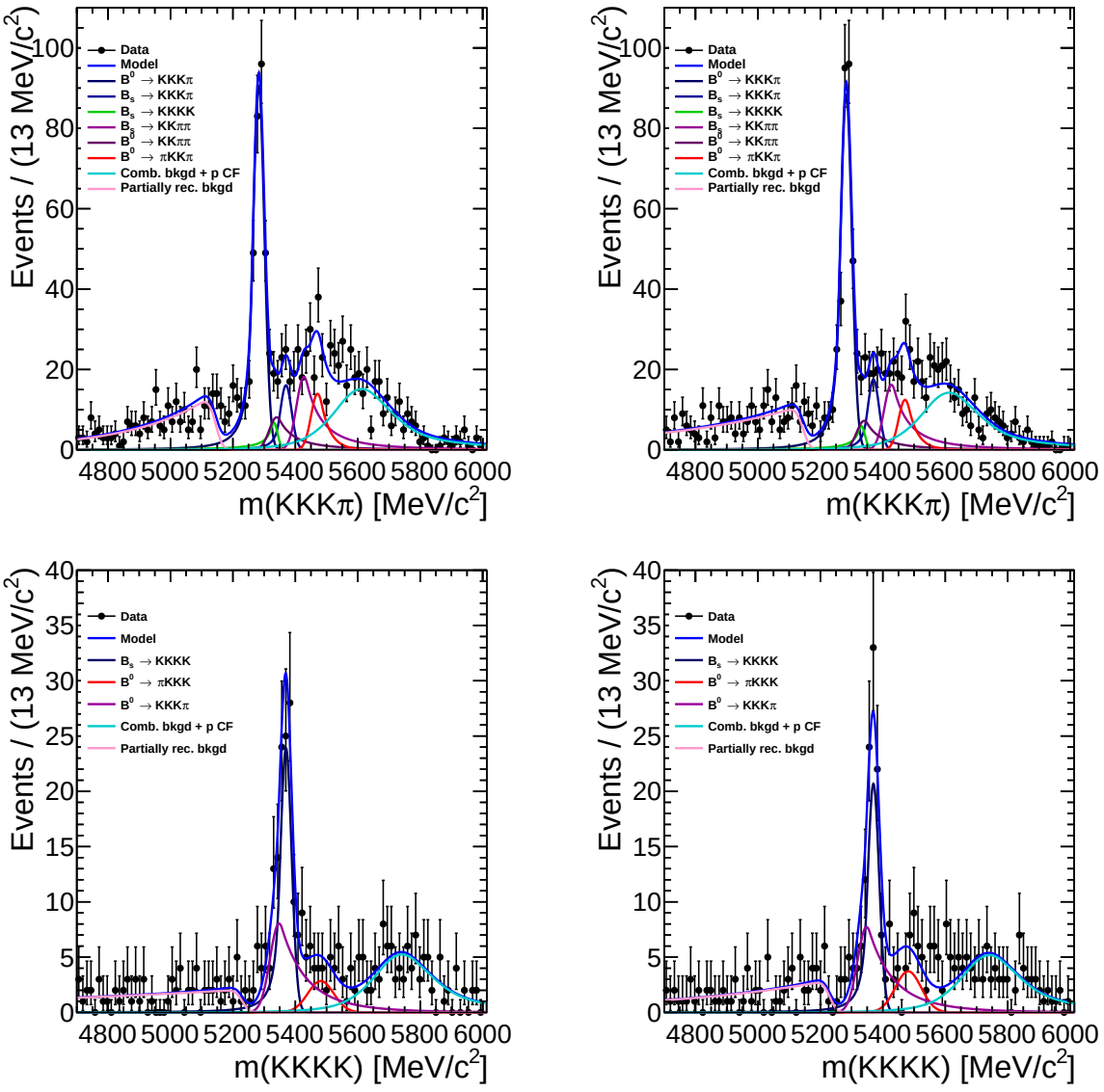

Figure C.6: RHSB events of 2011 $X_b^0 \to pKK\pi$ and $X_b^0 \to pKKK$ spectra reconstructed as $K\pi\pi\pi$ and $KK\pi\pi$, respectively, by selecting a proton (left-column) and an anti-proton (right-column), with a milder proton PID cut of ProbNN$p > 0.30$.

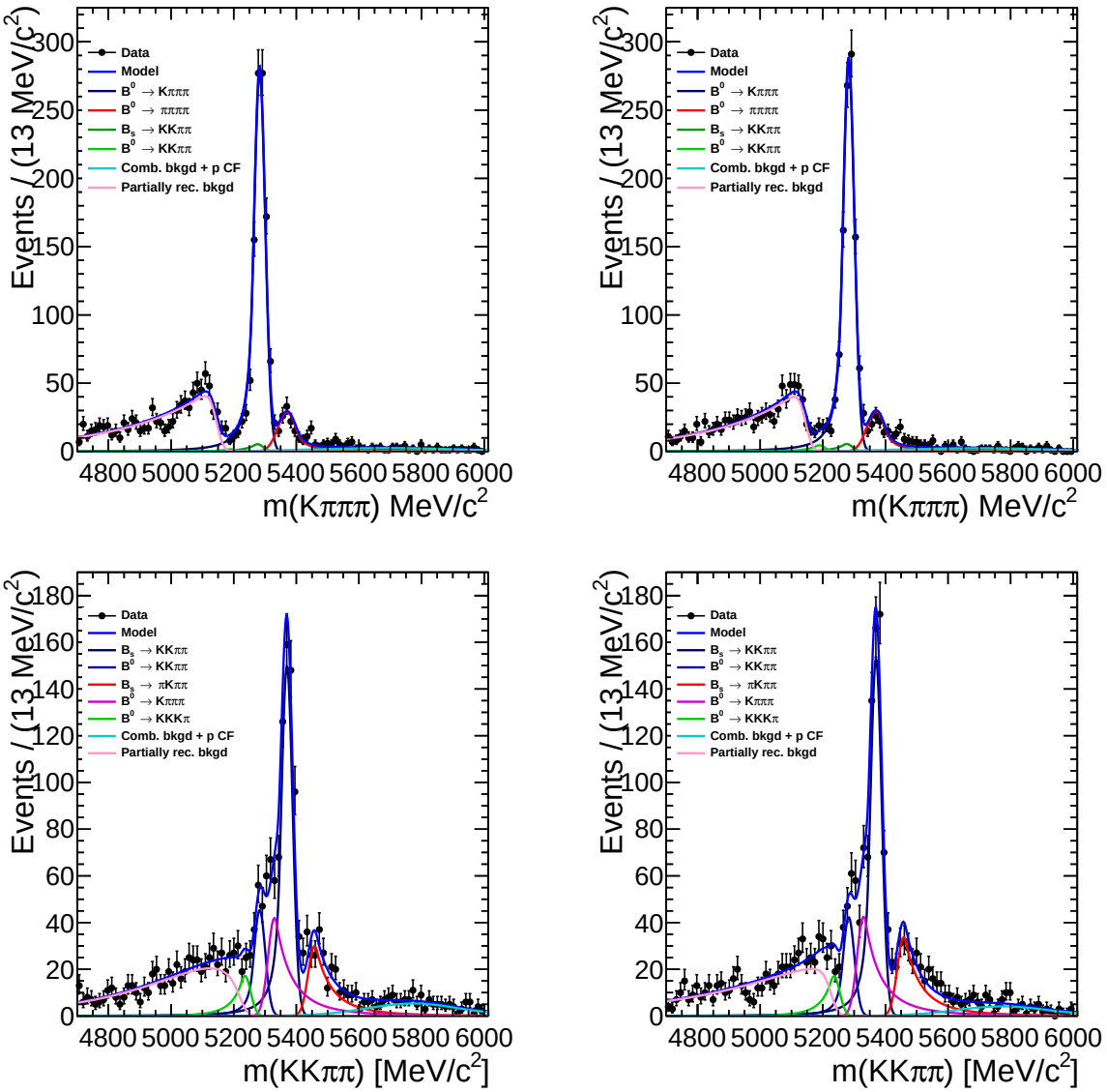

Figure C.7: RHSB events of 2012 $X_b^0 \to p\pi\pi\pi$ and $X_b^0 \to pK\pi\pi$ spectra reconstructed as $K\pi\pi\pi$ and $KK\pi\pi$, respectively, by selecting a proton (left-column) and an anti-proton (right-column), with a milder proton PID cut of ProbNN$p > 0.30$.

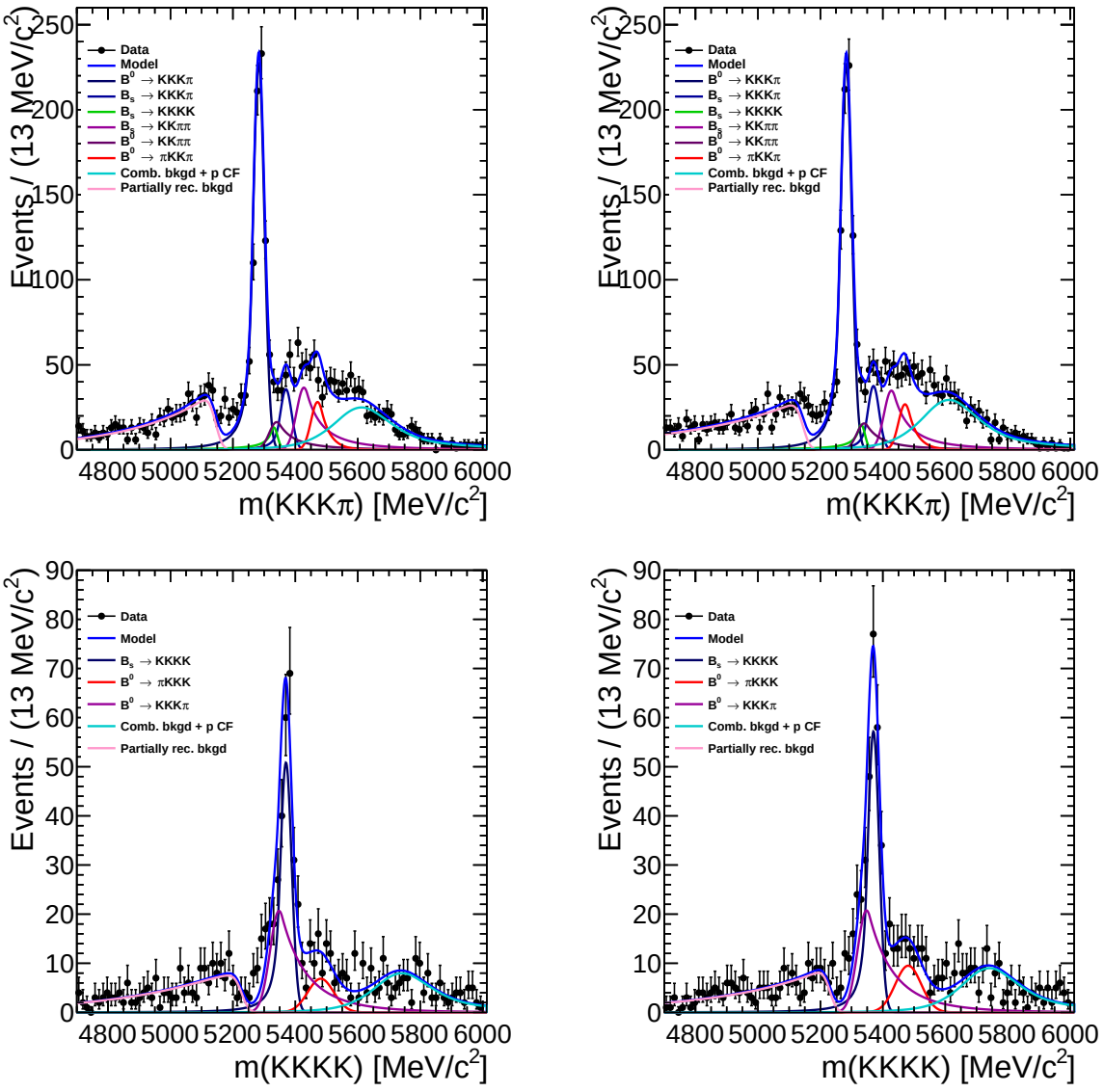

Figure C.8: RHSB events of 2012 $X_b^0 \to pKK\pi$ and $X_b^0 \to pKKK$ spectra reconstructed as $K\pi\pi\pi$ and $KK\pi\pi$, respectively, by selecting a proton (left-column) and an anti-proton (right-column), with a milder proton PID cut of ProbNN$p > 0.30$.

C.3 Shapes for the signals for the $\Delta\mathcal{A}^{CP}$ measurements.

This appendix presents the fit to the signal simulated events. The PDF that is used to model the signal contributions is a double Crystall Ball function. For the reader's convenience, the mathematical description is reminded here.

The double Crystal Ball function (DCB) is, roughly-speaking, a Gaussian with asymmetric tails. It allows to take into account a radiative tail or the imperfections of the tracking, with a left or a right tail, respectively. The mathematical description of a Crystal Ball PDF of variable m is given by:

$$P(m;\alpha,n,\mu,\sigma) = \mathcal{N}\cdot\begin{cases}\exp(-(m-\mu)^2/2\sigma^2), & \text{if } (m-\mu)/\sigma > -\alpha\\ (\frac{n}{|\alpha|})^n\exp(-\alpha^2/2)(\frac{n-\alpha^2}{|\alpha|}-\frac{m-\mu}{\sigma})^{-n}, & \text{if } (m-\mu)/\sigma \leq -\alpha\ ,\end{cases} \tag{C.1}$$

where $\mathcal{N}$ is the normalization and m is the invariant mass. The turnover point and the tail parameter are denoted α and n, respectively. This PDF is used in order to model the signal contributions.

Table C.1 summarizes the values of the parameters of the fit. The fit results are displayed in Fig. C.9 and C.10.

Table C.1: Fit parameters obtained in the fit to signal shape for the $\Delta\mathcal{A}^{CP}$ measurements.

Year	Fit parameters						
	μ	α_1	α_2/α_1	n_1	n_2/n_1	f_2	σ/σ_{ref}
$\Lambda_b^0 \to p\pi\pi\pi$:							
2011	5620.739±0.256	1.390±0.322	-1.447±0.495	1.589±0.171	1.195±0.215	0.516±0.219	1.043±0.019
2012	5620.651±0.185	1.150±0.260	-1.863±0.483	1.686±0.172	1.068±0.142	0.364±0.113	1.058±0.016
$\Lambda_b^0 \to pK\pi\pi$:							
2011	5620.773±0.195	1.725±0.115	-0.895±0.185	1.494±0.101	1.684±0.253	0.704±0.120	0.997±0.016
2012	5620.875±0.157	1.341±0.201	-1.542±0.285	1.522±0.111	1.250±0.140	0.372±0.099	$\sigma_{ref.} = 14.224 \pm 0.141$
$\Lambda_b^0 \to pKK\pi$:							
2011	5621.150±0.196	1.245±0.282	-1.639±0.463	1.858±0.205	1.297±0.246	0.317±0.124	0.959±0.016
2012	5621.007±0.145	1.301±0.173	-1.535±0.246	1.673±0.120	1.319±0.144	0.327±0.077	0.957±0.013
$\Lambda_b^0 \to pKKK$:							
2011	5620.902±0.156	1.477±0.246	-1.344±0.272	1.791±0.176	1.429±0.203	0.301±0.113	0.908±0.014
2012	5621.012±0.121	1.309±0.233	-1.634±0.326	1.923±0.180	1.096±0.136	0.219±0.073	0.913±0.012
$\Xi_b^0 \to pK\pi\pi$:							
2011	5789.366±0.202	1.069±0.254	-1.816±0.489	1.713±0.168	1.487±0.245	0.280±0.086	1.035±0.017
2012	5789.623±0.166	1.194±0.302	-1.808±0.539	1.718±0.167	1.107±0.179	0.333±0.128	1.037±0.014
$\Xi_b^0 \to pK\pi K$:							
2011	5789.359±0.188	1.300±0.235	-1.448±0.333	1.831±0.159	1.306±0.205	0.327±0.109	0.995±0.016
2012	5789.604±0.145	1.016±0.293	-2.096±0.667	1.993±0.238	1.088±0.184	0.236±0.087	0.992±0.013
$\Xi_b^0 \to pKKK$:							
2011	5789.544±0.151	1.698±0.181	-1.119±0.195	1.748±0.120	1.340±0.186	0.465±0.144	0.930±0.014
2012	5789.460±0.139	1.821±0.219	-0.966±0.298	1.790±0.107	1.370±0.245	0.574±0.229	0.941±0.012

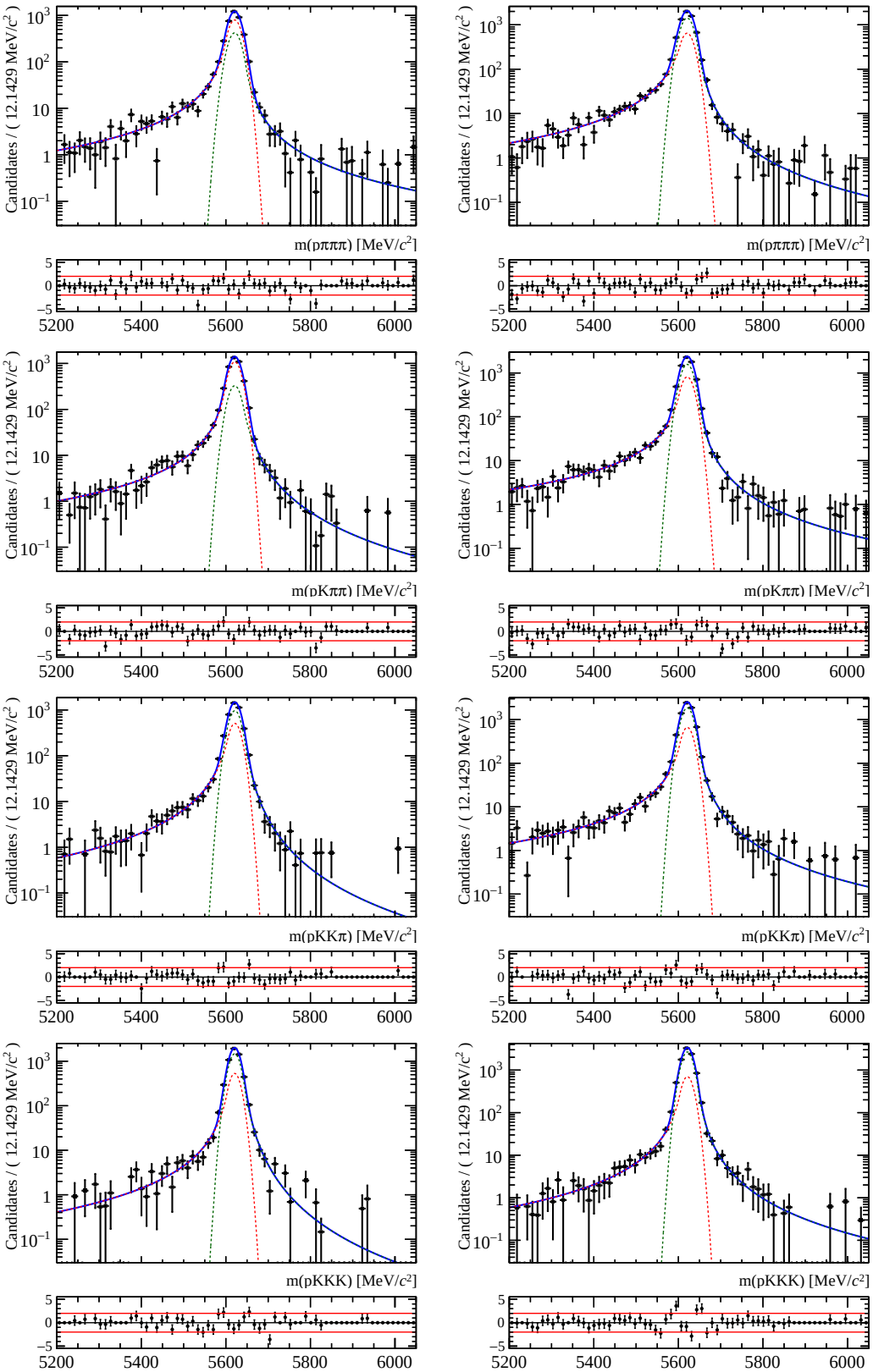

Figure C.9: Signal invariant mass distribution fitted with DCB PDF for the modes (in order from top to bottom) $\Lambda_b^0 \to p\pi\pi\pi$, $\Lambda_b^0 \to pK\pi\pi$, $\Lambda_b^0 \to pKK\pi$ and $\Lambda_b^0 \to pK^-K^+K^-$ for years (left column) 2011 and (right column) 2012.

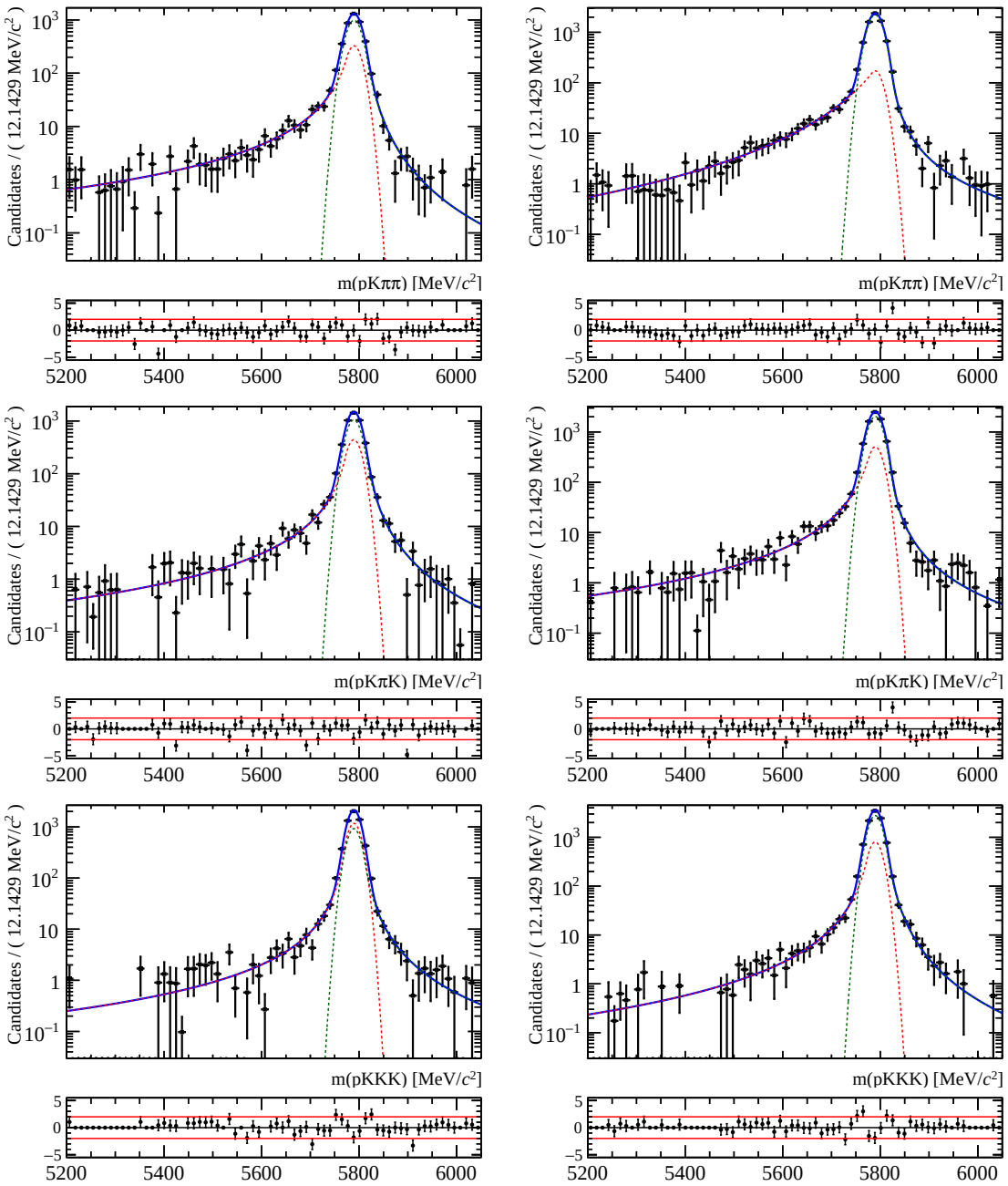

Figure C.10: Signal invariant mass distribution fitted with DCB PDF for the modes (in order from top to bottom) $\Xi_b^0 \to pK\pi\pi$, $\Xi_b^0 \to pK\pi K$ and $\Xi_b^0 \to pKKK$ for years (left column) 2011 and (right column) 2012.

C.4 Shapes of the signal-crossfeeds for the $\Delta\mathcal{A}^{CP}$ measurements and cross-feed factors.

This appendix presents the fit to the signal cross-feed simulated events. The PDF that is used to model the signal cross-feed contributions is (as for the signal) a double Crystall Ball function.

This PDF is used in order to model signal cross-feed contributions (composed of true signal events appearing in an other spectrum because of a misidentification of a pion or a kaon). Table C.2 summarizes the values of the parameters of the fit. The fit results are displayed in Fig. C.11 to C.13 for the fit to the 2012 simulated sample.

We remind here that the yield of a cross-feed is constrained to the corresponding signal yield in its respective spectrum by a relevant misidentification efficiency f. These factors are calculated by taking the ratios of selection efficiencies and PID efficiencies as a cross-feed and as a signal. PID efficiencies are measured in simulated events properly reweighted to match the identification performance as measured in calibration data .

This f factor is given by:

$$f = \frac{\epsilon^{\text{Sel.}}_{\text{CF}} \cdot \epsilon^{\text{PID}}_{\text{CF}}}{\epsilon^{\text{Sel.}}_{\text{Sig.}} \cdot \epsilon^{\text{PID}}_{\text{Sig.}}} \tag{C.2}$$

where $\epsilon^{\text{PID}}_{\text{CF}}$ and $\epsilon^{\text{PID}}_{\text{Sig.}}$ are the average efficiencies of misidentifying the candidates as cross-feed and identifying as signal, respectively, while the $\epsilon^{\text{Sel.}}_{\text{CF}}$ and $\epsilon^{\text{Sel.}}_{\text{Sig.}}$ are the average efficiencies in selecting the candidates as cross-feed or signal, respectively. The $\epsilon^{\text{Sel.}}_{\text{CF}}$ and $\epsilon^{\text{Sel.}}_{\text{Sig.}}$ includes the BDT selection efficiency and the mass window cut. The values of the factors are reported in Table C.3.

Table C.2: Fit parameters obtained in the fit to crossfeeds shapes. The number of digits is automatically defined to be three in order to ensure in all cases the presence of at least two significant digits.

Cross-feed	Year	Fit parameters							
		α_1	α_2/α_1	n_1	n_2/n_1	σ_1	σ_1/σ_2	μ	f_2
$\Lambda_b^0 \to p\pi\pi\pi$ as $pK\pi\pi$	2011	0.542±0.036	-1.047±0.077	2.373±0.237	1.024±0.115	18.939±1.138	1.037±0.066	5672.265±1.271	0.133±0.021
	2012	0.709±0.036	-0.886±0.052	3.111±0.228	0.673±0.054	21.544±0.965	0.912±0.046	5672.266±0.929	0.160±0.020
$\Lambda_b^0 \to p\pi\pi\pi$ as $pKK\pi$	2011	1.186±0.075	-0.240±0.027	0.952±0.148	3.732±0.236	11.563±0.344	2.316±0.088	5750.946±4.085	0.073±0.009
	2012	0.610±0.054	-0.311±0.030	3.960±0.289	1.019±0.136	30.055±1.016	0.627±0.052	5738.252±3.620	0.075±0.009
$\Lambda_b^0 \to p\pi\pi\pi$ as $pK\pi K$	2011	0.160±0.027	-0.987±0.051	1.704±0.252	15.000±0.005	10.158±0.112	2.497±0.089	5760.708±2.588	0.055±0.008
	2012	0.255±0.033	-0.534±0.040	4.909±0.403	14.994±0.010	11.412±0.328	1.902±0.085	5758.644±2.497	0.080±0.010
$\Lambda_b^0 \to pK\pi\pi$ as $p\pi\pi\pi$	2011	0.226±0.025	-10.193±2.499	5.863±2.358	0.302±0.255	22.636±1.808	0.964±0.225	5563.744±2.582	0.862±0.055
	2012	0.177±0.014	-12.602±2.579	29.686±15.686	0.059±0.037	19.640±1.273	1.099±0.227	5566.359±1.999	0.849±0.044
$\Lambda_b^0 \to pK\pi\pi$ as $pKK\pi$	2011	1.594±0.096	-0.104±0.008	1.771±0.307	11.946±9.783	25.300±1.460	0.643±0.050	5672.358±1.579	0.264±0.033
	2012	1.418±0.068	-0.174±0.011	1.476±0.163	4.189±1.075	20.824±0.958	0.924±0.055	5673.921±1.148	0.246±0.026
$\Lambda_b^0 \to pK\pi\pi$ as $pK\pi K$	2011	0.461±0.033	-0.417±0.032	5.480±1.417	1.084±0.322	29.194±1.895	0.509±0.033	5668.500±1.570	0.072±0.015
	2012	1.194±0.067	-0.220±0.015	1.813±0.238	2.380±0.446	26.864±1.362	0.683±0.040	5674.278±1.330	0.159±0.023
$\Lambda_b^0 \to pK\pi\pi$ as $pKKK$	2011	0.354±0.042	-0.319±0.032	6.859±0.345	14.997±0.008	17.177±0.700	1.065±0.070	5741.420±4.355	0.048±0.008
	2012	1.451±0.081	-0.046±0.009	1.800±0.207	14.998±0.006	49.481±1.034	0.209±0.028	5735.995±3.470	0.084±0.010
$\Lambda_b^0 \to pKK\pi$ as $pK\pi\pi$	2011	0.437±0.056	-2.303±1.041	1.580±0.240	4.606±0.922	18.940±1.575	0.784±0.328	5569.561±2.002	0.933±0.048
	2012	0.158±0.013	-13.756±2.160	12.237±4.798	0.170±0.076	17.535±1.110	1.183±0.129	5569.358±1.556	0.707±0.038
$\Lambda_b^0 \to pKK\pi$ as $pKKK$	2011	0.495±0.035	-0.465±0.036	3.148±0.581	1.446±0.325	14.735±0.957	1.085±0.072	5671.982±1.483	0.078±0.018
	2012	0.525±0.029	-0.614±0.036	2.893±0.345	1.218±0.160	19.325±0.906	0.930±0.044	5673.213±1.141	0.067±0.012
$\Lambda_b^0 \to pKKK$ as $pKK\pi$	2011	0.153±0.012	-17.586±4.446	76.644±35.294	0.014±0.011	22.130±1.419	0.586±0.210	5562.391±2.006	0.923±0.031
	2012	0.129±0.007	-10.908±2.447	73.338±36.544	0.057±0.032	18.090±0.988	0.893±0.172	5565.051±1.561	0.890±0.027
$\Lambda_b^0 \to pKKK$ as $pK\pi K$	2011	0.116±0.011	-14.342±3.132	59.641±21.232	0.073±0.050	15.945±1.273	1.292±0.192	5564.078±2.000	0.775±0.040
	2012	0.143±0.011	-14.852±3.022	33.111±11.295	0.083±0.050	17.762±1.059	1.117±0.153	5563.235±1.580	0.795±0.035
$\Xi_b^0 \to pK\pi\pi$ as $p\pi\pi\pi$	2011	0.195±0.016	-8.116±2.524	87.822±29.151	0.045±0.040	21.623±1.605	0.936±0.239	5735.476±2.538	0.839±0.053
	2012	0.217±0.017	-10.001±1.951	9.743±3.497	0.189±0.116	20.587±1.255	0.985±0.178	5736.907±1.887	0.830±0.045
$\Xi_b^0 \to pK\pi\pi$ as $pKK\pi$	2011	0.153±0.013	-2.959±0.182	18.700±2.663	0.125±0.029	14.975±1.018	1.485±0.101	5842.716±1.707	0.066±0.014
	2012	0.665±0.046	-0.560±0.044	3.440±0.505	0.761±0.140	25.715±1.395	0.693±0.039	5839.131±1.183	0.110±0.018
$\Xi_b^0 \to pK\pi\pi$ as $pK\pi K$	2011	0.208±0.019	-2.321±0.230	19.982±2.150	0.105±0.023	18.334±1.336	1.222±0.089	5844.720±1.756	0.070±0.016
	2012	0.409±0.028	-0.983±0.074	5.931±1.222	0.537±0.121	25.665±1.310	0.793±0.041	5841.368±1.274	0.064±0.013
$\Xi_b^0 \to pK\pi K$ as $pK\pi\pi$	2011	0.157±0.011	-13.145±3.573	108.026±0.008	0.018±0.023	21.417±1.428	0.858±2.838	5740.040±6.016	0.842±0.094
	2012	0.154±0.009	-11.842±1.740	30.902±13.780	0.100±0.014	20.010±0.579	0.922±0.094	5739.345±1.498	0.816±0.031
$\Xi_b^0 \to pK\pi K$ as $pKKK$	2011	0.141±0.013	-2.493±0.226	18.912±2.769	0.167±0.048	15.537±0.976	1.302±0.081	5841.439±1.630	0.031±0.009
	2012	0.543±0.035	-0.708±0.053	4.067±0.624	0.768±0.162	16.299±0.813	1.209±0.065	5842.949±1.128	0.124±0.020

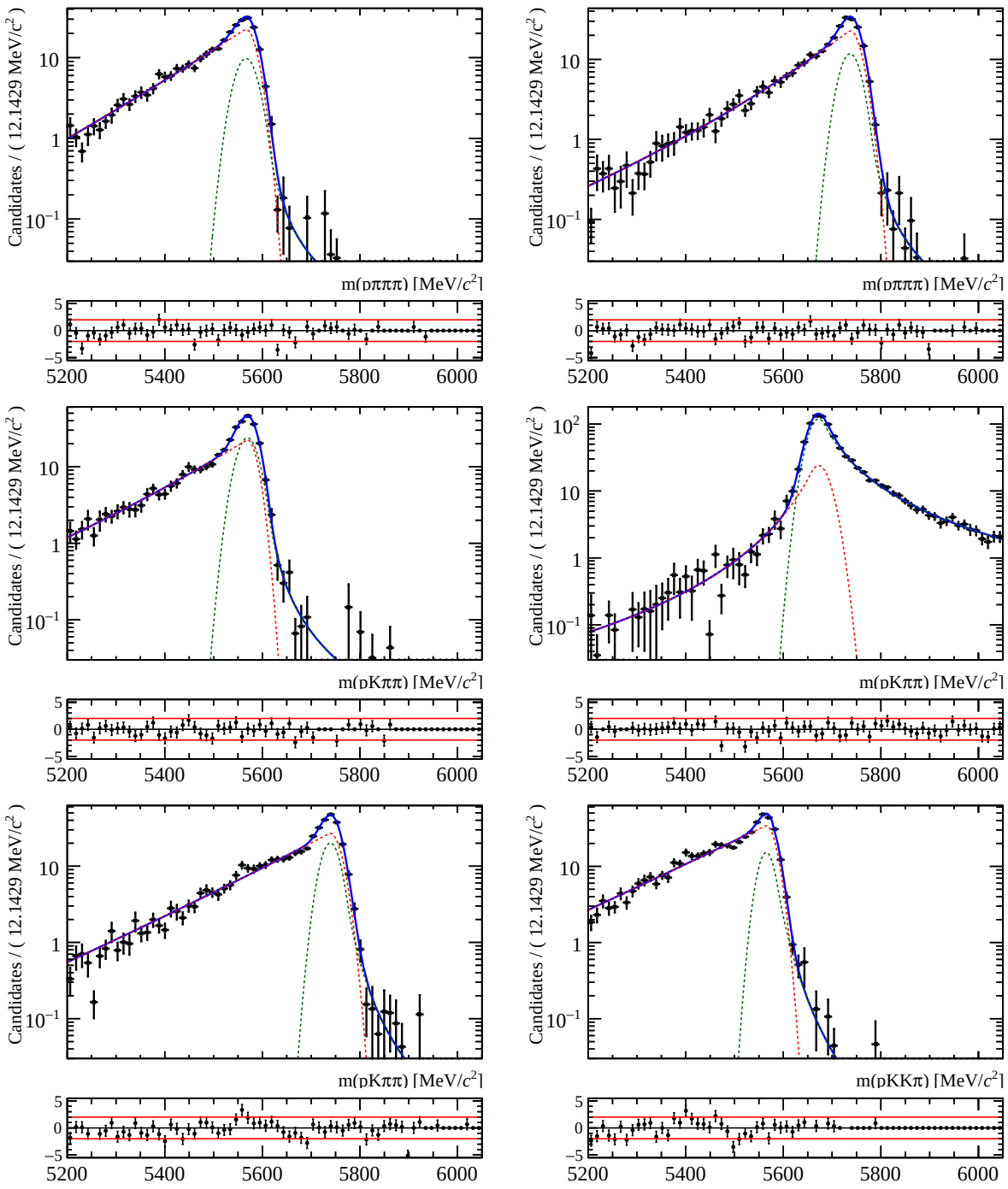

Figure C.11: Signal cross-feeds invariant mass distributions fitted with DCB PDF for the modes (in order from top to bottom) $\Lambda_b^0 \to pK\pi\pi$ as $p\pi\pi\pi$, $\Xi_b^0 \to pK\pi\pi$ as $p\pi\pi\pi$, $\Lambda_b^0 \to pKK\pi$ as $pK\pi\pi$, $\Lambda_b^0 \to p\pi\pi\pi$ as $pK\pi\pi$, $\Xi_b^0 \to pK\pi K$ as $pK\pi\pi$ and $\Lambda_b^0 \to pKKK$ as $pKK\pi$ for years 2012.

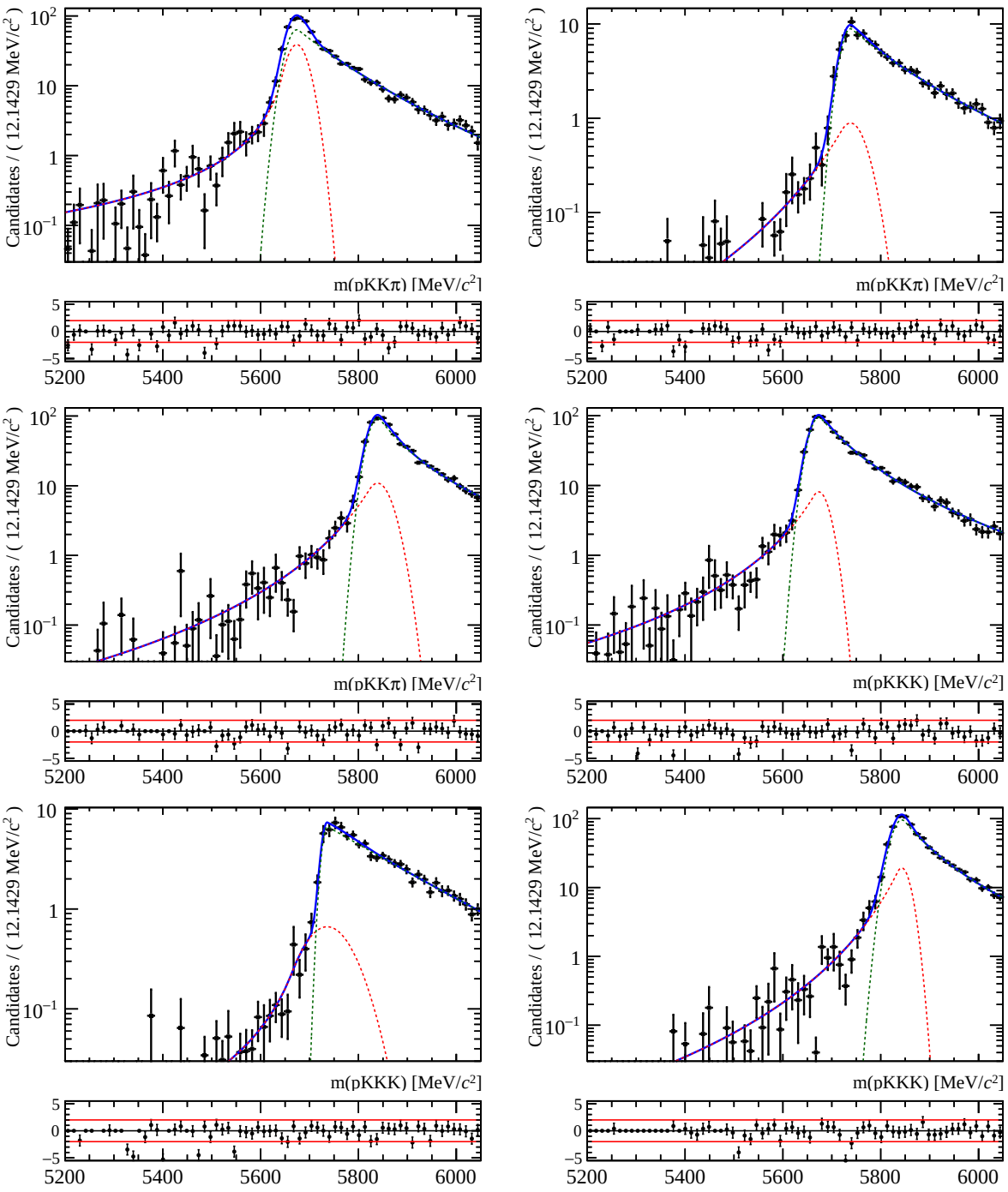

Figure C.12: Signal cross-feeds invariant mass distributions fitted with DCB PDF for the modes (in order from top to bottom) $\Lambda_b^0 \to pK\pi\pi$ as $pKK\pi$, $\Lambda_b^0 \to p\pi\pi\pi$ as $pKK\pi$ $\Xi_b^0 \to pK\pi\pi$ as $pKK\pi$, $\Lambda_b^0 \to pKK\pi$ as $pKKK$, $\Lambda_b^0 \to pK\pi\pi$ as $pKKK$ and $\Xi_b^0 \to pK\pi K$ as $pKKK$ for years 2012.

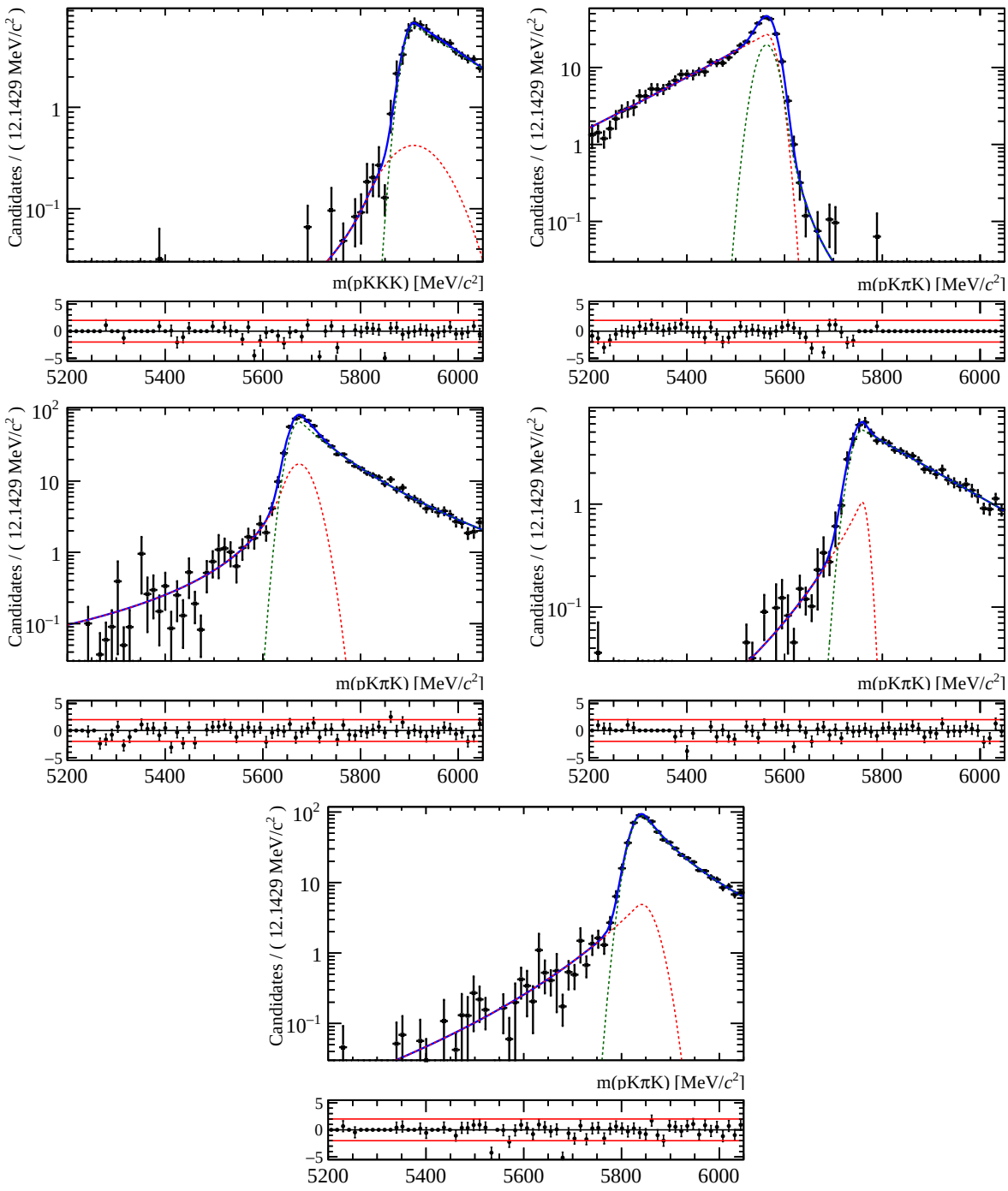

Figure C.13: Signal cross-feeds invariant mass distributions fitted with DCB PDF for the modes (in order from top to bottom) $\Xi_b^0 \to pK\pi\pi$ as $pKKK$, $\Lambda_b^0 \to pKKK$ as $pK\pi K$, $\Lambda_b^0 \to pK\pi\pi$ as $pK\pi K$, $\Lambda_b^0 \to p\pi\pi\pi$ as $pK\pi K$, $\Xi_b^0 \to pK\pi\pi$ as $pK\pi K$ for years 2012.

Table C.3: Cross-feed factors. The number of digits is automatically defined to be three in order to ensure in all cases the presence of at least two significant digits. The f factor must receive a factor 2 when two hadrons of the final state can be misidentified.

Crossfeeds	Efficiencies & CF-to-Signal factors (in %)					
	Year	$\epsilon_{\text{CF}}^{\text{PID}}$	$\epsilon_{\text{CF}}^{\text{Sel.}}$	$\epsilon_{\text{Sig.}}^{\text{PID}}$	$\epsilon_{\text{Sig.}}^{\text{Sel.}}$	f
$\Lambda_b^0 \to p\pi\pi\pi$ as $pK\pi\pi$	2011	6.483±0.087	73.495±0.452	47.641±0.298	73.498±0.453	13.607±1.647
	2012	6.673±0.067	65.670±0.366	49.174±0.208	65.332±0.367	13.641±1.562
$\Lambda_b^0 \to p\pi\pi\pi$ as $pKK\pi$	2011	0.889±0.026	69.160±0.474	47.641±0.298	73.498±0.453	5.000±0.194
	2012	0.912±0.022	59.956±0.379	49.174±0.208	65.332±0.367	5.000±0.240
$\Lambda_b^0 \to p\pi\pi\pi$ as $pK\pi K$	2011	0.640±0.015	69.193±0.474	47.641±0.298	73.498±0.453	5.000±0.194
	2012	0.663±0.013	60.006±0.379	49.174±0.208	65.332±0.367	5.000±0.241
$\Lambda_b^0 \to pK\pi\pi$ as $p\pi\pi\pi$	2011	2.211±0.037	72.534±0.470	52.575±0.299	72.868±0.454	4.187±0.741
	2012	2.029±0.027	65.670±0.381	53.633±0.212	66.166±0.369	3.756±0.430
$\Lambda_b^0 \to pK\pi\pi$ as $pKK\pi$	2011	6.071±0.080	68.550±0.474	52.575±0.299	72.868±0.454	10.863±1.114
	2012	6.278±0.066	60.114±0.381	53.633±0.212	66.166±0.369	10.634±0.862
$\Lambda_b^0 \to pK\pi\pi$ as $pK\pi K$	2011	5.681±0.070	68.570±0.474	52.575±0.299	72.868±0.454	10.169±1.114
	2012	5.819±0.059	60.083±0.381	53.633±0.212	66.166±0.369	9.852±0.862
$\Lambda_b^0 \to pK\pi\pi$ as $pKKK$	2011	0.784±0.026	68.544±0.476	52.575±0.299	72.868±0.454	1.403±0.168
	2012	0.787±0.018	59.974±0.383	53.633±0.212	66.166±0.369	1.329±0.123
$\Lambda_b^0 \to pKK\pi$ as $pK\pi\pi$	2011	2.657±0.045	74.093±0.472	57.311±0.308	70.832±0.478	4.849±0.482
	2012	2.490±0.032	65.286±0.384	58.783±0.225	60.491±0.384	4.571±0.428
$\Lambda_b^0 \to pKK\pi$ as $pKKK$	2011	6.454±0.085	69.880±0.482	57.311±0.308	70.832±0.478	11.111±1.389
	2012	6.702±0.070	59.311±0.386	58.783±0.225	60.491±0.384	11.180±1.025
$\Lambda_b^0 \to pKKK$ as $pKK\pi$	2011	3.467±0.053	70.178±0.463	61.921±0.291	70.110±0.445	5.604±0.970
	2012	3.218±0.038	60.038±0.371	64.148±0.209	59.842±0.356	5.033±0.767
$\Lambda_b^0 \to pKKK$ as $pK\pi K$	2011	2.751±0.045	70.203±0.456	61.921±0.291	70.110±0.445	4.449±0.970
	2012	2.560±0.033	60.320±0.365	64.148±0.209	59.842±0.356	4.022±0.767
$\Xi_b^0 \to pK\pi\pi$ as $p\pi\pi\pi$	2011	2.218±0.037	75.337±0.453	53.754±0.298	75.410±0.450	4.122±0.741
	2012	2.058±0.027	68.112±0.368	56.077±0.211	68.331±0.365	3.658±0.430
$\Xi_b^0 \to pK\pi\pi$ as $pKK\pi$	2011	6.095±0.082	71.967±0.471	53.754±0.298	75.410±0.450	10.821±1.114
	2012	6.181±0.066	63.977±0.378	56.077±0.211	68.331±0.365	10.321±0.862
$\Xi_b^0 \to pK\pi\pi$ as $pK\pi K$	2011	5.733±0.078	72.026±0.471	53.754±0.298	75.410±0.450	10.186±1.114
	2012	5.983±0.062	63.994±0.378	56.077±0.211	68.331±0.365	9.992±0.862
$\Xi_b^0 \to pK\pi K$ as $pK\pi\pi$	2011	3.311±0.049	74.811±0.458	58.528±0.305	74.430±0.456	5.685±0.482
	2012	2.958±0.034	66.235±0.376	60.665±0.219	64.091±0.378	5.040±0.428
$\Xi_b^0 \to pK\pi K$ as $pKKK$	2011	6.310±0.079	74.075±0.459	58.528±0.305	74.430±0.456	10.730±1.389
	2012	6.853±0.074	63.728±0.380	60.665±0.219	64.091±0.378	11.233±1.025

C.5 Shapes of the B decays for $\Delta\mathcal{A}^{CP}$ measurements and cross-feed factors.

This appendix presents the fit to the simulated events of B mesons decays. The PDF that is used to model those contributions is a Cruijff function. For the reader's convenience, the mathematical description is reminded here: the Cruijff function is an asymmetric function, composed of two Gaussian functions with shared mean μ but two different width σ's and two tail-correction parameters. Mathematically, the function is given by

$$P(m;\mu,\sigma_L,\sigma_R,\alpha_L,\alpha_R) = \mathcal{N}\cdot\begin{cases}\exp(-(m-\mu)^2/2(\sigma_L^2+\alpha_L(m-\mu)^2)), & \text{if } m\leq\mu\\ \exp(-(m-\mu)^2/2(\sigma_R^2+\alpha_R(m-\mu)^2)), & \text{if } m>\mu\end{cases} \tag{C.3}$$

where μ, σ_L (σ_R) and α_L (α_R) are the turnover points, the width of the left Gaussian (right Gaussian) and the left tail-correction parameter (right tail-correction parameter), respectively. Table C.4 summarizes the values of the parameters of the fit. The fit results are displayed in Fig. C.14 to C.16.

In addition, let's remind here that the cross-spectra factors are calculated using:

$$f = \frac{\epsilon_{\mathrm{X}}^{\mathrm{Sel.}}\cdot\epsilon_{\mathrm{X}}^{\mathrm{PID}}}{\epsilon_{\mathrm{Ref.}}^{\mathrm{Sel.}}\cdot\epsilon_{\mathrm{Ref.}}^{\mathrm{PID}}}, \tag{C.4}$$

where $\epsilon_{\mathrm{X}}^{\mathrm{PID}}$ and $\epsilon_{\mathrm{Ref.}}^{\mathrm{PID}}$ are the average efficiencies of misidentifying the B physics event as an event in X spectrum and misidentifying as an event in the reference spectrum, respectively, while the $\epsilon_{\mathrm{X}}^{\mathrm{Sel.}}$ and $\epsilon_{\mathrm{Ref.}}^{\mathrm{Sel.}}$ are the average efficiencies of selecting the B physics event as an event in the X spectrum and in the reference spectrum, respectively. The values of these factors are reported in Table C.5

Table C.4: Fit parameters obtained in the fit to B physics shapes.

B physics bkg.	Fit parameters				
	Year	σ_L	σ_R	α_R	μ
$B^0\to\pi\pi\pi\pi$ as $p\pi\pi\pi$	2011	40.543±21.002	267.712±61.781	0.034±0.124	5449.541±32.349
	2012	30.602±14.098	264.312±33.853	0.096±0.084	5424.285±19.870
$B^0\to K\pi\pi\pi$ as $p\pi\pi\pi$	2011	46.939±10.635	149.179±21.063	0.169±0.039	5461.642±16.264
	2012	51.580±10.258	185.767±19.602	0.178±0.034	5461.886±15.296
$B^0\to\pi K\pi\pi$ as $pK\pi\pi$	2011	68.954±23.072	173.898±45.528	0.118±0.092	5548.008±38.330
	2012	62.713±15.456	197.879±34.769	0.124±0.068	5532.417±25.951
$B_s^0\to KK\pi\pi$ as $pK\pi\pi$	2011	64.292±18.942	168.591±39.115	0.171±0.070	5579.297±34.177
	2012	72.047±11.713	203.861±30.363	0.192±0.062	5591.199±20.523
$B_s^0\to\pi KK\pi$ as $pKK\pi$	2011	55.636±32.494	212.984±191.639	0.119±0.230	5607.222±55.487
	2012	56.579±21.703	215.479±61.178	0.146±0.151	5604.113±37.021
$B^0\to KKK\pi$ as $pK\pi\pi$	2011	201.819±59.472	200.004±91.358	0.156±0.199	5505.228±121.331
	2012	150.650±64.736	269.981±26.188	0.165±0.135	5470.811±67.688
$B^0\to KKK\pi$ as $pKK\pi$	2011	49.795±12.389	159.994±6.705	0.165±0.021	5488.234±13.820
	2012	60.795±6.886	188.992±15.418	0.185±0.028	5508.376±11.119
$B^0\to KK\pi K$ as $pK\pi K$	2011	39.884±9.833	145.984±21.295	0.159±0.039	5481.289±17.098
	2012	43.414±0.262	182.711±14.736	0.161±0.033	5485.575±0.038
$B^0\to\pi KKK$ as $pKKK$	2011	54.813±27.949	193.455±62.246	0.120±0.132	5531.918±46.469
	2012	57.844±21.924	207.031±55.782	0.135±0.120	5541.839±37.373
$B_s^0\to KKKK$ as $pKKK$	2011	39.956±5.630	153.340±13.900	0.166±0.028	5572.842±9.886
	2012	48.820±6.258	179.035±17.558	0.184±0.036	5587.990±11.014

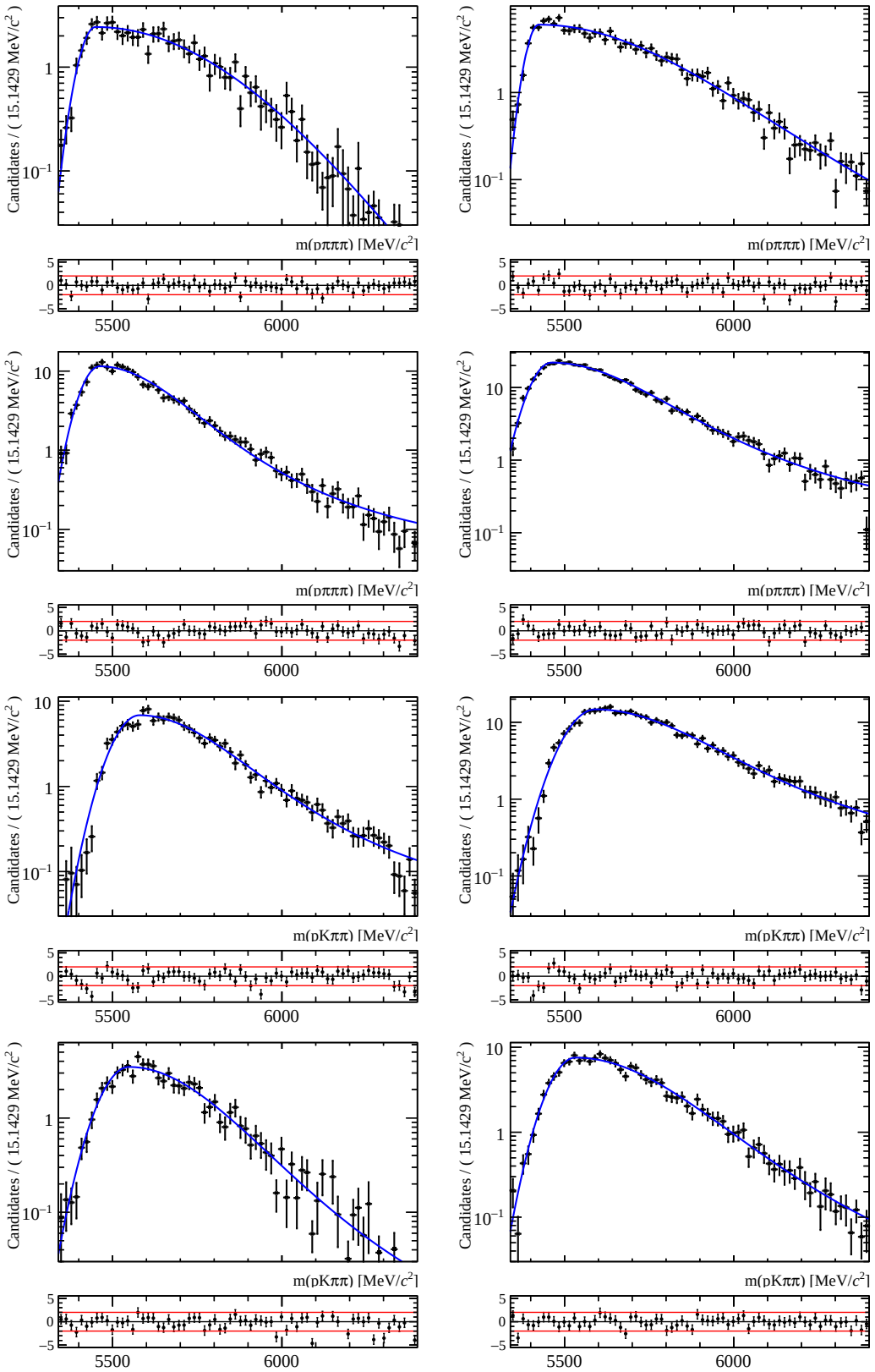

Figure C.14: B physics backgrounds invariant mass distribution fitted with Cruijff PDF for the modes (in order from top to bottom) $B^0 \to \pi\pi\pi\pi$ as $p\pi\pi\pi$, $B^0 \to K\pi\pi\pi$ as $p\pi\pi\pi$, $B_s^0 \to KK\pi\pi$ as $pK\pi\pi$ and $B^0 \to \pi K\pi\pi$ as $pK\pi\pi$ for years (left column) 2011 and (right column) 2012.

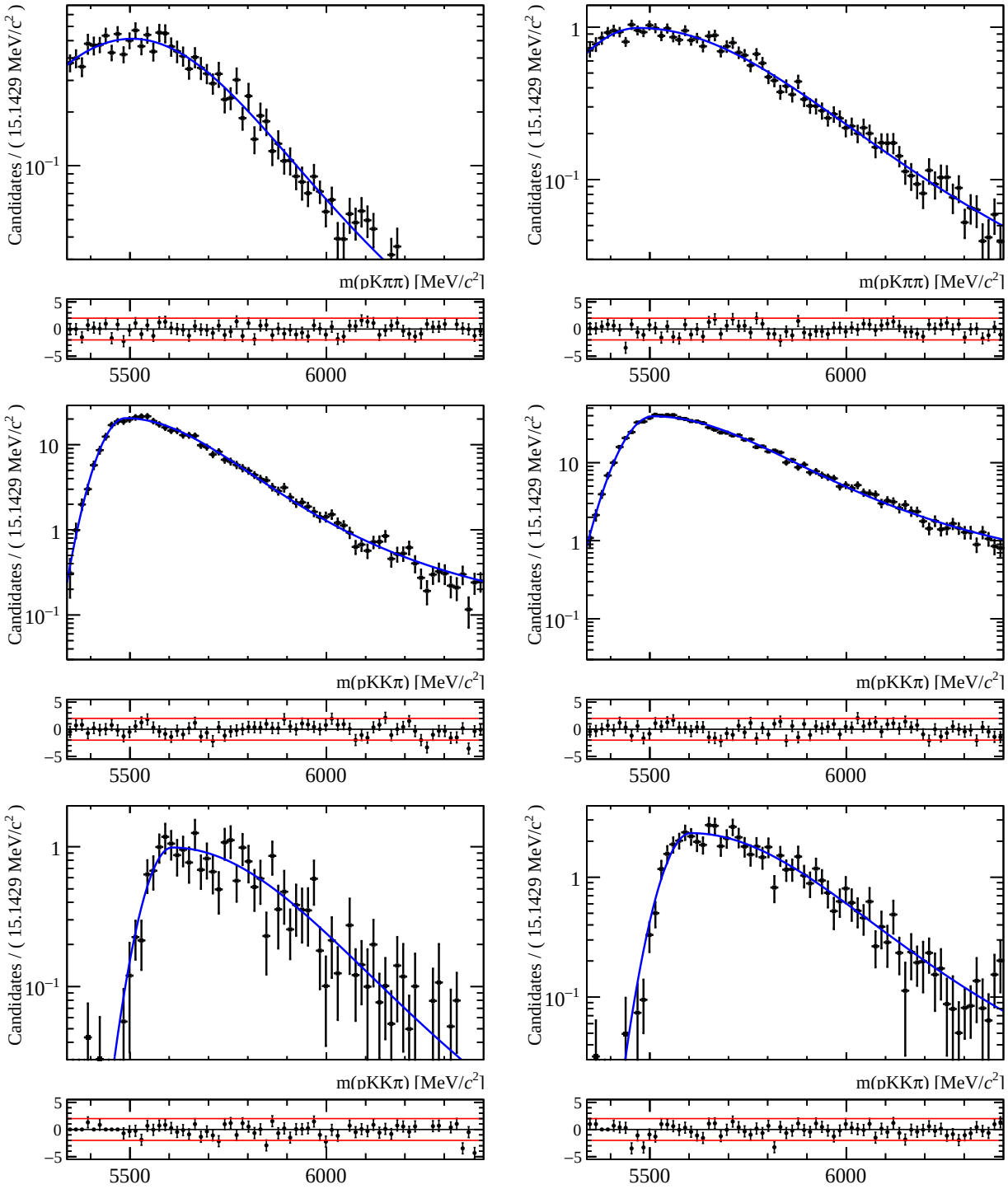

Figure C.15: B physics backgrounds invariant mass distribution fitted with Cruijff PDF for the modes (in order from top to bottom) $B^0 \to KKK\pi$ as $pK\pi\pi$, $B^0 \to KKK\pi$ as $pKK\pi$ and $B_s^0 \to \pi KK\pi$ as $pKK\pi$ for years (left column) 2011 and (right column) 2012.

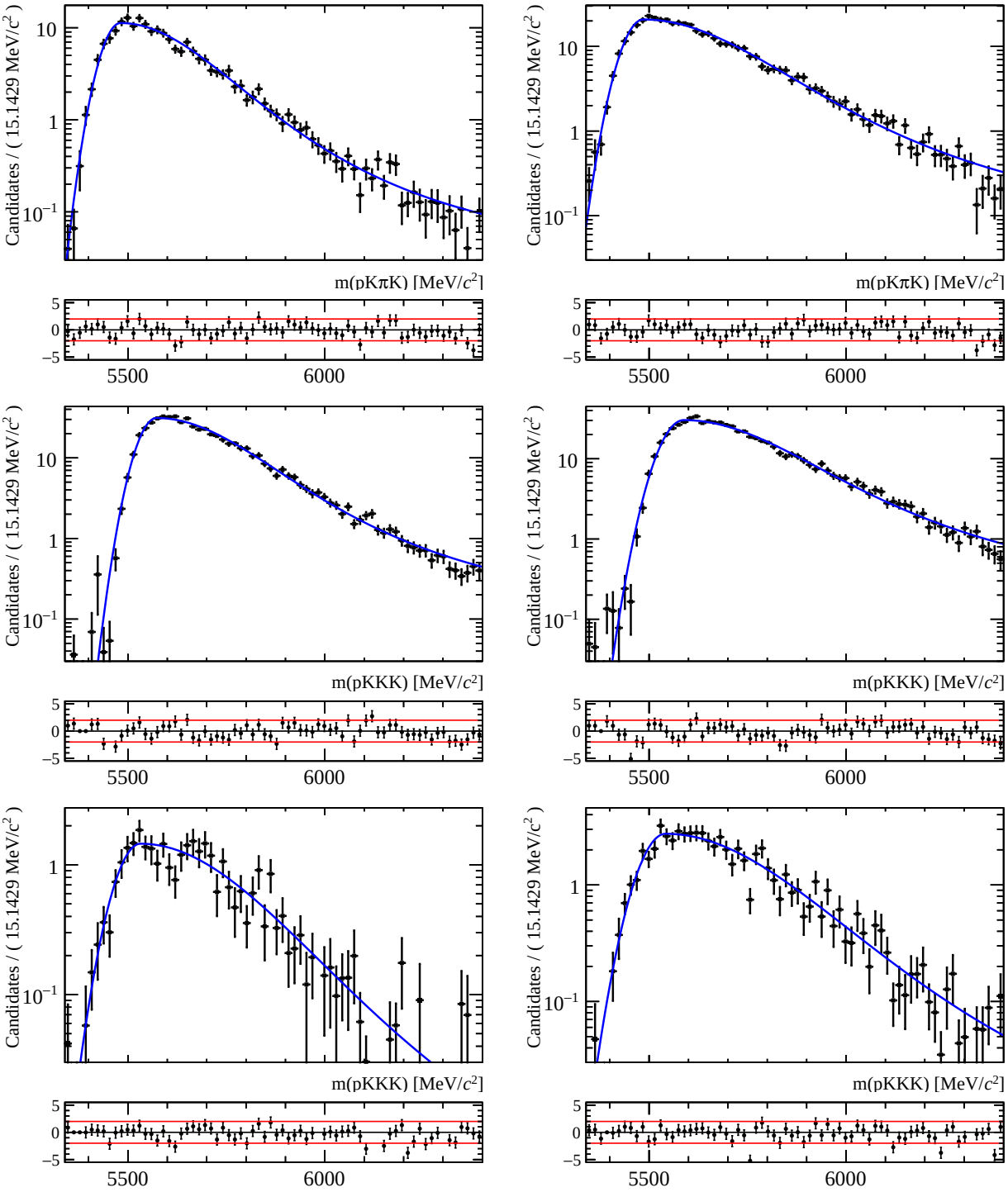

Figure C.16: B physics backgrounds invariant mass distribution fitted with Cruijff PDF for the modes (in order from top to bottom) $B^0 \to KK\pi K$ as $pK\pi K$, $B_s^0 \to KKKK$ as $pKKK$ and $B^0 \to \pi KKK$ as $pKKK$ for years (left column) 2011 and (right column) 2012.

Table C.5: B physics cross-spectra factors. The number of digits is automatically defined to be three in order to ensure in all cases the presence of at least two significant digits.

B physics	Efficiencies & X-to-Reference factors (in %)			
	Year	$\epsilon_{\mathrm{X}}^{\mathrm{PID}}$	$\epsilon_{\mathrm{X}}^{\mathrm{Sel.}}$	f
$B^0 \to K\pi\pi\pi$ as $p\pi\pi\pi$	2011	2.797±0.029	36.252±0.420	Ref.
	2012	3.439±0.017	34.619±0.293	Ref.
$B^0 \to \pi K\pi\pi$ as $pK\pi\pi$	2011	3.325±0.054	10.625±0.228	34.840±1.081
	2012	2.834±0.026	14.686±0.191	34.960±0.650
$B^0 \to KKK\pi$ as $pKK\pi$	2011	3.274±0.027	58.483±0.533	Ref.
	2012	4.101±0.015	54.256±0.366	Ref.
$B^0 \to KK\pi K$ as $pK\pi K$	2011	3.409±0.041	27.360±0.365	48.716±1.060
	2012	4.170±0.023	25.341±0.251	47.488±0.649
$B^0 \to \pi KKK$ as $pKKK$	2011	3.930±0.100	3.900±0.138	8.005±0.363
	2012	3.411±0.052	4.480±0.106	6.868±0.200
$B^0 \to KKK\pi$ as $pK\pi\pi$	2011	0.132±0.002	55.547±0.520	3.816±0.083
	2012	0.155±0.001	53.216±0.363	3.702±0.049
$B_s^0 \to KK\pi\pi$ as $pK\pi\pi$	2011	2.812±0.036	50.271±0.706	Ref.
	2012	3.714±0.020	47.868±0.484	Ref.
$B_s^0 \to \pi KK\pi$ as $pKK\pi$	2011	3.662±0.105	6.014±0.245	15.580±0.830
	2012	3.134±0.050	8.272±0.201	14.581±0.455

Appendix D

Appendix to Chapter 5

D.1 Fit results for the branching fraction measurements

The values of the parameters used in the simultaneous fit to the data for branching fractions measurements are reported in Table D.1.

Table D.1: Floating parameters of the simultaneous fit to the data of 2011 and 2012 for the branching fractions measurements. The individual particle and antiparticle are blinded.

Floating parameter	Value (in Λ_b^0/Ξ_b^0 spectra)	Value (in $\overline{\Lambda}_b^0/\overline{\Xi}_b^0$ spectra)
Parameters shared 2011 and 2012 :		
μ (Λ_b^0)	5624.27 ± 0.07	
μ (Ξ_b^0) - μ (Λ_b^0)	172.52 ± 0.39	
2012 σ_{core} (Signal $\Lambda_b^0 \to pK\pi\pi$) [ref]	16.47 ± 0.22	
$\mathcal{N}$ ($B^0 \to \pi\pi\pi\pi$ in $p\pi\pi\pi$) / $\mathcal{N}$ ($B^0 \to K\pi\pi\pi$ in $p\pi\pi\pi$)	0.425 ± 0.065	← shared
Parameters for 2011 spectra :		
$\mathcal{N}$ (Signal $\Lambda_b^0 \to p\pi\pi\pi$)	XXX ± XXX	XXX ± XXX
$\mathcal{N}$ (Signal $\Lambda_b^0 \to pK\pi\pi$)	XXX ± XXX	XXX ± XXX
$\mathcal{N}$ (Signal $\Lambda_b^0 \to pKK\pi$)	XXX ± XXX	XXX ± XXX
$\mathcal{N}$ (Signal $\Lambda_b^0 \to pKKK$)	XXX ± XXX	XXX ± XXX
$\mathcal{N}$ (Signal $\Xi_b^0 \to pK\pi K$)	XXX ± XXX	XXX ± XXX
$\mathcal{N}$ (Signal $\Xi_b^0 \to pK\pi\pi$)	XXX ± XXX	XXX ± XXX
$\mathcal{N}$ (Signal $\Xi_b^0 \to pKKK$)	XXX ± XXX	XXX ± XXX
$\mathcal{N}$ (Signal $\Lambda_b^0 \to (\Lambda_c^+ \to pK\pi)\pi$)	2760.8 ± 53.0	2666.2 ± 52.1
$\mathcal{N}$ (Combinatorics in $p\pi\pi\pi$)	40.5 ± 17.2	44.0 ± 17.4
$\mathcal{N}$ (Combinatorics in $pK\pi\pi$)	156.9 ± 29.7	107.4 ± 26.8
$\mathcal{N}$ (Combinatorics in $pKK\pi$)	204.1 ± 33.1	175.4 ± 30.4
$\mathcal{N}$ (Combinatorics in $pKKK$)	116.5 ± 27.8	76.1 ± 25.3
$\mathcal{N}$ (Combinatorics in $pK\pi K$)	82.9 ± 24.2	33.4 ± 21.4
$\mathcal{N}$ (CF $B^0 \to K\pi\pi\pi$ in $p\pi\pi\pi$)	72.7 ± 14.8	74.1 ± 13.7
$\mathcal{N}$ (CF $B_s^0 \to K\pi\pi K$ in $pK\pi\pi$)	22.5 ± 11.1	46.8 ± 14.3
$\mathcal{N}$ (CF $B^0 \to KKK\pi$ in $pKK\pi$)	89.5 ± 14.2	78.9 ± 14.5
$\mathcal{N}$ (CF $B_s^0 \to KKKK$ in $pKKK$)	31.2 ± 12.4	27.4 ± 11.3
$\mathcal{N}$ (CF $B \to$ 5-body in $pKKK$)	26.5 ± 14.6	30.2 ± 14.5
$\mathcal{N}$ (CF $B \to$ 5-body in $pKK\pi$)	8.9 ± 8.0	41.1 ± 13.3
$\mathcal{N}$ (CF $B \to$ 5-body in $pK\pi K$)	11.6 ± 8.6	1.9 ± 5.1
$\mathcal{N}$ (CF $B \to$ 5-body in $pK\pi\pi$)	43.3 ± 21.0	8.5 ± 11.1
$\mathcal{N}$ (CF $B \to$ 5-body in $p\pi\pi\pi$)	45.4 ± 14.9	35.8 ± 12.4
$\mathcal{N}$ (PR from $\Lambda_b^0 \to$ 5-body in $p\pi\pi\pi$)	133.1 ± 17.0	123.8 ± 16.3
$\mathcal{N}$ (PR from $\Lambda_b^0 \to$ 5-body in $pK\pi\pi$)	410.7 ± 29.7	428.7 ± 27.6
$\mathcal{N}$ (PR from $\Lambda_b^0 \to$ 5-body in $pKK\pi$)	52.3 ± 18.4	32.0 ± 18.3
$\mathcal{N}$ (PR from $\Lambda_b^0 \to$ 5-body in $pKKK$)	41.5 ± 16.7	31.8 ± 16.0
$\mathcal{N}$ (PR from $\Xi_b^0 \to$ 5-body in $pK\pi K$)	39.1 ± 25.5	67.2 ± 25.6
$\mathcal{N}$ (PR from $\Lambda_b^0 \to$ 5-body in $(\Lambda_c^+ \to pK\pi)\pi$)	908.2 ± 30.9	855.8 ± 30.0
c (Combinatorics in charmless decays)	0.029 ± 0.019	← shared
p (PR from Λ_b^0/Ξ_b^0 + 5-body)	0.468 ± 0.257	← shared
s (PR from Λ_b^0/Ξ_b^0 + 5-body)	-9.386 ± 15.306	← shared
p (PR from Λ_b^0 + 5-body in $(\Lambda_c^+ \to pK\pi)\pi$)	0.158 ± 0.091	← shared
s (PR from Λ_b^0 + 5-body in $(\Lambda_c^+ \to pK\pi)\pi$)	-12.168 ± 4.802	← shared

$r = (\ \sigma_{\text{core}}\ \Lambda_b^0 \to p\pi\pi\pi)/(\sigma_{\text{ref}})$	1.019 ± 0.024	← shared
$r = (\ \sigma_{\text{core}}\ \Lambda_b^0 \to pK\pi\pi)/(\sigma_{\text{ref}})$	1.010 ± 0.019	← shared
$r = (\ \sigma_{\text{core}}\ \Lambda_b^0 \to pKK\pi)/(\sigma_{\text{ref}})$	0.949 ± 0.023	← shared
$r = (\ \sigma_{\text{core}}\ \Lambda_b^0 \to pKKK)/(\sigma_{\text{ref}})$	0.917 ± 0.018	← shared
$r = (\ \sigma_{\text{core}}\ \Xi_b^0 \to pK\pi\pi)/(\sigma_{\text{ref}})$	1.036 ± 0.026	← shared
$r = (\ \sigma_{\text{core}}\ \Xi_b^0 \to pK\pi K)/(\sigma_{\text{ref}})$	1.001 ± 0.023	← shared
$r = (\ \sigma_{\text{core}}\ \Xi_b^0 \to pKKK)/(\sigma_{\text{ref}})$	0.918 ± 0.019	← shared
σ_{core} (Signal $\Lambda_b^0 \to (\Lambda_c^+ \to pK\pi)\pi$)	16.86 ± 0.21	← shared
$f_{\text{CF}}(\Lambda_b^0 \to pKKK$ in $pK\pi)$	0.140 ± 0.018	← shared
$f_{\text{CF}}(\Lambda_b^0 \to pKKK$ in $pK\pi K)$	0.044 ± 0.010	← shared
$f_{\text{CF}}(\Lambda_b^0 \to pKK\pi$ in $pKKK)$	0.115 ± 0.014	← shared
$f_{\text{CF}}(\Lambda_b^0 \to pKK\pi$ in $pK\pi\pi)$	0.049 ± 0.005	← shared
$f_{\text{CF}}(\Lambda_b^0 \to pK\pi\pi$ in $pKKK)$	0.041 ± 0.002	← shared
$f_{\text{CF}}(\Lambda_b^0 \to pK\pi\pi$ in $pKK\pi)$	0.110 ± 0.009	← shared
$f_{\text{CF}}(\Lambda_b^0 \to pK\pi\pi$ in $p\pi\pi\pi)$	0.077 ± 0.015	← shared
$f_{\text{CF}}(\Lambda_b^0 \to pK\pi\pi$ in $pK\pi K)$	0.110 ± 0.009	← shared
f_{CF}(PR from Λ_b^0 + 5body in $pK\pi\pi$ in $pKK\pi$)	0.246 ± 0.036	← shared
$f_{\text{CF}}(\Lambda_b^0 \to p\pi\pi\pi$ in $pKK\pi)$	0.100 ± 0.004	← shared
$f_{\text{CF}}(\Lambda_b^0 \to p\pi\pi\pi$ in $pK\pi\pi)$	0.301 ± 0.028	← shared
$f_{\text{CF}}(\Lambda_b^0 \to p\pi\pi\pi$ in $pK\pi K)$	0.050 ± 0.002	← shared
$f_{\text{CF}}(\Xi_b^0 \to pK\pi K$ in $pKKK)$	0.108 ± 0.014	← shared
$f_{\text{CF}}(\Xi_b^0 \to pK\pi K$ in $pK\pi\pi)$	0.115 ± 0.010	← shared
$f_{\text{CF}}(\Xi_b^0 \to pK\pi\pi$ in $pKK\pi)$	0.108 ± 0.011	← shared
$f_{\text{CF}}(\Xi_b^0 \to pK\pi\pi$ in $p\pi\pi\pi)$	0.041 ± 0.007	← shared
$f_{\text{CF}}(\Xi_b^0 \to pK\pi\pi$ in $pK\pi K)$	0.103 ± 0.011	← shared
$f_{\text{CF}}(B^0 \to K\pi\pi\pi$ in $pK\pi\pi)$	0.331 ± 0.014	← shared
$f_{\text{CF}}(B^0 \to KKK\pi$ in $pKKK)$	0.078 ± 0.005	← shared
$f_{\text{CF}}(B^0 \to KKK\pi$ in $pK\pi\pi)$	0.037 ± 0.001	← shared
$f_{\text{CF}}(B^0 \to KKK\pi$ in $pK\pi K)$	0.476 ± 0.014	← shared
$f_{\text{CF}}(B_s^0 \to K\pi\pi K$ in $pKK\pi)$	0.145 ± 0.011	← shared
Parameters for 2012 spectra :		
$\mathcal{N}$ (Signal $\Lambda_b^0 \to p\pi\pi\pi$)	XXX ± XXX	XXX ± XXX
$\mathcal{N}$ (Signal $\Lambda_b^0 \to pK\pi\pi$)	XXX ± XXX	XXX ± XXX
$\mathcal{N}$ (Signal $\Lambda_b^0 \to pKK\pi$)	XXX ± XXX	XXX ± XXX
$\mathcal{N}$ (Signal $\Lambda_b^0 \to pKKK$)	XXX ± XXX	XXX ± XXX
$\mathcal{N}$ (Signal $\Xi_b^0 \to pK\pi K$)	XXX ± XXX	XXX ± XXX
$\mathcal{N}$ (Signal $\Xi_b^0 \to pK\pi\pi$)	XXX ± XXX	XXX ± XXX
$\mathcal{N}$ (Signal $\Xi_b^0 \to pKKK$)	XXX ± XXX	XXX ± XXX
$\mathcal{N}$ (Signal $\Lambda_b^0 \to (\Lambda_c^+ \to pK\pi)\pi$)	6223.4 ± 79.4	5892.9 ± 77.3
$\mathcal{N}$ (Combinatorics in $p\pi\pi\pi$)	77.3 ± 38.1	103.7 ± 37.6
$\mathcal{N}$ (Combinatorics in $pK\pi\pi$)	416.9 ± 62.2	424.5 ± 60.7
$\mathcal{N}$ (Combinatorics in $pKK\pi$)	318.8 ± 50.5	401.9 ± 53.2
$\mathcal{N}$ (Combinatorics in $pKKK$)	315.9 ± 45.9	343.8 ± 47.2
$\mathcal{N}$ (Combinatorics in $pK\pi K$)	187.4 ± 40.4	215.6 ± 40.0
$\mathcal{N}$ (CF $B^0 \to K\pi\pi\pi$ in $p\pi\pi\pi$)	242.0 ± 27.1	257.2 ± 27.9
$\mathcal{N}$ (CF $B_s^0 \to K\pi\pi K$ in $pK\pi\pi$)	177.4 ± 30.6	121.2 ± 25.1
$\mathcal{N}$ (CF $B^0 \to KKK\pi$ in $pKK\pi$)	231.5 ± 25.7	194.2 ± 24.0
$\mathcal{N}$ (CF $B_s^0 \to KKKK$ in $pKKK$)	74.8 ± 20.3	98.2 ± 22.6
$\mathcal{N}$ (CF $B \to$ 5-body in $pKKK$)	90.1 ± 26.0	50.1 ± 21.3

$\mathcal{N}$ (CF $B \to$ 5-body in $pKK\pi$)	159.0 ± 27.2	206.2 ± 32.1
$\mathcal{N}$ (CF $B \to$ 5-body in $pK\pi K$)	68.7 ± 20.7	51.3 ± 17.4
$\mathcal{N}$ (CF $B \to$ 5-body in $pK\pi\pi$)	200.7 ± 46.5	258.4 ± 49.7
$\mathcal{N}$ (CF $B \to$ 5-body in $p\pi\pi\pi$)	191.6 ± 29.5	127.3 ± 25.0
$\mathcal{N}$ (PR from $\Lambda_b^0 \to$ 5-body in $p\pi\pi\pi$)	315.3 ± 27.2	299.0 ± 25.8
$\mathcal{N}$ (PR from $\Lambda_b^0 \to$ 5-body in $pK\pi\pi$)	866.7 ± 46.3	884.5 ± 45.6
$\mathcal{N}$ (PR from $\Lambda_b^0 \to$ 5-body in $pKK\pi$)	136.0 ± 28.8	93.0 ± 29.8
$\mathcal{N}$ (PR from $\Lambda_b^0 \to$ 5-body in $pKKK$)	33.4 ± 23.1	87.2 ± 24.2
$\mathcal{N}$ (PR from $\Xi_b^0 \to$ 5-body in $pK\pi K$)	47.5 ± 37.5	37.1 ± 36.5
$\mathcal{N}$ (PR from $\Lambda_b^0 \to$ 5-body in $(\Lambda_c^+ \to pK\pi)\pi$)	2044.6 ± 46.1	1888.1 ± 44.3
c (Combinatorics in charmless decays)	0.020 ± 0.015	← shared
p (PR from Λ_b^0/Ξ_b^0 + 5-body)	0.576 ± 0.244	← shared
s (PR from Λ_b^0/Ξ_b^0 + 5-body)	-13.695 ± 16.795	← shared
p (PR from Λ_b^0 + 5-body in $(\Lambda_c^+ \to pK\pi)\pi$)	0.161 ± 0.059	← shared
s (PR from Λ_b^0 + 5-body in $(\Lambda_c^+ \to pK\pi)\pi$)	-13.592 ± 3.186	← shared
$r = (\ \sigma_{\rm core}\ \Lambda_b^0 \to p\pi\pi\pi)/(\sigma_{\rm ref})$	1.049 ± 0.020	← shared
$r = (\ \sigma_{\rm core}\ \Lambda_b^0 \to pKK\pi)/(\sigma_{\rm ref})$	0.950 ± 0.019	← shared
$r = (\ \sigma_{\rm core}\ \Lambda_b^0 \to pKKK)/(\sigma_{\rm ref})$	0.893 ± 0.015	← shared
$r = (\ \sigma_{\rm core}\ \Xi_b^0 \to pK\pi\pi)/(\sigma_{\rm ref})$	1.027 ± 0.024	← shared
$r = (\ \sigma_{\rm core}\ \Xi_b^0 \to pK\pi K)/(\sigma_{\rm ref})$	0.994 ± 0.020	← shared
$r = (\ \sigma_{\rm core}\ \Xi_b^0 \to pKKK)/(\sigma_{\rm ref})$	0.921 ± 0.017	← shared
$\sigma_{\rm core}$ (Signal $\Lambda_b^0 \to (\Lambda_c^+ \to pK\pi)\pi$)	16.49 ± 0.14	← shared
$f_{\rm CF}$(CF $\Lambda_b^0 \to pKKK$ in $pKK\pi$)	0.114 ± 0.014	← shared
$f_{\rm CF}$(CF $\Lambda_b^0 \to pKKK$ in $pK\pi K$)	0.036 ± 0.008	← shared
$f_{\rm CF}$(CF $\Lambda_b^0 \to pKK\pi$ in $pKKK$)	0.116 ± 0.010	← shared
$f_{\rm CF}$(CF $\Lambda_b^0 \to pKK\pi$ in $pK\pi\pi$)	0.046 ± 0.004	← shared
$f_{\rm CF}$(CF $\Lambda_b^0 \to pK\pi\pi$ in $pKKK$)	0.021 ± 0.001	← shared
$f_{\rm CF}$(CF $\Lambda_b^0 \to pK\pi\pi$ in $pKK\pi$)	0.108 ± 0.007	← shared
$f_{\rm CF}$(CF $\Lambda_b^0 \to pK\pi\pi$ in $p\pi\pi\pi$)	0.064 ± 0.011	← shared
$f_{\rm CF}$(CF $\Lambda_b^0 \to pK\pi\pi$ in $pK\pi K$)	0.104 ± 0.006	← shared
$f_{\rm CF}$(PR from Λ_b^0 + 5body in $pK\pi\pi$ in $pKK\pi$)	0.227 ± 0.029	← shared
$f_{\rm CF}$(CF $\Lambda_b^0 \to p\pi\pi\pi$ in $pKK\pi$)	0.102 ± 0.005	← shared
$f_{\rm CF}$(CF $\Lambda_b^0 \to p\pi\pi\pi$ in $pK\pi\pi$)	0.297 ± 0.023	← shared
$f_{\rm CF}$(CF $\Lambda_b^0 \to p\pi\pi\pi$ in $pK\pi K$)	0.050 ± 0.002	← shared
$f_{\rm CF}$(CF $\Xi_b^0 \to pK\pi K$ in $pKKK$)	0.112 ± 0.010	← shared
$f_{\rm CF}$(CF $\Xi_b^0 \to pK\pi K$ in $pK\pi\pi$)	0.101 ± 0.009	← shared
$f_{\rm CF}$(CF $\Xi_b^0 \to pK\pi\pi$ in $pKK\pi$)	0.103 ± 0.009	← shared
$f_{\rm CF}$(CF $\Xi_b^0 \to pK\pi\pi$ in $p\pi\pi\pi$)	0.037 ± 0.004	← shared
$f_{\rm CF}$(CF $\Xi_b^0 \to pK\pi\pi$ in $pK\pi K$)	0.101 ± 0.009	← shared
$f_{\rm CF}(B^0 \to K\pi\pi\pi$ in $pK\pi\pi)$	0.334 ± 0.009	← shared
$f_{\rm CF}(B^0 \to KKK\pi$ in $pKKK)$	0.067 ± 0.003	← shared
$f_{\rm CF}(B^0 \to KKK\pi$ in $pK\pi\pi)$	0.036 ± 0.001	← shared
$f_{\rm CF}(B^0 \to KKK\pi$ in $pK\pi K)$	0.471 ± 0.009	← shared
$f_{\rm CF}(B_s^0 \to K\pi\pi K$ in $pKK\pi)$	0.131 ± 0.006	← shared

D.2 Dynamics of the decay and reference frame

The helicity angle of a track h_i is defined as the angle between the direction of the momentum of the track h_i in the rest frame of its mother and the direction of the momentum of its mother in the h_i's grandmother rest frame (or in the LAB). The angle Φ is the angle between the two decay planes present in the process. The representation of this definition is displayed on the f igure D.1.

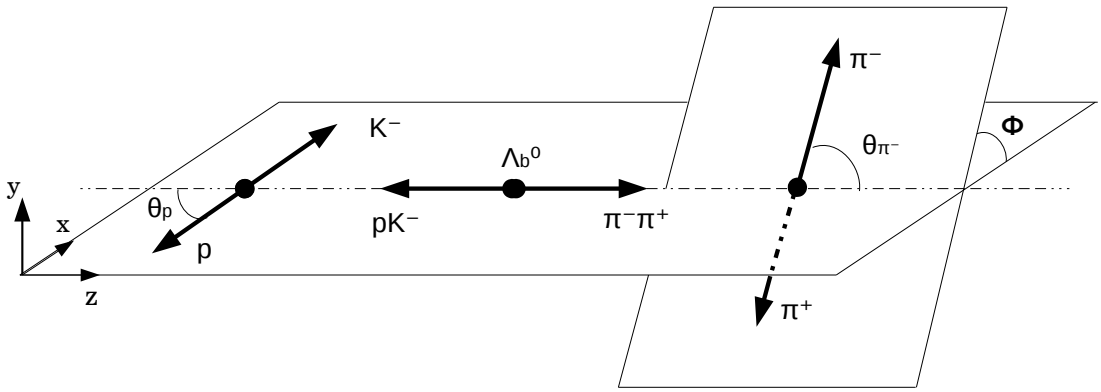

Figure D.1: Definition of the helicity angles and the angle between the two decay planes.

For example, in the decay $\Lambda_b^0 \to \Lambda^* \rho^0 \to pK^-\pi^+\pi^-$, we first perform a rotation to align z-axis with the direction of $(\overrightarrow{p}_{\pi^-} + \overrightarrow{p}_{\pi^+})$, in the rest frame of Λ_b^0. The helicity axis direction is defined in the equation D.1.

$$\overrightarrow{e}_{hel.} = -\frac{\overrightarrow{p}_{K^-}^{\{\Lambda_b^0\}} + \overrightarrow{p}_{p}^{\{\Lambda_b^0\}}}{|\overrightarrow{p}_{K^-}^{\{\Lambda_b^0\}} + \overrightarrow{p}_{p}^{\{\Lambda_b^0\}}|}. \tag{D.1}$$

where the superscript "{}" stands for the rest frame of reference taken for the momentum $\overrightarrow{p}$. The cosine of the helicity angle for the particles present in the final state is then defined in the following equations.

$$\cos\theta_p = -\frac{\overrightarrow{p}_{p}^{\{\Lambda^*\}}}{|\overrightarrow{p}_{p}^{\{\Lambda^*\}}|} \cdot \overrightarrow{e}_{hel}. \tag{D.2}$$

$$\cos\theta_{\pi^+} = \frac{\overrightarrow{p}_{\pi^+}^{\{\rho^0\}}}{|\overrightarrow{p}_{\pi^+}^{\{\rho^0\}}|} \cdot \overrightarrow{e}_{hel}. \tag{D.3}$$

We can also define the decay angle ϕ_{hel}. ϕ_{hel} is the angle between the two decay planes of the process. In that respect, we define the normal vectors of the two decay planes as the

following :

$$\overrightarrow{n}_{pK} = \frac{\overrightarrow{p}^{\{\Lambda_b^0\}}_{K^-} \wedge \overrightarrow{p}^{\{\Lambda_b^0\}}_{p}}{|\overrightarrow{p}^{\{\Lambda_b^0\}}_{K^-} \wedge \overrightarrow{p}^{\{\Lambda_b^0\}}_{p}|}. \tag{D.4}$$

$$\overrightarrow{n}_{\pi\pi} = \frac{\overrightarrow{p}^{\{\Lambda_b^0\}}_{\pi^+} \wedge \overrightarrow{p}^{\{\Lambda_b^0\}}_{\pi^-}}{|\overrightarrow{p}^{\{\Lambda_b^0\}}_{\pi^+} \wedge \overrightarrow{p}^{\{\Lambda_b^0\}}_{\pi^-}|}. \tag{D.5}$$

Thanks to the equation D.4 and D.5 we define the cosine of the decay angle as given in equation D.6.

$$\cos\phi_{hel.} = \overrightarrow{n}_{pK} \cdot \overrightarrow{n}_{\pi\pi}. \tag{D.6}$$

D.3 Fit to the data with free cross-feed factor in $pKKK$.

Figure D.2 and D.3 show the fit results in which the factor which constrains the cross-feed contributions that proceed via a simultaneous misidentification of two tracks of the final state in $pKKK$ spectrum is free.

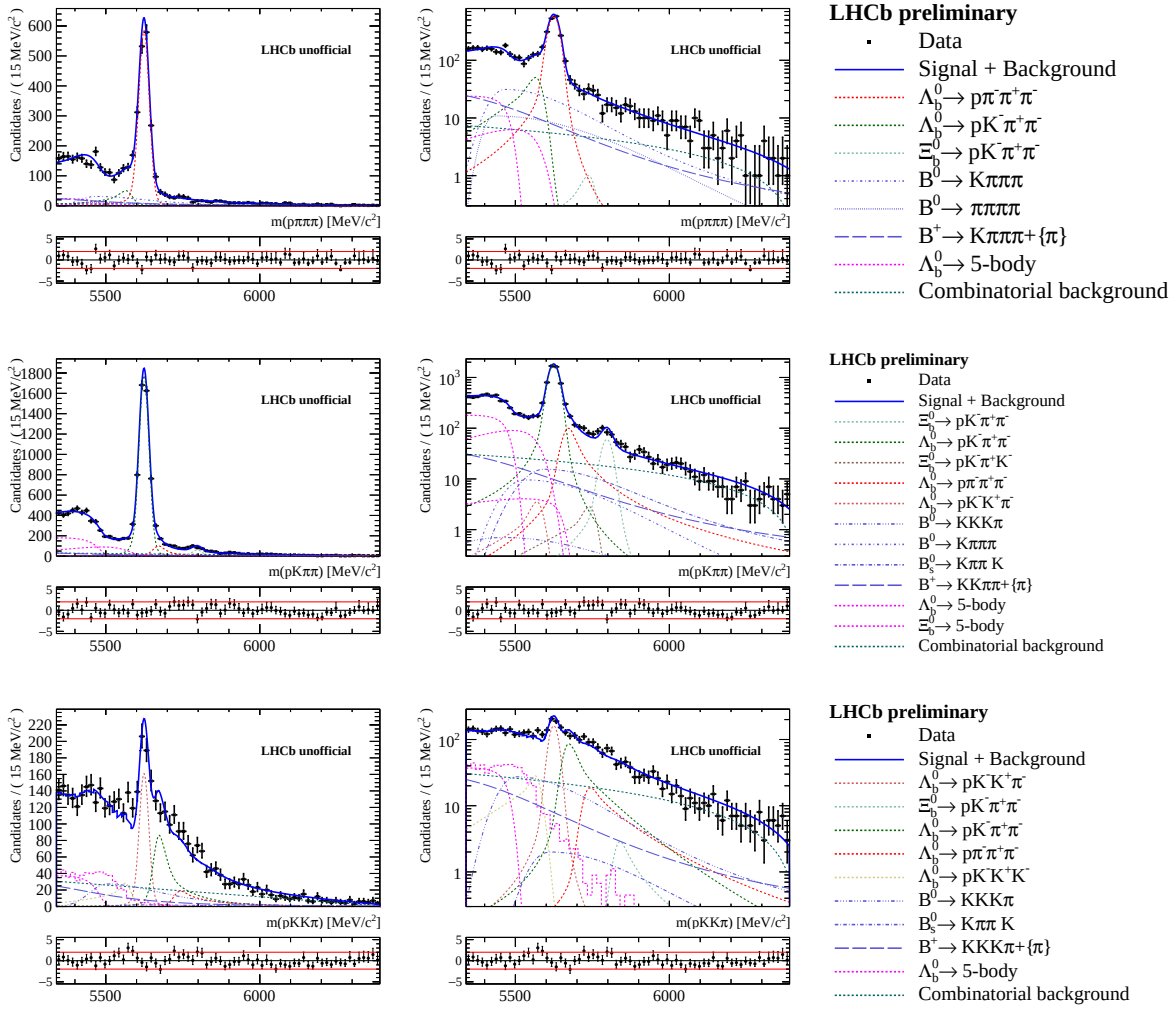

Figure D.2: Invariant mass distributions superimposed to the results of the fit to the [from top to bottom] $X_b^0 \to p\pi\pi\pi$, $X_b^0 \to pK\pi\pi$ and $X_b^0 \to pKK\pi$ spectra for the addition of the 2011 and 2012 data samples.

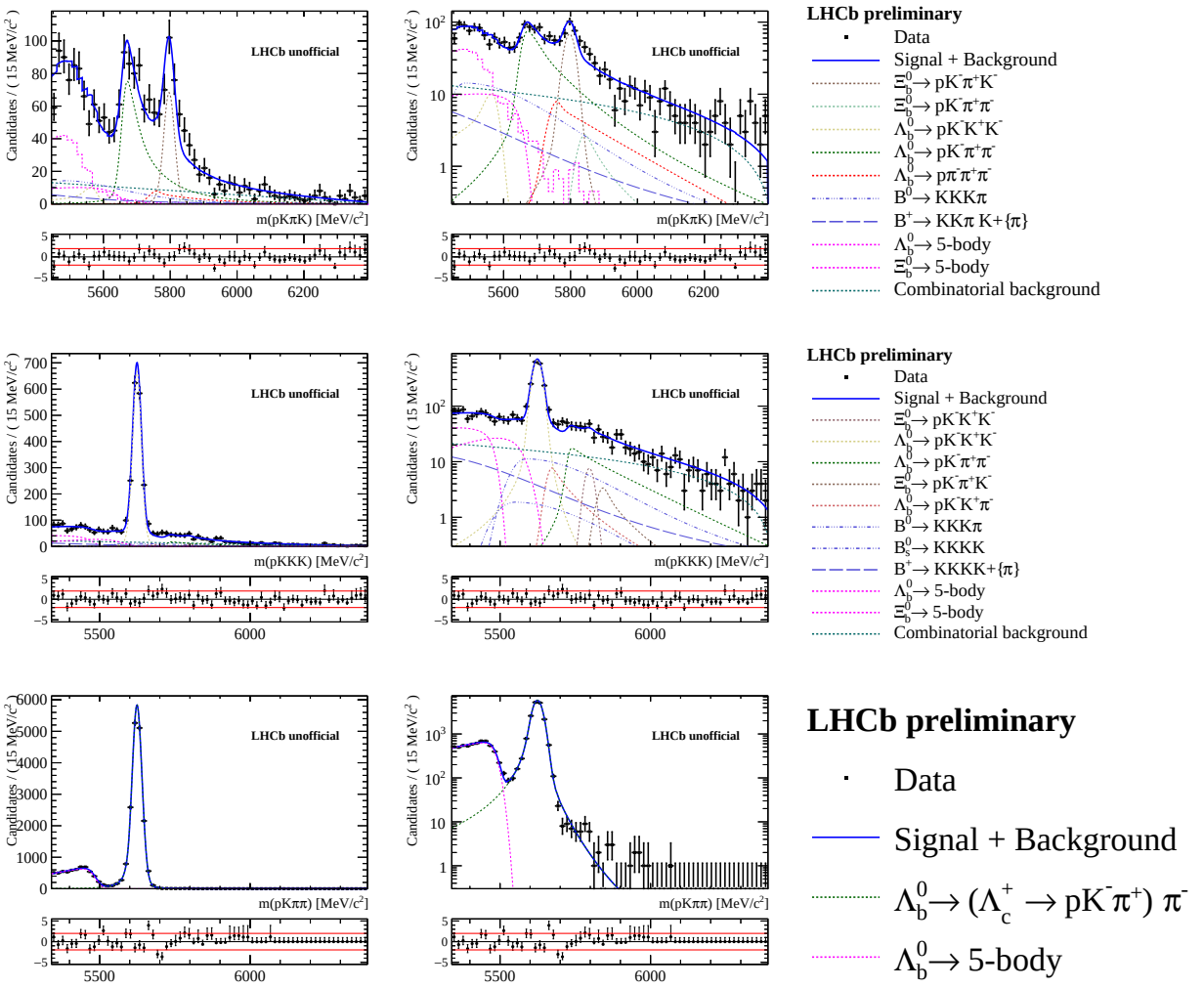

Figure D.3: Invariant mass distributions superimposed to the results of the fit to the [from top to bottom] $X_b^0 \to pK\pi K$, $X_b^0 \to pKKK$ and $X_b^0 \to (\Lambda_c^+ \to pK\pi)\pi$ spectra for the addition of the 2011 and 2012 data samples.

Appendix E

Appendix to Chapter 7

E.1 Two and three body invariant-mass distributions for 2012 data

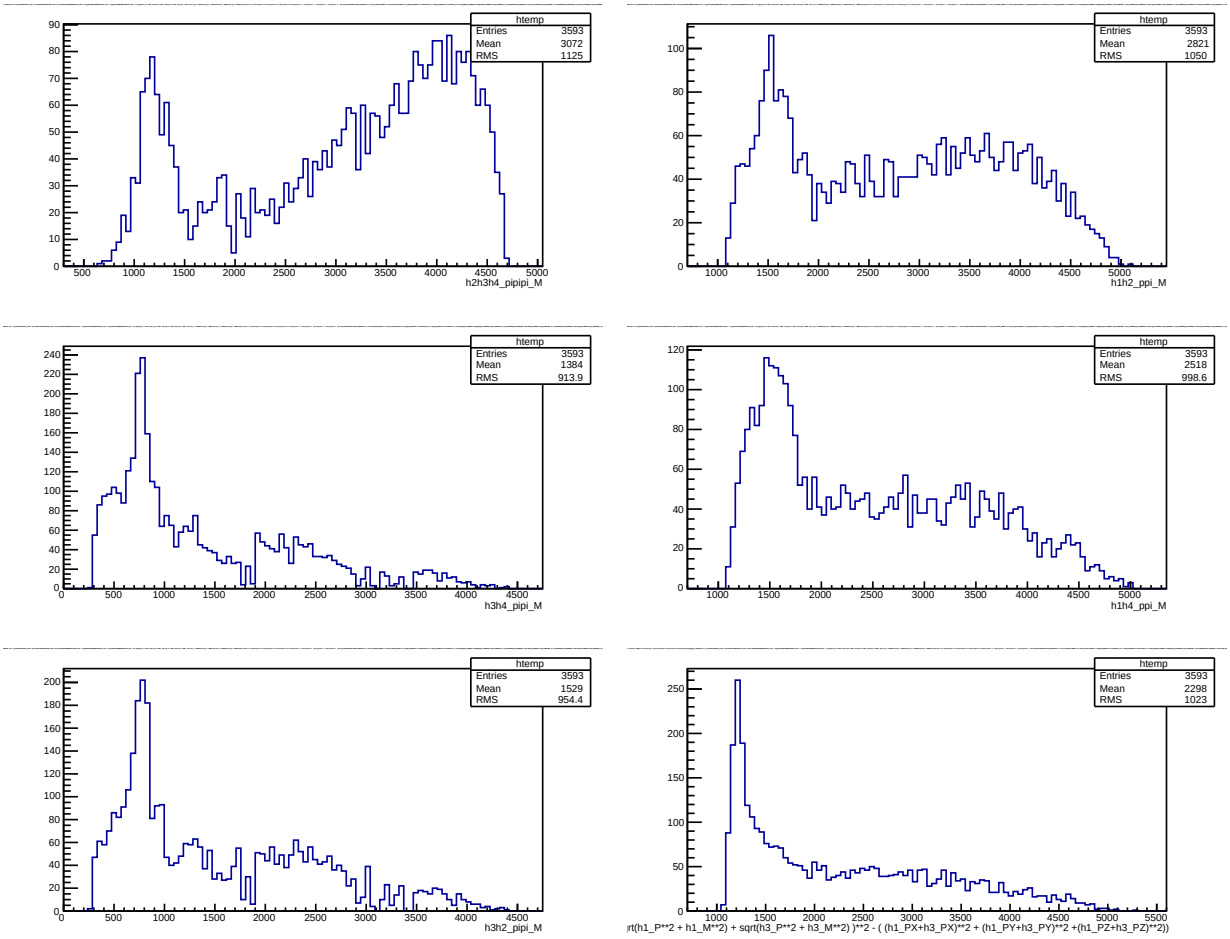

Figure E.1: Two and three body invariant-mass distributions considering $\Lambda_b^0 \to p\pi^-\pi^+\pi^-$ 2012 events. From left to right, top to bottom: $m(h_2h_3h_4)$, $m(h_1h_2)$, $m(h_3h_4)$, $m(h_1h_4)$, $m(h_3h_2)$, $m(h_1h_3)$ distributions where h_is stand for p, π^-, π^+ and π^-, respectively.

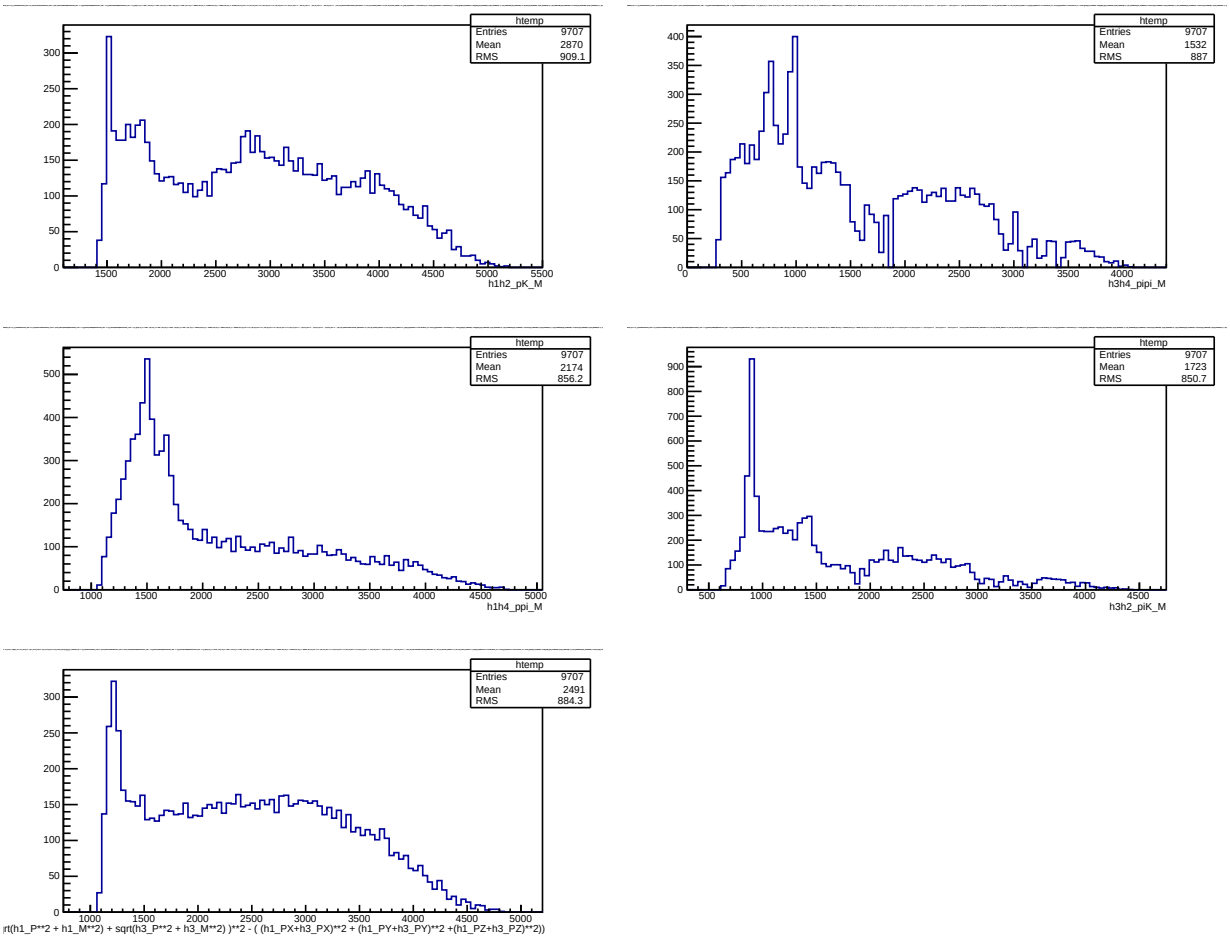

Figure E.2: Two and three body invariant-mass distributions considering $\Lambda_b^0 \to pK^-\pi^+\pi^-$ 2012 events. From left to right, top to bottom: $m(h_1h_2)$, $m(h_3h_4)$, $m(h_1h_4)$, $m(h_3h_2)$, $m(h_1h_3)$ distributions where h_is stand for p, K^-, π^+ and π^-, respectively.

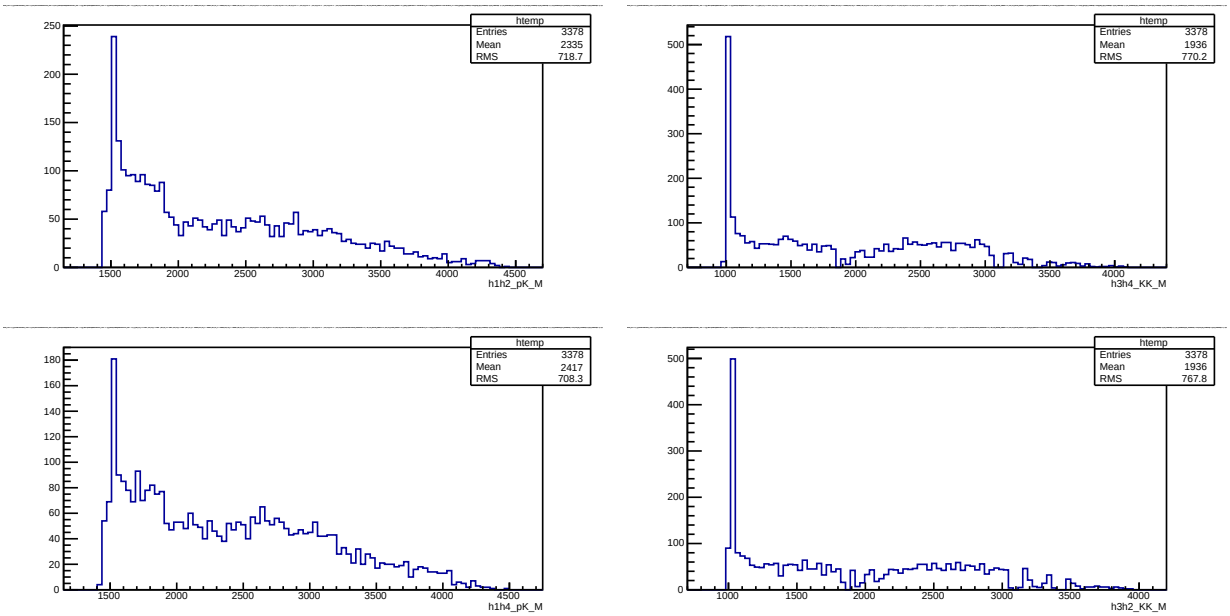

Figure E.3: Two and three body invariant-mass distributions considering $\Lambda_b^0 \to pK^-K^+K^-$ 2012 events. From left to right, top to bottom: $m(h_1h_2)$, $m(h_3h_4)$, $m(h_1h_4)$, $m(h_3h_2)$ distributions where h_is stand for p, K^-, K^+ and K^-, respectively.

E.2 Fit results using full phase space of data in linear scale.

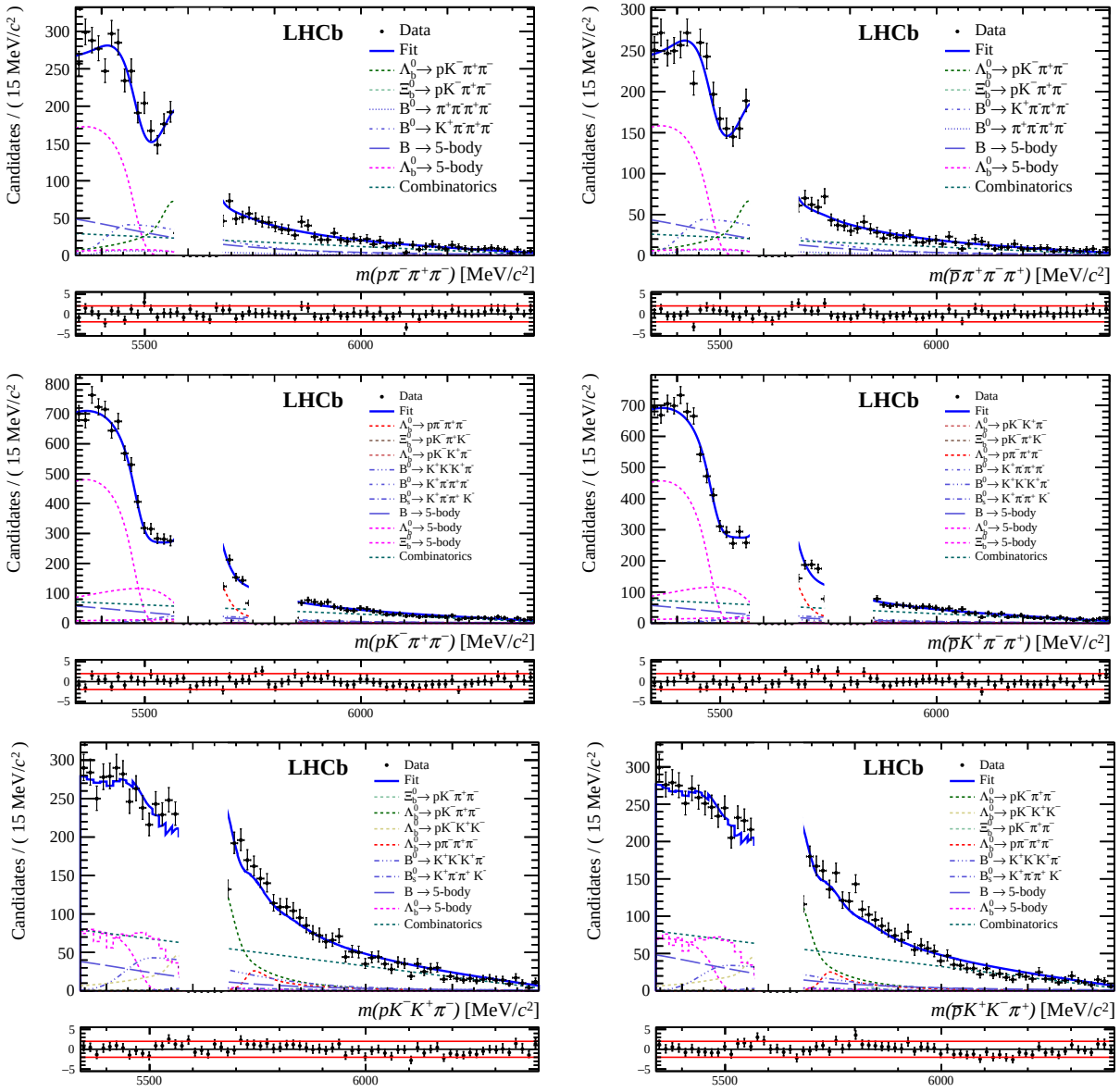

Figure E.4: Superimposed fit results for the [from top to bottom] $X_b^0 \to p\pi\pi\pi$, $X_b^0 \to pK\pi\pi$ and $X_b^0 \to pKK\pi$ spectra using the full phase space data. Plots in the left-column are for the spectra with X_b^0 and on the right-column for the spectra with $\overline{X}{}_b^0$.

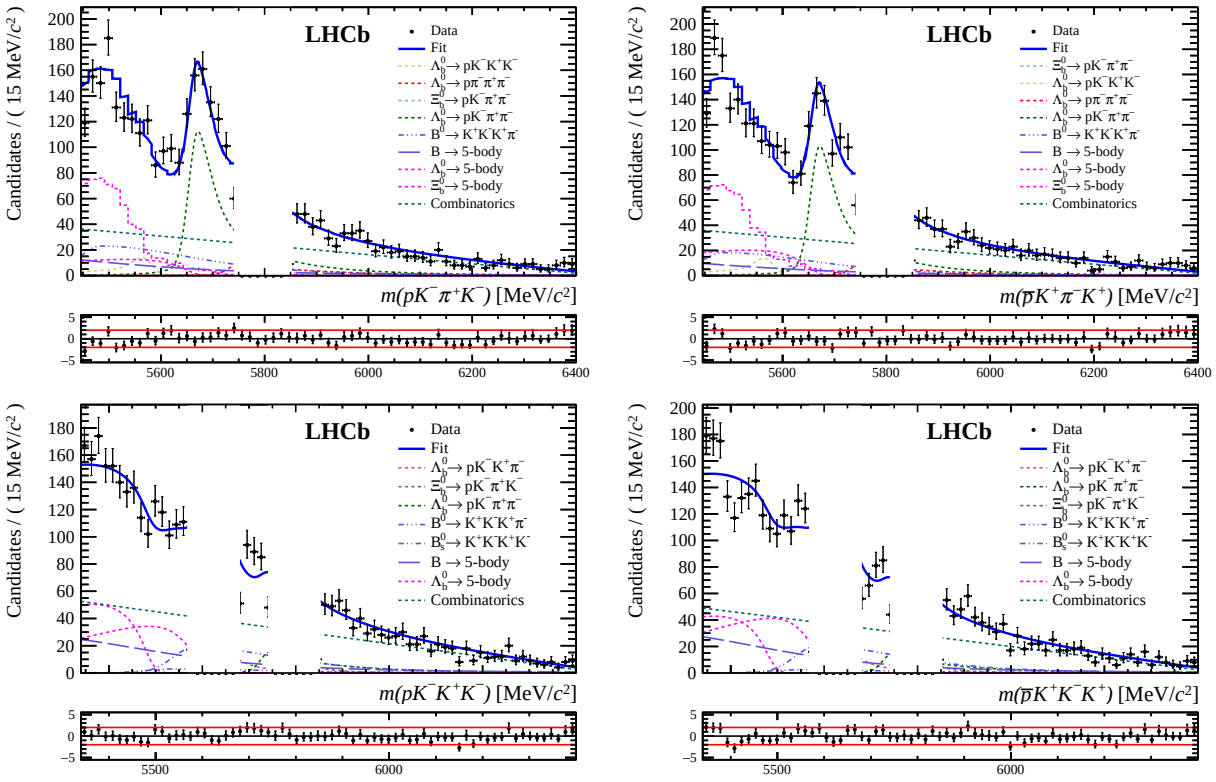

Figure E.5: Superimposed fit results for the [top] $X_b^0 \to pK\pi K$ and [bottom] $X_b^0 \to pKKK$ spectra using the full phase space data of 2011 and 2012. Plots in the left-column are for the spectra with X_b^0 and on the right-column for the spectra with $\overline{X}_b^0$.

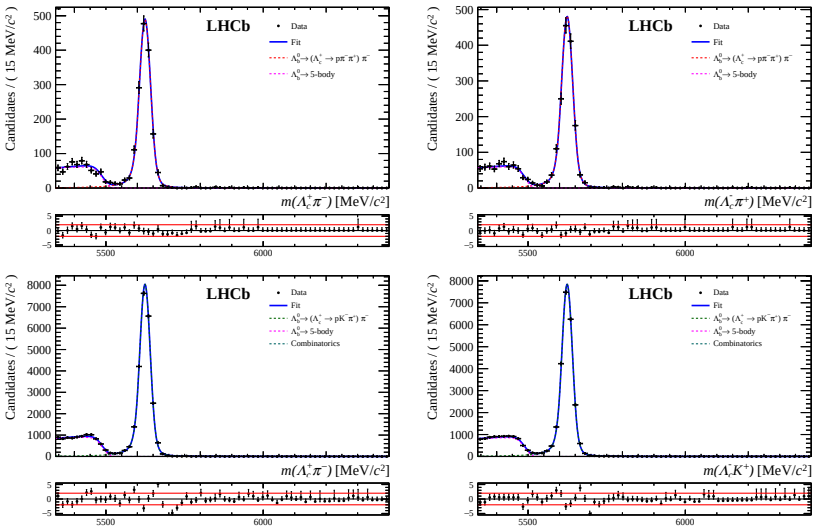

Figure E.6: Superimposed fit results for the [from top to bottom] $X_b^0 \to (\Lambda_c^+ \to p\pi\pi)\pi$, $X_b^0 \to (\Lambda_c^+ \to pK\pi)\pi$ spectra using the full phase space data of 2011 and 2012. Plots in the left-column are for the spectra with X_b^0 and on the right-column for the spectra with $\overline{X}_b^0$.

E.3 Fit results for the inclusive $\Delta\mathcal{A}^{CP}$ measurements

Table E.1: Floating parameters of the simultaneous fit to the TIS data sample of 2011 and 2012.

Floating parameter	Value (in Λ_b^0/Ξ_b^0 spectra)	Value (in $\overline{\Lambda}_b^0/\overline{\Xi}_b^0$ spectra)
Parameters shared 2011 and 2012 :		
μ (Ξ_b^0) - μ (Λ_b^0)	172.61 ± 0.37	
2012 σ_{core} (Signal $\Lambda_b^0 \to pK\pi\pi$) [ref]	16.55 ± 0.16	
$\mathcal{N}$ ($B^0 \to \pi\pi\pi\pi$ in $p\pi\pi\pi$) / $\mathcal{N}$ ($B^0 \to K\pi\pi\pi$ in $p\pi\pi\pi$)	0.180 ± 0.029	← shared
Parameters for 2011 spectra :		
$\mathcal{N}$ (Signal $\Lambda_b^0 \to p\pi\pi\pi$)	X.XXX ± X.XXX	X.XXX ± X.XXX
$\mathcal{N}$ (Signal $\Lambda_b^0 \to pK\pi\pi$)	X.XXX ± X.XXX	X.XXX ± X.XXX
$\mathcal{N}$ (Signal $\Lambda_b^0 \to pKK\pi$)	X.XXX ± X.XXX	X.XXX ± X.XXX
$\mathcal{N}$ (Signal $\Lambda_b^0 \to pKKK$)	X.XXX ± X.XXX	X.XXX ± X.XXX
$\mathcal{N}$ (Signal $\Xi_b^0 \to pK\pi K$)	X.XXX ± X.XXX	X.XXX ± X.XXX
$\mathcal{N}$ (Signal $\Xi_b^0 \to pK\pi\pi$)	X.XXX ± X.XXX	X.XXX ± X.XXX
$\mathcal{N}$ (Signal $\Xi_b^0 \to pKKK$)	X.XXX ± X.XXX	X.XXX ± X.XXX
$\mathcal{N}$ (Signal $\Lambda_b^0 \to (\Lambda_c^+ \to p\pi\pi)\pi$)	291.9 ± 17.3	300.5 ± 17.5
$\mathcal{N}$ (Signal $\Lambda_b^0 \to (\Lambda_c^+ \to pK\pi)\pi$)	4550.2 ± 68.3	4356.0 ± 66.9
$\mathcal{N}$ (Signal $\Xi_b^0 \to (\Xi_c^+ \to pK\pi)\pi$)	57.1 ± 8.3	51.7 ± 8.1
$\mathcal{N}$ (Signal $\Lambda_b^0 \to (\Xi_c^+ \to pK\pi)\pi$)	-0.8 ± 4.8	-7.6 ± 4.8
$\mathcal{N}$ (Combinatorics in $p\pi\pi\pi$)	159.0 ± 24.8	144.7 ± 24.5
$\mathcal{N}$ (Combinatorics in $pK\pi\pi$)	414.8 ± 43.1	342.5 ± 40.3
$\mathcal{N}$ (Combinatorics in $pKK\pi$)	484.4 ± 45.3	453.4 ± 42.7
$\mathcal{N}$ (Combinatorics in $pKKK$)	295.7 ± 37.7	233.6 ± 34.2
$\mathcal{N}$ (Combinatorics in $pK\pi K$)	182.1 ± 31.8	159.6 ± 30.4
$\mathcal{N}$ (Combinatorics in $(\Lambda_c^+ \to pK\pi)\pi$)	19.8 ± 10.2	1.1 ± 13.8
$\mathcal{N}$ (Combinatorics in $(\Xi_c^+ \to pK\pi)\pi$)	19.9 ± 9.7	0.0 ± 1.9
$\mathcal{N}$ (CF $B^0 \to K\pi\pi\pi$ in $p\pi\pi\pi$)	105.0 ± 18.4	119.4 ± 18.1
$\mathcal{N}$ (CF $B_s^0 \to K\pi\pi K$ in $pK\pi\pi$)	64.3 ± 17.1	70.1 ± 18.5
$\mathcal{N}$ (CF $B^0 \to KKK\pi$ in $pKK\pi$)	147.5 ± 20.7	109.8 ± 18.1
$\mathcal{N}$ (CF $B_s^0 \to KKKK$ in $pKKK$)	57.4 ± 16.6	46.8 ± 14.2
$\mathcal{N}$ (CF $B^0 \to$ 5-body in $pKKK$)	21.7 ± 13.2	57.1 ± 18.9
$\mathcal{N}$ (CF $B^0 \to$ 5-body in $pKK\pi$)	64.0 ± 15.5	82.3 ± 18.4
$\mathcal{N}$ (CF $B^0 \to$ 5-body in $pK\pi K$)	24.6 ± 12.5	18.7 ± 10.5
$\mathcal{N}$ (CF $B^0 \to$ 5-body in $pK\pi\pi$)	85.0 ± 27.5	84.7 ± 26.7
$\mathcal{N}$ (CF $B^0 \to$ 5-body in $p\pi\pi\pi$)	71.2 ± 17.2	83.3 ± 17.5
$\mathcal{N}$ (PR from $\Lambda_b^0 \to$ 5-body in $p\pi\pi\pi$)	269.5 ± 22.9	202.0 ± 21.5
$\mathcal{N}$ (PR from $\Lambda_b^0 \to$ 5-body in $pK\pi\pi$)	772.8 ± 37.8	701.3 ± 35.6
$\mathcal{N}$ (PR from $\Lambda_b^0 \to$ 5-body in $pKK\pi$)	81.3 ± 26.1	87.9 ± 25.9
$\mathcal{N}$ (PR from $\Lambda_b^0 \to$ 5-body in $pKKK$)	91.0 ± 24.0	59.8 ± 23.0
$\mathcal{N}$ (PR from $\Xi_b^0 \to$ 5-body in $pK\pi K$)	53.0 ± 33.5	82.8 ± 33.8
$\mathcal{N}$ (PR from $\Lambda_b^0 \to$ 5-body in $(\Lambda_c^+ \to p\pi\pi)\pi$)	94.2 ± 10.0	94.6 ± 10.0
$\mathcal{N}$ (PR from $\Lambda_b^0 \to$ 5-body in $(\Lambda_c^+ \to pK\pi)\pi$)	1681.1 ± 42.2	1540.9 ± 40.4
$\mathcal{N}$ (PR from $\Xi_b^0 \to$ 5-body in $(\Xi_c^+ \to pK\pi)\pi$)	90.0 ± 12.4	111.5 ± 11.7
c (Combinatorics in charmless decays)	0.046 ± 0.011	← shared
c (Combinatorics in charmed decays)	-0.023 ± 0.000	← shared

p (PR from Λ_b^0/Ξ_b^0 + 5-body in charmless spectra)	0.661 ± 0.175	← shared
s (PR from Λ_b^0/Ξ_b^0 + 5-body in charmless spectra)	-13.891 ± 19.401	← shared
p (PR from Λ_b^0 + 5-body in $(\Lambda_c^+ \to pK\pi)\pi$)	0.053 ± 0.045	← shared
s (PR from Λ_b^0 + 5-body in $(\Lambda_c^+ \to pK\pi)\pi$)	-2.342 ± 2.294	← shared
$r = (\ \sigma_{\rm core}\ \Lambda_b^0 \to p\pi\pi\pi)/(\sigma_{\rm ref})$	1.045 ± 0.017	← shared
$r = (\ \sigma_{\rm core}\ \Lambda_b^0 \to pK\pi\pi)/(\sigma_{\rm ref})$	1.003 ± 0.013	← shared
$r = (\ \sigma_{\rm core}\ \Lambda_b^0 \to pKK\pi)/(\sigma_{\rm ref})$	0.962 ± 0.016	← shared
$r = (\ \sigma_{\rm core}\ \Lambda_b^0 \to pKKK)/(\sigma_{\rm ref})$	0.922 ± 0.012	← shared
$r = (\ \sigma_{\rm core}\ \Xi_b^0 \to pK\pi\pi)/(\sigma_{\rm ref})$	1.038 ± 0.017	← shared
$r = (\ \sigma_{\rm core}\ \Xi_b^0 \to pK\pi K)/(\sigma_{\rm ref})$	0.995 ± 0.016	← shared
$r = (\ \sigma_{\rm core}\ \Xi_b^0 \to pKKK)/(\sigma_{\rm ref})$	0.930 ± 0.013	← shared
$\sigma_{\rm core}$ (Signal $\Lambda_b^0 \to (\Lambda_c^+ \to p\pi\pi)\pi$)	17.42 ± 0.53	← shared
$\sigma_{\rm core}$ (Signal $\Lambda_b^0 \to (\Lambda_c^+ \to pK\pi)\pi$)	16.92 ± 0.14	← shared
$\sigma_{\rm core}$ (Signal $\Lambda_b^0 \to (\Xi_c^+ \to pK\pi)\pi$)	14.00 ± 2.75	← shared
$\sigma_{\rm core}$ (Signal $\Xi_b^0 \to (\Xi_c^+ \to pK\pi)\pi$)	17.95 ± 1.63	← shared
$f_{\rm CF} = (\Lambda_b^0 \to pKKK$ in $pKK\pi)$	0.144 ± 0.017	← shared
$f_{\rm CF} = (\Lambda_b^0 \to pKKK$ in $pK\pi K)$	0.041 ± 0.009	← shared
$f_{\rm CF} = (\Lambda_b^0 \to pKK\pi$ in $pKKK)$	0.116 ± 0.014	← shared
$f_{\rm CF} = (\Lambda_b^0 \to pKK\pi$ in $pK\pi\pi)$	0.049 ± 0.005	← shared
$f_{\rm CF} = (\Lambda_b^0 \to pK\pi\pi$ in $pKKK)$	0.041 ± 0.002	← shared
$f_{\rm CF} = (\Lambda_b^0 \to pK\pi\pi$ in $pKK\pi)$	0.126 ± 0.008	← shared
$f_{\rm CF} = (\Lambda_b^0 \to pK\pi\pi$ in $p\pi\pi\pi)$	0.074 ± 0.011	← shared
$f_{\rm CF} = (\Lambda_b^0 \to pK\pi\pi$ in $pK\pi K)$	0.123 ± 0.008	← shared
$f_{\rm CF}$ = PR from Λ_b^0 + 5body in $pK\pi\pi$ in $pKK\pi)$	0.307 ± 0.028	← shared
$f_{\rm CF} = (\Lambda_b^0 \to p\pi\pi\pi$ in $pKK\pi)$	0.101 ± 0.004	← shared
$f_{\rm CF} = (\Lambda_b^0 \to p\pi\pi\pi$ in $pK\pi\pi)$	0.293 ± 0.024	← shared
$f_{\rm CF} = (\Lambda_b^0 \to p\pi\pi\pi$ in $pK\pi K)$	0.050 ± 0.002	← shared
$f_{\rm CF} = (\Xi_b^0 \to pK\pi K$ in $pKKK)$	0.113 ± 0.014	← shared
$f_{\rm CF} = (\Xi_b^0 \to pK\pi K$ in $pK\pi\pi)$	0.115 ± 0.010	← shared
$f_{\rm CF} = (\Xi_b^0 \to pK\pi\pi$ in $pKK\pi)$	0.113 ± 0.011	← shared
$f_{\rm CF} = \Xi_b^0 \to pK\pi\pi$ in $p\pi\pi\pi)$	0.041 ± 0.007	← shared
$f_{\rm CF} = (\Xi_b^0 \to pK\pi\pi$ in $pK\pi K)$	0.107 ± 0.011	← shared
$f_{\rm CF} = (B^0 \to K\pi\pi\pi$ in $pK\pi\pi)$	0.349 ± 0.011	← shared
$f_{\rm CF} = (B^0 \to KKK\pi$ in $pKKK)$	0.080 ± 0.004	← shared
$f_{\rm CF} = (B^0 \to KKK\pi$ in $pK\pi\pi)$	0.038 ± 0.001	← shared
$f_{\rm CF} = (B^0 \to KKK\pi$ in $pK\pi K)$	0.488 ± 0.011	← shared
$f_{\rm CF} = (B_s^0 \to K\pi\pi K$ in $pKK\pi)$	0.156 ± 0.008	← shared

Parameters for 2012 spectra :		
$\mathcal{N}$ (Signal $\Lambda_b^0 \to p\pi\pi\pi)$	X.XXX ± X.XXX	X.XXX ± X.XXX
$\mathcal{N}$ (Signal $\Lambda_b^0 \to pK\pi\pi)$	X.XXX ± X.XXX	X.XXX ± X.XXX
$\mathcal{N}$ (Signal $\Lambda_b^0 \to pKK\pi)$	X.XXX ± X.XXX	X.XXX ± X.XXX
$\mathcal{N}$ (Signal $\Lambda_b^0 \to pKKK)$	X.XXX ± X.XXX	X.XXX ± X.XXX
$\mathcal{N}$ (Signal $\Xi_b^0 \to pK\pi K)$	X.XXX ± X.XXX	X.XXX ± X.XXX
$\mathcal{N}$ (Signal $\Xi_b^0 \to pK\pi\pi)$	X.XXX ± X.XXX	X.XXX ± X.XXX
$\mathcal{N}$ (Signal $\Xi_b^0 \to pKKK)$	X.XXX ± X.XXX	X.XXX ± X.XXX
$\mathcal{N}$ (Signal $\Lambda_b^0 \to (\Lambda_c^+ \to p\pi\pi)\pi)$	734.0 ± 27.3	697.0 ± 26.6
$\mathcal{N}$ (Signal $\Lambda_b^0 \to (\Lambda_c^+ \to pK\pi)\pi)$	11512.9 ± 108.7	11013.7 ± 106.2
$\mathcal{N}$ (Signal $\Xi_b^0 \to (\Xi_c^+ \to pK\pi)\pi)$	112.2 ± 12.3	106.6 ± 12.5
$\mathcal{N}$ (Signal $\Lambda_b^0 \to (\Xi_c^+ \to pK\pi)\pi)$	-3.1 ± 9.0	6.3 ± 11.8

$\mathcal{N}$ (Combinatorics in $p\pi\pi\pi$)	297.3 ± 54.6	272.1 ± 53.0
$\mathcal{N}$ (Combinatorics in $pK\pi\pi$)	986.0 ± 90.9	952.6 ± 89.8
$\mathcal{N}$ (Combinatorics in $pKK\pi$)	1093.6 ± 78.2	1095.7 ± 78.9
$\mathcal{N}$ (Combinatorics in $pKKK$)	745.4 ± 71.2	677.5 ± 70.5
$\mathcal{N}$ (Combinatorics in $pK\pi K$)	582.8 ± 59.2	589.5 ± 57.4
$\mathcal{N}$ (Combinatorics in $(\Lambda_c^+ \to pK\pi)\pi$)	56.9 ± 16.5	21.3 ± 13.2
$\mathcal{N}$ (Combinatorics in $(\Xi_c^+ \to pK\pi)\pi$)	41.8 ± 13.8	19.7 ± 9.8
$\mathcal{N}$ (CF $B^0 \to K\pi\pi\pi$ in $p\pi\pi\pi$)	444.2 ± 36.6	464.5 ± 37.2
$\mathcal{N}$ (CF $B_s^0 \to K\pi\pi K$ in $pK\pi\pi$)	339.7 ± 41.0	347.0 ± 40.8
$\mathcal{N}$ (CF $B^0 \to KKK\pi$ in $pKK\pi$)	474.4 ± 36.9	400.3 ± 34.1
$\mathcal{N}$ (CF $B_s^0 \to KKKK$ in $pKKK$)	211.6 ± 33.2	244.8 ± 35.3
$\mathcal{N}$ (CF $B^0 \to$ 5-body in $pKKK$)	297.0 ± 44.3	277.1 ± 44.8
$\mathcal{N}$ (CF $B^0 \to$ 5-body in $pKK\pi$)	399.0 ± 40.0	509.0 ± 43.8
$\mathcal{N}$ (CF $B^0 \to$ 5-body in $pK\pi K$)	163.7 ± 29.7	134.0 ± 27.0
$\mathcal{N}$ (CF $B^0 \to$ 5-body in $pK\pi\pi$)	630.6 ± 70.8	610.2 ± 70.2
$\mathcal{N}$ (CF $B^0 \to$ 5-body in $p\pi\pi\pi$)	495.6 ± 42.6	413.7 ± 39.8
$\mathcal{N}$ (PR from $\Lambda_b^0 \to$ 5-body in $p\pi\pi\pi$)	630.2 ± 37.3	542.2 ± 35.0
$\mathcal{N}$ (PR from $\Lambda_b^0 \to$ 5-body in $pK\pi\pi$)	1784.1 ± 63.4	1751.2 ± 61.7
$\mathcal{N}$ (PR from $\Lambda_b^0 \to$ 5-body in $pKK\pi$)	359.2 ± 43.6	314.6 ± 43.5
$\mathcal{N}$ (PR from $\Lambda_b^0 \to$ 5-body in $pKKK$)	167.3 ± 37.8	181.8 ± 39.1
$\mathcal{N}$ (PR from $\Xi_b^0 \to$ 5-body in $pK\pi K$)	68.6 ± 56.0	111.7 ± 56.0
$\mathcal{N}$ (PR from $\Lambda_b^0 \to$ 5-body in $(\Lambda_c^+ \to p\pi\pi)\pi$)	286.0 ± 17.3	262.1 ± 16.6
$\mathcal{N}$ (PR from $\Lambda_b^0 \to$ 5-body in $(\Lambda_c^+ \to pK\pi)\pi$)	4111.2 ± 66.0	3929.0 ± 64.4
$\mathcal{N}$ (PR from $\Xi_b^0 \to$ 5-body in $(\Xi_c^+ \to pK\pi)\pi$)	220.4 ± 20.0	223.6 ± 19.7
c (Combinatorics in charmless decays)	0.053 ± 0.008	← shared
c (Combinatorics in charmed decays)	-0.004 ± 0.000	← shared
p (PR from Λ_b^0/Ξ_b^0 + 5-body in charmless spectra)	0.593 ± 0.110	← shared
s (PR from Λ_b^0/Ξ_b^0 + 5-body in charmless spectra)	-11.472 ± 4.227	← shared
p (PR from Λ_b^0 + 5-body in $(\Lambda_c^+ \to pK\pi)\pi$)	0.120 ± 0.030	← shared
s (PR from Λ_b^0 + 5-body in $(\Lambda_c^+ \to pK\pi)\pi$)	-6.412 ± 1.549	← shared
$r = (\ \sigma_{\text{core}}\ \Lambda_b^0 \to p\pi\pi\pi)/(\sigma_{\text{ref}})$	1.059 ± 0.014	← shared
$r = (\ \sigma_{\text{core}}\ \Lambda_b^0 \to pKK\pi)/(\sigma_{\text{ref}})$	0.958 ± 0.013	← shared
$r = (\ \sigma_{\text{core}}\ \Lambda_b^0 \to pKKK)/(\sigma_{\text{ref}})$	0.904 ± 0.011	← shared
$r = (\ \sigma_{\text{core}}\ \Xi_b^0 \to pK\pi\pi)/(\sigma_{\text{ref}})$	1.041 ± 0.014	← shared
$r = (\ \sigma_{\text{core}}\ \Xi_b^0 \to pK\pi K)/(\sigma_{\text{ref}})$	0.997 ± 0.013	← shared
$r = (\ \sigma_{\text{core}}\ \Xi_b^0 \to pKKK)/(\sigma_{\text{ref}})$	0.941 ± 0.012	← shared
σ_{core} (Signal $\Lambda_b^0 \to (\Lambda_c^+ \to p\pi\pi)\pi$)	18.21 ± 0.37	← shared
σ_{core} (Signal $\Lambda_b^0 \to (\Lambda_c^+ \to pK\pi)\pi$)	16.67 ± 0.09	← shared
σ_{core} (Signal $\Lambda_b^0 \to (\Xi_c^+ \to pK\pi)\pi$)	18.16 ± 5.55	← shared
σ_{core} (Signal $\Xi_b^0 \to (\Xi_c^+ \to pK\pi)\pi$)	18.10 ± 1.23	← shared
$f_{\text{CF}} = (\Lambda_b^0 \to pKKK$ in $pKK\pi)$	0.127 ± 0.014	← shared
$f_{\text{CF}} = (\Lambda_b^0 \to pKKK$ in $pK\pi K)$	0.035 ± 0.007	← shared
$f_{\text{CF}} = (\Lambda_b^0 \to pKK\pi$ in $pKKK)$	0.120 ± 0.010	← shared
$f_{\text{CF}} = (\Lambda_b^0 \to pKK\pi$ in $pK\pi\pi)$	0.046 ± 0.004	← shared
$f_{\text{CF}} = (\Lambda_b^0 \to pK\pi\pi$ in $pKKK)$	0.021 ± 0.001	← shared
$f_{\text{CF}} = (\Lambda_b^0 \to pK\pi\pi$ in $pKK\pi)$	0.120 ± 0.006	← shared
$f_{\text{CF}} = (\Lambda_b^0 \to pK\pi\pi$ in $p\pi\pi\pi)$	0.062 ± 0.007	← shared
$f_{\text{CF}} = (\Lambda_b^0 \to pK\pi\pi$ in $pK\pi K)$	0.107 ± 0.005	← shared
$f_{\text{CF}} = (\ \text{PR from}\ \Lambda_b^0$ + 5body in $pK\pi\pi$ in $pKK\pi)$	0.260 ± 0.021	← shared
$f_{\text{CF}} = (\Lambda_b^0 \to p\pi\pi\pi$ in $pKK\pi)$	0.103 ± 0.005	← shared

$f_{\rm CF} = (\Xi_b^0 \to pK\pi\pi$ in $pKK\pi)$	0.112 ± 0.009	← shared
$f_{\rm CF} = (\Xi_b^0 \to pK\pi\pi$ in $p\pi\pi\pi)$	0.037 ± 0.004	← shared
$f_{\rm CF} = (\Xi_b^0 \to pK\pi\pi$ in $pK\pi K)$	0.107 ± 0.009	← shared
$f_{\rm CF} = (B^0 \to K\pi\pi\pi$ in $pK\pi\pi)$	0.350 ± 0.006	← shared
$f_{\rm CF} = (B^0 \to KKK\pi$ in $pKKK)$	0.069 ± 0.002	← shared
$f_{\rm CF} = (B^0 \to KKK\pi$ in $pK\pi\pi)$	0.037 ± 0.000	← shared
$f_{\rm CF} = (B^0 \to KKK\pi$ in $pK\pi K)$	0.475 ± 0.006	← shared
$f_{\rm CF} = (B_s^0 \to K\pi\pi K$ in $pKK\pi)$	0.146 ± 0.005	← shared

Table E.2: Floating parameters of the simultaneous fit to the TOS data sample of 2011 and 2012. Only the yields are reported since all other parameters are shared between the TIS and TOS samples.

Floating parameter	Value (in Λ_b^0/Ξ_b^0 spectra)	Value (in $\overline{\Lambda}_b^0/\overline{\Xi}_b^0$ spectra)
Parameters for 2011 spectra :		
$\mathcal{N}$ (2011 Signal $\Lambda_b^0 \to p\pi\pi\pi$)	X.XXX ± X.XXX	X.XXX ± X.XXX
$\mathcal{N}$ (2011 Signal $\Lambda_b^0 \to pK\pi\pi$)	X.XXX ± X.XXX	X.XXX ± X.XXX
$\mathcal{N}$ (2011 Signal $\Lambda_b^0 \to pKK\pi$)	X.XXX ± X.XXX	X.XXX ± X.XXX
$\mathcal{N}$ (2011 Signal $\Lambda_b^0 \to pKKK$)	X.XXX ± X.XXX	X.XXX ± X.XXX
$\mathcal{N}$ (2011 Signal $\Xi_b^0 \to pK\pi K$)	X.XXX ± X.XXX	X.XXX ± X.XXX
$\mathcal{N}$ (2011 Signal $\Xi_b^0 \to pK\pi\pi$)	X.XXX ± X.XXX	X.XXX ± X.XXX
$\mathcal{N}$ (2011 Signal $\Xi_b^0 \to pKKK$)	X.XXX ± X.XXX	X.XXX ± X.XXX
$\mathcal{N}$ (2011 Signal $\Lambda_b^0 \to (\Lambda_c^+ \to p\pi\pi)\pi$)	172.0 ± 13.2	160.6 ± 12.8
$\mathcal{N}$ (2011 Signal $\Lambda_b^0 \to (\Lambda_c^+ \to pK\pi)\pi$)	2551.3 ± 51.1	2508.4 ± 50.7
$\mathcal{N}$ (2011 Signal $\Xi_b^0 \to (\Xi_c^+ \to pK\pi)\pi$)	31.3 ± 6.4	30.3 ± 6.4
$\mathcal{N}$ (2011 Signal $\Lambda_b^0 \to (\Xi_c^+ \to pK\pi)\pi$)	7.5 ± 5.0	6.3 ± 3.9
$\mathcal{N}$ (2011 Combinatorics in $p\pi\pi\pi$)	140.2 ± 23.1	141.4 ± 21.1
$\mathcal{N}$ (2011 Combinatorics in $pK\pi\pi$)	294.6 ± 39.1	336.4 ± 36.0
$\mathcal{N}$ (2011 Combinatorics in $pKK\pi$)	296.9 ± 33.6	368.0 ± 34.3
$\mathcal{N}$ (2011 Combinatorics in $pKKK$)	170.7 ± 27.3	193.9 ± 28.4
$\mathcal{N}$ (2011 Combinatorics in $pK\pi K$)	164.0 ± 26.8	128.1 ± 25.4
$\mathcal{N}$ (2011 Combinatorics in $(\Lambda_c^+ \to pK\pi)\pi$)	11.3 ± 7.2	6.1 ± 6.1
$\mathcal{N}$ (2011 Combinatorics in $(\Xi_c^+ \to pK\pi)\pi$)	13.8 ± 7.6	21.4 ± 10.3
$\mathcal{N}$ (2011 CF $B^0 \to K\pi\pi\pi$ in $p\pi\pi\pi$)	84.9 ± 15.1	59.9 ± 15.0
$\mathcal{N}$ (2011 CF $B_s^0 \to K\pi\pi K$ in $pK\pi\pi$)	37.1 ± 13.4	38.9 ± 14.4
$\mathcal{N}$ (2011 CF $B^0 \to KKK\pi$ in $pKK\pi$)	89.0 ± 15.9	61.7 ± 14.1
$\mathcal{N}$ (2011 CF $B_s^0 \to KKKK$ in $pKKK$)	27.4 ± 12.2	22.4 ± 10.7
$\mathcal{N}$ (2011 CF $B^0 \to$ 5-body in $pKKK$)	11.3 ± 9.8	28.9 ± 14.0
$\mathcal{N}$ (2011 CF $B^0 \to$ 5-body in $pKK\pi$)	36.7 ± 12.1	45.3 ± 14.4
$\mathcal{N}$ (2011 CF $B^0 \to$ 5-body in $pK\pi K$)	17.6 ± 9.9	13.0 ± 8.4
$\mathcal{N}$ (2011 CF $B^0 \to$ 5-body in $pK\pi\pi$)	39.3 ± 21.4	44.6 ± 20.8
$\mathcal{N}$ (2011 CF $B^0 \to$ 5-body in $p\pi\pi\pi$)	54.3 ± 14.2	47.3 ± 14.4
$\mathcal{N}$ (2011 PR from $\Lambda_b^0 \to$ 5-body in $p\pi\pi\pi$)	130.9 ± 17.7	118.9 ± 17.3
$\mathcal{N}$ (2011 PR from $\Lambda_b^0 \to$ 5-body in $pK\pi\pi$)	383.0 ± 27.4	393.2 ± 27.7
$\mathcal{N}$ (2011 PR from $\Lambda_b^0 \to$ 5-body in $pKK\pi$)	45.3 ± 18.9	24.3 ± 19.3
$\mathcal{N}$ (2011 PR from $\Lambda_b^0 \to$ 5-body in $pKKK$)	57.8 ± 17.1	20.6 ± 16.4
$\mathcal{N}$ (2011 PR from $\Xi_b^0 \to$ 5-body in $pK\pi K$)	0.0 ± 15.6	49.9 ± 26.1
$\mathcal{N}$ (2011 PR from $\Lambda_b^0 \to$ 5-body in $(\Lambda_c^+ \to p\pi\pi)\pi$)	68.1 ± 8.4	69.4 ± 8.6
$\mathcal{N}$ (2011 PR from $\Lambda_b^0 \to$ 5-body in $(\Lambda_c^+ \to pK\pi)\pi$)	863.4 ± 30.3	859.5 ± 30.2

$\mathcal{N}$ (2011 PR from $\Xi_b^0 \to$ 5-body in $(\Xi_c^+ \to pK\pi)\pi$)	46.9 ± 9.6	28.6 ± 9.2
2011 c (Combinatorics in charmless decays)	0.113 ± 0.062	← shared
Parameters for 2012 spectra :		
$\mathcal{N}$ (2012 Signal $\Lambda_b^0 \to p\pi\pi\pi$)	X.XXX ± X.XXX	X.XXX ± X.XXX
$\mathcal{N}$ (2012 Signal $\Lambda_b^0 \to pK\pi\pi$)	X.XXX ± X.XXX	X.XXX ± X.XXX
$\mathcal{N}$ (2012 Signal $\Lambda_b^0 \to pKK\pi$)	X.XXX ± X.XXX	X.XXX ± X.XXX
$\mathcal{N}$ (2012 Signal $\Lambda_b^0 \to pKKK$)	X.XXX ± X.XXX	X.XXX ± X.XXX
$\mathcal{N}$ (2012 Signal $\Xi_b^0 \to pK\pi K$)	X.XXX ± X.XXX	X.XXX ± X.XXX
$\mathcal{N}$ (2012 Signal $\Xi_b^0 \to pK\pi\pi$)	X.XXX ± X.XXX	X.XXX ± X.XXX
$\mathcal{N}$ (2012 Signal $\Xi_b^0 \to pKKK$)	X.XXX ± X.XXX	X.XXX ± X.XXX
$\mathcal{N}$ (2012 Signal $\Lambda_b^0 \to (\Lambda_c^+ \to p\pi\pi)\pi$)	417.0 ± 20.6	419.9 ± 20.7
$\mathcal{N}$ (2012 Signal $\Lambda_b^0 \to (\Lambda_c^+ \to pK\pi)\pi$)	6066.2 ± 78.9	6179.2 ± 79.5
$\mathcal{N}$ (2012 Signal $\Xi_b^0 \to (\Xi_c^+ \to pK\pi)\pi$)	69.4 ± 9.4	66.8 ± 10.0
$\mathcal{N}$ (2012 Signal $\Lambda_b^0 \to (\Xi_c^+ \to pK\pi)\pi$)	5.0 ± 7.9	8.9 ± 7.2
$\mathcal{N}$ (2012 Combinatorics in $p\pi\pi\pi$)	310.6 ± 46.0	266.3 ± 45.8
$\mathcal{N}$ (2012 Combinatorics in $pK\pi\pi$)	714.1 ± 78.8	716.8 ± 70.7
$\mathcal{N}$ (2012 Combinatorics in $pKK\pi$)	767.9 ± 60.1	774.3 ± 60.5
$\mathcal{N}$ (2012 Combinatorics in $pKKK$)	522.5 ± 54.1	537.9 ± 54.6
$\mathcal{N}$ (2012 Combinatorics in $pK\pi K$)	451.5 ± 47.8	492.8 ± 46.5
$\mathcal{N}$ (2012 Combinatorics in $(\Lambda_c^+ \to pK\pi)\pi$)	27.1 ± 11.2	9.4 ± 8.8
$\mathcal{N}$ (2012 Combinatorics in $(\Xi_c^+ \to pK\pi)\pi$)	31.0 ± 11.9	42.2 ± 13.4
$\mathcal{N}$ (2012 CF $B^0 \to K\pi\pi\pi$ in $p\pi\pi\pi$)	257.0 ± 29.1	298.8 ± 29.9
$\mathcal{N}$ (2012 CF $B_s^0 \to K\pi\pi K$ in $pK\pi\pi$)	191.1 ± 31.2	187.7 ± 30.9
$\mathcal{N}$ (2012 CF $B^0 \to KKK\pi$ in $pKK\pi$)	262.9 ± 28.0	209.7 ± 25.9
$\mathcal{N}$ (2012 CF $B_s^0 \to KKKK$ in $pKKK$)	106.8 ± 24.6	121.2 ± 26.3
$\mathcal{N}$ (2012 CF $B^0 \to$ 5-body in $pKKK$)	154.7 ± 32.7	148.7 ± 33.2
$\mathcal{N}$ (2012 CF $B^0 \to$ 5-body in $pKK\pi$)	222.6 ± 30.4	281.5 ± 33.2
$\mathcal{N}$ (2012 CF $B^0 \to$ 5-body in $pK\pi K$)	101.9 ± 23.2	79.7 ± 21.2
$\mathcal{N}$ (2012 CF $B^0 \to$ 5-body in $pK\pi\pi$)	344.1 ± 53.5	354.3 ± 53.2
$\mathcal{N}$ (2012 CF $B^0 \to$ 5-body in $p\pi\pi\pi$)	307.7 ± 34.2	273.6 ± 32.0
$\mathcal{N}$ (2012 PR from $\Lambda_b^0 \to$ 5-body in $p\pi\pi\pi$)	271.3 ± 27.5	334.1 ± 28.0
$\mathcal{N}$ (2012 PR from $\Lambda_b^0 \to$ 5-body in $pK\pi\pi$)	864.7 ± 45.7	807.8 ± 43.3
$\mathcal{N}$ (2012 PR from $\Lambda_b^0 \to$ 5-body in $pKK\pi$)	161.4 ± 30.6	140.5 ± 30.5
$\mathcal{N}$ (2012 PR from $\Lambda_b^0 \to$ 5-body in $pKKK$)	108.4 ± 27.5	69.9 ± 27.2
$\mathcal{N}$ (2012 PR from $\Xi_b^0 \to$ 5-body in $pK\pi K$)	52.3 ± 42.0	53.2 ± 41.2
$\mathcal{N}$ (2012 PR from $\Lambda_b^0 \to$ 5-body in $(\Lambda_c^+ \to p\pi\pi)\pi$)	147.0 ± 12.5	152.1 ± 12.6
$\mathcal{N}$ (2012 PR from $\Lambda_b^0 \to$ 5-body in $(\Lambda_c^+ \to pK\pi)\pi$)	2041.7 ± 46.6	1981.4 ± 45.8
$\mathcal{N}$ (2012 PR from $\Xi_b^0 \to$ 5-body in $(\Xi_c^+ \to pK\pi)\pi$)	96.6 ± 14.6	98.4 ± 15.1
2012 c (Combinatorics in charmless decays)	0.112 ± 0.047	← shared

E.4 Fit results in Low2x2BodyMass configuration in linear scale.

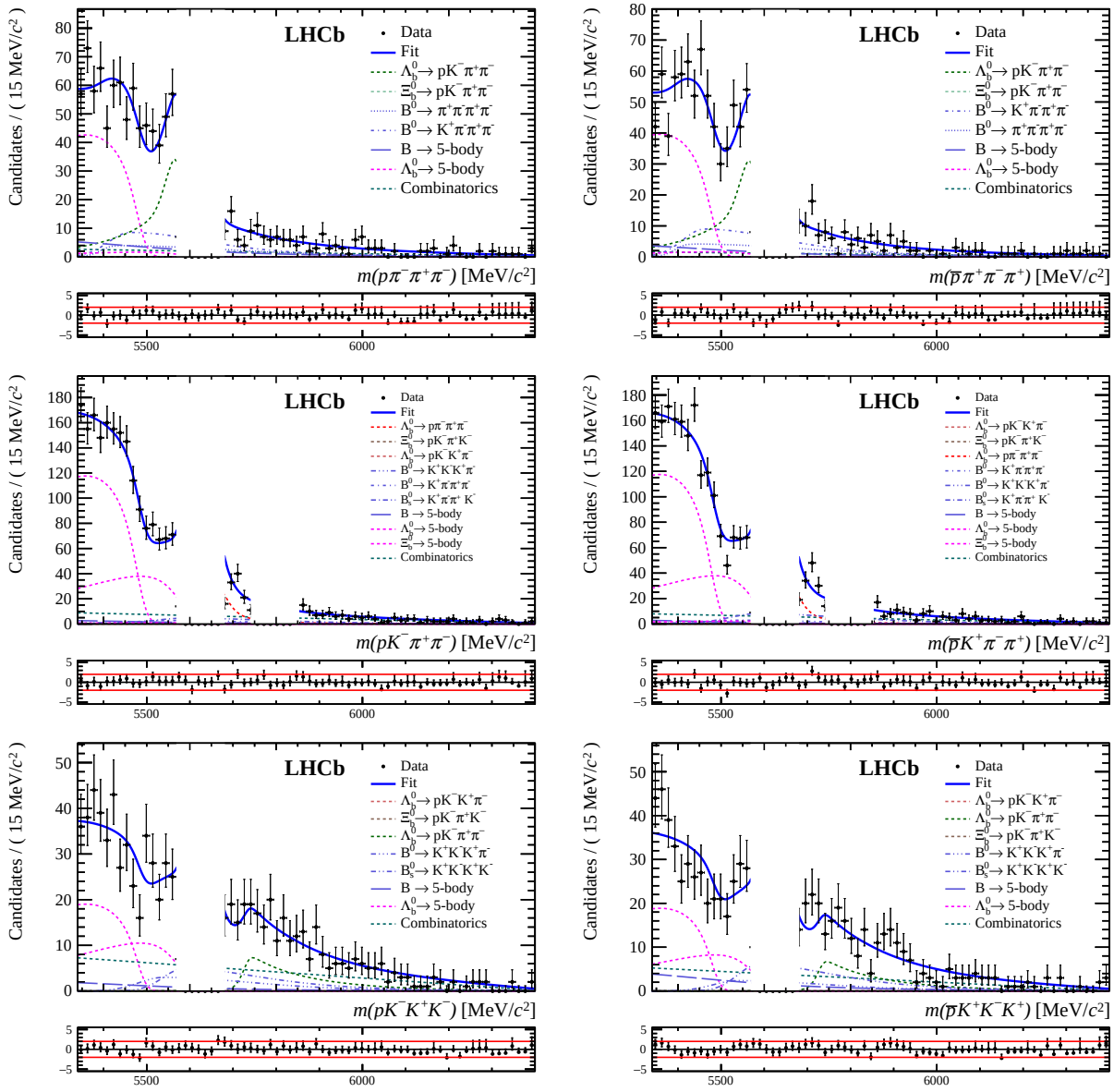

Figure E.7: (From top to bottom) $p\pi\pi\pi$, $pK\pi\pi$, $pKKK$ invariant-mass spectra for (first column) X_b data (TIS, TOS, 2011 and 2012 samples combined) and (second column) $\bar{X}_b$ data (TIS, TOS, 2011 and 2012 samples combined) considering Low2x2BodyMass set of cuts.

E.5 Fit results for specific decays in linear scale.

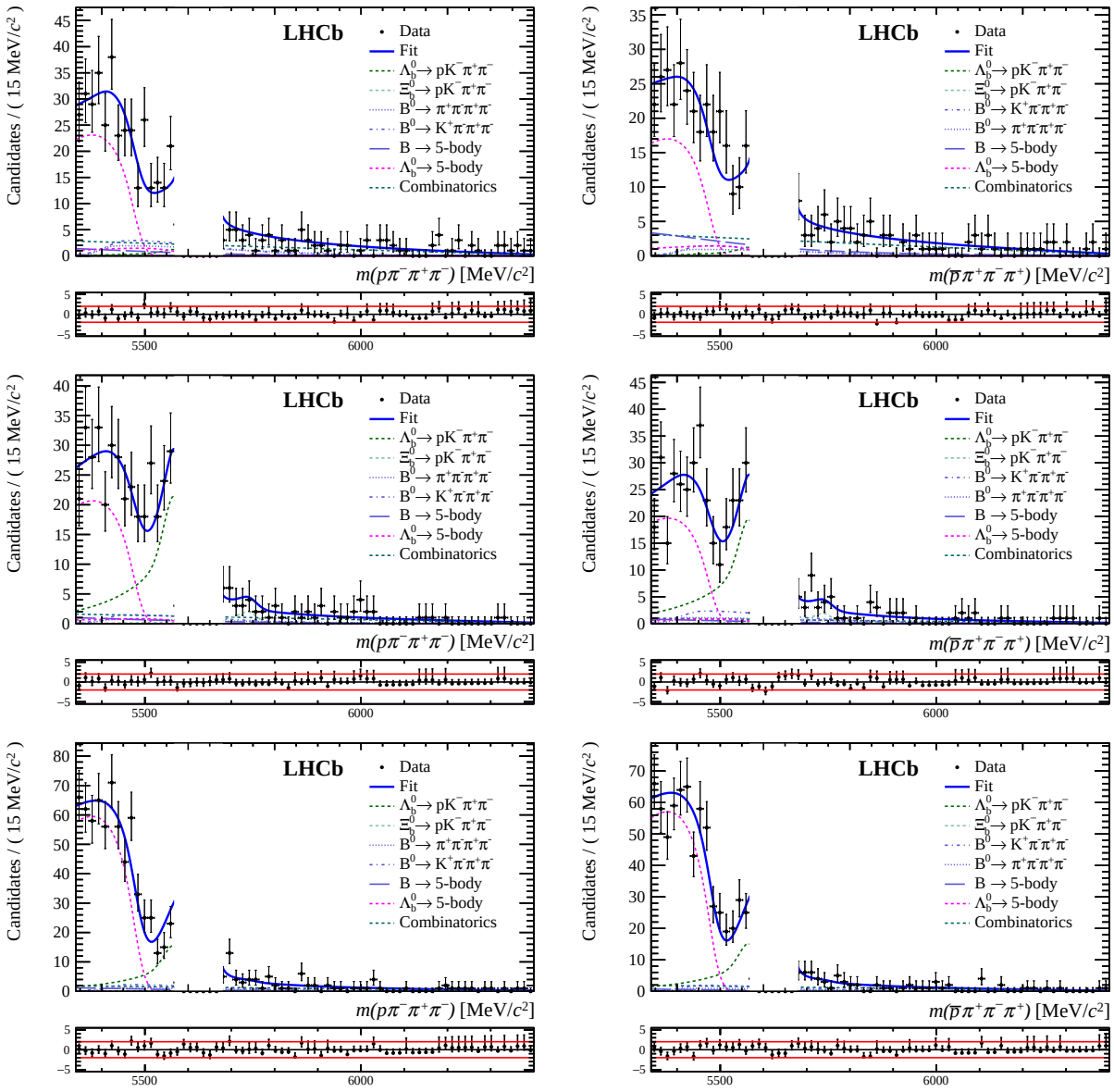

Figure E.8: $p\pi\pi\pi$ invariant-mass spectra considering (from top to bottom) $\Lambda_b^0 \to pa_1$, $\Lambda_b^0 \to N^{*0}\rho^0$ (f^0), $\Lambda_b^0 \to \Delta^{++}\pi^-\pi^-$ resonances for (first column) X_b^0 data (TIS, TOS, 2011 and 2012 samples combined) and (second column) $\overline{X}_b^0$ data (TIS, TOS, 2011 and 2012 samples combined).

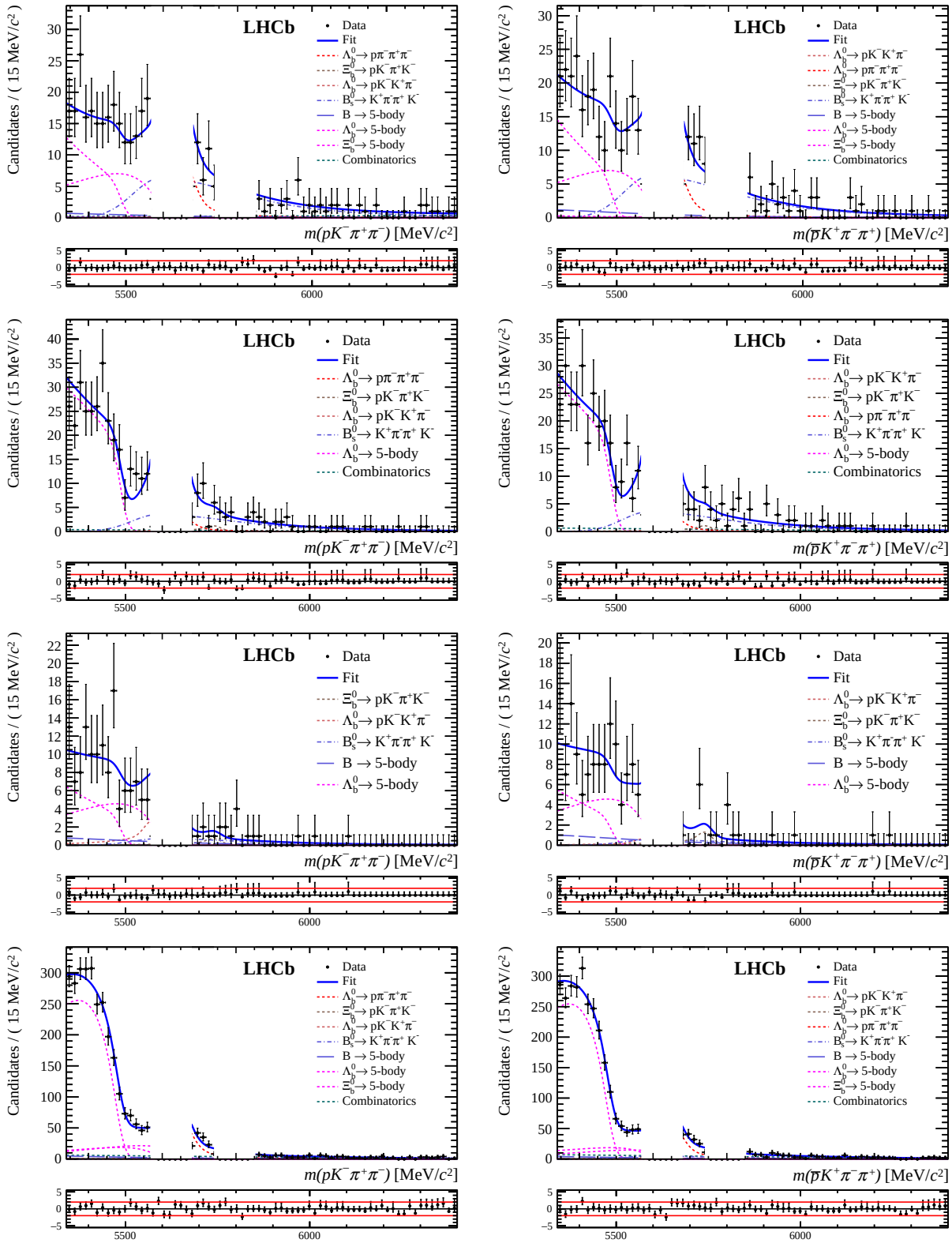

Figure E.9: $pK\pi\pi$ invariant-mass spectra considering (from top to bottom) $\Lambda_b^0 \to pK_1$, $\Lambda_b^0 \to N^*(1520)^0 K^{*0}$, $\Lambda_b^0 \to \Lambda^*(1520)^0\rho^0(f^0)$, $\Lambda_b^0 \to \Delta^{++}K^-\pi^-$ decays for (first column) X_b^0 data (TIS, TOS, 2011 and 2012 samples combined) and (second column) $\overline{X}_b^0$ data (TIS, TOS, 2011 and 2012 samples combined).

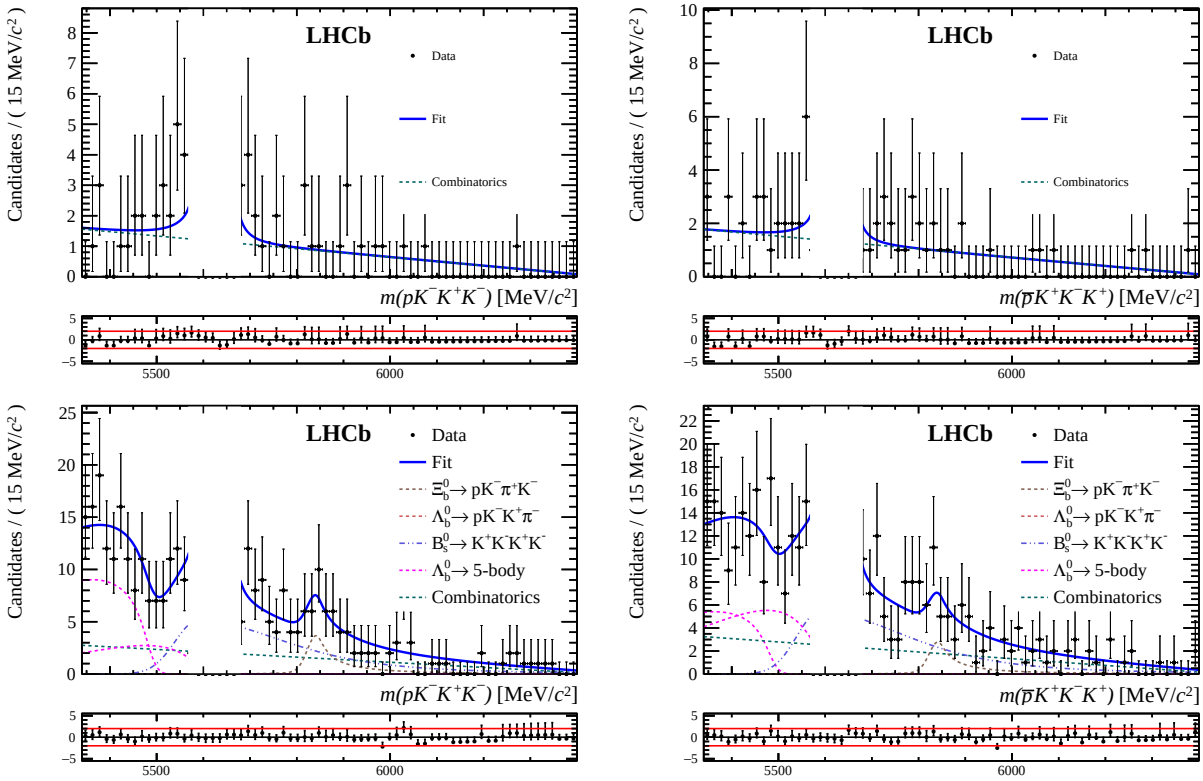

Figure E.10: $pKKK$ invariant-mass spectra considering (from top to bottom) $\Lambda_b^0 \to \Lambda^*(1520)^0\phi^0$ and $\Lambda_b^0 \to pK^-_{\text{highmass}}\phi^0$ decays for (first column) X_b^0 data (TIS, TOS, 2011 and 2012 samples combined) and (second column) $\overline{X}_b^0$ data (TIS, TOS, 2011 and 2012 samples combined).

Appendix F

Preliminary study of $B^0 \to K^{*0}(K^+\pi^-)\tau^+\tau^-$ decay

This section presents an exploratory work on the reconstruction of the decay $B^0 \to K^{*0}\tau^+\tau^-$ by making use of a simulated signal sample. As a word of caution, I want to stress in those lines that this appendix is only aiming at presenting the development of a partial reconstruction that might be of interest in a future and complete analysis.

F.1 Motivations

In the Standard Model, the couplings between electroweak gauge bosons and the three lepton families are equal: the $W^\pm \to l^\pm \nu_l$ or $Z^0 \to l^\pm l^\mp$ decay amplitudes are hence proportional to the same vertex factors whatever the final state is, resulting in the Lepton Flavour Universality (LFU). For instance, measurements of the $Z^0 \to l^\pm l^\mp$ ($l^\pm = e^\pm, \mu^\pm, \tau^\pm$) decay widths are providing so far compatible results within uncertainties [8]. Lepton Flavour Universality Violation (LFUV) might however arise in quark transitions, for which different New Physics (NP) processes can come into play.

In that respect, several experimental measurements present tensions with respect to the SM predictions: measurements of the differential branching fractions of electroweak penguin processes with dileptons in the final state such as, for instance, $B^0 \to K^{(*)}\mu^+\mu^-$ and $B_s^0 \to \phi\mu^+\mu^-$ are indeed deviating from SM theoretical expectations [50–52]. Anomalies have as well been observed through R_K, R_{K^*}, R_D, R_{D^*} observables that are defined in equations (F.1). Current discrepancies with respect to the SM for these ratios, that may constitute hints of NP, are displayed in Table F.1.

$$R_{K^{(*)}} = \frac{\mathcal{B}(B^0 \to K^{(*)}\mu^+\mu^-)}{\mathcal{B}(B^0 \to K^{(*)}e^+e^-)} \tag{F.1a}$$

$$R_{D^{(*)}} = \frac{\mathcal{B}(B^+ \to D^{(*)}\tau^-\overline{\nu}_\tau)}{\mathcal{B}(B^+ \to D^{(*)}l^-\overline{\nu}_\ell)} \tag{F.1b}$$

Conversely to the measurements previously discussed, rare decay processes impliying the third-lepton generation (we refer here to $b \to s\tau^+\tau^-$ processes) have not been observed so far. The τ-lepton has a special status:

- measurements would permit the access to angular variables related to the τ polarisation,

Observable	SM prediction	Experimental measurements	Tension (σ)
R_D	0.300 ± 0.008 [43]	$0.403 \pm 0.040 \pm 0.024$ [43]	2.2[a]
R_{D^*}	0.252 ± 0.003 [43]	$0.310 \pm 0.015 \pm 0.008$ [43]	3.4[a]
R_K	1[b]	$0.745^{+0.090}_{-0.074} \pm 0.036$ [53]	2.6
R_{K^*}	1[b]	$0.66\ ^{+0.11}_{-0.07} \pm 0.03$ [c] [54]	$2.1 - 2.3$
		$0.69\ ^{+0.11}_{-0.07} \pm 0.05$ [c] [54]	$2.4 - 2.5$

[a] Recent LHCb measurement of $R_{D^{*-}}$ brings the combined discrepancy of R_D and R_{D^*} to 4.1σ [55].
[b] The SM prediction is exactly 1 but small and well-understood effects related to the leptons masses.
[c] R_{K^*} has been measured in bins of $m^2_{l^\pm l^\mp}$.

Table F.1: Current SM predictions and experimental measurements of R_K, R_{K^*}, R_D, R_{D^*}.

- the large mass of the τ-lepton may improve the sensitivity of NP contributions: for instance in the two-Higgs-doublet-models, the coupling between Higgs boson and lepton is proportional to the τ mass [56],

- and it would complete the comparisons with the two others family (μ, e): to sort out the NP models, should the anomalies be confirmed with light flavours.

Henceforth, this part is dedicated to $B^0 \to K^{*0}(K^+\pi^-)\tau^+\tau^-$ decay mode, for which a Feynman decay-representation is displayed on Fig. F.1. The actual SM prediction of the branching fraction gives $\mathcal{O}(10^{-7})$ [57,58], value that remains far below the present upper limit set on a similar decay mode $\mathcal{B}(B \to K^+\tau^+\tau^-) < \mathcal{O}(10^{-3})$ [59] (this limit is expected to be improved by the Belle II experiment though). The goal of the preliminary analysis presented in this Section is to reconstruct $B^0 \to K^{*0}(K^+\pi^-)\tau^+\tau^-$ decay with $\tau^\pm \to \pi^\pm\pi^\mp\pi^\pm\overset{(-)}{\nu}_\tau$ and figure out whether the B^0 mass can be determined with an acceptable resolution.

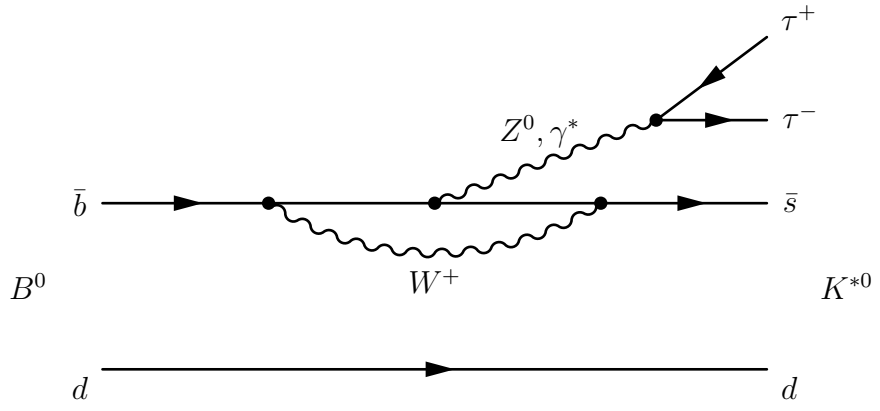

Figure F.1: Feynman diagram of $B^0 \to K^{*0}(K^+\pi^-)\tau^+\tau^-$ decay in the SM. NP contributions can for instance imply Z' boson instead of Z^0.

If so, LHCb could provide an experimental limit on the branching fraction of this decay, although the expected number of reconstructed signal events (with some assumptions) is dramatically low ($\mathcal{N}_{\text{sig}} \simeq 0.6$ using Eq. (F.2)) Any disagreement with the SM prediction on

this yield and hence, on the branching fraction, could be an additional hint of NP.

$$\mathcal{N}_{\text{sig}} = 2 \int \mathcal{L}dt \cdot \sigma_{b\bar{b}} \cdot f_{B^0} \cdot \mathcal{B}(B^0 \to K^{*0}(K^+\pi^-)\tau^+\tau^-) \cdot \mathcal{B}(\tau \to 3\pi)^2 \cdot \epsilon_{\text{rec.}}\epsilon_{acc.}\epsilon_{trigger}. \quad \text{(F.2a)}$$

$$\text{with} \begin{cases} \int \mathcal{L}dt = & 3\,\text{fb}^{-1} & : & \text{Run I integrated luminosity} \\ \sigma_{b\bar{b}} \sim & 295\mu\text{b} & : & b\text{-pair production cross-section (7 TeV) [60]} \\ f_{B^0} \sim & 40\% & : & (b \to B^0) \text{ hadronisation fraction [8]} \\ \mathcal{B}(B^0 \to K^*\tau\tau) \sim & \mathcal{O}(10^{-7}) & : & \text{prediction of SM branching fraction} \\ \mathcal{B}(\tau \to 3\pi)^2 \sim & 0.8\% & : & \text{branching fraction [8]} \\ \epsilon_{\text{rec.,acc,trigg}} \sim & 0.1\% & : & \text{reconstruction, acceptance and trigger efficiencies} \end{cases} \quad \text{(F.2b)}$$

F.2 Partial Reconstruction of $B^0 \to K^{*0}(K^+\pi^-)\tau^+\tau^-$

As soon as neutrinos are in the $B^0 \to K^{*0}(K^+\pi^-)\tau^+\tau^-$ possible final states, the kinematics (hence the B quadri-vector) is not fully-reconstructible at LHCb. This section presents a partial reconstruction of the decay: it consists in the determination of the missing (neutrinos) components by using the topological informations of the decay. Simulated sample of the $B^0 \to K^{*0}(K^+\pi^-)\tau^+(\pi^+\pi^-\pi^+\overline{\nu}_\tau)\tau^-(\pi^-\pi^+\pi^-\nu_\tau)$ decay has been generated and is used in order to perform this partial reconstruction, whose procedure is described in this section. I underline here again that this approach is exploratory. The backgrounds are not considered in this analysis yet.

F.2.1 Method

Figure F.2 is illustrating the topology of the $B^0 \to K^{*0}(K^+\pi^-)\tau^+(\pi^+\pi^-\pi^+\overline{\nu}_\tau)\tau^-(\pi^-\pi^+\pi^-\nu_\tau)$ decay. Considering that the π's and K^{*0} are fully reconstructed, we have a total of 6 degrees of freedom (the 2 momentum vectors of the neutrinos). The decay is however sufficiently constrained by considering energy-momentum conservation equations, the mass of the τ leptons and flight distances. The procedure is hence detailed through the following equations.

Considering energy and momenta conservation at one Tertiary-Vertex (TV) position, one can write:

$$\sqrt{m^2_{\tau^-} + p^2_{\tau^-}} = \sqrt{m^2_{\pi_t} + p^2_{\pi_t}} + p_{\nu_\tau} \quad \text{(F.3a)}$$

$$\vec{p_{\tau^-}} = \vec{p_{\pi_t}} + \vec{p_{\nu_\tau}}. \quad \text{(F.3b)}$$

where π_t stands for the sum of the π's (daughters of the τ decaying) 4-vectors. We can indeed consider that the τ decay as a 2-body decay as soon as the π's are fully reconstructible within LHCb acceptance. Defining the parallel component as the direction of the τ decaying (given by the Secondary (SV) and Tertiary Vertices positions), one can write Eq. (F.3b) as:

$$\begin{cases} \vec{0} = & \vec{p_{\pi_t}}^{\perp} + \vec{p_{\nu_\tau}}^{\perp}, \\ \vec{p_{\tau^-}}^{\parallel} = & \vec{p_{\pi_t}}^{\parallel} + \vec{p_{\nu_\tau}}^{\parallel}. \end{cases} \quad \text{(F.4)}$$

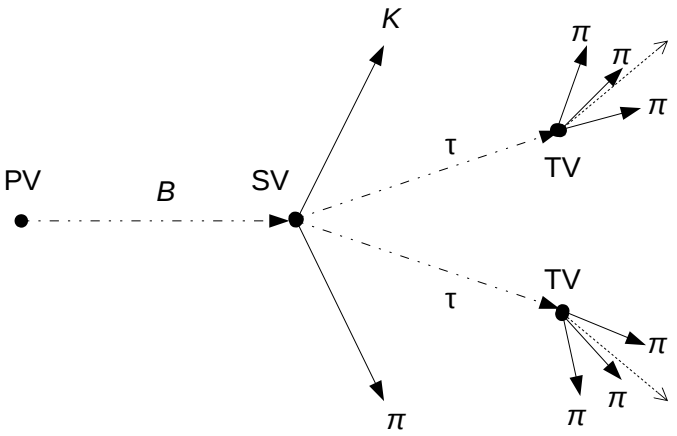

Figure F.2: Illustration of the $B^0 \to K^{*0}(K^+\pi^-)\tau^+(\pi^+\pi^-\pi^+\overline{\nu}_\tau)\tau^-(\pi^-\pi^+\pi^-\nu_\tau)$. PV, SV, and TV correspond to the Primary, Secondary and Tertiary vertices, respectively. The dotted lines represent the non-reconstructed particles. Conversely, the plain lines are the particles that can be reconstructed in the detector.

Squaring both sides of Eq. (F.3a), provides

$$m^2_{\tau-} = E^2_{\pi_t} + p^2_{\nu_\tau} + 2p_{\nu_\tau}E_{\pi_t} - p^{\parallel,2}_{\pi_t} - p^{\parallel,2}_{\nu_\tau} - 2p^{\parallel}_{\nu_\tau}p^{\parallel}_{\pi_t}, \tag{F.5a}$$

$$\Leftrightarrow\quad m^2_{\tau-} = E^2_{\pi_t} + p^{\perp,2}_{\nu_\tau} - p^{\parallel,2}_{\pi_t} + 2(p_{\nu_\tau}E_{\pi_t} - p^{\parallel}_{\nu_\tau}p^{\parallel}_{\pi_t}), \tag{F.5b}$$

$$\Leftrightarrow\quad m^2_{\tau-} = E^2_{\pi_t} + p^{\perp,2}_{\nu_\tau} - p^{\parallel,2}_{\pi_t} + 2(p_{\nu_\tau}E_{\pi_t} - p^{\parallel}_{\nu_\tau}p^{\parallel}_{\pi_t}). \tag{F.5c}$$

Rearranging the expression and considering that $p^{\perp,2}_{\nu_\tau} = p^{\perp,2}_{\pi_t}$, Eq. (F.5c) becomes

$$K = \sqrt{p^{\parallel,2}_{\nu_\tau} + p^{\perp,2}_{\nu_\tau}}E_{\pi_t} - p^{\parallel}_{\nu_\tau}p^{\parallel}_{\pi_t}, \tag{F.6a}$$

$$\text{with}\quad 2K = m^2_\tau - E^2_{\pi_t} + p^{\parallel,2}_{\pi_t} - p^{\perp,2}_{\pi_t},$$
$$= (m^2_\tau - m^2_{\pi_t} - 2p^{\perp,2}_{\pi_t}). \tag{F.6b}$$

Squaring both sides of Eq. (F.6a) eventually provides a quadratic equation, into which $p^{\parallel}_{\nu_\tau}$ is the only unknown quantity

$$p^{\parallel,2}_{\nu_\tau}(p^{\parallel,2}_{\pi_t} - E^2_{\pi_t}) + 2p^{\parallel}_{\nu_\tau}Kp^{\parallel}_{\pi_t} + K^2 - p^{\perp,2}_{\pi_t}E^2_{\pi_t} = 0. \tag{F.7}$$

We hence can compute the discriminant Δ of Eq. (F.7) as

$$\Delta = 4\left[K^2p^{\parallel,2}_{\pi_t} - \left(p^{\parallel,2}_{\pi_t} - E^2_{\pi_t}\right)\left(K^2 - p^{\perp,2}_{\pi_t}E^2_{\pi_t}\right)\right], \tag{F.8a}$$

$$\Leftrightarrow\quad \Delta = 4E^2_{\pi_t}\left(p^{\parallel,2}_{\pi_t}p^{\perp,2}_{\pi_t} + K^2 - p^{\perp,2}_{\pi_t}E^2_{\pi_t}\right), \tag{F.8b}$$

$$\Leftrightarrow\quad \Delta = E^2_{\pi_t}\left(m^2_\delta - 4p^{\perp,2}_{\pi_t}m^2_\tau\right), \tag{F.8c}$$

$$\text{with}\quad m_\delta = m^2_\tau - m^2_{\pi_t},$$

and consequently determine the missing parallel component of the ν_τ as a function of known quantities through:

$$p^{\parallel}_{\nu_\tau} = \frac{(m_\delta - 2p^{\perp,2}_{\pi_t})}{2(p^{\perp,2}_{\pi_t} + m^2_{\pi_t})}\cdot p^{\parallel}_{\pi_t} \pm \frac{\sqrt{m^2_\delta - 4m^2_\tau p^{\perp,2}_{\pi_t}}}{2(p^{\perp,2}_{\pi_t} + m^2_{\pi_t})}\cdot E_{\pi_t}. \tag{F.9}$$

For each TV, one can determine the missing parallel ν_τ component and hence, the τ momentum and eventually the B invariant mass. For each event, we have four possible solutions of the B^0 invariant mass (two per TV) hereafter denoted as *rr, rw, wr, ww* for *right-right, right-wrong, wrong-right, wrong-wrong* respectively. The *right* solution is determined according to the *true* value, by using partial reconstruction procedure on a *true*[a] simulated data sample: the closest solution to the *true* value is taken as *right*. This is obviously a cheated way of selecting solutions that cannot be use while running on real data.

F.2.2 Commissioning the partial reconstruction

In order to check the partial reconstruction equations, we make use of a *true* simulated data sample. Are compared on Fig. F.3 the partial recontructed momentum distributions of ν_τ, $\overline{\nu}_\tau$ and $\tau^\pm$ with the true distributions. Since resolutions effects are not taken into account the two distributions are the same and validate the equations system.
The B^0 invariant mass distributions for each type of solution is provided on Fig. F.4. One can observe that the *rr* solution is not exactly a line. This is due to rounding errors of simulated observables at the time of producing the tuples.
Now that the implementation of the method is validated, it is time to turn to fully simulated events to examine the resolution sensitivities.

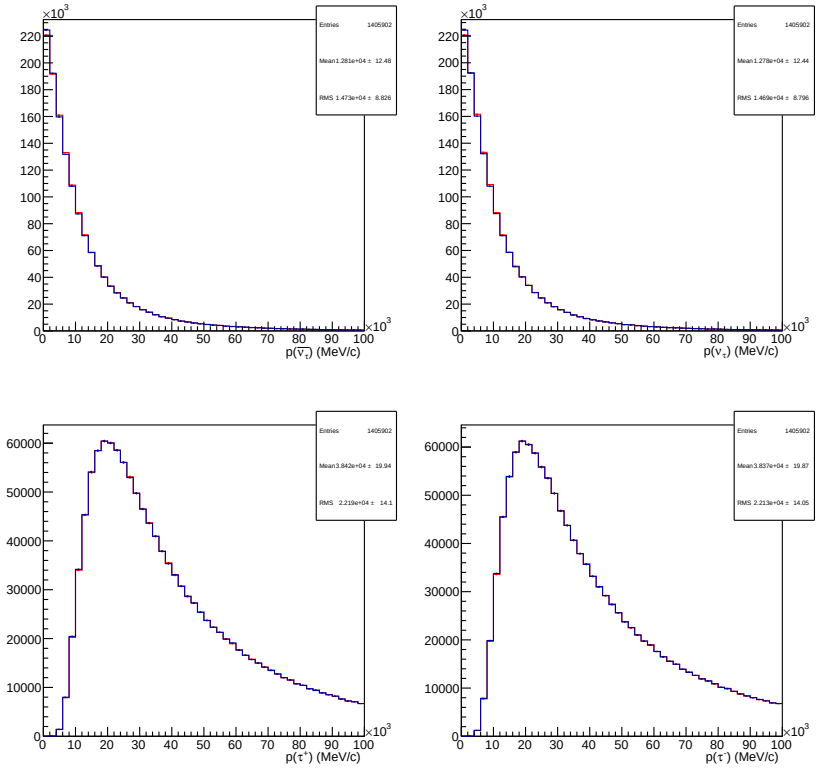

Figure F.3: (From top to bottom, left to right) ν_τ, $\overline{\nu}_\tau$, τ^+ and τ^- momentum distributions using the partial reconstruction procedure (blue line) that is compared to the true distributions (red line)

[a] *true* means that the detector response has not been simulated. Eventual resolution effects are consequently not considered at this stage.

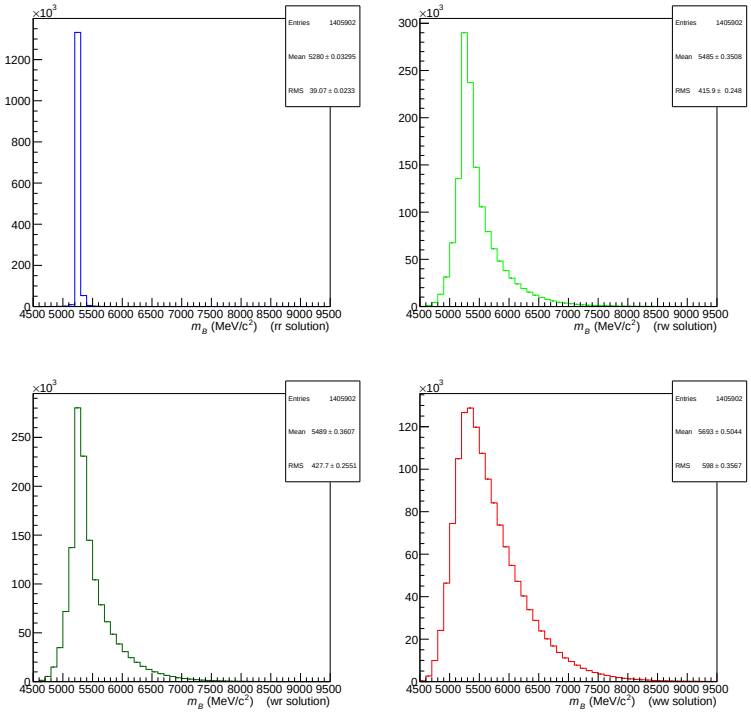

Figure F.4: Invariant mass distribution of B^0 by using pure simulated data sample. The four type of solutions are displayed and indicated in title of x-axis.

F.2.3 Impact of experimental resolutions.

The resolution on B^0 signal peak comes from the determination of the π_t and $K\pi$ momenta and the PV, SV and TVs positions. For instance, as soon as the SV is used to determine the two τ's directions as well as the B^0 direction, we expect a dramatic degradation of the B^0 resolution due to the uncertainties on the SV position. The values of those quantities as given by the *reconstruction*[b] are hence implemented in the procedure presented so far. In order to get an estimation of the experimental resolution, a gaussian fit to the difference between the *true* B^0 invariant mass distribution and the reconstructed one, for each type of solution, is provided on Fig. F.5. Only the left part of the distribution is fitted: the resolution number should be compared with the ~ 10 MeV/c^2 resolution of fully reconstructed decays, and only the heart of the distribution is of interest, since the right-handed tail is a direct consequence of resolution effects. The resolution on the rr B^0 invariant mass is eventually found to be $\sigma_{\text{rec}} = 303 \pm 6$ MeV/c^2.

As previously emphasized, making use of the *true* simulation sample in order to select the *right* or *wrong* solutions cannot be use while looking at real data. In a further analysis on real data, one can however model the wrong solutions and subtract these contributions to the sum of the four invariant masses. Following the same strategy as for the rr solution, a gaussian fit to the left part of the sum of the four solution invariant mass distributions is displayed on Fig. F.6. The resolution is found to be $\sigma_{\text{all}} = 322 \pm 4$. This result is encouraging: despite detector experimental resolutions and unknown neutrinos components, the $B^0 \to K^{*0}(K^+\pi^-)\tau^+\tau^-$ candidates are reconstructible. However, resolutions effects brings the term under the square root in Eq. F.9 to negative value: the immediate consequence is a low reconstruction efficiency (found to be around 12%)

[b] *reconstruction* means that we are considering the values provided by the simuation of the detector response, taking consequently into account resolution effects.

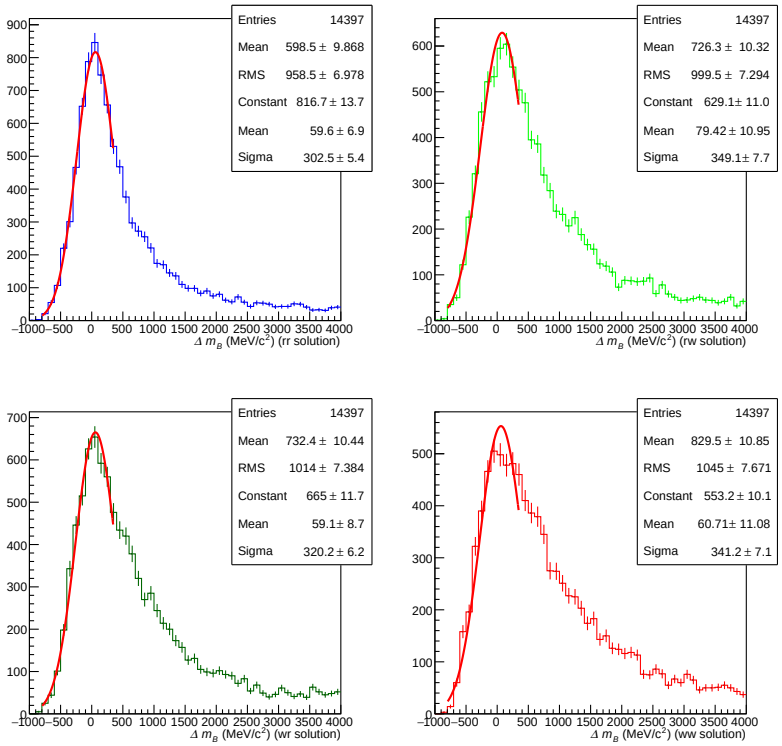

Figure F.5: Fit to the the difference between the *true* B^0 invariant mass distribution and the reconstructed one, for each type of solution.

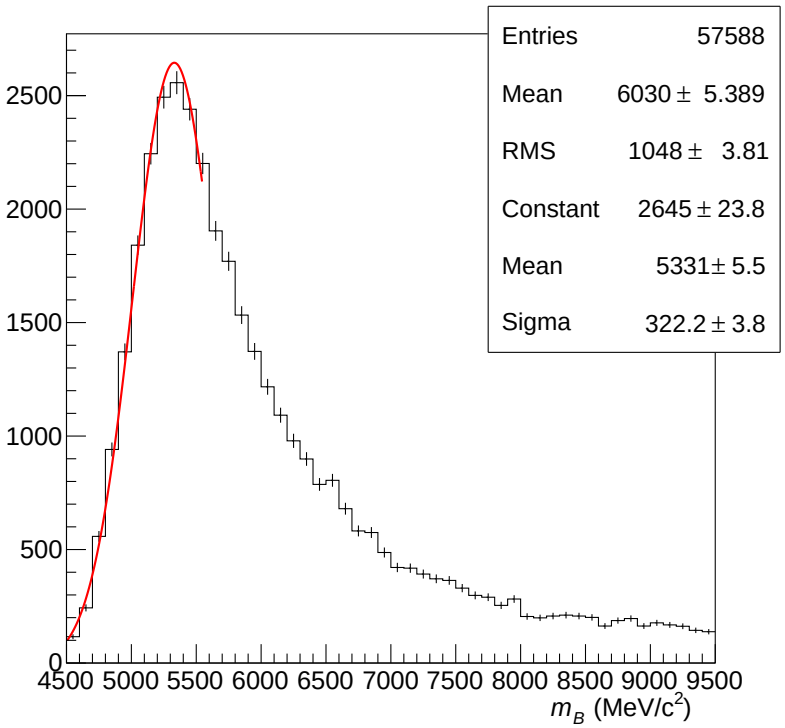

Figure F.6: Fit to the sum of the four solution invariant mass distributions.

F.3 Conclusions and discussion on the reconstruction

The procedure presented in the previous section is aiming at the reconstruction of the $B^0 \to K^{*0}(K^+\pi^-)\tau^+\tau^-$ decay. The final state contains neutrinos that makes the B^0 invariant mass difficult to determine. It has been shown from a simulated sample, that a partial-reconstruction method permits to reconstruct the invariant mass of interest with an acceptable resolution, by taking advantage of the kinematical and topological properties of the decay. Several comments are in order:

- The reconstruction efficiency is suffering from resolution effects on the expression of the parallel component of the neutrino momentum. For instance, a very short τ's flight-distance would prevent from a proper SV-TV distinction. It has eventually been checked that requiring a large B^0 and/or τ flight-distance is indeed improving the resolution of the B^0 signal peak.

- Only a simulated signal sample has been used in the reconstruction. As a next step, one has to consider potential background sources. The partial-reconstruction procedure might bring other contributions under the signal peak, making more difficult the background subtraction/veto.

- Aternative τ final states can also be envisaged. For instance, the decay $\tau^- \to \mu^-\overline{\nu}_\mu\nu_\tau$ presents some advantages: an improvement of the acceptance efficieny would be in order and an improvement of the selection and trigger efficiencies can be expected as well, since muons are well reconstruced in LHCb. However, the positions of the TVs would be unknown, letting the B^0 direction as the only possibility to determine the missing neutrinos components. The partial reconstruction method is in that case only approximate but can provide invaluable additional discriminating variables.

Appendix G

Résumé

Les particules élémentaires ainsi que leurs interactions (forte, faible et électromagnétique) sont actuellement décrites par le Modéle Standard (MS) des particules. Les données accumulées dans le cadre de la physique des Hautes Énergies sont, depuis des décennies, décrites et comprises par le MS. Bien que de récentes mesures réalisées par LHCb (basée au CERN à Genève) révélent quelques tensions par rapport à ces prédictions, on peut raisonnablement considérer que le construction du MS est un succès, récemment consolidé et validé par la découverte d'une résonance bosonique au LHC jusqu'alors compatible avec le boson de Brout-Englert-Higgs. Bien qu'il se suffise à lui-même, le MS est incomplet : par exemple, l'asymétrie matière-antimatière visible dans l'Univers ne peut, à l'heure actuelle, être complétement décrite par le MS. Une partie de ce document est dédiée à la recherche de la violation *CP* et les mesures d'asymétries *CP* sont actuellement interprétables par le MS. Des asymétries non-nulles, violant *CP*, ont été observées dans des désintégrations de mésons K et B. À l'inverse, la violation de *CP* n'a jamais été observée dans des désintégrations de baryons, bien que plusieurs mesures réalisées par la collaboration LHCb semblent indiquer l'existence d'asymétries *CP* non-nulles dans des désintégrations de baryons beaux.

Le travail présenté dans ce document est dédié à l'étude des désintégrations faibles de deux baryons beaux, Λ_b^0 ($|udb\rangle$) et Ξ_b^0 ($|usb\rangle$), et utilise des échantillons de données enregistrés par l'expérience LHCb en 2011 et en 2012. Les expériences BaBar et Belle opéraient à des énergies dans le centre de masse inférieures au seuil de production des baryons beaux. À l'inverse, la production abondante des baryons Λ_b^0 et Ξ_b^0 dans les collisions proton-proton ainsi que la grande probabilité pour un quark b d'hadroniser en un baryon beau au Large Hadron Collider (LHC), donne à l'expérience LHCb l'opportunité d'étudier les désintégrations multicorps sans charme de baryons beaux.

Une part significative de cette étude est dédiée aux mesures des rapports d'embranchements des désintégrations sans charme à quatre corps des baryons Λ_b^0 et Ξ_b^0. Dans le MS, ces désintégrations procèdent simultanément via les transitions de quarks $b \to u$ (à l'arbre) et $b \to d,s$ (transitions à courant neutre de type pingouin). La différence de phase faible induite par cette interférence est *a priori* une opportunité de rechercher la violation *CP* dans ces désintégrations de baryons beaux. De plus, ces désintégrations sans charme à quatre corps contiennent des structures résonantes, simultanément dans la région non-baryonique de basse masse à deux corps (*i.e.* les masses invariantes de $\pi^+\pi^-$, $K^\pm\pi^\mp$, K^+K^-) ainsi que dans la region baryonique de basse masse (*i.e.* les masses invariantes de pK, $p\pi$). Par conséquent, la différence de phases fortes induite par l'interférence de ces amplitudes peut augmenter l'effet d'une asymétrie *CP*. Des mesures d'asymétries *CP* ($\Delta\mathcal{A}^{CP}$) dans les modes

de désintgrations discutés plus haut sont présentées dans ce document. Certaines sont produites dans des régions de l'espace des phases afin de favoriser la présence de structures résonantes. Ainsi, sept désintégrations inclusives de Λ_b^0 et Ξ_b^0 sont simultanément étudiées: $\Lambda_b^0 \to p\pi^-\pi^+\pi^-$, $\Lambda_b^0 \to pK^-\pi^+\pi^-$, $\Lambda_b^0 \to pK^-K^+\pi^-$, $\Lambda_b^0 \to pK^-K^+K^-$, $\Xi_b^0 \to pK^-\pi^+\pi^-$, $\Xi_b^0 \to pK^-\pi^+K^-$ and $\Xi_b^0 \to pK^-K^+K^-$ ainsi que des désintégrations spécifiques qui inclut plusieurs résonances intermédiaires comme, par exemple, $\Lambda_b^0 \to pa_1$, $\Lambda_b^0 \to \Delta^{++}K^-\pi^-$ ou $\Lambda_b^0 \to \Lambda^*(1520)^0\phi^0$.

G.1 Éléments de théorie.

G.1.1 Le Modèle Standard

Le Modèle Standard (MS) des particules est une théorie quantique des champs basée sur une invariance locale de jauge. Les particules élémentaires ainsi que leurs interactions sont décrites par un Lagrangien dont l'invariance, selon des transformations locales et continues, est imposée. Une symétrie génère les interactions et est construite à partir des groupes de symétrie $SU(3)_C$, $SU(2)_L$ et $U(1)_Y$ pour l'interaction forte, faible et électromagnétique, respectivement. Actuellement, la force gravitationnelle n'est pas incluse dans le MS et n'est, en conséquence, pas discutée dans ce document.

Le secteur électrofaible du MS est basé sur l'invariance locale de jauge du groupe de symétrie $SU(2)_L \otimes U(1)_Y$ et a été formalisé par S.L.Glashow, S.Weinberg and A.Salam [1–3]. Un mécanisme de brisure spontanée de symétrie est cependant nécessaire afin de fournir une masse aux fermions fondamentaux ainsi qu'aux bosons. Ce mécanisme est discuté un peu plus loin dans ces lignes. Les générateurs des groupes de symétrie $SU(2)_L$ et $U(1)_Y$ sont l'isospin faible (matrices de Pauli σ_α) et l'hypercharge faible qui sont associés aux champs $\overrightarrow{W}_\mu = (W_\mu^1, W_\mu^2, W_\mu^3)$ et B_μ, respectivement.

Expérimentallement, il a été observé que la symétrie de parité est maximallement violée par l'interaction faible [4] : en terme d'hélicité, seuls les fermions gauches et les antifermions droits peuvent participer aux désintégrations par courant chargé (donc $SU(2)_L$). La théorie électrofaible sépare, par conséquent, les composantes gauches et droites des spineurs, comme $\psi = \psi_L + \psi_R$, où $\psi_L(\psi_R)$ sont les projections du champ spinoriel sur l'état gauche (droit) d'hélicité, respectivement associées aux doublets (Q_L, L_L) et singulets (q_R, l_R^d) de $SU(2)$. On peut noter que le singulet l_R^u (qui pourrait représenter les neutrinos droits stériles) n'est pas discuté davantage. Les deux composantes des doublets, appellées "up" (q_L^u, l_L^u) et "down" (q_L^d, l_L^d), sont des états propres d'isospin faible et sont associées aux valeurs propres $+1/2$ et $-1/2$, respectivement.

L'interaction électrofaible peut donc s'écrire, dans la base de l'interaction, comme Eq. (G.1) et Eq. (G.2) pour les quarks et les leptons, repectivement, en respectant la notation introduite dans la Table G.1.

Table G.1: Représentation des champs fermioniques par génŕation dans la base de l'interaction ainsi que les opérateurs quantiques associés.

	Champ fermioniques par génération			Opérateurs quantiques	
	1st	2nd	3rd	Isospin I_3	Charge Q
Quarks:					
Q_L	$\begin{pmatrix} u \\ d \end{pmatrix}_L$	$\begin{pmatrix} c \\ s \end{pmatrix}_L$	$\begin{pmatrix} t \\ b \end{pmatrix}_L$	$\begin{pmatrix} \frac{1}{2} & 0 \\ 0 & -\frac{1}{2} \end{pmatrix}$	$\begin{pmatrix} \frac{2}{3} & 0 \\ 0 & -\frac{1}{3} \end{pmatrix}$
q_R^u	u_R	c_R	t_R	0	$+\frac{2}{3}$
q_R^d	d_R	s_R	b_R	0	$-\frac{1}{3}$
Leptons:					
L_L	$\begin{pmatrix} \nu_e \\ e \end{pmatrix}_L$	$\begin{pmatrix} \nu_\mu \\ \mu \end{pmatrix}_L$	$\begin{pmatrix} \nu_\tau \\ \tau \end{pmatrix}_L$	$\begin{pmatrix} \frac{1}{2} & 0 \\ 0 & -\frac{1}{2} \end{pmatrix}$	$\begin{pmatrix} 0 & 0 \\ 0 & -1 \end{pmatrix}$
l_R^d	e_R	μ_R	τ_R	0	-1

$$\begin{aligned} \mathcal{L}_{\text{kin.}}^{\text{quarks}} &= i\overline{Q}_L(\partial^\mu + \frac{i}{2}gW_\alpha^\mu\sigma_\alpha + \frac{i}{6}g'B^\mu)\gamma_\mu Q_L \\ &+ i\overline{q^u}_R(\partial^\mu + ig'\frac{2}{3}B^\mu)\gamma_\mu q_R^u + i\overline{q^d}_R(\partial^\mu - \frac{i}{3}g'B^\mu)\gamma_\mu q_R^d \end{aligned} \tag{G.1}$$

$$\mathcal{L}_{\text{kin.}}^{\text{leptons}} = i\overline{L}_L(\partial^\mu + \frac{i}{2}gW_\alpha^\mu\sigma_\alpha - \frac{i}{2}g'B^\mu)\gamma_\mu L_L + i\overline{l^d}_R(\partial^\mu - ig'B^\mu)\gamma_\mu l_R^d \tag{G.2}$$

G.1.2 Matrice de Cabibbo-Kobayashi-Maskawa

Les bosons de l'interaction faible acquièrent une masse via le mécanisme de brisure spontanée de symétrie (mécanisme de Brout-Englert-Higgs [5–7]). Un doublet de champs scalaires complexes est ajouté au Lagrangien, et la symétrie est spontanément brisée lorsque qu'un des minima possibles est choisi. Choisir $\phi_1 = \phi_2 = \phi_4 = 0$, ϕ_3 donne une valeur attendue dans le vide non nulle donnée par

$$\langle 0|\phi|0\rangle = \frac{1}{\sqrt{2}}\begin{pmatrix} 0 \\ v \end{pmatrix}, \quad \text{with} \quad v = \left(-\frac{\mu^2}{\lambda}\right)^{1/2}. \tag{G.3}$$

Ainsi, les couplages du champ de Higgs au champs fermioniques sont décrits par les couplages de Yukawa, et peuvent s'écrire comme

$$\mathcal{L}_\mathcal{Y} = -\lambda_{ij}^u\overline{Q}_{Li}\phi u_{Rj} - \lambda_{ij}^d\overline{Q}_{Li}\phi d_{Rj} - \lambda_{ij}^d\overline{L}_{Li}\phi l_{Rj}^d, \tag{G.4}$$

où i, j sont des indices de générations, Q_L et L_L sont les doublets gauches, u_R, d_R et l_R^d sont les singulets droits de $SU(2)_L \otimes U(1)_Y$. $\lambda_{ij}^{d,u}$ sont des matrices complexes 3×3 des couplages de type down et up. Lorsque le champ de Higgs acquiert une valeur attendue dans le vide non nulle, des termes de masses (pour les quarks par exemple) apparaissent

$$\begin{aligned} \mathcal{L}_\mathcal{Y} &= -\left(\frac{\lambda_{ij}^d \cdot v}{\sqrt{2}}\right)\overline{d}_{Li}d_{Rj} - \left(\frac{\lambda_{ij}^u \cdot v}{\sqrt{2}}\right)\overline{u}_{Li}u_{Rj} + ... \\ &= -\mathcal{M}_{ij}^d\overline{d}_{Li}d_{Rj} - \mathcal{M}_{ij}^u\overline{u}_{Li}u_{Rj} + ... \end{aligned} \tag{G.5}$$

où $\mathcal{M}_{ij}^{u,d}$ sont des matrices de masses de dimension 3 dans la base de l'interaction. Il peut être utile de passer des états propres de l'interaction aux états propres de masse afin de mettre en évidence la masse "physique" des particules. Cette transformation est possible en introduisant des matrices unitaires $\mathcal{U}_L^{u(d)}$ et $\mathcal{U}_R^{u(d)}$. On a

$$M_{ij}^{u(d)} = \mathcal{U}_L^{u(d)} \mathcal{M}_{ij}^{u(d)} \mathcal{U}_R^{u(d)\dagger} = \begin{pmatrix} m_{u(d)} & 0 & 0 \\ 0 & m_{c(s)} & 0 \\ 0 & 0 & m_{t(b)} \end{pmatrix}, \tag{G.6}$$

où les éléments de la diagonale sont les masses des quarks. Généralement, il est d'usage d'utiliser les transformations pour les quarks de type "down". Ainsi, on a

$$Q_L = \begin{pmatrix} u_L \\ d_L \end{pmatrix} = (\mathcal{U}_L^{u\dagger})_j \begin{pmatrix} u_{Lj}^m \\ (\mathcal{U}_L^u \mathcal{U}_L^{d\dagger})_{jk} d_{Lk}^m \end{pmatrix}. \tag{G.7}$$

où m identifie les états propres de masse. Les termes $(\mathcal{U}_L^u \mathcal{U}_L^{d\dagger})_{jk}$ sont des éléments d'une matrice complexe 3×3 appelée la matrice de Cabibbo-Kobayashi-Maskawa [9, 10] dont l'expression générique est donnée par l'Eq. G.8.

$$V_{CKM} = (\mathcal{U}_L^u \mathcal{U}_L^{d\dagger}) = \begin{pmatrix} V_{ud} & V_{us} & V_{ub} \\ V_{cd} & V_{cs} & V_{cb} \\ V_{td} & V_{ts} & V_{tb} \end{pmatrix}. \tag{G.8}$$

Les courants faibles chargés sont par conséquent modifiés par la transformation des états propres de l'interaction vers les états propres de masse, et les éléments de la matrice CKM apparaissent grâce à cette opération. Le Lagrangien (qui est invariant selon les rotations de $SU(2)$)) devient, dans la base des états propres de masse :

$$\mathcal{L}_{\text{kin.}}^{quarks,m} = \frac{ig}{\sqrt{2}} (\overline{u^m}_{Li} \gamma^\mu (\mathcal{U}_{ik}^u \mathcal{U}_{kj}^{d\dagger}) d_{Lj}^m W_\mu^+ + \overline{d^m}_{Li} \gamma^\mu (\mathcal{U}_{ik}^d \mathcal{U}_{kj}^{u\dagger}) u_{Lj}^m W_\mu^-) + \frac{ig}{2} \overline{Q}_{Li} \gamma^\mu \sigma_3 W_3^\mu Q_{Li}, \tag{G.9}$$

où l'on peut voir qu'un mélange de saveur est possible dans les interactions par courants chargés. Le dernier terme n'est pas modifié : il n'existe pas de changement de saveur par courant neutre (FCNC) au premier ordre.

Plusieurs paramétrisations de la matrice CKM sont possibles. Bien que la matrice soit de dimension 3 et contiennent 9 éléments complexes, son unitarité fournit 9 relations indépendantes. De plus, il y a 6 phases arbitraires liées à chacun des quarks, et définir une seule de ces phases permet d'obtenir une référence pour 5 d'entre elles. 3 paramètres réels et une phase complexe violant *CP* sont suffisants pour paramétriser la matrice CKM. Altomari et Wolfenstein produisent une paramétrisation qui permet une visualisation explicite de la hiérarchie entre les différents mélange de saveurs. On a donc

$$V_{CKM} = \begin{pmatrix} 1 - \lambda^2/2 & \lambda & A\lambda^3(\rho - i\eta) \\ -\lambda & 1 - \lambda^2/2 & A\lambda^2 \\ A\lambda^3(1 - \rho - i\eta) & -A\lambda^2 & 1 \end{pmatrix} + \mathcal{O}(\lambda^4), \tag{G.10}$$

où la hiérarchie entre les termes est gouvernée par l'odre du paramètre λ. Les éléments de la diagonale sont égaux à 1 au premier ordre: les procédés impliquant des quarks de la même génération sont favorisés.

G.1.3 Violation de la symétrie *CP*

Experimentallement, il est possible d'observer une violation *CP* en étudiant trois phénomènes. Considèrons le processus $B^0 \to f$ et $\overline{B}^0 \to \overline{f}$ où les états initiaux B^0, $\overline{B}^0$ et finaux f, $\overline{f}$, sont CP-conjugués. Il est possible de définir les amplitudes comme

$$A = \langle f|\mathcal{H}|B\rangle \tag{G.11}$$
$$\overline{A} = \langle \overline{f}|\mathcal{H}|\overline{B}\rangle \tag{G.12}$$

où A et $\overline{A}$ contiennent des phases faibles associées aux éléments de matrice CKM, qui sont modifiés sous la transformation *CP*. La violation directe de la symétrie *CP* a donc lieu lorsque le rapport $\left|\frac{\bar{A}}{A}\right|$ est différent de 1. Par conséquent, les rapports d'embranchements des deux processus (*CP*-conjugués) doivent être différents. La violation directe de la symétrie *CP* a été observée pour la première fois dans les désintégrations de mésons K en 2001 [14] et dans les désintégrations de mésons B en 2004 [15, 16]. Une partie du travail présenté dans ce document est dédié à la recherche de la violation directe de la symétrie *CP* dans les désintégrations de baryons. Une asymétrie non nulle implique une différence entre les largeurs de désintégration des deux processus *CP*-conjugués, données par

$$\Gamma(i \to f) \neq \Gamma(\bar{i} \to \overline{f}) \qquad \text{avec} \qquad \begin{cases} \Gamma(i \to f) = |A(i \to f)|^2 \\ \Gamma(\bar{i} \to \overline{f}) = |\overline{A}(\bar{i} \to \overline{f})|^2 \end{cases}. \tag{G.13}$$

Si on considère une désintégration qui implique deux amplitudes déphasé es A_1 et A_2, on peut écrire :

$$A = A_1 + A_2 = |A_1|e^{i\phi_1}e^{i\delta_1} + |A_2|e^{i\phi_2}e^{i\delta_2}, \tag{G.14}$$
$$\overline{A} = \overline{A}_1 + \overline{A}_2 = |A_1|e^{-i\phi_1}e^{i\delta_1} + |A_2|e^{-i\phi_2}e^{i\delta_2}. \tag{G.15}$$

où δ_i (ϕ_i) sont les phases fortes (faibles) et (ne) sont (pas) conservé es sous une transformation *CP*. Le calcul de l'asymétrie *CP* A_{CP} donne

$$A_{CP} = \frac{|A|^2 - |\overline{A}|^2}{|A|^2 + |\overline{A}|^2} = \frac{2|A_1||A_2|\sin(\phi_1 - \phi_2)\sin(\delta_1 - \delta_2)}{|A_1|^2 + |A_2|^2 + 2|A_1||A_2|\cos(\phi_1 - \phi_2)\cos(\delta_1 - \delta_2)}. \tag{G.16}$$

Cette expression implique qu'au moins deux amplitudes déphasées doivent interférer afin d'observer une asymétrie. Une difference de phase faible non nulle (qui vient directement des éléments de la matrice CKM) ainsi qu'une différence de phase forte non nulle (possible grâce aux interactions dans l'état final par exemple) sont necessaires à l'observation d'une asymétrie *CP*. Ces conditions motivent les différentes mesures qui sont réalisées ici: de nombreuses interférences sont attendues dans les modes de désintégrations qui sont étudiées. De plus, des mesures sont faites pour d'autres modes qui doivent favoriser la présence de résonance forte dans l'état final.

G.2 Modes de désintégrations étudiés

Des désintégrations sans charme à quatre corps sont étudiés afin de (1) mesurer des rapports d'embranchements et (2) de chercher des asymétries *CP* en mesurant l'observable A_{CP}. Les baryons étudiés sont Λ_b^0 et Ξ_b^0. Ils furent observés pour la premiè re fois par les collaborations UA1 et CDF, respectivement.

Les modes de désintégrations sont (en considérant $X_b = \{\Lambda_b^0, \Xi_b^0\}$) $\Lambda_b^0 \to p\pi^-\pi^+\pi^-$, $X_b \to pK^-\pi^+\pi^-$, $\Lambda_b^0 \to pK^-K^+\pi^-$, $\Xi_b^0 \to pK^-\pi^+K^-$ et $X_b \to pK^-K^+K^-$. Une expérience de comptage permet la mesure directe d'une asymétrie *CP* modulo les corrections instrumentales et les asymétries de production. Afin de maitriser ces inconnues, des désintégrations de X_b à quatre corps impliquant soit un Λ_c^+ ou Ξ_c^+ sont utilisées comme canaux de contrôle. Les modes $\Lambda_b^0 \to (\Lambda_c^+ \to p\pi^-\pi^+)\pi^-$, $\Lambda_b^0 \to (\Lambda_c^+ \to pK^-\pi^+)\pi^-$ et $\Xi_b^0 \to (\Xi_c^+ \to pK^-\pi^+)\pi^-$ sont par conséquent utilisés pour contrôler les effets expérimentaux cités plus haut dans la recherche d'asymétries *CP*. Enfin, les rapports d'embranchements des modes sans charme discutés ici sont déterminés par rapport au rapport d'embranchement de la désintégration $\Lambda_b^0 \to (\Lambda_c^+ \to pK^-\pi^+)\pi^-$.

G.3 Le LHC et LHCb

La recherche du boson de Brout-Englert-Higgs fut une des principales motivations pour la création du Large Hadron Collider (LHC), successeur du collisionneur Large Electron Positron (LEP) au CERN (Centre Européen pour la Recherche Nucléaire). C'est un collisionneur constitué de deux anneaux supraconducteurs de 27 km installés dans le tunnel originel du LEP, à environ 100 mètres de profondeur. Deux faisceaux de protons se rencontrent à différents points d'intersection avec une énergie dans le centre de masse de 13 TeV depuis 2015. Cette caractéristique fait du LHC le collisionneur le plus énergétique jamais construit. Les LHC réalisa des collisions avec une énergie dans le centre de masse de 7 TeV en 2011 et de 8 TeV en 2012 (lors du Run I).

G.3.1 Le complexe d'accélération du LHC

L'énergie requise lors des collisions nécessite un complexe d'accélération dont une représentation est donnée sur la Fig. G.1. La source de proton est une bouteille d'hydrogène dont les protons sont isolés par un champ éléctrique. Le voyage des protons commence avec un accélérateur linéaire (LINAC 2) et se poursuit avec le Proton Synchrotron Booster (PSB). Celui-ci produit des faisceaux de 1.4 GeV. Le Proton Synchrotron (PS) et le Super Proton Synchrotron (SPS) suivent et accélèrent les protons à une énergie de 450 GeV. Enfin, les faisceaux sont livrés aux anneaux finaux, qui accélèront les faisceaux jusqu'à l'énergie nominale. Les collisions ont finalement lieu au quatre points d'intersection où différents detecteurs et expériences sont installés.

G.3.2 L'expérience LHCb

L'expérience LHCb est une des quatre expériences qui collectent les données fournies par le LHC. L'expérience est dédiée à l'étude des saveurs lourdes (processus impliquant des quarks *b*-, *c*- ou des leptons τ). En plus des phénomènes violant *CP* (ainsi que la recherche de phases violant *CP* au-delà de celle du MS), LHCb scrute les désintégrations rares de particules de saveur lourdes afin de rechercher des écarts aux prédictions du MS. LHCb est un spectromètre instrumenté sur une couverture angulaire allant de 10 mrad à 300 mrad, commme représenté sur la Figure G.2.

Plusieurs sous-détecteurs sont utilisés par l'expérience LHCb : un système de reconstruction des traces chargées est construit autour d'un aimant assurant l'existence d'un champ magnétique de 4 T.m. À l'avant de l'aimant (*i.e.* vers le point de collision), ce système est composé d'un localisateur de vertex à haute résolution (VELO) ainsi que de stations de déclenchement. Une excellente discrimination des traces de K et de π est assurée par la

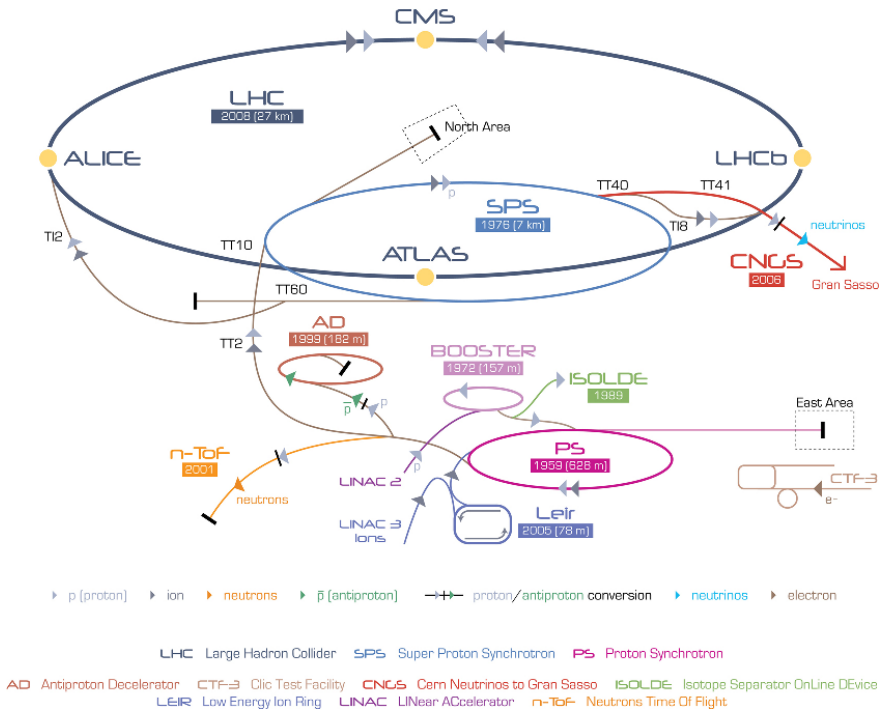

Figure G.1: Représentation schématique du complexe d'accélération du LHC.

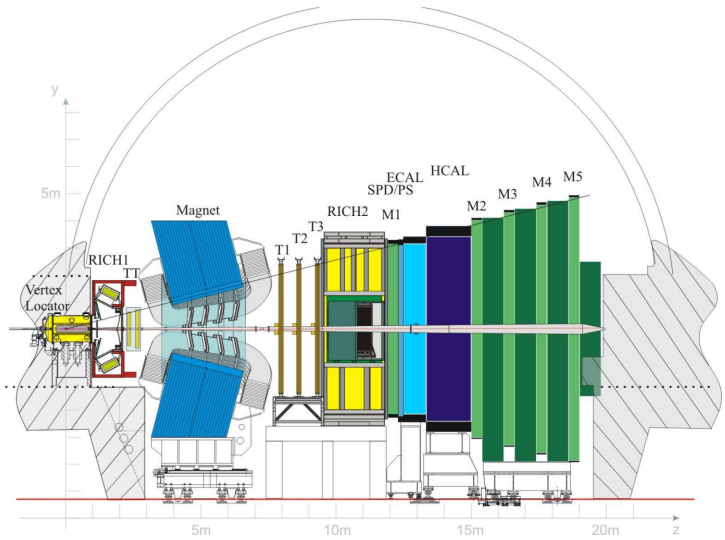

(a) Vue schématique.

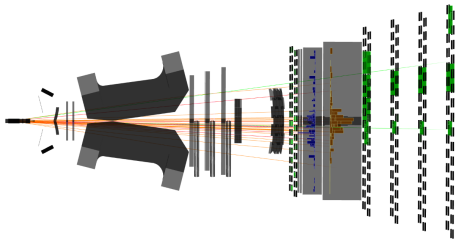

(b) Représentation d'un événement .

Figure G.2: Vue du détecteur LHCb. L'axe z est aligné avec la direction du faisceau et l'axe y est vertical.

présence de deux compteurs Cherenkov (RICH1 et RICH2) qui sont respectivement placés à l'avant et à l'arrière de l'aimant. Aussi, le sytème calorimétrique est composé entre autre d'un calorimètre électronique et d'un calorimètre hadronique. Enfin, l'identification des muons est renforcée par la présence d'un systeme dédié.

G.3.3 Sytème de déclenchement

Un système de déclenchement est utilisé afin de réduire la quantité de données enregistrées, en ne conservant que les événements d'intérêt. Celui-ci est divisé en deux parties: le niveau 0 (L0) et les niveaux supérieurs (HLT). Le L0 utilise les sous-détecteurs les plus rapides (comme le VELO et les calorimètres) pour une prise de décision rapide. Les événements de signaux qui passent le L0 sont donc associés à des traces reconstruites et des critères de sélection peuvent être établis en fonction de l'origine du déclenchement : on parle de décision L0TOS (Trigger On Signal) si un candidat du signal est responsable du déclenchement ou de L0TIS (Trigger Independent of Signal) si le déclenchement est dû à d'autres particules produites dans la collision. Dans ce document, des mesures de rapports d'embranchement de désintégrations sans charme à quatre corps de Λ_b^0 et Ξ_b^0 sont établis. De plus, des mesures d'asymétries $\Delta\mathcal{A}^{CP}$ sont réalisées. Bien que la majorité des outils sont communs aux deux types de mesures, de différents critères sont utilisés pour le rapport de déclenchement.

- Pour les rapports d'embranchement, il est important de minimiser la variation d'efficacité sur l'espace des phases des désintégrations d'intérêt. En conséquence, les candidats de signal sont sélectionnés à partir d'événements pour lesquels la décision L0TIS est satisfaite.
- À l'inverse, les décisions L0TOS et L0TIS sont considérées pour les mesures $\Delta\mathcal{A}^{CP}$. Ceci implique cependant de corriger l'asymétrie mesurée des effets d'une décisions L0TOS.

Sélection des signaux et ajustement aux données.

G.3.4 Echantillons de données - Simulation

Les données utilisées dans cette analayse furent collectées par l'expérience LHCb, pendant le Run I du LHC (à une énergie dans le centre de masse de 7 TeV pour 2011 et de 8 TeV pour 2012). Le nombre d'événements est conséquent et des critères de sélection sont établis (on parle de "Stripping") afin de rejeter les événements qui ne présentent pas d'intérêt pour les analyses réalisées. Deux lignes de Stripping distinctes sont utilisées, correspondant aux deux années de prise de données.
Des échantillons de données simulées Monte Carlo (MC) sont utilisés afin d'étudier signaux et bruits de fond et de modéliser les différentes distributions de masse invariante. Les événements MC sont produits dans la configuration **MagDown** et **MagUp**. En ce qui concerne les signaux, la simulation contient deux types (*a priori* extrêmes) de dynamiques de désintégrations : l'une est non résonante et l'autre considère des désintégrations à deux corps, impliquant N^{*0} ou Λ^{*0} en association avec une résonance mesonique de basse masse. Ce mélange sera avantageusement utilisé dans la détermination des incertitudes systématiques relatives à l'espace des phases de la désintégration : la "vraie" dynamique du signal est *a priori* inconnue et devrait être contenue entre ces deux cas extrêmes.
Ainsi, la région basse de la masse invariante de deux corps est préservée par cette première sélection: par exemple, la présence attendue de $\Lambda^{*0}(1520)$ and $N^{*0}(1520)$ oblige la

préservation de la masse invariante de ph. Pour ce faire, aucun critère cinématique n'est appliqué aux masses invariantes de deux corps. Ce choix permet d'une part de mesurer des rapports d'embranchements avec une variation d'efficacité sur l'espace des phases acceptable (pour une certaine configuration du système de déclenchement). D'autre part, ceci permet la recherche d'asymétrie CP dans des régions basses de masse invariante.

G.3.5 Sélection

Les candidats de baryons beaux neutres, (notés X_b) sont formés à partir d'un proton, sélectionné à l'aide de critères dit de PID (Particle Identification), ainsi que de trois traces chargées additionnelles. Plusieurs critères sont considérés afin de sélectionner les candidats de signal. Pour ne citer que quelques-uns d'entre eux: lorsque que plus d'un vertex primaire (PV) est reconstruit, le candidat X_b est associé au PV qui forme le plus petit χ^2_{IP}, où χ^2_{IP} est la différence en terme de χ^2 entre un PV reconstruit avec ou sans le candidat considéré. Le candidat X_b doit être suffisamment séparé du PV et pour associer une trace additionnelle au PV, la qualité de la reconstruction du vertex associé au candidat doit être significativement améliorée lorsque que cette trace est considérée. Aussi, chacune des quatre traces présentes dans l'état final ne doit avoir une impulsion telle que $p < 100\,\text{GeV}/c$, valeur pour laquelle il y a une faible discrimination entre pion/kaon/proton. Enfin, des critères de sélection de PID sont appliqués, afin d'obtenir une discrimination efficace entre kaons et pions et d'associer le candidat reconstruit à un des différent spectre d'état final $p\pi\pi\pi$, $pK\pi\pi$, $pKK\pi$, $pK\pi K$ et $pKKK$.

Trois catégories de bruits de fond peuvent significativement contribuer dans la région de masse invariante considérée. Ceux-ci sont discutés plus en détail dans les pages qui suivent mais comme la sélection vise le rejet de ces différentes sources, introduisons-les dès maintenant: on peut distinguer les bruits de fond dit de "cross-feed" (contamination d'événements de signal pour lesquels au moins une trace est mal identifiée), les désintégrations sans charme à quatre corps de meson beaux et le bruit de fond combinatoire (association de traces avec au moins une trace indépendante du vertex d'intérêt.).

Afin de réduire la contribution des cross-feeds et d'obtenir des spectres mutuellement exclusifs, des variables de sélection (notés ProbNN) sont utilisées. Celles-ci permettent d'estimer la probabilité pour une trace d'être (ou de ne pas être) d'une certaint nature (*e.g.* ProbNNπ devrait être de 1 pour un pion et de 0 pour un kaon). Une coupure sur les variables ProbNN est donc déterminée afin de réaliser une séparation π-K. Une illustration de la distribution des kaons et des pions dans le plan (ProbNNK, ProbNNπ) est fournie Fig. G.3. Les imperfections de la simulation nécessitent cependant une correction : des figures d'efficacités sont donc construites à partir d'échantillons de calibration et la cinématique simulée est utilisée afin de pondérer événement par événement, l'efficacité d'un événement de passer un critère de sélection. Enfin, la coupure optimale est déterminée à l'aide de Figure de Mérite de Punzi.

Le reject du bruit de fond combinatoire est effectué grâce à un discriminant multivarié, basé sur un arbre de décision boosté (BDT). Les candidats ainsi que les événements de haute masse invariante de l'échantillon simulé de $\Lambda_b^0 \to p\pi^-\pi^+\pi^-$, sont repectivement utilisés comme échantillons de signal et de bruit de fond. Le BDT utilise plusieurs variables discriminantes et topologiques, comme par exemple, l'impulsion transverse, la pseudo-rapidité, la qualité de la mesure de la distance de vol ou du paramètre d'impact... Le BDT produit donc une seule et unique variable discriminante, en tenant compte des corrélations non-linéaires

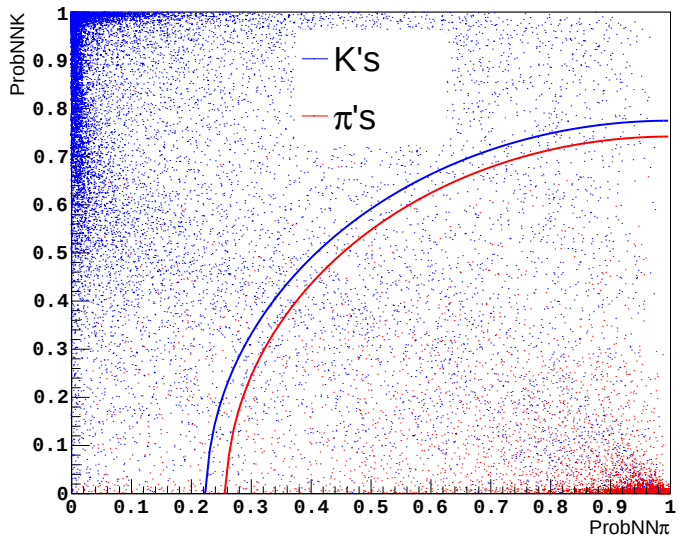

Figure G.3: Illustration des distributions de kaons et de pions dans le plan (ProbNNK, ProbNNπ), à partir d'événements simulées de la désintégration $\Lambda_b^0 \to pK^-\pi^+\pi^-$.

qui existent entre les variables d'entrées. Enfin, la coupure utilisée dans l'analyse des rapports d'embranchements est déterminée en maximisant une Figure de Mérite et fournit une efficacité de signal d'environ 70%. Une réoptimisation de cette coupure est réalisée dans le cadre des mesures de $\Delta\mathcal{A}^{CP}$, en minimisant l'incertitude statistique de l'observable.

Quelque soit le spectre étudié ($p\pi\pi\pi$, $pK\pi\pi$, $pKK\pi$, $pK\pi K$ et $pKKK$ ou canaux de contrôle), le proton fait parti de l'état final. L'efficacité des signaux et des cross-feeds seront donc les mêmes (aux distributions cinématiques près) quelque soit le critère de sélection en ProbNNp qui est appliqué. Une coupure est cependant nécessaire pour réduire et/ou rejeter le bruit de fond provenant des désintégrations à quatre ou cinq corps de mésons $B^0_{d,s}$ et B^+ . Ces bruits de fond peuvent être conséquents (rapports d'embranchement attendus de l'ordre de $\mathcal{O}(10^{-4})$) et peuvent être à l'origine d'importante asymétrie CP. Afin de réduire ces contributions de bruit de fond, un coupure est choisie à ProbNN$p > 0.50$. Bien qu'arbitraire, cette valeur permet de rejeter un nombre significatif de bruits de fond tout en conservant la majorité des événements de signal. Comme pour le cas des π et K, la variable ProbNNp n'est pas correctement décrite par la simulation. L'utilisation d'échantillons de calibration (désintégrations inclusives de Λ_c^+ dans ce cas) sont utilisés pour repondérer la simulation et déterminer les efficacités d'identification.

Enfin, un certain nombre de désintégrations charmées d'un baryon beau neutre en deux corps ($\Lambda_c^+ h$, $\Xi_c h$), en trois corps Dph ou en une combinaison contenant un charmonium ($c\bar{c}ph$) peuvent produire le même état final que le signal d'intérêt. Ainsi, plusieurs masse invariantes, correspondant aux désintégrations possibles, sont explicitement reconstruites et "interdites" en utilisant un critère de sélection sur la masse invariante reconstruite (veto). Pour illustration, les critères utilisés sont reportés dans la Table G.2

G.3.6 Ajustement simultané aux données.

Un ajustement aux données des différentes distributions de masse invariantes reconstruites selon les cinq hypothèses d'état final, ainsi qu'aux données des canaux de contrôle, est réalisé.

Table G.2: Liste des vetos de résonances charmées appliqués dans la sélection.

Résonances charmées	Désintégration	Sélection appliquée (masses en MeV/c^2)
Λ_c^+	$\Lambda_c^+ \to p\pi^-\pi^+$	$\lvert 2283.00 - h_1h_2h_3\_p\pi\pi\rvert > 30.$ et $\lvert 2283.00 - h_1h_4h_3\_p\pi\pi\rvert > 30.$
	$\Lambda_c^+ \to pK^-\pi^+$	$\lvert 2262.50 - h_1h_2h_3\_pK\pi\rvert > 52.5$ et $\lvert 2262.50 - h_1h_4h_3\_pK\pi\rvert > 52.5$
	$\Lambda_c^+ \to pK^-K^+$	$\lvert 2283.00 - h_1h_2h_3\_pKK\rvert > 30.$ et $\lvert 2283.00 - h_1h_4h_3\_pKK\rvert > 30.$
Ξ_c^+	$\Xi_c^+ \to pK^-\pi^+$	$\lvert 2467.80 - h_1h_2h_3\_pK\pi\rvert > 30.$ et $\lvert 2467.80 - h_1h_4h_3\_pK\pi\rvert > 30.$
$\overset{(-)}{D^0}$	$\overset{(-)}{D^0} \to \pi^-\pi^+$	$\lvert 1864.84 - h_2h_3\_\pi\pi\rvert > 30.$ et $\lvert 1864.84 - h_4h_3\_\pi\pi\rvert > 30.$
	$\overset{(-)}{D^0} \to K^-K^+$	$\lvert 1864.84 - h_2h_3\_KK\rvert > 30.$ et $\lvert 1864.84 - h_4h_3\_KK\rvert > 30.$
	$D^0 \to \pi^+K^-$	$\lvert 1864.84 - h_2h_3\_K\pi\rvert > 30.$ et $\lvert 1864.84 - h_4h_3\_K\pi\rvert > 30.$
	$\overline{D}^0 \to \pi^-K^+$	$\lvert 1864.84 - h_2h_3\_\pi K\rvert > 30.$ et $\lvert 1864.84 - h_4h_3\_\pi K\rvert > 30.$
D^+	$D^+ \to \pi^+K^-\pi^+$	$\lvert 1869.61 - h_2h_3h_4\_\pi K\pi\rvert > 30.$
D_s^+	$D_s^+ \to K^+K^-\pi^+$	$\lvert 1968.30 - h_2h_3h_4\_KK\pi\rvert > 30.$ et $\lvert 1968.30 - h_2h_3h_4\_\pi KK\rvert > 30.$
	$D_s^+ \to \pi^+\pi^-\pi^+$	$\lvert 1968.30 - h_2h_3h_4\_\pi\pi\pi\rvert > 30.$
J/ψ	$J/\psi \to \pi^+\pi^-$	$\lvert 3096.92 - h_2h_3\_\pi\pi\rvert > 50.$ et $\lvert 3096.92 - h_4h_3\_\pi\pi\rvert > 50.$
	$J/\psi \to K^+K^-$	$\lvert 3096.92 - h_2h_3\_KK\rvert > 50.$ et $\lvert 3096.92 - h_4h_3\_KK\_\mathrm{M}\rvert > 50.$
χ_{c0}	$\chi_{c0} \to \pi^+\pi^-$	$\lvert 3414.75 - h_2h_3\_\pi\pi\rvert > 50.$ et $\lvert 3414.75 - h_4h_3\_\pi\pi\rvert > 50.$
	$\chi_{c0} \to K^+K^-$	$\lvert 3414.75 - h_2h_3\_KK\rvert > 50.$ et $\lvert 3414.75 - h_4h_3\_KK\_\mathrm{M}\rvert > 50.$
$X \to \mu^+\mu^-$		$!(h_1\_\mathrm{isMuon} == 1 \;\&\&\; h_2\_\mathrm{isMuon} == 1)$ et $!(h_3\_\mathrm{isMuon} == 1 \;\&\&\; h_4\_\mathrm{isMuon} == 1)$
		$!(h_2\_\mathrm{isMuon} == 1 \;\&\&\; h_3\_\mathrm{isMuon} == 1)$ et $!(h_1\_\mathrm{isMuon} == 1 \;\&\&\; h_4\_\mathrm{isMuon} == 1)$

Cet ajustement est simultané, et consiste à maximiser, événement par événement, une fonction de vraisemblance étendue. L'échantillon de données est divisé en fonction de la charge du proton, de l'année de prise de données (ainsi que du critère du système de déclenchement pour le cas de l'analyse $\Delta\mathcal{A}^{CP}$). Les composantes du modèle utilisé par l'ajustement sont, en plus du signal, le bruit de fond partiellement reconstruit des désintégrations à 5 corps de X_b, les cross-feeds, les désintégrations à 4 ou 5 corps de mésons B et la combinatoire. Pour chaque échantillon, la fonction de vraisemblance s'écrit :

$$\ln \mathcal{L} = \sum_i \ln \left(\sum_j N_j P_{j,i} \right) - \sum_j N_j \tag{G.17}$$

où N_j est le nombre d'événements lié à la composante j et P_i désigne la probabilité de l'événement i. L'utilisation d'un ajustement simultané aux données est motivé par les constations suivantes : les information des spectres non-charmés (*i.e* de signal) et charmés (canaux de contrôle) sont intriquées, par exemple, par la présence des contaminations de bruit de fond et de signaux (cross-feed), par la pondération commune des critères de PID, par des paramètres physiques comme la masse reconstruite du baryon candidat (pour ne citer qu'eux). L'ajustement simultané de paramètres partagés entre les signaux et les canaux de contrôle, ainsi que l'utilisation de contraintes (éduqués des données) afin de contrôler les cross-feeds, permet d'intégrer un certain nombre d'incertitudes comme incertitude statistique de l'ajustement. Le nombre total de paramètres ajustés est d'environ 200 (300) pour la détermination des rapports d'embranchements ($\Delta\mathcal{A}^{CP}$). Voici quelques contraintes prises en compte dans l'ajustement :

- La valeur de la masse des baryons Λ_b^0 et Ξ_b^0 est partagée entre les spectres de signal et de contrôle.

- La différence de masse entre Λ_b^0 et Ξ_b^0 est contrainte selon une loi Gaussiène à la valeur du PDG.
- Les rapports des largeurs des fonctions des différents signaux sont contraints aux valeurs obtenues par l'ajustement aux données simulées. La largeur de référence est celle de $\Lambda_b^0 \to pK^-\pi^+\pi^-$ (2012).
- Les nombres d'événements des contaminations de cross-feed sont contraints aux nombres d'événements des signaux correspondants par un facteur qui tient compte des efficacités de sélection et d'identification (PID).
- Les nombres d'événements des bruits de fond venant des désintégrations à 4 ou 5 corps de mésons B sont similairement contraints aux nombres d'événements mesurés dans la région haute de masse invariante.

Plusieurs autres contraintes, liées aux partages des paramètres utilisés dans la modélisation des contributions physiques, sont aussi utilisées dans la statégie. Celles-ci sont discutées dans les sections suivantes.

G.3.7 Observables d'intérêt

Les rapports d'embranchements et les asymétrie $\Delta\mathcal{A}^{CP}$ sont directement calculés lors de l'ajustement aux données en utilisant la matrice de covariance ainsi que les nombres d'événements des signaux et des canaux de contrôle. Afin d'éviter un biais de mesure, l'analyse est dans un premier temps construite à l'aveugle. Tant que les contributions de bruits de fond ne sont pas décrites de manière satisfaisante et sous contrôle, la valeur mesurée des observables d'intérêt n'est pas accessible. Les observables sont les suivantes :

Les rapports d'embranchements sont donnés par :

$$\begin{aligned} R(X_b^0 \to ph^{'}h^{''}h^{'''}) &\equiv \frac{\mathcal{B}(X_b^0 \to ph^{'}h^{''}h^{'''})}{\mathcal{B}(\Lambda_b^0 \to \Lambda_c^+\pi^-)} \cdot \frac{f_{X_b}}{f_{\Lambda_b^0}}, \\ &= \frac{\epsilon^{\text{geo.}}_{\Lambda_b^0\to\Lambda_c^+\pi^-}}{\epsilon^{\text{geo.}}_{X_b^0\to ph^{'}h^{''}h^{'''}}} \cdot \frac{\epsilon^{\text{sel.}}_{\Lambda_b^0\to\Lambda_c^+\pi^-}}{\epsilon^{\text{sel.}}_{X_b^0\to ph^{'}h^{''}h^{'''}}} \cdot \frac{\epsilon^{\text{PID}}_{\Lambda_b^0\to\Lambda_c^+\pi^-}}{\epsilon^{\text{PID}}_{X_b^0\to ph^{'}h^{''}h^{'''}}} \cdot \frac{1}{\epsilon^{\text{veto}}_{X_b^0\to ph^{'}h^{''}h^{'''}}} \cdot \frac{\mathcal{N}_{X_b^0\to ph^{'}h^{''}h^{'''}}}{\mathcal{N}_{\Lambda_b^0\to\Lambda_c^+\pi^-}}, \end{aligned}$$

où $\mathcal{B}$ représente le rapport d'embranchement et $f_{X_b}/f_{\Lambda_b^0}$ et la fraction d'hadronisation relative de $b \to X_b$ par rapport à $b \to \Lambda_b^0$. De gauche à droite, les rapports d'efficacité sont liés à l'acceptance géométrique, aux critères de sélection, aux critères de PID et aux vetos des bruits de fond charmés. Le nombre d'événement mesuré pour le mode de signal et le mode de normalisation est respectivement représenté par $\mathcal{N}_{X_b^0\to ph^{'}h^{''}h^{'''}}$ et $\mathcal{N}_{\Lambda_b^0\to\Lambda_c^+\pi^-}$.

L'asymétrie $\mathcal{A}^{CP}$ et la différence $\Delta\mathcal{A}^{CP}$ sont données par:

$$\mathcal{A}^{CP} = \frac{\mathcal{N}(X_b^0) - \overline{\mathcal{N}}(\overline{X}_b^0)}{\mathcal{N}(X_b^0) + \overline{\mathcal{N}}(\overline{X}_b^0)} \quad \text{et} \tag{G.18}$$

$$\Delta\mathcal{A}^{CP} = \frac{\mathcal{N}(X_b^0) - \overline{\mathcal{N}}(\overline{X}_b^0)}{\mathcal{N}(X_b^0) + \overline{\mathcal{N}}(\overline{X}_b^0)} - \frac{\mathcal{N}_{\text{C}}(X_b^0) - \overline{\mathcal{N}}_{\text{C}}(\overline{X}_b^0)}{\mathcal{N}_{\text{C}}(X_b^0) + \overline{\mathcal{N}}_{\text{C}}(\overline{X}_b^0)}, \tag{G.19}$$

respectivement, où $\mathcal{N}_C$ et $\overline{\mathcal{N}}_C$ dans l'Eq. G.19 sont les nombres d'événements du mode de contrôle. L'échantillon de données utilisé est divisé en fonction de la charge du proton, de l'année de prise de données et des deux conditions du système de déclenchement (afin de corriger les asymétries liées aux efficacités L0TOS). Le même modèle d'ajustement aux données est utilisé pour les deux types de mesures.

G.4 Identification des sources de bruits de fond et modèle d'ajustement aux données.

La structure du bruit de fond des désintégrations à 4 corps des baryons Λ_b^0 et Ξ_b^0 est riche. On peut envisager au moins six catégories de bruits de fond:

- **Les bruits de fond qui piquent sous le signal**, qui viennent des désintégrations charmées par exemple. Comme vu précédemment dans la section discutant la sélection, le seul moyen de réduire ces bruits de fond à des niveaux abordables est d'appliquer des vetos en terme de masse invariante. Dans cette analyse, les états intermédiaires explicitement interdits sont Λ_c^+, Ξ_c^+, D^+, D_s^+, D^0, χ_{c0} et J/ψ. Rappelons ici que les désintégrations impliquant Λ_c^+ ou Ξ_c^+ sont utilisés comme canaux de contrôle dans la détermination des $\Delta\mathcal{A}^{CP}$ afin de maitriser au premier ordre, les asymétries de détection et de production. Pour les rapports d'embranchements, le mode de normalisation est $\Lambda_b^0 \to (\Lambda_c^+ \to pK\pi)\pi$.

- **Bruits de fond partiellement reconstruits** : désintégrations en 5 corps de Λ_b^0 ou Ξ_b^0 où une particle est manquante. Les contributions dominantes de cette catégorie de bruit de fond sont les désintégrations à 5 corps où un π^0 est manquant. Le seuil considéré dans la modélisation de cette contribution est donné par la différence entre la masse du baryon beaux Λ_b^0 ou Ξ_b^0 et la masse du π^0. Les bruits de fond partiellement reconstruits pour lesquels un photon est manquant sont aussi considérés. Ces contributions sont par ailleurs contraintes à la hiérachie connue entre des désintégrations analogues de mésons B.

- **Contamination de cross-feed** qui sont des événements de signal qui peuvent apparaitre comme un bruit de fond si au moins une trace est mal identifiée. Bien que l'optimisation des critères de sélection de PID réduit ces contributions, un nombre significatif d'événements de signal peuvent encore apparaitre comme un bruit de fond. Comme introduit précédemment, le nombre d'événements d'une contamination de cross-feed est contraint au nombre d'événements du signal correspondant par un facteur qui tient compte des efficacités de sélection et d'identification (PID). L'utilisation de ces contraintes permet un contrôle efficace de ces contributions.

- **Les désintégrations de mésons B en 4 ou 5 corps** peuvent apparaitre comme sources de bruit fond si un proton est identifié comme un π ou un kaon. Plusieurs sources dominantes sont envisagées, incluant $B^0 \to \pi^+\pi^-\pi^+\pi^-$, $B^0 \to K^+\pi^-\pi^+\pi^-$, $B^0 \to K^+K^-K^+\pi^-$, $B_s^0 \to K^+\pi^-\pi^+K^-$ et $B_s^0 \to K^+K^-K^+K^-$. Seul un critère de sélection sur la variable ProbNNp est susceptible de réduire ces contributions. Cependant, une étude approfondie est nécessaire afin d'estimer le nombre d'événements encore présent dans les spectres de signal. Cette étude est détaillée dans la section suivante.

- **Combinatoire** d'une ou plusieurs traces sans rapport avec le mode de désintégration d'intérêt. La topologie et la cinématique des ces événements de bruit de fond diffèrent suffisamment de ceux du signal pour limiter leur présence en utilisant des critères de selection multivariés.

Ces contributions sont considérés dans la construction du modèle d'ajustement aux données.

G.4.1 Anatomie de la région de haute masse invariante

La détermination du nombre d'événements de bruit de fond provenant des désintégrations à 4 ou 5 corps de mésons B n'est actuellement pas possible : les rapports d'embranchement inclusifs des mésons B ne sont pas mesurés. Ces contributions de bruits de fond sont particulièrement inquiétantes car elles peuvent significativement contribuer aux effets d'asymétrie CP. Le contrôle de ces contributions est donc nécessaire. Une estimation est cependant possible, en utilisant la région de haute masse invariante : l'idée est de reconstruire la masse invariante de quatre particules de l'état final en tenant compte des états finaux attendus dans les désintégrations de mésons B. Par exemple, pour le spectre de $\Lambda_b^0 \to p\pi^-\pi^+\pi^-$, le proton est hypothétiquement considéré comme un K pour estimer le nombre d'événements du mode $B^0 \to K\pi\pi\pi$. Pour éviter la découverte prématurée du nombre d'événements de signal (qui sont maintenus cachés pour éviter un biais d'analyse), seuls les événements de la région de haute masse invariante sont considérés. Ainsi, un ajustement à ces données est réalisé afin d'identifier et de quantifier les contributions dominantes.

- Dans chaque spectre de haute masse, une contribution dominante venant d'une désintégration de méson B doit apparaitre via une confusion d'identification ($K \to p$). Ces modes contaminent par ailleurs les autres spectres via une confusion d'identification ($K \to \pi$) ou ($\pi \to K$).

- De manière analogue, les contaminations de signaux (cross-feed) doivent aussi être présentes dans la région de haute masse. Les contributions issues d'une confusion $\pi \to p$ doivent aussi être présentes.

- Un bruit de fond partiellement reconstruit issu des désintégrations $B \to 5$ corps pour lesquelles une trace n'est pas reconstruite est aussi attendu.

- Un bruit de fond combinatoire est aussi attendu.

Le but de cet ajustement aux données n'est pas d'avoir une compréhesion fine de la région de haute masse invariante mais bien d'identifier et d'estimer les contributions dominantes. Les contributions sous-dominantes sont controllées par des contraintes qui sont directement dérivées d'échantillons de calibration. Par exemple, la détermination du nombre d'événements de $B^0 \to K^+\pi^-\pi^+\pi^-$ attendus dans le spectre de $K\pi\pi\pi$ permet de contraindre le nombre d'événements de $B^0 \to K^+\pi^-\pi^+\pi^-$ dans le spectre de $KK\pi\pi$ en utilisant l'équation suivante :

$$(N_{K\pi\pi\pi})_2 = 2 * \frac{\epsilon_2^{\text{sel.}} * \epsilon_2^{\text{PID}}}{\epsilon_1^{\text{sel.}} * \epsilon_1^{\text{PID}}} * (N_{K\pi\pi\pi})_1 \tag{G.20}$$

où l'indice (1) indique le spectre où le mode est trouvé ($K\pi\pi\pi$ dans cet exemple) et où l'indice (2) indique le spectre dans lequel la contribution apparait comme un cross-feed ($KK\pi\pi$ dans

cet exemple). Le facteur deux vient du fait que un π parmi les deux de l'état final peut être mal identifié. Chaque contribution de contamination est donc implémentée dans le modèle d'ajustement aux données avec cette contrainte sur son nombre d'événements .
La fonction modélisant les désintégrations de B est déterminée à partir d'événements simulés. Les contributions de bruits de fond partiellement reconstruits sont modélisés par une fonction Argus convoluée avec une Gaussiènne. Ce type de contribution est non-négligeable, et le nombre d'événements mesuré dans la région de haute masse invariante est utilisé pour contraindre ces contributions dans l'ajustement aux données des spectres de signaux $X_b^0 \to phh'h''$. Une illustration des ajustements aux données de la région de haute masse invariante est donnée Fig. G.4

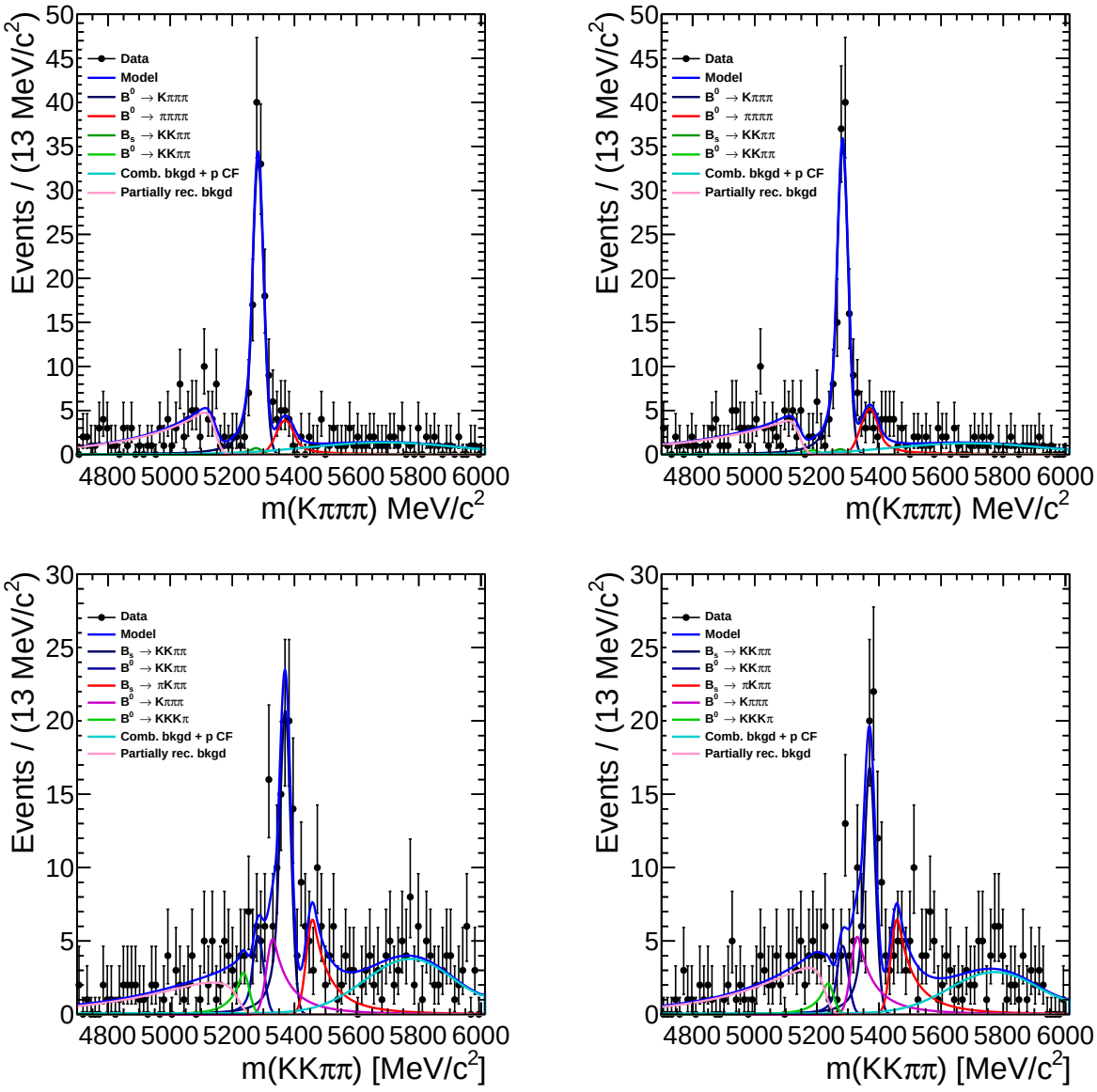

Figure G.4: Spectre de masse invariante pour les événements de la région de haute masse (2012) des spectres [de haut en bas] $X_b^0 \to p\pi\pi\pi$ reconstruit comme $B^0 \to K\pi\pi\pi$ et $X_b^0 \to pK\pi\pi$ reconstruit comme $B_s^0 \to KK\pi\pi$ (gauche) avec p and (droite) $\bar{p}$ séparés.

Le nombre d'événements des contributions de bruits de fond venant des désintégrations de mésons B est donc estimé pour l'analyse des rapports d'embranchements et la mesure des variables $\Delta\mathcal{A}^{CP}$ séparemment.

G.4.2 Modèle d'ajustement aux données.

Comme introduit précédemment, un ajustement aux données des différents spectres de masse invariante est réalisé, et ce, simultanément. Cet ajustement permet de mesurer le nombre d'événements pour chaque mode de signal, et d'extraire rapports d'embranchement et $\Delta\mathcal{A}^{CP}$. Le même modèle est utilisé pour les deux types de mesure.
Les différences entre les performances d'identification du proton dans l'échantillon de calibration et dans les données de l'analyse nécessitent une pondération des efficacités ainsi que des fonctions utilisées dans la modélisation des signaux et des bruits de fond (elles-même déterminées à partir de données simulées.) Cette pondération est réalisée en tenant compte de la variation d'efficacités entre les différents régimes cinématiques (impulsion, pseudo-rapidité , multiplicité). Le découpage utilisé lors de la production des cartes d'efficacité est reporté dans le tableau G.3

Table G.3: Découpage utilisé pour la production des cartes d'efficacité d'identification $\text{PID}_{K\pi}$ et PID_p. Les limites reportés ici permettent d'avoir le même nombre d'événements .

Particle type (year)	p binning boundaries (in GeV/c^2)	η binning boundaries	N_{tracks}
K's (2011)	{3000; 9300; 15600; 18515; 28325; 40097; 59717; 100000}	{1.5; 2.4975; 2.7075; 3.0575; 3.3725; 3.7225; 4.0025; 5.0}	{0;100;150;200; 270;500}
K's (2012)	{3000; 9300; 15600; 16553; 26363; 38135; 57755; 100000}	{1.5; 2.4625; 2.6725; 2.9875; 3.3025; 3.6525; 3.8975; 5.0}	{0;100;150;200; 270;500}
π's (2011)	{3000; 9300; 15600; 16553; 24401; 36173; 55793; 100000}	{1.5; 2.4625; 2.7075; 3.0225; 3.3375; 3.6875; 3.9675; 5.0}	{0;100;150;200; 270;500}
π's (2012)	{3000; 9300; 14591; 15600; 24401; 34211; 53831; 100000}	{1.5; 2.4275; 2.6375; 2.9525; 3.2675; 3.6175; 3.8975; 5.0}	{0;100;150;200; 270;500}
p's (2011)	{3000; 9300; 15600; 18515; 28325; 40097; 59717; 100000}	{1.5; 2.4975; 2.7075; 3.0575; 3.3725; 3.7225; 4.0025; 5.0}	{0;100;150;200; 270;500}
p's (2012)	{3000; 9300; 15600; 16553; 26363; 38135; 57755; 100000}	{1.5; 2.4625; 2.6725; 2.9875; 3.3025; 3.6525; 3.8975; 5.0}	{0;100;150;200; 270;500}

Les contributions de signal, cross-feeds et bruits de fond issus des désintégrations de mésons B sont modélisés à partir de données simulées. Les paramètres sont utilisés dans l'ajustement aux données "réelles" (sauf la position du pic pour le signal et les cross-feeds). Un exemple de la modélisation du signal $\Lambda_b^0 \to pK^-K^+K^-$ est reportésur la figure G.5. Les efficacités d'identification sont calculées à l'aide de données simulées et sont utilisées pour contraindre le nombre d'événements des contributions de bruits de fond. La combinatoire ainsi que la plupart des bruits de fonds partiellement reconstruits sont quant à eux laissés libres dans l'ajustement aux données : ces contributions sont en effet attendues comme dominantes dans les régions de haute et basse masse invariante, respectivement.

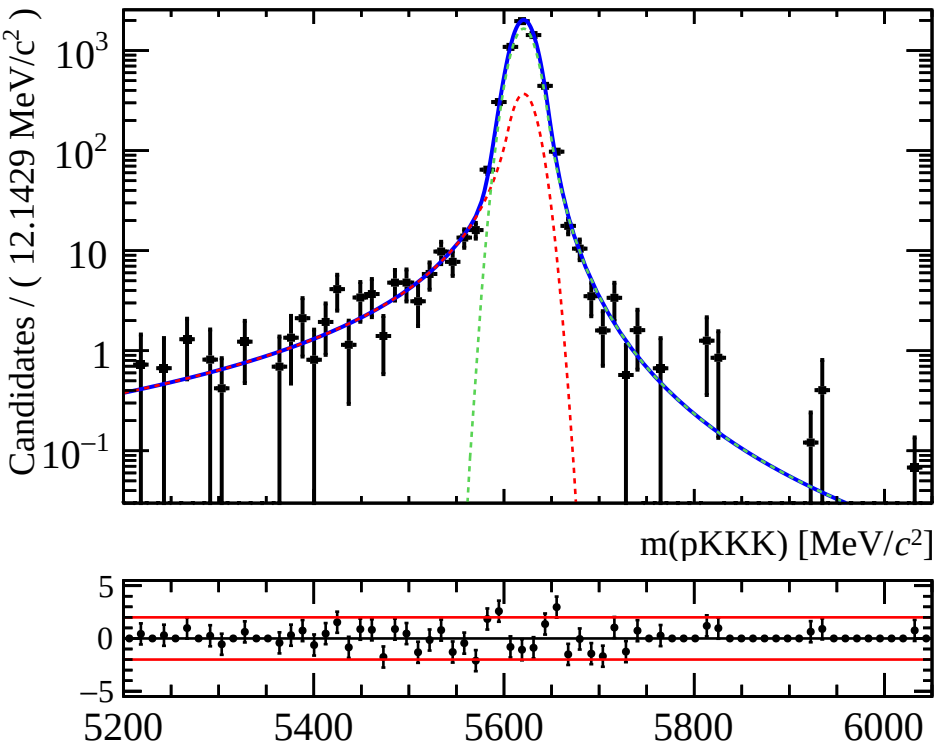

Figure G.5: Distribution de masse invariante du signal $\Lambda_b^0 \to pK^-K^+K^-$, modélisé par une fonction Double Crystal Ball. Cette fonction est utilisée pour la détermination du rapport d'embranchement correspondant.

G.5 Mesures des rapports d'embranchements.

L'observable utilisée dans la dérivation des rapports d'embranchements des modes de désintégration d'intérêt est la quantité R, définie par

$$
\begin{aligned}
R(X_b^0 \to p h^{'} h^{''} h^{'''}) &\equiv \frac{\mathcal{B}(X_b^0 \to p h^{'} h^{''} h^{'''})}{\mathcal{B}(\Lambda_b^0 \to \Lambda_c^+ \pi^-)} \cdot \frac{f_{X_b}}{f_{\Lambda_b^0}}, \\
&= \frac{\epsilon^{\text{geo.}}_{\Lambda_b^0 \to \Lambda_c^+ \pi^-}}{\epsilon^{\text{geo.}}_{X_b^0 \to p h^{'} h^{''} h^{'''}}} \cdot \frac{\epsilon^{\text{sel.}}_{\Lambda_b^0 \to \Lambda_c^+ \pi^-}}{\epsilon^{\text{sel.}}_{X_b^0 \to p h^{'} h^{''} h^{'''}}} \cdot \frac{\epsilon^{\text{PID}}_{\Lambda_b^0 \to \Lambda_c^+ \pi^-}}{\epsilon^{\text{PID}}_{X_b^0 \to p h^{'} h^{''} h^{'''}}} \cdot \frac{1}{\epsilon^{\text{veto}}_{X_b^0 \to p h^{'} h^{''} h^{'''}}} \cdot \frac{\mathcal{N}_{X_b^0 \to p h^{'} h^{''} h^{'''}}}{\mathcal{N}_{\Lambda_b^0 \to \Lambda_c^+ \pi^-}},
\end{aligned}
\tag{G.21}
$$

où $\mathcal{B}$ représente le rapport d'embranchement et $f_{X_b}/f_{\Lambda_b^0}$ et la fraction d'hadronisation relative de $b \to X_b$ par rapport à $b \to \Lambda_b^0$. De gauche à droite, les rapports d'efficacité sont liés à l'acceptance géométrique, aux critères de sélection, aux critères de PID et aux vetos des bruits de fond charmés. Le nombre d'événement mesuré pour le mode de signal et le mode de normalisation est respectivement représenté par $\mathcal{N}_{X_b^0 \to p h^{'} h^{''} h^{'''}}$ et $\mathcal{N}_{\Lambda_b^0 \to \Lambda_c^+ \pi^-}$.

Les figures reportées dans cette section correspondent à l'addition des spectres séparé par charge (p et $\bar{p}$). Le modèle d'ajustement aux données fut développé en aveugle. La collaboration LHCb valida la modélisation, et l'addition des spectres fut découverte. Les figures G.6 à G.10 présentent les résultats de l'ajustement simultané aux données des cinq spectres d'intérêt. La figure G.11 présente le resultat pour le mode de normalisation. Tous les modes de désintégrations sont pour la première fois observés à l'exception de $\Xi_b^0 \to p K^- K^+ K^-$. La Table G.4 présente le nombre d'événements observés.

Table G.4: Nombre d'événements mesurés pour chaque mode de signal, déterminé par l'addition des résultats obtenue dans les spectres séparés par charge et par année. Les rapports signal (S) sur bruits de fonds (B, toutes sources confondues) dans une fenêtre de masse invariante large de ± 3 fois la largeur du signal, sont donnés. L'intervalle de masse invariante correspondant est reporté dans la dernière colonne.

Decay mode	Signal yield	S/B	$\pm 3\sigma$ range (MeV/c^2)
$\Lambda_b^0 \to p\pi^-\pi^+\pi^-$	1809 ± 48	4.9 ± 0.3	[5573.9, 5674.6]
$\Lambda_b^0 \to pK^-\pi^+\pi^-$	5193 ± 76	7.7 ± 0.4	[5574.4, 5674.2]
$\Lambda_b^0 \to pK^-K^+\pi^-$	444 ± 30	0.71 ± 0.06	[5577.4, 5671.1]
$\Lambda_b^0 \to pK^-K^+K^-$	1706 ± 46	8.1 ± 0.7	[5579.0, 5674.6]
$\Xi_b^0 \to pK^-\pi^+\pi^-$	183 ± 22	0.59 ± 0.09	[5747.9, 5846.2]
$\Xi_b^0 \to pK^-\pi^+K^-$	199 ± 21	0.81 ± 0.10	[5747.4, 5846.2]
$\Xi_b^0 \to pK^-K^+K^-$	27 ± 14	0.14 ± 0.08	[5752.7, 5840.8]
$\Lambda_b^0 \to (\Lambda_c^+ \to pK^-\pi^+)\pi^-$	16518 ± 133	—	[5573.7, 5674.8]

G.5.1 Ajustement aux données du spectre $p\pi\pi\pi$

La figure G.6 montre un signal inambigu du mode $\Lambda_b^0 \to p\pi^-\pi^+\pi^-$. La modélisation du bruit de fond décrit les données de manière satisfaisante. Comme la région de haute masse est exclusivement composée des contributions venant des désintégrations de mésons B et du bruit de fond combinatoire, ce résultat valide la modélisation de ces contributions. Les bruits de fond partiellement reconstruits sont également bien décrits par la fonction ARGUS.

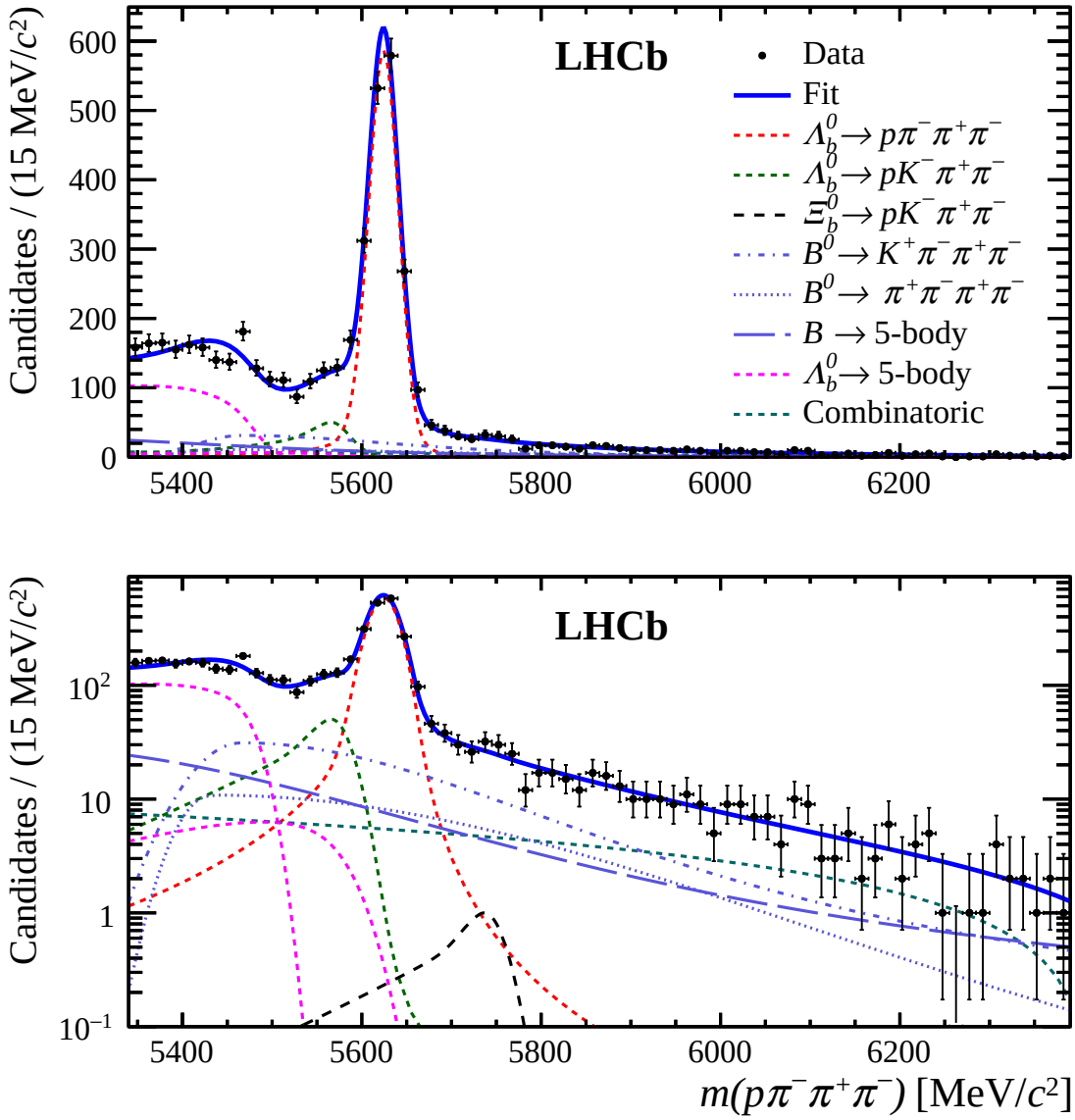

Figure G.6: Résultat de l'ajustement aux candidats de masse invariante du spectre $p\pi\pi\pi$ avec une échelle (haut) logarithmique et (bas) linéaire. Les différentes composantes utilisées sont indiquées dans la légende. La contribution $\Lambda_b^0 \to$ 5-body décrit le bruit de fond radiatif partiellement reconstruit $\Lambda_b^0 \to p\pi^-\eta'$ et le bruit de fond partiellement reconstruit $\Lambda_b^0 \to p\pi^-\pi^+\pi^-\pi^0$ pour lequel un π^0 n'est pas reconstuit. Cette dernière domine à basse masse.

G.5.2 Ajustement aux données du spectre $pK\pi\pi$

La figure G.7 montre un signal inambigu du mode $\Lambda_b^0 \to pK^-\pi^+\pi^-$ ainsi que le mode $\Xi_b^0 \to pK^-\pi^+\pi^-$. On peut noter ici que la structure du bruit de fond est riche. Comme indiqué précédemment, l'avantage du fit simultané est de pouvoir utiliser les informations du spectre précédent (et donc des suiants également) pour contraindre certaintes contributions présentes dans le spectre (*i.e.* la contamination du signal $\Lambda_b^0 \to p\pi^-\pi^+\pi^-$). Ici encore, les bruits de fond partiellement reconstruits sont correctement décrits par la fonction ARGUS. Cependant, quelques différences entre les données et le modèle sont visibles, notamment dans la région de haute masse invariante. La significance de ces écarts n'est cependant pas plus grande que deux déviations standard et ces derniers sont couverts par l'ampleur de la variation considérée dans l'estimation des incertitudes systématiques.

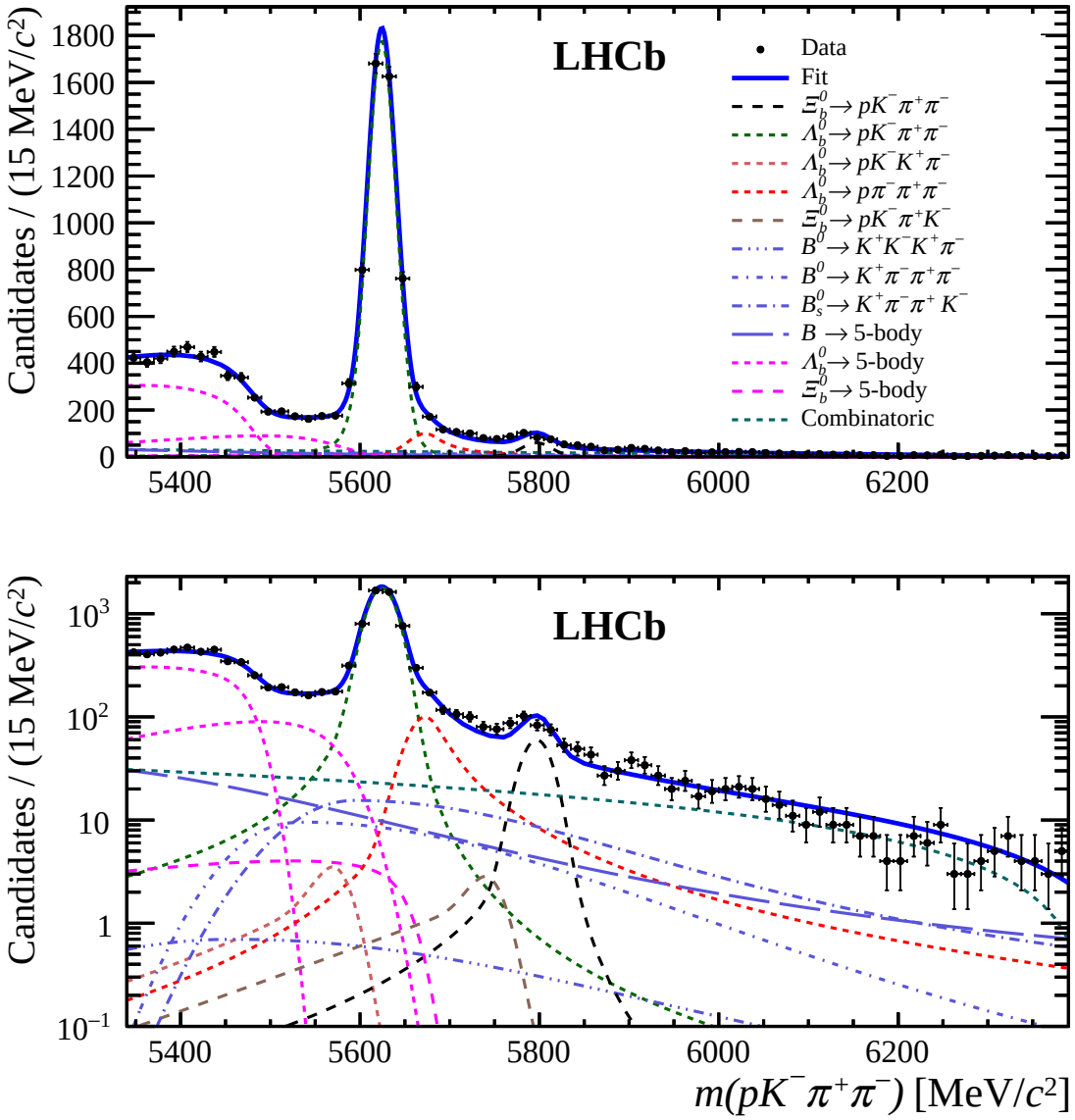

Figure G.7: Résultat de l'ajustement aux candidats de masse invariante du spectre $pK\pi\pi$ avec une échelle (haut) logarithmique et (bas) linéaire. Les différentes composantes utilisées sont indiquées dans la légende. La contribution $\Lambda_b^0 \to$ 5-body décrit le bruit de fond radiatif partiellement reconstruit $\Lambda_b^0 \to pK^-\eta'$ et le bruit de fond partiellement reconstruit $\Lambda_b^0 \to pK^-\pi^+\pi^-\pi^0$ pour lequel un π^0 n'est pas reconstuit. Cette dernière domine à basse masse.

G.5.3 Ajustement aux données du spectre $pKK\pi$

La figure G.8 montre un signal inambigu du mode $\Lambda_b^0 \to pK^-K^+\pi^-$. Ici encore, on peut noter que la structure du bruit de fond est riche. La fonction en histogramme modèle le cross-feed du mode partiellement reconstruit $\Lambda_b^0 \to p\pi^-\pi^+\pi^-\pi^0$. Cette contribution est la seule directement déterminée des données.

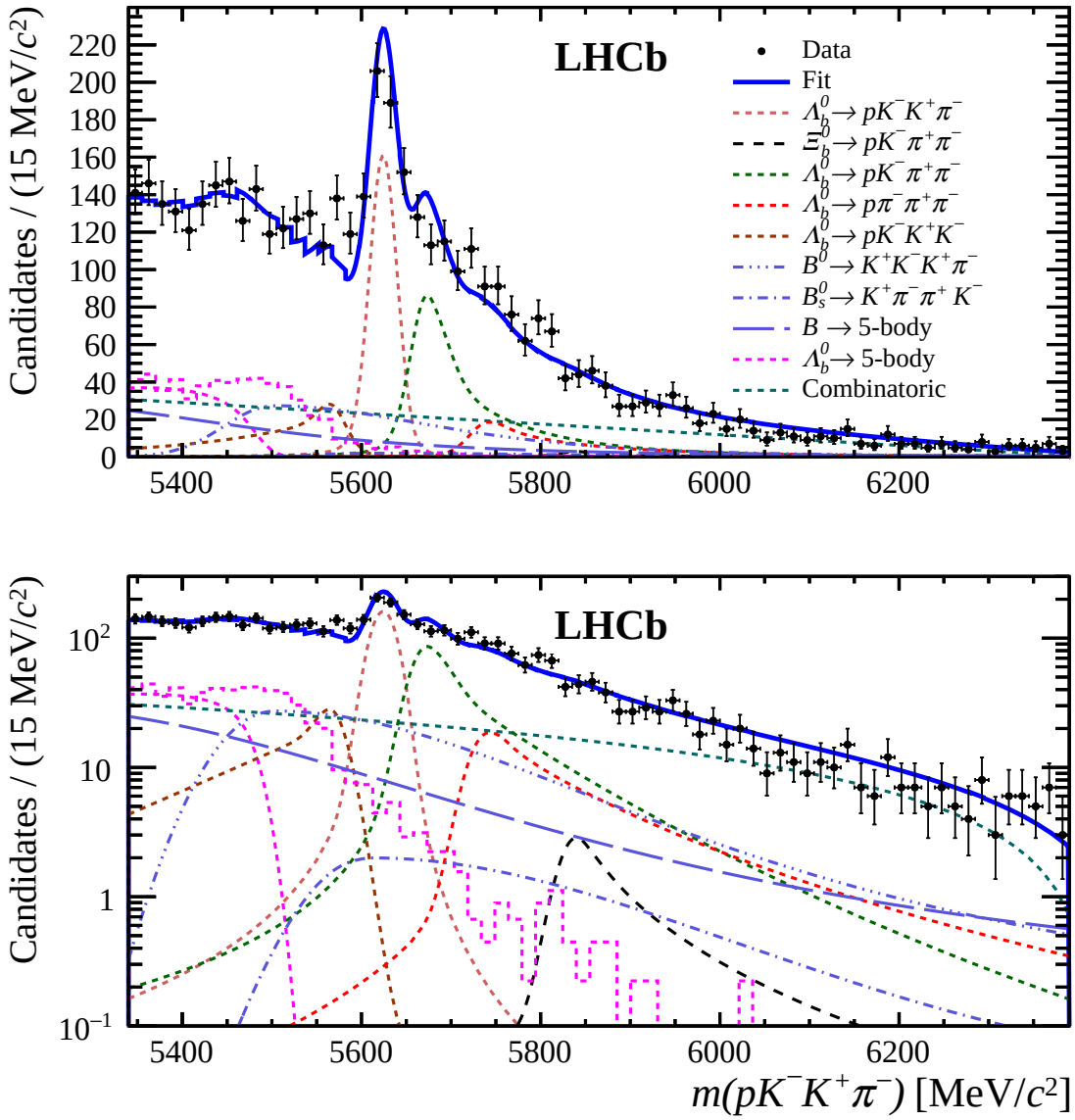

Figure G.8: Résultat de l'ajustement aux candidats de masse invariante du spectre $pKK\pi$ avec une échelle (haut) logarithmique et (bas) linéaire. Les différentes composantes utilisées sont indiquées dans la légende. La contribution $\Lambda_b^0 \to$ 5-body décrit le bruit de fond partiellement reconstruit $\Lambda_b^0 \to pK^-\pi^+\pi^-\pi^0$ pour lequel un π^0 n'est pas reconstuit, le bruit de fond partiellement reconstruit $\Lambda_b^0 \to pK^-\pi^+\pi^-\pi^0$ où un pion est confondu avec un kaon, et le mode partiellement reconstruit $\Lambda_b^0 \to pK^-K^+\pi^-\pi^0$.

G.5.4 Ajustement aux données du spectre $pK\pi K$

La figure G.9 montre un signal inambigu du mode $\Xi_b^0 \to pK^-\pi^+\pi^-$. Comme pour le spectre $pK\pi\pi$, quelques différences entre les données et le modèle sont visibles, notamment dans la région de haute masse invariante. Ces écarts sont couverts par l'ampleur de la variation considérée dans l'estimation.

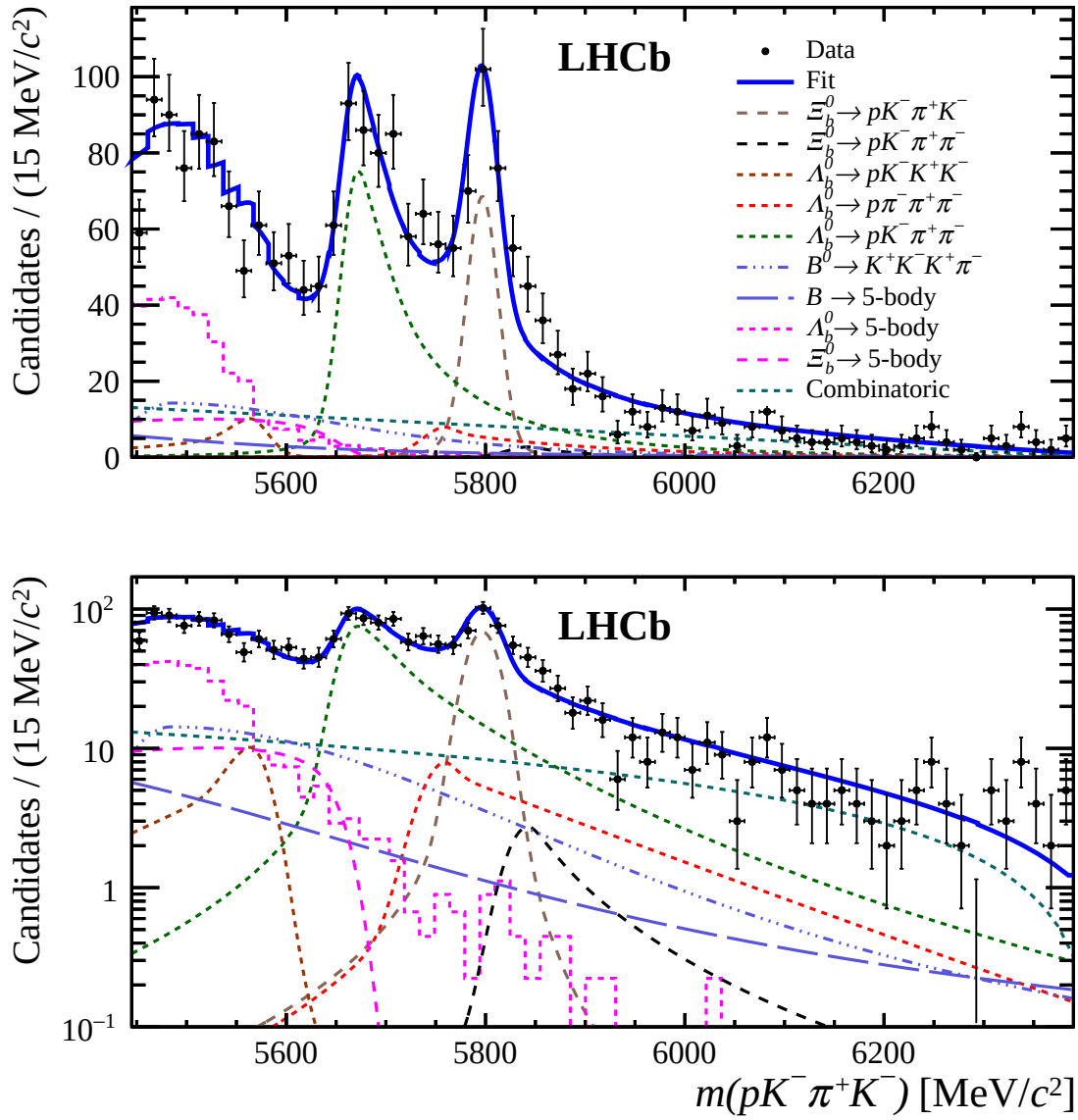

Figure G.9: Résultat de l'ajustement aux candidats de masse invariante du spectre $pK\pi K$ avec une échelle (haut) logarithmique et (bas) linéaire. Les différentes composantes utilisées sont indiquées dans la légende.

G.5.5 Ajustement aux données du spectre $pKKK$

La figure G.9 montre un signal inambigu du mode $\Lambda_b^0 \to pK^-K^+K^-$. Le mode de désintégration $\Xi_b^0 \to pK^-K^+K^-$ est cependant mesuré avec une significance de 2.3σ. Les contributions de bruits de fond sont correctement modélisés.

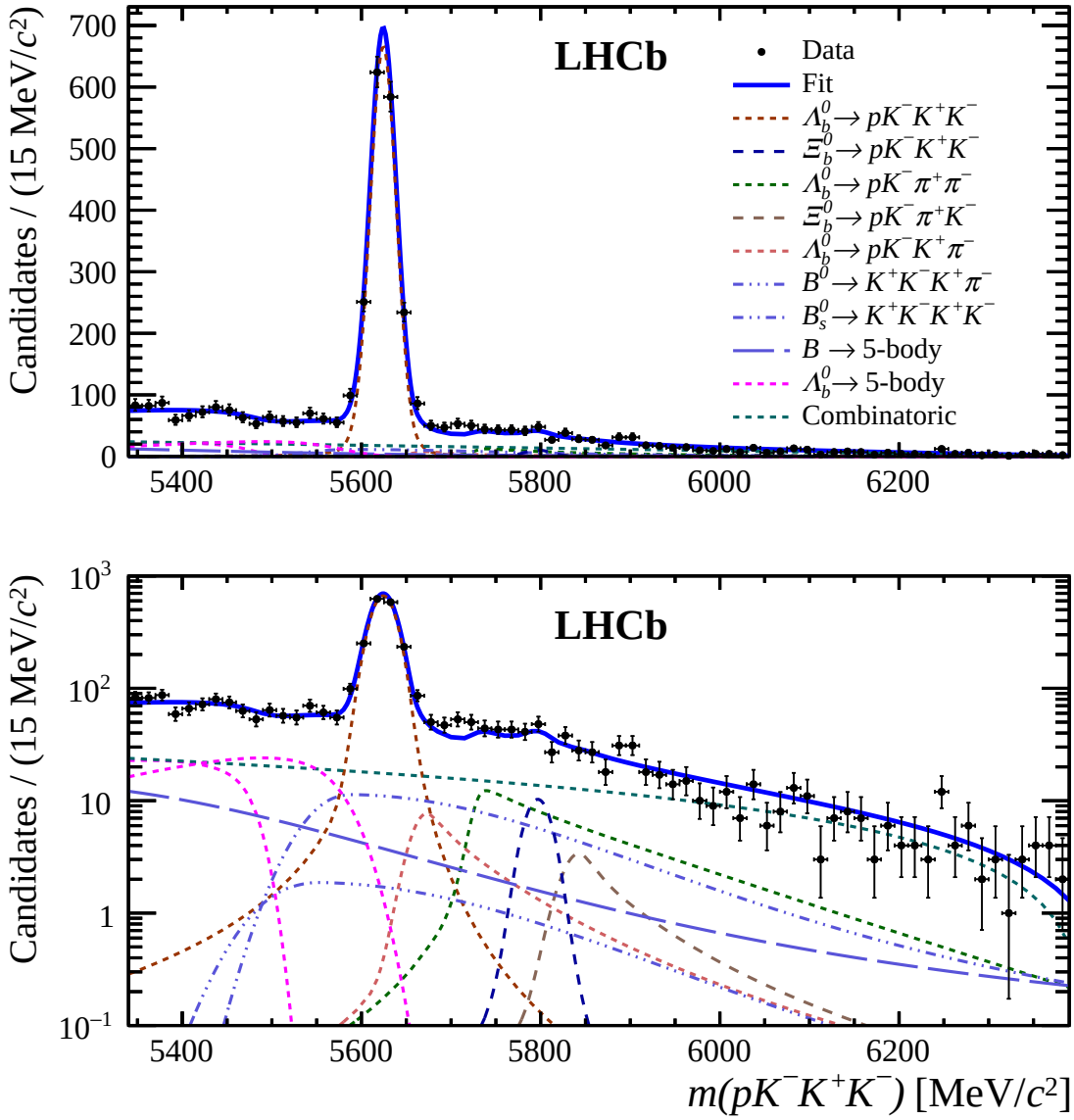

Figure G.10: Résultat de l'ajustement aux candidats de masse invariante du spectre $pKKK$ avec une échelle (haut) logarithmique et (bas) linéaire. Les différentes composantes utilisées sont indiquées dans la légende. La contribution $\Lambda_b^0 \to$ 5-body décrit les bruits de fond partiellement reconstruits $\Lambda_b^0 \to pK^-K^+K^-\gamma$ and $\Lambda_b^0 \to pK^-K^+K^-\pi^0$ où γ et π^0 ne sont pas reconstruits, respectivement.

G.5.6 Ajustement aux données du spectre $\Lambda_c^+ \pi$

La figure G.11 montre un signal inambigu du mode $\Lambda_b^0 \to (\Lambda_c^+ \to p\pi^-\pi^+)\pi^-$. La seule source de bruit de fond est le bruit de fond partiellement reconstruit.

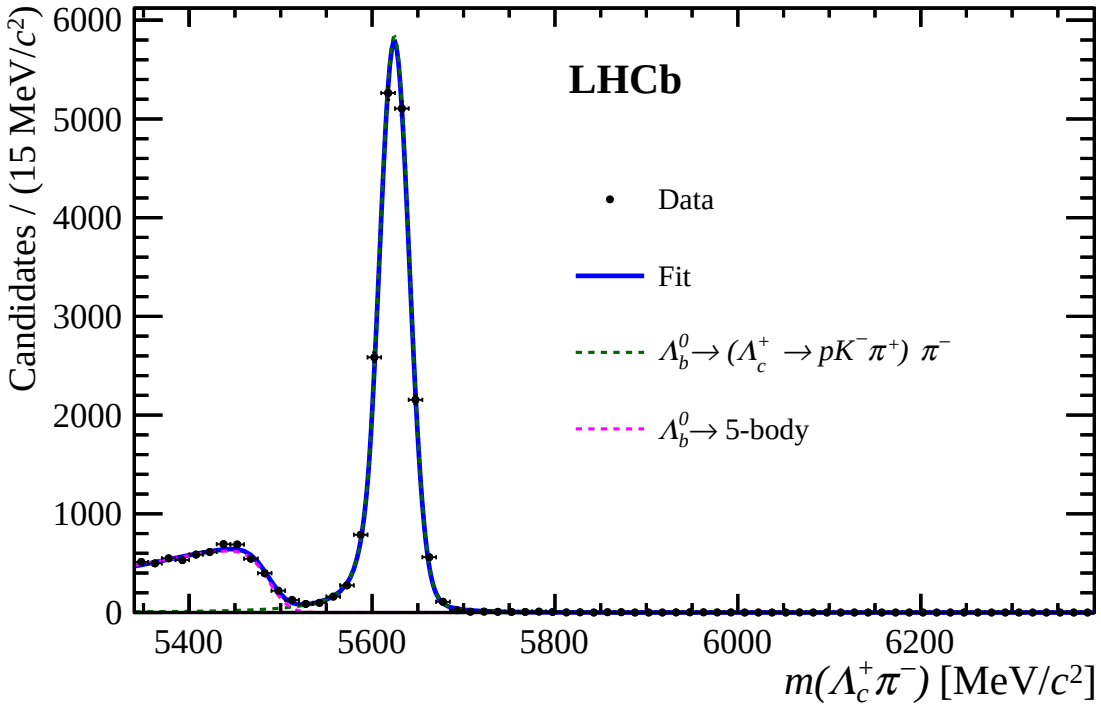

Figure G.11: Résultat de l'ajustement aux candidats de masse invariante du spectre $\Lambda_c^+\pi^-$. Les différentes composantes utilisées sont indiquées dans la légende.

G.6 Calcul des efficacités

Les efficacités sont déterminées à partir de donneées simulées. Cette simulation a été générée avec un mélange abitraire de deux types de cinématiques, considérées comme extrêmes. Par exemple, la désintégration $\Lambda_b^0 \to pK^-\pi^+\pi^-$ procède dans la simulation via les désintégrations à deux corps $\Lambda_b^0 \to \Lambda^*(1520)^0\rho(770)^0$, $\Lambda_b^0 \to \Lambda^*(1520)^0 f_2(1270)$ or $\Lambda_b^0 \to N^*(1520)^0 K^*(892)$. En principe, la variation d'efficacité sur l'espace des phases doit dépendre des coordonnées de l'espace des phases mais la dynamique de la désintégration est *a priori* inconnue, et une correction des efficacités par les données nécessiterait une pondération à 5 dimensions. Il a été constaté qu'un échantillon de donnée satisfaisant la condition de déclenchement L0TIS, présente une variation d'efficacité sur l'espace des phases qui est globalement constante. Une incertitude systématique est propagée sur la mesure du rapport d'embranchement pour tenir compte de cette approximation. De plus, toute la sélection des événements de signal a été dessinée dans le but de préserver l'espace des phases de la désintégration . Une illustration de la variation d'efficacité sur l'espace des phases est donnée Fig G.12.
Seuls les événements pour lesquels le système de déclenchement est indépendant du signal sont donc utilisés dans la détermination des rapports d'embranchements.

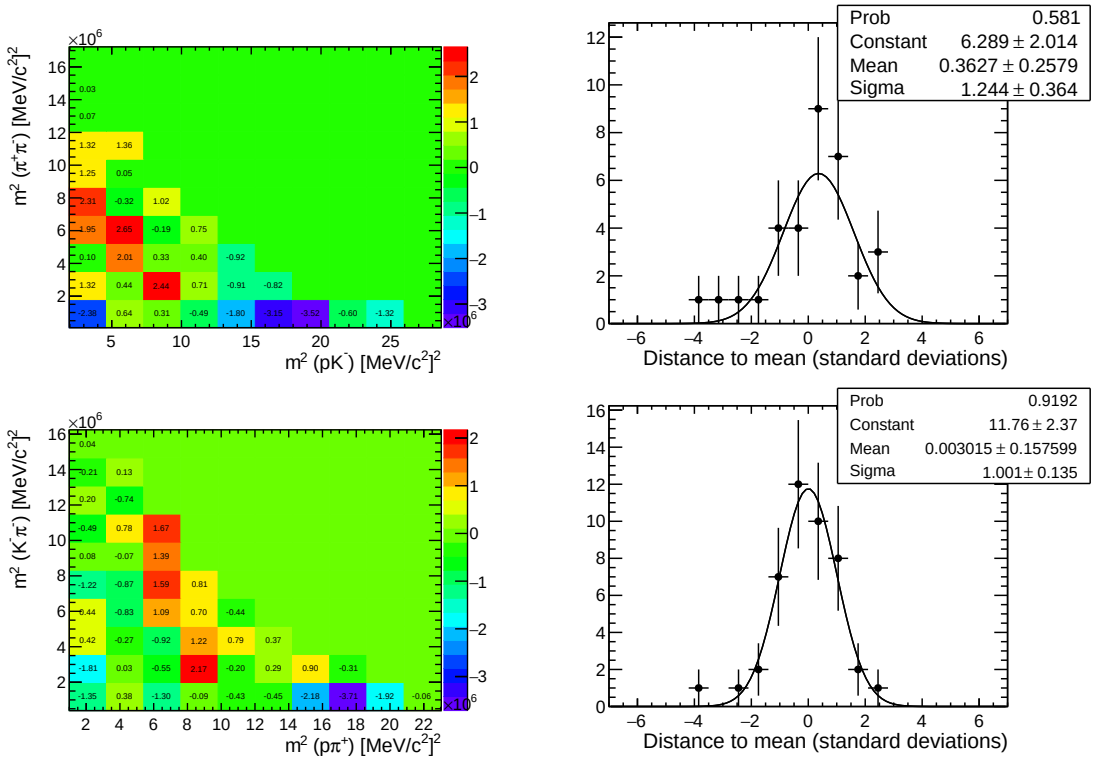

Figure G.12: Événements de simulation sélectionnés avec la condition L0TIS. Gauche: distribution d'efficacité sur l'espace de phase, en coordonnée de masse invariante (au carré) de deux corps où chaque bin contient la distance à la valeur moyenne de la carte exprimée en nombre de déviations standard. La distribution des ces distances est reportée sur la figure de droite. Une variation peut être considérée comme uniforme si la distribution est compatible avec une gaussiène centrée en 0 et de largeur 1.

G.6.1 Rapports d'efficacités - récapitulatif

La table G.5 présente les rapports d'efficacités nécessaires au calcul du rapport d'embranchement. Seules les efficacités des vetos sont déterminées directement des données, en inférant le nombre d'événements rejetés via l'utilisation d'une interpolation linéaire sur la région rejetée.

Table G.5: Rapports d'efficacité (mode de normalisation sur signal) pour 2011 (première ligne) et 2012 (deuxième ligne). La dernière colonne présente l'efficacité des critères de rejet des bruits de fond charmés (appliquée au signal uniquement). Pour le mode $\Xi_b^0 \to pK^-K^+K^-$ qui n'est pas observé, l'efficacité de veto est déterminée à partir de données simulées. La différence avec l'efficacité moyenne mesurée pour les modes Ξ_b^0 est reportée dans le tableau.

Désintégration	Rapports d'efficacités			
	Acceptance	Selection	PID	Vetos
$\Lambda_b^0 \to p\pi^-\pi^+\pi^-$	1.070 ± 0.003	0.433 ± 0.011	1.018 ± 0.013	0.693 ± 0.028
	1.050 ± 0.004	0.425 ± 0.009	1.046 ± 0.010	0.712 ± 0.017
$\Lambda_b^0 \to pK^-\pi^+\pi^-$	1.020 ± 0.003	0.438 ± 0.011	0.922 ± 0.012	0.758 ± 0.032
	1.004 ± 0.004	0.432 ± 0.009	0.958 ± 0.009	0.744 ± 0.016
$\Lambda_b^0 \to pK^-K^+\pi^-$	0.978 ± 0.003	0.462 ± 0.012	0.846 ± 0.011	0.742 ± 0.099
	0.970 ± 0.004	0.468 ± 0.010	0.874 ± 0.008	0.765 ± 0.050
$\Lambda_b^0 \to pK^-K^+K^-$	0.928 ± 0.003	0.445 ± 0.012	0.783 ± 0.010	0.751 ± 0.036
	0.916 ± 0.003	0.452 ± 0.010	0.801 ± 0.007	0.787 ± 0.026
$\Xi_b^0 \to pK^-\pi^+\pi^-$	1.019 ± 0.003	0.431 ± 0.011	0.902 ± 0.011	0.652 ± 0.082
	1.009 ± 0.004	0.424 ± 0.009	0.917 ± 0.008	0.659 ± 0.109
$\Xi_b^0 \to pK^-\pi^+K^-$	0.979 ± 0.003	0.434 ± 0.011	0.829 ± 0.010	0.689 ± 0.074
	0.969 ± 0.004	0.450 ± 0.010	0.847 ± 0.008	0.752 ± 0.081
$\Xi_b^0 \to pK^-K^+K^-$	0.929 ± 0.003	0.425 ± 0.011	0.764 ± 0.009	0.819 ± 0.123
	0.922 ± 0.003	0.429 ± 0.009	0.771 ± 0.007	

G.6.2 Incertitudes systématiques

Plusieurs sources d'incertitudes systématiques sont considérées. Seules les sources dominantes sont reportées et discutées ici.

- Les paramètres des fonctions utilisées dans l'ajustement aux données sont établis par un ajustement aux données simulées. Ceux-ci sont ensuite fixés dans l'ajustement aux données réelles. Afin d'estimer une incertitudes systématiques pour couvrir ce choix, des pseudo-expériences sont générées et la valeur des paramétres varient en prenant en compte leur matrice de corrélation. La distribution des résultats de ces pseudo-epériences est utilisée pour estimer une incertitude (de l'ordre de 1 à 2%).

- Dans l'analyse, on considère qu'il n'y a pas de variation d'efficacité sur l'espace des phases. Une incertitude systématique est estimée afin de couvrir cette hypothèse: la différence entre les efficacités déterminées pour les deux cinématiques extrêmes (présentes dans la simulation) est prise comme intervalle d'incertitudes. L'effet varie d'un mode à l'autre et peut atteindre 5%.

Pour illustration, les tables G.6 et G.7 présentent les différentes sources de systématiques liées au modèle d'ajustement aux données et aux efficacités, respectivement.

Table G.6: Incertitudes systématiques liées au modèle de l'ajustement aux données de (première ligne) 2011 (seconde ligne) 2012. De gauche à droite, celles-ci sont liées aux paramètres fixes des fonctions du modèle, le choix du modèle de combinatoire, la forme utilisée pour signaux et cross-feeds, les bruits de fond partiellement reconstruits $\Lambda_b^0 \to pK^-\pi^+\pi^-\pi^0$ (PR1) et $\Lambda_b^0 \to p\pi^-\eta'$ (PR2) et les facteurs de cross-feed. La dernière colonne présente l'incertitude globale liée au modèle.

Mode de désintégration	Incertitudes systématiques (%)							$\sigma_{\text{Tot.}}$ (%)
	$\sigma_{\text{Pars.}}$	$\sigma_{\text{Comb.}}$	$\sigma_{\text{Sig.}}$	$\sigma_{\text{CF.}}$	σ_{PR1}	σ_{PR2}	$\sigma_{f_{\text{CF}}}$	
$\Lambda_b^0 \to p\pi^-\pi^+\pi^-$	$\pm$ 1.1	< 0.1	$\pm$ 0.8	$\pm$ 0.3	—	$\pm$ 0.1	—	$\pm$ 1.4
	$\pm$ 0.7	< 0.1	$\pm$ 0.8	$\pm$ 0.2	—	< 0.1	—	$\pm$ 1.2
$\Lambda_b^0 \to pK^-\pi^+\pi^-$	$\pm$ 0.8	$\pm$ 0.3	$\pm$ 0.7	< 0.1	—	—	—	$\pm$ 1.1
	$\pm$ 0.9	$\pm$ 0.3	$\pm$ 0.7	$\pm$ 0.3	—	—	—	$\pm$ 1.3
$\Lambda_b^0 \to pK^-K^+\pi^-$	$\pm$ 1.5	$\pm$ 1.5	$\pm$ 0.9	$\pm$ 1.2	$\pm$ 7.2	—	$\pm$ 3.5	$\pm$ 8.5
	$\pm$ 1.1	$\pm$ 1.0	$\pm$ 0.7	$\pm$ 1.0	$\pm$ 4.7	—	$\pm$ 3.1	$\pm$ 5.9
$\Lambda_b^0 \to pK^-K^+K^-$	$\pm$ 0.9	$\pm$ 0.6	$\pm$ 1.4	< 0.1	—	—	< 0.1	$\pm$ 1.8
	$\pm$ 0.8	$\pm$ 0.4	$\pm$ 1.0	< 0.1	—	—	< 0.1	$\pm$ 1.4
$\Xi_b^0 \to pK^-\pi^+\pi^-$	$\pm$ 1.8	$\pm$ 1.0	$\pm$ 2.3	$\pm$ 1.5	—	—	$\pm$ 1.8	$\pm$ 3.5
	$\pm$ 1.0	$\pm$ 2.4	$\pm$ 0.5	$\pm$ 1.5	—	—	$\pm$ 1.0	$\pm$ 3.1
$\Xi_b^0 \to pK^-\pi^+K^-$	$\pm$ 1.9	$\pm$ 1.0	$\pm$ 0.7	$\pm$ 0.7	$\pm$ 2.9	—	$\pm$ 3.7	$\pm$ 5.2
	$\pm$ 1.5	$\pm$ 0.7	$\pm$ 0.7	$\pm$ 1.3	$\pm$ 2.2	—	$\pm$ 4.8	$\pm$ 5.8
$\Xi_b^0 \to pK^-K^+K^-$	$\pm$ 6.4	$\pm$ 10	$\pm$ 1.5	$\pm$ 0.5	—	—	$\pm$ 2.2	$\pm$ 13
	$\pm$ 3.9	$\pm$ 8.9	$\pm$ 2.0	$\pm$ 0.6	—	—	< 0.1	$\pm$ 10

G.7 Rapports d'embranchements

Six modes de désintégrations sont significativement observés. Le mode $\Xi_b^0 \to pK^-K^+K^-$ est mesuré avec une significance de 2.3 σ. Pour ce mode, des intervalles de 90% (et 95%) de degré de confiance sont déterminés en utilisant une inférence de Feldman-Cousins. Les rapports d'embranchements absolus sont :

$$\begin{aligned}
\mathcal{B}(\Lambda_b^0 \to p\pi^-\pi^+\pi^-) &= (1.90 \pm 0.06 \pm 0.10 \pm 0.16 \pm 0.07) \cdot 10^{-5}, \\
\mathcal{B}(\Lambda_b^0 \to pK^-\pi^+\pi^-) &= (4.55 \pm 0.08 \pm 0.20 \pm 0.39 \pm 0.17) \cdot 10^{-5}, \\
\mathcal{B}(\Lambda_b^0 \to pK^-K^+\pi^-) &= (0.37 \pm 0.03 \pm 0.04 \pm 0.03 \pm 0.01) \cdot 10^{-5}, \\
\mathcal{B}(\Lambda_b^0 \to pK^-K^+K^-) &= (1.14 \pm 0.03 \pm 0.07 \pm 0.10 \pm 0.05) \cdot 10^{-5},
\end{aligned}$$

où la première incertitude est statistique et le deuxième est d'origine systématique. Les deux dernières incertitudes viennent de la connaissance des rapports d'embranchements $\mathcal{B}(\Lambda_b^0 \to \Lambda_c^+\pi^-)$ et $\mathcal{B}(\Lambda_c^+ \to pK^-\pi^+)$ dans cet ordre.

$$\begin{aligned}
\mathcal{B}(\Xi_b^0 \to pK^-\pi^+\pi^-) \cdot f_{\Xi_b^0}/f_{\Lambda_b^0} &= (1.72 \pm 0.21 \pm 0.25 \pm 0.15 \pm 0.07) \cdot 10^{-6}, \\
\mathcal{B}(\Xi_b^0 \to pK^-\pi^+K^-) \cdot f_{\Xi_b^0}/f_{\Lambda_b^0} &= (1.56 \pm 0.16 \pm 0.19 \pm 0.13 \pm 0.06) \cdot 10^{-6}, \\
\mathcal{B}(\Xi_b^0 \to pK^-K^+K^-) \cdot f_{\Xi_b^0}/f_{\Lambda_b^0} &\in [0.11{-}0.25] \cdot 10^{-6} \text{ at } 90\% \text{ C.L.}
\end{aligned}$$

Les mesures reportées ici sont compatibles avec la hiérachie CKM. De plus, des limites sur les rapports d'embranchements inclusifs des désintégrations $B \to 4$ corps sont connues.

Table G.7: Incertitudes systématiques liées aux efficacités pour (première ligne) 2011 (seconde ligne) 2012. De gauche à droite, celles-ci sont liées au processus de reconstruction des traces, au PID, à l'efficacité de détection, à la variation d'efficacité sur l'espace des phases ainsi qu'aux vetos. La dernière colonne présente l'incertitude globale liée au modèle.

Mode de désintégration	Incertitudes sytématiques (%)					$\sigma_{\text{Tot.}}$ (%)
	$\sigma_{\text{trk.}}$	$\sigma_{\text{PID.}}$	$\sigma_{\text{Det.}}$	$\sigma_{\text{PhSp.}}$	σ_{Veto}	
$\Lambda_b^0 \to p\pi^-\pi^+\pi^-$	± 0.3	± 1.3	± 0.6	± 3.2	± 4.0	± 5.2
	± 0.5	± 0.8	± 0.4	± 4.1	± 2.4	± 4.8
$\Lambda_b^0 \to pK^-\pi^+\pi^-$	± 0.3	± 1.3	—	± 3.6	± 4.1	± 5.5
	± 0.5	± 0.9	—	± 3.0	± 2.1	± 3.7
$\Lambda_b^0 \to pK^-K^+\pi^-$	± 0.3	± 1.2	± 0.4	± 2.9	± 13	± 14
	± 0.4	± 0.9	± 0.3	± 3.2	± 6.5	± 7.3
$\Lambda_b^0 \to pK^-K^+K^-$	± 0.2	± 1.2	—	± 4.2	± 4.8	± 6.4
	± 0.4	± 0.8	—	± 3.8	± 3.3	± 5.1
$\Xi_b^0 \to pK^-\pi^+\pi^-$	± 0.3	± 1.3	—	± 2.6	± 13	± 14
	± 0.5	± 0.9	—	± 3.0	± 17	± 18
$\Xi_b^0 \to pK^-\pi^+K^-$	± 0.2	± 1.2	± 0.4	± 2.9	± 11	± 12
	± 0.4	± 0.9	± 0.3	± 2.9	± 11	± 13
$\Xi_b^0 \to pK^-K^+K^-$	± 0.2	± 1.2	—	± 3.7	± 15	± 16
	± 0.4	± 0.8	—	± 3.8	± 15	± 16

Par contraste, les rapports d'embranchements inclusifs des désintégrations $B \to 3$ corps contenant les même transitions de quarks dans le MS ont été mesurés et permettent une comparaison raisonnable. Ici encore, les ordres de magnitudes des rapports d'embranchements sont compatibles.

L'établissement de ces signaux ouvre une nouvelle voie pour la recherche de la violation de l'asymétrie *CP*. La prochaine partie discute ces mesures.

G.8 Mesures d'asymétrie $\Delta\mathcal{A}^{CP}$

Les mesures d'asymétrie $\Delta\mathcal{A}^{CP}$ des six modes observés sont réalisées à partir de l'ajustement aux données présentés dans les sections précédentes. Nous rappelons ici que les critères de sélection sur les valeurs de ProbNNp et de BDT sont réoptimisés en fonction des erreurs statistiques des observables $\Delta\mathcal{A}^{CP}$ (dont la valeur centrale est inconnue).

G.8.1 L'ensemble des mesures

Trois types de mesure sont considérés. Le premier considère l'ensemble des données (mesures inclusives). Les deux suivants visent à inclure ou favoriser la présence de phase forte dans l'état final qui peuvent accentuer l'effet induit par la différence de phase faible. Par exemple, mesurer $\Delta\mathcal{A}^{CP}$ dans la désintégration $\Lambda_b^0 \to pa_1$ permet d'accéder à une région de l'espace des phases pouvant contenir de forts effets, qui ne seraient pas nécessairement visibles dans la mesure inclusive de la désintégration $\Lambda_b^0 \to p\pi^-\pi^+\pi^-$. L'ensemble des mesures

est résumé dans le tableau G.8.

Table G.8: Liste des modes de désintégrations utilisés pour mesurer $\Delta\mathcal{A}^{CP}$. Low2x2BodyMass (LBM) désigne la région de basse masse de 2x deux corps.

Spectre	Mesures inclusives	Low2x2BodyMass	Sélection de résonance
$X_b^0 \to p\pi\pi\pi$	$\Lambda_b^0 \to p\pi^-\pi^+\pi^-$	$\Lambda_b^0 \to p\pi^-\pi^+\pi^-$	$\Lambda_b^0 \to pa_1$ $\Lambda_b^0 \to \Delta^{++}\pi^-\pi^-$ $\Lambda_b^0 \to N^*(1520)^0\rho^0(f^0)$
$X_b^0 \to pK\pi\pi$	$\Lambda_b^0 \to pK^-\pi^+\pi^-$ $\Xi_b^0 \to pK^-\pi^+\pi^-$	$\Lambda_b^0 \to pK^-\pi^+\pi^-$	$\Lambda_b^0 \to pK_1$ $\Lambda_b^0 \to \Delta^{++}K^-\pi^-$ $\Lambda_b^0 \to \Lambda^*(1520)^0\rho^0(f^0)$ $\Lambda_b^0 \to N^*(1520)^0K^{*0}$
$X_b^0 \to pKKK$	$\Lambda_b^0 \to pK^-K^+K^-$	$\Lambda_b^0 \to pK^-K^+K^-$	$\Lambda_b^0 \to \Lambda^*(1520)^0\phi^0$ $\Lambda_b^0 \to pK^-_{\text{highmass}}\phi^0$
$X_b^0 \to pKK\pi$	$\Lambda_b^0 \to pK^-K^+\pi^-$		
$X_b^0 \to pK\pi K$	$\Xi_b^0 \to pK^-\pi^+K^-$		

G.8.2 Corrections des asymétries

Les sources d'incertitudes (liées au modèle d'ajustement aux données par exemple) sont indépendantes de charge et donc une correction sur la mesure n'est pas nécessaire (contrairement au cas des rapports d'embranchements). Le modèle d'ajustement aux données a en effet été dessiné dans le but de prendre en compte ces incertitudes. Cependant, des incertitudes aymétriques de charges peuvent être induites par d'autres effets, discutés ci-dessous. Ces sources ont été identifiées et leur effet quantifié avant la découverte des résultats. Pour illustration, les incertitudes systématiques sont reportées dans la Table G.9.

- **Asymétrie de détection liée au système de déclenchement** : une antiparticule va probablement faire l'expérience d'une interaction nucléaire avant une particule. Cet effet peut provoquer une asymétrie qui doit être mesurée afin de corriger les mesures $\Delta\mathcal{A}^{CP}$. Des échantillons de calibration sont utilisés afin d'estimer cette asymétrie systématique et l'incertitude sur sa détermination est propagée comme incertitude systématique, pour toutes les mesures de $\Delta\mathcal{A}^{CP}$.

- **Asymétrie de détection des particules** : il existe une asymétrie entre les efficacités de détection entre proton et antiproton ou K^+ et K^-. Ici encore, Des échantillons de calibration sont utilisés afin d'estimer cette asymétrie systématique et l'incertitude sur sa détermination est propagée comme incertitude systématique, pour toutes les mesures de $\Delta\mathcal{A}^{CP}$.

- **Asymétrie liée au PID** : à partir d'échantillons de calibration, les efficacités de PID sont déterminées séparemment pour proton et antiproton. Les mesures de $\Delta\mathcal{A}^{CP}$ sont corrigées de l'asymétrie correspondante mesurée.

Table G.9: Incertitudes systématiques par sources pour chaque mode pour les données de 2011. L'index "*" indique les modes pour lesquels les échantillons de 2011 et 2012 sont combinés.

Mode de désintégration	Incertitudes absolues (%)				Total (%)
	σ_{L0}	σ_K	σ_p	σ_{PID}	
$\Lambda_b^0 \to p\pi^-\pi^+\pi^-$	± 0.11	—	± 0.20	± 0.84	± 0.87
$\Lambda_b^0 \to pK^-\pi^+\pi^-$	± 0.10	± 0.17	± 0.20	± 0.83	± 0.88
$\Lambda_b^0 \to pK^-K^+\pi^-$	± 0.11	—	± 0.21	± 0.82	± 0.85
$\Lambda_b^0 \to pK^-K^+K^-$	± 0.11	± 0.15	± 0.20	± 0.83	± 0.88
$\Xi_b^0 \to pK^-\pi^+\pi^-$	± 0.09	± 0.17	± 0.20	± 0.84	± 0.88
$\Xi_b^0 \to pK^-\pi^+K^-$	± 0.09	± 0.15	± 0.20	± 0.83	± 0.88
$\Lambda_b^0 \to p\pi^-\pi^+\pi^-$	± 0.10	—	± 0.16	± 0.72	± 0.74
$\Lambda_b^0 \to pK^-\pi^+\pi^-$	± 0.09	± 0.17	± 0.17	± 0.68	± 0.73
$\Lambda_b^0 \to pK^-K^+K^-$	± 0.09	± 0.16	± 0.17	± 0.75	± 0.79
$\Lambda_b^0 \to pa_1$	± 0.18	—	± 0.20	± 0.97	± 1.01
$\Lambda_b^0 \to N^*(1520)^0\rho^0(f^0)$	± 0.08	—	± 0.12	± 0.47	± 0.49
$\Lambda_b^0 \to \Delta^{++}\pi^-\pi^-$	± 0.09	—	± 0.18	± 0.96	± 0.99
$\Lambda_b^0 \to pK_1$ *	± 0.11	± 0.16	± 0.14	± 0.58	± 0.63
$\Lambda_b^0 \to \Lambda^*(1520)^0\rho^0(f^0)$ *	± 0.04	± 0.12	± 0.12	± 0.36	± 0.40
$\Lambda_b^0 \to N^*(1520)^0K^{*0}$	± 0.06	± 0.15	± 0.14	± 0.64	± 0.67
$\Lambda_b^0 \to \Delta^{++}K^-\pi^-$	± 0.09	± 0.22	± 0.19	± 0.96	± 1.01
$\Lambda_b^0 \to \Lambda^*(1520)^0\phi^0$ *	± 0.05	± 0.11	± 0.10	± 0.30	± 0.33
$\Lambda_b^0 \to pK^-_{\text{highmass}}\phi^0$ *	± 0.06	± 0.15	± 0.14	± 0.58	± 0.61

G.8.3 Résultats

.

Comme pour le cas des rapports d'embranchements, le nombre d'événements mesuré permet la mesure des $\Delta\mathcal{A}^{CP}$. 18 mesures sont réalisées. Pour illustration, le résultat de l'ajustement aux données du spectre $\Lambda_b^0 \to pK^-\pi^+\pi^-$ est reporté Fig G.13. Le modèle décrit les données de manière satisfaisante pour tous les spectres considérés. Rappelons ici encore que ce modèle fut construit à l'aveugle, et que les résultats présentés dans ce document n'ont pas eu besoin d'être retouchés. Les observables $\Delta\mathcal{A}^{CP}$ reçoivent cependant (comme discuté dans la section précédente) des corrections afin de prendre en compte les effets d'asymétries expérimentales. Ainsi, la mesure d'asymétrie *CP* est donnée par :

$$\Delta\mathcal{A}^{CP} = \Delta\mathcal{A}^{CP}{}_{\text{raw}} - \delta^{\text{L0}} + \Delta A_K - \Delta A_P - \Delta A_{PID}, \tag{G.22}$$

où δ^{L0}, ΔA_K, ΔA_P et ΔA_{PID} sont des corrections liées aux asymétries du système de déclenchement, de la détection des protons et des kaons ainsi que efficacités de PID, respectivement. Les mesures de $\Delta\mathcal{A}^{CP}$ sont faites pour chaque année de prise de données et la combinaison des résulats est la moyenne pondérée des incertitudes statistiques et des incertitudes systématiques non-corrélées.

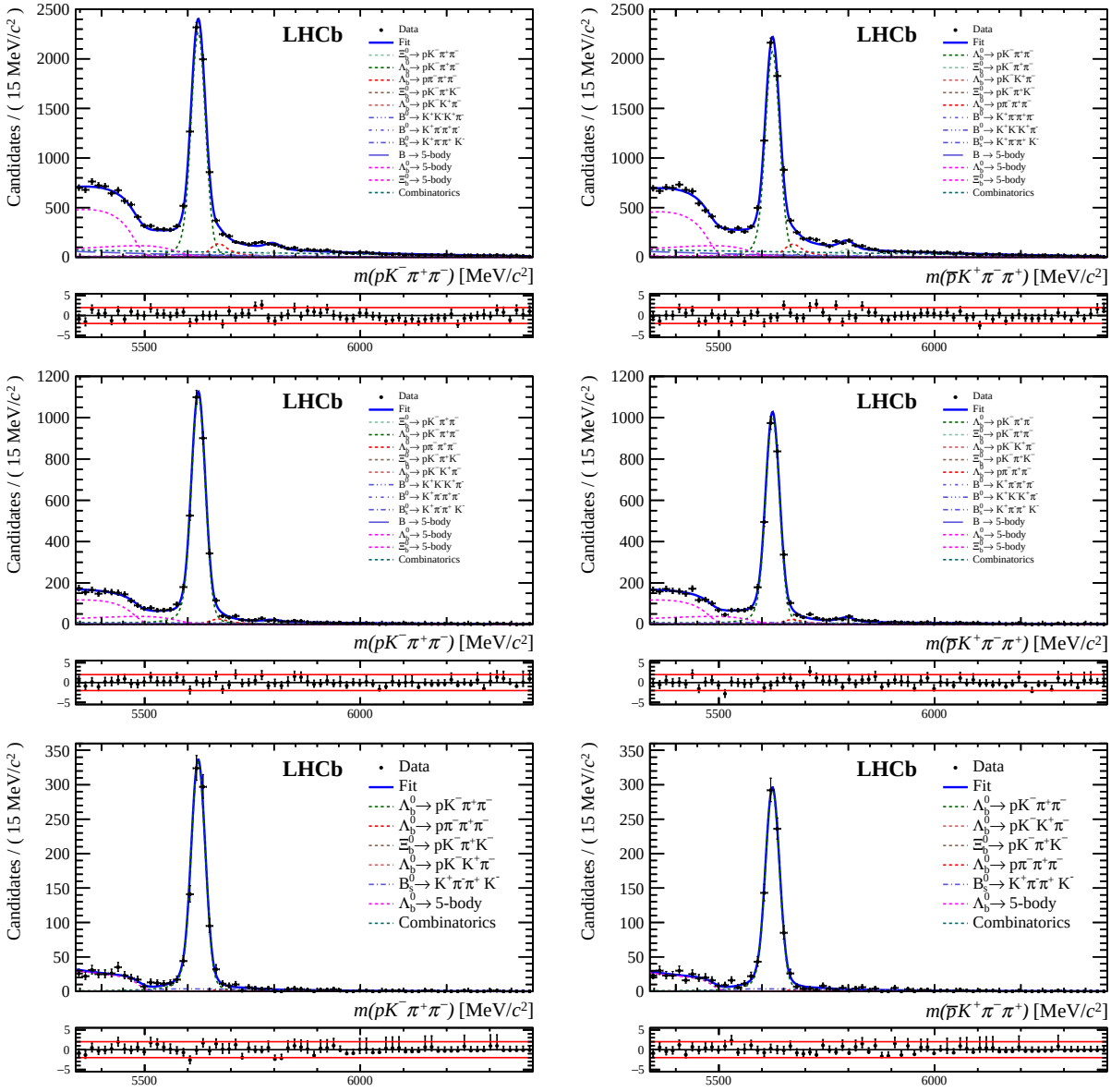

Figure G.13: Résultat de l'ajustement aux données pour les modes de désintégrations $\Lambda_b^0 \to pK^-\pi^+\pi^-$ (inclusif et Low2x2BodyMass) et $\Lambda_b^0 \to N^*(1520)^0 K^{*0}$. De gauche à droite: spectre avec X_b^0 et spectre avec $\overline{X}_b^0$.

Les valeurs de $\Delta\mathcal{A}^{CP}$ inclusives sont données ci-dessous :

$$\begin{aligned}
\Delta\mathcal{A}^{CP}(\Lambda_b^0 \to p\pi^-\pi^+\pi^-)(\%) &= 1.1 \pm 2.5 \pm 0.5 \\
\Delta\mathcal{A}^{CP}(\Lambda_b^0 \to pK^-\pi^+\pi^-)(\%) &= 3.2 \pm 1.1 \pm 0.5 \\
\Delta\mathcal{A}^{CP}(\Lambda_b^0 \to pK^-K^+\pi^-)(\%) &= -6.9 \pm 4.9 \pm 0.5 \\
\Delta\mathcal{A}^{CP}(\Lambda_b^0 \to pK^-K^+K^-)(\%) &= 0.2 \pm 1.8 \pm 0.5 \\
\Delta\mathcal{A}^{CP}(\Xi_b^0 \to pK^-\pi^+\pi^-)(\%) &= -16.8 \pm 10.4 \pm 0.5 \\
\Delta\mathcal{A}^{CP}(\Xi_b^0 \to pK^-\pi^+K^-)(\%) &= -6.8 \pm 8.0 \pm 0.5.
\end{aligned}$$

Les mesures pour les régions de basse masse de deux corps sont:

$$\begin{aligned}
\Delta\mathcal{A}^{CP}(\Lambda_b^0 \to p\pi^-\pi^+\pi^-)(\%) &= 3.7 \pm 4.1 \pm 0.5 \\
\Delta\mathcal{A}^{CP}(\Lambda_b^0 \to pK^-\pi^+\pi^-)(\%) &= 3.5 \pm 1.5 \pm 0.5 \\
\Delta\mathcal{A}^{CP}(\Lambda_b^0 \to pK^-K^+\pi^-)(\%) &= 2.7 \pm 2.3 \pm 0.5,
\end{aligned}$$

Enfin, les mesures pour les désintégrations à deux corps sont :

$$\begin{aligned}
\Delta\mathcal{A}^{CP}(\Lambda_b^0 \to pa_1)(\%) &= -1.5 \pm 4.2 \pm 0.6 \\
\Delta\mathcal{A}^{CP}(\Lambda_b^0 \to N^*(1520)^0\rho^0(f^0))(\%) &= 2.0 \pm 4.9 \pm 0.3 \\
\Delta\mathcal{A}^{CP}(\Lambda_b^0 \to \Delta^{++}\pi^-\pi^-)(\%) &= 0.1 \pm 3.2 \pm 0.6 \\
\Delta\mathcal{A}^{CP}(\Lambda_b^0 \to pK_1)(\%) &= 4.7 \pm 3.5 \pm 0.7 \\
\Delta\mathcal{A}^{CP}(\Lambda_b^0 \to \Lambda^*(1520)^0\rho^0(f^0))(\%) &= 0.6 \pm 6.0 \pm 0.4 \\
\Delta\mathcal{A}^{CP}(\Lambda_b^0 \to N^*(1520)^0K^{*0})(\%) &= 5.5 \pm 2.5 \pm 0.4 \\
\Delta\mathcal{A}^{CP}(\Lambda_b^0 \to \Delta^{++}K^-\pi^-)(\%) &= 4.4 \pm 2.6 \pm 0.6 \\
\Delta\mathcal{A}^{CP}(\Lambda_b^0 \to \Lambda^*(1520)^0\phi^0)(\%) &= 4.3 \pm 5.6 \pm 0.4 \\
\Delta\mathcal{A}^{CP}(\Lambda_b^0 \to pK^-_{\rm highmass}\phi^0)(\%) &= -0.7 \pm 3.3 \pm 0.7.
\end{aligned}$$

où la première incertitude est statistique et la seconde est d'origine systématique. Aucune violation de la symétrie *CP* est significativement observée. Une comparaison éduquée entre les résultats présentés dans ce document et la preuve de violation *CP* dans $\Lambda_b^0 \to p\pi^-\pi^+\pi^-$ reportée par la collaboration LHCb nécessite une analyse en amplitude à 5 dimensions afin d'identifier les amplitudes responsables de l'indication de la violation *CP* dans les deux analyses.

La quête pour la première observation de la violation *CP* dans les désintégrations de baryons continue. La quantité de données du RunII est 5 fois plus conséquente que celle utilisée dans cette analyse, et sera l'opportunité de compléter ce programme.

Bibliography

[1] A. Salam, *Weak and Electromagnetic Interactions*, Conf. Proc. **C680519** (1968) 367.

[2] S. Weinberg, *A Model of Leptons*, Phys. Rev. Lett. **19** (1967) 1264.

[3] S. L. Glashow, *Partial Symmetries of Weak Interactions*, Nucl. Phys. **22** (1961) 579.

[4] C. S. Wu *et al.*, *Experimental Test of Parity Conservation in Beta Decay*, Phys. Rev. **105** (1957) 1413.

[5] F. Englert and R. Brout, *Broken Symmetry and the Mass of Gauge Vector Mesons*, Phys. Rev. Lett. **13** (1964) 321.

[6] P. W. Higgs, *Broken symmetries, massless particles and gauge fields*, Phys. Lett. **12** (1964) 132.

[7] P. W. Higgs, *Broken Symmetries and the Masses of Gauge Bosons*, Phys. Rev. Lett. **13** (1964) 508.

[8] Particle Data Group, C. Patrignani *et al.*, *Review of particle physics*, Chin. Phys. **C40** (2016) 100001, and 2017 update.

[9] N. Cabibbo, *Unitary Symmetry and Leptonic Decays*, Phys. Rev. Lett. **10** (1963) 531.

[10] M. Kobayashi and T. Maskawa, *CP-Violation in the Renormalizable Theory of Weak Interaction*, Prog. Theor. Phys. **49** (1973) 652.

[11] L. Wolfenstein, *Parametrization of the Kobayashi-Maskawa Matrix*, Phys. Rev. Lett. **51** (1983) 1945.

[12] CKMfitter group, J. Charles *et al.*, *Current status of the Standard Model CKM fit and constraints on $\Delta F = 2$ new physics*, Phys. Rev. **D91** (2015) 073007, arXiv:1501.05013, updated results and plots available at http://ckmfitter.in2p3.fr/.

[13] J. H. Christenson *et al.*, *Evidence for the 2π Decay of the K_2^0 Meson*, Phys. Rev. Lett. **13** (1964) 138.

[14] NA48, L. Iconomidou-Fayard, *Results on CP violation from the NA48 experiment at CERN*, Int. J. Mod. Phys. **A17** (2002) 3012, arXiv:hep-ex/0110028, [,92(2001)].

[15] NA48, A. Lai *et al.*, *A Precise measurement of the direct CP violation parameter Re(epsilon-prime / epsilon)*, Eur. Phys. J. **C22** (2001) 231, arXiv:hep-ex/0110019.

[16] BABAR Collaboration, B. Aubert *et al.*, *Direct CP Violating Asymmetry in $B^0 \to K^+\pi^-$ Decays*, Phys. Rev. Lett. **93** (2004) 131801.

[17] LHCb collaboration, R. Aaij *et al.*, *First observation of CP violation in the decays of B_s^0 mesons*, Phys. Rev. Lett. **110** (2013) 221601, arXiv:1304.6173.

[18] BABAR Collaboration, B. Aubert *et al.*, *Observation of CP Violation in the B^0 Meson System*, Phys. Rev. Lett. **87** (2001) 091801.

[19] Belle Collaboration, K. Abe *et al.*, *Observation of Large CP Violation in the Neutral B Meson System*, Phys. Rev. Lett. **87** (2001) 091802.

[20] C. Albajar *et al.*, *First observation of the beauty baryon Λ_b in the decay channel $\Lambda_b \to J/\psi\Lambda$ at the CERN proton-antiproton collider*, Physics Letters B **273** (1991), no. 4 540.

[21] CDF, T. Aaltonen *et al.*, *Observation of the Ξ_b^0 Baryon*, Phys. Rev. Lett. **107** (2011) 102001, arXiv:1107.4015.

[22] LHCb collaboration, R. Aaij *et al.*, *Measurement of matter-antimatter differences in beauty baryon decays*, Nature Physics **13** (2017) 391 LHCb-PAPER-2016-030, CERN-EP-2016-212, arXiv:1609.05216.

[23] LHCb, A. A. Alves, Jr. *et al.*, *The LHCb Detector at the LHC*, JINST **3** (2008) S08005.

[24] S. Monteil, *Mesures de précision électrofaibles*, habilitation à diriger des recherches, Université Blaise Pascal - Clermont-Ferrand II, Dec., 2009, HDR 280.

[25] LHCb collaboration, *LHCb magnet: Technical Design Report*, CERN-LHCC-2000-007. LHCb-TDR-001.

[26] LHCb collaboration, *LHCb VELO (VErtex LOcator): Technical Design Report*, CERN-LHCC-2001-011. LHCb-TDR-005.

[27] LHCb collaboration, *LHCb outer tracker: Technical Design Report*, CERN-LHCC-2001-024. LHCb-TDR-006.

[28] LHCb collaboration, *LHCb inner tracker: Technical Design Report*, CERN-LHCC-2002-029. LHCb-TDR-008.

[29] LHCb collaboration, *LHCb RICH: Technical Design Report*, CERN-LHCC-2000-037. LHCb-TDR-003.

[30] LHCb collaboration, *LHCb calorimeters: Technical Design Report*, CERN-LHCC-2000-036. LHCb-TDR-002.

[31] LHCb collaboration, *LHCb muon system: Technical Design Report*, CERN-LHCC-2001-010. LHCb-TDR-004.

[32] R. Aaij *et al.*, *Performance of the LHCb Vertex Locator*, JINST **9** (2014) 09007, arXiv:1405.7808.

[33] LHCb VELO Group, H. L. Snoek, *The LHCb VELO: Performance and radiation damage*, Nucl. Instrum. Meth. **A765** (2014) 35.

[34] A. Puig, *The LHCb trigger in 2011 and 2012*, Tech. Rep. LHCb-PUB-2014-046. CERN-LHCb-PUB-2014-046, CERN, Geneva, 2014.

[35] L. Breiman, J. H. Friedman, R. A. Olshen, and C. J. Stone, *Classification and regression trees*, Wadsworth international group, Belmont, California, USA, 1984.

[36] Y. Freund and R. E. Schapire, *A decision-theoretic generalization of on-line learning and an application to boosting*, J. Comput. Syst. Sci. **55** (1997) 119.

[37] G. Punzi, *Sensitivity of searches for new signals and its optimization*, in *Statistical Problems in Particle Physics, Astrophysics, and Cosmology* (L. Lyons, R. Mount, and R. Reitmeyer, eds.), p. 79, 2003. arXiv:physics/0308063.

[38] LHCb, R. Aaij *et al.*, *Updated branching fraction measurements of $B^0_{(s)} \to K^0_S h^+ h'^-$ decays*, JHEP **11** (2017) 027, arXiv:1707.01665.

[39] LHCb, R. Aaij *et al.*, *Measurement of branching fractions of charmless four-body Λ^0_b and Ξ^0_b decays*, JHEP **02** (2018) 098, arXiv:1711.05490.

[40] M. Adinolfi *et al.*, *Performance of the LHCb RICH detector at the LHC*, Eur. Phys. J. **C73** (2013) 2431, arXiv:1211.6759.

[41] M. Vesterinen and D. Mueller, *Measurement of the Kaon Detection Asymmetry using Double-tagged Partially Reconstructed D^0 Decays*, Tech. Rep. LHCb-INT-2013-054. CERN-LHCb-INT-2013-054, CERN, Geneva, Nov, 2013.

[42] G. J. Feldman and R. D. Cousins, *Unified approach to the classical statistical analysis of small signals*, Phys. Rev. **D57** (1998) 3873.

[43] HFLAV, Y. Amhis *et al.*, *Averages of b-hadron, c-hadron, and τ-lepton properties as of summer 2016*, Eur. Phys. J. **C77** (2017), no. 12 895, arXiv:1612.07233.

[44] Belle, J. Dalseno *et al.*, *Measurement of Branching Fraction and First Evidence of CP Violation in $B^0 \to a_1^{\pm}(1260)\pi^{\mp}$ Decays*, Phys. Rev. **D86** (2012) 092012, arXiv:1205.5957.

[45] A. Martin Sanchez, P. Robbe, and M.-H. Schune, *Performances of the LHCb L0 Calorimeter Trigger*, .

[46] F. Betti *et al.*, *Measurement of CP violation in $\Lambda^0_b \to pK^-$ and $\Lambda^0_b \to p\pi^-$ decays at LHCb*, LHCb-ANA-2018-002.

[47] C. S. Kim, Y. Kwon, J. Lee, and W. Namgung, *Test of factorization hypothesis from exclusive nonleptonic B decays*, Phys. Rev. **D65** (2002) 097503, arXiv:hep-ph/0108004.

[48] J. Zhu, H.-W. Ke, and Z.-T. Wei, *The decay of $\Lambda_b \to p\ K^-$ in QCD factorization approach*, Eur. Phys. J. **C76** (2016), no. 5 284, arXiv:1603.02800.

[49] H.-Y. Cheng, *Nonfactorizable corrections to hadronic weak decays of heavy mesons*, arXiv:hep-ph/9506340.

[50] LHCb collaboration, R. Aaij *et al.*, *Differential branching fractions and isospin asymmetries of $B \to K^{(*)}\mu^+\mu^-$ decays*, JHEP **06** (2014) 133, arXiv:1403.8044.

[51] LHCb, R. Aaij *et al.*, *Measurements of the S-wave fraction in $B^0 \to K^+\pi^-\mu^+\mu^-$ decays and the $B^0 \to K^*(892)^0\mu^+\mu^-$ differential branching fraction*, JHEP **11** (2016) 047, arXiv:1606.04731, [Erratum: JHEP04,142(2017)].

[52] LHCb, R. Aaij *et al.*, *Angular analysis and differential branching fraction of the decay $B^0_s \to \phi\mu^+\mu^-$*, JHEP **09** (2015) 179, arXiv:1506.08777.

[53] LHCb collaboration, R. Aaij *et al.*, *Test of lepton universality using $B^+ \to K^+\ell^+\ell^-$ decays*, Phys. Rev. Lett. **113** (2014) 151601, arXiv:1406.6482.

[54] LHCb, R. Aaij *et al.*, *Test of lepton universality with $B^0 \to K^{*0}\ell^+\ell^-$ decays*, JHEP **08** (2017) 055, arXiv:1705.05802.

[55] LHCb, R. Aaij *et al.*, *Measurement of the ratio of the $B^0 \to D^{*-}\tau^+\nu_\tau$ and $B^0 \to D^{*-}\mu^+\nu_\mu$ branching fractions using three-prong τ-lepton decays*, Phys. Rev. Lett. **120** (2018), no. 17 171802, arXiv:1708.08856.

[56] T. M. Aliev, M. Savci, A. Ozpineci, and H. Koru, *Two higgs doublet model and lepton polarization in the $b \to k\tau^+\tau^-$*, Journal of Physics G: Nuclear and Particle Physics **24** (1998), no. 1 49.

[57] HPQCD Collaboration, C. Bouchard *et al.*, *Standard model predictions for $b \to k\ell^+\ell^-$ with form factors from lattice qcd*, Phys. Rev. Lett. **111** (2013) 162002.

[58] J. F. Kamenik, S. Monteil, A. Semkiv, and L. V. Silva, *Lepton polarization asymmetries in rare semi-tauonic $b \to s$ exclusive decays at FCC-ee*, Eur. Phys. J. **C77** (2017), no. 10 701, arXiv:1705.11106.

[59] BaBar, J. P. Lees *et al.*, *Search for $B^+ \to K^+\tau^+\tau^-$ at the BaBar experiment*, Phys. Rev. Lett. **118** (2017), no. 3 031802, arXiv:1605.09637.

[60] LHCb, R. Aaij *et al.*, *Measurement of the b-quark production cross-section in 7 and 13 TeV pp collisions*, Phys. Rev. Lett. **118** (2017), no. 5 052002, arXiv:1612.05140, [Erratum: Phys. Rev. Lett.119,no.16,169901(2017)].